Geology, Alteration, and Mineralisation of the Golpu Porphyry and Wafi Epithermal Deposit, Morobe Province, Papua New Guinea

Marc Rinne
M.Sc.

Submitted in fulfilment of the requirements for the degree of
Doctor of Philosophy

February, 2015

UNIVERSITY
OF TASMANIA

CODES

Declaration of Originality

This thesis contains no material which has been accepted for a degree or diploma by the University or any other institution, except by way of background information and duly acknowledged in the thesis, and to the best of my knowledge and belief, contains no material previously published or written by another person except where due acknowledgement is made in the text of the thesis.

Date:

Signature:

Authority of Access

Copying and communication of any part of this thesis is prohibited until August 2016; following that time, limited copying and communication is permitted in accordance with the Copyright Act 1968.

Abstract

The Golpu porphyry and Wafi epithermal deposit of Papua New Guinea contains contrasting styles of epithermal veins and alteration that overprinted early-formed porphyry-style mineralisation. Golpu is the easternmost and oldest porphyry deposit in a previously unrecognised belt that includes most of the porphyry deposits in the New Guinea Orogen. This metallogenic belt was formed in an orogenic regime that was driven by west-directed, low-angle subduction of an antiformal slab of oceanic lithosphere (the Solomon Sea Plate).

The regional stratigraphy at Golpu comprises Mesozoic metasedimentary rocks of lower to middle greenschist metamorphic facies. These rocks were intruded in the study area by Golpu and Nambonga diorites, which have calc-alkaline to high-K calc-alkaline arc geochemical characteristics. Early porphyry veins and alteration followed emplacement of the Golpu diorites. Porphyry activity culminated in the main stage of Cu-Au mineralisation around 8.67 ± 0.02 Ma, resulting in an unusually high-grade (1 Gt @ 0.90% Cu and 0.63 ppm Au) and vertically elongated (> 1.8 km) orebody. Golpu sulfides define a zonation pattern from chalcopyrite with trace bornite, to chalcopyrite > pyrite, to distal pyrite > chalcopyrite. They also define zonation in sulfur isotopic compositions (e.g., $\delta^{34}S_{sulfides}$ from proximal -0.9 to distal +2.0 ‰).

A maar-diatreme breccia complex was emplaced after the Golpu porphyry mineralisation, followed by the main stage of Wafi epithermal mineralisation and alteration. Zones of pervasive high sulfidation alteration containing quartz, alunite, pyrophyllite, kaolinite, dickite, and diaspore occur above and overprint the Golpu porphyry. These zones contain vein and disseminated pyrite - covellite - chalcocite - tennantite ± enargite ± bornite atop the porphyry, to distal disseminated pyrite - sphalerite ± tennantite. $\delta^{34}S_{alunite}$ values vary from +6.3 ‰, directly above Golpu, to +19.4 ‰, 600 metres west of Golpu.

An arcuate zone of intermediate sulfidation epithermal carbonate - sulfide ± quartz ± adularia veins and montmorillonite - chlorite ± muscovite ± illite alteration occurs along the margins of the high sulfidation domain. Most of the Wafi epithermal gold resource (136 Mt @ 1.70 ppm Au) occurs in the intermediate sulfidation zone nearest the Wafi high sulfidation alteration. The intermediate sulfidation epithermal mineralisation transitions down the north-dipping Compass fault into the Golpu porphyry environment, where sparse veins of tennantite - sphalerite - galena - chalcopyrite are interpreted as the basal component of intermediate sulfidation epithermal veins.

The temporal and spatial configuration of veins and alteration assemblages at Golpu and Wafi indicate that the Golpu porphyry was the causative intrusive complex for both porphyry and epithermal mineralisation. Uplift and exhumation during the life of the porphyry system was driven by low-angle subduction, and resulted in a shift from porphyry to epithermal magmatic-hydrothermal activity over a period of 0.25 to 0.40 m.y..

Acknowledgements

This study was jointly sponsored by Newcrest and Harmony. I am grateful for the rare opportunity to work on the Wafi-Golpu project, and for the considerable logistical support. I thank all the Morobe Mining Joint Ventures staff for their support over the past several years. I am especially thankful to Dave Finn and Stuart Hayward, who ensured that I was well looked after during my field visits. Dave Finn, thank you for responding so helpfully to my many e-mails and requests for information. Additional thanks to Mike Erceg, Simon Shakesby, Doug Menzies, John Holliday, and many others who have helped shape this project.

To my principal supervisor, Dave Cooke, thank you for your guidance, your patience, and your encouraging words in seeing this project to completion. You've given me the chance to see many amazing places during the course of my candidature, for which I am truly grateful. To Anthony Harris, my advisor at Newcrest, thank you for your support; this project would not be the same (let alone exist) without your involvement. To Janina Micko, my co-supervisor during the first part of my candidature, your unwavering kindness continues to amaze. To Nic Jansen, my co-supervisor (and part-time pilot / scuba diver / sea dog / banjo picker), thank you for your edits, your sound advice, and your encouragement.

Modelling the geology and alteration zonation in a volume of rock as huge and diverse as Wafi-Golpu was a daunting task. The resulting model is built on the cumulative efforts of site geologists, past and present, and on the field investigations and interpretations of giants the likes of Richard Sillitoe and Terry Leach. This thesis would simply not have been possible without their work.

This work also benefited from conversations with Bob Loucks, Bruce Gemmell, Jeremy Richards, and others. Several parts of this thesis were completed thanks to the analytical work of Charlotte Allen, Matt Heizler, Rob Creaser, and Stafford McKnight. I am grateful for the assistance of members of staff at CODES and UTas, including but not limited to Sarah Gilbert, Leonid Danyushevsky, Jay Thompson, Sandrin Feig, Karsten Goemann, Garry Davidson, Anya Reading, Ron Berry, Tony Crawford, Katie McGoldrick, Karen Mollross, Rose Pongratz, and Peter Cornish. To Jocelyn McPhie, thank you for your support, especially during the last few months of this process. To Pete Hollings, previously my M.Sc. supervisor in Canada, thank you for your continued encouragment; I am glad to know you as a mentor.

I cannot properly put into words how grateful I am for my friends and family. Evan, Erin, Nic, Steph, Angela E., Dan, Selina, Roisin, Rose, Sam, Vic, and others, thank you for making my time in Tasmania so memorable. You kept me (functionally?) sane with a regimen of harmonised group singing, hockey, ridiculous dancing, sugar shuffle tournaments, and expensive breakfasts.

As always, love and thanks to my parents, Rob and Minelle, and my siblings, Leanne, Eric, and Rochelle. To my wife, Angela, I love you. I could not have done this without you, for a million reasons too cheesy to list here. Thank you for occasionally kicking me outside for some needed fresh air!

Table of Contents

List of Figures

Chapter 1

Chapter 2

Chapter 3

Chapter 4

List of Tables

Chapter 3

Chapter 4

Chapter 5

Chapter 1
Introduction

1.1 Introduction

Porphyry systems, which include both porphyry deposits and their near-surface manifestations such as high sulfidation epithermal deposits and lithocaps (Sillitoe, 2010), are important in at least three general respects. Firstly, they are typically a product of subduction-related processes. Their large sizes, global distribution, and history of formation from the Archean to the present (e.g.: Barley, 1982; Davies and Luhta, 1978; Ayres et al., 1982; Groves et al., 2005) makes them a significant mechanism for heat and volatile transfer from mantle to near-surface above convergent tectonic margins. Secondly, they record evidence for the behaviour of fluids and rock during the magmatic to epithermal transition and across significant temperature, pressure, pH, and Eh gradients (e.g.: Hedenquist et al., 2000; Einaudi et al., 2003). Thirdly and of more practical concern is that they can concentrate copper, gold, silver, molybdenum, tungsten, tin, and other metals in a small volume of mineable rock. Of current global metal inventories, about 3/4 of the copper, 1/2 of the molybdenum, ~ 1/5 of the gold, and most of the rhenium are mined from porphyry deposits (Sillitoe, 2010).

The Wafi-Golpu deposit of Papua New Guinea is a recently discovered giant porphyry Cu-Au system that contains contrasting styles of epithermal veins and alteration, which have overprinted substantial porphyry-style mineralisation. This close spatial and temporal overlap of several mineralisation styles provides an excellent opportunity to investigate genetic links between porphyry and epithermal environments within a larger porphyry system.

1.2 Review of Porphyry-Epithermal Systems

Porphyry deposits are spatially, temporally, and genetically associated with porphyritic intrusions of mostly felsic composition (John et al., 2010). They occur in clusters along convergent plate settings when and where mantle-derived oxidised and sulfur-undersaturated magmas are produced, but they do not erupt to surface (Wilkinson, 2013). Instead, magmas intrude to depths of a few kilometres below the surface, and volatile exsolution creates magmatic brine and vapour (Roedder, 1971; Henley and McNabb, 1978; Hedenquist and Lowenstern, 1994). The exsolution of volatiles from the magma causes an increase in hydrostatic pressure. Once this pressure exceeds the lithostatic pressure (+ tensile strength of the rock), the host rock fails, allowing for the violent escape of magmatic fluids through fractures (Burnham, 1979). These fractures, propagated by the catastrophic brittle failure of the wallrock, develop mostly above and around the upper edges of the intrusions, and they are the focus of magmatic-hydrothermal alteration and associated mineralisation in most porphyry deposits (e.g., Brimhall, 1977). The pressure release and volatile loss that occurs during rock failure also results in the crystallisation of groundmass in the causative intrusion, producing a porphyritic texture (Burnham, 1967).

Porphyry deposits form in environments that also produce (or require) uplift, so that recently-formed porphyry deposits are more common at higher elevations (Fig. 1.1). Although porphyry deposits have been forming since the Archean (Ayres et al., 1982; Groves et al., 2005), their occurrence in the upper crust of convergent settings – zones of uplift and erosion – results in a strong preservation bias: about half of the known

porphyry copper deposits are younger than 59 Ma (Fig. 1.1; Singer et al., 2008). Even the most conservative estimate for erosion rates in arid regions outside of orogenic belts (red line in Fig. 1.1 B) would result in the loss of deposits older than 60 Ma without post-mineralisation burial.

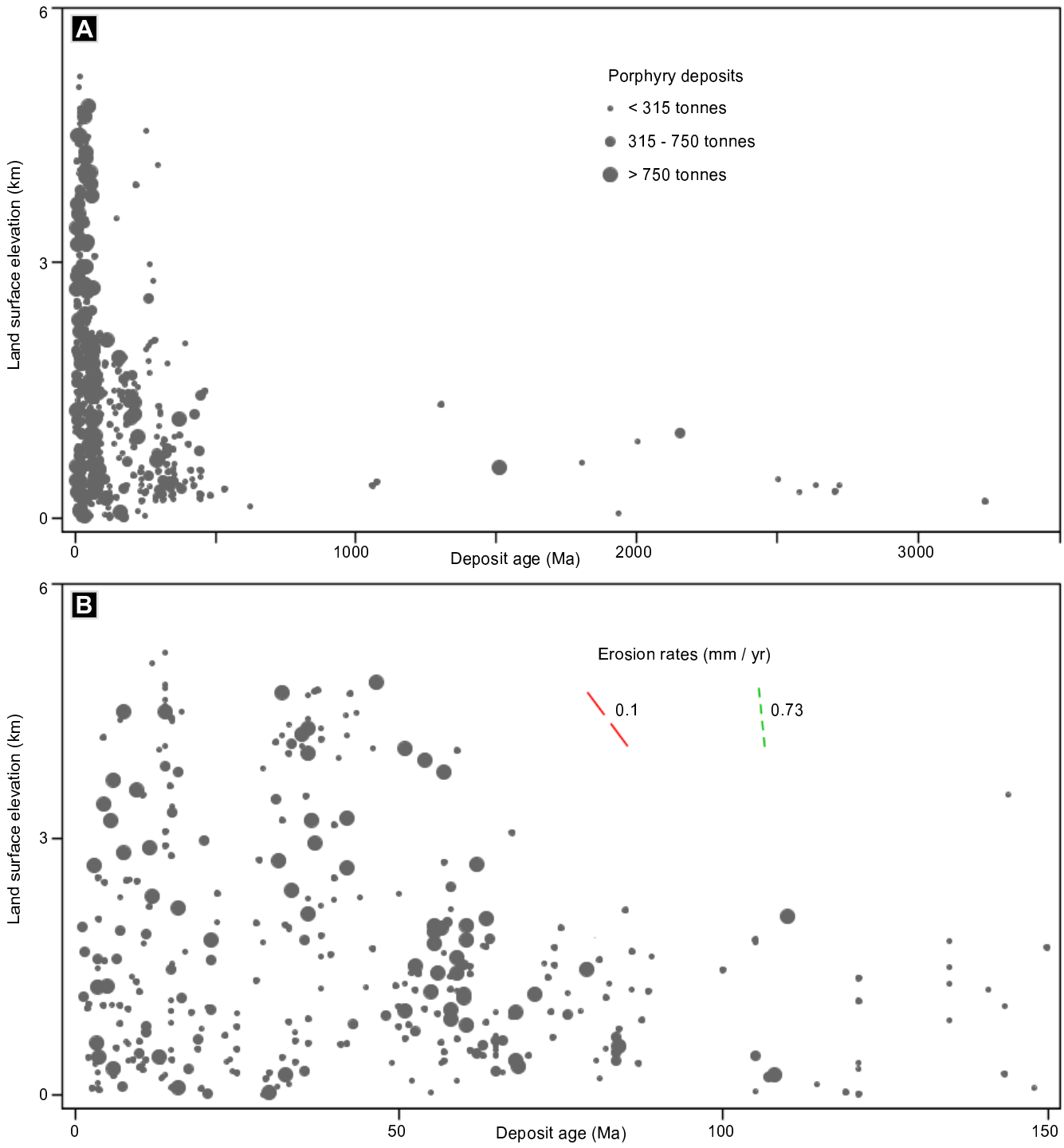

Figure 1.1: Current land elevation at porphyry deposit coordinates versus age, for (A) all deposits with known age and (B) deposits 150 Ma and younger. The elevation of the centre of any given ore deposit may be above (in the case of partially exhumed deposits) or below the current land surface, but a correlation with uplifted environments is nonetheless indicated. Erosion rates shown in B are from Montgomery and Brandon (2002), with slopes indicating the slowest rate measured in regions outside of tectonically active areas (0.1 mm/yr) and a rate typical for orogenic belts (0.73 mm/yr). Elevations used are from NASA SRTM3 topography data, corresponding to the coordinates of 612 porphyry deposits in Singer et al. (2005).

Epithermal deposits comprise veins and altered rocks in the uppermost kilometre of active volcanic-hydrothermal environments. Although they are not exclusively porphyry-related, many epithermal deposits or occurrences have a clear spatial and genetic association with underlying porphyry systems. Some documented examples indicate that porphyry and overlying epithermal systems share not only the same regional tectonic and structural controls, but also the same magmatic heat and (to some extent) fluid source (e.g., the Lepanto epithermal and Far South East porphyry deposits; Arribas, 1995; Hedenquist et al., 1998; Sillitoe and Hedenquist, 2003).

High sulfidation (alunite - kaolinite) epithermal deposits are formed by the ascent of acidic magmatic fluids (± some mixing with oxidising meteoric waters), and contain mostly disseminated ore and pervasive to texturally selective acid leaching in upward-flaring zones (White, 1991; Arribas, 1995). As for advanced argillic alteration in general, a strong structural control in high sulfidation systems typically results in alteration zones that overprint underlying porphyry-related potassic, sericitic, or propylitic alteration (John et al., 2010). Intermediate and low sulfidation (adularia - sericite ± quartz - carbonate) deposits may form by the interaction of fluids with wallrock in similar porphyry-related environments, but – unlike the acid-stable high sulfidation systems – they are vein-dominated and involve near-neutral-pH fluids (Hedenquist et al., 2000). Intermediate sulfidation vein systems have higher sulfide contents, higher silver contents, higher fluid salinities, and lower gold contents than low sulfidation systems (Hedenquist et al., 2000). Transitions from high sulfidation (acid-stable) to intermediate sulfidation (neutral-pH stable) alteration and vein systems have been documented in the shallow portions of some porphyry-epithermal systems (i.e., carbonate - sulfide veins at the edges of lithocaps; Sillitoe, 2010).

Porphyry-epithermal deposits are characterised by an upward and outward kilometre-scale zonal arrangement of veins and alteration assemblages. This zoning is largely a result of the mass and heat transfer from their associated porphyry intrusions into the surrounding environment. Key processes in deposit formation involve (1) the separation of magmatic fluid into magmatic brine and low density vapour (associated with porphyry mineralisation + potassic, sericitic, and propylitic veins and alteration), followed by (2) interactions of the low density vapour component with overlying and laterally adjacent wallrock and water (resulting in epithermal veins and alteration; Hedenquist et al., 2000). John et al. (2010) summarised these processes as follows:

1) Dense, high-temperature magmatic brines add K, SiO_2, CO_2, H, and S to wallrock nearest the intrusions (i.e., potassic alteration and porphyry mineralisation).
2) Moving away from the intrusion, magmatic brines are of lower temperature and lower K^+ / Na^+ or K^+ / H^+ ratios. They add H^+, K^+, S^{2-}, and SiO_2 (sericitic alteration) to more distal O_2, CO_2, S^{2-}, and H^+ (propylitic alteration, with possible input from ambient fluid in host rock).
3) Later lower density and temperature fluids with higher H^+ / K^+ ratios result in addition of H^+ and S^{2-} (and loss of K^+, Na^+, Ca^{2+}) in upward-flaring zones that may cross-cut earlier stages (late sericitic to intermediate argillic alteration).
4) Moving towards surface, the more buoyant magmatic vapour component may condense to H_2SO_4-bearing fluids of very low pH, leaving intensely acid-altered rocks with residual quartz (e.g., Stoffregen, 1987; Sillitoe, 1995; Cooke and Simmons, 2000). These structurally controlled fluids may also migrate laterally over long distances to produce a wide lithocap. High S contents in this same acidic fluid may

also result in high sulfidation veins and alteration with alunite, pyrite, covellite, digenite, tennantite, enargite, or bornite (Hedenquist et al., 2000). The addition of significant gold during this stage may require continued separation of magmatic vapour and brine at gradually increasing pressures, which would occur during cooling of the underlying intrusion (Heinrich et al., 2004).

5) Depending on the hydrogeology, fault architecture, or general seismicity of the shallow environment, fluids from steps (3) or (4) may cool, boil, or mix with more oxidising and lower salinity meteoric water to result in low to intermediate sulfidation vein systems. Transitions from hot and / or acidic fluids to cool and / or near-neutral pH fluids may also occur by water-rock interaction alone, which is strongly dependent on rock types and water : rock ratios (e.g., Hedenquist et al., 1994).

1.3 Study Objectives

This thesis investigates the characteristics and genesis of the Golpu and Wafi deposits, including the timing of hydrothermal systems involved, and the spatial relationships between the shallow epithermal and deeper porphyry-related domains of veins and alteration. A genetic model is produced to describe the tectonic triggers to Golpu and similar-age porphyry deposits in New Guinea. Several exploration vectors towards porphyry and high sulfidation mineralised centers are also identified as an outcome of this research.

1.4 Thesis Organisation

This thesis is structured as follows:

Chapter Two (regional geology) contains a review of the tectonic history and metallogeny of the Papua New Guinea region. The regional geology, structure, and seismicity of the area are integrated in a new tectonic-metallogenic model for Golpu and other porphyry deposits of the New Guinea Orogen. This work establishes the regional context for Chapter Three, which documents the deposit scale geology of Wafi-Golpu.

The host lithostratigraphy to the Golpu and Wafi deposits is described in Chapter Three using core logs completed by the author and site geologists, together with geochemical data and structural interpretations. Some previously unrecognised elements, including sedimentary packages and fault zones, are proposed based on relationships observed in the existing database. Least-altered geochemistry and mineralogy is defined in each of the lithological units identified, and an interpretation of the host rock geometry is presented in plan and cross sections as a basis for comparison to alteration chemistry and mineralogy in later chapters. Possible contradictions or ambiguities in the previous interpretation of some features, including fault orientations and the genetic interpretations of certain rock units, are discussed.

Chapter Four (alteration and mineralisation) presents most of the field and laboratory work completed during the course of this study. It documents the vein and alteration events of the Golpu and Wafi deposits, described in interpreted order of their formation. Alteration section diagrams are presented in terms of mineral assemblages compiled using quantitative XRD, visible and IR spectra, petrographic and scanning electron microscopy, and LA-ICPMS data collected during the course of this work. Comparisons of the paragenetic sequence, scale, and zoning relationships of the vein and alteration assemblages at Golpu and Wafi are made to those documented in other porphyry and epithermal deposits.

Chapter Five (geochronology and geochemistry of alteration and mineralisation) documents the absolute timing and geochemistry of Golpu and Wafi vein and alteration events. Microprobe U-Pb, Re-Os, and Ar-Ar geochronological results are presented to further constrain the paragenesis described in Chapter Four, tracing the development of Golpu and Wafi from porphyry intrusion to epithermal events. Alteration geochemistry is further explored with respect to mass balance changes, sulfur isotopic compositions, and gold deportment in the porphyry and epithermal mineral assemblages.

The data and arguments presented in the earlier chapters are considered in Chapter Six (genetic model and conclusions) in order to: 1) provide a genetic model for Golpu and Wafi, emphasising that Golpu formed in an unusual low-angle subduction environment; 2) summarise the evidence for the spatial, temporal, and genetic links between the Golpu porphyry and Wafi epithermal environments; and 3) highlight the most informative vectors to porphyry and epithermal centers, including some applicable in barren lithocap environments. This synopsis is followed by a discussion of the implications of this study, and proposals of future work that may be of value. Detailed petrographic descriptions (Appendix A), core logs (Appendix B), lithotype and assay modelling methods (Appendix C), modal abundance and core photography methods (Appendix D), X-ray diffraction results (Appendix E), and SWIR mineral identification results (Appendix F) are also provided. Geochemical data including radiogenic isotopic results, XRD traces, and SWIR spectra are provided as digital appendices.

1.5 Previous Work

The Golpu and Wafi deposits have been the subject of many studies, most notably: a M.Sc. thesis at the University of Western Australia (Tau-Loi, 1996); AusIMM conference presentations and abstracts (Leach and Erceg, 1990; Erceg et al., 1991; Corbett, 1994); and reviews in several deposit syntheses (e.g., Corbett and Leach,1998; Sillitoe, 1999; Sillitoe, 2010). This thesis also makes use of previous work not available in the public domain, particularly the MMJV drill hole database and a series of reports on petrographic and XRD data collected by Terry Leach and associates from 1989-1996. Their original data cannot be reproduced in the appendices, but the sources of data are noted wherever used.

1.6 Location and Access

The Wafi-Golpu system is located in the Morobe Province of New Guinea, about 65 km WSW of the port city of Lae (Fig. 1.2 A). Access by road is from Lae via Timini, when local conditions allow, or by helicopter. The Wafi field office is located at 6° 53’ S and 146° 27’ E, at an elevation of about 410 m.

1.7 Exploration History

Although alluvial gold was reported in the Wafi River around 1930, it was not until 1977 – ten years following the discovery of the Wamum porphyry prospect northwest of Wafi – that CRA workers discovered gold-bearing pyritic rock in the Wafi River, including one sample with 22g/t Au (Shedden, 1979). CRA continued exploration near the Wafi River by stream, soil, and ridge sampling, to eventually define part of the

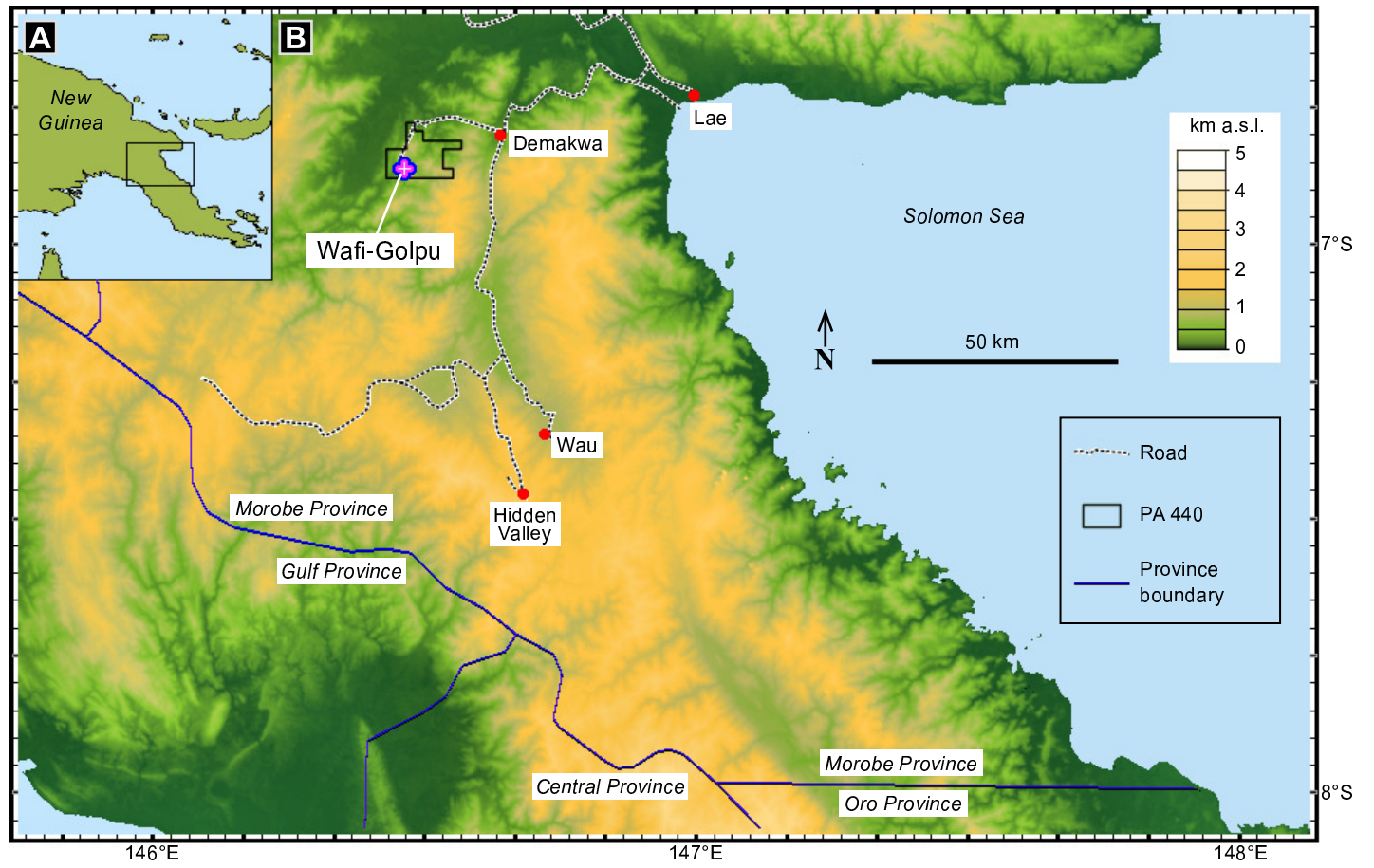

Figure 1.2: Map showing the location of the Wafi-Golpu project. A) Area of map B is outlined. B) Wafi-Golpu is located in Prospecting Authority 440 (PA 440, outlined), approximately 65 km WSW of Lae and 65 km NNW of the Hidden Valley mine. C) View from Wafi Hill, looking SW to the Watut River valley (distant background at right side of photo).

Wafi high sulfidation deposit in 1980 (Curtis and Ryan, 1997). About 8.5 km of core was then drilled from 1983 to 1986 in the Wafi area, leading to mine feasibility studies on the Wafi deposit in 1990 under then-joint venture partners Elders Mining PNG (Erceg et al., 1991). Richard Sillitoe, consulting for CRA in 1990, was the first worker to suggest that a unit previously described as conglomerate was a diatreme breccia pipe (Erceg, 2008).

Also in 1990, Terry Leach, Greg Corbett, and Mike Erceg together recognised a zonation from propylitic to advanced argillic alteration assemblages in the Wafi lithocap, based largely on mineralogy determined by X-ray diffraction. They developed an alteration model predicting a high temperature upflow zone directly overlying the then-unknown Golpu porphyry stocks (Corbett and Leach, 1998). Erceg (2008) highlights the role that Terry Leach played in the recognition of Wafi as a zoned high sulfidation deposit, including this anecdote:

> *Terry flew to site. I pulled out the XRD map. Terry pulled out a box of colouring pencils (a good geologist is never without his colouring pencils!) and within 20 minutes had contoured the XRD data into the zoned alteration map, had recognised the system as a high sulfidation system, and had modelled a hot acid magmatic fluid upflow zone ...* (Erceg, 2008)

The drilling program that was undertaken in 1990, the last year of the CRA-Elders joint venture, was partly aimed to test this upflow zone (Curtis and Ryan, 1997; Erceg, 2008). This led to the first intersection of significant high sulfidation Cu mineralisation overprinting porphyritic diorite (Golpu) in 1990. At the time, this portion of the high sulfidation deposit was named Rafferty's Copper Zone – after the captain of a WWII Superfortress wreck near Wafi site (Erceg, 2008). The strongly quartz- and alunite-altered Golpu diorite was not targeted for further drill definition at depth.

CRA continued to define the Rafferty's copper deposit from 1990 to 1995, at which time Wafi-Golpu was recognised as a high sulfidation and porphyry system (Tau-Loi, 1996). In 1996, CRA intersected the first interval recognised as intermediate sulfidation style Wafi mineralisation; at this point, Wafi-Golpu was deemed a high sulfidation deposit with some intermediate to low sulfidation characteristics, and a minor porphyry component near surface. The deeper and higher grade portions of the Golpu resource remained largely untested for nearly a decade. By 2003, then-owners Abelle Limited had defined the Golpu porphyry resource to 100 million tonnes at 1.3 % copper and 0.6 g/t gold (Harmony annual report, 2003), or about a tenth of its current size.

Harmony acquired Abelle and the Wafi-Golpu project in 2003, and drilled the first deep and high grade intersections of Golpu porphyry below the high sulfidation overprint. Since 2005, drilling has been concentrated mostly on the Golpu porphyry copper-gold component. In 2008, Harmony entered into a 50:50 joint venture with Newcrest, forming Morobe Mining Joint Ventures. To date, over 190 kilometres of core have been drilled in 490 holes, and deep drill definition has drastically increased the total Golpu resource estimate to 1 billion tonnes at 0.63 ppm Au, 0.90 % Cu, and 1.1 ppm Ag, to a total estimated 12.4 million ounces of gold and 5.4 million tonnes of copper (Newcrest Mining Ltd. reserve announcement, December 2012). The Wafi-Golpu deposit therefore figures among the largest Cu-Au porphyry deposits of the SW Pacific, similar to Ok Tedi or Panguna in terms of total metal endowment (e.g,. Cooke et al., 2005), with copper and gold grades approaching those of the giant Grasberg deposit (Pollard et al., 2005).

Chapter 2
Regional Geology

2.1 Introduction

This chapter reviews the regional geology of Papua New Guinea from the perspective of key factors in the formation, character, and preservation of the Wafi-Golpu system. The tectonic model presented here establishes the regional framework for a deposit genetic model, and is applicable to other porphyry deposits in the New Guinea Orogen.

The growth of Papua New Guinea by oblique subduction-accretion of island arc and oceanic plateau terranes against a continental nucleus presents nearly the full suite of processes and tectonic elements involved in the growth of continents, with convergence and uplift rates among the fastest measured on Earth (Dewey and Bird, 1970; Tregoning et al., 2000). This has resulted in several generations of calc-alkaline Cu-Au (±Mo) and alkaline Cu-Au porphyry and epithermal deposits.

2.2 Tectonic History and District Metallogeny

Papua New Guinea is located along the western Pacific Rim, a zone of active subduction with associated seismicity and volcanism that extends south through Fiji and New Zealand and north to the Philippines and Japan (Fig. 2.1). The country is on the northern margin of the Indo-Australian Plate, sharing the same basement rock units as in Australia, namely the Owen-Stanley metamorphic complex (Williamson and Hancock, 2005).

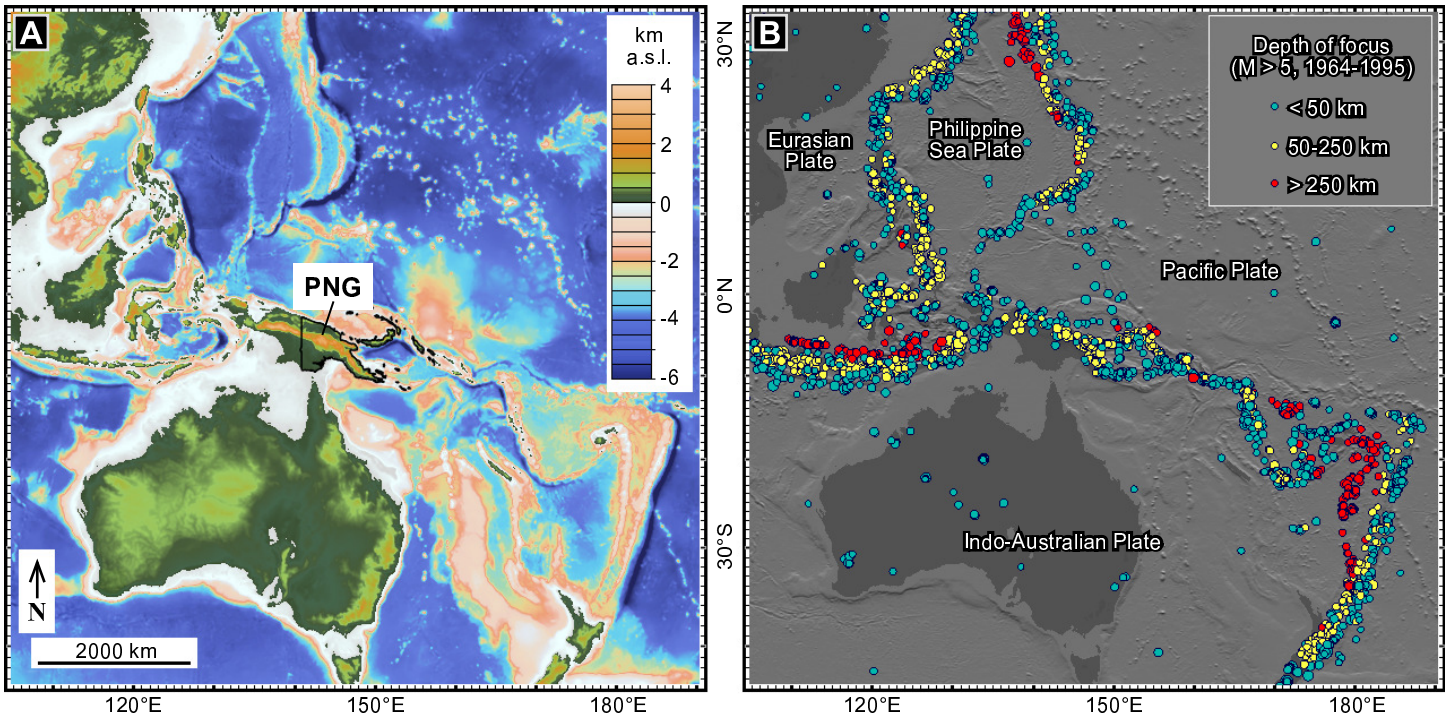

Figure 2.1: A) Map showing the location of Papua New Guinea (PNG) along the west Pacific Rim, which can be broadly traced by the belts of seismic and volcanic activity. B) Seismic data show northward subduction of the Indo-Australian Plate and mostly westward subduction of the Pacific Plate. This figure was produced with GeoMapApp (geomapapp.org) with topography data from Ryan et al. (2009). Seismic data are from the International Seismological Centre (2009) and Engdahl and Villaseñor (2002).

Tectonic history

The PNG region is a mosaic of tectonic elements that accommodate westward movement of the Pacific Plate (currently at 78 mm/yr) and northward movement of the Indo-Australian Plate (60 mm/yr; Corbett, 2005). Figures 2.2 and 2.3 provide a summary of the tectonic development and associated metallogenic belts of the region from 70 Ma to present. Numbered elements in these figures are discussed in the text. The tectonic development of PNG has been taking place within a zone of interaction between relatively westward- and northward-migrating plates since about the Cretaceous (Loffler, 1977), although the locations and numbers of plate boundaries have changed over time.

Proto-continental New Guinea partially separated from the northern part of the Australian continent during the Paleocene opening of the Coral Sea basin around 60 Ma (Fig. 2.2 D **- 1**). This rifting was halted in the Eocene (~ 40 Ma) by the northward migration of the Indo-Australian Plate (Kearey et al., 2009). The Owen Stanley rocks that host the Golpu deposit were probably in place near the proto-continental New Guinea margin by 70 Ma. Alternatively, they were deposited on adjacent continental shelf and accreted during obduction of the Papuan Ophiolite at 58.3 ± 0.4 Ma (Lus et al., 2004).

A north-dipping subduction zone was initiated during the Eocene to the north of the New Guinea proto-continent, producing the Sepik Arc (Fig. 2.2 F **- 2**). This arc was accreted to New Guinea from the Late Eocene through the Oligocene (the Sepik Event). It caused an early stage of uplift and regional metamorphism to the south − the New Guinea Orogen − and terminated volcanism along the Sepik Arc at around 22 Ma (Findlay et al., 1997).

In the Late Eocene, southwest-dipping subduction along the Kilinailau-Manus Trench began far north of the mainland (Fig. 2.2 F **- 3**). Oligocene to Miocene arc magmatism related to the Kilinailau subduction formed most of the New Guinea and Solomon Islands (Fig. 2.2 F **- 4**).

The Ontong Java Plateau is a plume-derived Cretaceous oceanic plateau sequence that is 60 million cubic kilometres in volume (Gladczenko et al., 1997; Mahoney et al., 1993). It is the largest of Earth's large igneous provinces and is estimated to have reached the Kilinailau subduction zone around 22 - 20 Ma (Fig. 2.2 H **- 5**; Bruns et al., 1989). This resulted in southeast to northwest closure of subduction along the Kilinailau Trench, as well as uplift, erosion, and an end to arc volcanism in the New Guinea Islands.

Subduction along the Trobriand-Wewak Trench initiated around 20 Ma in response to the plateau-triggered closure of Kilinailau subduction (Fig. 2.3 B **- 6**; Hall, 1997). This southward dipping Trobriand-Wewak subduction zone resulted in the Maramuni Arc (Fig. 2.3 B - line of black circles labeled **7**), during an episode of continental arc magmatism which was most active from 17 - 10 Ma (Knesel et al., 2008; Findlay et al., 1997).

Golpu intruded around 8.8 Ma (Chapter Three), possibly as part of the Maramuni magmatic arc generated by southward Trobriand-Wewak subduction, but after southward subduction. It may be better described as a post-Maramuni porphyry deposit (section 2.5).

Several significant changes to the tectonic configuration and regional stress field occurred between 15 and 4 Ma. Until this point, uplift in the New Guinea Orogen occurred mostly along orogen-parallel (ESE-trending) thrust faults and fold axial planes. East to west closure of the Trobriand trench started around 15 - 12 Ma (Hill and Raza, 1999), replaced by northward-directed subduction along the New Britain Trench

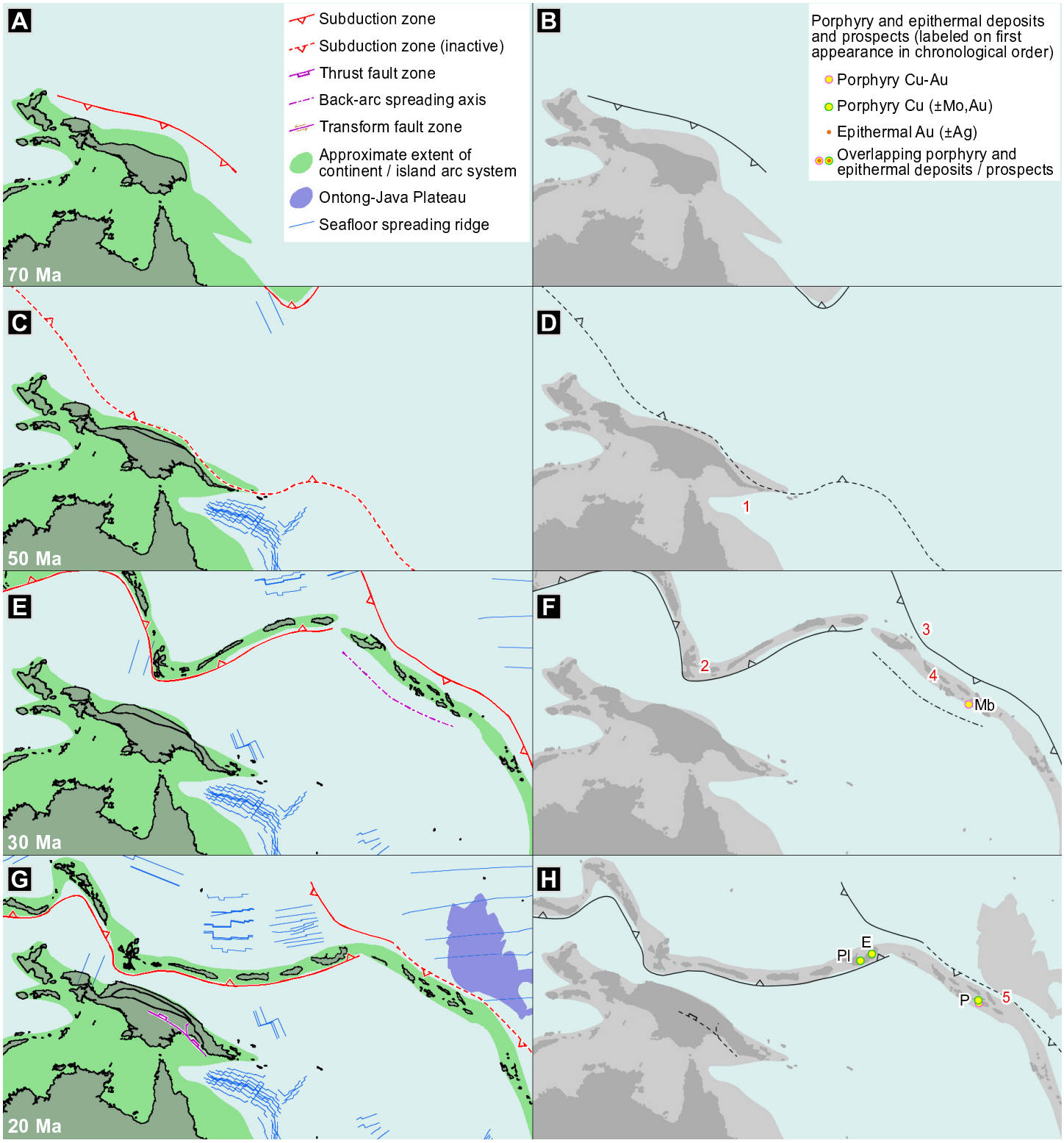

Figure 2.2: Tectonic development of the PNG region from 70 to 20 Ma. Ages are indicated in the left column (bottom left of each frame). The right column (panels B, D, F, and H) shows the appearance of porphyry and epithermal deposits, with deposit ages mostly from Singer et al. (2008). Red numbers refer to elements or events discussed in the text. Plate and spreading ridge locations and rotations are based on GPlates software (as in Boyden et al., 2011), with some adjustments after Hall (2002). Deposit name abbreviations are: (in panel F) Mb - Mbetilonga; (panel H) E - Esis, P - Poha, Pl - Plesyumi.

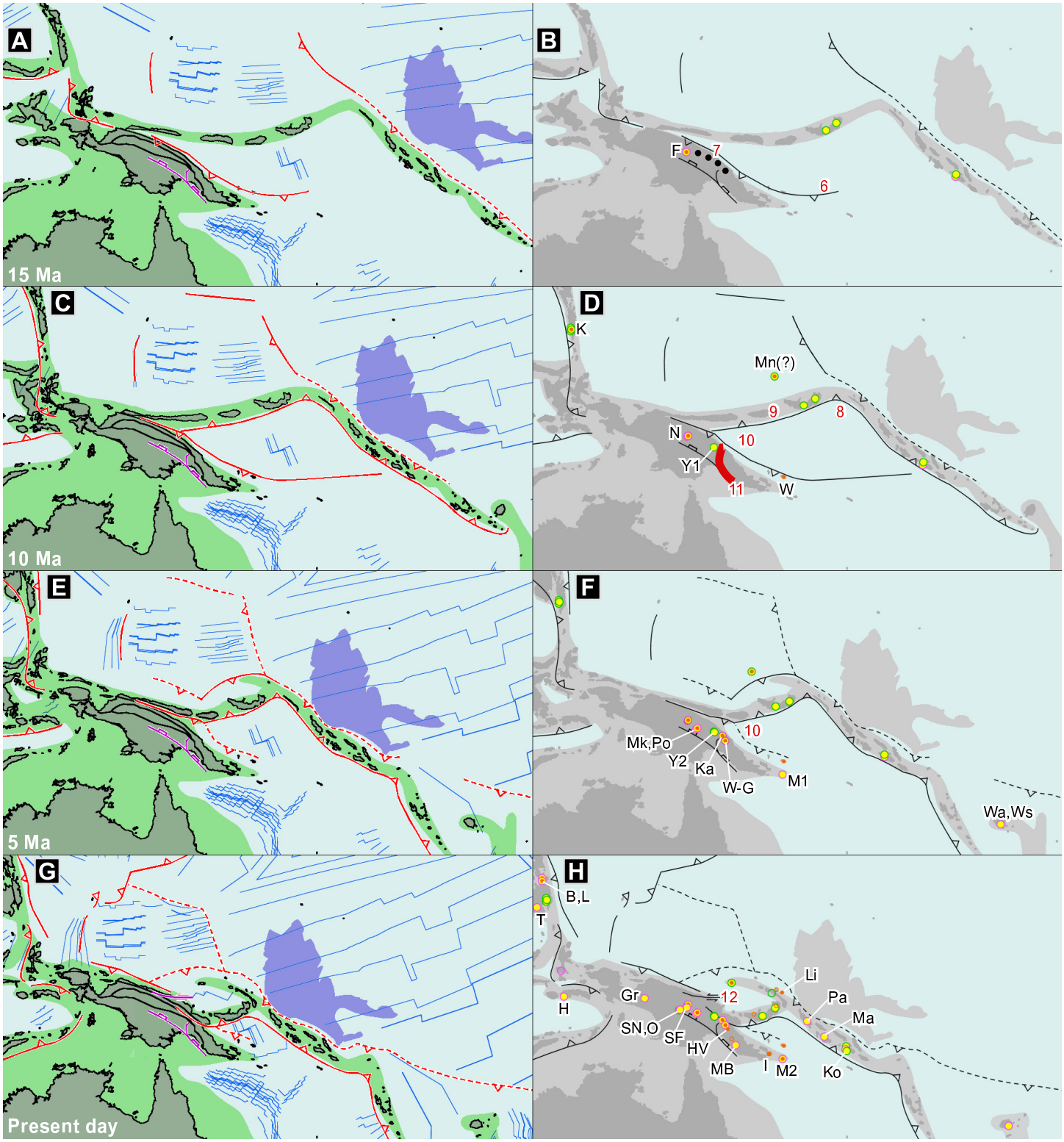

Figure 2.3: Tectonic development of the PNG region from 15 Ma to present day. The legend is the same as in Figure 2.2. The right column shows the appearance of porphyry and epithermal deposits, using ages mostly from Singer et al. (2008). Red numbers refer to elements or events discussed in the text. Plate and spreading ridge locations and rotations are based on GPlates software (as in Boyden et al., 2011), with some adjustments after Hall (2002). Deposit name abbreviations are: (in panel B) F - Frieda; (panel D) Mn - Manus Island prospects, N - Nena, Y1 - Early Yandera, W - Woodlark, K - Kingking and adjacent; (panel F) Ka - Kainantu, W-G - Wafi-Golpu, M1 - Misima, MK - Mt Kare, Po - Porgera, Wa - Wainaulo, Ws - Waisoi; (panel H) HV - Hidden Valley, MB - Mt. Bini / Kodu / Ofi, SF - Star Mt Futik, H - Hila, SN - Star Mt Nong River, Ma - Mase, B - Boyongan, L - Luna-Asiga, Pa - Panguna, Gr - Grasberg, M2 - Umuna, I - Imwauna, Ko - Koloula, O - Ok Tedi, Li - Lihir, T - Tampakan.

(Fig. 2.3 D - **8**), where it continues to the present day. This reversal in subduction direction occurred during the docking of the Melanesian Arc with New Guinea (Fig. 2.3 D - **9**), effectively turning the Solomon Sea Plate into a westward-migrating wedge with both north- and south-dipping subducted margins (Fig. 2.3 D,F - **10**; as identified by Ripper, 1982). Relative westward motion of this plate into New Guinea resulted in an E-W oriented stress field and the start of significant uplift by E-dipping thrusts in the Aure Deformation Zone (Fig. 2.3 D - red line labeled **11**; Buddin,1993).

The most active period of uplift in the New Guinea Orogen occurred from 12 to 4 Ma (Hill and Raza, 1999). This was most pronounced in the Aure Deformation Zone, with structures consistent with an E-W oriented stress field: mostly N-trending and E-dipping thrust faults and subhorizontal fold axial planes, as well as possible NNW-trending extensional faults (Williamson and Hancock, 2005). Golpu diorites intruded around this time (Chapter Three).

Post-Golpu tectonic history

Uplift of up to 4.5 km is estimated to have occurred in the New Guinea Orogen between 8 and 5 Ma (Crowhurst et al., 1996), with erosion of ~ 3 km exposing many of the Maramuni (and later) intrusions and mineralisation, including the Wafi-Golpu deposit. Following the most pronounced episode of uplift and erosion through the Central Range from 8 to 4 Ma (Sapiie et al., 1999), oblique subduction along the north coast of New Guinea has shifted to mostly sinistral strike-slip motion at a current rate of about 11 cm per year. Most of this motion is now accommodated along the Bewani-Torricelli Fault Zone (Fig. 2.3 H - **12**), and a smaller perpendicular vector component is accommodated by thrust faulting along the shallow N-dipping Ramu-Markham fault zone (south of **12** in Fig. 2.3 H; Cloos et al., 2005).

Offshore, the opening of the Woodlark Basin at 6 Ma and the Manus Basin at 3.5 Ma separated the New Guinea Islands, producing their present-day configuration (Taylor et al., 1999; Hall, 2002; Williamson and Hancock, 2005). These back-arc volcanic centres, along with arc volcanism related to subduction along the New Britain Trench, contribute the bulk of current volcanic activity in Papua New Guinea.

2.3 Regional Geology

Papua New Guinea has been divided into several mostly WNW-trending lithotectonic domains (Fig. 2.4) on the basis of rock types and ages, locations of thrust faults, and topography (Williamson and Hancock, 2005). The Fly Platform is a mostly flat-lying and undeformed sequence of Triassic to Tertiary marine sedimentary rocks and Quaternary volcanic and volcaniclastic rocks overlying the Australian Craton. The Papuan Fold Belt consists of folded and thrust-faulted equivalents of the Fly Platform rocks. These are overlain by Quaternary stratovolcanoes, and are host to several exposed Miocene to Pleistocene intrusions and associated porphyry deposits (e.g., Porgera, Ok Tedi; Williamson and Hancock, 2005; Fig. 2.3 F,H).

The New Guinea Thrust Belt consists of several stacked thrust sheets derived from the Fly Platform and Papuan Fold Belt, and is also host to some porphyry mineralisation (e.g., Frieda, Nena; Fig. 2.3 B,D). The Eastern Fold Belt, the eastern extension of the New Guinea Orogen, is extensively faulted along its western margin in the Aure Deformation Zone (Fig. 2.4). The Owen Stanley Thrust Belt comprises the Owen Stanley

metamorphic complex (Cretaceous metasedimentary rocks), along with the Papuan Ultramafic Belt, which has been thrust atop the younger Eastern Fold Belt via the Bogoro Thrust (Williamson and Hancock, 2005).

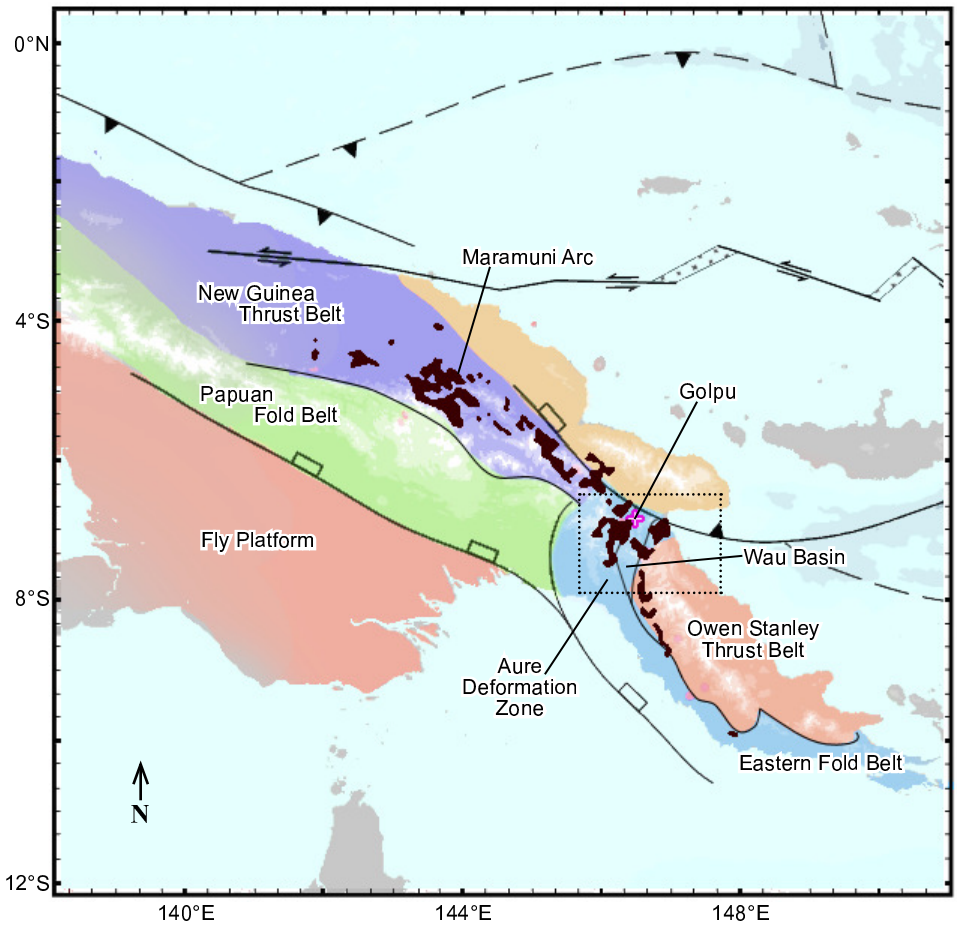

Figure 2.4: Lithotectonic domains of New Guinea on the basis of rock types and ages, locations of thrust faults, and topography (Williamson and Hancock, 2005, with structures from Buddin, 1993). Maramuni Arc intrusions (labeled) are from Cloos et al. (2005). Golpu is located in the Wau basin, along the eastern part of the N-S Aure Deformation Zone. The box shows the location of regional geology and structure maps of the Markham area (Figs. 2.5 and 2.6).

The Markham area of NE New Guinea (outlined in Fig. 2.4) includes the Wau Basin, which occurs along the eastern part of the Aure Deformation Zone. The Markham area consists of Australian cratonic basement of Mesozoic age (Owen Stanley rocks) overthrust by an ophiolite suite around 60 Ma (Fig. 2.5). These rocks were folded in a N-S oriented stress field and metamorphosed during the Sepik subduction-accretion event (~ 40 Ma). Low-lying regions were filled by sediments with variable volcanic input around 30 - 10 Ma (Omaura and Langimar units), parts of which contain submarine shelf facies limestone. These rocks were then faulted and folded by an E-W oriented stress field during development of the Aure Deformation Zone, mostly from 12 - 4 Ma, and mostly along the Wau Basin in central and western parts the Markham Area (Figs. 2.5 and 2.6). The region was then intruded by Maramuni continental arc magmas (Morobe granodiorite).

Units younger than Morobe granodiorite make up only a small part of the map area (Fig. 2.5). These rocks were deposited by shallow water sedimentation with some volcanic input (Otibanda and Babwaf units). They are cut by late intermediate to felsic intrusions and overlain by volcanic products (Edie porphyry and Bulolo volcanic rocks) that are associated with epithermal deposits of the Morobe Goldfield (Nelson et al., 1990).

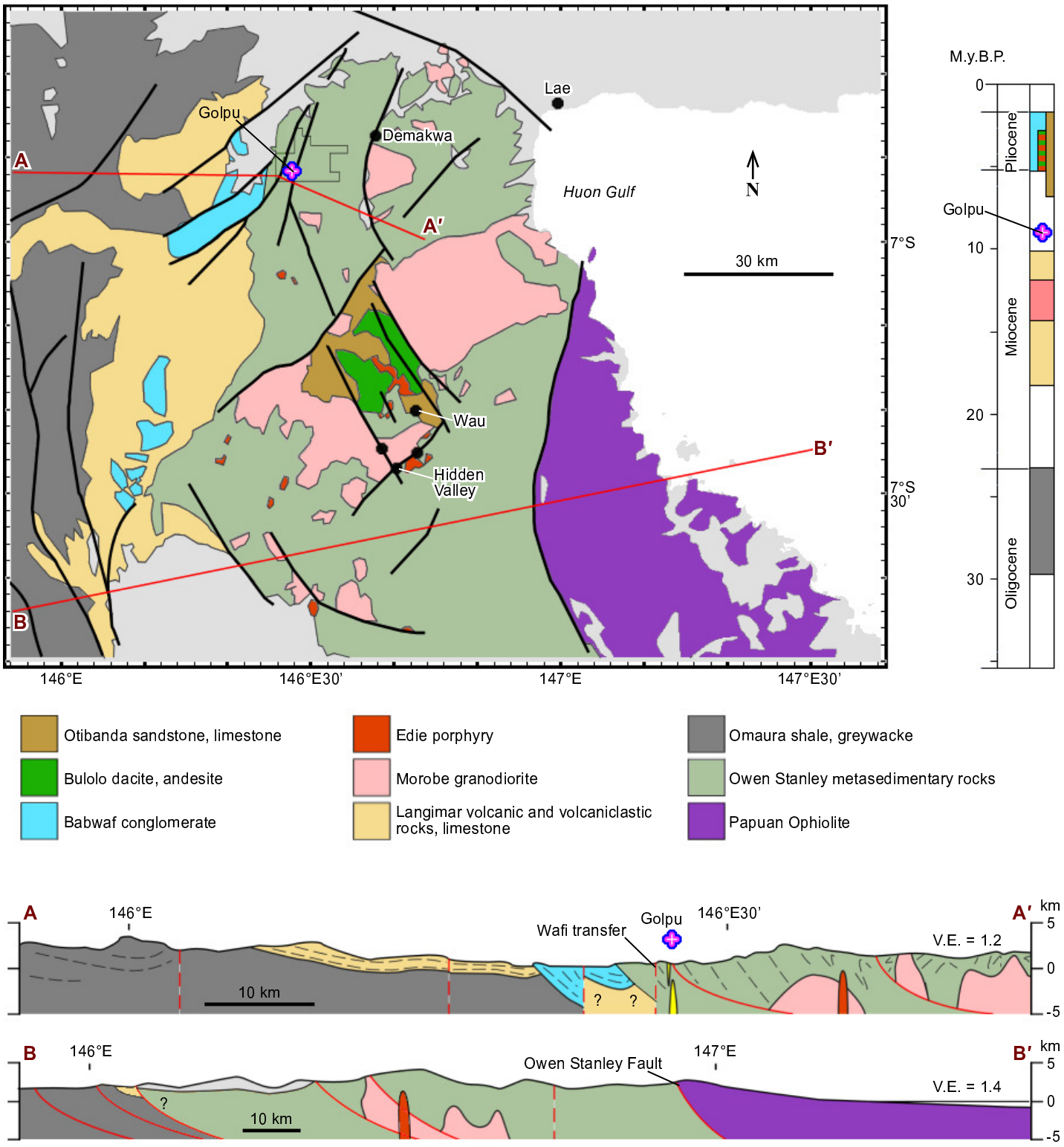

Figure 2.5: Geological map and sections of the Markham area. Approximate ages of units shown are indicated on the stratigraphic column (at right), except for the Owen Stanley metasedimentary rocks (Jurassic to Cretaceous age) and the Papuan Ophiolite, which formed ca. 71 - 65 Ma, before its emplacement at 58.3 ± 0.4 Ma (Lus et al., 2004). Geology compiled from Dow (1977), Tingey and Grainger (1976), Grainger (1970), Erceg et al. (1991), and Leach and Erceg (1991), with fault traces based on interpretations by Corbett (1990). Section A is modified from Grainger and Pillinger (1972; their section A-D) and section B is modified from D'Addario et al. (1974; their section F-G).

The Papuan Ophiolite (Fig. 2.5) is a layered series of up to 8 km of ultramafic rock (harzburgites and pyroxenites, locally cumulate) overlain by 4 km of gabbro and an upper 4 km of basalt with some sheeted dyke outcrops (Davies and Smith, 1971; Davies, 2012). The oceanic basalt crystallised between 71 and 65 Ma, and was thrust atop the Owen Stanley rocks at 58.3 ± 0.4 Ma (Lus et al., 2004; Davies, 2012).

The Owen Stanley metasedimentary rocks (Fig. 2.5) are host to most of the Wafi-Golpu deposit. In order of abundance, these are interbedded metasiltstones, metasandstones, and clast-supported metaconglomerates, which occur in beds that are centimetres to tens of metres thick (Tau-Loi and Andrew, 1998). Detrital zircons of 120 - 107 Ma (Kopi et al., 2000) and rounded gabbroic clasts (Erceg et al., 1991) reflect partly igneous source rocks during sedimentation on the passive northern margin of PNG. Most of the metaconglomerate clasts have been slightly elongated parallel to the regional planar metamorphic fabric, which is generally north-trending and dipping 40 - 60° E to SE. Apart from the amphibolite facies zone adjacent to the Papuan Ophiolite, these rocks have undergone regional greenschist facies metamorphism, resulting in a typical assemblage of actinolite - albite - chlorite - quartz, with a weak planar fabric evident in hand sample (Erceg et al., 1991). Lower to middle greenschist facies is generally reported (e.g., Davies, 2012), consistent with the mineral assemblage in least-altered samples in this study (Chapter Three). Most metamorphism is of late Cretaceous age, with a later Eocene event around 44 - 32 Ma (Davies and Williamson, 2001).

The Omaura shale and greywacke are located in the western part of the Markham area (Fig. 2.5). They contain reef facies limestone and are interpreted by Tingey and Grainger (1976) to have accumulated into low-lying parts of the Aure Deformation Zone around 25 Ma. These rocks were then extensively folded and faulted, and overthrust by the older Owen Stanley rocks.

The Langimar Beds consist of volcaniclastic pebble to cobble conglomerates with a tuffaceous matrix, unconformably overlying the Omaura Formation and some of the Owen Stanley rocks (Fig. 2.5; Tingey and Grainger, 1976). They contain interbedded sandstone and biohermal (reef) limestone interpreted by Smit et al. (1974) as shelf facies. The reported Middle Miocene age is from foraminifera (Dow et al., 1974). Andesite "agglomerate" has been reported in some of the basal contacts (Tingey and Grainger, 1976).

The Morobe granodiorite (Fig. 2.5) is a suite of Miocene intrusions that consist mostly of granodiorite, diorite, and monzonite. They intruded the Owen Stanley metasedimentary rocks around 14.5 - 12 Ma (K-Ar and Rb-Sr ages; Tingey and Grainger, 1976). The Morobe granodiorite is considered to be part of the Maramuni magmatic arc (e.g., Garwin et al., 2005). Maramuni intrusions in general are in places cut by, and elsewhere cross-cut, thrust faults (Verave and Kawagle, 2010).

The Babwaf conglomerate is a poorly consolidated but well sorted conglomerate with minor sandstone and siltstone beds. These are interpreted as a shallow water sedimentary facies by Tingey and Grainger (1976). They unconformably overlie or are in fault contact with older units in the western part of the map area (Fig. 2.5). They occur several kilometres west of Golpu and have not been documented in the local study area (Chapter Three).

The Otibanda Formation is a Late Miocene to Late Pliocene sequence containing several hundred metres of interbedded sandstone, conglomerate, tuff, and limestone. These mostly lacustrine and fluvial rocks crop out near the Bulolo units (Fig. 2.5), and are locally gold-bearing (Plane, 1972; Fisher, 1975).

The Edie porphyry is a series of biotite- and hornblende-phyric andesite to dacite stocks and dykes, generally smaller and of distinctly younger age than Morobe granodiorite stocks (Fig. 2.5). A K-Ar hornblende age of 4.5 ± 0.4 Ma has been reported by Cussen et al. (1986) for this stage of intrusions. These are the youngest intrusions exposed in the Markham area and were probably involved in the formation of the Morobe Goldfield epithermal deposits (Nelson et al., 1990).

The Bulolo volcanic rocks consist of felsic ignimbrite several hundred metres thick with minor andesite, interpreted to be the extrusive equivalent of the Edie porphyry. These crop out near the Morobe Goldfield deposits but are not present near Golpu (Fig. 2.5).

2.4 Regional Structure

The Wafi-Golpu deposit is located in the eastern part of the Aure Deformation Zone, which is a belt of E- to NNE-dipping thrusts and folds in the New Guinea Orogen (Figs. 2.4 and 2.6). The thrusts are most evident in the Oligocene to Miocene clastic sedimentary rocks immediately west of the Owen Stanley thrust belt (e.g., faults through the Omaura greywacke in the southwest corner of Figs. 2.5 and 2.6). The east-dipping thrusts are part of a lateral ramp architecture identified by Pohn (2000) using side-looking radar. Such structures are common in fold-and-thrust belts such as the Appalachians (Pohn, 2000). Most thrust faults in this belt occurred from 12 - 4 Ma and probably post-date most of the Morobe intrusions (e.g., Fig. 2.5). Golpu diorites intruded around the time of this east-dipping thrust development.

Some NNE-trending structures, such as the Wafi fault (Fig. 2.6), may be transfer (i.e., vertical) faults. These types of structures are visible through most of the New Guinea Orogen as linear aeromagnetic features (Hill et al., 2002). Their roots may have played a significant role in the locations of Maramuni magmas (e.g., Corbett, 1994).

NNW-trending faults in the region have generally been reported as extensional, implying either normal or transtensional motion. For instance, the Watut and Wandumi Faults (Fig. 2.6) are described by Corbett (1994) as normal faults that define the NNW-trending Bulolo Graben. However, D'Addario et al. (1974) imply in their sections that these NNW-trending structures are NNE-dipping thrusts.

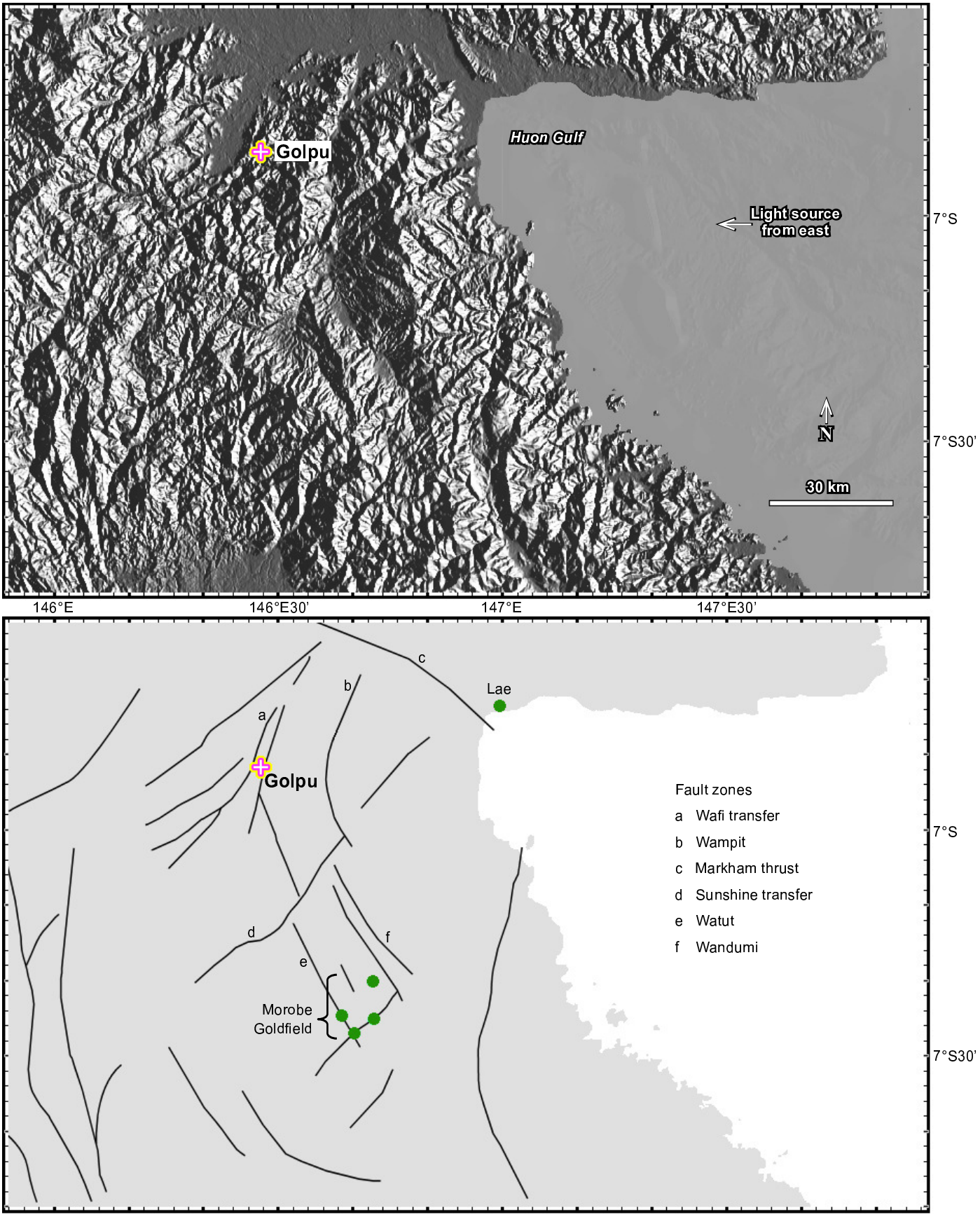

Figure 2.6: Maps showing the major structures of the Markham area. A) Topographic model with west-facing light source highlights topography built by east-dipping thrust stacks (see sections in Fig. 2.5). B) Same map area with major fault traces labeled. Most fault traces were interpreted by Corbett (1990) based on topography and side looking radar.

2.5 Discussion

Hill and Raza (1999) suggested that Maramuni magmatism ceased at 12 Ma. If the Maramuni Arc is strictly defined by magmas that intruded during southward subduction, then the Golpu diorites (ca. 8.8 Ma; Chapter Three) post-date this magmatic arc by several million years. They are interpreted to have intruded during later Aure deformation in a period of low-angle westward subduction.

The transition from south- to north-directed subduction east of Golpu during the southward docking of the Melanesian arc resulted in an antiformal, westward-subducting plate that remains approximately flat below New Guinea for several hundred kilometres west of the Huon Gulf. Seismic data and mantle tomographic evaluations show that rather than tearing during westward migration of the north-dipping New Britain trench, the south-dipping oceanic crust has remained attached to the westward migrating Solomon Sea Plate, forming the inverted U-shaped feature identified by Ripper (1982) and Pegler et al. (1995; Fig. 2.7). A similar configuration, involving west-directed subduction of a wedge-shaped slab, is interpreted to have been present during intrusive activity at Golpu (e.g., Fig. 2.3 C-F).

Subduction of this north- and south-dipping wedge has a component of low-angle subduction to the west (section A-A′ in Fig. 2.8), and may have triggered generation of the Golpu deposit. A key role for low-angle subduction was proposed by Cooke et al. (2005) for several porphyry deposits including the supergiant Grasberg and central Chilean deposits. The U-shaped feature related to flat westward subduction of the Solomon Sea Plate is visible in the seismic data as far west as 143°E (Fig. 2.7; farther if the oldest and westernmost parts of the slab are now aseismic), so this feature may explain the westward younging of post-Maramuni porphyry deposits from Golpu towards Ok Tedi (Fig. 2.9).

Based on this review of the available evidence, I propose that there are two metallogenic belts in the New Guinea Orogen. The Maramuni belt formed between 17 and 12 Ma, and includes the Frieda, Nena, and early Yandera deposits. The second, more richly endowed belt is defined by a series of westward-younging deposits that includes Golpu (the earliest in this belt) and younger deposits east of Grasberg (Fig. 2.9). It is defined here as the Post-Maramuni belt.

2.6 Summary

The Golpu diorites intruded greenschist facies Owen Stanley metasedimentary rocks in the eastern part of the Aure Deformation Zone. The deposit formed ~ 3 m.y. after the end of the porphyry-generating Maramuni Event. Golpu is the first formed and easternmost deposit in a younger belt of low-angle subduction-related deposits. Epithermal mineralisation in the nearby Morobe Goldfield occurred in the latest stages of regional magmatism, 4 - 5 m.y. after Golpu intrusion.

Figure 2.7 (next page): An inverted U-shaped and approximately flat subducting slab (the Solomon Sea Plate) is visible in the seismic data at least as far west as 143°E (sections B, C, D) and in the mantle tomographic model of Tregoning and Gorbatov (2004; section C). Current plate boundaries including spreading and transform ridges are visible in the plan sections 1-3. Seismic data are from the International Seismological Centre (2009), and mantle tomographic sections are from Hall and Spakman (2002) and Tregoning and Gorbatov (2004). Parts of this figure were produced with GeoMapApp (geomapapp.org), using topography data from Ryan et al. (2009).

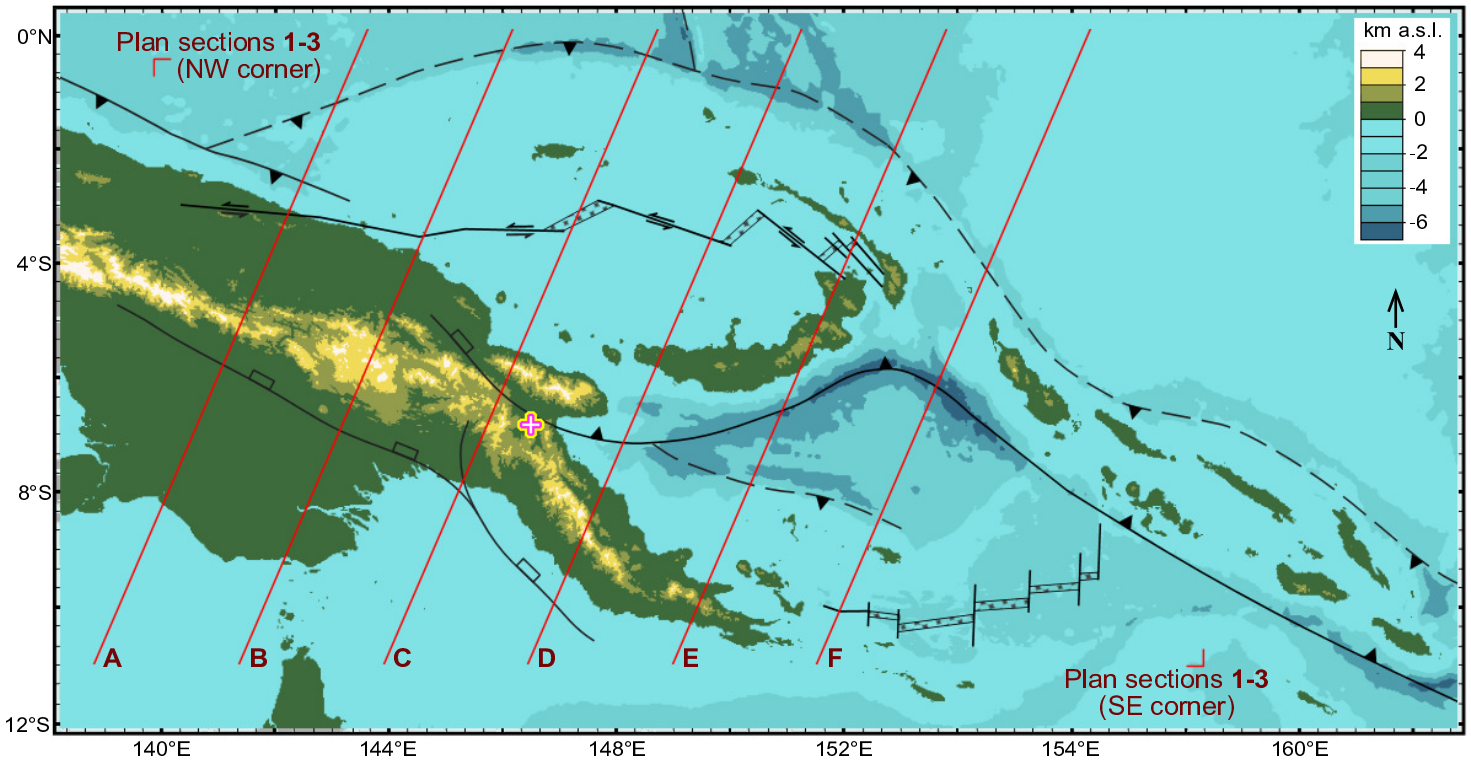
Plan sections 1-3
(NW corner)
km a.s.l.
4
2
0
-2
-4
-6
N
A
B
C
D
E
F
Plan sections 1-3
(SE corner)
0°N
4°S
8°S
12°S
140°E
144°E
148°E
152°E
154°E
160°E

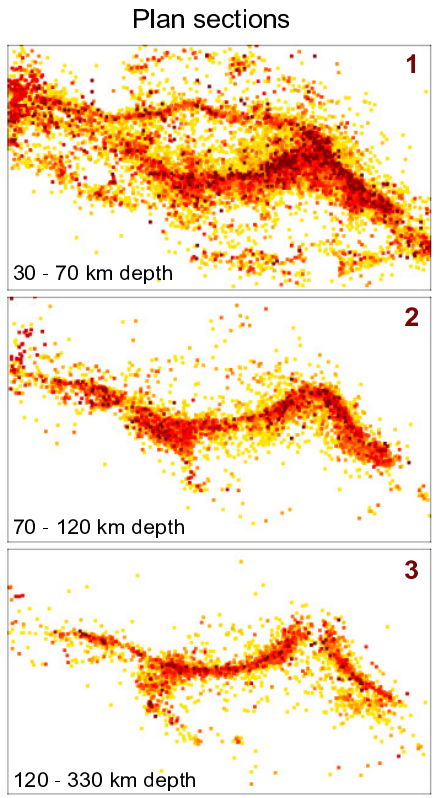
Plan sections
1
30 - 70 km depth
2
70 - 120 km depth
3
120 - 330 km depth

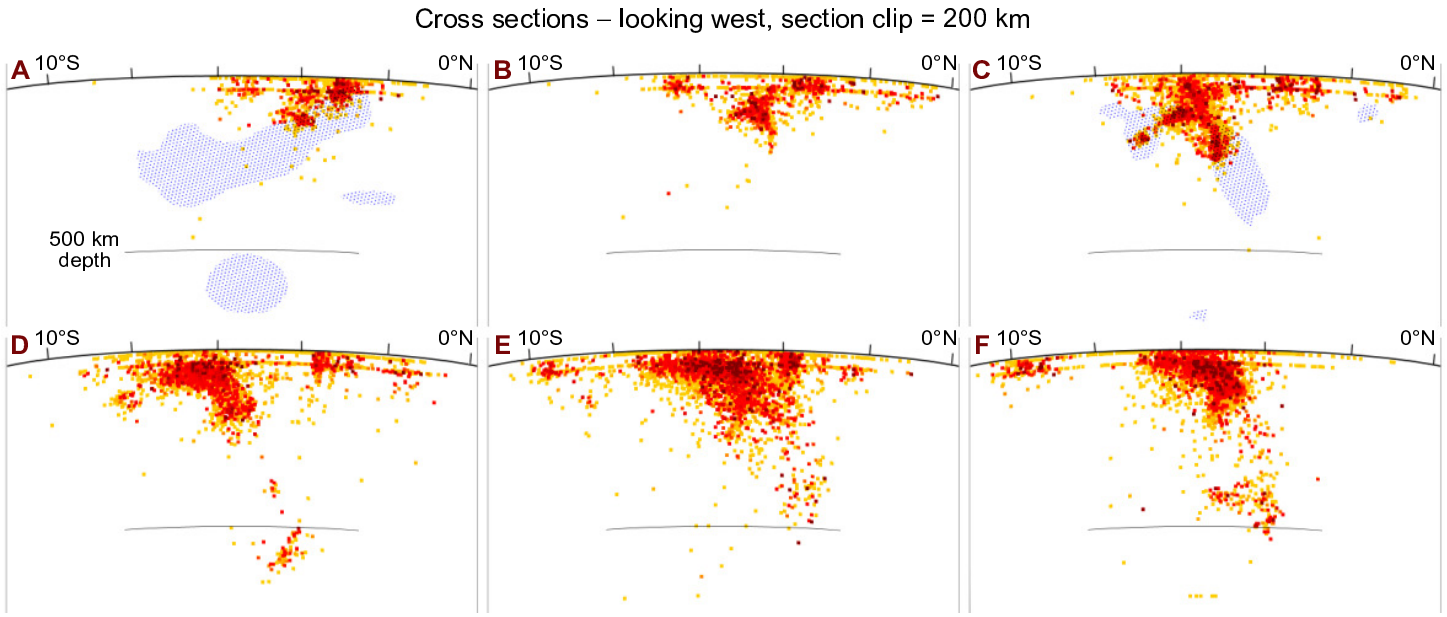
Cross sections – looking west, section clip = 200 km
A 10°S 0°N
B 10°S 0°N
C 10°S 0°N
500 km depth
D 10°S 0°N
E 10°S 0°N
F 10°S 0°N

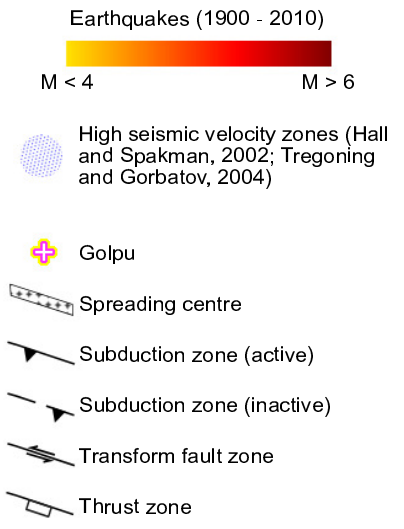
Earthquakes (1900 - 2010)
M < 4
M > 6
High seismic velocity zones (Hall and Spakman, 2002; Tregoning and Gorbatov, 2004)
Golpu
Spreading centre
Subduction zone (active)
Subduction zone (inactive)
Transform fault zone
Thrust zone

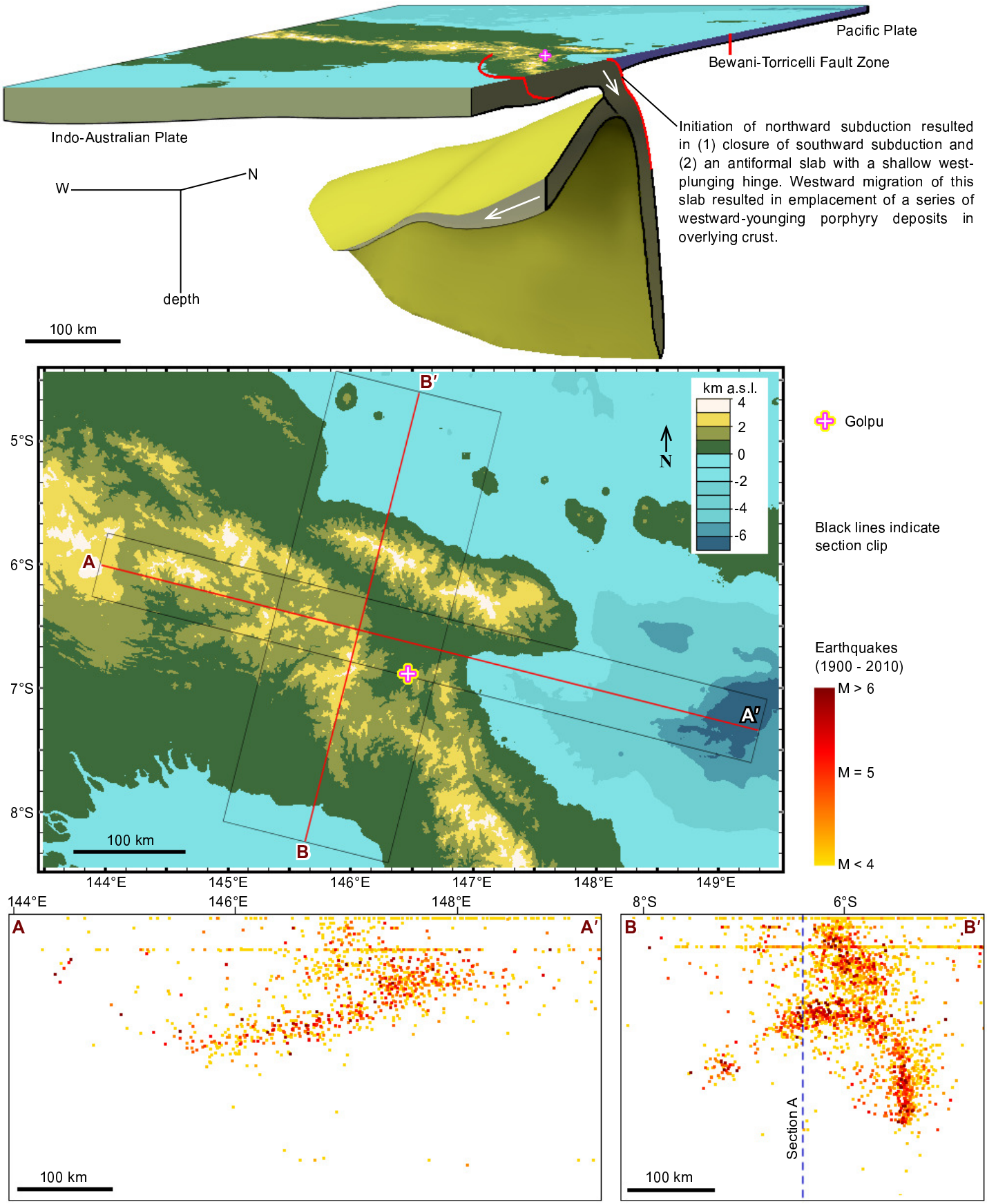

Figure 2.8: Model and sections illustrating the low-angle westward dip (A-A′) and antiformal or inverted U-shaped geometry (B-B′) of the Solomon Sea Plate subducting westward below the New Guinea Orogen. The seismogenic zone does not disappear west of 144°E; see for example section B in Figure 2.7. Seismic data are from the International Seismological Centre (2009). Parts of this figure were produced with GeoMapApp (geomapapp.org), using topography data from Ryan et al. (2009).

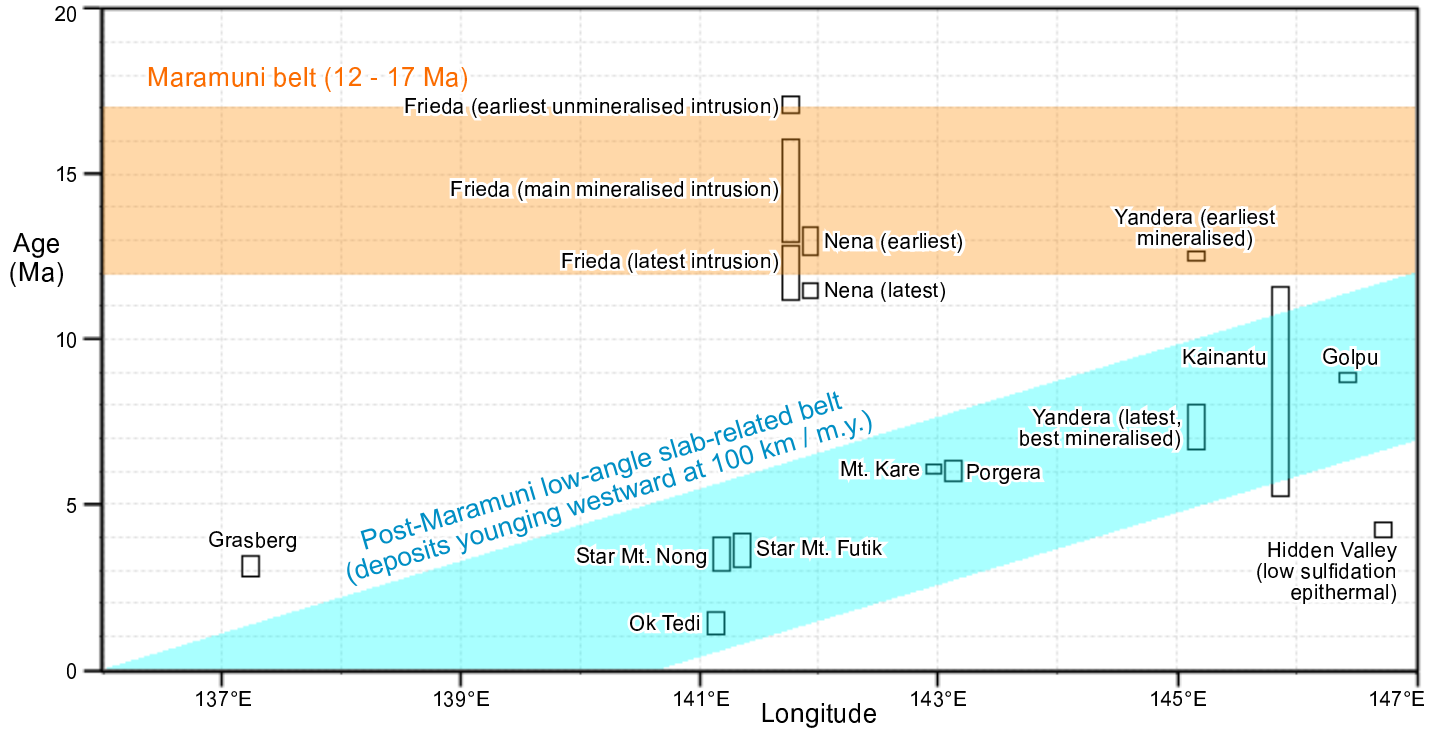

Figure 2.9: Age (bars indicate error or estimated range in references) versus longitude of porphyry deposits in New Guinea, showing two major belts of porphyry generation. The later belt includes Golpu and youngs westward by about 100 km / m.y.. The Yandera deposit may contain a better-mineralised post-Maramuni porphyry intrusion after an earlier, weakly mineralised Maramuni intrusion. The Grasberg and Ok Tedi deposits are probably not related to the two belts indicated. Dates are from Grant and Nielsen (1975), Whalen et al. (1982), Nelson et al. (1990), Bainbridge et al. (1998), Highlands Pacific 2003 annual report, Singer et al. (2008), and this study (Chapter Three).

The tectonic development of the Papua New Guinea region during the Cenozoic involved many stages of arc initiation, closure, and accretion, resulting in several arc- or orogen-parallel belts of porphyry deposits in both continental and oceanic arc settings. The most important events with respect to Golpu were:

1) The collision of the Ontong Java Plateau with the Melanesian Arc around 22 Ma resulted in the start of Trobriand-Wewak subduction, with associated porphyry-epithermal deposits forming from 17 - 12 Ma.
2) The closure of southward Trobriand subduction and initiation of northward subduction from 15 - 12 Ma, in conjunction with accretion of the Melanesian Arc to the northern margin of New Guinea, resulted in a wedge-shaped Solomon Sea Plate with a component of shallow westward subduction below Golpu.
3) Shallow westward subduction of the Solomon Sea Plate contributed to significant uplift in the New Guinea Orogen, by E-dipping thrusts that were most pronounced in the Aure Deformation Zone. The compression, uplift, and exhumation primarily driven by the collision with this west-directed slab were key in the formation of the Wafi-Golpu porphyry-epithermal system. Progressively younger deposits were formed west of Golpu in conjunction with the slab-associated compressional regime (± volatile or metal source; e.g., Cooke et al., 2005).

Chapter 3
Wafi-Golpu District Geology

3.1 Introduction

This chapter documents the host stratigraphy, igneous rocks, and faults at Golpu and Wafi. This information provides the framework necessary for a detailed evaluation of the structural, mineralogical, and chemical controls on porphyry and epithermal alteration and mineralisation in later chapters. New U-Pb geochronology results in this chapter constrain the timing of emplacement of the Golpu intrusive complex and Cu-Au mineralisation. Whole rock geochemistry data are used to evaluate the tectonic setting of Golpu.

3.2 Methods

The density and depth of drilling through the study area allows for very large and well-constrained geology sections. The map and sections presented in this chapter are based on modelling of core log data collected by MMJV and previous site geologists, up to October 2012, with adjustments using my drill core logs. Lithotype volumes were modelled using Leapfrog software, and clipped to within 200 metres of drill core locations. A detailed description of the method used to produce these volumes and sections is provided in Appendix C. The diorite volumes are based in part on a model by P. Dunham in October 2012 (unpublished data), with adjustments using lithology volumes generated in Leapfrog with a vertical structural trend.

For the least-altered rocks described in this chapter, modal mineral abundances have been established based on thin section petrography supplemented by image processing and X-ray diffraction (XRD) analyses. A total of 159 polished thin sections were examined in order to identify alteration and vein assemblages, and overprinting and cross-cutting relationships. Detailed petrographic descriptions for selected samples, including least-altered lithotypes, are provided in Appendix A.

Images and image mosaics of polished thin sections were processed using imageJ software for modal mineral abundance. This was applied to phenocryst, sulfide, fragment, and vein abundances in key samples; otherwise, modal abundances given in Appendix A were estimated visually in thin section. More details of the image processing methods are provided in Appendix D.

X-ray diffraction traces were collected from 70 drill core samples from the study area, including 11 least-altered samples. The sample powders were analysed by S. McKnight (University of Ballarat), under the following conditions: Siemens D500 and D501 diffractometers were used with Fe-filtered CoK_{α} X-rays at 36 kV and 30 mA; the diffractograms / XRD profiles were collected by step scans with a starting angle of 5 $^{o}2\theta$, at conventional scan rates (1 degree or 2 theta per minute), and ending at 76 $^{o}2\theta$. McKnight used SiroQuant 3.0 software to identify and estimate the relative proportions of minerals in each sample. Smectite-bearing samples were air-dried and glycolated in order to better resolve the clay contents. The XRD results for each sample are provided in Appendix E, and XRD traces are provided in Appendix G.

A total of 87 whole core samples were submitted for analysis of major and trace elements at Acme Analytical Laboratories in Vancouver, Canada. Samples were crushed to 200 mesh, and pulps were heated to 105 °C before analysis. Major element oxides were determined by inductively coupled plasma - mass

spectrometry (ICP-MS) following lithium borate fusion and acid digestion. Loss on ignition (LOI) values were obtained by heating to 1000 °C. The concentrations of 49 trace elements, including the lanthanide series, were determined by ICP-MS after hot 4 acid digestion (HNO_3 - $HClO_4$ - HF followed by HCl) of 30 g pulp samples. The whole rock data, including analytical detection limits and sample descriptions, are provided in Appendix G.

Notes on rock nomenclature

"Metapelite" is the term used in the MMJV logs for metasedimentary rock with grains smaller than sand size. Although "pelite" has been applied on the basis of grain size alone (it is an obsolete synonym of mudstone; e.g., Bates & Jackson, 1987) the term metapelite has the additional connotation of higher alumina content (i.e., metamorphosed fine-grained sedimentary rock with high primary clay or mica content; Schmid et al., 2007), which does not accurately describe most of the quartz-rich metasiltstone in the study area. In this thesis, the terms metasiltstone, metasandstone, and metaconglomerate are used. These terms are based on average grain sizes of < 0.06 mm, 0.06 - 2 mm, and > 2 mm, respectively (Schmid et al., 2007).

Previous workers have used the genetic name "Wafi Diatreme" to describe the large breccia unit in the centre of the study area (e.g., Leach and Erceg, 1990; Sillitoe, 1999; Sillitoe, 2010). However, in order to keep observations and interpretations separate, the name "Wafi breccia complex" is used here.

3.3 Wafi-Golpu District Geology

The study area is 6 x 4.5 km, centred over the Wafi-Golpu system in the SW corner of Prospecting Authority 440 (Fig. 3.1). The study area contains broadly E- to ESE-dipping Owen Stanley metasedimentary rocks that were intruded by the Nambonga and Golpu diorite stocks, and cut by the Wafi breccia complex. These rocks are unconformably overlain by Hekeng Andesite and Wafi Conglomerate locally. The rock units are shown in the following map and cross sections (Figs. 3.2 to 3.7) and are described in detail in section 3.4. The geometry of the multiphase Golpu intrusive complex is shown in plan view in Figure 3.8.

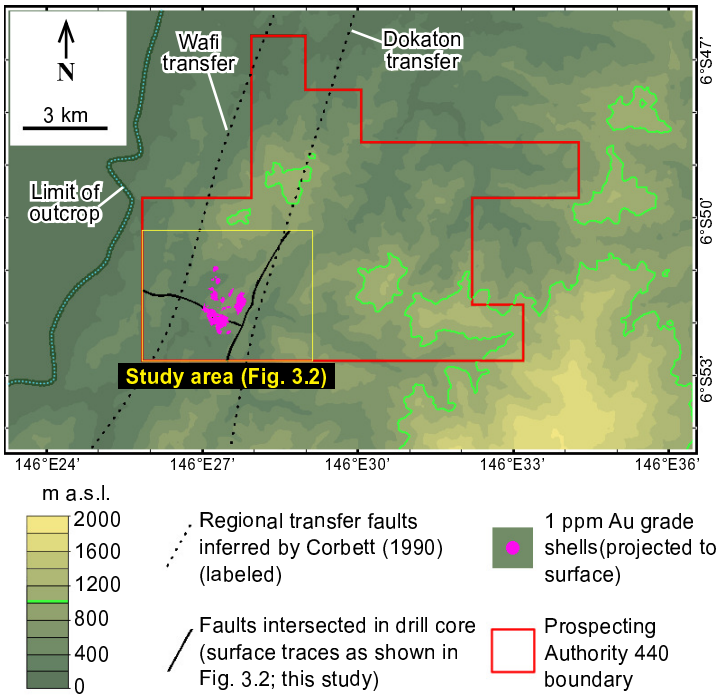

Figure 3.1: The study area is located in the SW corner of Prospecting Authority 440. Except for units shown in Figure 3.2, all mapped outcrop in this figure is Owen Stanley metasedimentary rock, covered by fluvial sediments west of the outcrop limit (labeled). Gold grade shells show the location of Wafi and Golpu mineralisation projected to surface (as in Fig. 3.2 A). The regional transfer structures were interpreted by Corbett (1990) on the basis of topography and side-looking radar (Figs. 2.5 and 2.6). I interpret an east-dipping thrust to occur near, or in place of, the Dokaton transfer, based on intersections in drill core (section 3.5). This figure was generated in part using GeoMapApp (http://www.geomapapp.org) with topography data from Ryan et al. (2009).

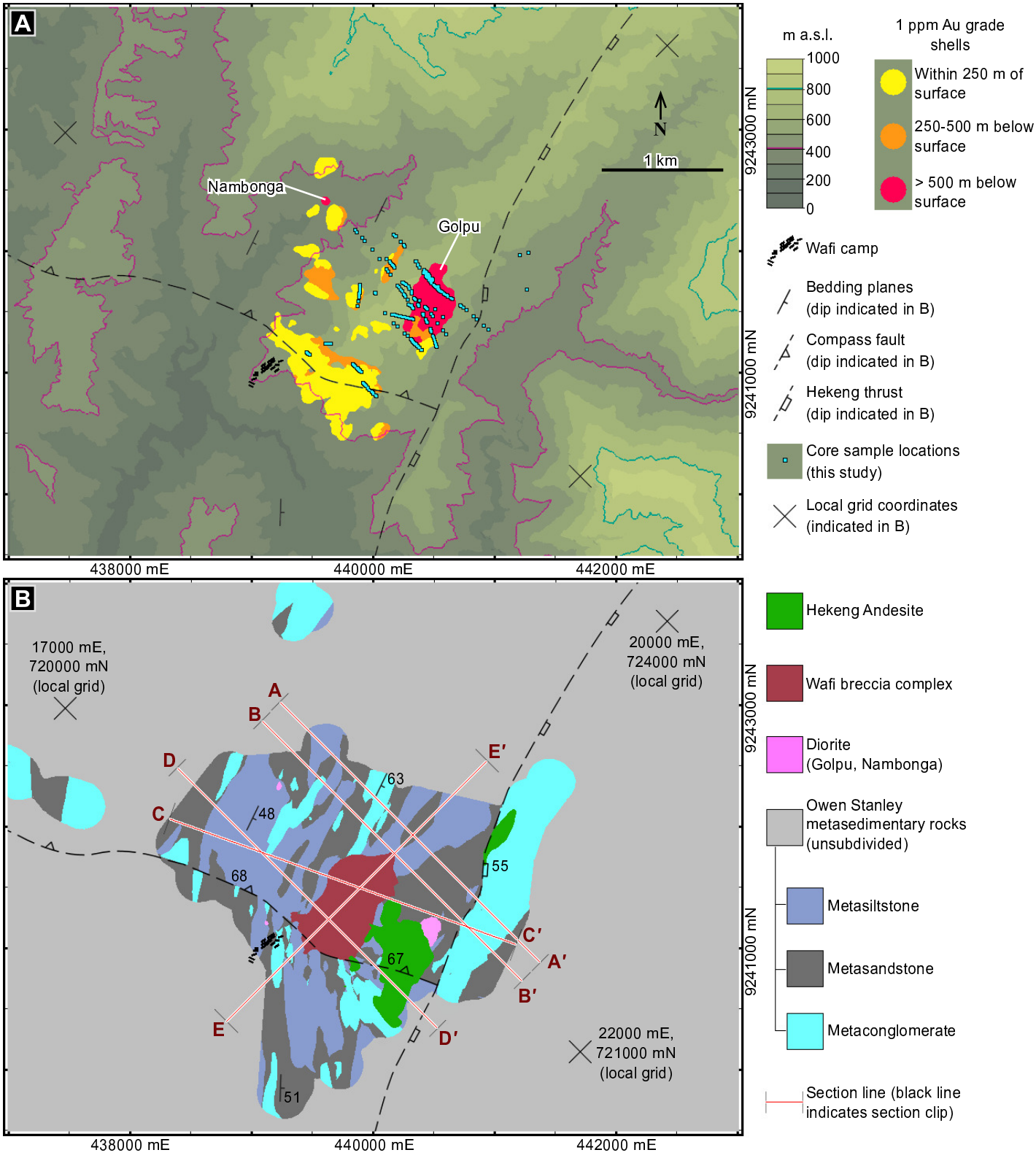

Figure 3.2: Maps of the Wafi property. A) Topography with sample locations and 1 ppm Au grade shells projected to surface. Grade shells deeper than 500 metres show hypogene Nambonga and Golpu porphyry mineralisation (labeled). Those shallower than 500 metres show Wafi epithermal mineralisation. B) Simplified plan geology map, looking below overburden. From mapping by MMJV geologists and consultants, with adjustments and subdivision of Owen-Stanley rocks using lithologies in drill core. Sections A-E are shown in Figures 3.3 to 3.7.

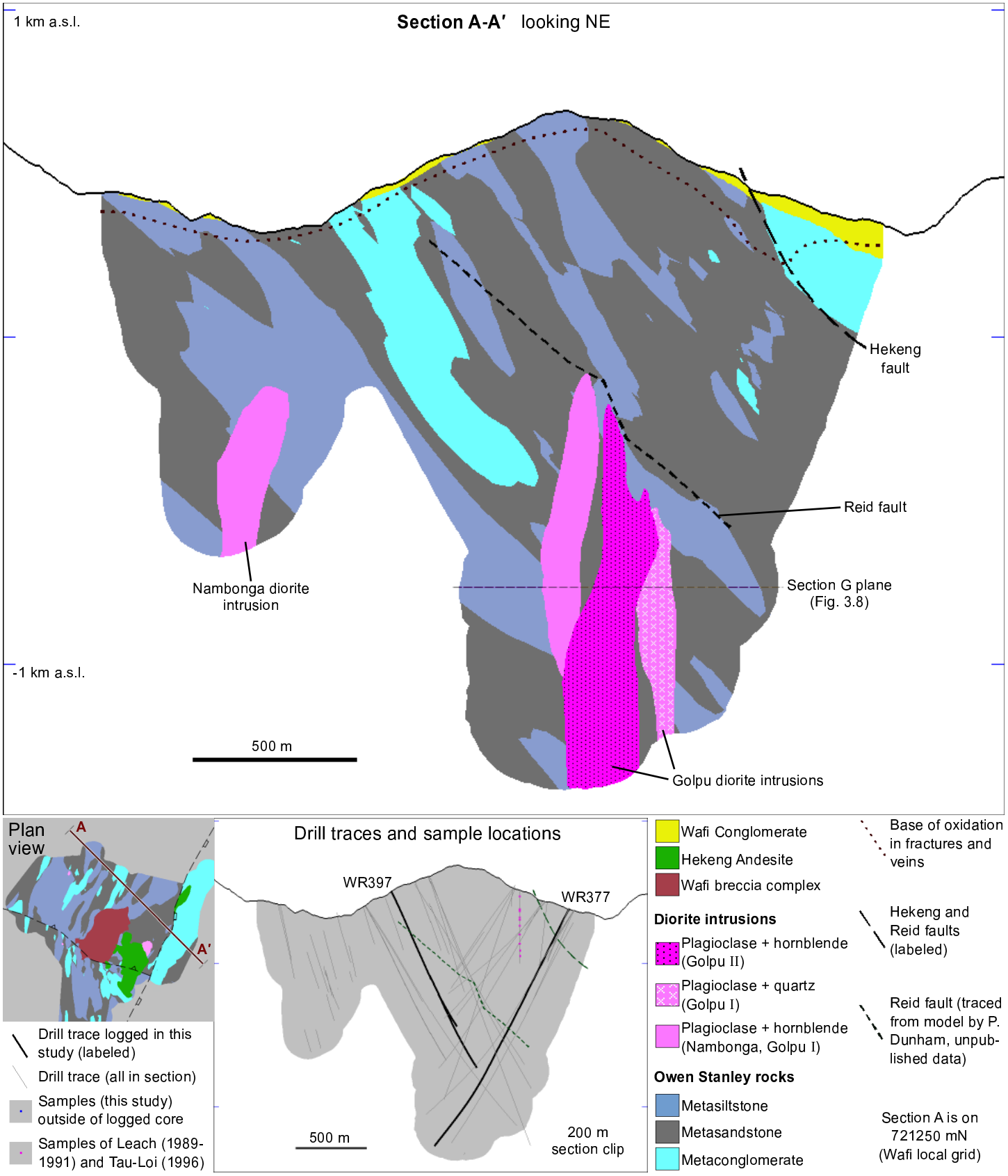

Figure 3.3: Geology section A-A′, looking NE. Rock volumes were built using the Leapfrog compositing methods discussed in the text, based on core logs by MMJV geologists and the author. The oxidation profile, Reid fault trace, and diorite outlines are also based on models by P. Dunham (unpublished data, 2012). The bottom image is the same section showing the location of drill traces logged and sampled in this study (thick lines), along with all other drill traces (thin lines) and other sources of petrographic and XRD data used in this study (Tau-Loi, 1996; and Leach, 1989-1996). The section clip applies only to the drill traces and sample locations.

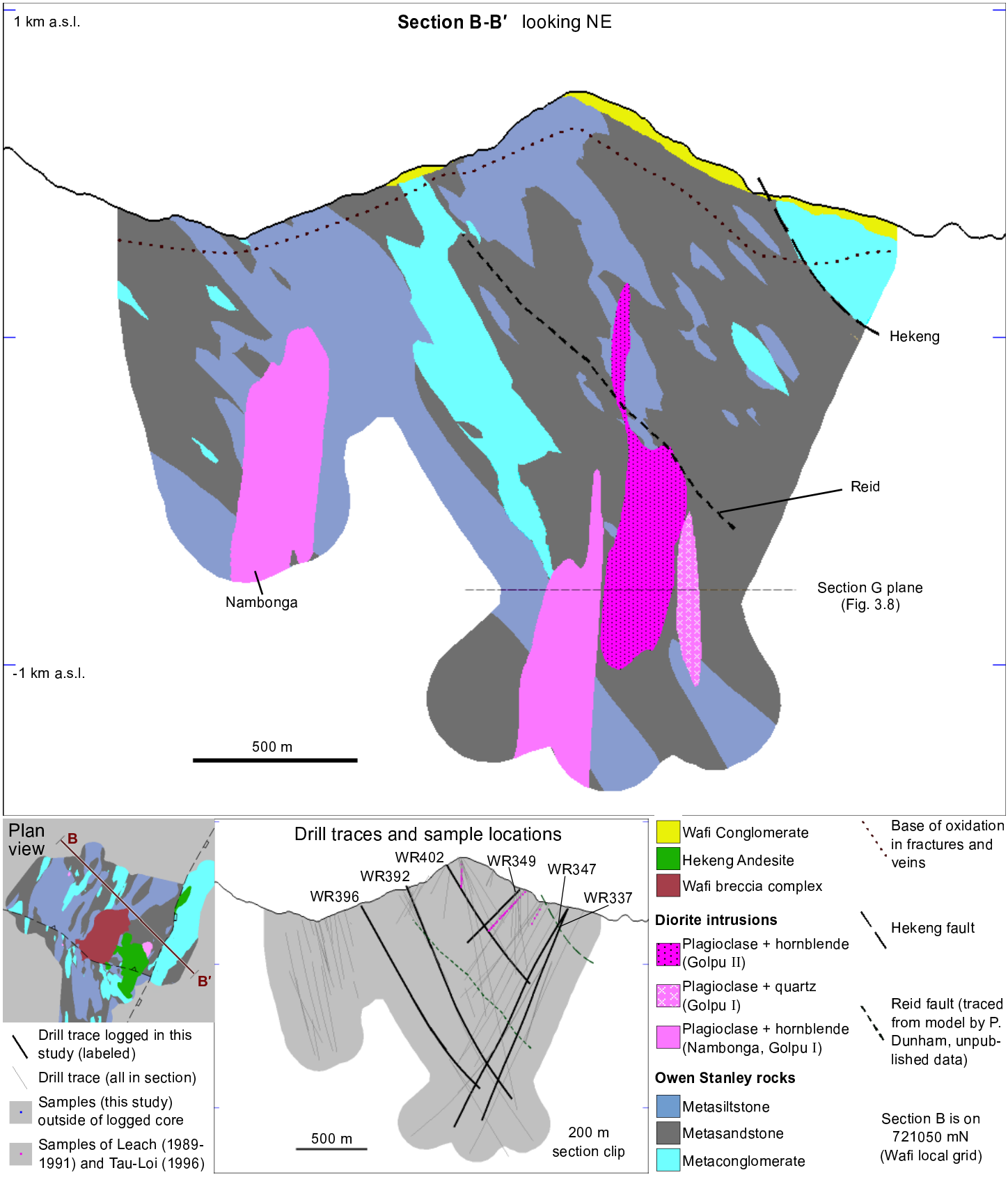

Figure 3.4: Geology section B-B′, looking NE. As in section A, Golpu consists of three diorite intrusions. Although two of the Golpu intrusions appear to be rootless in this section, they are vertically continuous both to the NE and SW of the section. Methods and data sources (MMJV geologists, P. Dunham) are as described in Figure 3.3.

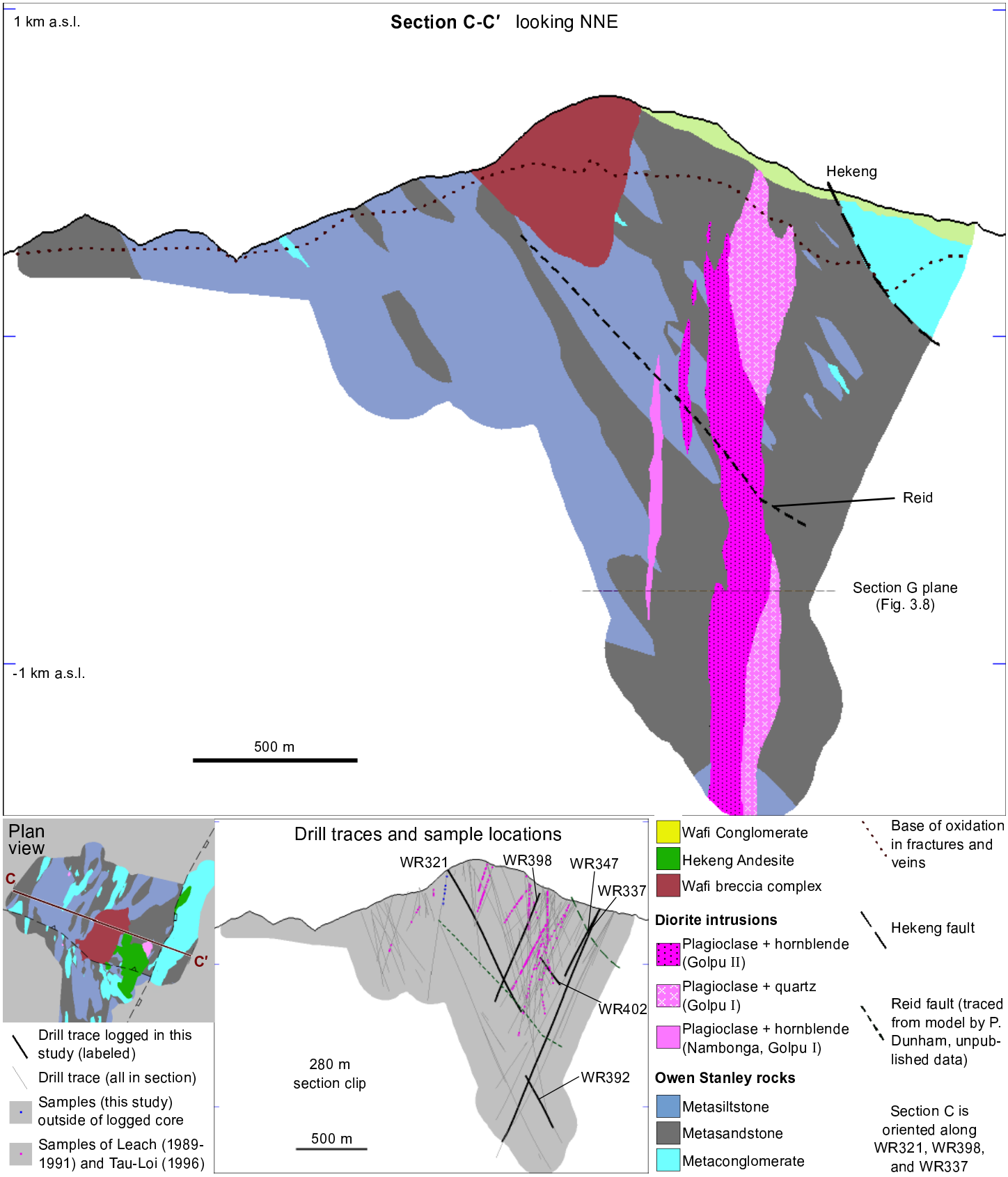

Figure 3.5: Geology section C-C′, looking NNE. This shows the thin NNE-trending geometry of the Golpu intrusions as well as the deepest drilled extent of the Wafi breccia complex. Methods and data sources (MMJV geologists, P. Dunham) are as described in Figure 3.3.

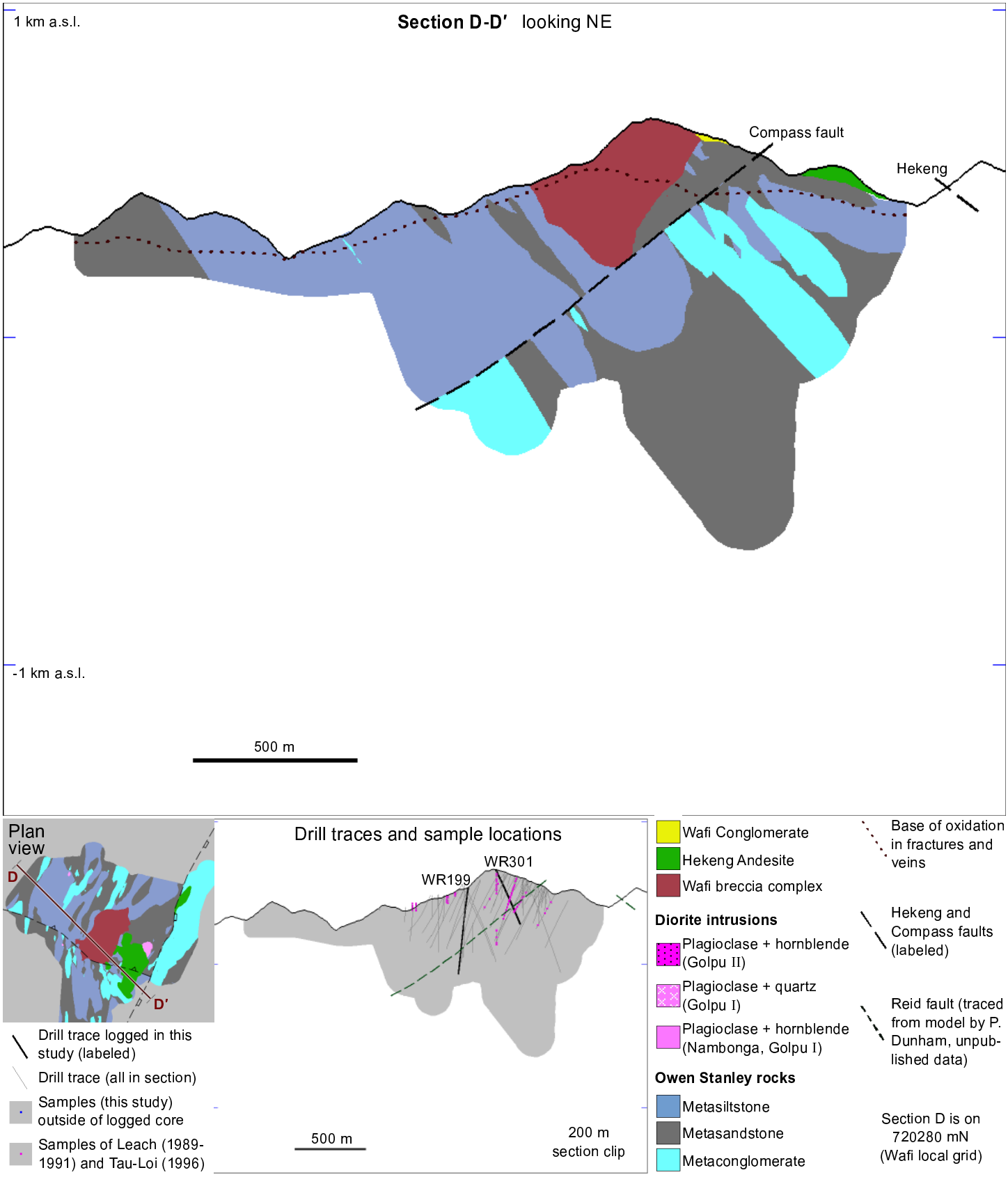

Figure 3.6: Geology section D-D′, looking NE. The steep eastern margin of the Wafi breccia complex is evident in this section, along with the main outcrop of Hekeng Andesite unconformably overlying Owen Stanley metasedimentary rock. The Compass fault dips 65 - 70° N, but has a shallow apparent dip due to the orientation of the section. Methods and data sources (MMJV geologists, P. Dunham) are as described in Figure 3.3.

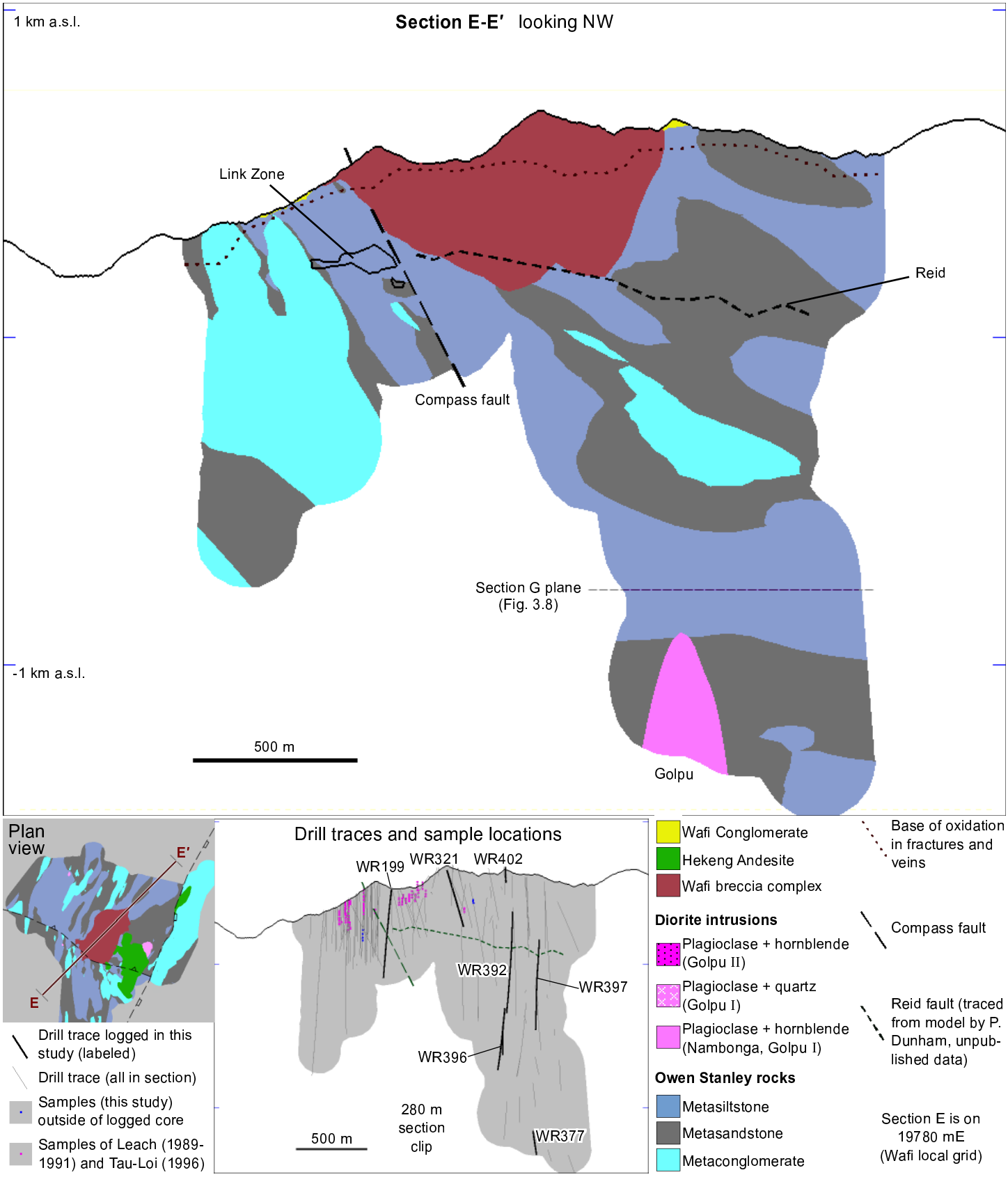

Figure 3.7: Geology section E-E′, looking NW. This section shows the maximum length (1050 m) of the Wafi breccia complex, its southern margin occurring partly along the Compass fault. The western edge of the Golpu intrusive complex is also visible. Link Zone (outlined after P. Dunham, unpublished data) contains the highest gold grades at Wafi, as epithermal veins along and up to a few hundred metres south of the Compass fault (Chapter Four). Methods and data sources (MMJV geologists, P. Dunham) are as described in Figure 3.3.

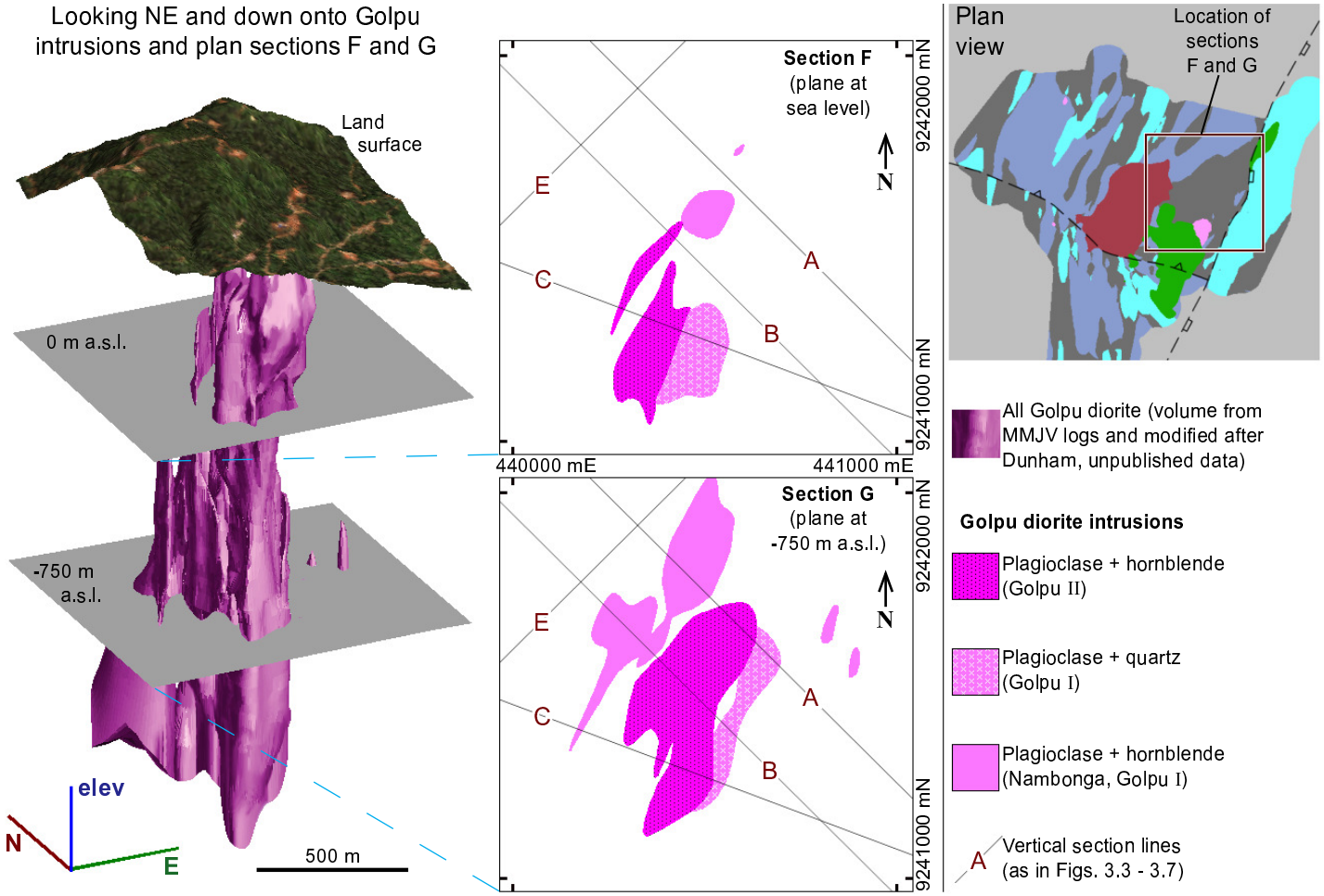

Figure 3.8: Geology sections F and G, showing the distribution of Golpu diorite intrusions in plan view. The 3-dimensional view at left is looking approximately along the NNE strike of the Golpu intrusions. The diorite volume is based on core logs by MMJV geologists and modified after a model by P. Dunham (unpublished data). The three intrusive phases of the Golpu diorite complex are shown in the plan sections, and consist of a plagioclase + hornblende-phyric diorite to the N and NW, a plagioclase + quartz-phyric diorite to the E and SE which outcrops nearly to the surface (below overburden), and a last hornblende + plagioclase-phyric diorite which has intruded between (and partly along the contacts of) the previous two phases. This last phase of intrusion is associated with the main stage of Golpu porphyry mineralisation (Chapter Four). Coordinates are in AMG66.

3.4 Descriptions of Rock Units

Rocks of the study area are described in this section from oldest to youngest. The rock photos in Figures 3.9 to 3.18 illustrate characteristics of the least-altered rock types, unless otherwise stated in the image caption.

3.4.1 Owen Stanley Metasedimentary Rocks

Age: Jurassic to Mid-Cretaceous. Detrital zircons: 120 - 107 Ma (Kopi et al., 2000). Inherited zircons in Golpu diorites are of mostly Mesozoic age (this study; Table 3.2).

Collectively, Owen Stanley metasedimentary rocks make up 96 % of the surface map area in Figure 3.2 (ignoring overburden), and 71 % of the drill intervals. Individual beds vary from laminae (sub-millimetre) to about 30 metres thick, with most bedding planes approximately parallel to the regional stratigraphy (e.g., Fig. 3.9 A). Some bedding packages, such as conglomerate-dominant units with minor interbedded sandstone,

are up to 350 metres thick and can be traced in drill core about a kilometre along stratigraphy (e.g., the metaconglomerate package that is in between the Nambonga and Golpu intrusions in Figs. 3.3, 3.4, and 3.7).

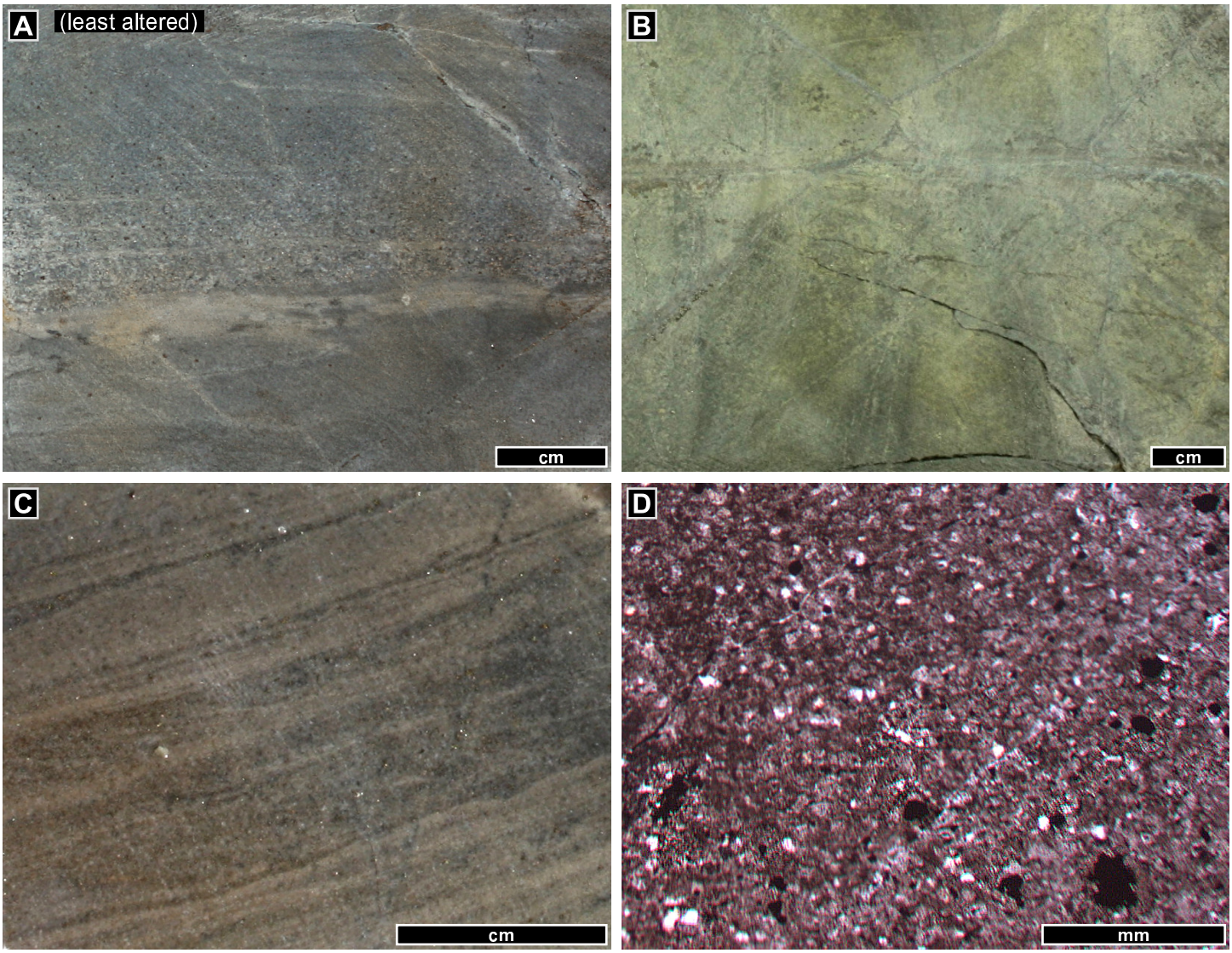

Figure 3.9: Representative core and thin section photos of Owen Stanley metasiltstone. A) Least-altered metasiltstone with an upward-fining bed. The bedding plane near image centre is parallel to the drill core (WR397, 96.0 m). B) Massive metasiltstone with a green colour due to chlorite - muscovite alteration (WR337, 382.6 m). C) Finely laminated metasiltstone (WR392, 235.4 m). D) Thin section image of typical metasiltstone, showing protolith quartz grains of mostly silt size (1 / 16 mm). Opaque grains are pyrite (plane polarised light / PPL; WR199, 285.0 m).

Metasiltstone

Metasiltstone makes up approximately 55 % of the Owen Stanley metasedimentary rock in drill core. It is the most common rock type in the study area. Least-altered samples have a grey-green colour (Fig. 3.9 A), with a lighter colour in samples with higher quartz content. Based on thin section and XRD results, the least-altered metasiltstones contain 30 - 50 vol % quartz, 20 - 50 % plagioclase, 4 - 20 % chlorite, 4 - 10 % pyrite, and minor magnetite, clay, and actinolite (Table 3.1; Appendix A). Grains visible in thin section are mostly rounded quartz and plagioclase (Fig. 3.9 D). The matrix in least-altered samples contains the micas that are generally too fine grained to identify in thin section.

Table 3.1: Summary of the mineralogy of least-altered metasedimentary rocks

Lithotype	Sample location	Summary of bulk mineralogy (vol % by quantitative XRD)
Meta-siltstone	WR397, 353.2 m	40 % quartz, 23 % plagioclase (albite < labradorite), 16 % chlorite, 5 % pyrite, 10 % kaolinite or dickite
	WR323, 457.7 m	42 % plagioclase (albite > labradorite), 33 % quartz, 6 % pyrite, 9 % smectite, 4 % chlorite
Meta-sandstone	WR347, 98.8 m	44 % plagioclase (albite > labradorite), 21 % chlorite, 13 % augite, 12 % actinolite, 2 % pyrite
	WR392, 150.2 m	47 % plagioclase (albite < labradorite), 25 % chlorite, 15 % quartz, 3 % talc, 2 % calcite, 2 % pyrite
	WR392, 276.3 m	30 % plagioclase (albite < labradorite), 32 % chlorite, 18 % quartz, 8 % actinolite, 3 % pyrite, 2 % augite
	WR396, 44.0 m	50 % plagioclase (albite < labradorite), 21 % actinolite, 19 % quartz, 2 % pyrite, 2 % orthoclase
Meta-conglomerate	WR377, 218.6 m	34 % plagioclase (albite > labradorite), 21 % actinolite, 21 % chlorite, 10 % augite, 4 % epidote, 3 % quartz
	WR396, 284.7 m	56 % plagioclase (albite < labradorite), 19 % actinolite, 11 % quartz, 3 % pyrite

Note: totals do not add to 100 % because trace components are not presented in this table.

Metasandstone

The metasandstone has a grey-green colour similar to the metasiltstone, but contains grains that are visible in hand sample (Fig. 3.10 A). Clast-supported arenite is predominant, occurring in massive to weakly bedded packages composed of poorly sorted, sub-rounded to rounded plagioclase and quartz grains 0.3 - 2 mm across (Fig. 3.10 A-C). Some metasandstone occurs as minor interbeds with metasiltstone (Fig. 3.10 D). The metasandstone units consist of 30 - 50 vol % plagioclase, 15 - 40 % chlorite, trace to 25 % actinolite, trace to 20 % quartz, 2 - 5 % pyrite, and minor augite, orthoclase, magnetite, calcite, talc, and muscovite in some samples.

Metaconglomerate

Metaconglomerate makes up about 12 % of the drilled Owen Stanley metamorphic rock. Most of the metaconglomerate intervals contain poorly sorted and well-rounded clasts that are 0.5 - 9 cm in diameter. The clasts are slightly elongated along bedding planes or unit contacts, and vary from clast-supported to sandy matrix-supported textures (Fig. 3.11 A-D). About half of the metaconglomerate contacts are gradational, fining over several tens of metres into pebbly conglomerate and adjacent sandstone (Appendix B). The rocks are consistently polymictic and show little variation in the relative abundance of clast types. About 35 % of the clasts are sandstone, 25 % are mottled green and white gabbroic clasts with relict equigranular plagioclase and augite (Fig. 3.11 A-D), 20 % are dark chlorite - actinolite - plagioclase clasts (with higher chlorite content than most siltstone or sandstone), and 20 % are lighter quartz-rich siltstone clasts. Selective replacement of the dark (chlorite - actinolite) and mottled gabbroic clasts is a common feature in many of the altered samples (Chapter Four). The colour and bulk mineralogy of these units are similar to the metasandstone, with 30 - 60 %

plagioclase, 15 - 30 % actinolite, trace to 30 % chlorite, trace to 20 % quartz, and the remainder including augite, pyrite, magnetite, and epidote (Table 3.1; Appendix A).

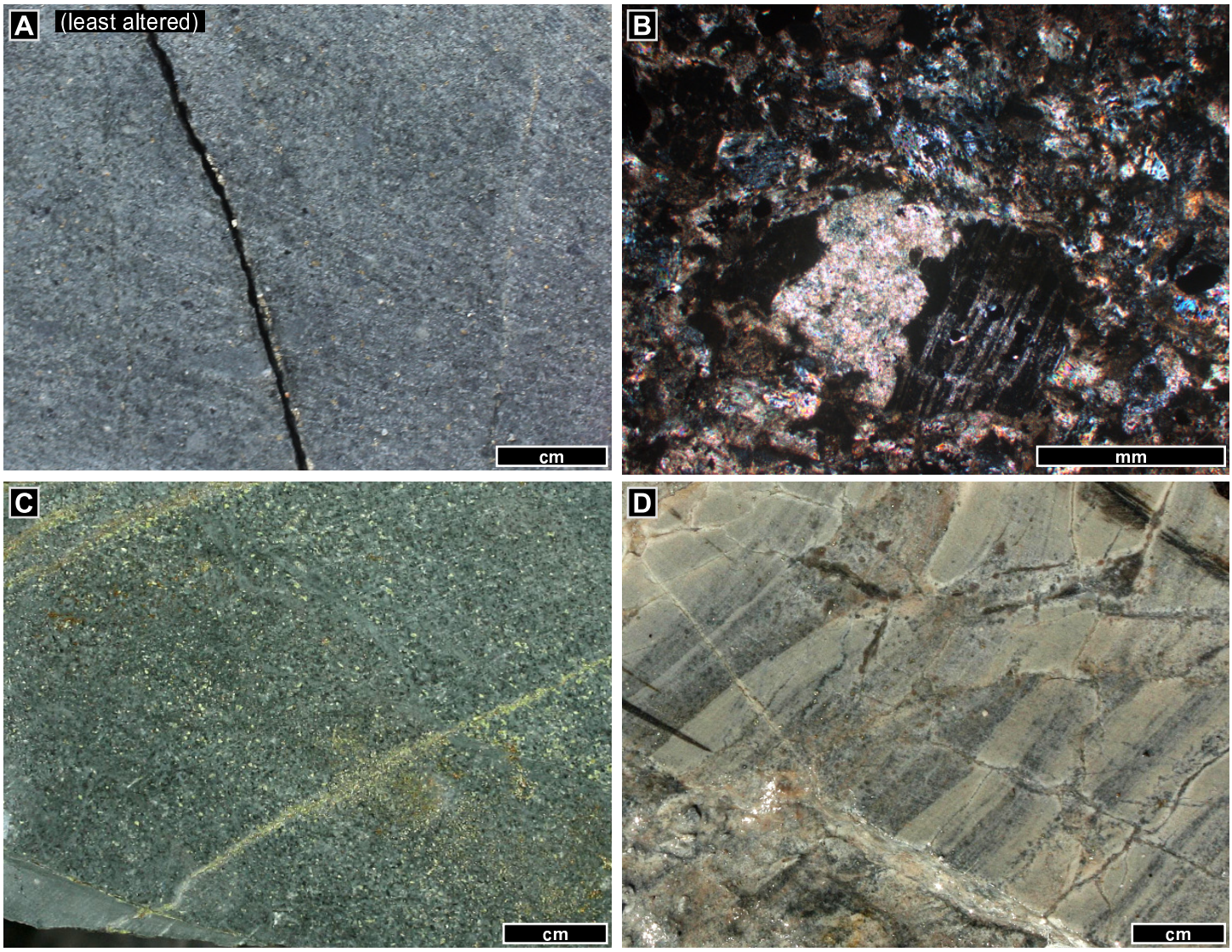

Figure 3.10: Representative core and thin section photos of Owen Stanley metasandstone. A) Least-altered medium-grained metasandstone (WR377, 761.0 m). B) Thin section image of the same sample, showing a plagioclase clast 2 mm across. The clast and surrounding matrix have been altered and / or metamorphosed to chlorite, muscovite, and trace actinolite (cross polarised light / XPL; WR377, 761.0 m). C) Massive to weakly bedded metasandstone as in A and B, but propylitic alteration has produced a greener colour than in A. Epidote has selectively replaced many of the plagioclase clasts. A bedding contact with metasiltstone is visible at the bottom left (WR397, 34.7 m). D) Interbedded metasandstone and metasiltstone. Upward fining from darker sandstone to lighter siltstone is visible at the top left (WR397, 331.4 m).

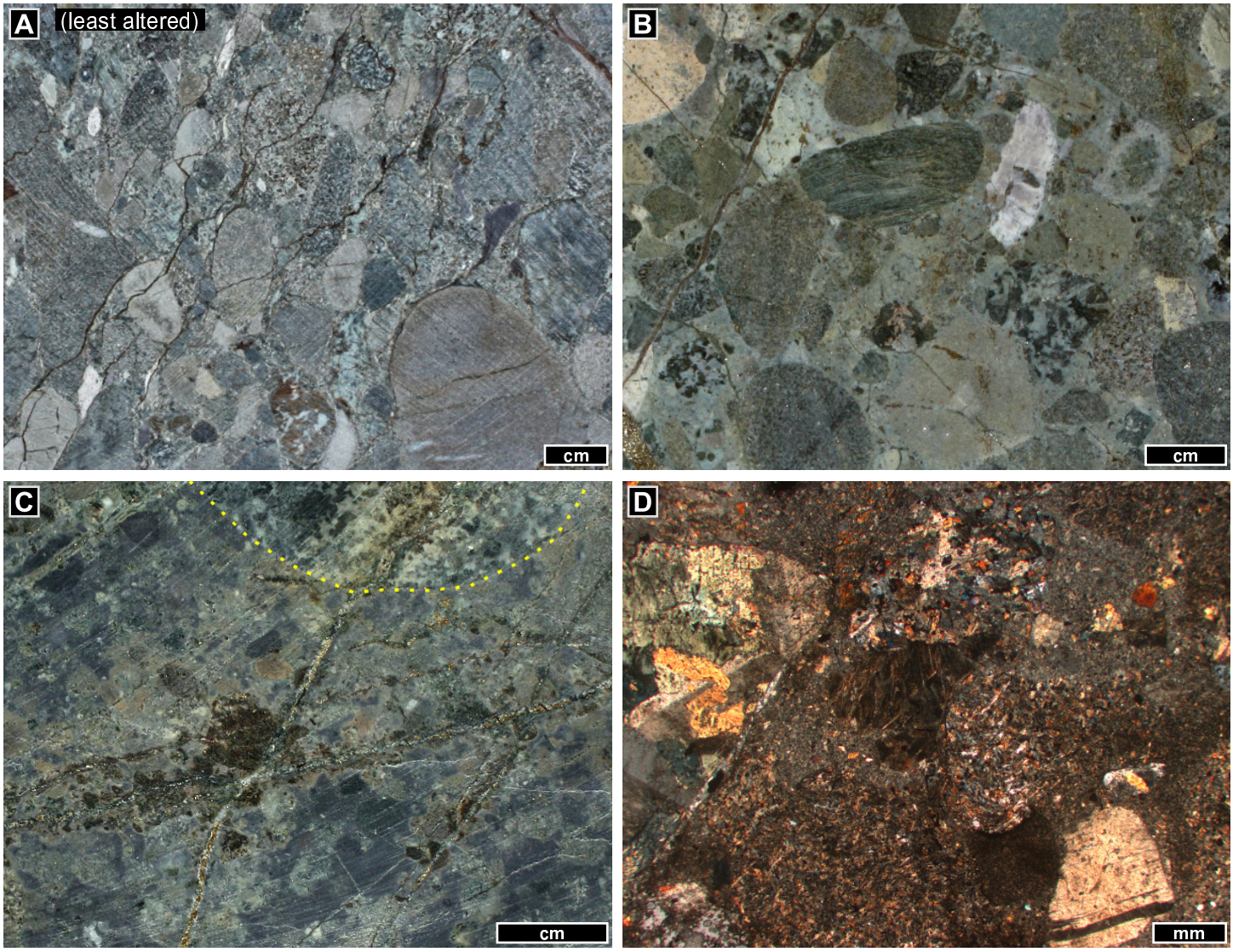

Figure 3.11: Representative photos of Owen Stanley metaconglomerate. A) Least-altered metaconglomerate consisting mostly of slightly elongated sandstone, siltstone, and gabbroic clasts (WR377, 216.7 m). B) Weakly propylitic altered metaconglomerate. Several mottled green and white gabbroic clasts are visible in this image (WR392, 109.0 m). C) Biotite vein halos are only developed in gabbroic clasts in this mostly propylitic altered sample. One large gabbroic clast margin is marked at the top of the image (WR396, 284.7 m). D) Thin section image of a least-altered (propylitic) part of the rock in C, showing a gabbro clast (at left) containing pyroxene and plagioclase, a relict plagioclase clast at bottom right, and a chlorite - muscovite and trace biotite-altered matrix (XPL; WR396, 284.7 m).

3.4.2 Nambonga Intrusion

Age: 10.33 ± 0.5 to 9.95 ± 0.5 Ma (K-Ar hornblende age; Tau-Loi, 1996).

The Nambonga diorite is interpreted to be the oldest intrusion in the study area, based on dating by Tau-Loi (1996; Table 3.2). It is a hornblende- and plagioclase-phyric porphyritic diorite. A small dyke of the intrusion crops out at surface (Fig. 3.2 B). The Nambonga diorite is less altered, and contains lower Cu and Au contents than the Golpu diorites (Morehari et al., 2009; Chapter Four). The Nambonga diorite was not investigated during this study.

Table 3.2: Geochronology of Nambonga and Golpu diorite intrusions

Intrusive phase	Sample ID	Age ± 2σ (Ma)	Dating method	Number of zircon analyses used	Inherited zircon ages (Ma)	Source
Nambonga	N5	10.33 ± 0.50	K-Ar (hornblende)	n/a	n/a	Tau-Loi (1996)
	H6	9.95 ± 0.50				
Stage I plagioclase- and quartz-phyric Golpu	392-1790.0	8.79 ± 0.17	U-Pb (zircon)	20	192 - 240, 604, 48	This study
	392-1830.9	8.93 ± 0.20		29		
Stage I hornblende- and plagioclase-phyric Golpu	397-1084.0	9.01 ± 0.14	U-Pb (zircon)	22	42, 112, 203	This study
Stage II hornblende- and plagioclase-phyric Golpu	321-H	8.86 ± 0.19	U-Pb (zircon)	12	12 - 18, 374	A. Harris (2010)
	220-H	8.70 ± 0.19		11		
	392-1413.0	8.86 ± 0.22		23		This study
	392-1280.5	8.59 ± 0.22		27		

Sample names are in drillhole-metres format, where possible. U-Pb zircon results are error weighted ^{208}Pb corrected ^{206}Pb / ^{238}U ages, including samples collected by A. Harris (2010). The U-Pb sample locations are shown in Figure 3.12.

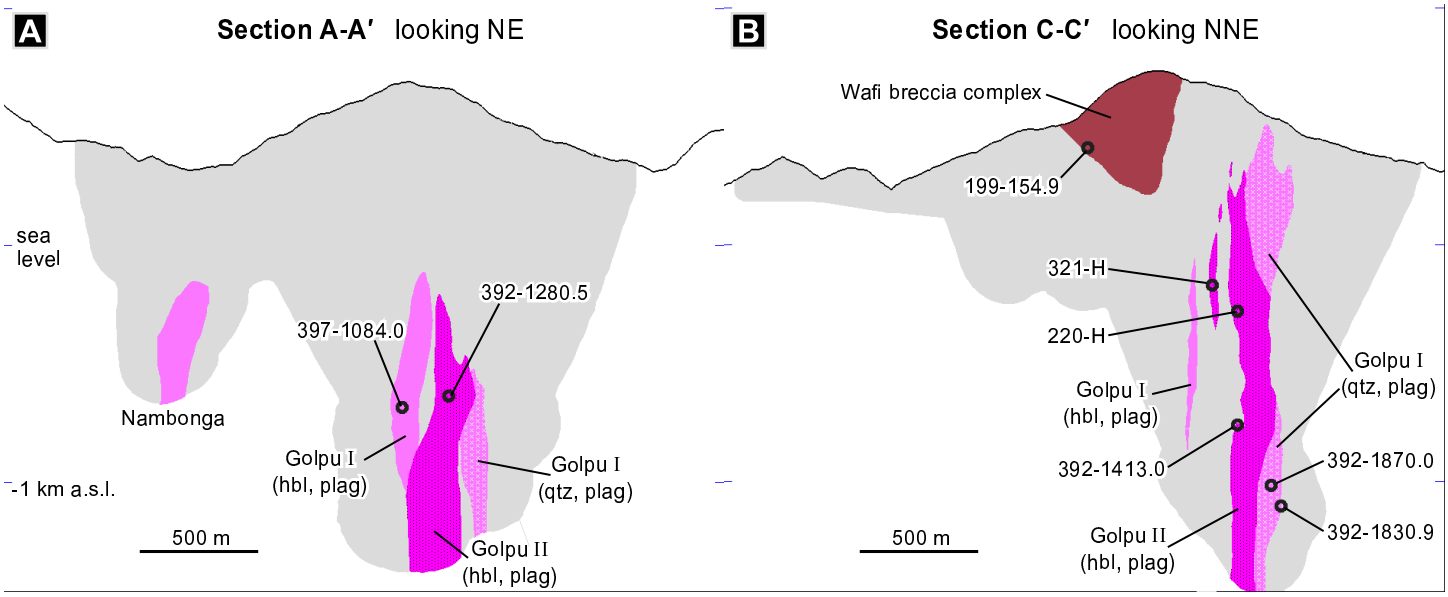

Figure 3.12: Sections showing the locations of samples used for U-Pb geochronology of Golpu diorites. The section clip for sample locations is 280 metres, except for sample 392-1280.5 (projected NE onto section A) and sample 199-154.9 (projected NNE onto section C). A) U-Pb samples in section A. Light grey indicates the extent of rock defined by drilling (as shown in Fig. 3.3). B) U-Pb samples in section C. Detailed geology in section C is shown in Figure 3.5.

Table 3.3: Summary of the mineralogy and primary phenocryst content of least-altered Golpu diorites

Diorite stage	Sample	Summary of bulk mineralogy[1] or primary phenocryst content[2]
Stage I plagioclase- and quartz-phyric	Primary phenocrysts (average)	81 % plagioclase, 11 % biotite, 7 % quartz, 1 % hornblende
	WR392, 1728.0 m	42 % plagioclase (albite > labradorite), 25 % quartz, 19 % muscovite, 7 % biotite, 2 % pyrite
Stage I hornblende- and plagioclase-phyric	Primary phenocrysts (average)	31 % hornblende, 69 % plagioclase (estimated on basis of phenocryst habit in altered samples)
Stage II hornblende- and plagioclase-phyric	Primary phenocrysts (average)	75 % plagioclase, 21 % hornblende, 4 % biotite
	WR347, 1075.0 m	29 % plagioclase (albite < labradorite), 30 % quartz (~ 15 % as veins), 16 % orthoclase, 6 % biotite, 7 % kaolinite, 2 % magnetite,

[1]XRD totals do not add up to 100 because trace components are not presented in this table. Note that least-altered sample results do not reflect primary magmatic or protolith content due to alteration, especially of hornblende, biotite, and plagioclase (see text).
[2]Primary phenocryst contents are modal % estimates of phenocrysts only, normalised to 100 %, from thin sections (Appendix A).

3.4.3 Golpu Intrusions

Ages: 9.01 ± 0.14 to 8.59 ± 0.22 Ma (Table 3.2).

The Golpu intrusive complex contains three diorite intrusions (Figs. 3.3 to 3.8). Each intrusion can be distinguished on the basis of the relative abundance of quartz, plagioclase or relict plagioclase, and relict (biotite-replaced) hornblende phenocrysts (Table 3.3, Fig. 3.16 D). Least-altered samples of all three phases have calc-alkaline to high-K calc-alkaline diorite compositions (Fig. 3.16 A-F).

Stage I plagioclase- and quartz-phyric Golpu diorite

The stage I Golpu intrusion is a mottled grey porphyritic diorite with 80 - 90 % phenocrysts that are 1.5 - 2 mm in diameter (sparse quartz phenocrysts are 5 mm across). The diorite has a quartz-rich groundmass with fine-grained biotite, plagioclase, and magnetite (Fig. 3.13 A,B). Of the phenocrysts, 60 - 90 % are plagioclase, 10 - 30 % are biotite (microphenocrysts with sharp margins), and 5 - 10 % are quartz (Table 3.2; Appendix A). A few intervals contain up to 5 % sparsely distributed hornblende replaced by biotite, as subhedral rhombs < 1.5 mm long. The plagioclase phenocrysts are prismatic or tabular to rounded, and are zoned in almost all samples (where preserved). The bulk mineralogy of this rock (including groundmass) is summarised in Table 3.2, but note that the XRD totals do not reflect primary magmatic compositions; unlike the Owen Stanley rocks, least-altered samples of the all three diorite phases are at least weakly altered to muscovite, biotite, chlorite, orthoclase, and / or chalcopyrite. Thin section estimates of average primary phenocryst contents (Table 3.2) and bulk primary mineralogy (Fig. 3.16 D) are better estimates of the primary magmatic compositions. The key features of the plagioclase- and quartz-phyric diorite are the sparse quartz phenocrysts,

which can still be identified in strongly altered intervals, abundant primary biotite, and a hard quartz-rich groundmass.

Stage I hornblende- and plagioclase-phyric Golpu diorite

Least-altered examples of the stage I hornblende- and plagioclase-phyric Golpu diorite contain only relict chlorite-, biotite-, and muscovite-altered phenocrysts of hornblende and plagioclase. Relative proportions of hornblende and plagioclase have been estimated from observations of relict crystal habits (Fig. 3.13 C,D). Phenocrysts make up 50 - 80 % of the rock, of which about a third are relict subhedral hornblende rhombs or hexagons (0.6 - 3 mm in diameter), and two thirds are relict rectangular plagioclase (< 2 mm long). This unit does not contain quartz phenocrysts.

Stage II hornblende- and plagioclase-phyric Golpu diorite

The youngest Golpu intrusion is a mottled grey or grey-green crowded porphyritic diorite with approximately 70 - 90 % subhedral to euhedral relict phenocrysts that are 0.5 - 3 mm long, set in a grey plagioclase- and quartz-rich groundmass (Fig. 3.14 A-F). Relict subhedral to euhedral hornblende phenocrysts are present in all samples, and constitute between 15 and 50 % of the phenocrysts. Variations in hornblende contents are gradual over tens of metres, occur throughout the intrusion, and are not marked by intrusive contacts. This intrusion (including groundmass) has an overall lower quartz content than the stage I plagioclase- and quartz-phyric intrusion (Table 3.2).

The stage II Golpu diorite occurs as several dykes ≥ 20 cm wide in its shallower portions (e.g., WR402, Appendix B), with phenocrysts < 2 mm long. Contacts of these dykes with Owen Stanley rocks are sharp, mostly planar, and have a weak planar fabric defined by the preferred alignment of phenocrysts near the contacts (e.g., Fig. 3.14 C). The main stock and its connected dykes are oriented NNE. Most diorite in individual drillholes are separated by at least a few metres of metasedimentary rock (e.g., WR392, WR396, WR397; Appendix B). Rare intervals containing diorite-diorite contacts are ambiguous with respect to both the exact location and the order of intrusion due to the intense quartz veining and orthoclase alteration along the stage II diorite margins (D. Finn, pers. comm., 2011).

Breccia veins with angular diorite and quartz-veined diorite fragments in biotite- and chlorite-cemented hydrothermal sandstone infill (Fig. 3.15 E-F) occur throughout the intrusion, along with several pegmatitic biotite patches with irregular margins (Fig. 3.15 C). Parts of the intrusion also contain poorly preserved round patches of biotite, chlorite, and chalcopyrite up to 3 cm across (Fig. 3.15 A,B).

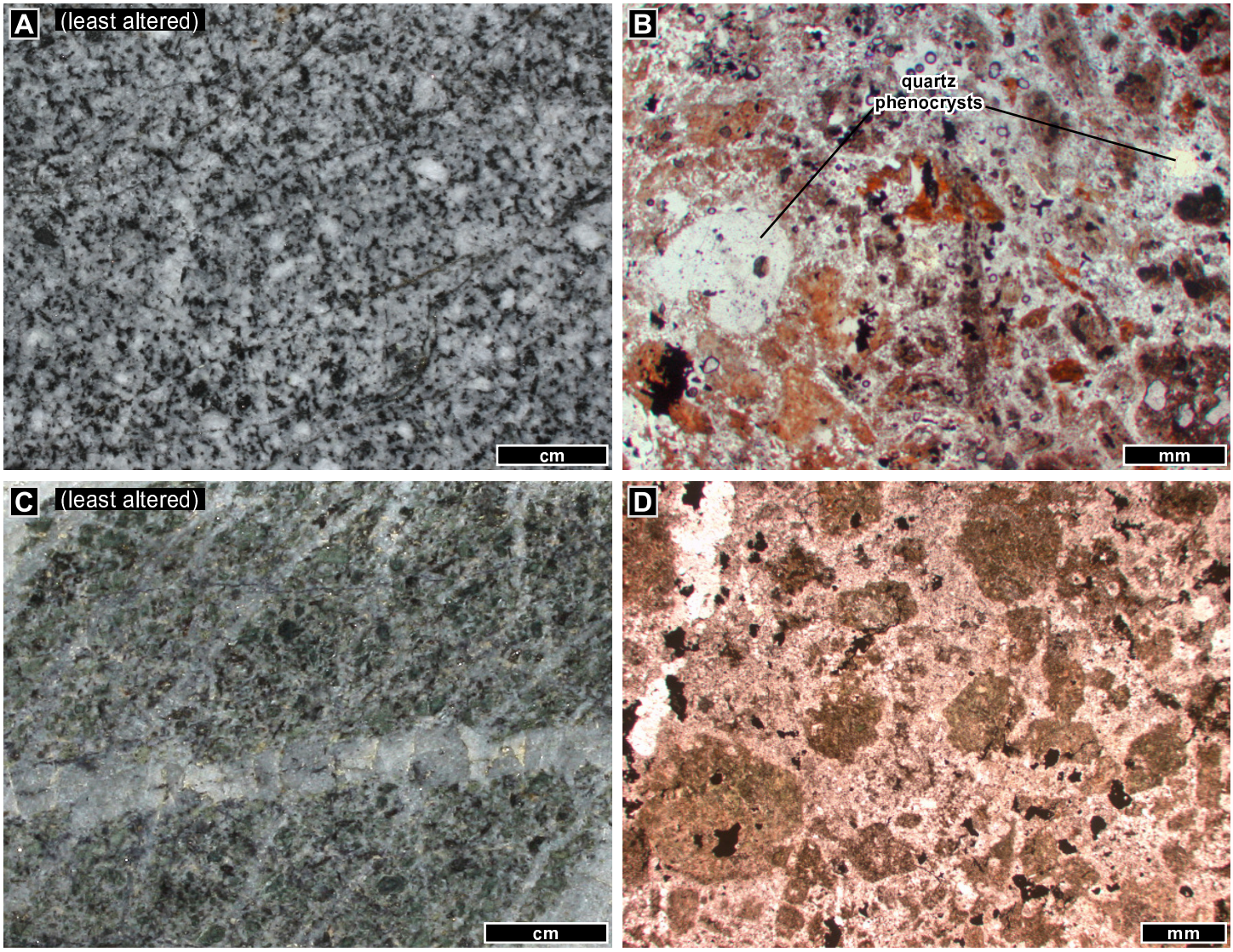

Figure 3.13: Representative core and thin section photos of early (stage I) Golpu intrusions. A) Least-altered plagioclase- and quartz-phyric diorite with abundant biotite as phenocrysts and in groundmass (WR392, 1775.0 m). B) Thin section of the same intrusive phase as in A, showing quartz phenocrysts (labeled), muscovite- and biotite-altered plagioclase phenocrysts (dusty laths) and primary magmatic biotite (phenocrysts in centre of image, and groundmass; WR392, 1728.3 m). C) Hornblende- and plagioclase-phyric stage I diorite. This least-altered sample contains strong texturally selective alteration, with chlorite-, biotite-, and muscovite-altered phenocrysts that can be identified by crystal habit (WR396, 1377.6 m). D) Thin section of the same intrusive phase as in C, showing chlorite-biotite-altered relict subhedral hornblende phenocrysts. Opaque minerals are pyrite, magnetite, and trace chalcopyrite (PPL; WR396, 1309.0 m).

Figure 3.14 (next page): Representative core and thin section photos of the stage II Golpu plagioclase- and hornblende-phyric diorite. A) Typical appearance of scattered black subhedral hornblende phenocrysts (altered to biotite) and more abundant pale green to white plagioclase (altered to chlorite and muscovite; WR392, 1532.5 m). B) Thin section image from the same interval as in A, showing a rhomb-shaped relict hornblende phenocryst replaced by biotite with diffuse or flaky margins (WR392, 1546.3 m). C) Hornblende-phyric dyke, with a sharp intrusive contact with biotite-altered wallrock (WR402, 564.4 m). D) Thin section image showing a higher than typical abundance of relict phenocrysts of hornblende (brown subhedral rhombs) compared to plagioclase (white laths). Groundmass is plagioclase, quartz, and secondary biotite - muscovite (PPL; WR321, 949.4 m). E) Intense selective orthoclase alteration highlights unusually sparse subhedral hornblende phenocrysts (replaced by biotite; plagioclase altered white; WR392, 1398.0 m). F) Stage II Golpu diorite is associated with the main stage of porphyry mineralisation (Chapter Four) and contains disseminated chalcopyrite, pyrite, and magnetite (reflected light; WR392, 1546.3 m).

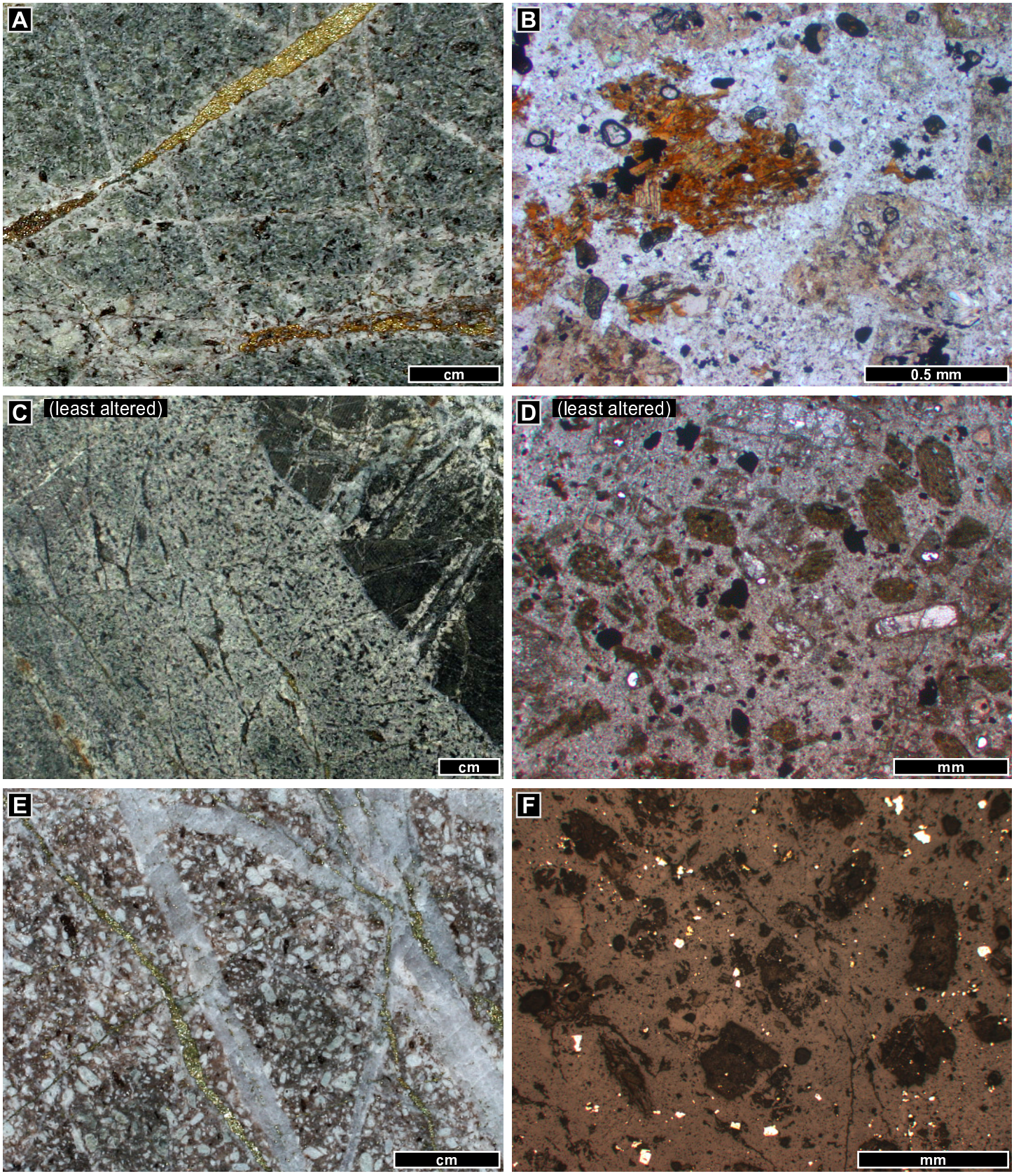

Figure 3.14: Representative core and thin section photos of the stage II Golpu plagioclase- and hornblende-phyric diorite. Image captions are provided on the previous page.

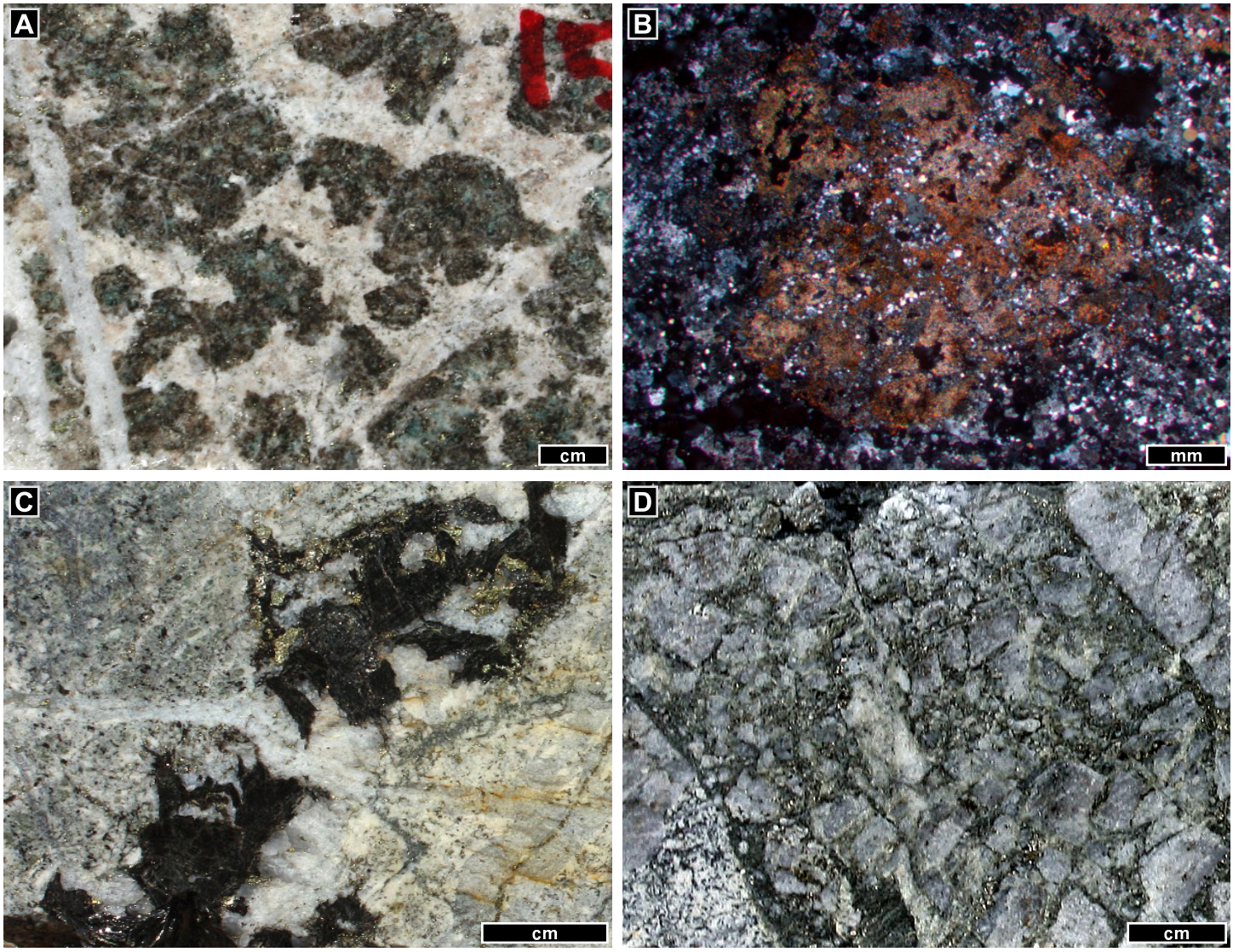

Figure 3.15: Core photos of magmatic-hydrothermal textures in the stage II hornblende- and plagioclase-phyric Golpu diorite. A) Round patches (up to 60 vol %) of biotite (~ 3 / 4) and chlorite (~ 1 / 4), partly overprinted by orthoclase alteration, 30 - 35 metres from the diorite contact (WR396, 1501.0 m). B) Thin section of the same sample as in A, showing a small zone of biotite (+ chlorite) with diffuse margins into fine orthoclase-altered diorite (XPL; WR396, 1501.0 m). C) Coarse-grained biotite in stage II diorite (WR392, 1466.2 m). D) Breccia veins (WR347, 1012.0 m), discussed in the text.

Table 3.4: Geochemistry of least-altered igneous rocks in the study area

Rock type	Stage I Golpu diorites		Stage II Golpu diorite (hornblende- and plagioclase-phyric)		Wafi breccia complex	Hekeng Andesite
Sample ID	392-1728.3	396-1339.7	337-991.5	392-1546.3	199-155.3	315-315.8
Sample description	Moderate orthoclase and muscovite altered plagioclase- and quartz-phyric Golpu diorite	Strong quartz and orthoclase altered hornblende- and plagioclase-phyric Golpu diorite*	Weak muscovite - chlorite - biotite altered diorite with finely disseminated magnetite	Moderate orthoclase - biotite altered diorite with finely disseminated magnetite, bornite, and chalcopyrite	Moderate muscovite - pyrite altered Wafi breccia complex, containing fragments of diorite and wallrock	Least-altered plagioclase-phyric Hekeng Andesite
SiO_2	63.72	82.18	62.40	56.80	57.10	61.32
TiO_2	0.47	0.19	0.26	0.28	0.78	0.52
Al_2O_3	16.18	5.63	10.39	12.46	16.54	17.19
Fe_2O_3	5.10	4.02	17.55	10.19	11.67	6.23
MnO	0.02	0.35	0.05	0.04	<0.01	0.05
MgO	2.19	0.43	0.85	1.03	0.02	2.38
CaO	1.20	0.74	0.40	1.26	0.06	0.82
Na_2O	4.33	0.33	1.65	1.82	0.02	2.47
K_2O	2.61	2.72	3.55	6.07	0.07	2.10
P_2O_5	0.11	0.05	<0.01	0.09	0.19	0.15
S	2.63	2.24	1.16	7.03	8.09	3.35
LOI†	3.30	3.00	1.90	6.40	13.30	6.60
Sum	99.23	99.67	99.02	96.41	99.75	99.83
La	4.6	2.9	1.1	5.5	11.6	10.9
Ce	9.3	7.3	1.7	10.9	23.5	23.6
Pr	1.14	0.86	0.23	1.43	2.69	2.88
Nd	5.4	3.1	1.4	7.0	11.2	10.1
Sm	1.00	0.93	0.29	1.75	1.71	2.64
Eu	0.51	0.41	0.16	0.56	0.53	0.88
Gd	1.03	0.78	0.37	1.87	1.53	2.64
Tb	0.21	0.16	0.05	0.32	0.20	0.50
Dy	1.16	0.80	0.33	1.53	0.74	2.84
Ho	0.33	0.21	0.08	0.38	0.19	0.69
Er	0.69	0.55	0.16	1.18	0.60	1.85
Tm	0.13	0.10	0.03	0.18	0.12	0.31
Yb	0.99	0.40	0.29	0.92	0.82	2.16
Lu	0.14	0.07	0.05	0.20	0.18	0.29
Ag	0.71	0.76	1.02	8.16	1.67	0.13
As	3.3	7.4	<0.5	214.6	531.2	9.4
Au	0.86	0.21	0.44	0.89	0.07	0.07
Co	8.0	11.6	9.2	27.4	17.6	12.6
Cr	3.8	4.5	7.1	4.2	5.4	4.7
Cu	8932.6	3995.7	7667.1	36760.0	400.1	283.6
Ga	18.8	6.6	25.9	15.9	7.0	17.0
Hf	2.5	1.1	1.6	1.8	2.3	2.6
Hg	<0.01	0.03	<0.01	0.17	0.89	0.04
Mo	8.6	349.0	2.1	2.5	2.4	16.3
Nb	6.6	1.0	2.1	2.2	4.7	4.3
Ni	12.6	12.8	10.7	49.9	50.3	6.2
Pb	4.8	14.3	1.9	861.5	169.4	19.2
Rb	57.4	33.9	34.8	78.2	1.4	46.0
Sn	2	2	2	5	5	4
Sr	163.8	31.7	55.5	71.3	791.0	108.1
Ta	0.3	0.2	0.1	0.3	0.4	0.3
Th	3.9	1.4	0.9	2.1	4.5	4.5
U	0.5	0.2	0.1	0.4	1.3	1.1
V	136	45	134	141	139	119
W	4.6	5.8	1.6	5.3	19.3	1.0
Y	6.7	4.1	2.2	11.9	5.2	16.3
Zr	84.5	32.4	53.7	73.3	86.3	102.0

Major element oxides and sulfur are reported in wt. %. Trace elements are reported in ppm. Some elements are omitted from this table, and are provided in Appendix G.
*Note that the least-altered sample of stage I hornblende- and plagioclase-phyric diorite is strongly altered. †Loss on ignition values include sulfur.

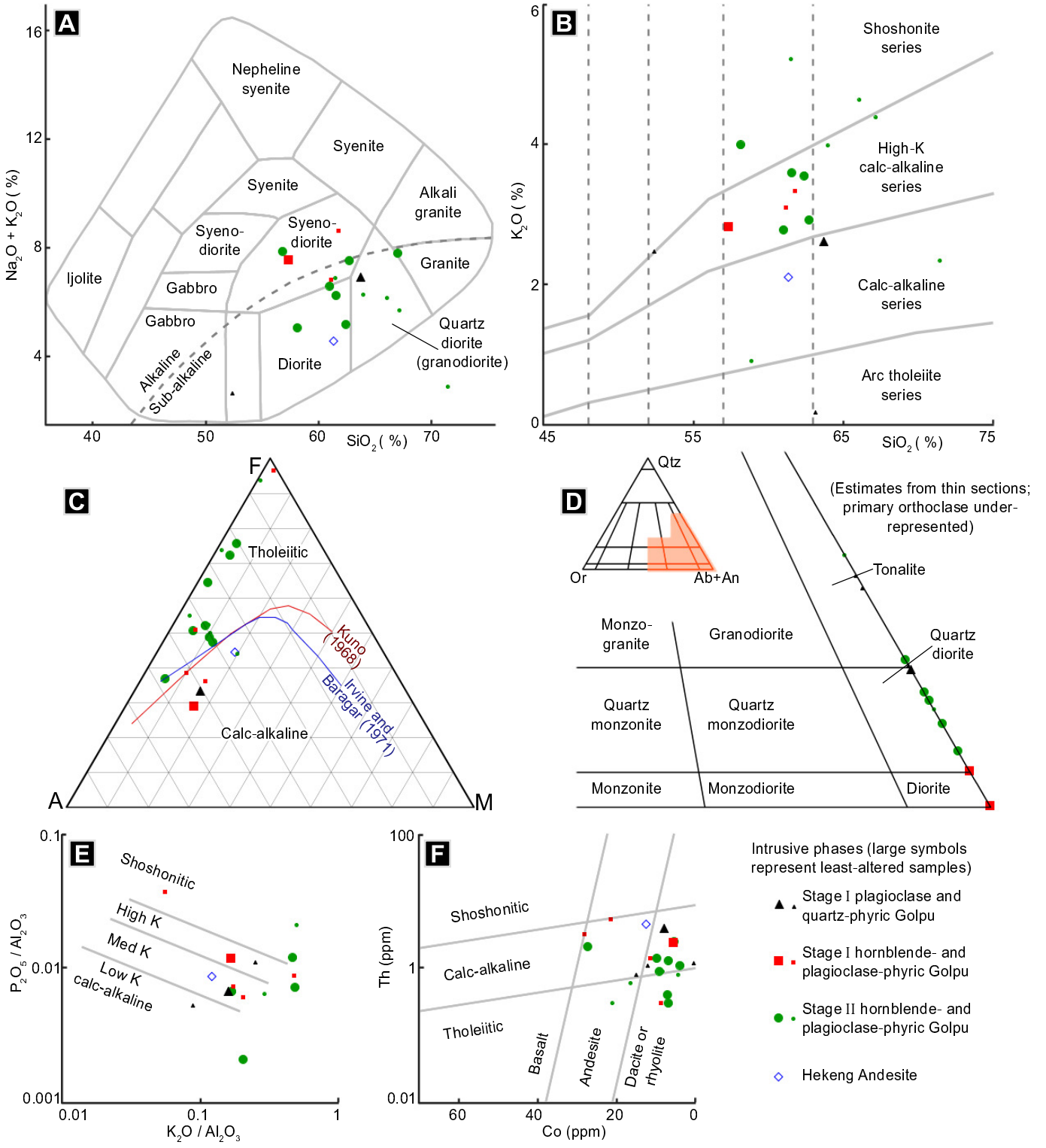

Figure 3.16: Selected whole rock geochemistry and mineralogy of the Golpu intrusions and Hekeng Andesite. Representative data are listed in Table 3.4, and all data are provided in Appendix G. A) Samples are of sub-alkaline to alkaline dioritic compositions in the TAS plutonic diagram of Cox et al. (1979). B) K_2O vs. SiO_2 of Peccerillo and Taylor (1976) indicate mostly high-K calc-alkaline character. C) AFM classifications (where F = FeO_{total}) of Kuno (1968) and Irvine and Baragar (1971) indicate calk-alkaline compositions for stage I Golpu intrusions and Hekeng Andesite. Least-altered stage II Golpu diorite contains finely disseminated magnetite, resulting in the trend towards Fe-rich compositions. D) Normative quartz, plagioclase, and orthoclase in Golpu samples (primary compositions estimated from thin section) indicate diorite to tonalite compositions, but a more accurate assessment of primary orthoclase would likely result in diorite to granodiorite compositions (diagram from Streckesen, 1976). E) P_2O5 / Al_2O_3 vs. K_2O / Al_2O_3 values, as applied by Crawford et al. (2007) to Vanuatu and Sunda arc lavas, are consistent with the medium- to high-K calc-alkaline character of Golpu diorites and Hekeng Andesite. F) Th vs. Co classification of Hastie et al. (2007) indicates samples of mostly calc-alkaline and felsic-intermediate composition.

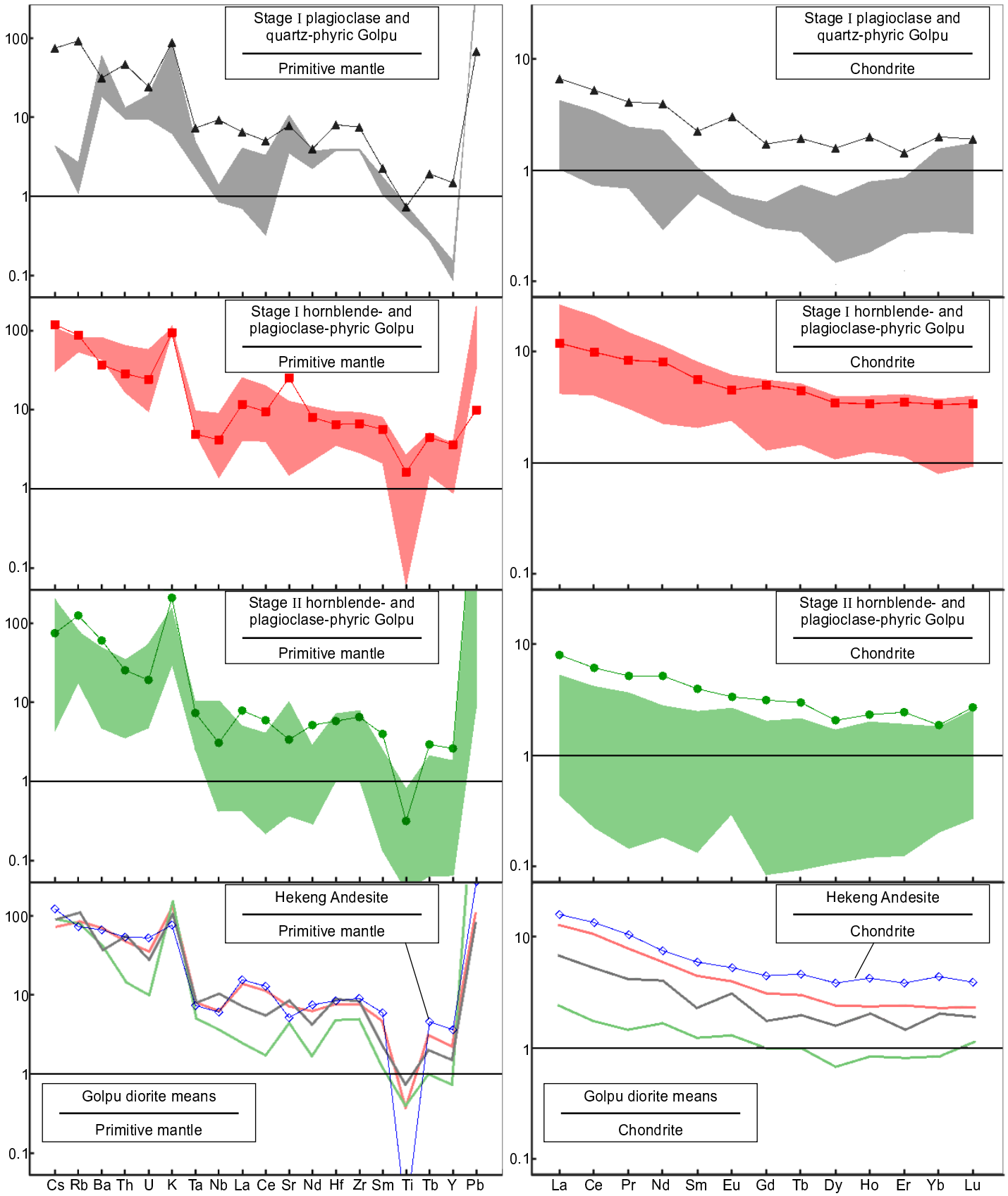

Figure 3.17: Trace element profiles of Golpu diorite intrusions and Hekeng Andesite, normalised to primitive mantle (left column) and chondrite (right column). Normalisation values are from Sun and McDonough (1989). Shaded areas show the range of compositions in altered diorite samples and are not considered to represent primary magmatic compositions. The representative profiles (lines with points) are from least-altered samples 392-1728.3, 377-1650.0, 392-1546.3, and 315-315.8. The data are provided in Appendix G. The sample legend is the same as in Figure 3.16.

3.4.4 Wafi Breccia Complex (a.k.a. Wafi Diatreme)

Age: 9.05 ± 0.23 Ma (interpreted age of entrained breccia fragments; maximum age of eruption).

The Wafi breccia complex is a large multiphase polymictic breccia unit that spans 1050 x 480 metres at surface, and tapers to at least 500 metres below surface (Figs. 3.2, 3.7). Most of this unit consists of fine-grained volcaniclastic material (tuff, fine-grained tuff breccia) that occurs mostly as infill to fragments or lapilli visible in hand sample (Fig. 3.18 A,C,E,F). Some massive to bedded units have fragments that are only visible in thin section (Fig. 3.18 B,D). Some of the massive tuffaceous units contain 30 - 50 % randomly oriented white euhedral to angular fragmented plagioclase crystals 0.5 - 1 mm long. Tau-Loi (1996) documented low-angle graded cross beds of fine pyroclastic material in outcrop, which he described as base surge deposits.

The coarse or visible fragment breccia component makes up about 90 % of the unit, with fragments in intervals 60 - 200 metres thick that are mostly upward-fining and more fragment-rich near their base (e.g., WR199, WR301, and WR321; Appendix B). These intervals are infill-supported chaotic breccias with 50 to 90 % fine-grained infill by volume. Of the fragments, 95 % are angular to sub-angular metasiltstone and metasandstone. Most are muscovite- or muscovite- and kaolinite-altered, but some are biotite-altered (Fig. 3.18 E). Rare fragments contain truncated quartz or quartz-pyrite veins (Fig. 3.18 F). Approximately 5 % of the fragments are sub-rounded to irregular amoeboid relict fragments of possible diorite (Fig. 3.18 C,E; see discussion). Fewer than 1 % of the fragments are fine plagioclase-phyric crystal tuff. Small dacitic dykes have been reported in parts of the breccia complex (Morehari et al., 2009). They do not occur in the drill core logged in this study, and the few thin intervals logged by MMJV workers do not correlate well across drill holes.

Most of the breccia complex has been strongly altered to quartz, alunite, pyrite, kaolinite, dickite, muscovite, and / or pyrophyllite (Chapter Four). In addition to the small grain size, the intensity of alteration impedes thin section identification of mineral phases (e.g., Fig. 3.18 D). However, XRD analysis of the least-altered fragment-rich sample shown in Figure 3.18 E identified 35 wt % plagioclase, 26 wt % biotite, 15 wt % orthoclase, 8 wt % pyrite, 7 wt % quartz, and 7 wt % muscovite (WR199, 155.3 m; Appendix E). This is consistent with muscovite and pyrite alteration of diorite and biotite-altered wallrock fragments.

The south and east contacts of the Wafi breccia complex with Owen Stanley rocks are poorly preserved due in part to intense hydrothermal alteration (Chapter Four). However, there are several well-preserved breccia veins within 60 metres of its eastern contact (Fig. 3.19 A-D) that I interpret to be cogenetic with the main breccia complex, on the basis of similar fragment types and timing with respect to biotite, muscovite - quartz - pyrite, and kaolinite - dickite veins and alteration (Chapter Four). These sharp-walled breccia veins are polymictic, chaotic, fragment- to infill-supported breccias with an average of 50 % subangular fragments. Approximately 55 % of the fragments are weakly muscovite- and kaolinite-altered metasiltstone (< 6 cm in diameter). About 35 % are grey-yellow muscovite-altered and quartz - pyrite veined metasiltstone and metasandstone, and 10 % are pyrite veined fragments of an earlier breccia phase that contains pyrite-veined wallrock fragments (< 2 cm in diameter) in a quartz cement to hydrothermal sandstone infill (Fig. 3.19 C). Parts of these breccia veins contain tan muscovite- and kaolinite-altered hydrothermal mudstone to sandstone without large fragments (Fig. 3.19 B).

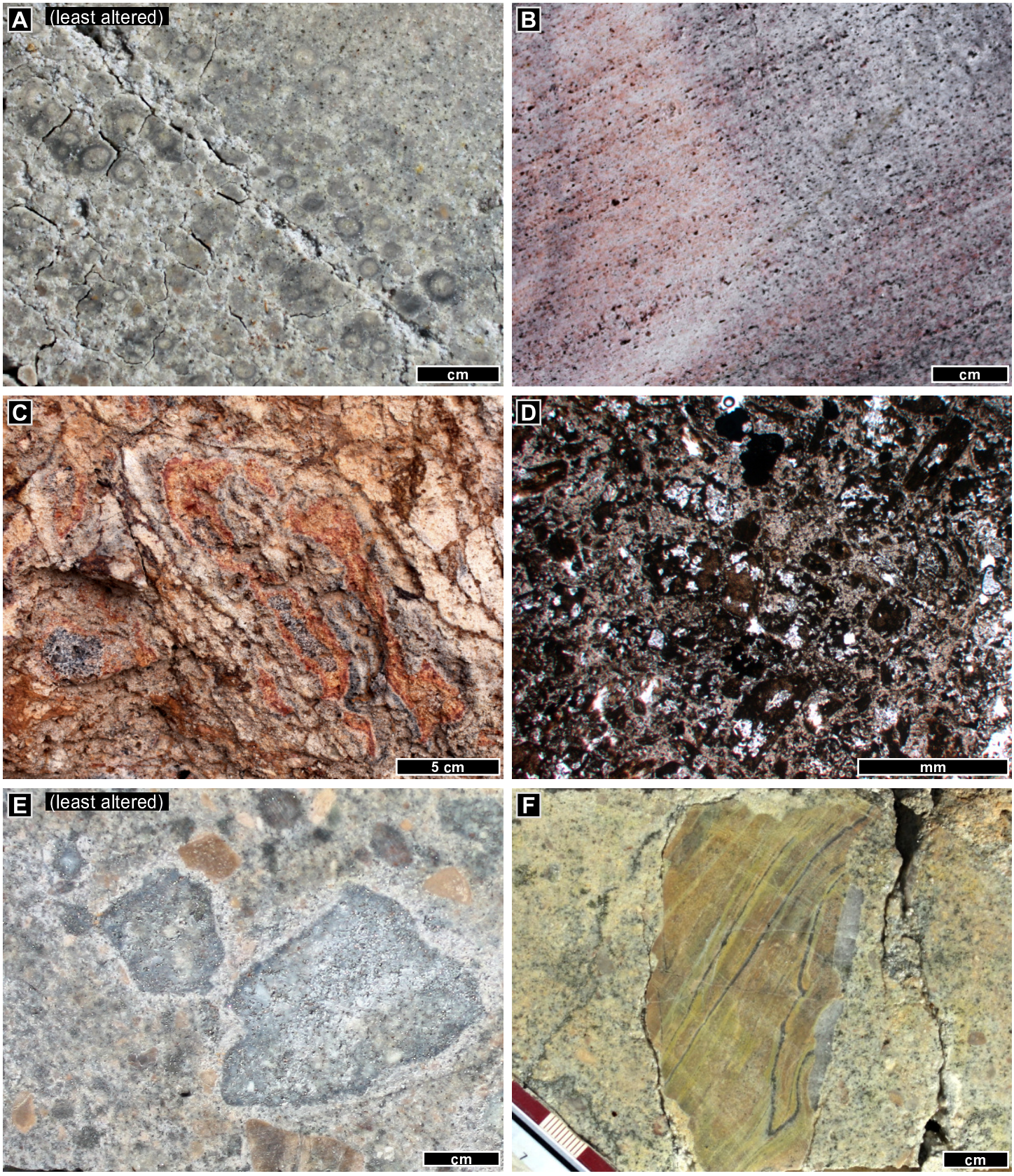

Figure 3.18: Representative photos of the Wafi breccia complex. Image captions are provided on the next page.

Figure 3.18 (previous page): Representative photos of the Wafi breccia complex. A) Weakly stratified, kaolinite- and muscovite-altered accretionary lapilli < 6 mm across (WR199, 132.4 m). B) Finely bedded tuff. Porosity is secondary (quartz - alunite - hematite altered sample; WR321, 8.9 m). C) Irregular amoeboid fragments or blocks (left and centre) of possible porphyritic diorite, similar to image E (outcrop near top of Wafi Hill). D) Photomicrograph of the fine-grained infill component that makes up most of the unit, with relict angular to sub-rounded fragments < 1 mm across (PPL; WR321, 150.0 m). E) Fragment size increases downhole in several layers over tens to hundreds of metres. Larger amoeboid fragments shown here are possibly diorite, and smaller fragments are poorly preserved biotite-altered Owen Stanley rock (muscovite - pyrite altered sample, WR199, 155.3 m). F) Metasedimentary wallrock fragments occur throughout the breccia complex, such as this tabular quartz-veined and muscovite-altered metasiltstone fragment which occurs 210 metres away from the nearest wallrock (WR199, 48.8 m).

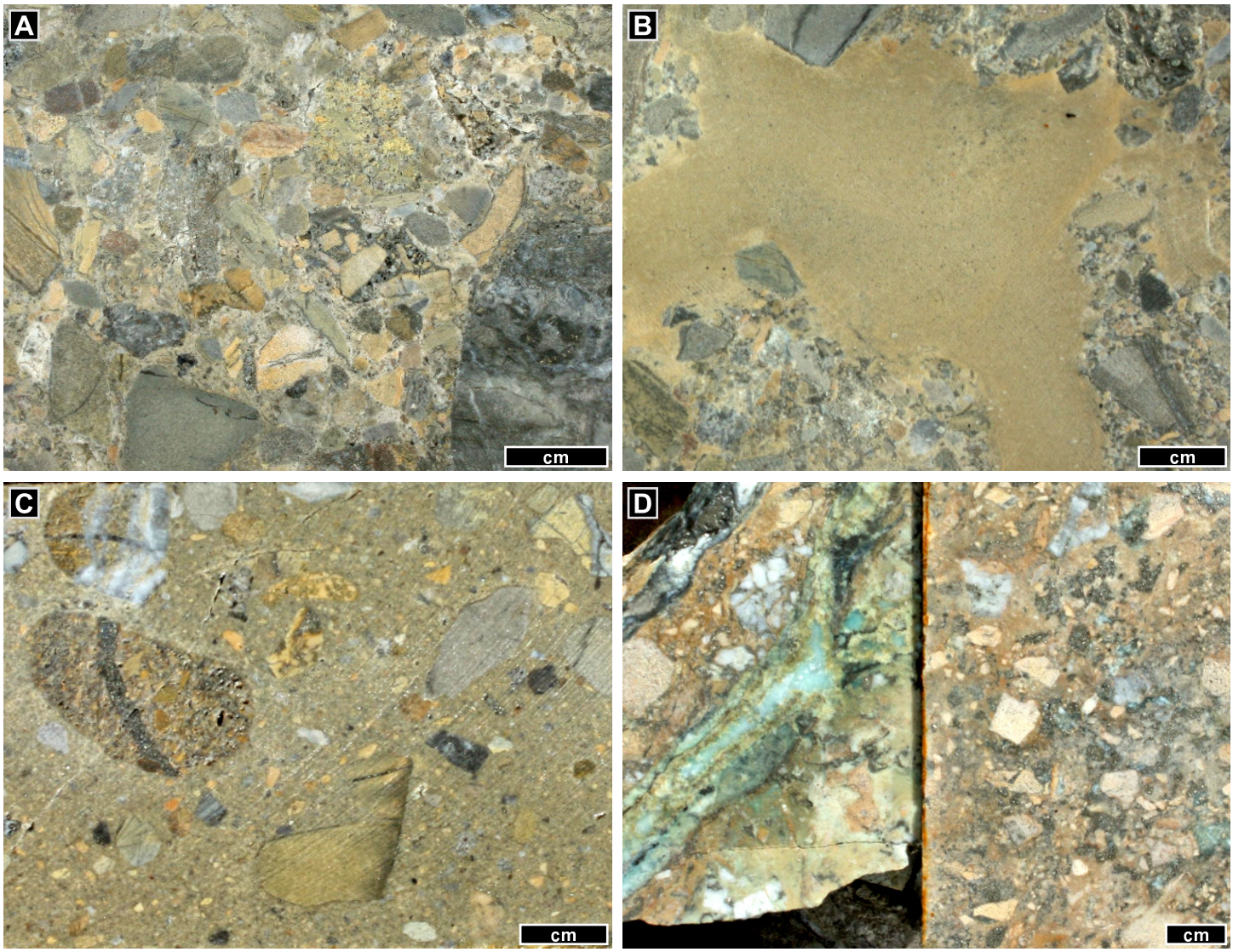

Figure 3.19: Core photos of breccia veins within 60 metres of the main Wafi breccia complex. A) Polymictic, chaotic, locally fragment-supported breccia vein with several fragment types discussed in the text (WR301, 296.0 m). B) Hydrothermal mudstone to sandstone with irregular margins, through the same breccia vein as in A (WR301, 296.8 m). C) Truncated quartz veins in several fragments and one breccia fragment (with quartz-cemented hydrothermal sandstone infill) cut by a quartz-pyrite vein (WR301, 299.3 m). D) Diffuse kaolinite - dickite veins occur near the margins of some of the breccia veins (Chapter Four; WR301, 317.2 m).

3.4.5 Post-Mineralisation Units

Hekeng Andesite

Age: No data, but a lack of alteration (apart from supergene oxidation) in this unit located atop the Golpu lithocap implies emplacement after the Golpu intrusions and the Wafi breccia complex.

The Hekeng Andesite unit occurs in outcrop (Fig. 3.20 E) as an unmineralised massive dyke < 70 metres wide, unconformably overlying metasedimentary rock (CRA Exploration Report, 1997). It contains about 25 - 40 % white plagioclase phenocrysts < 2 mm long in a grey-green (or red, where oxidised) chloritic groundmass (Tau-Loi, 1996). This unit does not occur in the drill core logged for this study. Whole rock geochemical results from a sample of this unit are shown in Table 3.4 and in Figures 3.16, 3.17, and 3.22.

Holocene cover

Age: 37 - 38 kyr B.P. (^{14}C age from Tau-Loi, 1996).

Parts of the study area, especially east of the Wafi breccia complex, are overlain by poorly consolidated Holocene sedimentary rock, shown as the Wafi Conglomerate in Figures 3.3 to 3.7. The Wafi Conglomerate consists of mostly rounded and tabular clasts of Owen Stanley rocks and minor carbonaceous material supported in a poorly sorted sandy matrix (Fig. 3.20 A,B). Fewer than 5 % of the clasts are cut by quartz veins truncated at clast margins. This unit is in places underlain by up to four metres of Hekeng Breccia, which contains angular to sub-rounded clasts of Owen Stanley rocks and porphyritic diorite in a hematite-oxidised matrix. A few of the larger clasts are white due to quartz - alunite alteration (Fig. 3.20 C,D). The Hekeng Breccia and Wafi Conglomerate are respectively interpreted as recent gravity- and water-transported sediments (i.e., talus / scree overlain by alluvial gravel; Morehari et al., 2009).

Surface oxidation profile

Tropical weathering in the study area has resulted in a zone of selective to locally pervasive oxidation (hematite with less abundant goethite and jarosite) about 20 - 130 metres thick (e.g., Fig. 3.18 F). The zone of fracture-hosted oxidation extends deeper, to about 320 metres below surface. The deepest extent of supergene oxidation is assocated with the east-dipping Hekeng fault (Figs. 3.3 to 3.6).

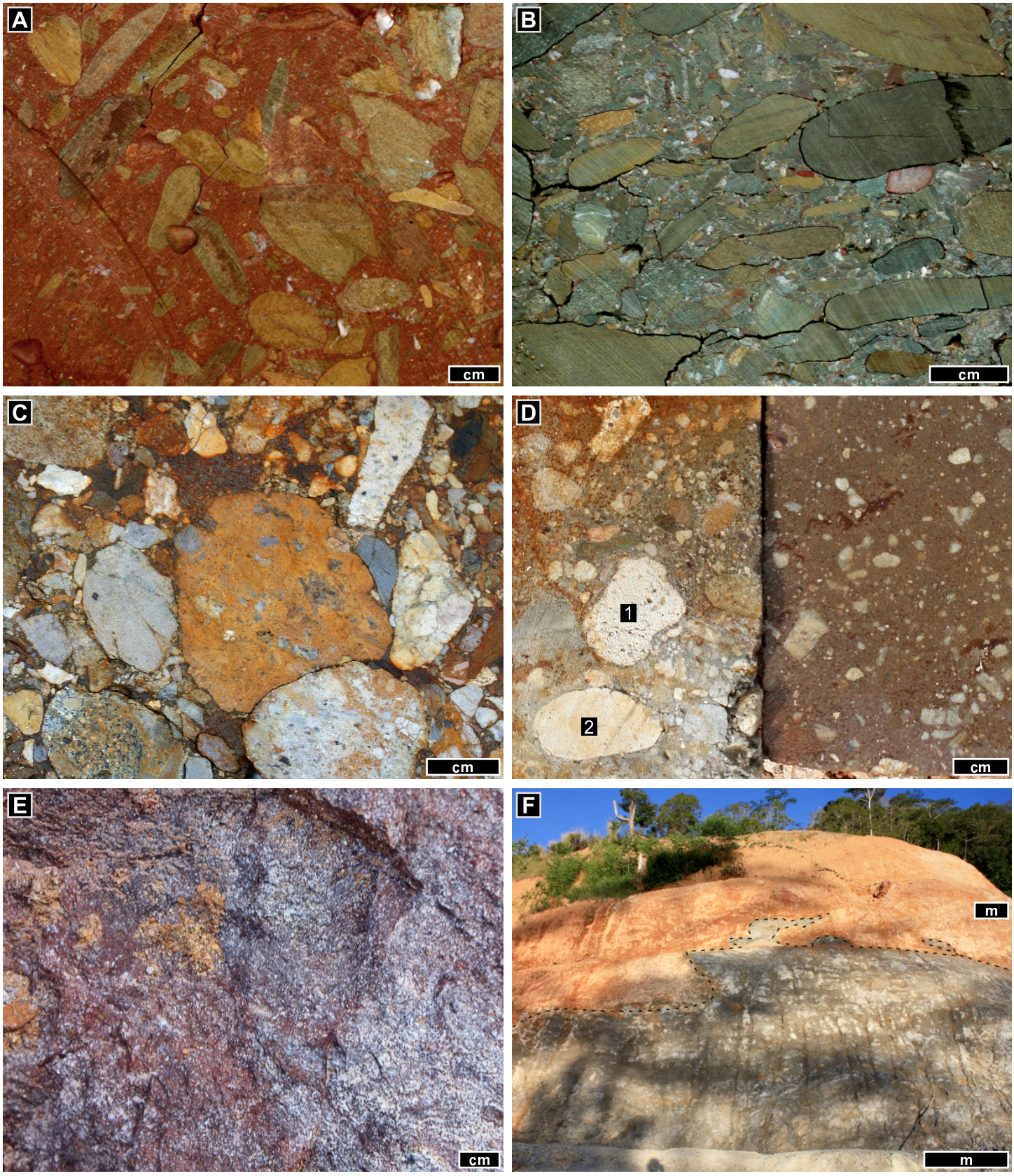

Figure 3.20: Post-mineralisation features in the study area. A) Oxidised Wafi Conglomerate, with matrix-supported angular to rounded clasts of altered and veined metasedimentary rock and quartz vein fragments (WR337, 31.3 m). B) Wafi Conglomerate below pervasive surface oxidation (WR437, 42.6 m). C) Fragment-supported Hekeng Breccia underlies the rock in B (WR347, 67.2 m). D) Hekeng Breccia containing kaolinite-altered (1), quartz- and alunite-altered (2), quartz vein, and metapelite fragments. This interval occurs within a few metres of Golpu diorite (WR398, 8.8 m). E) Outcrop of Hekeng Andesite, with small white plagioclase phenocrysts in a red (oxidised, but otherwise unaltered) groundmass. F) Machinery-exposed outcrop showing the tropical oxidation profile in Owen Stanley metasiltstone (marked with dashed line) near Wafi camp. Metre scales are approximate.

3.5 Local Structures

Broad structure of host stratigraphy

Corbett (1990) observed that bedding planes at Wafi dip to the east, whereas the weak regional metamorphic planar fabric of the host rocks dips NE to NNE. This is consistent with the orientations of major bedding packages in drill core that dip from 48° to 63° to the E-ESE (as shown in Figs. 3.2 - 3.7), and with a weak planar fabric that is near-parallel to the bedding planes where evident in drill core.

Faults

Many structural interpretations have been proposed for the study area (e.g., Corbett, 1990; Tau-Loi, 1996; and the EL440 annual report compiled by Morehari et al., 2009). The most recent structural interpretation (Morehari et al., 2009) identified two NNE-trending graben walls, and several NNW-trending vertical faults (Fig. 3.21 B). The graben bounding structures are interpreted largely on the basis of topography (C. Muller, pers. comm., 2011). Morehari et al. (2009) also noted shallow dipping faults around the Wafi breccia complex, interpreting them to be ring thrusts formed during diatreme eruption.

Rather than address the evidence for each structure or broad structural framework proposed by previous workers, the drill data were used to identify faults or fault zones according to either (1) evidence of offset or (2) evidence of the fault zone. The first criterion requires an abrupt change in alteration style or lithology across the proposed fault contact, and the second requires an interval identified as “fault gouge” or equivalent in a plane (i.e., across several drill holes).

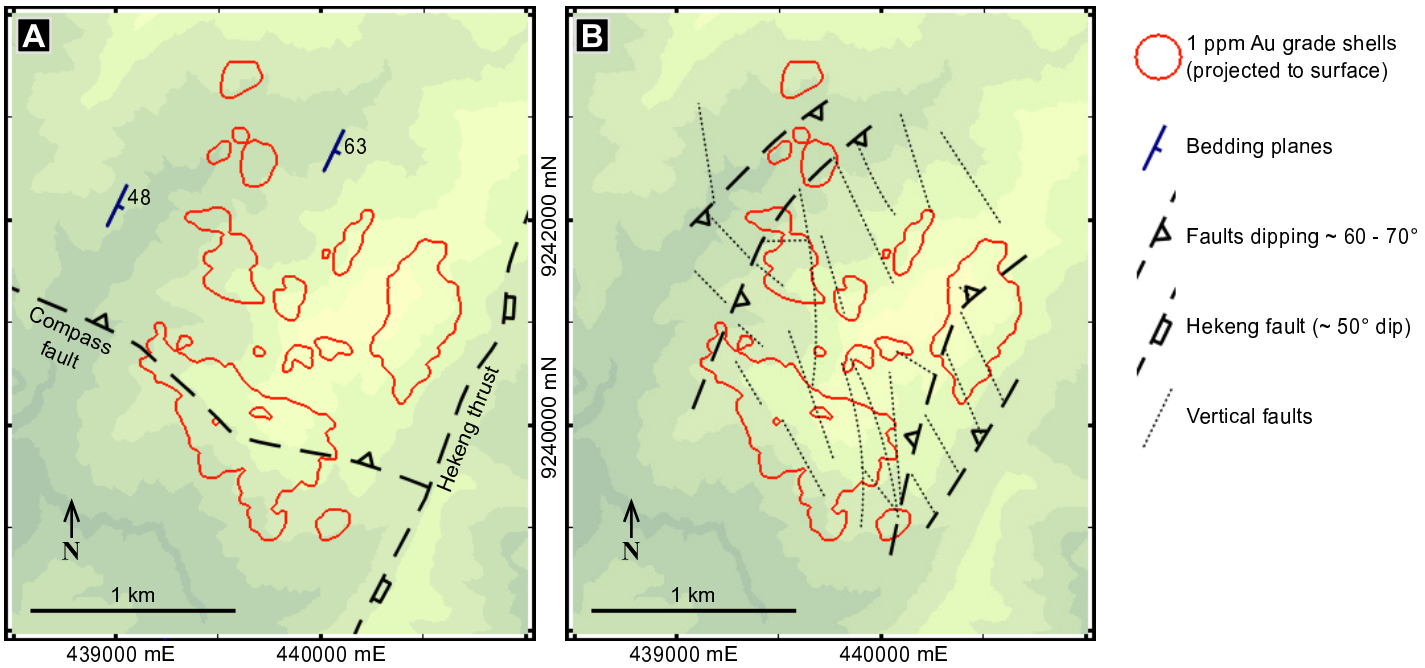

Figure 3.21: Summary of surface structural interpretations at Wafi. A) Fault and bedding planes proposed in this study entirely on the basis of drill data (see text). B) A recent structural interpretation compiled by Morehari et al. (2009).

Two zones that meet the above criteria for faults in drill core are the Compass fault and the Hekeng thrust (Fig 3.1 - 3.8 and 3.21 A). Clear offset of Owen Stanley units in drill core indicates that the Compass fault dips 65 - 70° NNE, towards and possibly into Golpu diorites, although its extent at depth is unclear (e.g., Fig. 3.7). The Hekeng fault dips 55° ENE, shallowing slightly with depth, and is defined by 2 - 15 metres of fault gouge in drill core that marks an abrupt transition from (least-altered) metaconglomerate-dominant to (propylitic- and sericitic-altered) metasandstone-dominant rocks (e.g., WR 377, 245.0 m; Appendix B). The abrupt change in alteration styles suggests that the Hekeng fault is a post-mineralisation structure. A third structure, the Reid fault, has been proposed by D. Finn and R. Reid (pers. comm., 2012) based on changes in Cu and Au grades across parts of its surface. The inferred location of the Reid fault is indicated in Figures 3.1 to 3.8, although I have not been able to identify the fault zone in my logged holes or in the MMJV core logs.

3.6 Discussion

3.6.1 Metamorphic Facies of Host Rocks

The least-altered metasiltstone, metasandstone, and metaconglomerate samples generally contain the same assemblage of plagioclase, quartz, chlorite, actinolite, pyrite, and trace magnetite. Some input from weak propylitic alteration is likely in some of these samples, but many of these samples were collected east of the post-mineralisation Hekeng thrust. Assuming this assemblage represents the regional metamorphic mineral assemblage, these rocks are of lower to middle (chlorite zone) greenschist metamorphic facies (in metapelites to metagreywackes; Winter, 2010). This is consistent with the metamorphic grade reported regionally (Davies, 2012), and accounts for the lack of biotite in least-altered samples.

3.6.2 Evidence that the Wafi Breccia Complex is a Diatreme

In 1990, field investigations at Wafi led R. Sillitoe to conclude that the Wafi breccia complex (at the time described as a conglomerate) was a diatreme (Erceg, 2008). Diatremes are a widespread component of porphyry systems, usually occurring after (and perhaps contributing to the cessation of) Cu-Au porphyry mineralisation (e.g., Sillitoe, 1985; Garcia, 1991). Pre-mineralisation diatremes are less common (e.g., Hehnke et al., 2012; Sillitoe et al., 2013).

A diatreme is formed by phreatomagmatic eruption and associated wallrock collapse (Self et al., 1980). This results in mostly ash-sized fragments, along with larger volcaniclastic and wallrock fragments that are reworked during wall collapse. Diatremes also have upward-flaring geometries as a result of eruption within 2500 metres of surface, with specific shapes depending on depth of explosions and competency of host and overlying rock (Vesperman and Schmincke, 2000).

A single diatreme may contain several distinct breccias, but the most common component is fine-grained breccia that contains fragments of country rock (Head and Wilson, 2002). Diatremes may grade into dykes at depth, and may be expressed at surface as maars (Vesperman and Schmincke, 2000). In the case of kimberlitic diatremes, dykes are common but are “small, rootless, sinuous, and pinch out laterally and vertically” (Head and Wilson, 2002). Late (diatreme contact-cutting) dykes are rare, indicating that diatremes are usually the closing

stage of magmatism (Head and Wilson, 2002).

A clear root zone to the Wafi breccia complex has yet to be intersected in drill core. However, the unit contains a large volume of fine tuffaceous infill and small breccia fragments (Fig. 3.18 D), an abundance of metasedimentary country rock fragments, and irregular dacite dykes within the main body of the Wafi breccia complex that are all consistent with the characteristics of diatremes (as described by Sillitoe, 1985; Vesperman and Schmincke, 2000; Head and Wilson, 2002; and Martin et al., 2007). Its origin by phreatomagmatic eruption is further supported by the following arguments:

- The U-Pb zircon age of 9.05 ± 0.23 Ma is consistent with a magmatic source and eruption after (or with) the last Golpu intrusions.
- The amoeboid fragments in Figure 3.18 C and E may be juvenile magmatic clasts, which would indicate a porphyritic magma invading (or contributing to the eruption of) a co-magmatic hydrothermal breccia pipe, as documented by Richards (2011; his Figure 8). Hydrothermally altered porphyritic fragments have also been reported in the diatreme (CRA Exploration report, 1997).
- The high biotite and orthoclase contents in the least-altered sample from WR199 – about 500 metres from the zone of potassic alteration around Golpu – suggest a Golpu-proximal source of fragments and / or magma, given that biotite and orthoclase are both present at less than trace amounts in the least-altered host rocks. They also indicate that eruption occurred after or at the end of Golpu intrusions and associated potassic alteration of wallrock.
- The accretionary lapilli in Figure 3.18 A may indicate a process wherein their outer layers accumulated by suspension of particles in a gas-fluidised environment. Such high-energy gas-fluidised conditions can be sustained in diatreme vents during eruptions (Gernon et al., 2009).
- The base surge beds documented by Tau-Loi (1996) may represent deposits in the subaerial parts of a maar-diatreme breccia complex (as in Davies et al., 2008).

3.6.3 Composition of Golpu Intrusions

The Golpu diorites have geochemical characteristics that are typical of intrusions related to Cu-Au porphyry deposits, as summarised in Table 3.5.

Table 3.5: Key characteristics of Golpu diorites compared to intrusions of porphyry deposits in general

General characteristics of porphyry deposit intrusions	Characteristics of Golpu diorites (all intrusions unless specified)
Calc-alkaline composition (high-K calc-alkaline intrusions generally associated with porphyry Cu-Au; Cooke et al., 2005)	Calc-alkaline to high-K calc-alkaline composition (e.g., Fig. 3.16, and least-altered stage II mean $Na_2O + K_2O$ = 7.0 wt %)
Intrusions of intermediate to felsic composition (Sillitoe, 2010)	Intermediate to felsic composition (e.g., least-altered stage II mean SiO_2 = 62.1 wt %, Co = 13.5 ppm, Zr/TiO_2 = 206)
Intrusions enriched in LILE and other fluid-mobile elements with respect to primitive mantle, with fractionated LREE and relative depletions in HFSE (i.e., profiles of arc magmatism; Ayuso, 2010)	Fractionated REE patterns (e.g., least-altered stage II mean La/Yb_{cn} = 3.2), with relative Ta, Nb, and Ti depletions (e.g., Fig. 3.17; stage II mean Nb/Nb* = 0.48)
Mineralising intrusions generally have lower total REE and relative depletions in MREE to HREE (Gd to Lu; Ayuso, 2010)	Stage II (main stage mineralising) Golpu diorites have lower total REE than stage I diorites, with convex chondrite-normalised MREE to HREE (e.g., Fig. 3.17 D)

3.6.4 Evidence for Arc Magmatic Processes

Porphyry deposits are generally associated with magmatic arcs in convergent settings or zones of active uplift (Sillitoe, 1972). Golpu and younger porphyry deposits in the New Guinea Orogen formed after south-directed Trobriand-Wewak subduction, in a setting in which crustal thickening – or impediment to volcanism – was driven by west-directed subduction of an antiformal slab complex (Chapter Two). Partial melts in this setting may have been derived by thickening of the lithosphere (Richards, 2009), or by the more common process of slab dehydration (wherein water contributed by the Solomon Sea Plate was the key driver of melting in overlying mantle). In either case, Golpu can be deemed a "postsubduction porphyry deposit" in that it is sourced from previously subduction-modified mantle of the type described by Richards (2009). Also regardless of the mechanisms driving partial melting, the magmas generated in this environment are expected to record a magmatic arc signature (Richards, 2009), because the ultimate source of the partial melts is Trobriand-Wewak subduction-modified upper mantle.

In Golpu diorite samples, measures of slab input of nonconservative elements (e.g., Rb or Th/Yb in Fig. 3.22; Pearce and Peate, 1995), and relative HFSE depletion (e.g., Ta/Yb < Th/Yb in Fig. 3.22 B) clearly point to arc magmatic processes. Additionally, the relative MREE to HREE depletion in some stage II diorite samples (e.g., Fig. 3.23 C) is a feature of mineralisation-associated arc magmas (Ayuso, 2010) that may indicate extensive fractionation of hornblende in the parent magma (i.e., a very hydrous parent magma; Rohrlach and Loucks, 2005). A more hydrous composition of the stage II diorite is also implied by the abundance of hornblende, and by textural evidence for local accumulations of volatile components in the crystallising magma. In particular, the sample shown in Figure 3.15 A and B, collected 35 metres from the stage II diorite intrusive contact, may be relict orbicular diorite. The pegmatitic patches (3.15 C) throughout the stage II intrusion similarly indicate local volatile accumulations (as in Candela, 1997). Veins (mostly quartz by volume) and vein breccias are also most abundant within and near the margins of the stage II diorite (Chapter Four).

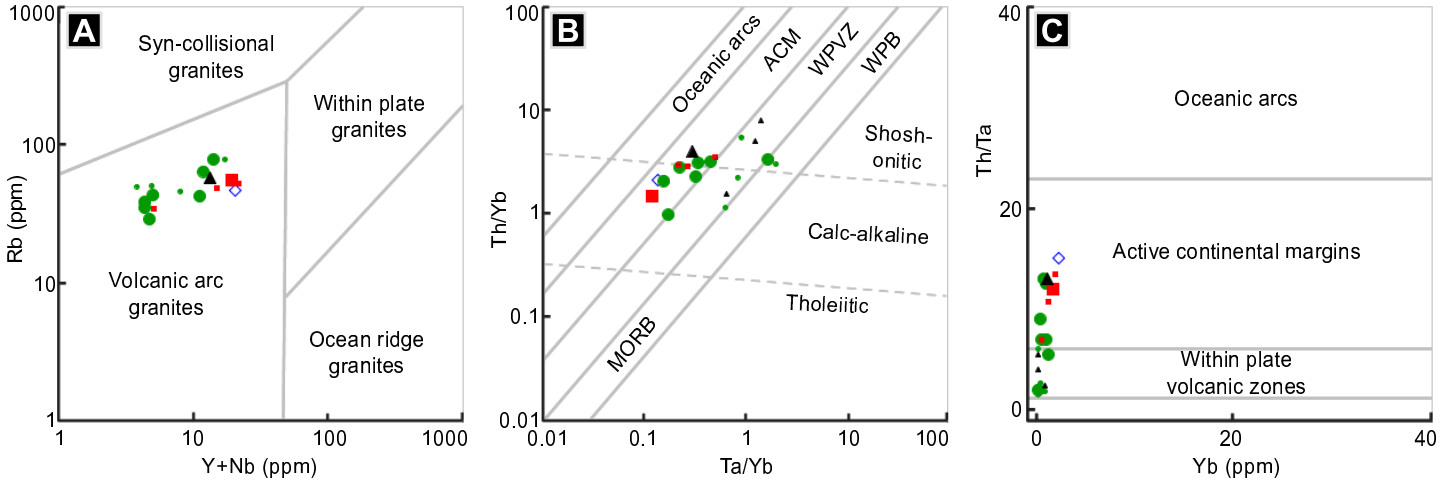

Figure 3.22: Tectonic discrimination diagrams for Golpu diorite and Hekeng Andesite samples. The sample legend is the same as in Fig. 3.16. A) Rb vs. Y+Nb of Pearce et al. (1984) showing lower incompatible element contents consistent with an arc setting (see text). B) Th/Yb vs. Ta/Yb of Pearce (1982) and (C) Th/Ta vs. Yb of Gorton and Schandl (2000) for felsic and intermediate rocks, with Golpu diorites mostly in the field of active continental margins. Abbreviations: ACM = Active continental margins; WPVZ = Within plate volcanic zones; WPB = Within plate basalts; MORB = Mid-ocean ridge basalts.

3.7 Summary

The regional stratigraphy at Wafi-Golpu comprises broadly E- to ESE-dipping metasedimentary rocks of lower to middle greenschist metamorphic facies. They were intruded by diorite stocks with magmatic arc geochemical characteristics, including calc-alkaline to high-K calc-alkaline and intermediate to felsic compositions. Figure 3.23 summarises the general transition from (1) early intrusions (stage I Golpu and Nambonga diorites) to (2) a narrow intrusion with several dykes running partly along previous intrusive contacts (stage II Golpu), to (3) explosive eruption to surface (the Wafi breccia complex). The roots of the Wafi breccia complex have not yet been defined by drilling.

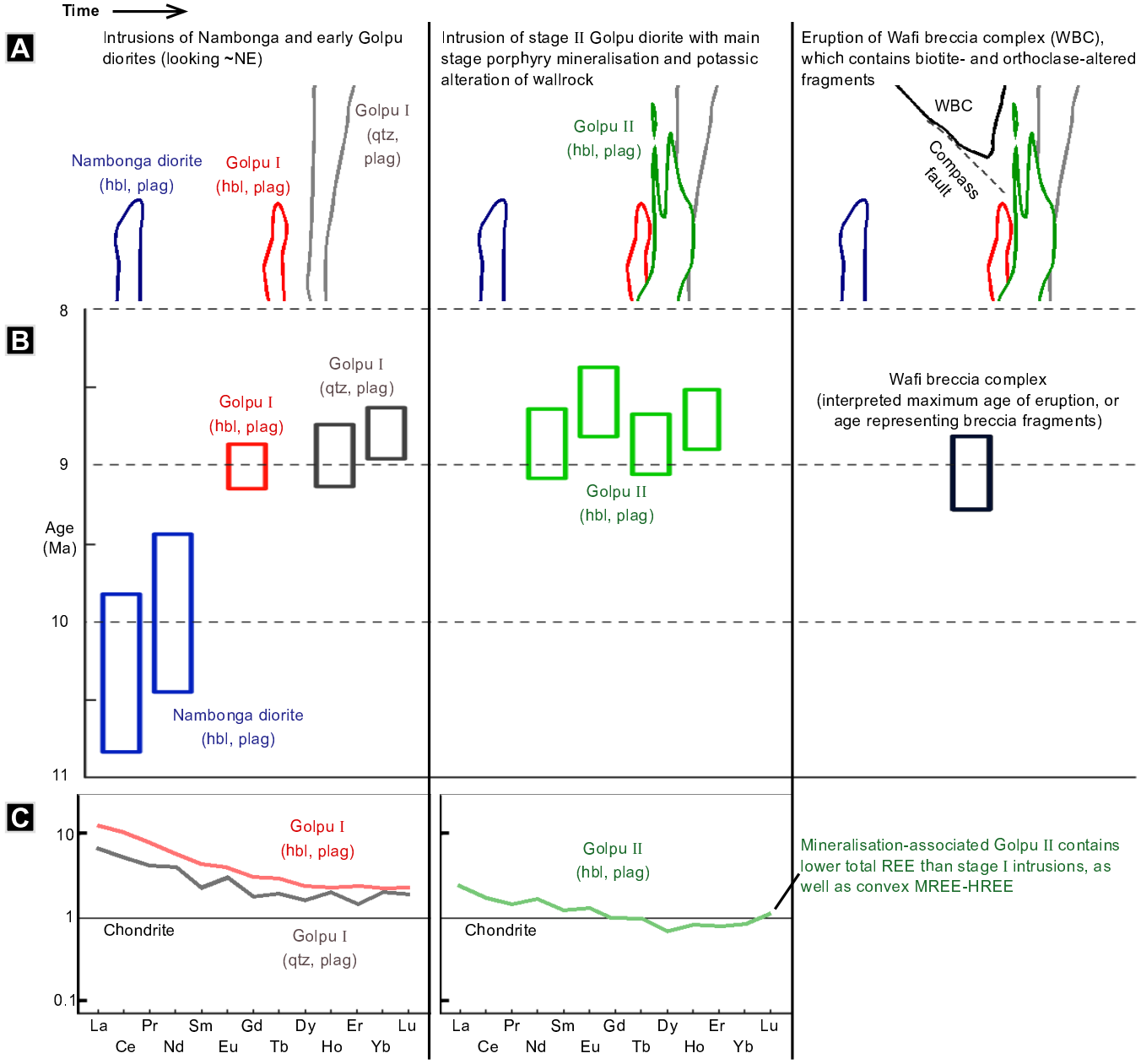

Figure 3.23: Summary of the timing and spatial relationships between igneous units in the study area. A) Schematic of intrusive and eruptive events from earliest (left) to latest (right). The third panel, showing the eruption of the Wafi breccia complex or diatreme, also indicates the location of the Compass fault as seen in NW-looking sections (e.g., Fig. 3.7). It extends from the southern diatreme margin towards the Golpu porphyry. B) Summary of geochronology results from this study and other workers, with age bars shown at 2σ. Samples and data sources are the same as in Table 3.2. All results shown are U-Pb (zircon) except for the Nambonga intrusive ages (K-Ar hornblende from Tau-Loi, 1996). C) Chondrite-normalised REE profiles of least-altered Golpu diorite sample means, as in Figure 3.17. Phenocryst abbreviations: hbl = hornblende; plag = plagioclase, qtz = quartz.

Chapter 4
Alteration and Mineralisation

4.1 Introduction

Coupled porphyry and high sulfidation epithermal deposits are generally characterised by an upward and outward-flaring zonal arrangement of veins and altered rocks (Chapter One). Studies of porphyry and epithermal deposits fundamentally rely on an understanding of the spatial and temporal relationships between their veins and altered rocks. For example, investigations into the behaviour of fluids and rocks in mid to shallow crust (e.g.: Einaudi et al., 2003; Heinrich, 2007), or the timescales and key processes involved in porphyry-epithermal mineralisation (e.g.: Arribas et al., 1995; Sillitoe, 1999; Masterman et al., 2005; Braxton et al., 2012) are all informed by the paragenesis of veins and alteration assemblages documented in individual deposit studies. Mineral exploration models are ultimately reliant on these same investigations (e.g., Chang et al., 2011).

The Wafi-Golpu deposit is a mineralogically complex system of veins and altered rocks. The hydrothermal mineral assemblages record a wide range of geological conditions, demonstrating transitions between porphyry, high sulfidation, and intermediate sulfidation epithermal environments. This chapter systematically documents the mineralogy, zonation, and relative timing of these contrasting vein and alteration assemblages. Comparisons of Wafi-Golpu's paragenetic sequence, scale, and zoning relationships are made to other well-documented porphyry and epithermal deposits. This information provides the basis for investigations into the fluid pH and temperature conditions, mineralising processes, and absolute timing of the vein and alteration events in Chapters Five and Six.

4.2 Methods and Terminology

4.2.1 Sources of Data

This study involved detailed graphic core logging of 13 drill holes for a total of 14,810 metres. Digitised versions of the graphic logs are provided in Appendix B. This information has been supplemented by core logs recorded by MMJV and previous site geologists, which include field observations of vein and altered rock mineralogy, intensity of alteration, and frequency of veins. Mineral ID and abundances were also recorded in the XRD and petrographic analyses of core samples by Leach (1989, 1990a, 1990b, 1990c, 1990d, 1991a, 1991b) and Tau-Loi (1996). Sample locations for these data are indicated in Figures 3.3 to 3.7. These data are the basis for the maps and cross sections of mineral distributions shown in this chapter.

Text searches of the MMJV geological descriptions have also been used to supplement the drill data. This has better defined the distribution of certain vein types in drill core (e.g., adularia, carbonates, sphalerite, galena), particularly in drill holes where vein type or vein abundance columns have not been completed by previous site geologists.

4.2.2 Analytical Methods

Mineral abundance estimates

The drill core mineralogy and modal abundances described in this chapter are based on thin section petrography with image processing, quantitative X-ray diffraction (XRD) analysis, short-wavelength infrared (SWIR) spectroscopy, and scanning electron microscopy (SEM). The image processing and XRD methods are described in Chapter Three, with imaging methods and XRD data provided in appendices D and E.

SWIR spectroscopy

A total of 423 infrared spectra were collected using the ASD Terraspec instrument, and a further 88 were collected from core samples using the Integrated Spectronics portable infrared microanalyser (PIMA). Two to five analyses were performed on each core sample, with an average spacing between core samples of 57 metres throughout the drill holes logged in this study. The analyses were recorded as representing either pervasively altered samples, vein halos, or vein material in each sample. Using The Spectral Geologist software, minerals were identified by comparing each spectrum to a reference database. The SWIR mineral identification results are provided in Appendix F, and the SWIR spectra are provided in the digital appendix.

Scanning electron microscopy

Electron microprobe data were collected from twelve key thin sections in order to (1) identify small (< 20 μm) and uncommon minerals, (2) better constrain the overall mineral abundance in samples containing high clay contents or very fine grained disseminated sulfides, and (3) acquire higher resolution images of cross-cutting vein-vein or vein-alteration relationships in samples where paragenesis was ambiguous. Samples were analysed using a Cameca SX100 electron microprobe at the Central Science Laboratory, University of Tasmania. Mineral Liberation Analysis (MLA) mapping and mineral identification was also performed on three samples. The mineral identification and abundance results from this work are provided in the digital appendix.

4.2.3 Terminology

Terms used in the descriptions of altered rock and vein textures, mineral habit, and mineral abundance are defined in Table 4.1. Vein types and mineral assemblages are generally named according to the minerals present (e.g., anhydrite - chalcopyrite - pyrite ± molybdenite veins, or pervasive alunite - kaolinite - quartz - pyrite altered rocks). Trace components, which are described in the text, are generally omitted from the names of vein types or alteration mineral assemblages. I have avoided some terminology such as the A - B - D vein classification of Gustafson and Hunt (1975). The high and intermediate sulfidation epithermal nomenclature of Hedenquist et al. (2000) is used in reference to the Wafi alunite - kaolinite and carbonate-bearing domains of epithermal veins and altered rocks. The term lithocap is used in the discussion to refer to the zone of pervasively alunite- and kaolinite- altered rocks at Wafi.

Table 4.1: Terminology of alteration and mineralisation used in this thesis

Term	Definition
Mineral assemblage	Two or more minerals that are intergrown, without a reaction front (Barton et al., 1963); textural evidence (e.g., exsolution lamellae) may further indicate that they precipatated at the same time (Augustithis, 1995)
Selective alteration	Alteration that has replaced specific minerals, preserving the original rock texture (Titley, 1982)
Pervasive alteration	Texturally destructive alteration that appears to have replaced all original minerals (Titley, 1982)
Vein	Rock fracture filled by minerals of hydrothermal origin
Vein halo	Pervasive or selectively pervasive alteration that occurs adjacent to vein margins, with diffuse contacts into wallrock (as in the "alteration envelope" of Titley, 1982)
Trace (abundance)	Comprising < 1 volume % of the rock
Hydrothermal sandstone	Breccia infill that consists of hydrothermally cemented fragments of < 2 mm in diameter, synonymous with rock flour of Sillitoe (1985) and breccia matrix of Davies et al. (2008)
Cryptocrystalline	Mineral grains that are not identifiable at 40 x magnification (generally < 10 μm across)
Microcrystalline	Mineral grains that are not visible in hand specimen, but can be identified at up to 40 x magnification (generally > 0.01 mm / 10 μm across)

4.3 Paragenesis

The sequence of veins and alteration assemblages in the Wafi-Golpu deposit are divided here into four stages, on the basis of cross-cutting and overprinting relationships (Fig. 4.1). The first two stages (I and II) comprise porphyry-style assemblages that are concentrically zoned about the Golpu diorites. Stage I (early Golpu) was a minor porphyry mineralising event associated with the stage I Golpu diorites described in Chapter Three. Stage II (main stage Golpu mineralisation) involved most of the porphyry Cu-Au mineralisation, which was associated with emplacement of the stage II hornblende-phyric Golpu diorite.

Stage III alteration and mineralisation has produced upward-flaring domains of quartz, muscovite, and pyrite veins and altered rocks. The Wafi breccia complex is interpreted to have erupted during stage III.

Stage IV (main stage Wafi mineralisation) comprises late assemblages that have overprinted the mineralised Golpu diorites as well as the Wafi breccia complex. The epithermal mineral assemblages are broadly zoned about the Golpu intrusions, with an outermost zone of carbonate - adularia - sulfide veins and montmorillonite - chlorite ± illite altered rocks (Figs. 4.1, 4.2).

The following subsections 4.3.1 to 4.3.4 systematically document the veins and altered rocks of Wafi-Golpu in chronological order, from porphyry to epithermal style veins and alteration. The interpreted mineral zoning and paragenesis is summarised in Figure 4.1.

Figure 4.1 (next page): Schematic illustration of zoning and paragenesis of veins and alteration in the Wafi-Golpu deposit. The earliest events are shown at the bottom of the diagram. Proximity to the Golpu diorites is indicated on the horizontal axis, with distance less than zero indicating veins or alteration within the intrusions. The vertical thickness of each mineral assemblage corresponds to relative abundance. Downward-flaring shapes (as in the stage II anhydrite - chalcopyrite veins) indicate greater abundance with depth, whereas upward-flaring shapes (as in the stage IV veins and alteration) indicate increasing abundance towards the present surface. The vertical red lines correspond to zones of gold mineralisation, with opacity indicating the relative contribution from each stage. Although the order of veins and alteration presented in this figure are representative of the overall sequence documented in this study, many of the changes in mineral assemblages are gradual and overlapping. For example, most of the stage II quartz - molybdenite veins formed early in stage II, but a few veins have cross-cut stage II orthoclase veins, implying a later timing. The format of this figure is after Masterman (2003).

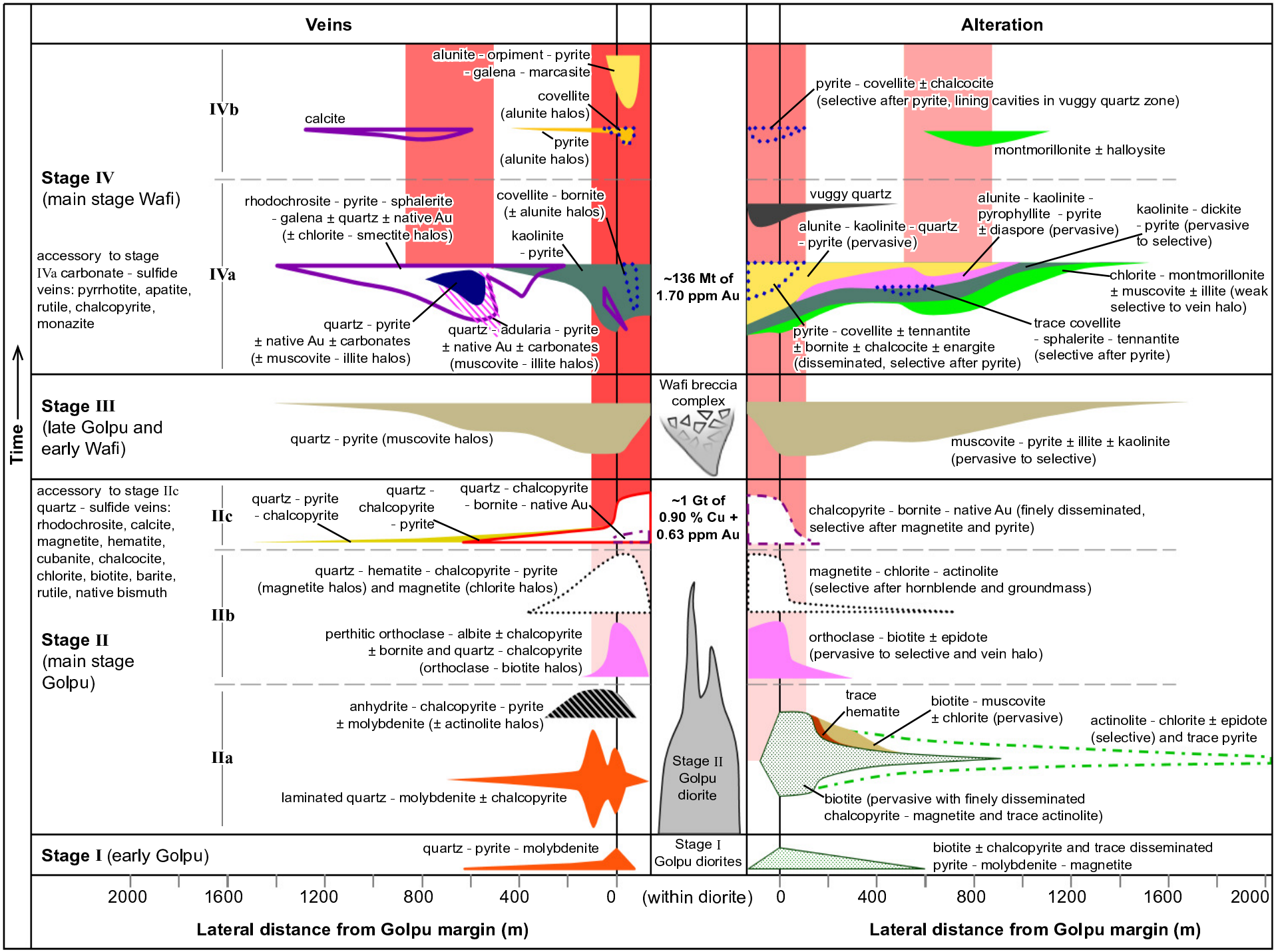
Veins
Alteration
Time
Stage IV
(main stage Wafi)
IVb
IVa
accessory to stage IVa carbonate - sulfide veins: pyrrhotite, apatite, rutile, chalcopyrite, monazite
alunite - orpiment - pyrite - galena - marcasite
covellite (alunite halos)
calcite
pyrite (alunite halos)
rhodochrosite - pyrite - sphalerite - galena ± quartz ± native Au (± chlorite - smectite halos)
covellite - bornite (± alunite halos)
kaolinite - pyrite
quartz - pyrite ± native Au ± carbonates (± muscovite - illite halos)
quartz - adularia - pyrite ± native Au ± carbonates (muscovite - illite halos)
~136 Mt of 1.70 ppm Au
pyrite - covellite ± chalcocite (selective after pyrite, lining cavities in vuggy quartz zone)
montmorillonite ± halloysite
vuggy quartz
alunite - kaolinite - pyrophyllite - pyrite ± diaspore (pervasive)
kaolinite - dickite - pyrite (pervasive to selective)
alunite - kaolinite - quartz - pyrite (pervasive)
chlorite - montmorillonite ± muscovite ± illite (weak selective to vein halo)
pyrite - covellite ± tennantite ± bornite ± chalcocite ± enargite (disseminated, selective after pyrite)
trace covellite - sphalerite - tennantite (selective after pyrite)
Stage III
(late Golpu and early Wafi)
quartz - pyrite (muscovite halos)
Wafi breccia complex
muscovite - pyrite ± illite ± kaolinite (pervasive to selective)
accessory to stage IIc quartz - sulfide veins: rhodochrosite, calcite, magnetite, hematite, cubanite, chalcocite, chlorite, biotite, barite, rutile, native bismuth
Stage II
(main stage Golpu)
IIc
IIb
IIa
quartz - pyrite - chalcopyrite
quartz - chalcopyrite - pyrite
quartz - chalcopyrite - bornite - native Au
~1 Gt of 0.90 % Cu + 0.63 ppm Au
chalcopyrite - bornite - native Au (finely disseminated, selective after magnetite and pyrite)
quartz - hematite - chalcopyrite - pyrite (magnetite halos) and magnetite (chlorite halos)
magnetite - chlorite - actinolite (selective after hornblende and groundmass)
perthitic orthoclase - albite ± chalcopyrite ± bornite and quartz - chalcopyrite (orthoclase - biotite halos)
orthoclase - biotite ± epidote (pervasive to selective and vein halo)
anhydrite - chalcopyrite - pyrite ± molybdenite (± actinolite halos)
trace hematite
biotite - muscovite ± chlorite (pervasive)
actinolite - chlorite ± epidote (selective) and trace pyrite
laminated quartz - molybdenite ± chalcopyrite
Stage II Golpu diorite
biotite (pervasive with finely disseminated chalcopyrite - magnetite and trace actinolite)
Stage I (early Golpu)
quartz - pyrite - molybdenite
Stage I Golpu diorites
biotite ± chalcopyrite and trace disseminated pyrite - molybdenite - magnetite
2000
1600
1200
800
400
0
(within diorite)
0
400
800
1200
1600
2000
Lateral distance from Golpu margin (m)
Lateral distance from Golpu margin (m)

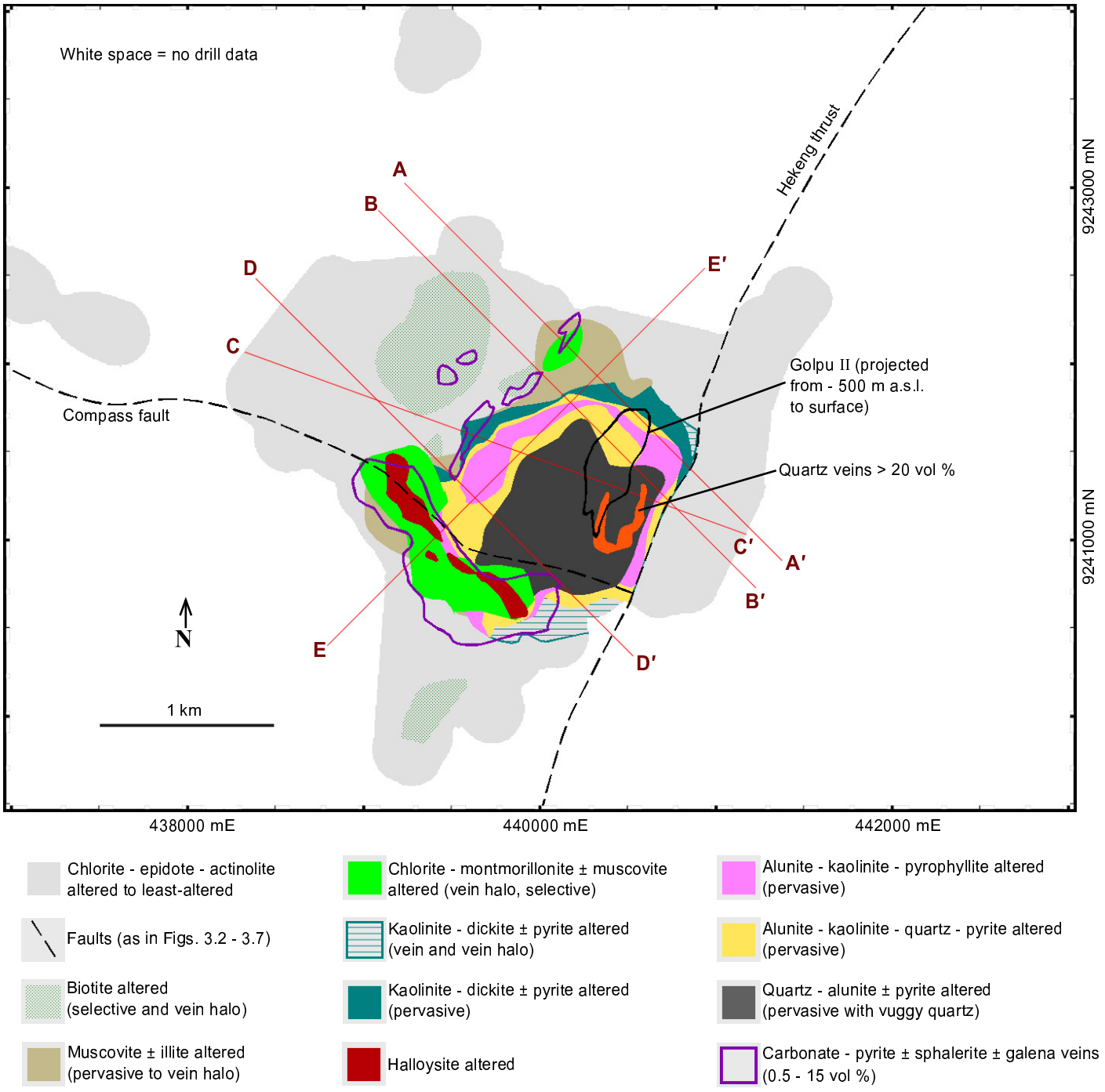

Figure 4.2: Map of veins and altered rocks of the Wafi-Golpu deposit, looking below overburden and the Hekeng andesite. For clarity, a projection of the stage II Golpu diorite is the only rock unit shown. The map area and section lines are the same as in the surface geology map (Fig. 3.2 B).

4.3.1 Stage I (Early Golpu)

The earliest stage of Golpu mineralisation (stage I; Fig. 4.3) comprises quartz - pyrite - molybdenite veins that occur along and near the intrusive margins of stage I diorites (Fig. 4.4 A-C), and finely disseminated chalcopyrite, pyrite, molybdenite, and magnetite in stage I diorites (Fig. 4.4 D,E). Least-altered diorite samples, farthest from the stage II diorite and assumed here to be most representative of stage I disseminated mineralisation, contain ~ 2.0 % pyrite, and less than 1.0 % each of chalcopyrite, magnetite, and molybdenite

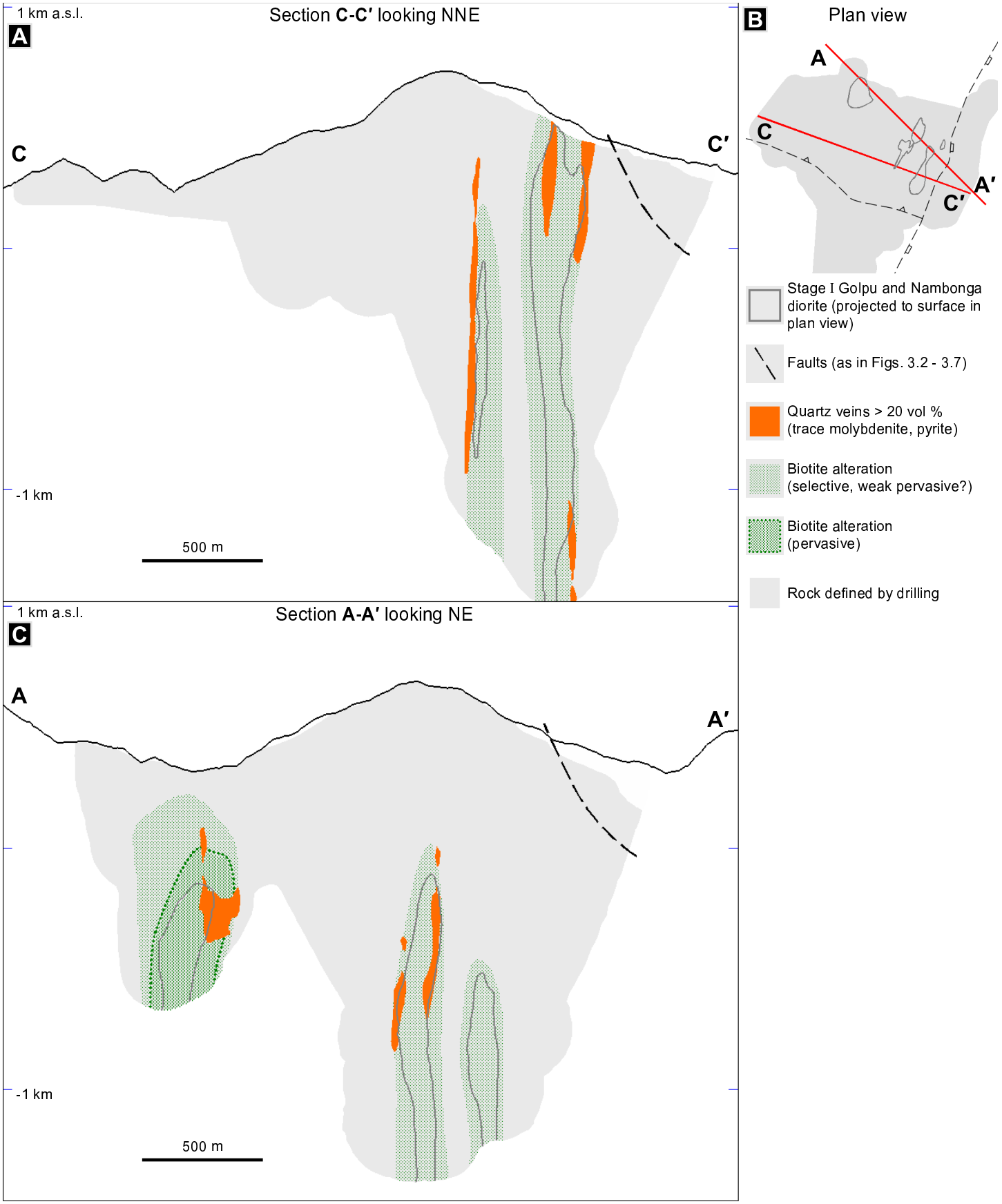

Figure 4.3: Stage I veins and alteration. Sections C-C′ (panel A) and A-A′ (panel C) show the estimated distribution of quartz veins and biotite alteration during early Golpu mineralisation. Diorite outlines are projected to surface in the plan view (panel B). Where intruded by the later Stage II diorite (outlined in Fig. 4.5), the diorite outlines and alteration zones are inferred. Also shown are zones of biotite alteration and quartz stockwork veins associated with the Nambonga stock.

(Appendix A). Biotite alteration of metasedimentary wallrock occured in stage I (Fig. 4.4 A,B), but its distribution is difficult to constrain due to overprinting by later events associated with the stage II diorite.

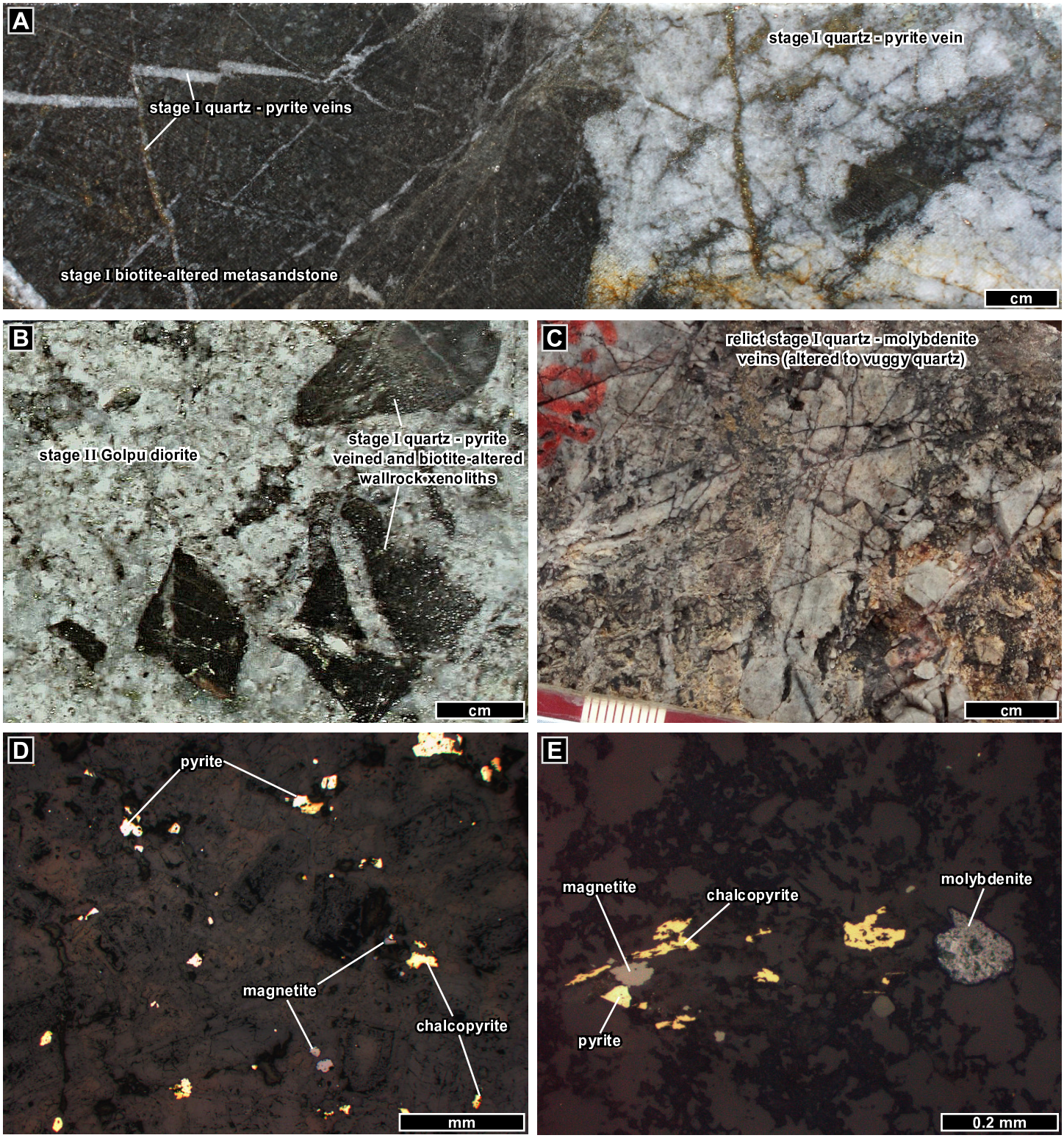

Figure 4.4: Stage I quartz - molybdenite - pyrite veins, biotite-altered rocks, and disseminated pyrite - chalcopyrite - magnetite mineralisation. A) Stage I quartz - pyrite veins and biotite-altered rock, adjacent to a stage I Golpu intrusion (WR 392, 1863.0 m). B) Biotite-altered wallrock fragments with truncated quartz - pyrite veins, within stage II Golpu diorite (WR396, 1499.7 m). C) Relict stage I stockwork quartz - molybdenite veins, overprinted by acid alteration. This is part of a metre interval containing 393 ppm Mo (WR398, 90.3 m). D) Stage I Golpu diorite (quartz- and plagioclase-phyric) contains disseminated pyrite, chalcopyrite, and magnetite (reflected PPL; WR392, 1851.5 m). E) Sparse disseminated molybdenite occurs with magnetite, pyrite, and chalcopyrite in stage I diorite (reflected PPL; WR392, 1728.3 m).

4.3.2 Stage II (Main Stage Golpu Mineralisation)

Stage IIa

Stage II veins and alteration are associated with, and are concentrically zoned about, the stage II diorite (Fig. 4.1). The first veins to have formed after intrusion of the stage II diorite are stage IIa quartz - molybdenite veins with trace chalcopyrite and pyrite (Figs. 4.5, 4.6 A-D). Most of the stage IIa quartz - molybdenite veins occur as a concentric array within 120 metres of the diorite intrusive margins (Fig. 4.1). A typical interval of this early stockwork contains 20 - 40 vol % quartz - molybdenite veins over 50 metres, and up to 70 vol % over a few metres (Appendix B). Some of the laminated quartz - molybdenite veins contain euhedral quartz terminating into anhydrite (e.g., Fig. 4.6 B). Stage IIa anhydrite - chalcopyrite - pyrite ± molybdenite veins, some of which have actinolite halos (Fig. 4.6 E-F), occur below -1 km a.s.l., or about 1.5 km below the current erosional surface (Fig. 4.5). They have cross-cut diorite, wallrock, and most of the quartz - molybdenite veins.

Alteration during stage IIa dominantly produced biotite with trace disseminated magnetite (± chalcopyrite), muscovite, and actinolite - chlorite ± epidote. The biotite alteration was most intense nearest the diorites, resulting in black rock with ~ 40 vol % biotite (Table 4.2). At about 180 metres from the diorite contacts, the biotite-altered rocks transition to either muscovite- or actinolite-bearing assemblages, depending on elevation (Figs. 4.1, 4.5). Specifically, below -600 m a.s.l., biotite-altered rocks (Fig. 4.6 A) transition through biotite - actinolite (Fig. 4.6 E) into distal actinolite - chlorite ± epidote altered rocks. Above -600 m a.s.l., biotite-altered rocks transition through muscovite (Fig. 4.7 A,B), into distal chlorite - actinolite ± epidote altered rocks (Fig. 4.7 D-G). Fine-grained hematite occurs in some intervals across the transition from biotite- to biotite- and muscovite-altered rocks, producing the red colour in Figure 4.7 A and B.

Table 4.2: Mineralogy of stage IIa biotite ± muscovite ± actinolite ± chlorite altered rocks

Sample description	Sample location	Summary of bulk mineralogy (vol % by quantitative XRD)
Intense, pervasive, biotite-altered metasandstone	WR402, 700.0 m	42 % biotite, 30 % plagioclase, 20 % quartz, 6 % muscovite
	WR398, 711.6 m	39 % biotite, 28 % quartz, 22 % albite, 4 % muscovite, 2 % chalcopyrite
Strong, pervasive to vein halo, biotite- and actinolite- altered metasiltstone and metasandstone, < 5 % anhydrite veins	WR377, 1890.0 m	46 % plagioclase (~labradorite), 19 % quartz, 17 % biotite, 10 % actinolite, 2 % chlorite, 2 % pyrite
	WR392, 1891.0 m	32 % plagioclase (~labradorite), 31 % biotite, 22 % quartz, 6 % actinolite, 6 % anhydrite
Strong, pervasive, muscovite- and biotite-altered metasandstone with red colour due to trace disseminated hematite	WR396, 975.8 m	40 % quartz, 25 % muscovite, 11 % chlorite, 10 % biotite, 9 % pyrite
Weak, pervasive to clast-selective, chlorite - actinolite ± epidote altered metasandstone and metaconglomerate (distal)	WR377, 218.6 m	32 % plagioclase (albite > labradorite), 21 % chlorite, 21 % actinolite, 10 % augite, 4 % epidote, 3 % quartz
	WR392, 276.3 m	32 % chlorite, 30 % plagioclase (~labradorite), 18 % quartz, 8 % actinolite, 3 % pyrite, 2 % augite, 2 % kaolinite - dickite

Note: totals do not add to 100 because trace components are not presented in this table.

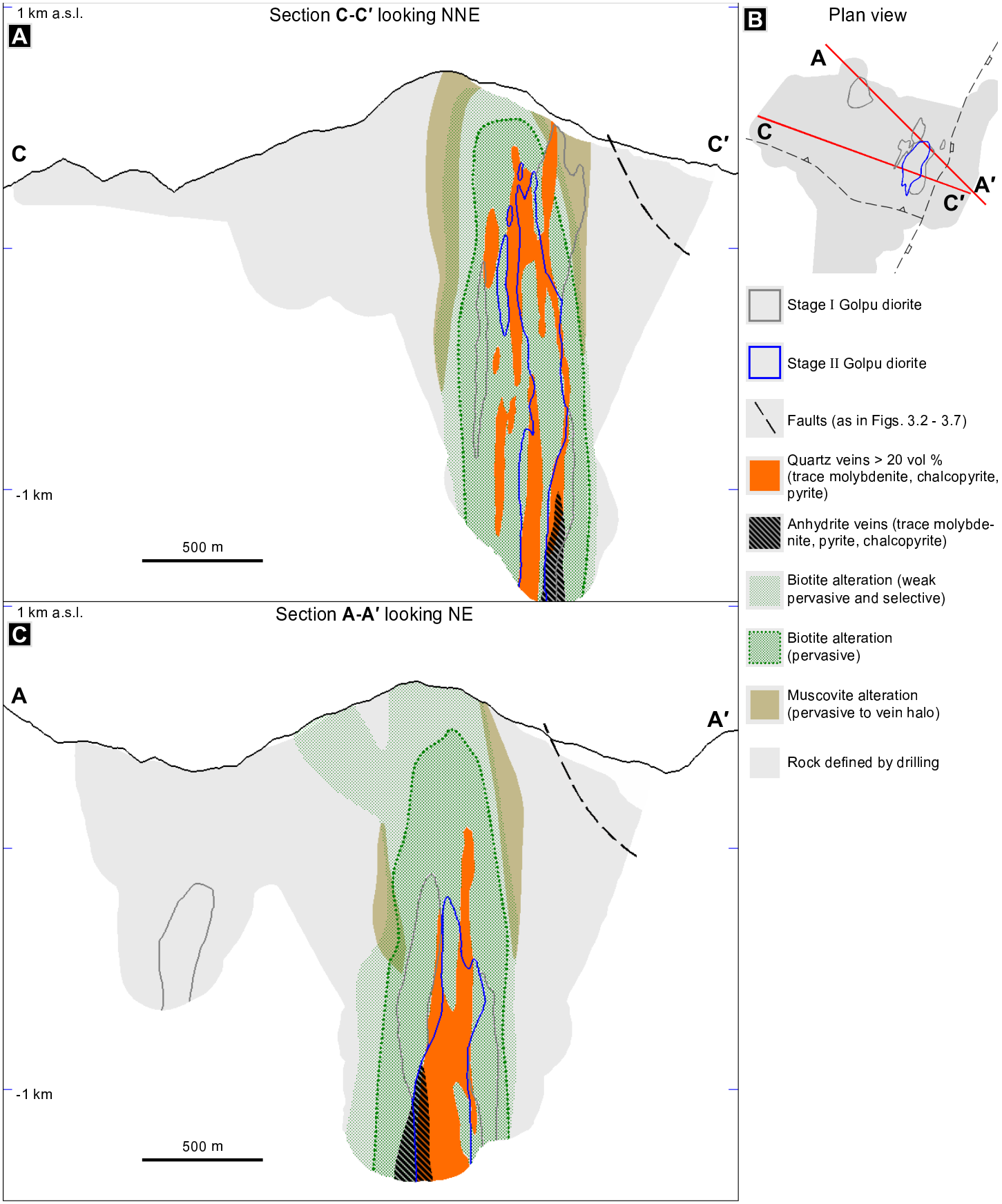

Figure 4.5: Stage IIa veins and alteration. Sections C-C′ (A) and A-A′ (C) show the distribution of quartz veins, anhydrite veins, biotite alteration, early muscovite alteration, and chlorite - epidote - actinolite alteration after intrusion of the Stage II Golpu diorite (outlined in blue). The diorite outlines are projected to surface in the plan view (B). Alteration zones overprinted by later quartz - alunite alteration and erupted by the Wafi breccia complex are inferred.

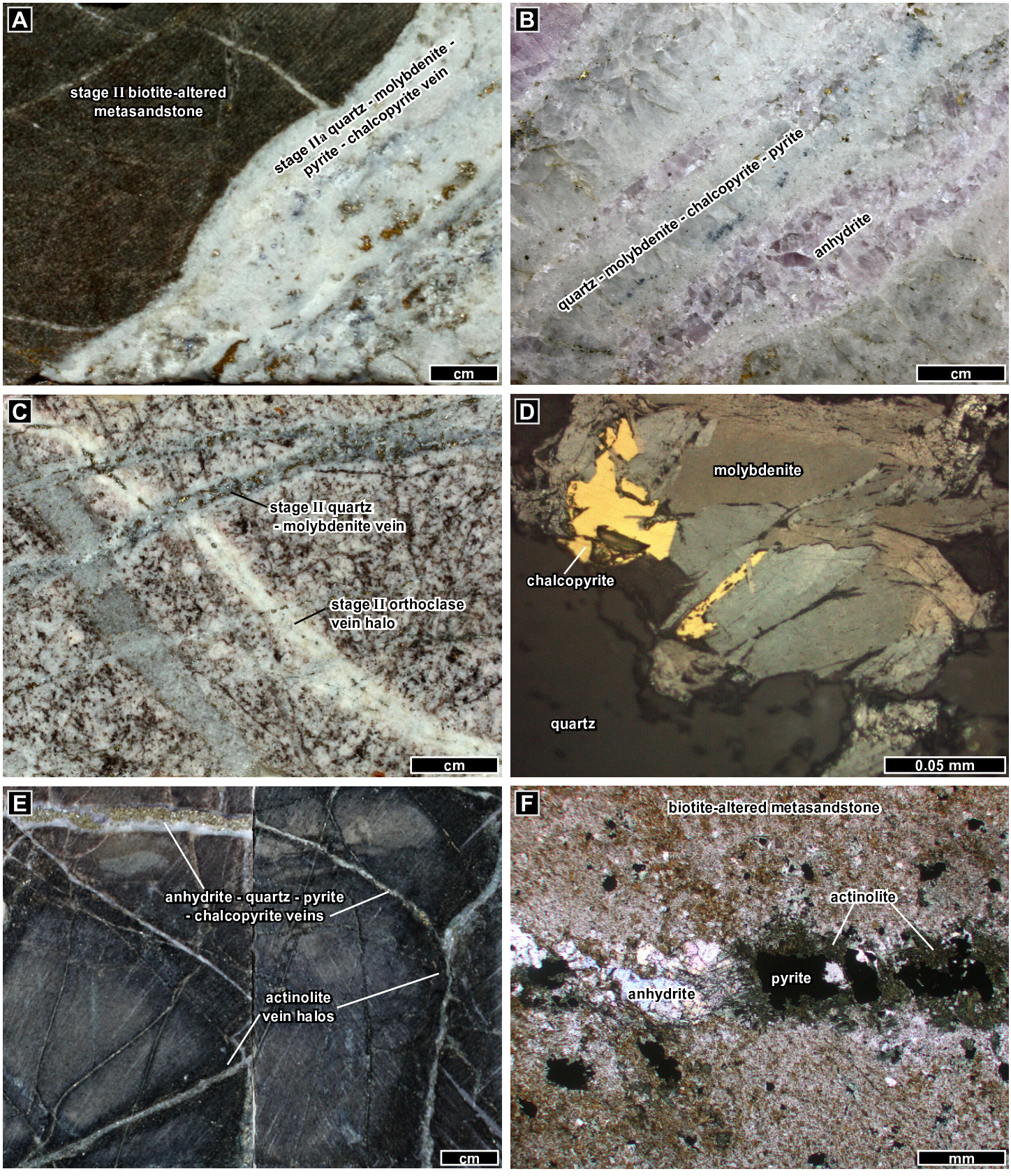

Figure 4.6: Stage IIa veins and altered rocks that are characteristic of the deeper parts of the Golpu deposit. A) Biotite-altered metasandstone that has been cut by a quartz - molybdenite - chalcopyrite - pyrite vein (WR392, 1583.8 m). B) Quartz - anhydrite - molybdenite - chalcopyrite - pyrite vein (WR377, 1791.5 m). C) The latest quartz - molybdenite veins cross-cut quartz and chalcopyrite veins with orthoclase halos (WR392, 1699.2 m). D) Chalcopyrite intergrown with molybdenite in a quartz - molybdenite vein (reflected partial XPL; WR392, 1662.6 m). E) Anhydrite - quartz - pyrite - chalcopyrite veins with actinolite - biotite halos in metasandstone (WR377, 1904.0 m). F) Thin section image of a vein as in (E), showing a dark green actinolite vein halo to an anhydrite - pyrite - chalcopyrite vein through biotite-altered metasandstone (PPL; WR392, 1891.0 m).

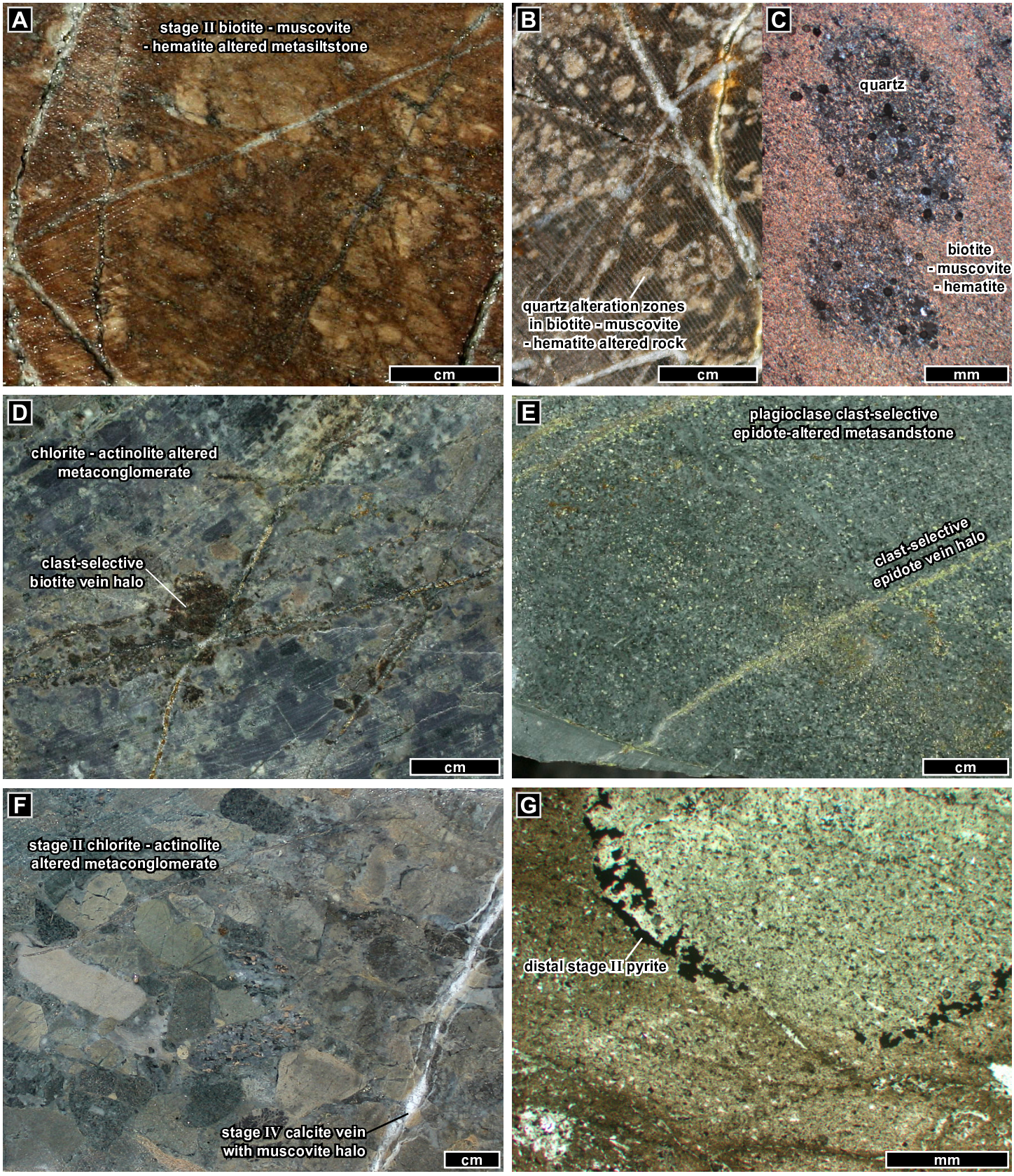

Figure 4.7: Stage IIa veins and altered rocks in shallower and distal parts of the study area. A) Fine-grained hematite occurs along the outward transition from stage II biotite- to muscovite-altered rocks (WR396, 975.8 m). B) Rounded zones of fine-grained quartz in biotite - muscovite - hematite altered rock (WR397, 1037.5 m). C) Photomicrograph of quartz in panel B (XPL). D) Distal clast-selective vein halo biotite in metaconglomerate (WR396, 284.7 m). E) Distal chlorite - actinolite - epidote alteration has resulted in selective and vein halo epidote alteration of plagioclase grains in metasandstone (WR397, 34.7 m). F) Weak distal chlorite - actinolite altered rock overprinted by weak clast-selective muscovite alteration (particularly along clast margins) and calcite veins (WR397, 113.9 m). G) Pyrite-rimmed clast in chlorite - actinolite and trace biotite-altered metasiltstone (PPL; WR397, 271.0 m).

Sparse, clast-selective biotite vein halos have been observed up to 600 metres from the nearest diorite (e.g., Fig. 4.7 D). This is unusual, as most distal stage IIa veins are limited to very sparse chlorite-epidote veins associated with weak clast-selective alteration (Fig. 4.1). The distal chlorite - actinolite ± epidote and trace pyrite alteration has, in many samples, produced a green colour (e.g., Fig. 4.7 E) distinct from the more blue-grey colour of least-altered metasedimentary host rocks. However, a distinction between weak distal chlorite - actinolite alteration and regional metamorphic rocks has not been possible at the scale of this study. This ambiguity in interpretation between distal alteration and regional greenschist facies metamorphism is also evident in the MMJV logs of distal drill core intervals, in which metasedimentary intervals are interchangeably categorised as “unaltered” or “propylitic,” without any evident zonation across drill holes.

Stage IIb

Stage IIb orthoclase - biotite and quartz - magnetite - hematite veins and altered rocks occur within and near the stage II diorite (Fig. 4.10). Orthoclase alteration has produced a pink colour throughout most of the originally grey-green stage II diorite (Fig. 4.8; Chapter Three). The orthoclase veins are sparsely distributed through the stage II diorite (Fig. 4.11 A-D), and contain early chalcopyrite - pyrite - bornite (e.g., Fig. 4.11 B). Most of the secondary orthoclase − in both veins and altered rocks − is perthitic, containing < 30 vol % irregular albite lamellae (Fig. 4.11 D). Halos of selective orthoclase alteration, after plagioclase phenocrysts and groundmass, occur with some stage II veins (Fig. 4.11 A,G,H). Orthoclase alteration was most intense through the stage II diorite, producing up to 45 vol % secondary orthoclase + albite in some samples (Table 4.3; Appendix E). Epidote occurs sporadically in a few intervals of orthoclase-altered stage II diorite (e.g., Fig. 4.9 B). Hornblende phenocrysts were most commonly replaced by biotite (Fig. 4.11 E,F), but some have rims of orthoclase (Fig. 4.11 D). In the stage I diorites, the orthoclase and magnetite alteration (along with chalcopyrite mineralisation and corresponding Cu, Fe, and K contents; Chapter Five) decrease in intensity with distance from the stage II diorite (e.g., WR392; Appendix B).

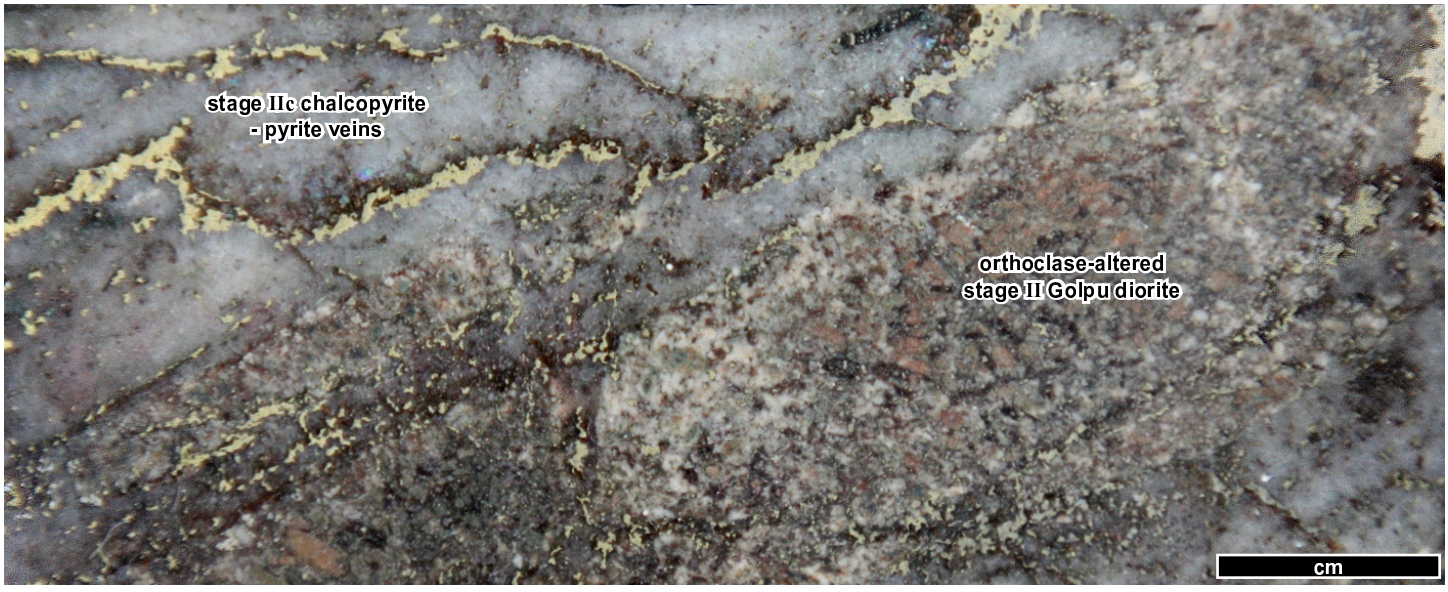

Figure 4.8: Stage IIb orthoclase-altered stage II diorite. The sample contains disseminated chalcopyrite, pyrite, and magnetite, and has been cross-cut by stage IIc chalcopyrite - pyrite veins (WR377, 1466.2 m).

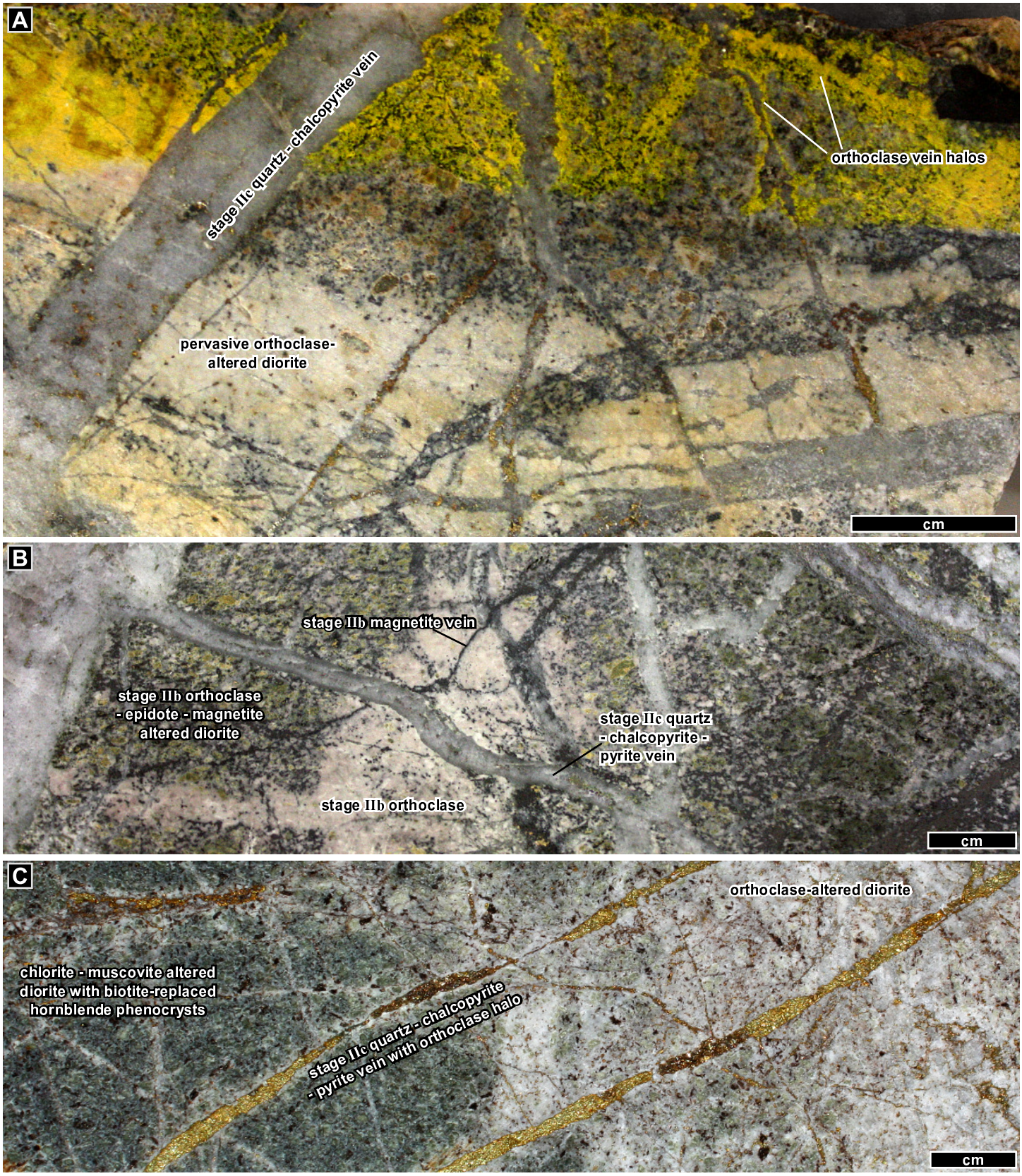

Figure 4.9: Stage II diorite containing stage IIb orthoclase, biotite, magnetite, and chlorite ± epidote ± muscovite. A) Pervasive stage IIb orthoclase, and orthoclase halos to stage IIc quartz - chalcopyrite veins (stained yellow; WR377, 1380.0 m). B) Stage IIb orthoclase- and epidote-altered diorite, cross-cut by stage IIb magnetite veins, and by stage IIc quartz - chalcopyrite veins (WR377, 1365.0 m). C) Subhedral hornblende phenocrysts have been altered to biotite (black), and plagioclase phenocrysts have been altered to chlorite - muscovite (at left) and orthoclase (at right). The sample is cross-cut by stage IIc chalcopyrite - pyrite veins with orthoclase halos (WR392, 1532.5 m).

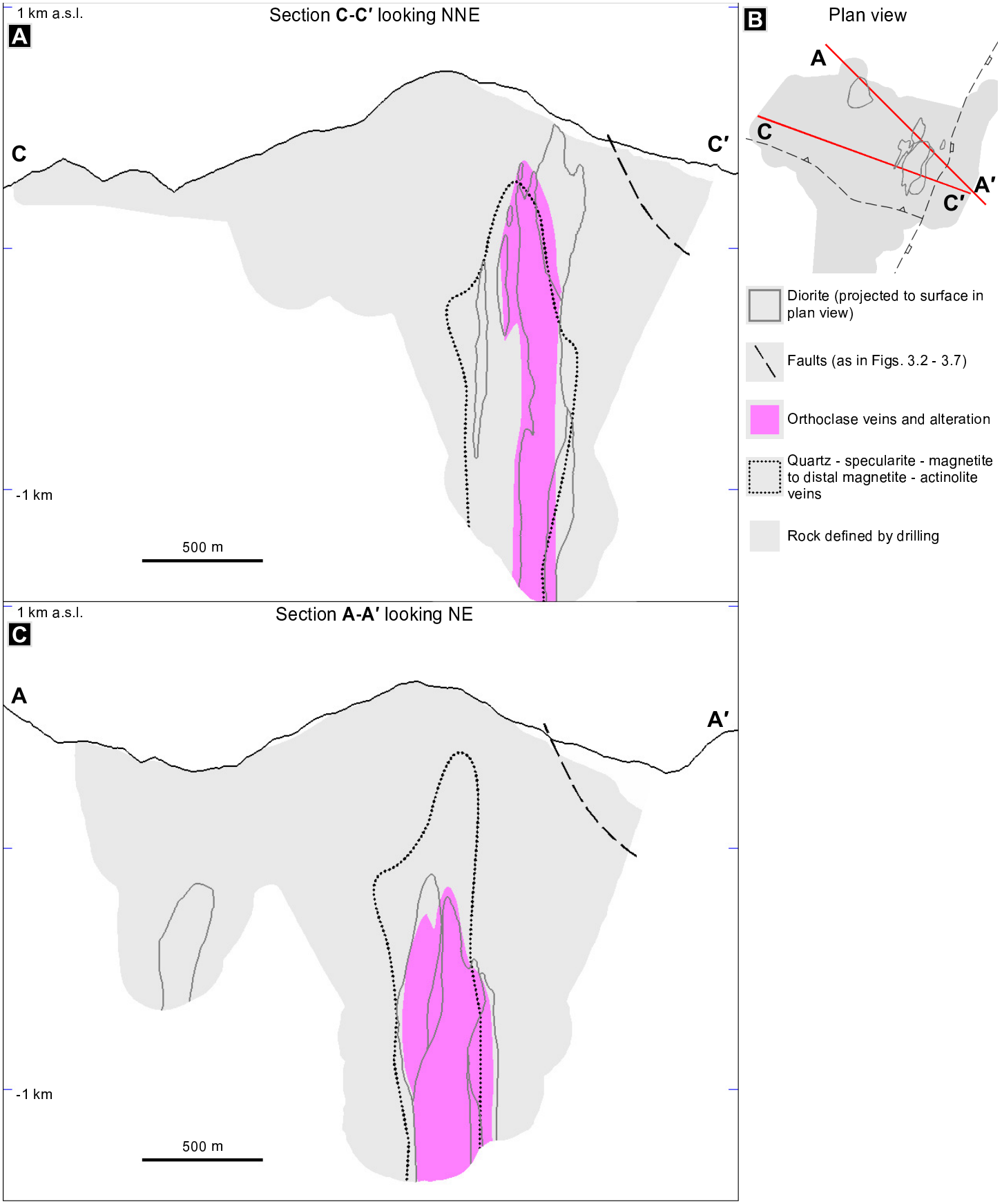

Figure 4.10: Stage IIb. Sections C-C′ (A) and A-A′ (C) show the distribution of orthoclase veins and alteration, which occurred mostly within the diorites, and quartz - specularite - magnetite veins to distal magnetite - actinolite veins with actinolite vein halos (see text). Section lines are shown in the plan view (B).

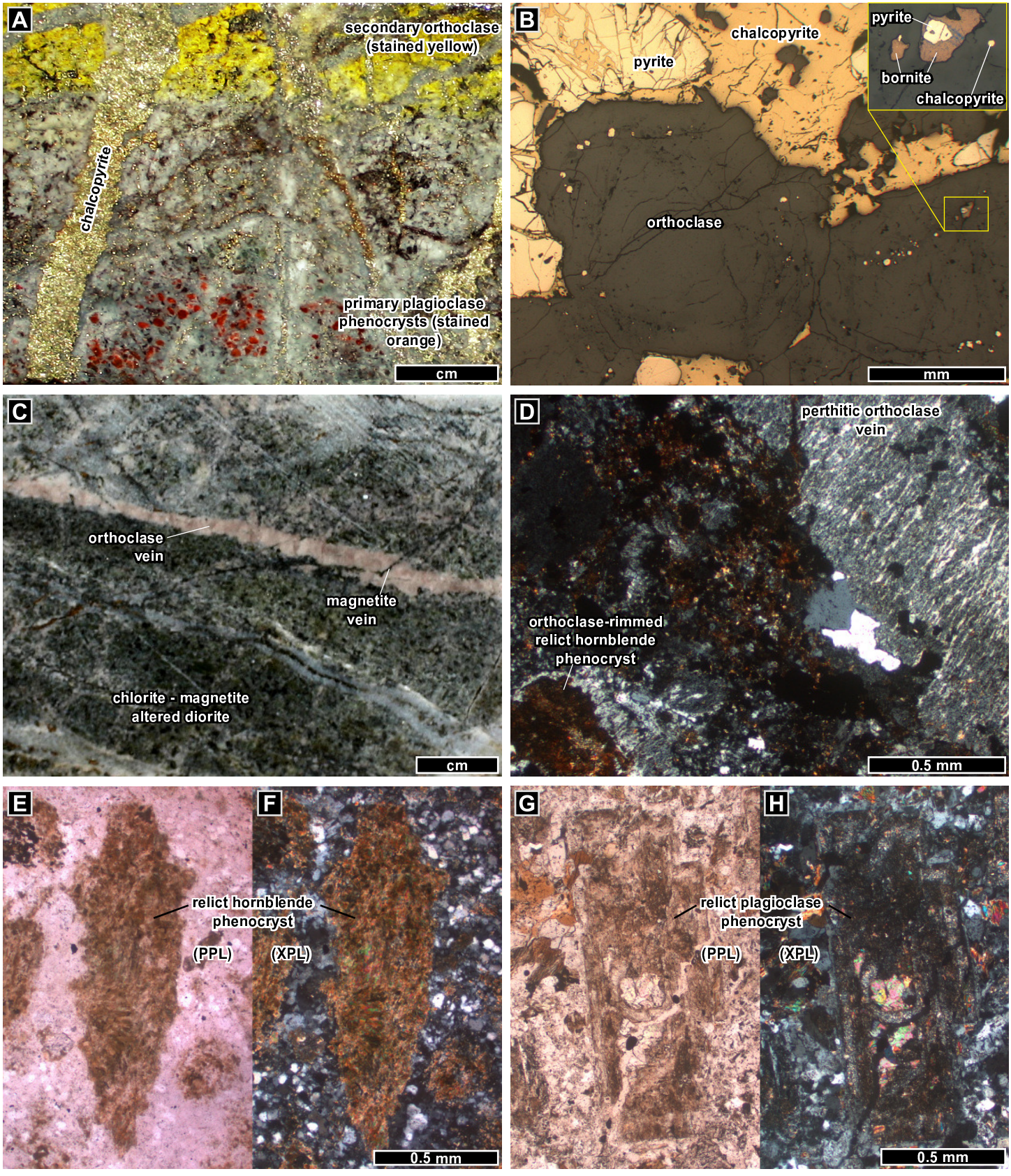

Figure 4.11: Stage IIb orthoclase - biotite veins and altered rocks. A) Feldspar stained sample showing secondary orthoclase (stained yellow) and primary plagioclase phenocrysts (stained orange; WR392, 1528.5 m). B) Inclusion trains of chalcopyrite - pyrite - bornite in orthoclase crystals (reflected PPL; WR377, 1246.0 m). C) Orthoclase vein through chlorite - magnetite - altered diorite, cross-cut by magnetite veins (WR377, 1306.6 m). D) Perthitic orthoclase along a vein margin (top right) and rimming a biotite-replaced hornblende phenocryst (bottom left; XPL; WR337, 1182.4 m). E) Hornblende phenocryst replaced by biotite with minor chlorite (PPL; WR396, 1309.0 m). F) As in panel E (XPL). G) Plagioclase phenocryst replaced by orthoclase (along rims and throughout crystal), calcite (centre of crystal), and biotite - muscovite (PPL; WR392, 1699.2 m). H) As in panel G (XPL).

Table 4.3: Mineralogy of stage IIb orthoclase-altered and porphyry mineralised diorite

Sample description	Sample location	Summary of bulk mineralogy (vol % by quantitative XRD)
Pervasive and vein halo orthoclase altered diorite, with ~ 5 - 15 % quartz - chalcopyrite veins	WR397, 1361.0 m	27 % quartz, 23 % orthoclase, 20 % plagioclase (~albite), 16 % biotite, 8 % chalcopyrite, 3 % chlorite
	WR377, 1182.4 m	49 % quartz, 20 % orthoclase, 15 % plagioclase (labradorite > albite), 3 % chalcopyrite, 2 % magnetite, 2 % muscovite

Totals do not add to 100 because trace components are not presented in this table.

Most of the stage IIb magnetite - hematite veins and alteration are spatially and temporally coincident with the orthoclase veins and alteration (Figs. 4.1, 4.10). Some have cross-cut orthoclase veins (e.g., Fig. 4.11 C), and a few occur up to 400 metres from the stage II diorite. Most of the distal veins are quartz - hematite - pyrite - chalcopyrite (Figs. 4.12, 4.13 A-E). The magnetite-dominant veins have chlorite - actinolite halos after biotite, whereas the hematite-dominant veins have disseminated magnetite halos (Figs. 4.12, 4.13 C-E). These veins have cross-cut quartz - molybdenite veins, and were cross-cut by quartz - chalcopyrite - pyrite veins. Magnetite - chlorite (± hematite and chalcopyrite) alteration has also occurred locally through the stage II diorite, resulting in green and strongly magnetic rock (as in the diorite shown in Fig. 4.11 C). This alteration was mostly selective after hornblende phenocrysts and groundmass (Fig. 4.13 F).

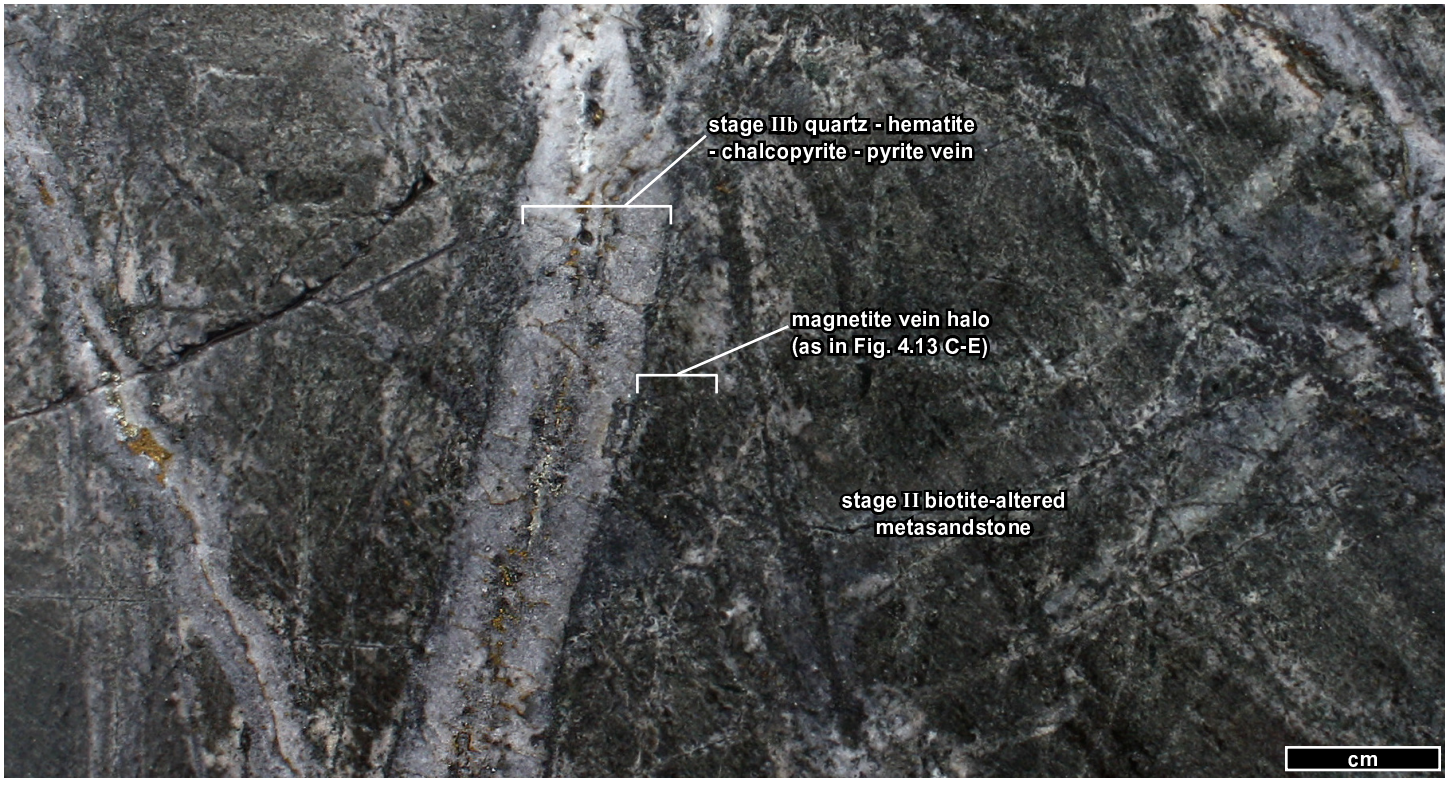

Figure 4.12: Stage IIb quartz - hematite (specularite) - chalcopyrite - pyrite veins with magnetite halos, which have cross-cut stage II biotite-altered metasandstone (WR402, 566.3 m).

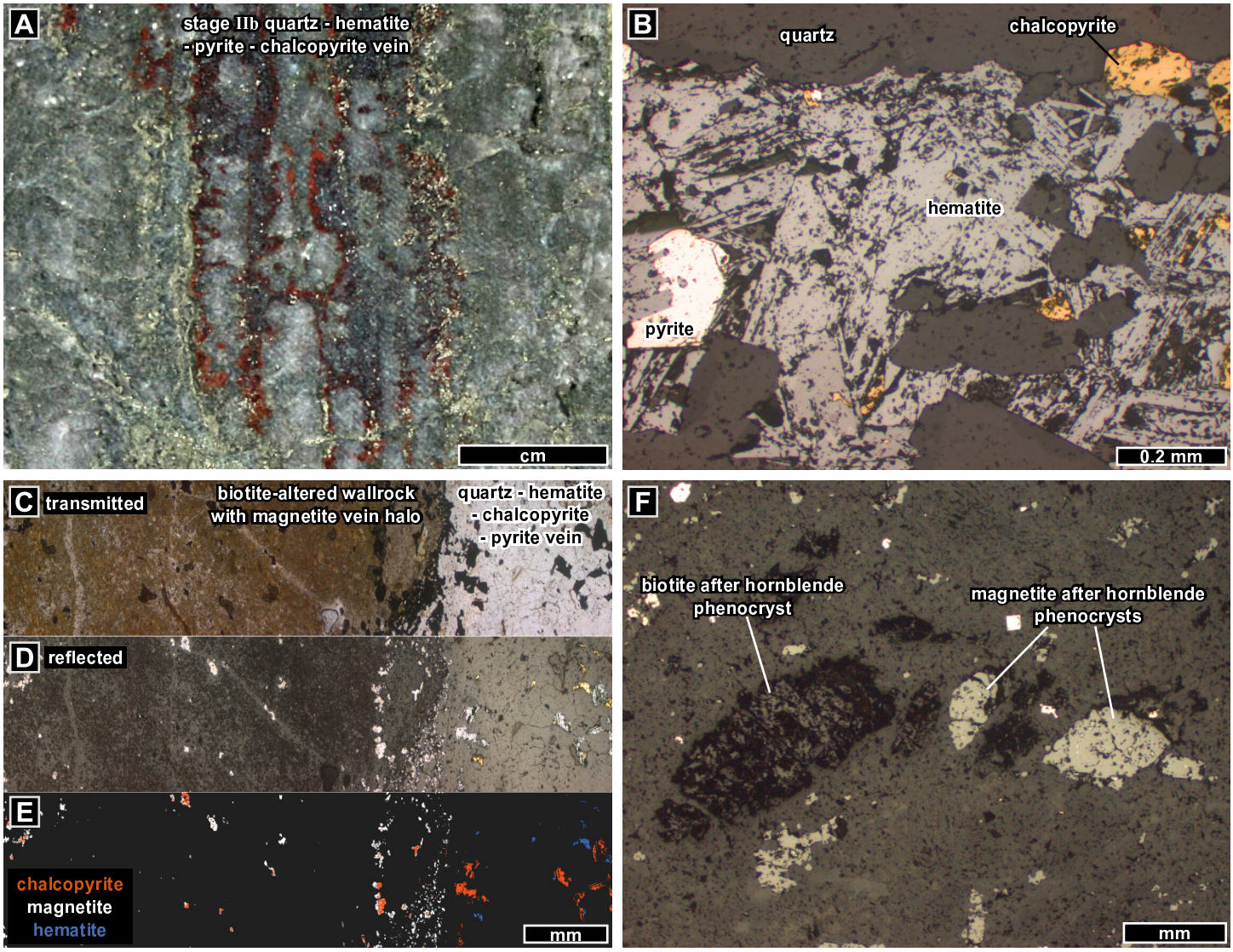

Figure 4.13: Stage IIb iron oxide veins and alteration associated with sulfides, orthoclase, and biotite. A) Laminated quartz - hematite (specularite) - pyrite - chalcopyrite vein (WR402, 686.0 m). B) Photomicrograph of pyrite and chalcopyrite interstitial to hematite laths, in a quartz - hematite (+ trace magnetite) vein (reflected PPL; WR402, 569.0 m). C) Same vein as in panel B, with a magnetite vein halo in biotite-altered metasiltstone at image left (PPL; WR402, 569.0 m). D) Vein in panel C, in reflected PPL. E) Vein in panel C, with minerals indicated. F) Selective magnetite (+trace hematite and chalcopyrite) and biotite alteration after hornblende phenocrysts in the stage II Golpu diorite (reflected PPL; WR337, 1182.4 m).

Stage IIc

Sulfides occur throughout the stage II veins and alteration, but most of the Golpu Cu-Au mineralisation occurred in stage IIc, which is the final stage of porphyry-concentric veins and alteration (Fig. 4.1). This main stage of Golpu porphyry mineralisation produced chalcopyrite, pyrite, and bornite veins and disseminations, mostly within the stage II diorite (Figs. 4.1, 4.14).

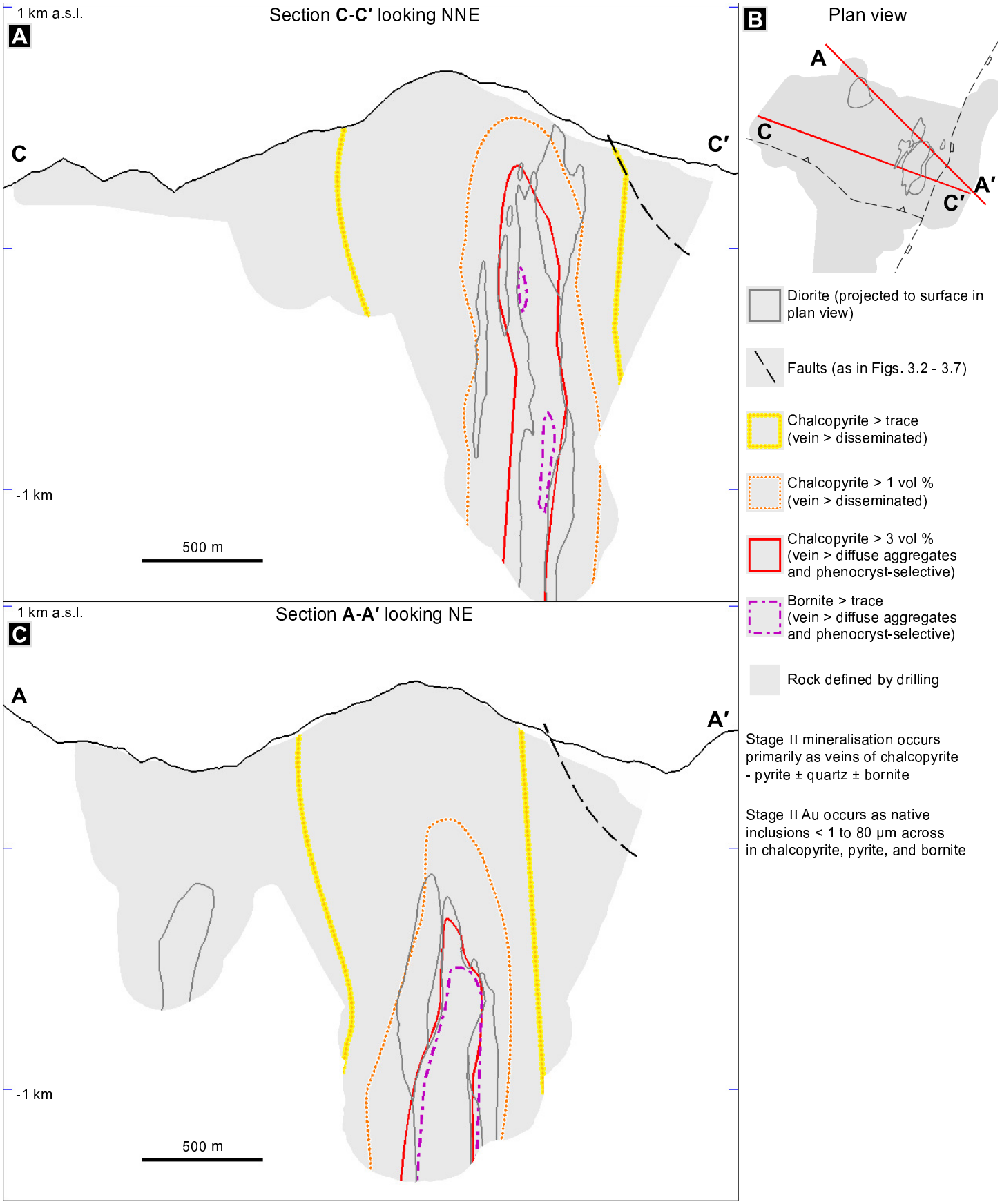

Figure 4.14: Stage IIc. Sections C-C′ (A) and A-A′ (C) show the zonation of sulfides, which occur primarily as veins in the stage II diorite. The outward transition from chalcopyrite > pyrite to pyrite > chalcopyrite occurs where chalcopyrite content decreases from 2 to 1 vol %. There are no domains of bornite > chalcopyrite. The trace and 1 % chalcopyrite zones are inferred where they have been overprinted or erupted by the Wafi breccia complex. Section lines and projections of the Golpu and Nambonga intrusions are shown in the plan view (B).

Stage IIc vein mineralisation

Quartz - chalcopyrite - pyrite ± bornite veins occur in both planar and irregular anastomosing sets throughout the stage II diorite (Figs. 4.8, 4.9, 4.15, 4.16 C, 4.21 F). Sulfides (dominantly chalcopyrite) also occur as breccia vein cement (e.g., Fig. 4.16 A) and diffuse veins with vein halos grading into disseminated sulfides (Fig. 4.16 B). The vein sulfide mineralogy defines a broad zonation pattern from chalcopyrite > bornite in the diorite centre, to chalcopyrite > pyrite (without bornite) in parts of the diorite, to pyrite > chalcopyrite around 100 metres from the intrusive margins (Figs. 4.1, 4.14). Vein bornite is most abundant in the deep northern portion of the stage II diorite (Fig. 4.14 C), where grades of > 8 wt % Cu and > 15 ppm Au can occur in some one metre intervals (Chapter Five). Where pyrite and bornite occur in the same veins, the pyrite occurs as fragments that formed slightly earlier than the bornite - chalcopyrite, based on overgrowth and replacement textures (e.g., Fig. 4.17 B). Sparse pyrite - chalcopyrite veins have been documented up to 800 metres from Golpu (Fig. 4.1).

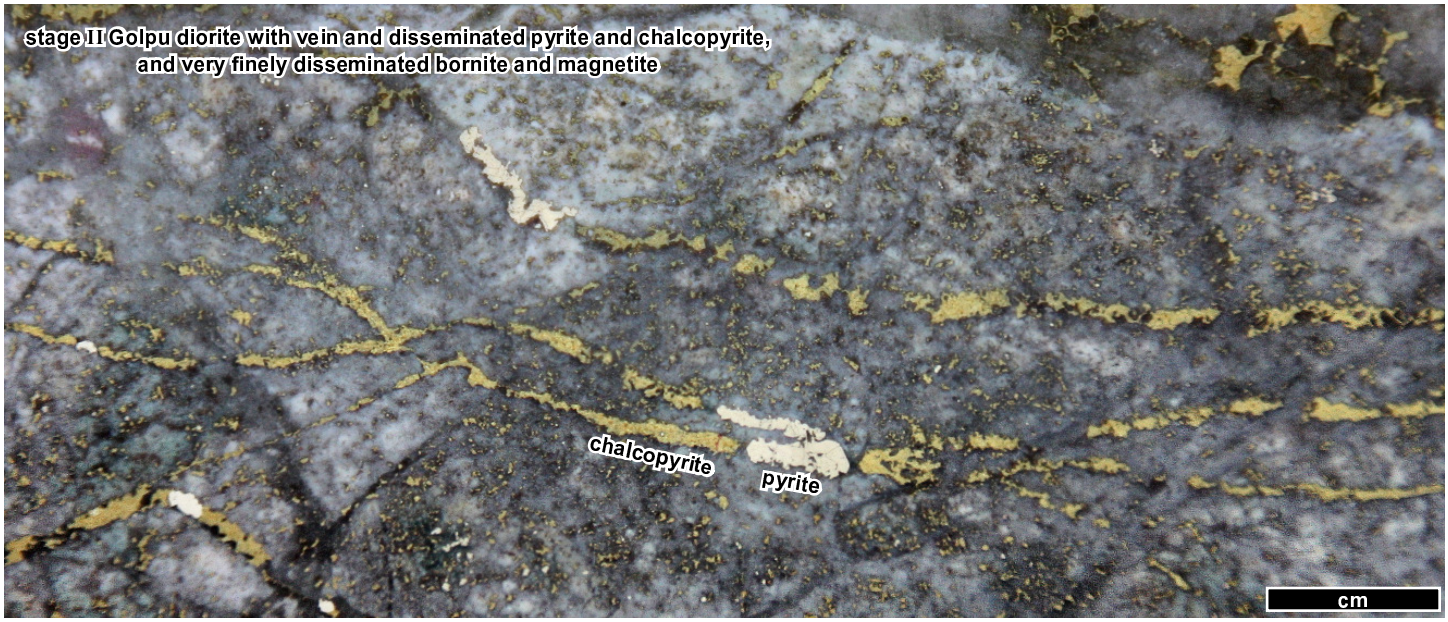

Figure 4.15: Typical appearance of mineralised stage II Golpu diorite, containing stage IIc quartz - chalcopyrite - pyrite veins and disseminations. Much of the rock is white due to perthite (orthoclase - albite) alteration. Trace bornite, magnetite, and native gold occur in this sample (e.g., Fig. 4.20 B). The corresponding metre assay yielded 3.43 ppm Au, 2.91 % Cu, and 3.0 ppm Ag (WR377, 1530.0 m).

Stage IIc disseminated mineralisation

The disseminated sulfide component makes up approximately a third of all porphyry mineralisation in the stage II Golpu diorite (e.g., Figs. 4.15, 4.16 B,D,E), and decreases to trace abundance within ~ 150 metres of the diorite contacts (Fig. 4.1). The disseminated sulfides occur as patchy diffuse aggregates (i.e., the disseminated grains are not evenly distributed at the hand sample scale, and are locally interconnected as in Fig. 4.16 B,D,E), and as rims to prior magnetite and pyrite (Fig. 4.16 D,E). The highest grade of dominantly disseminated mineralisation documented in this study occurs in the bornite zone, with 3.0 % chalcopyrite, 1.1 % pyrite, 0.5 % magnetite, and 0.1 % bornite (based on thin section image processing in WR377, 1453.4 m; Appendix A). The corresponding metre assay yielded 5.33 ppm Au, 4.31 % Cu, and 4.5 ppm Ag.

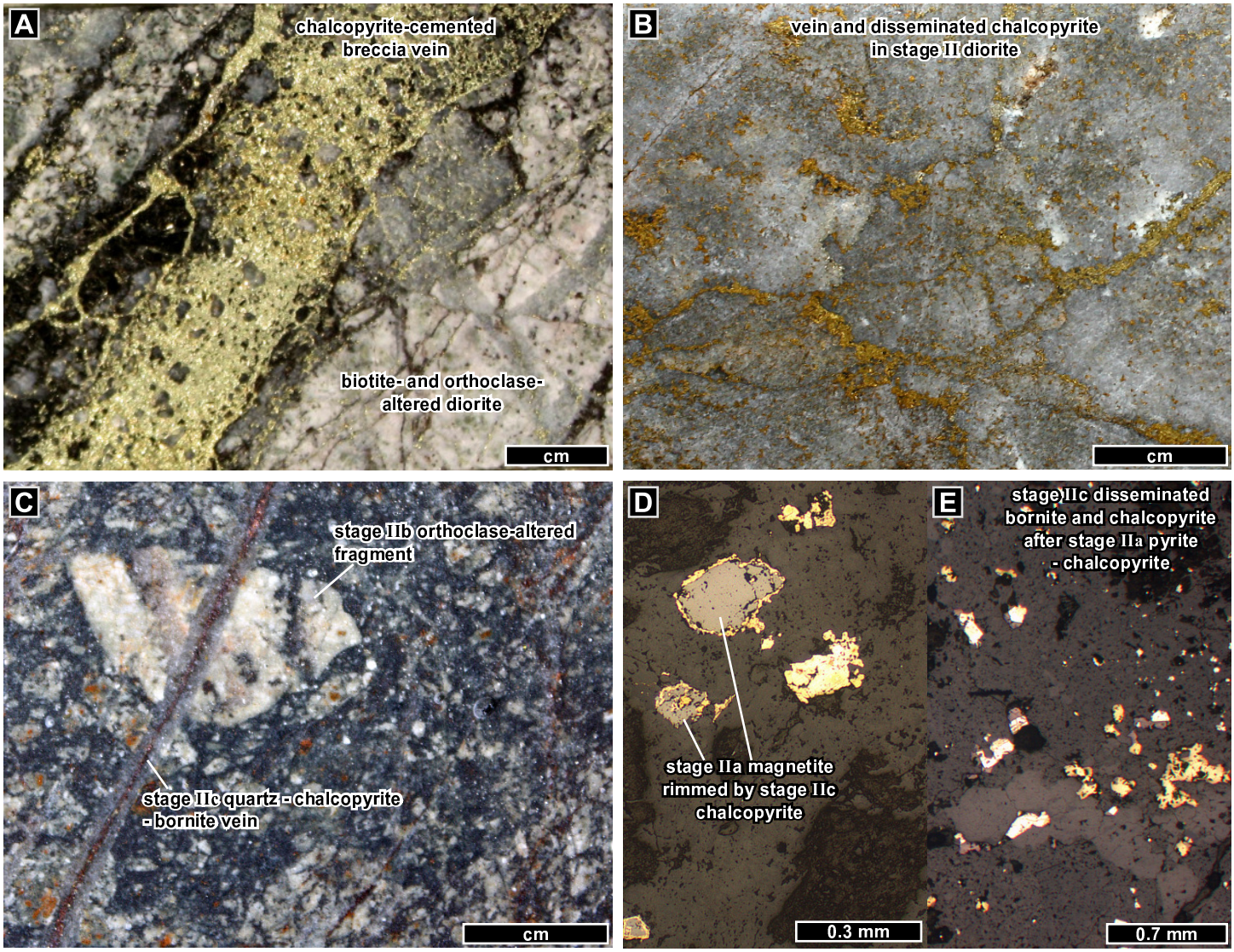

Figure 4.16: Stage IIc veins and disseminated sulfides (the main stage of Golpu porphyry mineralisation). A) Quartz - chalcopyrite veins and chalcopyrite - cemented breccia veins that have cross-cut biotite- and orthoclase-altered stage II diorite (WR397, 1361.0 m). B) Disseminated and vein mineralisation through stage II diorite. The corresponding interval contains 7.43 ppm Au, 4.0 wt. % Cu, and 4.9 ppm Ag (WR377, 1434.1 m). C) Breccia vein containing orthoclase-altered and quartz-veined diorite fragments and magnetite - chalcopyrite - bornite mineralised hydrothermal sandstone infill. It has been cross-cut by a quartz - chalcopyrite - bornite vein, at left (WR377, 1182.4 m). D) Disseminated chalcopyrite after magnetite (reflected PPL; WR397, 1361.0 m). E) Disseminated chalcopyrite - bornite after pyrite - chalcopyrite in stage II diorite (reflected PPL; WR392, 1546.3 m).

Outside of the stage II diorite, stage II disseminated sulfides occur as diffuse halos around stage IIc veins (Fig. 4.18 A), and as rims to disseminated sulfides in the stage I diorites (Fig. 4.18 B). Whereas most of the stage II diorite contains trace disseminated bornite (along with chalcopyrite, magnetite, and molybdenite), the wallrock contains only disseminated chalcopyrite and pyrite (along with trace molybdenite; Fig. 4.18 C).

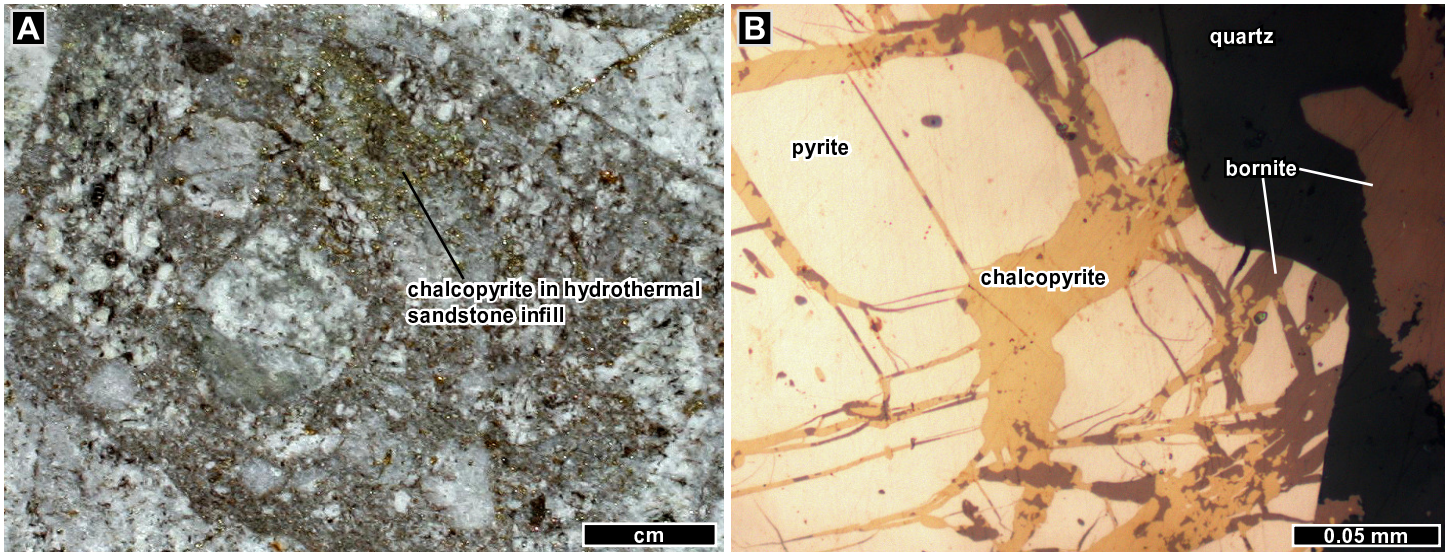

Figure 4.17: Stage IIc sulfides. A) Intrusive margin proximal breccia vein containing quartz-veined and orthoclase- and biotite-altered diorite fragments, in a hydrothermal sandstone infill containing disseminated chalcopyrite. The mineralised breccia has been cross-cut by chalcopyrite veins (e.g., at top right; WR392, 1548.7 m). B) Photomicrograph of bornite - chalcopyrite after pyrite in a stage IIc quartz - sulfide vein (reflected PPL; WR392, 1546.3 m).

Mineralised stage II diorite contains, on average, approximately 25 - 50 vol % quartz (vein + primary groundmass), 20 - 30 % perthitic orthoclase (orthoclase with albite lamellae), 10 - 20 % plagioclase, 5 - 10 % biotite (± chlorite ± muscovite, generally after hornblende phenocrysts), 2 - 5 % chalcopyrite (with metre-scale variations up to 25 %, depending on the density of veins), 1 - 3 % pyrite, 0 - 5 % magnetite, and 0 - 1 % bornite. Average stage II diorite contains 3 - 6 vol % chalcopyrite + pyrite + bornite.

Table 4.4: Mineralogy of stage IIc porphyry mineralised Golpu diorite

Sample description	Sample location	Summary of bulk mineralogy (vol % by quantitative XRD)
Well mineralised stage II diorite; vein halo orthoclase - biotite altered diorite, with 25 - 30 % quartz - chalcopyrite - pyrite veins and finely disseminated sulfides	WR377, 1116.4 m	37 % plagioclase (albite > labradorite), 27 % quartz, 23 % chalcopyrite, 3 % biotite, 3 % orthoclase
	WR392, 1402.0 m	33 % quartz, 22 % orthoclase, 21 % plagioclase (labradorite > albite), 10 % biotite, 6 % chalcopyrite, 2 % kaolinite - dickite, 2 % pyrite

Totals do not add to 100 because trace components are not presented in this table. Sample WR377, 1116.4 m was collected from a 1 metre interval that contains 1.2 ppm Au; the metre assay corresponding to sample WR392, 1402.0 m contains 8.5 ppm Au.

Stage IIc trace and accessory minerals

Stage IIc sulfides typically occur in sulfide or quartz + sulfide veins, but some sulfides are in sparse irregular patches or veins of coarse-grained biotite and perthitic orthoclase (Fig. 4.18 D-F). Other stage IIc accessory phases include rutile (Fig. 4.18 E, 4.21 E), chalcocite (Fig. 4.19 A), cubanite as exsolution lamellae in chalcopyrite (Fig. 4.19 B), sphalerite, galena, tennantite (Fig. 4.19 C), molybdenite (Fig. 4.19 D), barite (Fig. 4.19 E), rhodochrosite (Fig. 4.19 F), magnetite (Fig. 4.20 A,C, 4.21 A-D), hematite (Fig. 4.21 B), calcite (Fig. 4.21 A,E), and chlorite (Fig. 4.21 A). A single quartz-hosted inclusion of native bismuth 4 µm across was also observed by SEM in a stage II quartz - chalcopyrite - gold vein (sample WR397, 1359.3 m).

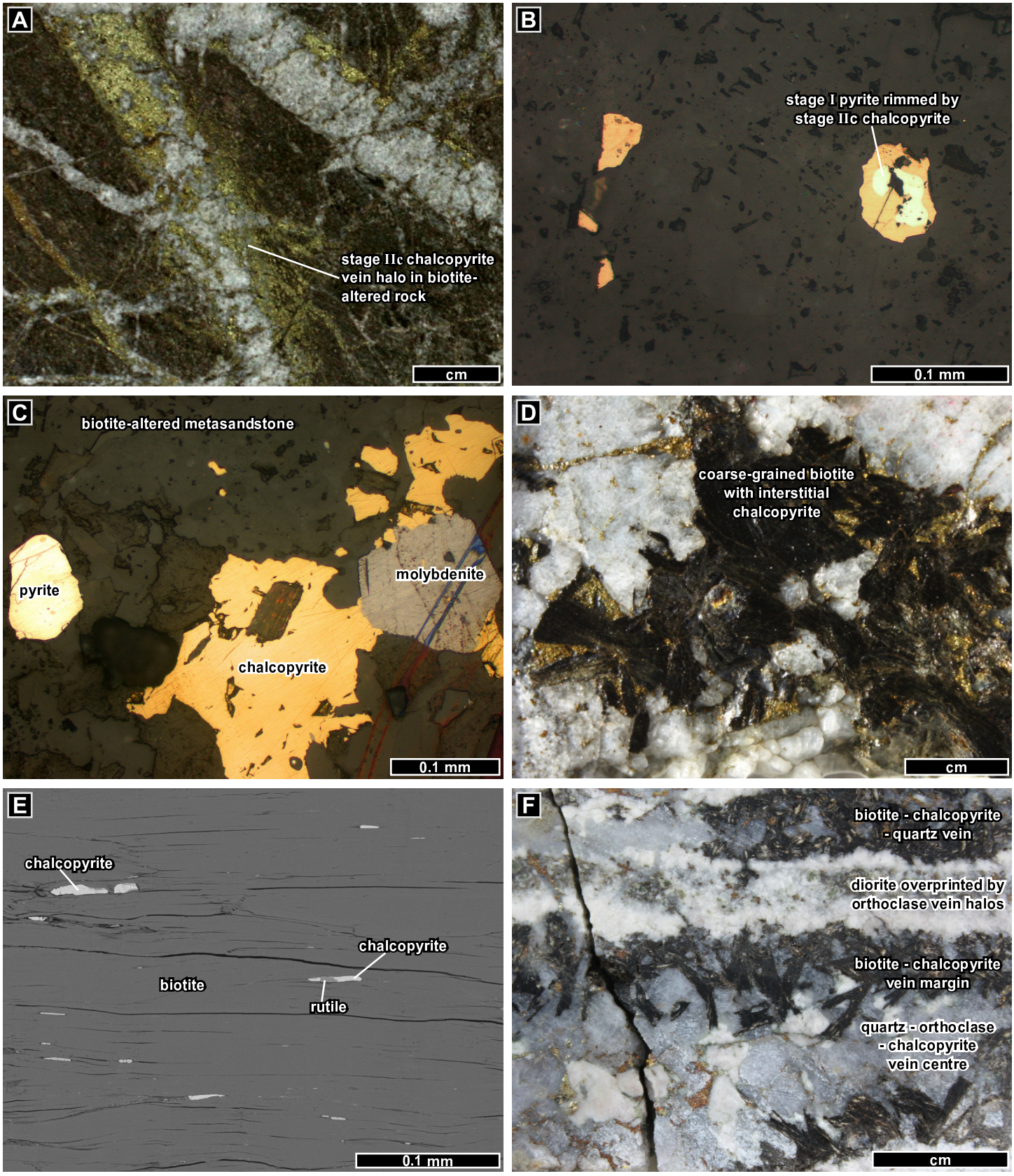

Figure 4.18: Stage IIc Golpu porphyry mineralisation. A) Diffuse chalcopyrite vein halo into biotite-altered metasandstone (WR392, 1662.0 m). B) Stage II chalcopyrite rimming disseminated pyrite in stage I diorite (reflected PPL; WR392, 1699.2 m). C) Disseminated sulfides in biotite-altered wallrock include pyrite, chalcopyrite, and molybdenite (reflected PPL; WR392, 1662.6 m). D) Chalcopyrite occurs with (interstitial to) coarse-grained biotite patches in stage II diorite (WR392, 1495.8 m). E) Chalcopyrite and rutile along cleavage planes of stage II biotite (backscattered electron image [SEM BSE]; WR392, 1495.8 m). F) Irregular pegmatitic biotite patches are in places transitional to veins, such as these biotite - chalcopyrite - bornite - quartz - orthoclase veins with orthoclase halos (WR377, 1328.6 m).

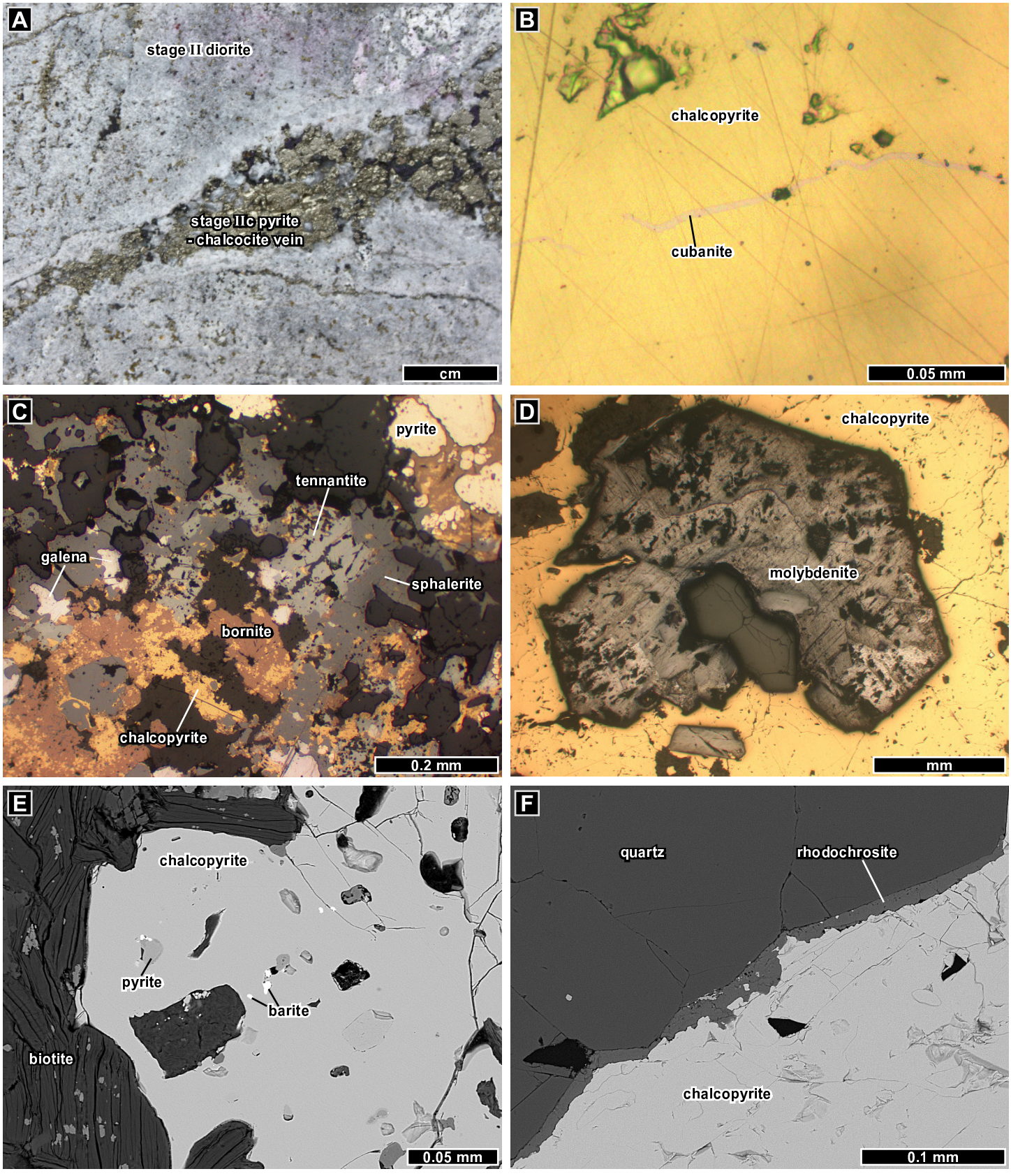

Figure 4.19: Stage IIc accessory minerals. A) Pyrite - chalcocite - quartz vein through diorite, with primary hypogene chalcocite as a cement to pyrite fragments (WR 377, 1581.2 m). B) Very thin lamellae of cubanite occur throughout the stage IIc chalcopyrite veins (reflected PPL; WR377, 1403.5 m). C) Galena, sphalerite, tennantite, bornite, chalcopyrite, and pyrite along a stage IIc vein margin (reflected PPL; WR392, 1546.3 m). D) Subhedral plate of molybdenite in a gold-bearing stage IIc chalcopyrite vein (reflected PPL; WR337, 1220.2 m). E) Barite and pyrite inclusions in a stage IIc gold-bearing chalcopyrite vein (SEM BSE; WR377, 1466.2 m). F) Rhodochrosite along the margin of a stage IIc gold-bearing chalcopyrite vein (SEM BSE; WR397, 1359.3 m).

Gold occurs as trace native inclusions < 5 to 80 µm across in chalcopyrite and pyrite (Figs. 4.20, 4.21). Many gold inclusions occur along chalcopyrite - pyrite and chalcopyrite - magnetite grain boundaries in veins and disseminated stage II sulfides (Fig. 4.20). Figure 4.21 D shows a gold inclusion in disseminated chalcopyrite.

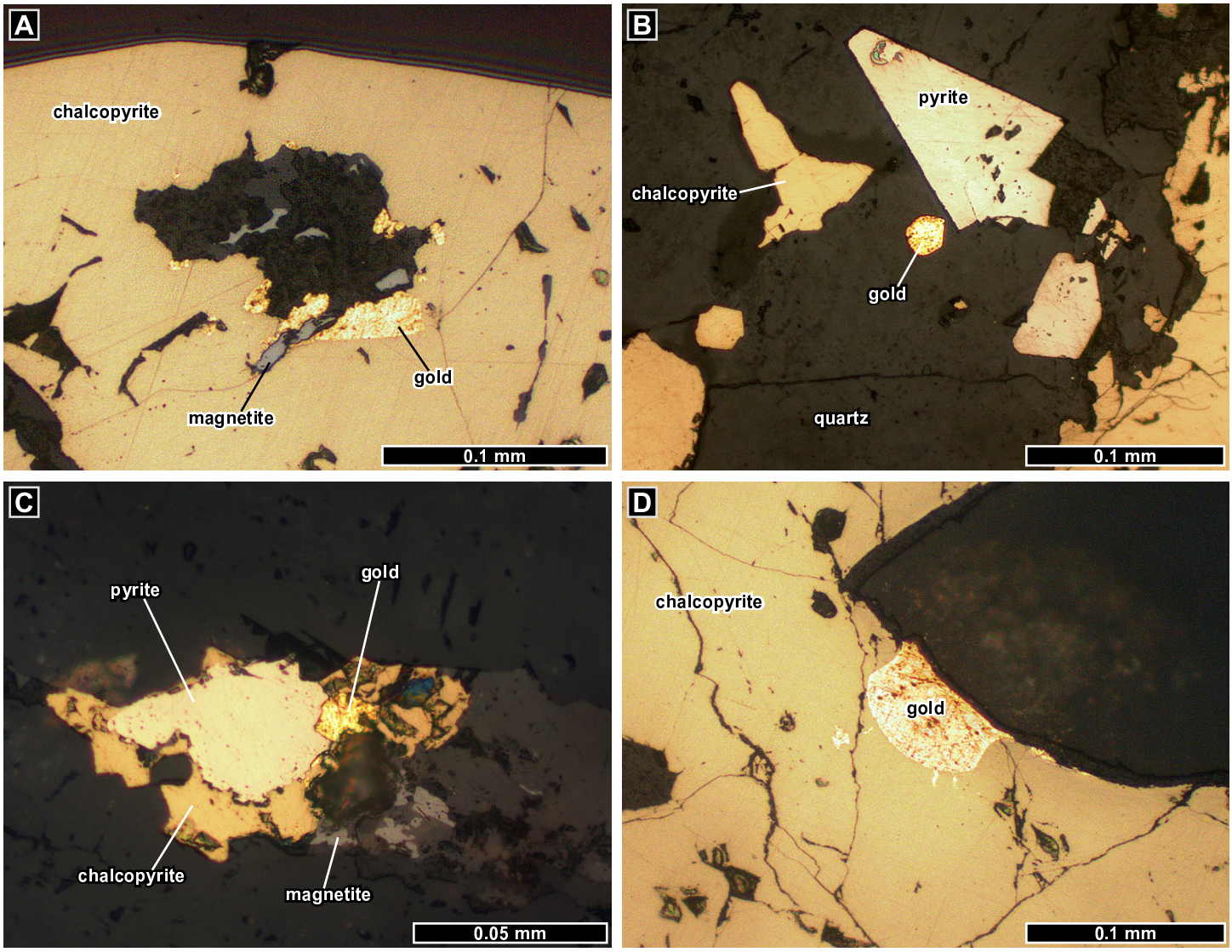

Figure 4.20: Stage IIc occurrences of native gold in Golpu porphyry mineralisation. All images are in reflected plane polarised light. A) Gold rimming magnetite in a chalcopyrite vein (WR337, 1220.2 m). B) Native gold inclusion surrounded by quartz, within a quartz - chalopyrite - pyrite vein (WR377, 1530.0 m). C) Gold grain at a pyrite - chalcopyrite grain boundary, within the central seam of a quartz - pyrite - chalcopyrite - magnetite vein (WR 377, 1171.5 m). D) Native gold grain ~ 80 µm in diameter, in a chalcopyrite vein (WR 337, 1220.2 m).

4.3.3 Stage III (Early Wafi / Late Golpu)

Stage III marks a change from diorite-concentric to upward-flaring zones of veins and alteration. It is defined by the first appearance of quartz - pyrite veins with muscovite halos that have cross-cut stage II biotite-, muscovite-, and chlorite- and actinolite-altered rocks (Fig. 4.22). There is a transition upwards from sparse pyrite veins with thin halos (e.g., Fig. 4.22 D) to wider muscovite halos, then to overlapping halos or pervasive muscovite alteration (Fig. 4.22 A-C). These upward-widening zones occur as shoulders to the stage II diorite

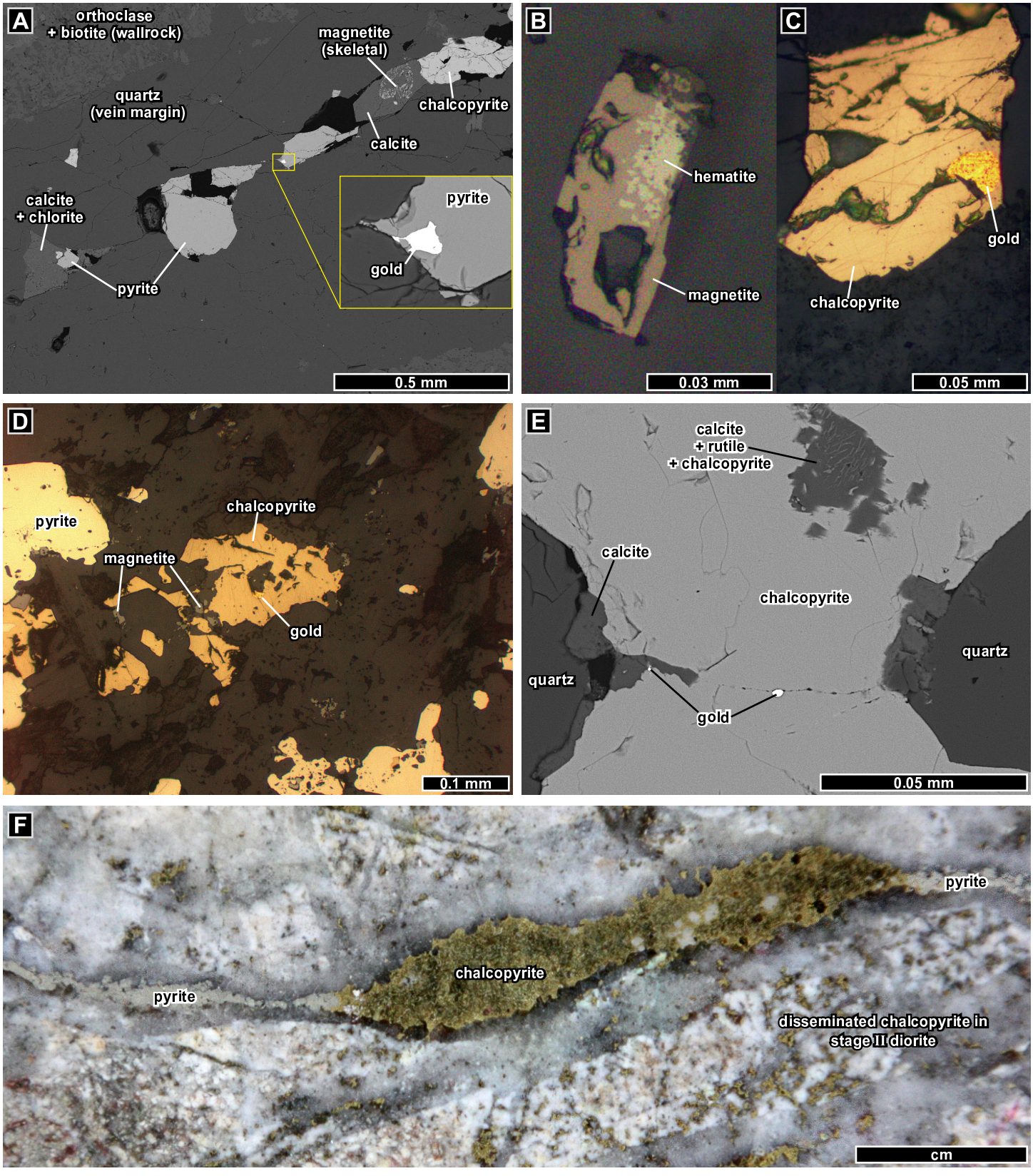

Figure 4.21: Stage IIc occurrences of native gold in Golpu. A) Central seam of a quartz - chalcopyrite vein with native gold, pyrite, chlorite, calcite, and skeletal (partically calcite-replaced) magnetite (SEM BSE; WR397, 1359.3 m). B) Magnetite - hematite inclusion near a stage IIc vein margin into a hematite - magnetite vein halo (reflected PPL; WR377, 1403.5 m). C) Native gold in chalcopyrite, within the same quartz - chalcopyrite - magnetite vein as in panel C (WR377, 1403.5 m). D) Gold in disseminated chalcopyrite - magnetite in stage II diorite (WR377, 1453.4 m). E) Calcite, rutile, and native gold in a chalcopyrite - pyrite - bornite vein (SEM BSE; WR397, 1359.3 m). F) Example of Golpu vein and disseminated sulfides that typically contain native gold inclusions. This sample is the same as in panel D (WR377, 1453.4 m).

(Figs. 4.1, 4.23), and their upper portions have been overprinted by stage IV alteration.

The Wafi breccia complex (Fig. 4.23) contains biotite- and orthoclase-altered fragments along with zircon grains of Golpu intrusive ages and older, and has been overprinted by stage IV veins and alteration (section 4.3.4). It is therefore interpreted to have erupted during stage III – that is, after stage II biotite - orthoclase alteration, and before stage IV kaolinite - alunite alteration. Curtis and Ryan (1997) reported mineralised porphyry fragments within the breccia complex from WR154, leading them to the same conclusion: the diatreme erupted after porphyry Cu mineralisation, and before kaolinite and alunite alteration.

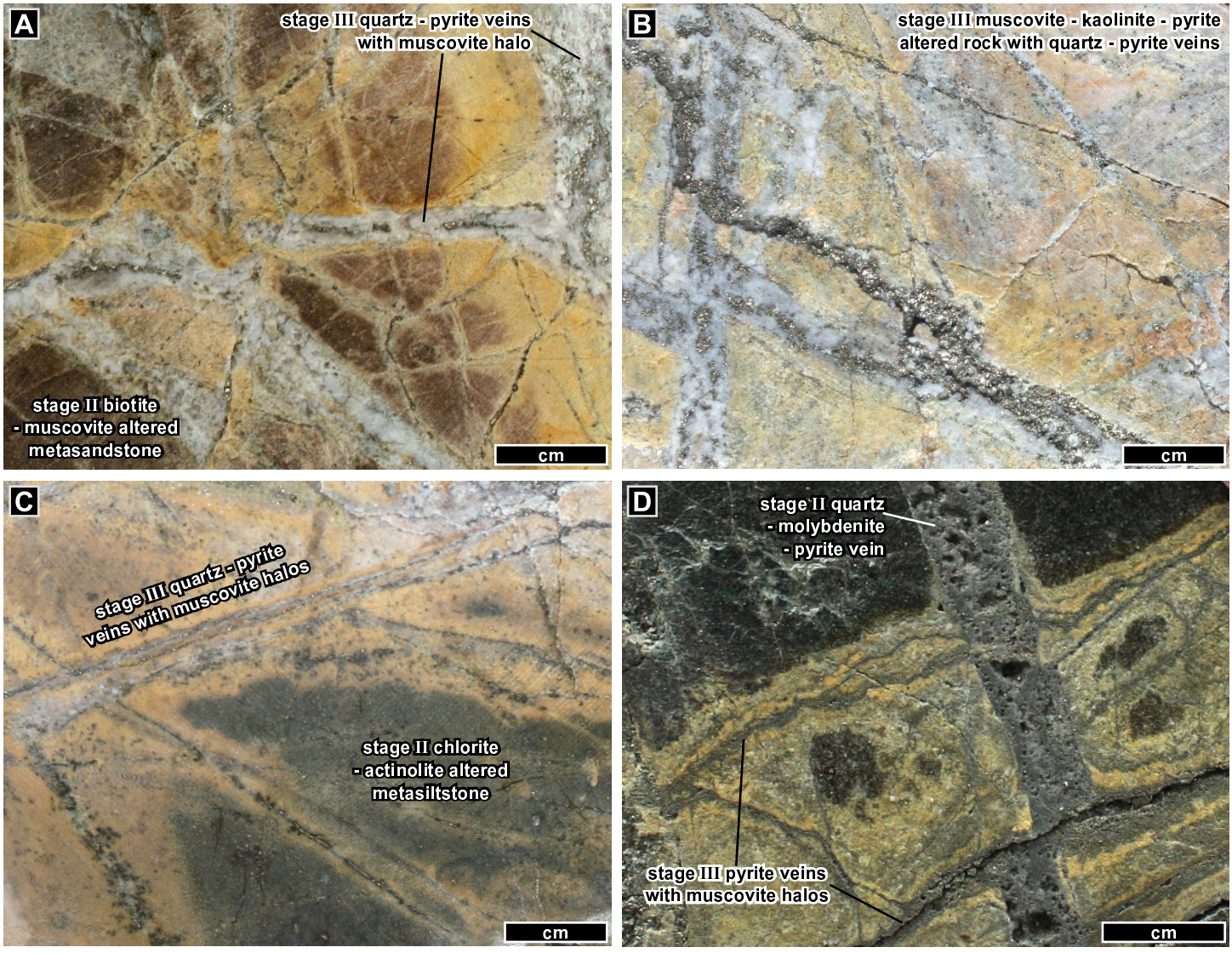

Figure 4.22: Stage III transitional quartz - pyrite veins and muscovite - pyrite altered rocks and vein halos. A) Muscovite vein halos in biotite - muscovite (+ trace hematite) altered metasandstone (WR337, 734.3 m). B) Pervasive muscovite - kaolinite - pyrite altered rock associated with stage III quartz - pyrite veins (WR392, 896.5 m). C) Deep quartz - pyrite veins with muscovite halos after chlorite - actinolite (+ trace epidote) altered pebbly metasiltstone (WR402, 1005.5 m). D) Pyrite veins with muscovite halos have cross-cut and offset biotite-altered and quartz - molybdenite - pyrite veined metasandstone (WR402, 662.7 m).

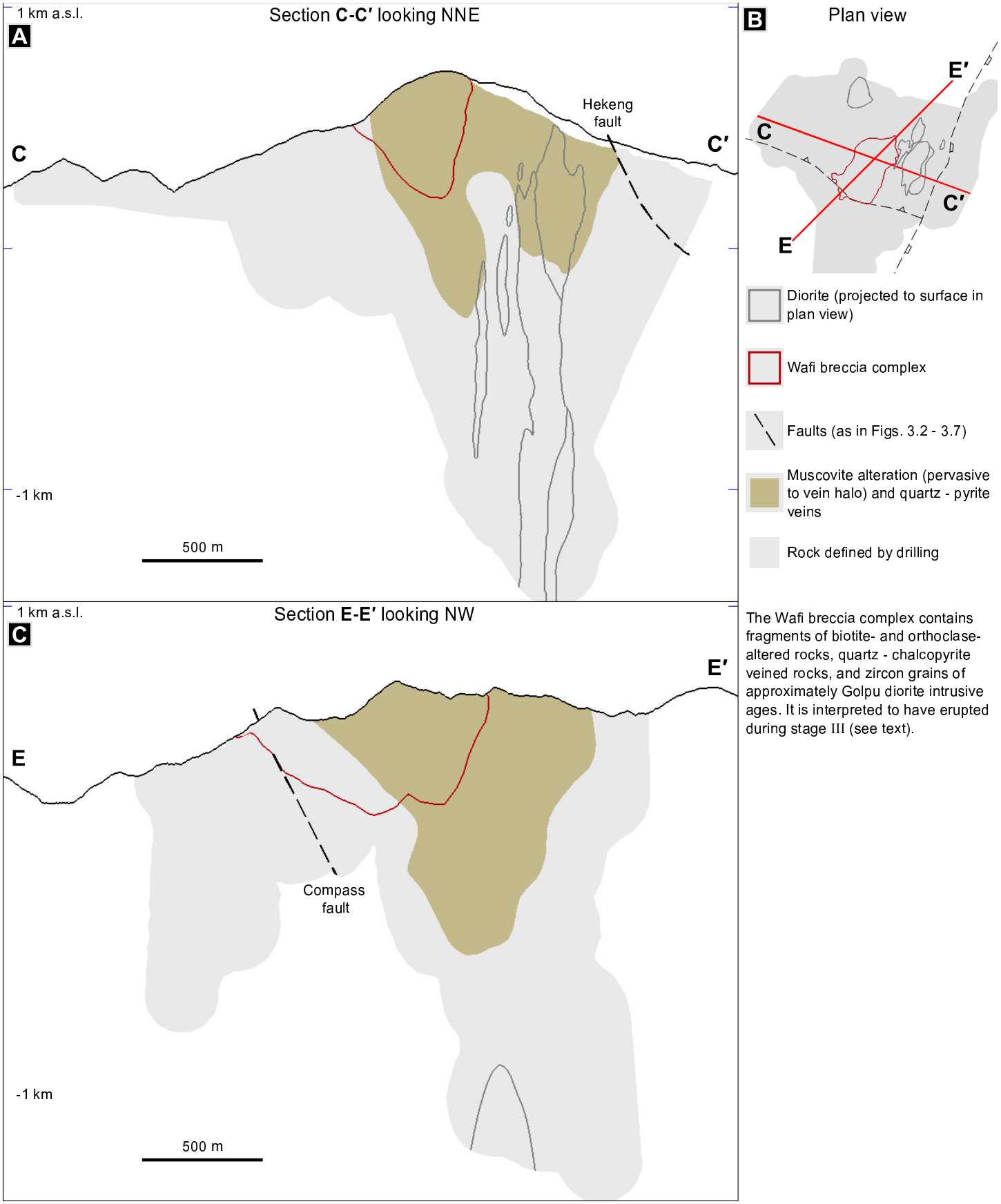

The Wafi breccia complex contains fragments of biotite- and orthoclase-altered rocks, quartz - chalcopyrite veined rocks, and zircon grains of approximately Golpu diorite intrusive ages. It is interpreted to have erupted during stage III (see text).

Figure 4.23: Stage III. Sections C-C′ (A) and E-E′ (C) show the distribution of muscovite alteration with disseminated pyrite, and quartz - pyrite veins with muscovite halos. The zone of stage III muscovite alteration in the Wafi breccia complex is inferred; some may have occurred before eruption. Section lines, projections of the Golpu and Nambonga intrusions, and the location of the Wafi breccia complex in outcrop are shown in the plan view (B).

4.3.4 Stage IV (Main Stage Wafi Mineralisation)

The main stage of Wafi epithermal mineralisation comprises two contrasting vein and alteration domains that are broadly zoned about the Golpu intrusive complex, as shown in simplified plan view in Figure 4.24. A high sulfidation (HS) epithermal domain occurs above and overprints the top of the Golpu diorites. This domain includes pyrite - covellite - tennantite ± bornite ± chalcocite ± enargite mineralisation near the current erosional surface, and transitions to sparse kaolinite - pyrite veins at depth (Fig. 4.25). The HS epithermal domain is described in section 4.3.4.1.

An intermediate sulfidation (IS) epithermal domain occurs along the periphery of the HS epithermal domain, particularly along the Compass fault and along east-dipping metaconglomerate units. The IS epithermal domain includes zones of gold-bearing vein and disseminated pyrite mineralisation that make up most of the Wafi epithermal deposit (Figs. 4.1, 4.25). The IS epithermal domain is described in section 4.3.4.2.

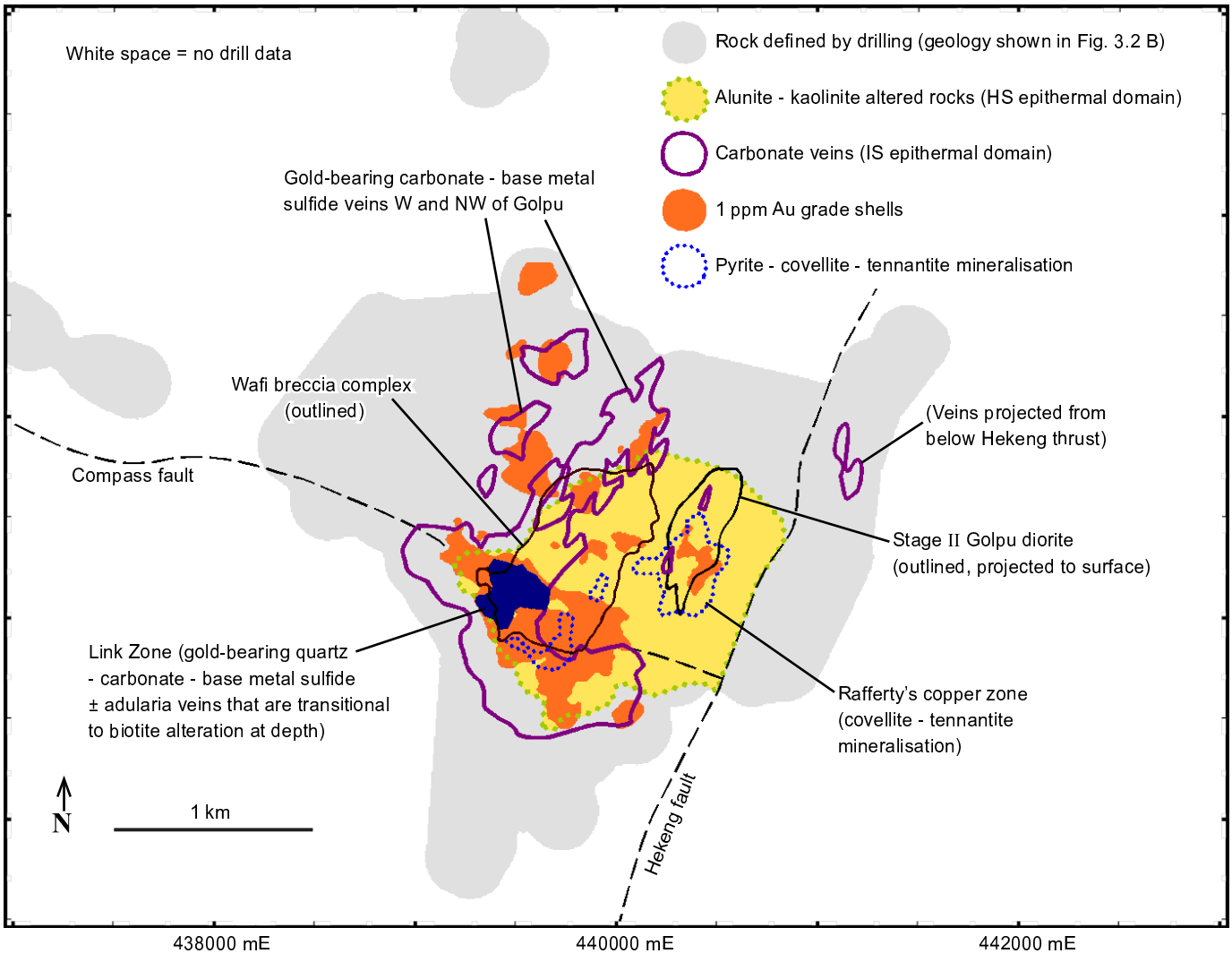

Figure 4.24: Simplified map of stage IV veins and altered rocks projected from within 500 metres of surface. The alunite - kaolinite domain occurs above, and overprints the top of, the Golpu diorites. The carbonate domain is peripheral to the alunite-altered rock, occurring mostly west and southwest of Golpu. Carbonate veins may make up as little as 0.5 % of the rock, but their occurrence within (and paucity outside of) the volume outlined is clearly documented in MMJV logs and other data. The labeled zones of epithermal mineralisation (Rafferty's copper zone, Link Zone, and carbonate veins west and northwest of Golpu) are described separately in the text. Link Zone, projected from depth, occurs along and south of the Compass fault, and does not intersect the upward-flaring Wafi breccia complex.

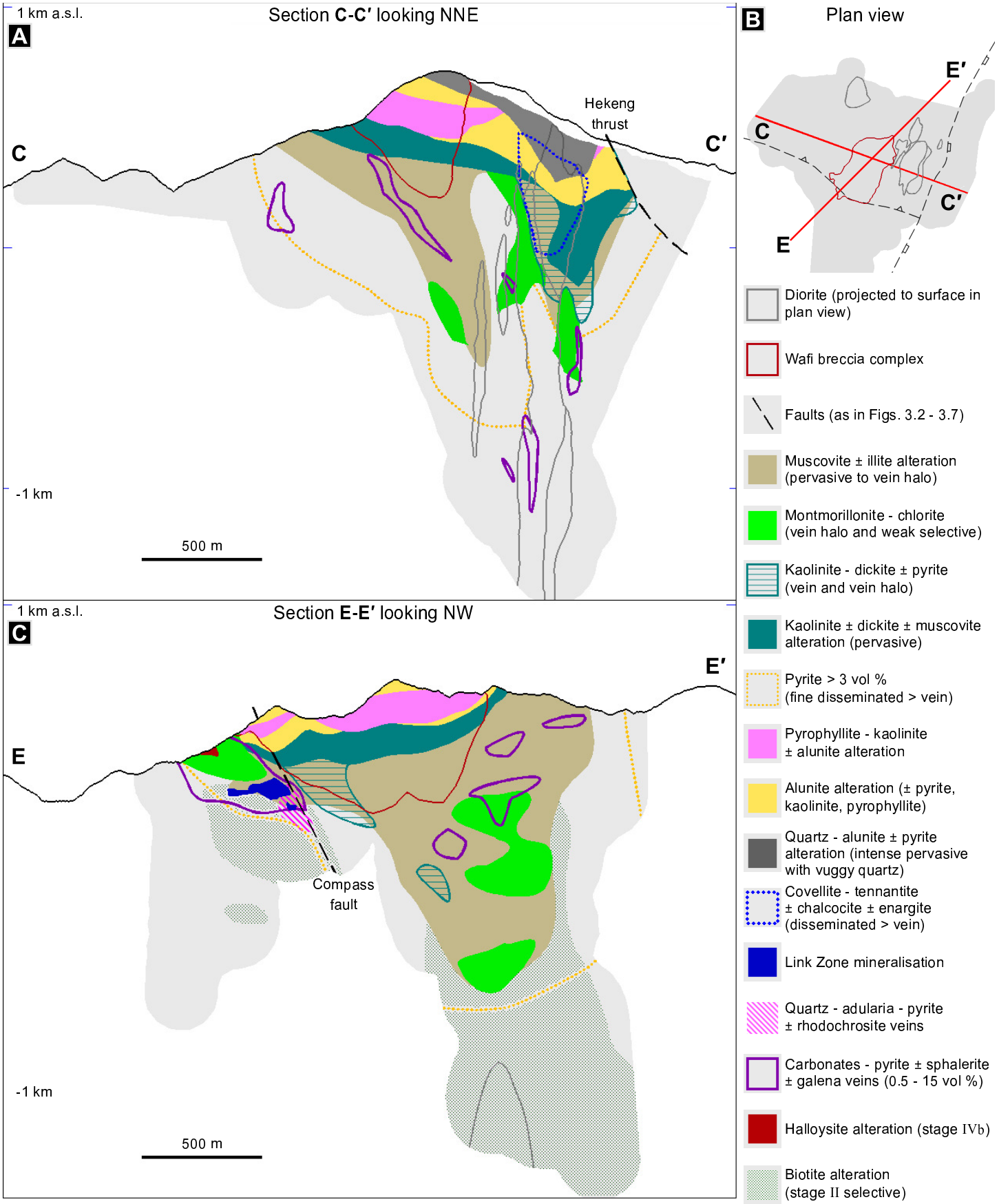

Figure 4.25: Stage IV. Sections C-C′ (A) and E-E′ (C) show main stage Wafi epithermal veins and alteration. All vein and alteration zones are stage IVa, except for the zones of biotite alteration (stage II), and some of the montmorillonite - halloysite alteration above Link Zone (stage IVb) shown in panel C. The upper limit of covellite-bearing mineralisation in panel A (section C-C′) corresponds with the base of supergene oxidation. Carbonates are mostly rhodochrosite, calcite, and kutnohorite.

4.3.4.1 Stage IVa high sulfidation epithermal veins and altered rocks

The lowermost portion of the stage IV HS epithermal domain features sparse kaolinite - pyrite ± muscovite ± dickite veins (Fig. 4.26 A, B, D). The deep kaolinite-bearing veins transition upwards into several zones of pervasive alteration. The zones of pervasive stage IVa alteration are broadly E-dipping, and their deepest parts are centred over the eastern shoulder of the Golpu intrusive complex (Fig. 4.25 A). They have overprinted the metasedimentary host rocks, the Wafi breccia complex, and the Golpu diorites.

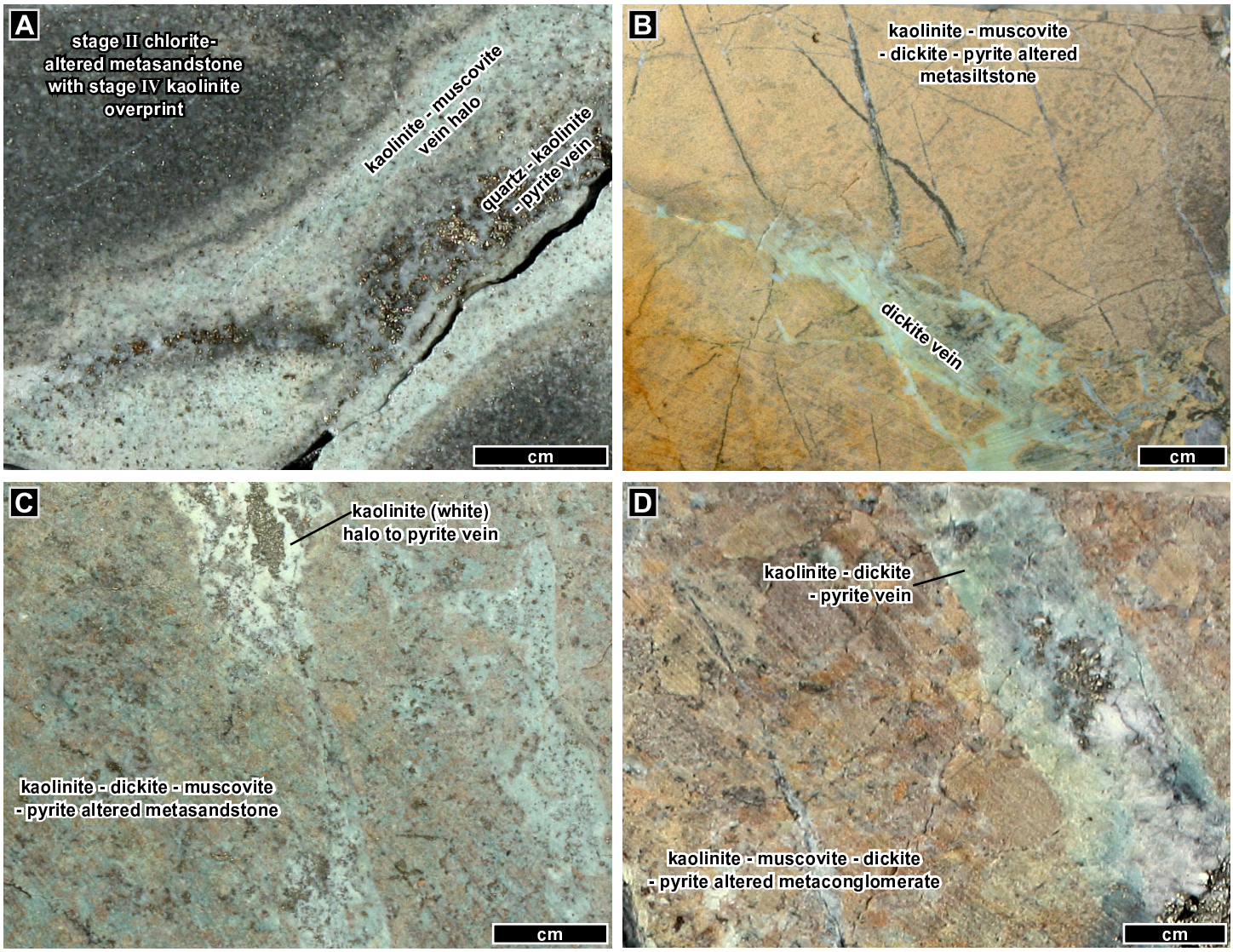

Figure 4.26: Stage IVa kaolinite-bearing veins and altered rocks that characterise the lower parts of the stage IV alunite - kaolinite alteration domain. The minerals listed in this figure were identified by SWIR and XRD. A) Deep quartz - kaolinite - pyrite vein with kaolinite - muscovite vein halo after chlorite (+ trace biotite and muscovite) altered metasandstone (WR397, 759.0 m). B) Dickite veins after kaolinite - muscovite - dickite - pyrite altered metasiltstone (WR337, 217.4 m). C) Pervasive kaolinite - dickite - muscovite - pyrite altered metasandstone (WR337, 500.5 m). D) Kaolinite - dickite - pyrite veins through kaolinite - muscovite - dickite - pyrite altered metaconglomerate (WR377, 549.0 m).

The lowermost zone of pervasive stage IVa altered rocks contains kaolinite, dickite, finely disseminated pyrite, and muscovite (Fig. 4.26 B-D). Average mineralogy in this zone comprises up to 45 vol % kaolinite to dickite, < 30 vol % muscovite, and < 7 vol % pyrite (Table 4.5). SWIR analyses indicate that illite is present in

some muscovite-bearing samples near the base of the pervasive kaolinite - dickite alteration zone. Elsewhere, illite is generally absent (Appendix F).

Table 4.5: Mineralogy of stage IVa kaolinite - dickite - muscovite - pyrite altered rocks (the lowermost zone of pervasive stage IV alteration)

Sample description	Sample location	Summary of bulk mineralogy (vol % by quantitative XRD)
Strong pervasive kaolinite - dickite - pyrite altered metasandstone	WR349, 188.4 m	47 % quartz, 41 % kaolinite - dickite*, 7 % pyrite
Moderate pervasive kaolinite - muscovite - pyrite altered metasandstone	WR337, 157.7 m	60 % quartz, 23 % kaolinite - dickite*, 7 % muscovite, 7 % pyrite
Strong pervasive muscovite - pyrite altered metasiltstone	WR315, 444.8 m	39 % quartz, 29 % muscovite, 17 % plagioclase (~ albite), 5 % biotite, 4 % pyrite, 2 % chlorite

*SWIR analyses indicate both kaolinite and dickite are present. Totals do not add to 100 because trace components are not presented in this table.

Moving upwards, the transition to stage IVa alunite - kaolinite altered rocks occurs between 10 and 200 metres above the base of pervasive kaolinite altered rocks (Fig. 4.25). This diffuse transition from kaolinite- to kaolinite- and alunite-altered rocks generally corresponds with a gradually lighter colour in drill core (e.g., Figs. 4.27 B, 4.28 A,C). Most of the alunite occurs as disseminated tabular crystals < 0.2 mm long (e.g., Fig. 4.28 B), along with kaolinite, pyrophyllite, pyrite, and / or quartz (Fig. 4.28).

Table 4.6: Mineralogy of stage IVa alunite - quartz - pyrite ± kaolinite ± pyrophyllite altered rocks (zones of pervasive alteration overlying the zone of pervasive kaolinite alteration)

Sample description	Sample location	Summary of bulk mineralogy (vol % by quantitative XRD)
Moderate pervasive muscovite - pyrite to (basal) alunite - pyrophyllite altered metasiltstone	WR321, 467.7 m	45 % quartz, 20 % muscovite, 18 % plagioclase (albite > labradorite), 10 % pyrite, 4 % alunite, 2 % pyrophyllite
Strong to intense pervasive pyrophyllite - alunite - pyrite altered Wafi breccia complex	WR321, 175.3 m	48 % quartz, 32 % pyrophyllite, 10 % alunite, 6 % pyrite, 3 % muscovite
	WR301, 184.0 m	49 % quartz, 26 % pyrophyllite, 16 % alunite, 5 % pyrite
Intense pervasive quartz - alunite altered Wafi breccia complex	WR301, 115.7 m	62 % quartz, 36 % alunite
	WR301, 229.2 m	83 % quartz, 13 % alunite
Vuggy quartz (intense remnant quartz altered stage I Golpu diorite)	WR398, 25.0 m	98 % quartz

Note: totals do not add to 100 because trace components are not presented in this table.

Stage IVa pyrophyllite alteration occurred near the lowermost zone of pervasive alunite alteration, particularly within the Wafi breccia complex (Fig. 4.25). The pyrophyllite is cryptocrystalline or masked by clay in samples from this study, and in hand sample appears white in association with alunite - quartz - pyrite ± kaolinite ± muscovite (Fig. 4.27 B). XRD spectra of Tau-Loi (1996) indicate the presence of trace aluminium phosphate-sulfate (APS) minerals in association with some of the alunite nearest the Golpu diorites. Trace

diaspore was also reported in four of 498 thin sections examined by Leach (1989, 1990a, 1990b, 1990c, 1991a, 1991b) through the Wafi breccia complex. There is no obvious discrete zone of diaspore alteration evident at Golpu.

The upward transition from alunite - kaolinite - pyrite ± pyrophyllite altered rocks into stage IVa quartz - alunite altered rocks is sharp and irregular (Fig. 4.29). The quartz - alunite alteration has destroyed much of the

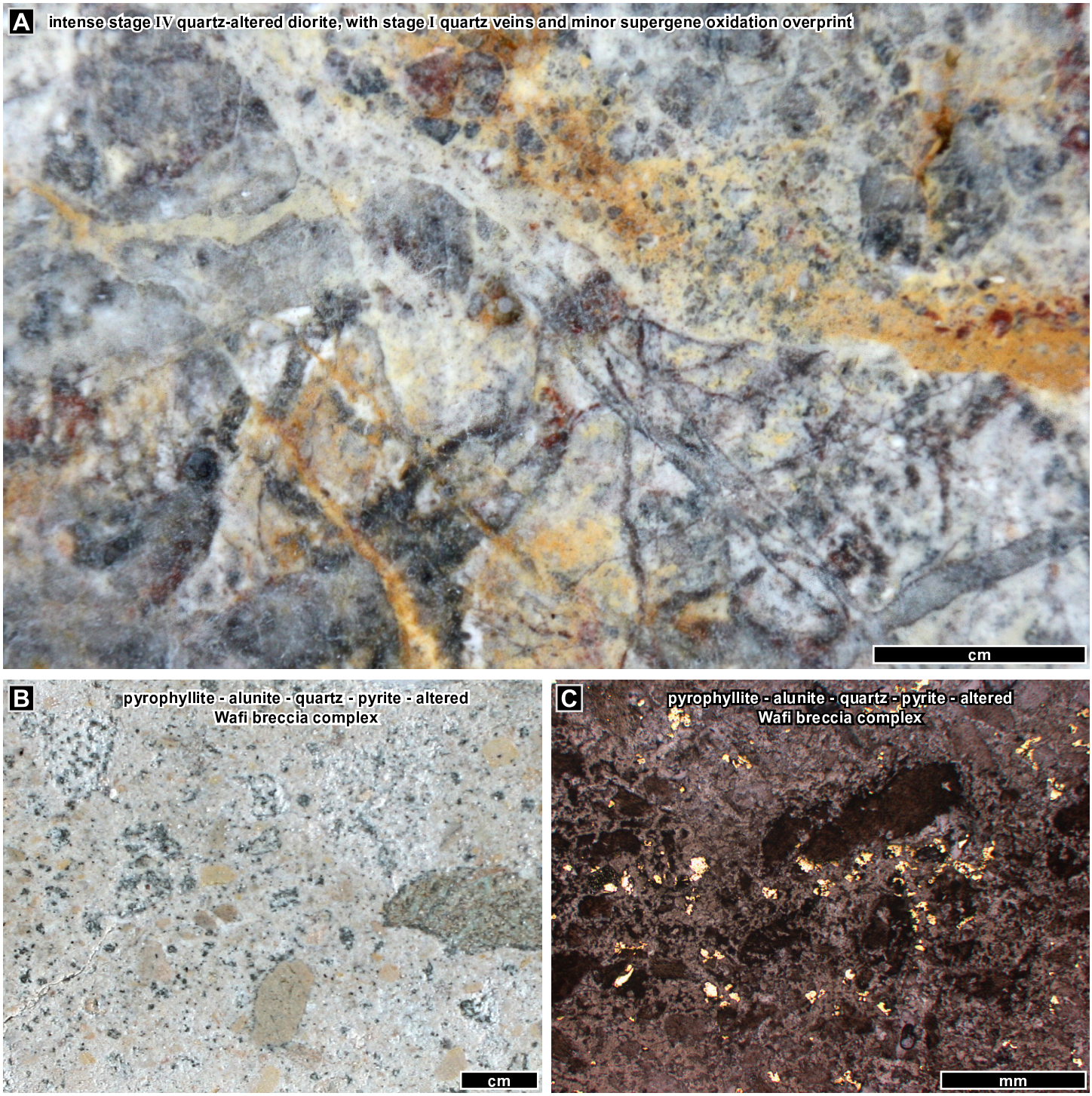

Figure 4.27: Stage IVa alunite-, pyrophyllite-, and quartz-altered rocks. A) Quartz veined and brecciated stage I Golpu diorite that has been intensely altered to remnant quartz, near the current erosional surface. The sample consists almost entirely of quartz, with some supergene hematite (WR398, 44.7 m). B) Pyrophyllite - alunite - quartz - pyrite - altered Wafi breccia complex. This sample contains 27 vol % pyrophyllite (WR301, 184.0 m). C) Photomicrograph of fine fragment-supported Wafi breccia, altered to mostly cryptocrystalline pyrophyllite - alunite - quartz - pyrite, as in image B (reflected PPL; WR301, 150.0 m).

protolith texture, but stockwork quartz veins are preserved locally as wormy remnants (Fig. 4.28 C). Most of the rock in the quartz - alunite zone consists of about 60 vol % quartz and 40 vol % alunite, with trace disseminated pyrite (Table 4.6).

Although dissolved cavities due to the stage IVa alteration are most common immediately above the Golpu diorites, patches of vuggy quartz occur throughout the quartz - alunite zone indicated in Figure 4.25. Within breccia veins near the Wafi breccia complex, the vuggy quartz alteration has dissolved the breccia infill (Fig. 4.28 D). In the Golpu diorites, vuggy quartz alteration has dissolved the diorite in between quartz stockwork veins, producing irregular vugs up to 1 cm across (Fig. 4.28 A). The remnant rock in the vuggy quartz zone consists almost entirely of quartz (Table 4.6), with molybdenite as a trace remnant in a few samples. The stage I laminated quartz - molybdenite veins shown in Figure 4.4 C (page 60) have, for example, retained 393 ppm Mo over one metre.

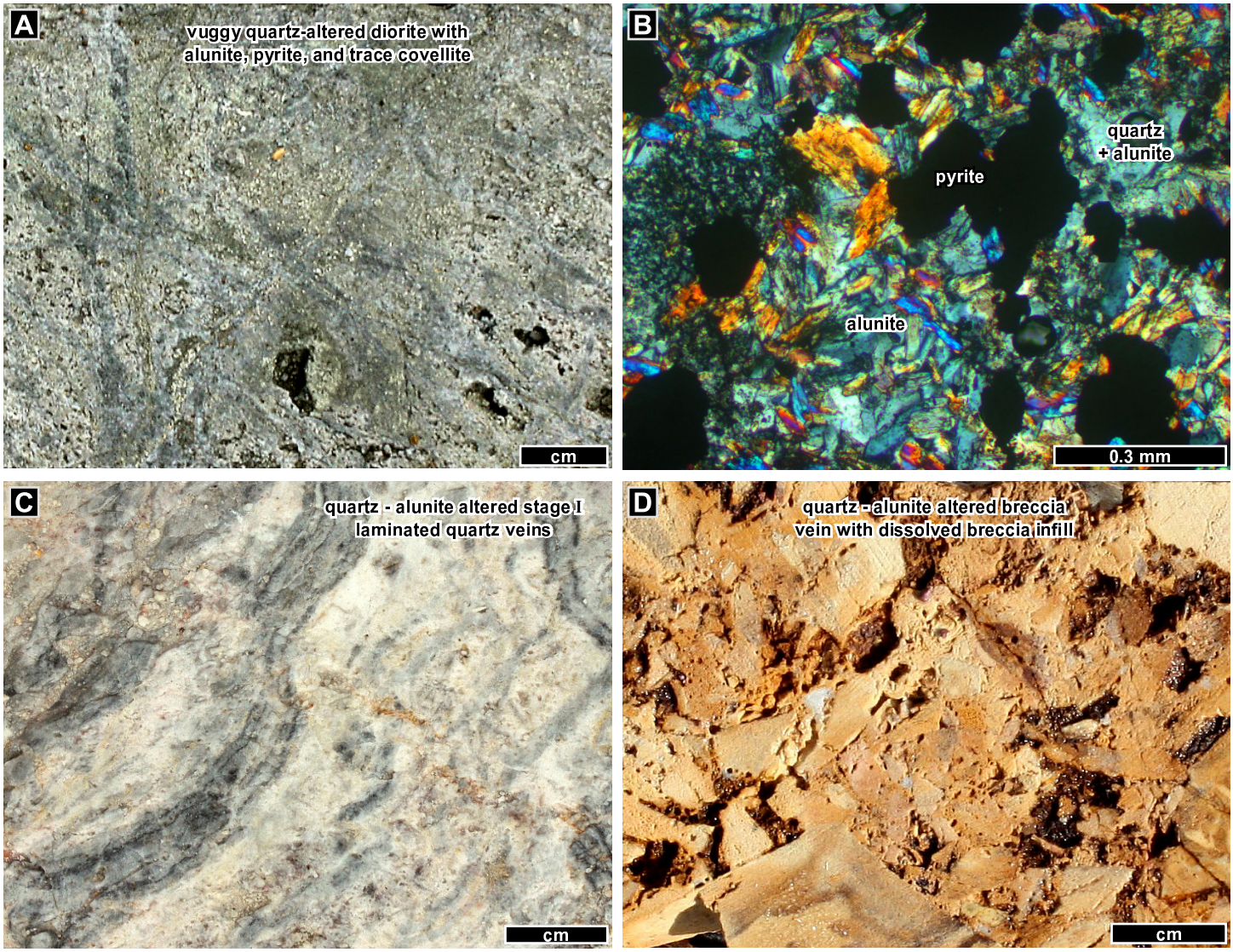

Figure 4.28: Stage IVa alunite-, pyrophyllite-, and quartz-altered rocks. A) Vuggy quartz after quartz-veined stage I diorite. Pyrite and trace covellite are finely disseminated and occur along the cavity walls (WR398, 118.9 m). B) Bladed alunite after diorite (opaque minerals are pyrite; XPL; WR398, 153.5 m). C) Quartz - alunite alteration after stage I stockwork quartz veins has resulted in a vermicular or wormy vein texture (WR398, 53.6 m). D) Quartz - alunite alteration (with later supergene hematite) has partly dissolved the infill to this chaotic, angular, fragment-supported breccia vein. The breccia contains some quartz-veined fragments (WR301, 229.2 m).

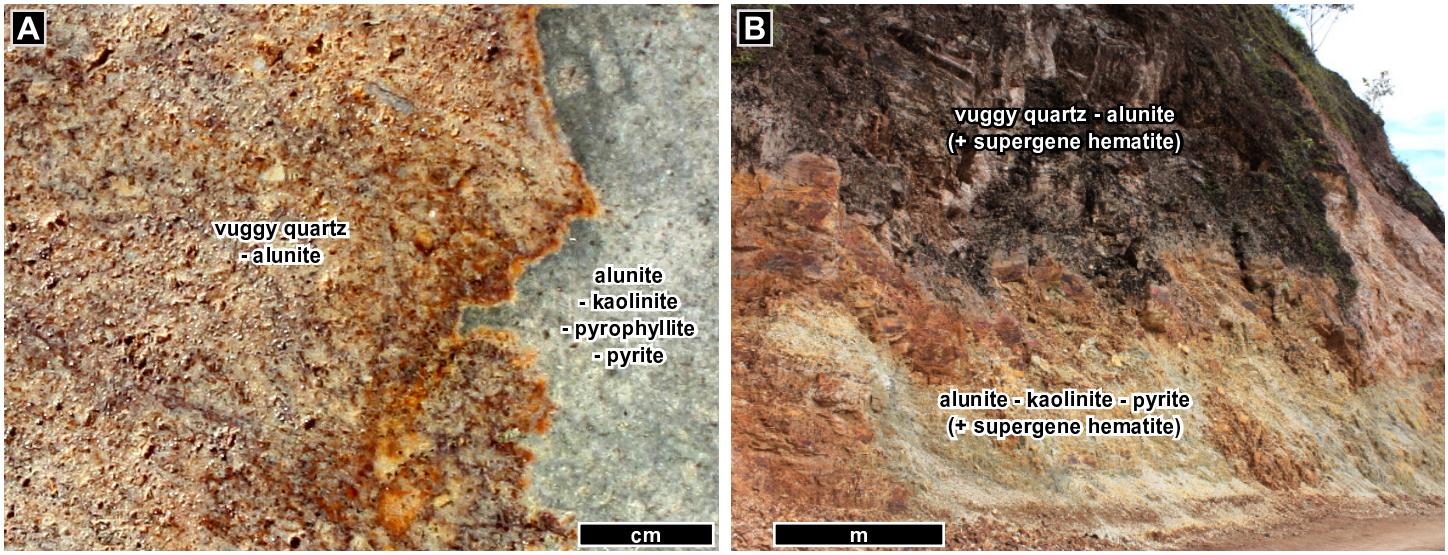

Figure 4.29: Stage IVa vuggy quartz - alunite transitions into alunite - kaolinite altered rock. A) Interface of vuggy quartz - alunite (+ pyrite, later hematite), into alunite - kaolinite - pyrophyllite - pyrite altered Wafi breccia (WR301, 161.9 m). B) Looking NE at outcrop of same interface as in image A, showing vuggy quartz - alunite overlying lighter coloured alunite - kaolinite - pyrite ± pyrophyllite altered metasedimentary rock. The metre scale applies to the foreground part of the image, at left.

Stage IVa pyrite - covellite - tennantite ± enargite mineralisation that has overprinted Golpu

Rafferty's copper zone (Fig. 4.24) comprises pyrite - covellite - tennantite mineralisation in an upward-flaring zone that has overprinted the uppermost Golpu diorite and adjacent 150 metres of wallrock (Figs. 4.1, 4.25). The stage IVa covellite and tennantite occur as veins and disseminated grains that were co-genetic with stage IVa alunite, kaolinite, and pyrite (Figs. 4.30 - 4.32). The covellite and tennantite together comprise up to 4 vol % of the rock, mostly occurring as very fine grains to irregular aggregates < 0.5 mm across, and as fine rims to pyrite (Figs. 4.30, 4.32 B-E). In some alunite-altered diorite samples, intergrown covellite, tennantite, and alunite occur as a diffuse rim to bornite - chalcopyrite (Fig. 4.32 B,C). Erceg (1991) interpreted this relationship as a high sulfidation overprint on pre-existing porphyry mineralisation.

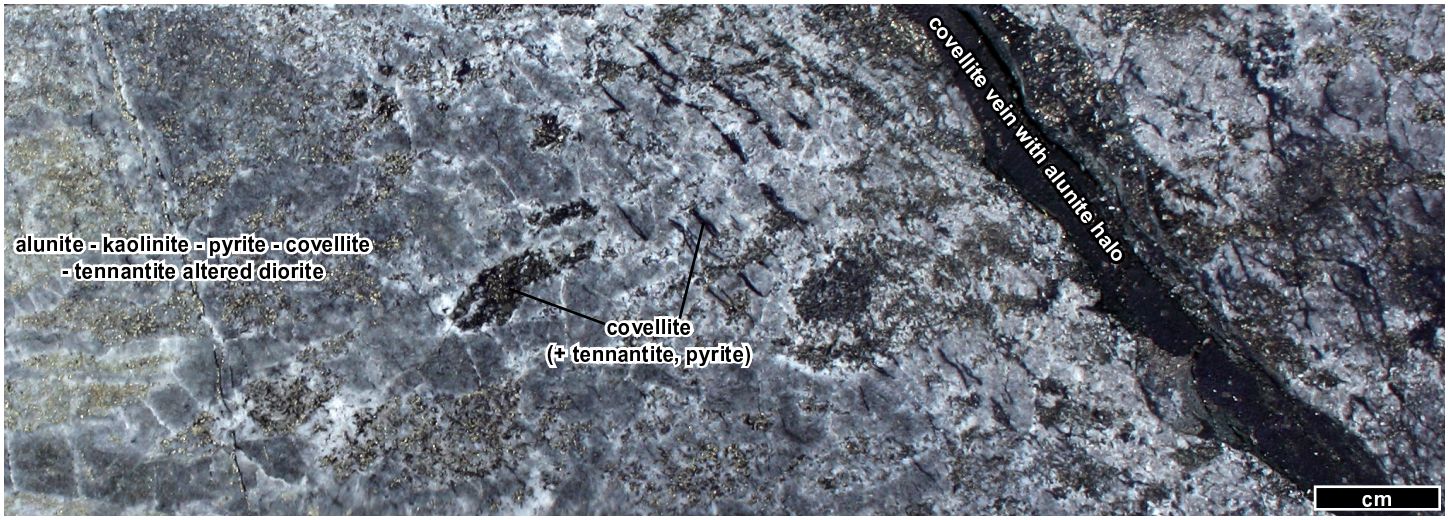

Figure 4.30: Stage IVa mineralisation in the alunite - kaolinite domain (Rafferty's Copper Zone). The quartz veined and alunite - kaolinite - pyrite altered diorite contains covellite and trace tennantite as fine disseminations and rims to pyrite. The covellite vein contains bornite fragments and an alunite (+ disseminated covellite) vein halo. The corresponding metre assay yielded 0.36 ppm Au and 3.2 wt. % Cu (WR398, 153.5 m).

Although tennantite is the only sulfosalt identified in samples from this study, about a quarter of the sulfosalt-bearing rocks at Wafi were reported by Leach (1989, 1990a, 1990b, 1990c, 1991a, 1991b), Purvis (1997), and Curtis and Ryan (1997) to contain trace enargite or luzonite in thin section. These enargite and luzonite bearing samples occur within the pyrite - covellite - tennantite mineralised zones labeled in Figure 4.24. The enargite - luzonite samples display no apparent zonation with respect to tennantite; that is, the sample data give no indication of changing enargite : tennantite ratios with depth or proximity to the Golpu diorites.

Near the upper eastern flank of stage II diorite, stage II disseminated hematite and veins (as in Fig. 4.7) have been overprinted by stage IV covellite mineralisation, resulting in an unusual peach-purple colour (Fig. 4.31). This small zone of overlapping vein and alteration zones is interpreted to record the overprinting of stage I porphyry mineralisation (quartz - pyrite - chalcopyrite veins in stage I diorite) by stage II hematite alteration (quartz - hematite veins and hematite alteration), followed by stage IV covellite mineralisation (kaolinite veins and alteration with disseminated and vein halo covellite; Fig. 4.31 B).

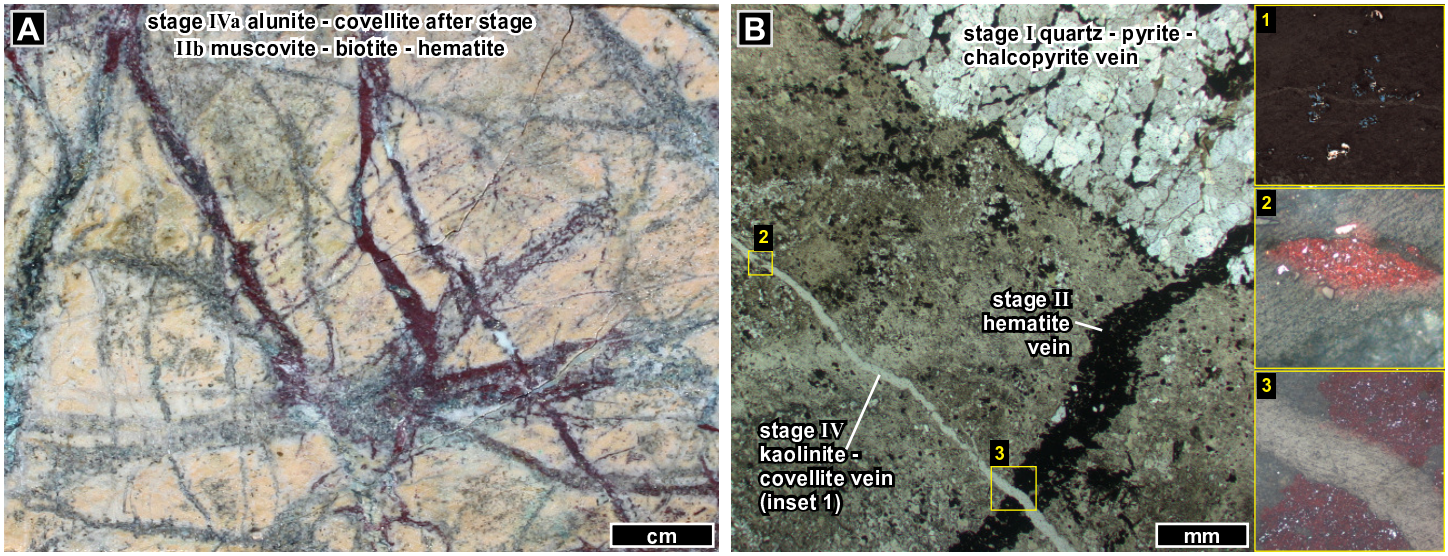

Figure 4.31: Stage IVa mineralisation near the base of the high sulfidation epithermal domain. A) Unusual colours resulting from hematite alteration (with stage II biotite - muscovite alteration) that has been overprinted by disseminated and vein halo covellite mineralisation (WR398, 345.7 m). B) Thin section of hematite- and covellite-altered rock as in image A (PPL; WR398, 358.9 m). In this sample, quartz - pyrite - chalcopyrite veins (top right) have been cross-cut by hematite veins (bottom right). These were in turn cross-cut by kaolinite veins associated with covellite alteration (e.g., covellite halo in inset 1), which contain fragments of the hematite veins (insets 2 and 3).

Stage IVa pyrite ± covellite ± sphalerite ± tennantite mineralisation near the Compass fault

Fine-grained pyrite hosts gold within the alunite - kaolinite - muscovite altered metasedimentary rocks southwest of Golpu, particularly near the Compass fault (Fig. 4.24; CRA Exploration Memorandum, 1997; Chapter Five). The gold-bearing pyrite mineralisation in the alunite-bearing rock is a minor component of the Wafi epithermal deposit; most epithermal gold occurs where carbonate veins have been documented (section 4.3.4.2). Trace covellite, tennantite, enargite, and rutile occur sporadically in association with pyrite in these distal alunite-bearing zones (Fig. 4.24). Their sporadic occurrence marked in Figure 4.24 is based on petrographic work by Leach (1989, 1990a, 1990b, 1990c, 1991a, 1991b), Purvis (1997), and Curtis and Ryan (1997) who described < 0.5 vol % combined covellite and sulfosalts in 18 of 498 thin sections of Wafi drill

core samples outside of Rafferty's copper zone. Trace disseminated sphalerite and galena also occur with pyrite towards the outer margins of the alunite - kaolinite altered rocks (Erceg et al., 1991), as shown in Figure 4.32 F and G.

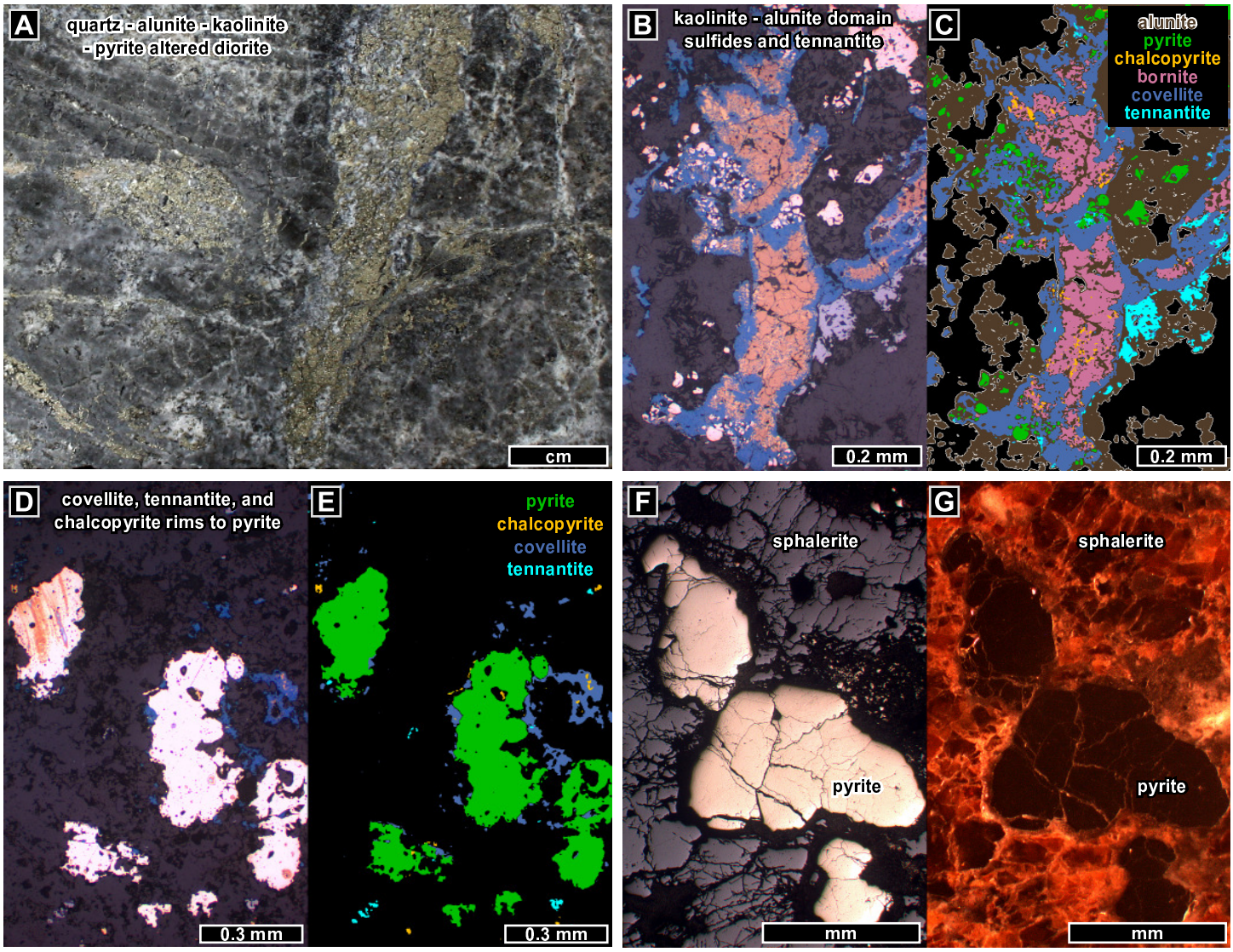

Figure 4.32: Stage IVa mineralisation in the high sulfidation epithermal domain. A) Typical appearance of stage I diorite that has been strongly altered to quartz, alunite, kaolinite, and pyrite, with trace tennantite, covellite, and chalcopyrite (WR398, 201.0 m). B) Tennantite, covellite, alunite, bornite, chalcopyrite, and pyrite in stage I diorite (reflected PPL). C) Stage IVa mineralisation as in panel B, with minerals indicated. The marked locations of alunite are based on SEM BSE imaging (WR398, 207.6 m). D) Covellite (+ trace chalcopyrite and tennantite) rimming stage IVa pyrite near the base of Rafferty's copper zone (reflected PPL). E) Minerals in panel D indicated (WR398, 207.0 m). F) Trace sphalerite occurs in association with pyrite - tennantite - alunite - kaolinite near the margins of the alunite - kaolinite alteration domain (reflected PPL; WR402, 220.0 m). G) Side lamp reflected PPL photomicrograph of minerals shown in panel F. Note red internal reflections in sphalerite.

4.3.4.2 Stage IVa intermediate sulfidation epithermal veins and altered rocks

The stage IVa IS epithermal domain is peripheral to the HS epithermal domain (Figs. 4.24, 4.25), and is characterised by rhodochrosite - base metal sulfide - quartz veins and montmorillonite - chlorite altered rocks (Figs. 4.33 - 4.37). The carbonate veins are most abundant between 500 and 1200 metres from the nearest diorite (Fig. 4.1), as a series of east-dipping veins to the west and northwest of Golpu. They occur in association with quartz - adularia - pyrite - arsenopyrite near the Compass fault (Fig. 4.24). Many of the carbonate veins are gold-bearing, and are lined by weak montmorillonite - chlorite to muscovite - illite alteration halos (Figs. 4.33, 4.34, 4.36 B). The veins are interpreted to have formed at the same time as the adjacent alunite - kaolinite alteration, on the basis of their close spatial relationship and the occurrence of gold along the transition from alunite- to carbonate-bearing assemblages (section 4.4.2.2).

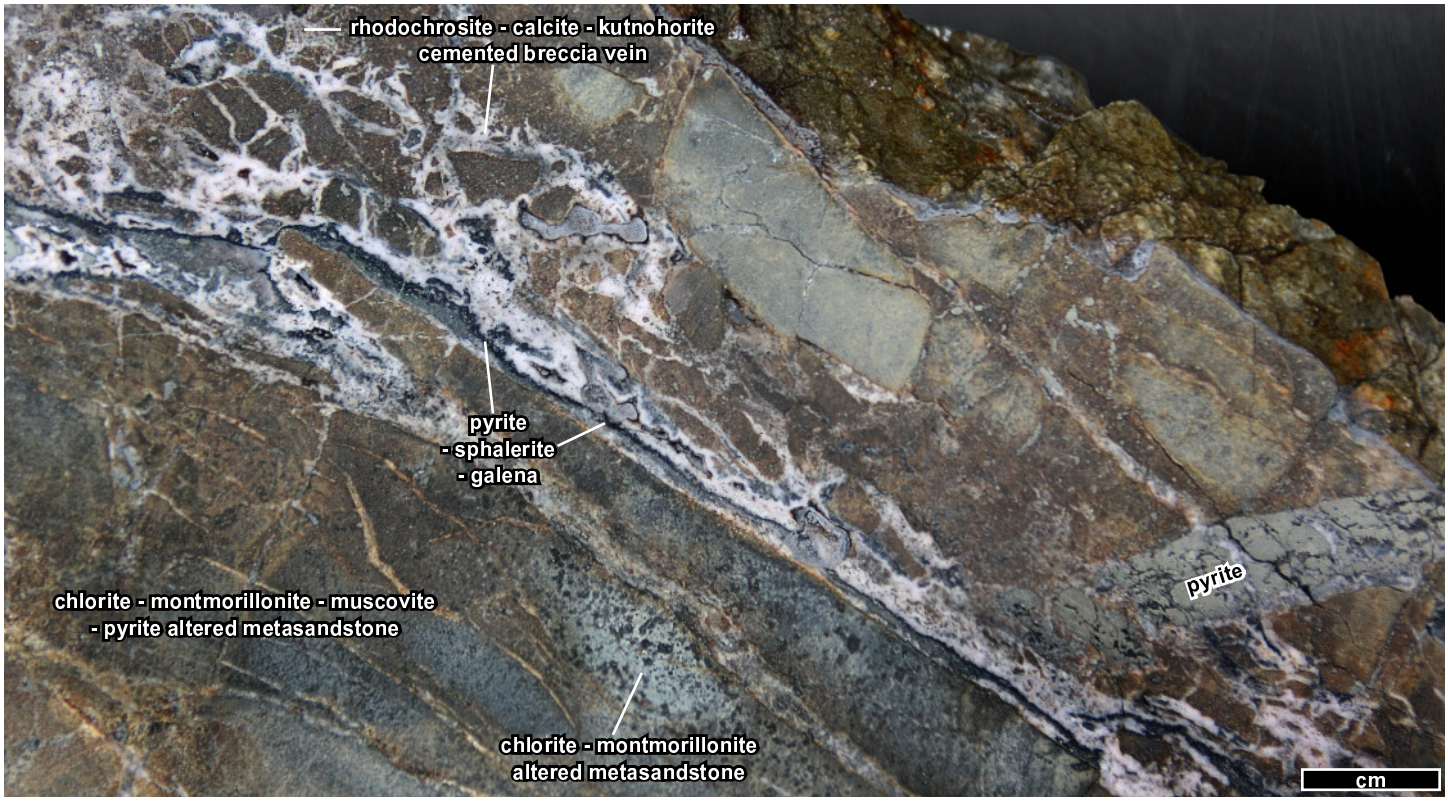

Figure 4.33: Stage IVa intermediate sulfidation epithermal veins and altered rock. Veins containing rhodochrosite, kutnohorite, calcite, pyrite, sphalerite, and galena transition to carbonate-cemented breccia veins with in-situ wallrock fragments. Fine-grained sulfides appear as dark bands in the veins. The metasandstone wallrock has been altered to chlorite, montmorillonite, and muscovite, and contains finely disseminated pyrite. Similar carbonate - base metal sulfide veins in nearby samples (e.g., WR392, 369.0 m) contain native gold. The corresponding metre assay for the sample shown yielded 1.9 ppm Au, 667 ppm As, and 0.9 % Mn (WR392, 326.5 m).

Stage IVa gold-bearing carbonate - base metal sulfide veins west and northwest of Golpu

East-dipping zones of carbonate - base metal sulfide veins can be traced for several hundred metres along Owen Stanley stratigraphy towards Golpu (Figs. 4.24, 4.25 A). These veins are sparse, making up < 5 volume % of core intervals near surface, but readily identified in drill core. They are most abundant within the metaconglomerate bedding units. The veins are carbonate-cemented multiphase breccias with 10 to 85 % rounded to angular sulfide fragments and sharp, irregular vein margins into previously altered wallrock. Most

are chaotic and infill-supported breccias; a few are rotated to jigsaw-fit and locally fragment-supported breccias (e.g., Figs. 4.33, 4.37 C). The breccia fragments consist, in decreasing order of abundance, of pyrite (some with native gold inclusions), sphalerite, galena, and quartz-cemented pyrite breccia (Figs. 4.33 - 4.36). Some pyrite fragments contain trace pyrrhotite inclusions. The infill, in order of decreasing abundance, is rhodochrosite, calcite, quartz, Mg-calcite, and kutnohorite cement.

Many of the carbonate - sulfide veins exhibit a chronological and vein wall-to-centre transition from quartz into carbonates with native gold-bearing pyrite. For example, the vein in Figure 4.36 C transitions from quartz - pyrite into carbonate - pyrite - sphalerite - galena - native gold, with euhedral quartz terminating into the zoned rhodochrosite cement at image left. Figure 4.37 A shows a vein wall to vein centre transition from quartz followed by Mn-, Ca-Mn-Mg-, and Ca-Mg-carbonates. The multiphase calcite-cemented breccia vein in Figure 4.37 C and D contains quartz-cemented pyrite fragments, indicating an early stage of quartz cement to the base metal sulfide breccia veins.

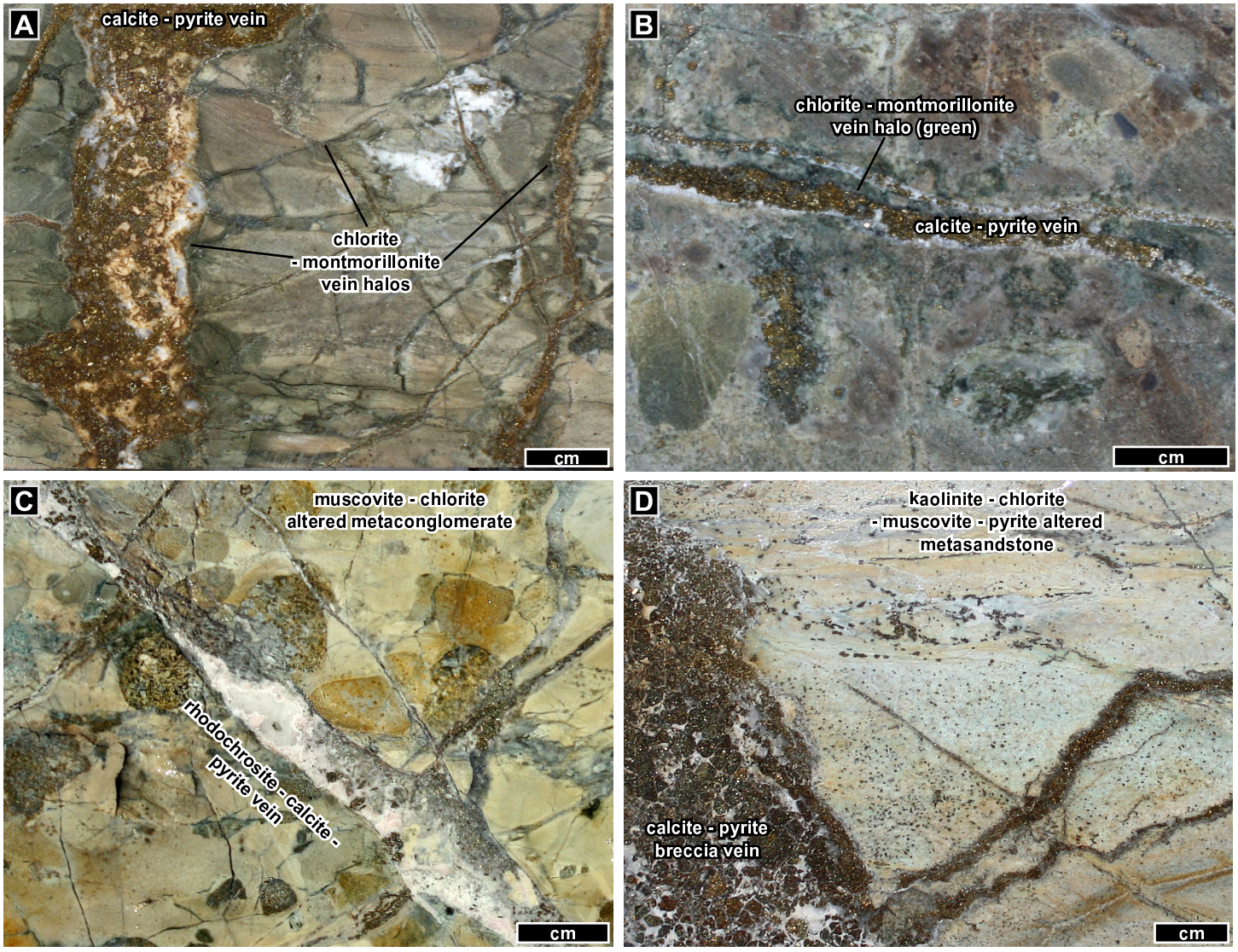

Figure 4.34: Stage IVa intermediate sulfidation epithermal veins and altered rocks. A) Calcite - pyrite veins with chlorite - montmorillonite halos after muscovite (+ trace kaolinite) altered metasiltstone (WR392, 232.1 m). B) Pyrite - calcite veins with chlorite - montmorillonite vein halos after chlorite - actinolite - muscovite altered metaconglomerate (WR 396, 648.0 m). C) Rhodochrosite - calcite vein with pyrite fragments in a muscovite - chlorite altered metaconglomerate (WR397, 123.5 m). D) Calcite-cemented breccia vein with pyrite fragments after kaolinite - chlorite - muscovite altered metasandstone (WR397, 64.4 m).

Stage IVa intermediate sulfidation altered rocks west and northwest of Golpu

Alteration associated with the carbonate veins was weak compared to that in the HS epithermal domain, with host rock textures and prior vein and alteration expressions generally preserved in between the vein halos (e.g., Fig. 4.34 B,C). The altered rocks contain chlorite - montmorillonite ± muscovite ± illite, which in total make up < 25 vol % of the rock (Table 4.7).

Table 4.7: Mineralogy of stage IV intermediate sulfidation epithermal alteration west of Golpu

Sample description	Sample location	Summary of bulk mineralogy (vol % by quantitative XRD)
Selective chlorite - montmorillonite altered metaconglomerate (adjacent to carbonate - pyrite veins)	WR396, 674.8 m	35 % quartz, 38 % plagioclase (~ labradorite), 9 % smectite group clays*, 6 % chlorite, 4 % pyrite
Moderate chlorite - muscovite - montmorillonite altered metasandstone with ~20 % quartz - carbonate - pyrite veins	WR397, 74.2 m	32 % pyrite, 31 % quartz, 8 % chlorite, 8 % muscovite, 8 % calcite, 4 % kaolinite - dickite*, 4 % ankerite

*SWIR analyses indicate montmorillonite is the primary clay mineral in these samples (Appendix F). Totals do not add to 100 because trace components are not presented in this table.

Stage IVa intermediate sulfidation epithermal veins at depth

Tennantite - sphalerite - galena - chalcopyrite veins < 2 mm wide have cross-cut stage II Golpu porphyry mineralisation and altered rocks (Fig. 4.35 B) at - 1 kilometre elevation (or 1500 metres from the top of stage II diorite; Fig. 4.25 A). Carbonate veins < 5 mm wide have also cross-cut stage II biotite altered and quartz - hematite veined wallrock within 500 metres of the top of stage II diorite (Fig. 4.35 A). These deep veins are interpreted to be the sparse basal component of stage IV IS epithermal veins (Fig. 4.25), on the basis of their mineralogy, and because they cross-cut stage II veins and altered rocks.

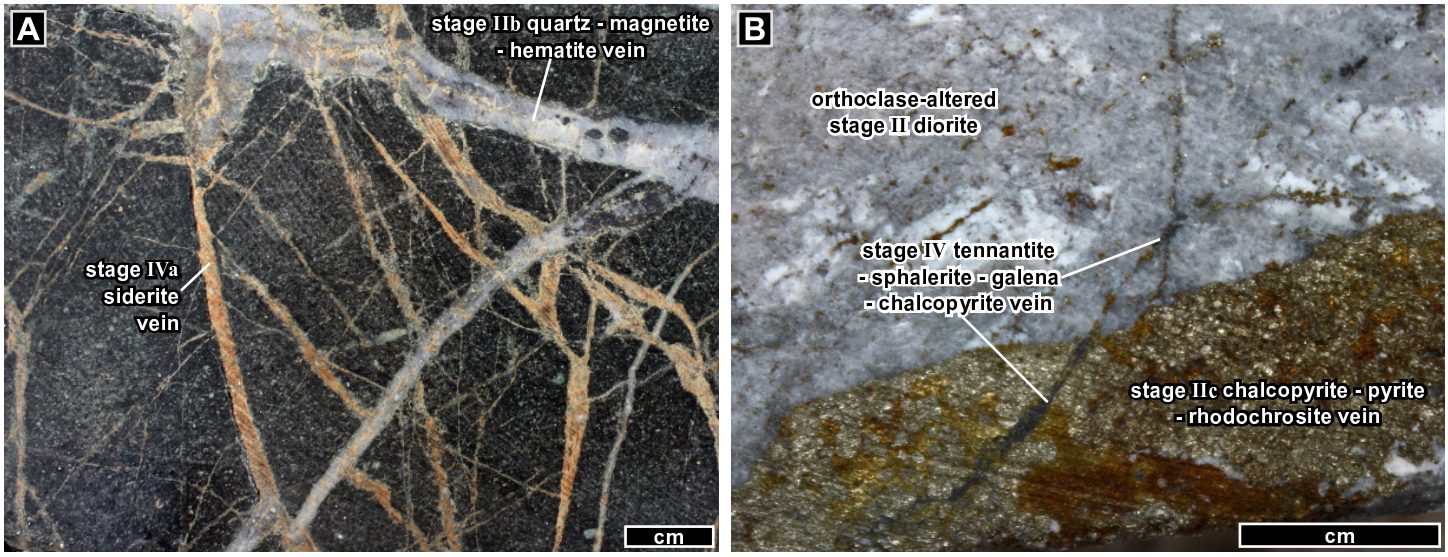

Figure 4.35: Stage IVa veins interpreted to be the basal component of stage IV intermediate sulfidation veins. Note the sample depth in both images. A) Carbonate veins (orange) cross-cut and locally offset biotite-altered and quartz - magnetite - hematite - veined metasandstone (WR402, 559.0 m). B) Tennantite - sphalerite - galena - chalcopyrite vein (labeled) after a chalcopyrite - pyrite - rhodochrosite vein (bottom), after orthoclase-altered stage II diorite (WR377, 1310.0 m).

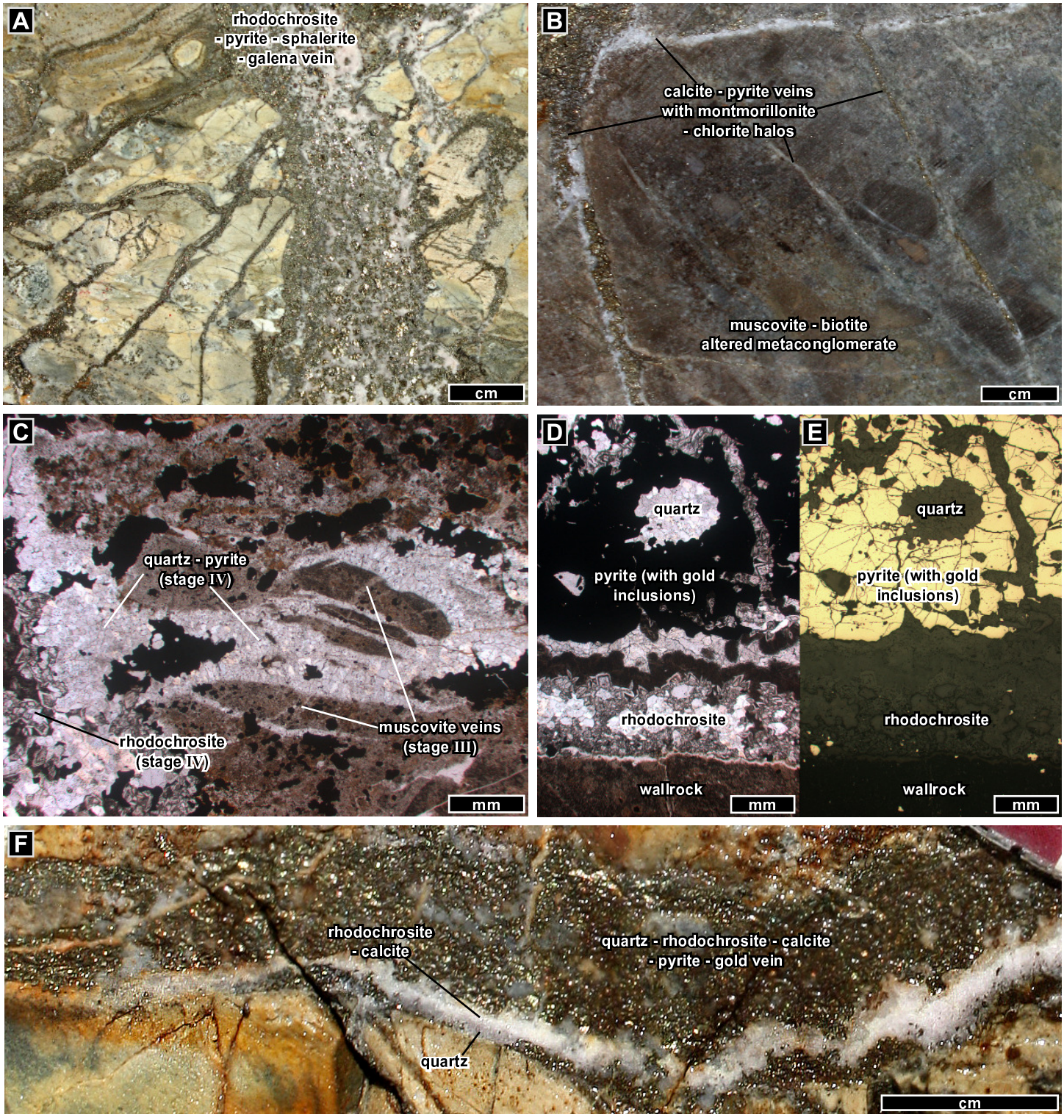

Figure 4.36: Stage IVa carbonate - base metal sulfide (intermediate sulfidation) veins and altered rocks. A) Rhodochrosite - pyrite - sphalerite - galena vein after muscovite-altered metaconglomerate (WR397, 123.0 m). B) Calcite - pyrite veins with montmorillonite - chlorite halos after muscovite (+ trace biotite) altered metaconglomerate. The vein halos are generally lighter than the muscovite - biotite altered wallrock in this sample (WR396, 674.8 m). C) Quartz - pyrite vein (middle of image) extends into quartz - rhodochrosite - calcite - pyrite - native gold vein (at left). This vein has cross-cut stage III to IV muscovite - kaolinite veins (middle of image) and altered rock (PPL; WR392, 369.0 m). D) Photomicrograph of the gold-bearing vein in panel C. Zoned rhodochrosite - calcite crystals radiate inward (towards top of image) from muscovite - kaolinite altered wallrock (bottom of image). The centre of the vein contains gold-bearing pyrite - rhodochrosite - quartz (as shown in Fig. 4.37 A). E) Photomicrograph of gold-bearing vein in panel D, shown in reflected PPL. F) Hand specimen of the gold-bearing vein shown in panels C, D, and E. The corresponding metre assay yielded 8.75 ppm Au, 1.7 ppm Ag, 1050 ppm As, 1.47 wt. % Mn, and 120 ppm Zn (WR392, 369.0 m).

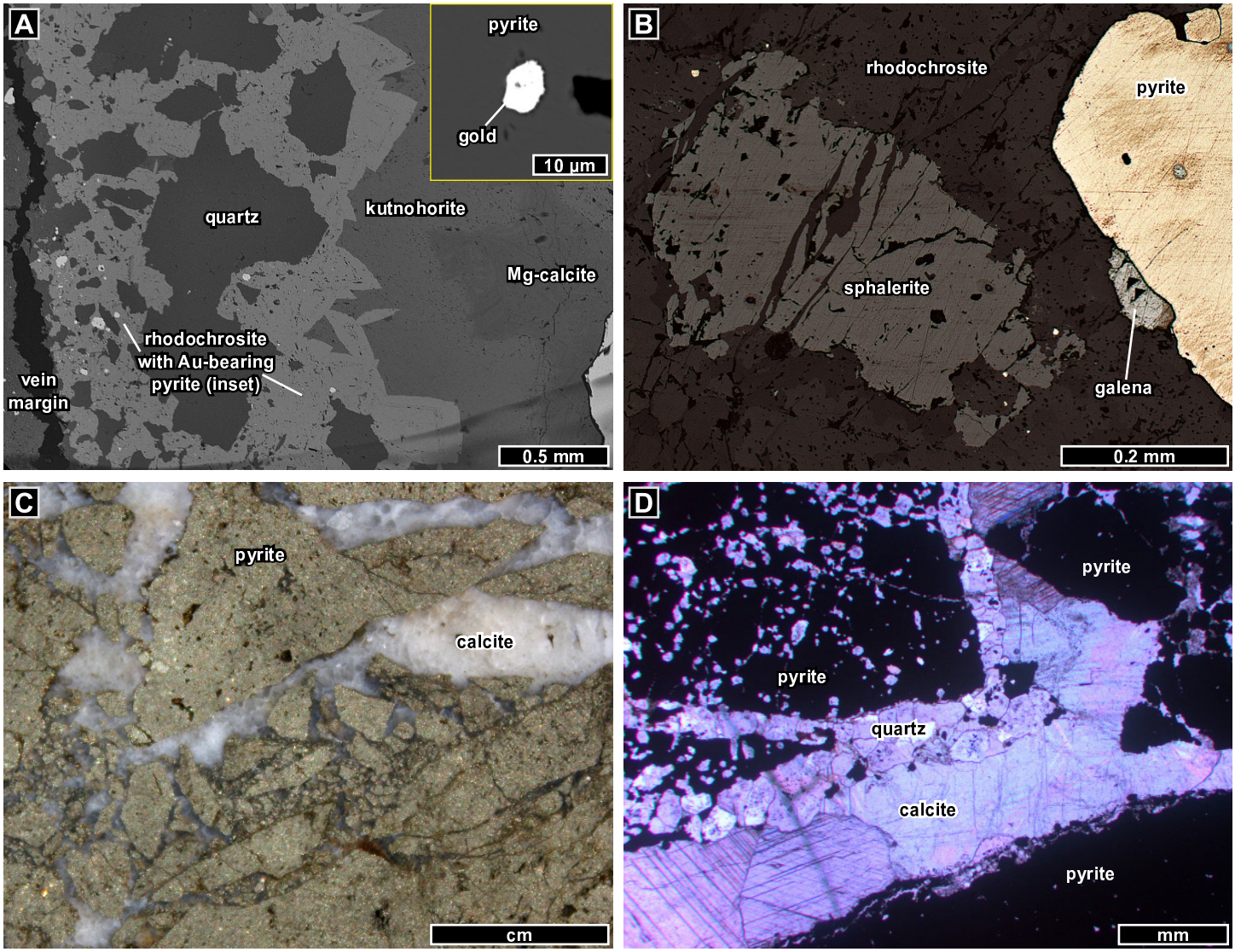

Figure 4.37: Stage IVa carbonate - base metal sulfide (intermediate sulfidation) veins. A) Transition from vein margin (left) to centre (right), from Mn- to Ca-Mn-Mg- to Ca-Mg-carbonates. Bright inclusions in rhodochrosite near the vein margin are locally gold-bearing pyrite. Inset shows a native gold grain in a rhodochrosite-hosted pyrite grain from the same sample (SEM BSE; WR 392, 369.0 m). B) Sphalerite, galena, and pyrite in a rhodochrosite vein (reflected PPL; WR397, 123.0 m). C) Calcite-cemented breccia vein with angular fragments of pyrite and quartz-cemented pyrite breccia (WR397, 395.5 m). D) Quartz-cemented breccia fragment (top left) from the same vein as in image C (PPL; WR397, 396.0 m).

Stage IVa intermediate sulfidation epithermal veins and disseminated pyrite near the Compass fault

Stage IVa IS epithermal mineralisation near the Compass fault includes a gold-rich zone of quartz - carbonate - pyrite ± arsenopyrite and disseminated pyrite ± arsenopyrite, and contains overlapping zones of adularia veins and stage II biotite-altered rocks (Figs. 4.25 C, 4.38 - 4.40). Carbonate veins are of much lower abundance near the Compass fault than in the previously described gold-bearing veins west of Golpu (e.g., Table 4.8). They occur throughout the carbonate veined volume indicated in Figures 4.24, 4.25, and 4.41, primarily as sub-millimetre veins of rhodochrosite, siderite, and ankerite intergrown with quartz and base metal sulfides (Leach, 1991; Curtis and Ryan, 1997).

Stage IVa veins and disseminated sulfides are most abundant in Link Zone, which contains up to 8 vol % pyrite (Fig. 4.39; Appendix A). Link Zone is the highest grade portion of the Wafi deposit, with 5.57 Mt at 6.57 ppm Au, or 16 % of the total contained gold in Wafi (Reid and Gossage, 2012). Link Zone has an east-dipping geometry that extends 380 metres along, and 320 metres south of, the Compass fault (Figs. 4.24, 4.25, 4.41; Dunham, 2012).

Adularia is a minor but widespread component of the Link Zone veins. The adularia occurs mostly along gold-bearing quartz - pyrite - arsenopyrite vein margins (Curtis and Ryan, 1997), and some adularia is intergrown with quartz in quartz - pyrite vein centres (e.g., Fig. 4.40 C,D,E).

The IS epithermal sulfide assemblage (including Link Zone ore) comprises pyrite and less abundant arsenopyrite, along with trace inclusions of pyrrhotite, sphalerite, chalcopyrite (Fig. 4.40 A,B), and native gold as microscopic inclusions in both pyrite and pyrrhotite (CRA Exploration memorandum, 1997). Accessory phases to the IS epithermal mineralisation include apatite, rutile, and monazite (e.g., Fig. 4.40 E,F).

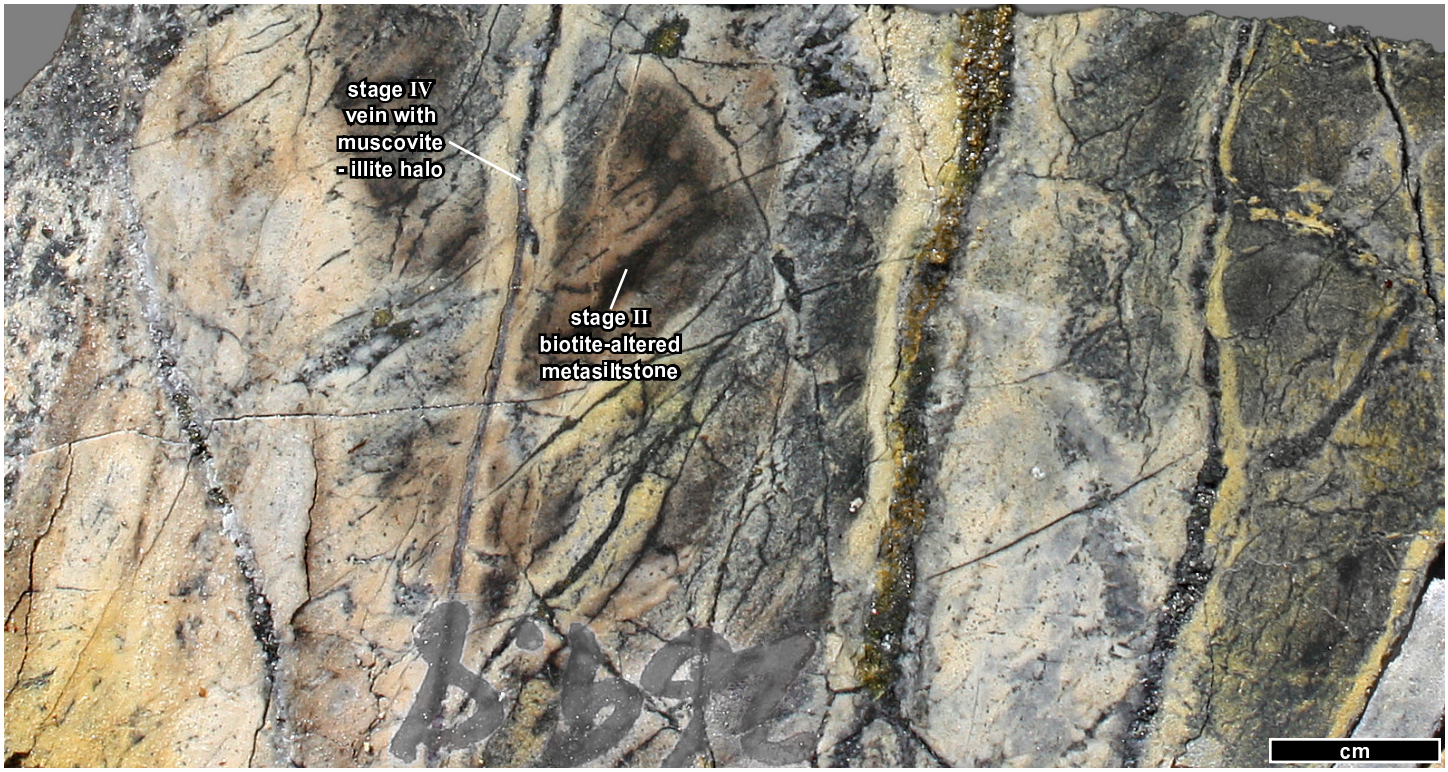

Figure 4.38: Stage IVa mineralisation in Link Zone comprises thin quartz - pyrite - arsenopyrite (± carbonates, adularia) veins with muscovite - illite vein halos. The veins cross-cut weak, pervasively biotite-altered rock near the Compass fault. Very fine-grained pyrite occurs throughout the sample (Fig. 4.39 B). The corresponding metre assay yielded 0.95 ppm Au (WR199, 269.8 m).

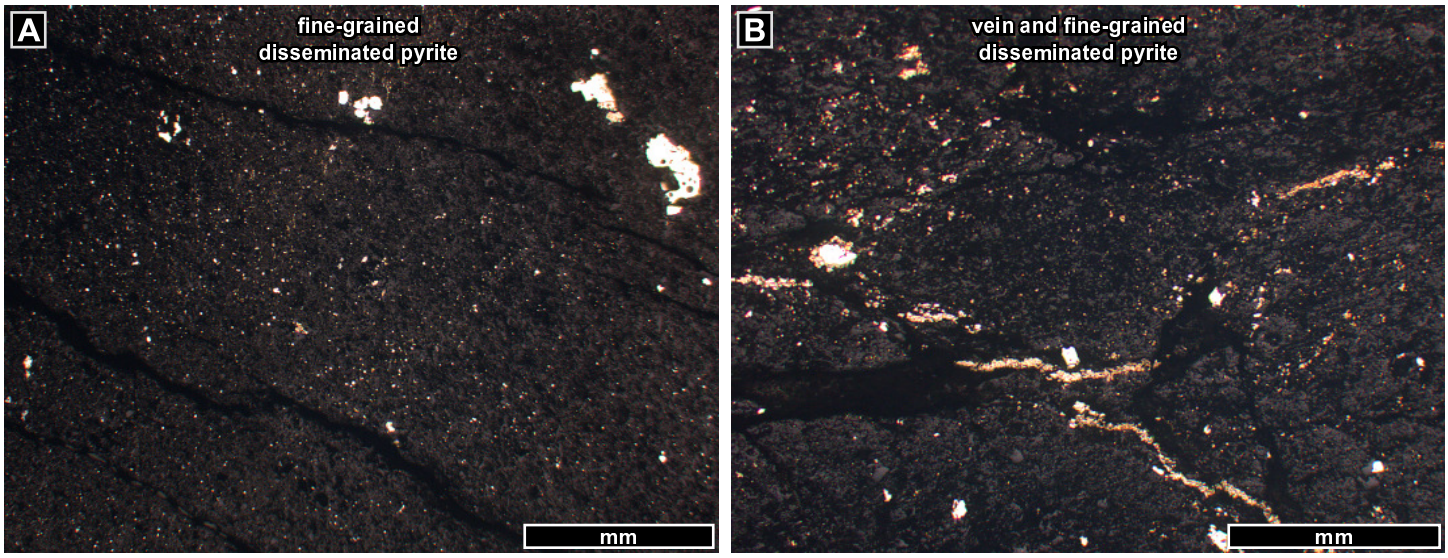

Figure 4.39: Photomicrographs of finely disseminated stage IVa pyrite that is characteristic of intermediate sulfidation mineralisation near the Compass fault. A) Link zone mineralisation contains abundant pyrite as very fine disseminations. The corresponding metre interval yielded 16 ppm Au, which is refractory in pyrite (Chapter Five; reflected PPL; WR177, 310.7 m). B) Vein and finely disseminated pyrite typical of Link Zone mineralisation, from the same sample as in Figure 4.38 (reflected PPL; WR199, 269.8 m).

Stage IVa intermediate sulfidation epithermal altered rocks near the Compass fault

Alteration in the IS epithermal domain near the Compass fault (including Link Zone) resulted primarily in vein halos of muscovite ± illite with finely disseminated pyrite (Fig. 4.38; Table 4.8). These altered rocks change southward into chlorite - actinolite altered rocks, northward into muscovite ± kaolinite altered rocks, and with depth (down the Compass fault) into biotite-altered rocks (e.g., Figs. 4.25 C, 4.38). Alteration between Link Zone and the current erosional surface produced chlorite - montmorillonite - muscovite, similar to the alteration associated with the carbonate - quartz - sulfide veins west of Golpu.

Table 4.8: Mineralogy of stage IV intermediate sulfidation alteration south and west of Golpu

Sample description	Sample location	Summary of bulk mineralogy (vol % by quantitative XRD)
Moderate pervasive muscovite altered metasiltstone with disseminated pyrite halos to quartz - pyrite - adularia - rhodochrosite veins (whole rock sample contains 15.3 ppm Au)	WR177, 389.8	60 % quartz, 20 % muscovite, 9 % orthoclase (adularia), 5 % pyrite, 3 % rhodochrosite
Strong vein halo muscovite - pyrite to quartz - carbonate - pyrite veins after weak pervasive biotite altered metasiltstone	WR 199, 337.9 m	47 % quartz, 26 % muscovite, 8 % biotite, 6 % kaolinite - dickite, 4 % pyrite, 3 % chalcopyrite, 2 % calcite
Strong pervasive muscovite - pyrite altered metasandstone with quartz - pyrite veins (whole tock sample contains 1.0 ppm Au)	WR177, 341.6 m	67 % quartz, 22 % muscovite, 7 % pyrite, 2 % biotite

Totals do not add to 100 because trace components are not presented in this table.

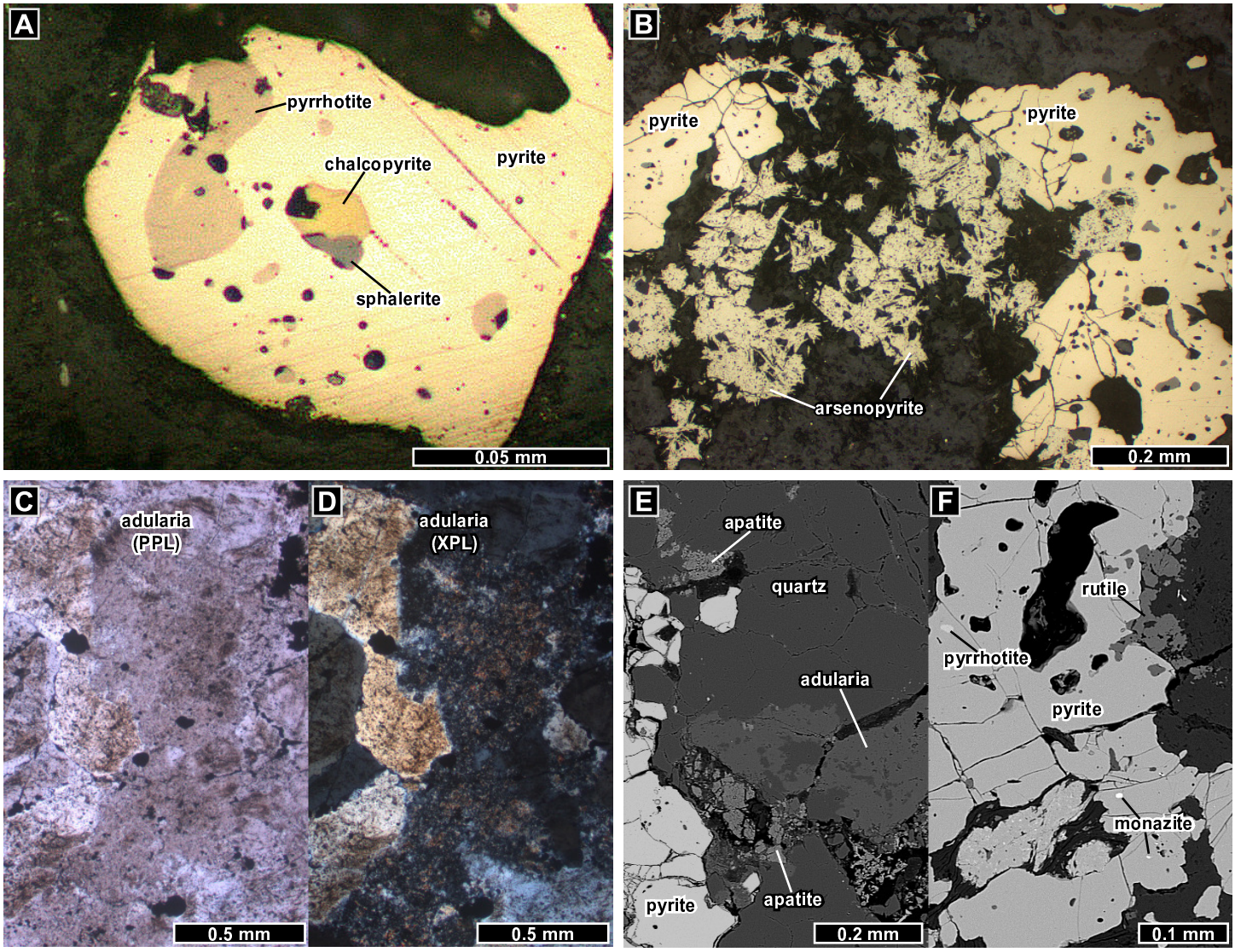

Figure 4.40: Photomicrographs of stage IVa quartz - adularia - carbonate - base metal sulfide veins in Link Zone. All images are from sample 199, 285.0 m, with a corresponding metre assay of 3.67 ppm Au. A) Pyrrhotite, chalcopyrite, and sphalerite inclusions in stage IVa disseminated pyrite (reflected PPL). B) Acicular arsenopyrite rimming stage IV pyrite (reflected PPL). C) Adularia in a quartz - adularia - pyrite vein (PPL). D) Adularia from panel C (XPL). E) Apatite, quartz, adularia, and pyrite in a stage IVa vein (SEM BSE). F) Pyrrhotite, rutile, monazite, and pyrite in the same vein as panel E (SEM BSE).

4.3.4.3 Fault and stratigraphic relationships with stage IV mineralisation

The Compass fault, which occurs partly along the southern margin of the Wafi breccia complex, has apparently controlled the location of most stage IV mineralisation, in both the HS and IS epithermal domains (Fig. 4.41). Of all drill holes in the study area, fourteen contain 10 metre intervals with greater than 15 ppm Au. All of these high grade intervals occur within 50 metres of the Compass fault (most occur in Link Zone, outlined in Fig. 4.41). Nearly all of the epithermal mineralised rock containing greater than 1.5 ppm Au occurs within 200 metres of the Compass fault (Fig. 4.41).

Morehari et al. (2009) suggested that host stratigraphy exerted a secondary structural control on mineralisation. The stage IVa pyrite-hosted gold mineralisation is reportedly best developed within metaconglomerate and metasandstone units nearest the Compass fault (Fig. 4.41), or along their contacts with

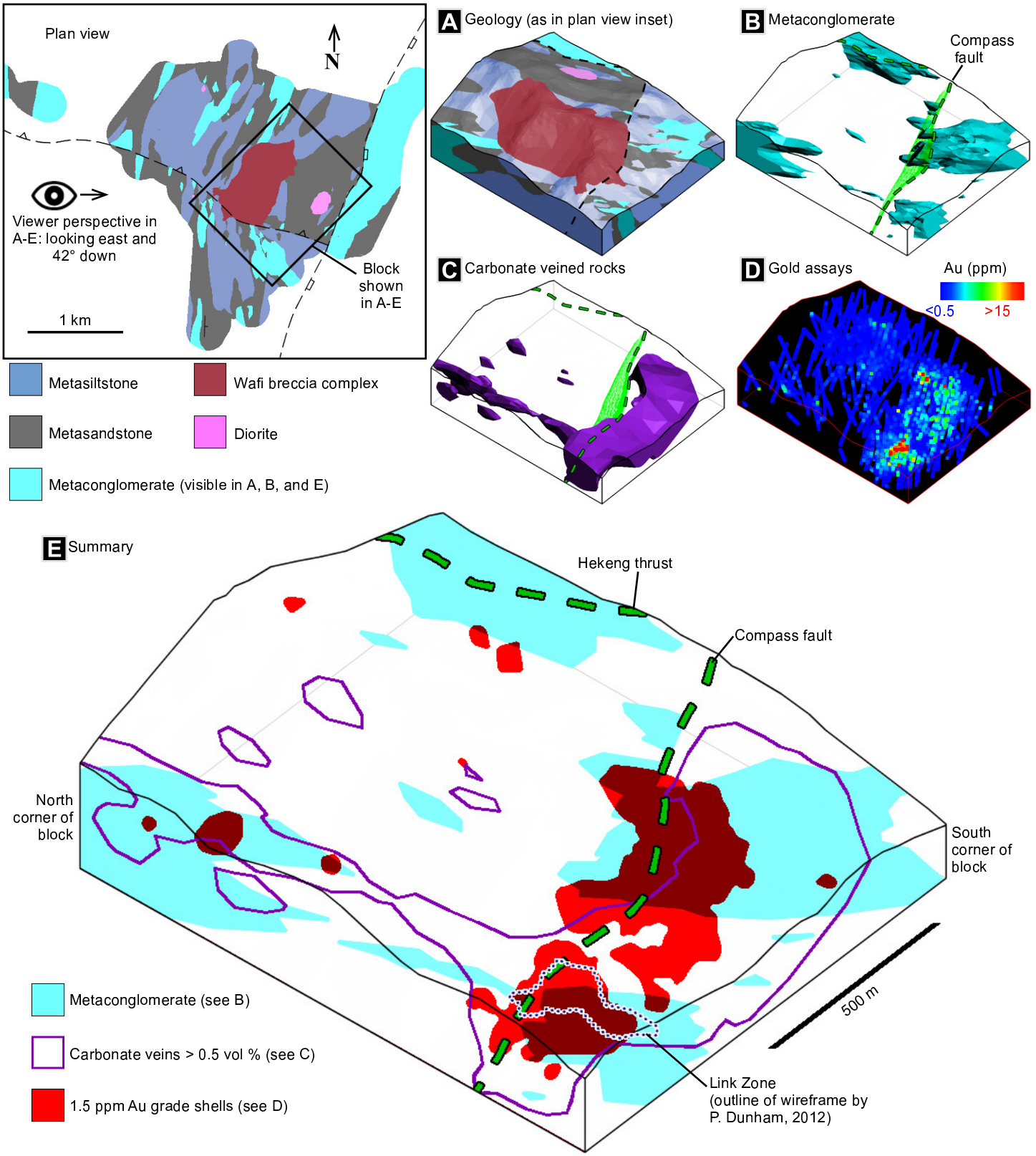

Figure 4.41: Stage IVa structural controls. Block models A-E summarise the spatial relationships between the Compass fault, host stratigraphic units, and Wafi epithermal carbonate veins and gold mineralisation. The inset is a surface geology map (as in Figure 3.2) indicating the location of the block shown in A-E. The perspective in all block model images is looking down and to the east – that is, looking along the host stratigraphy and approximately along the north-dipping Compass fault. A) Geology volumes below overburden, as shown in the inset map. B) East-dipping metaconglomerate units, shown as blue solids within the transparent block volume, are partly truncated by the Compass fault (labeled). C) Rock containing carbonate veins is indicated as a solid volume. D) Gold assays within the block volume indicate the locations of Wafi epithermal mineralisation. Assay data are described in more detail in Chapter Five. E) Summary block model showing the occurrence of (locally gold-bearing) carbonate veins along east-dipping metaconglomerate units (particularly to the north), and the occurrence of gold mineralisation near the Compass fault.

metasiltstone units (Morehari et al., 2009). The locally gold-bearing carbonate veins to the west and northwest of Golpu are, similarly, most abundant within east-dipping metaconglomerate units (e.g., the left portion of the block model in Fig. 4.41 E).

4.3.4.3 Stage IVb veins and altered rocks

Stage IVb vein and alteration events have resulted in volumetrically minor veins, sulfide rims, and clay overprints in the Wafi epithermal environment. The stage IVb events post-date the stage IVa veins and alteration in both the HS and IS epithermal domains (Fig. 4.1), but their paragenesis is otherwise not as clearly documented in stages I-IVa.

Stage IVb pyrite - covellite mineralisation within the vuggy quartz zone

Disseminated pyrite and trace covellite occur in the quartz-alunite altered rocks, and are very finely disseminated along cavity walls in some of the vuggy quartz samples (e.g., Fig. 4.28 A). The stage IVb covellite along cavity walls is interpreted to be the latest documented occurrence of covellite in the Wafi-Golpu paragenesis (Fig. 4.1). Because covellite and pyrite have not been preserved in the zone of supergene oxidation, the original extent of covellite-pyrite mineralisation in the vuggy quartz zone has not been determined.

Stage IVb covellite and pyrite veins with alunite halos

A few pyrite ± covellite veins < 1 mm wide have cross-cut kaolinite ± alunite ± muscovite altered rocks. These veins are sparse, and contain thin alunite halos (Fig. 4.42). They are interpreted to have occurred after the main stage of alunite ± kaolinite alteration (stage IVa), possibly contemporaneous with the pyrite - covellite mineralisation after vuggy quartz (as indicated in Fig. 4.1).

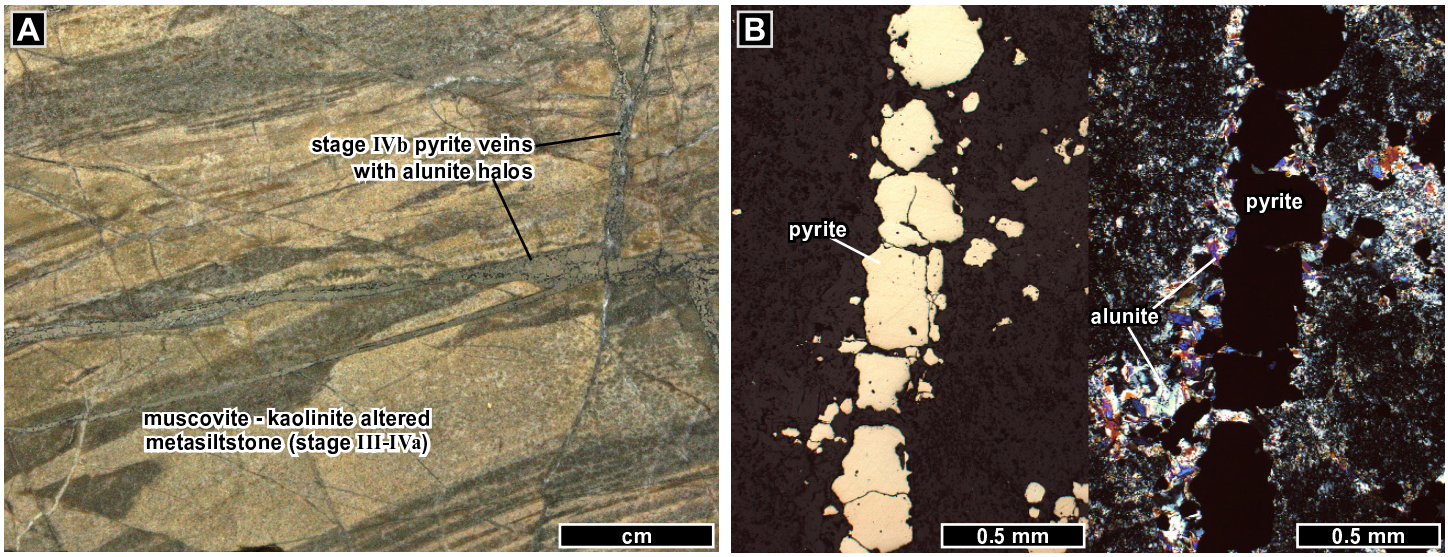

Figure 4.42: Stage IVb pyrite veins with alunite halos. A) Pyrite veins with alunite halos after kaolinite- and muscovite-altered metasiltstone (WR301, 315.6 m). B) Thin section of veins in image C, showing high-birefringence alunite laths < 0.1 mm long as a halo to a pyrite vein (reflected PPL at left, XPL at right; WR301, 315.6 m).

Stage IVb carbonate veins and montmorillonite - halloysite altered rocks

Most carbonate veins formed during stage IVa, but sparse calcite veins have reportedly cross-cut the gold-bearing quartz - carbonate - pyrite ± arsenopyrite veins in Link Zone (Curtis and Ryan, 1997; Fig. 4.1). These late calcite veins have not been identified in samples from this study. Assuming a common origin with the stage IVa mineralised carbonate veins (i.e., reflecting continued development of the same magmatic-hydrothermal system), these stage IVb calcite veins are interpreted to have occurred shortly after stage IVa. It is also possible that this event occurred later, but no suitable material for geochronological analysis was found to allow the two hypotheses to be tested.

Chlorite - montmorillonite - muscovite altered rocks above Link Zone transition towards surface into a sublinear zone of halloysite altered rocks. The halloysite was identified by Leach (1991) in 25 XRD samples, to a maximum depth of 190 metres from surface, or possibly 340 metres when including analyses for which halloysite identification was marked by Leach (1991) as uncertain. The halloysite-bearing zone is ~ 1100 metres long, and is visible in cross section in Figure 4.25 C and in plan view in Figure 4.2. It has not been sampled in this study, but its spatial overlap with alunite - pyrophyllite altered rocks (Fig. 4.25) suggests that it has occurred after the main stage of alunite - pyrophyllite alteration. The stage IVb montmorillonite - halloysite alteration may be contemporaneous with the post-mineralisation carbonate veins near Link Zone, as indicated in Figure 4.1.

Stage IVb alunite - orpiment - pyrite - galena - marcasite veins

A few sharp-walled alunite veins have cross-cut the covellite-mineralised and vuggy quartz-altered Golpu diorite. These alunite veins are interpreted as the last stage of all porphyry-epithermal veins and alteration documented in this study (Fig. 4.1). The thickest of these veins is 20 cm wide, and contains colloform bands of alunite, orpiment, pyrite, galena, and marcasite (Fig. 4.43; Appendix A).

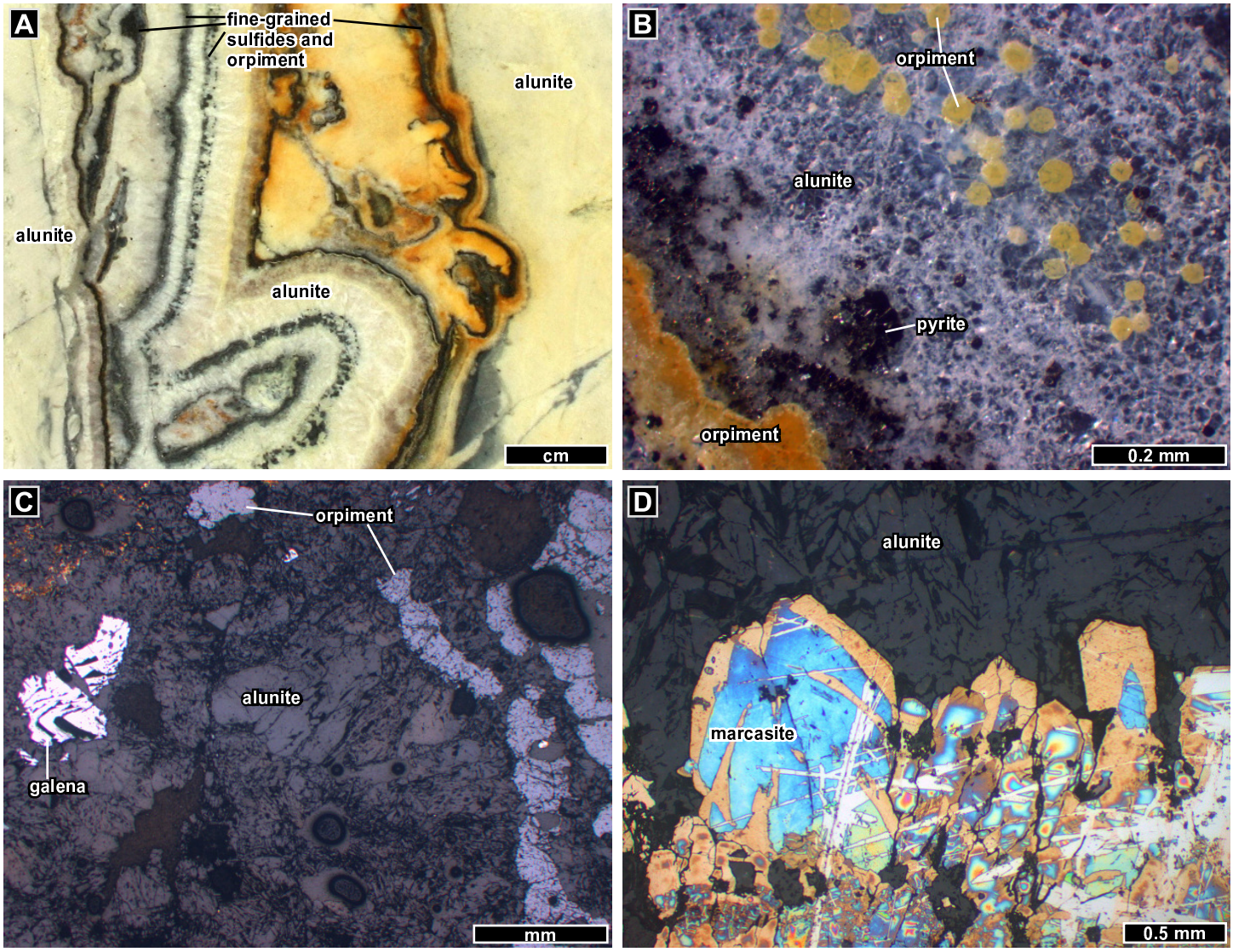

Figure 4.43: Photos of a stage IVb alunite vein, which cross-cuts covellite-mineralised Golpu diorite (all images are from WR398, 150.5 m). A) Colloform alunite bands ~ 5 cm from vein margin at left. The coarse central band (resembling a lowercase 'b') contains subhedral alunite laths up to 2.5 mm long. Dark bands are mostly pyrite and marcasite. B) Yellow orpiment bands (bottom left) and concentric radial growths (middle - upper right) in vein alunite (side lamp reflected PPL). C) Galena and orpiment in alunite (reflected PPL). D) Marcasite terminating towards vein centre (towards top of image) in alunite. Blue tarnish on the marcasite shows possible twinning planes or growth zones (reflected PPL).

4.4 Discussion

A major aim of this study is to investigate the relationship between the Golpu porphyry and Wafi epithermal environments (Chapter One). In order to fully address the spatial, temporal, and mineralogical complexity of Wafi-Golpu, each of the deposit components (Golpu porphyry, Wafi high sulfidation, and Wafi intermediate sulfidation) will here be compared to its respective deposit type. Arguments concerning the whole Wafi-Golpu system, specifically the genetic relationships between the porphyry and epithermal environments, are presented in context of geochemical and geochronological results in Chapters Five and Six.

4.4.1 Diorite-concentric Veins and Altered Rocks (Stages I and II)

The Golpu porphyry veins and altered rocks have the following characteristics in common with other calc-alkalic porphyry deposits (as recognised by Sillitoe, 1997; Einaudi et al., 2003; Wilson et al. 2007; Sillitoe, 2010; Sun et al., 2013):

- The Golpu porphyry ore consists primarily of vein and disseminated chalcopyrite, pyrite, and bornite. Bornite and pyrite do not occur together in equilibrium. Some bornite occurs as rims around disseminated pyrite, and some bornite - chalcopyrite veins contain pyrite fragments (e.g., Fig. 4.17 B).
- The ore-related alteration comprises biotite - perthite (orthoclase - albite) that transitions outwards to muscovite - chlorite and chlorite - actinolite - epidote alteration.
- Quartz veins are abundant, and make up a significant part of the main stage mineralising veins.
- The occurrence of magnetite - hematite intergrowths with, or shortly prior to, the main stage of Golpu mineralisation is a common feature of porphyry deposits, though perhaps not widely documented (Sun et al., 2013). The gold-bearing stage IIc veins with magnetite - hematite intergrowths (e.g., Fig. 4.21 B,C) are consistent with the argument that magnetite - hematite intergrowths are intrinsically linked to the reduction of sulfate to sulfide in the formation of giant porphyry deposits (Sun et al., 2013).
- Some stage II veins and altered rocks indicate that the Golpu magmatic fluids were relatively oxidised with respect to the metasedimentary host rocks. For example, the stage IIb hematite veins with magnetite halos in Figures 4.12 and 4.13 A-E indicate a redox gradient at the centimetre scale. The finely disseminated hematite along the porphyry-concentric transition from biotite- to muscovite- and chlorite-altered rocks in Figure 4.7 A and B indicates a redox gradient at the scale of hundreds of metres. Similar fine-grained hematite near the outer zone of biotite alteration has been documented around the Cadia porphyry deposits (Wilson et al., 2007).
- Golpu is hosted in rocks of low permeability (greenschist facies metasedimentary rocks), as is the case for many giant gold-rich porphyry deposits such as Grasberg (Sillitoe, 1997).

Some aspects of the Golpu deposit differ from the porphyry deposit characteristics compiled by Einaudi et al. (2003), Seedorff et al. (2005), and John et al. (2010):

- The hypogene Golpu ore has an elongate geometry, extending at least 1.8 kilometres vertically, and is open at depth (e.g., Fig. 4.14). Hypogene ore in most porphyry deposits occurs over a vertical interval of 1 - 1.5 km (Seedorff et al., 2005), although this figure may be limited by mining and drilling depths.
- The porphyry sulfides (dominantly chalcopyrite, pyrite, and bornite) are atypically abundant in the Golpu intrusions, making up 3 - 6 vol % of the stage II diorite intervals, compared to the average 1 - 2 vol % sulfides in most porphyry deposits (John et al., 2010). Likewise, the 1 Gt Golpu resource (porphyry ore including mineralised wallrock) contains 0.90 % Cu (Reid and Gossage, 2012), which is nearly double the median copper grade of 217 porphyry deposits reported by Singer et al. (2002).
- Some stage IIc veins contain chalcopyrite, pyrite, and magnetite. In particular, the co-existence of magnetite with pyrite in the same vein seam in Figure 4.21 A is unusual (Einaudi et al., 2003). The

calcite replacing skeletal magnetite in this gold-bearing vein may indicate an initial stage of magnetite-stable conditions at the time of gold mineralisation.

- Some of the accessory minerals to main stage Golpu porphyry mineralisation are unusual. Among 138 porphyry deposits compiled by John et al. (2010), barite occurs as a hypogene mineral in only 12.7 %, and rutile in 10 % of deposits. Native bismuth and cubanite, which occur as accessory phases to the stage IIc Golpu porphyry mineralisation, are reported by John et al. (2010) to occur in only 1 - 5 % of porphyry deposits.

4.4.2 Upward-flaring Veins and Altered Rocks (Stages III and IV)

4.4.2.1 High sulfidation epithermal domain

The Wafi alunite - kaolinite domain of veins and altered rocks contains several features characteristic of high sulfidation mineralisation (after Sillitoe, 1999; Sillitoe and Hedenquist, 2003; Einaudi et al., 2003; Jobin, 2004; and Sillitoe et al., 2013):

- The HS epithermal domain transitions upwards from sparse kaolinite - pyrite veins deep in the Golpu porphyry environment, to zones of pervasively altered rocks near the current erosional surface. The zones of pervasively altered rocks are broadly zoned about the Golpu porphyry, transitioning inward (towards Golpu) from kaolinite - dickite - pyrite, into alunite - kaolinite - pyrophyllite - pyrite ± diaspore, then alunite - kaolinite - quartz - pyrite assemblages. The central zone of residual quartz - alunite altered rocks contains zones of vuggy quartz, as is the case in many lithocaps (Sillitoe, 1999). In the quartz - alunite zone, acid alteration of Golpu quartz veins has resulted in undulating or wormy textures (Fig. 4.28 C) similar to the acid-altered stockwork veins in the upper parts of the Caspiche deposit (Sillitoe, 2013).
- High sulfidation mineralisation comprises vein-dominated styles at depth, transitioning upwards to disseminated mineralisation that is broadly lithologically controlled (as in the east-dipping zones of pervasive alunite - kaolinite altered rocks). Finely disseminated pyrite is the dominant ore mineral throughout the alunite - kaolinite domain. Sulfosalts, covellite, chalcocite, and bornite are less common components that occur as veins and pyrite-selective disseminations, and they are most abundant nearest the Golpu diorites, in Rafferty's copper zone (Figs. 4.24, 4.25).
- Some covellite - pyrite mineralisation occurred after vuggy quartz alteration, as is documented in other high sulfidation deposits (e.g., Sillitoe and Hedenquist, 2003). Most of the high sulfidation mineralisation, however, appears to have been co-genetic with stage IVa alunite (indicated by, for example, the alunite halos to covellite veins as in Fig. 4.30).
- Sphalerite occurs with pyrite and tennantite near the outer margins of the Wafi alunite-bearing zone. Sphalerite is reported to occur in many high sulfidation deposits (Sillitoe, 1999), and is generally interpreted to record a change (either spatial or temporal) from high to intermediate sulfidation states (e.g., Einaudi et al., 2003; Jobin, 2004). The latest (stage IVb) alunite - pyrite - orpiment - galena - marcasite veins (Fig. 4.43) similarly indicate a return to cooler conditions and lower sulfidation states.

Decreasing temperature and decreasing sulfidation state are thought to characterise late stage fluids through the lithocap environment (Einaudi et al., 2003).

4.4.2.2 Intermediate sulfidation epithermal domain

The domain of carbonate - base metal sulfide mineralisation is peripheral to the Wafi lithocap (Figs. 4.24, 4.25). It is mostly vein-dominated, comprising Mn-carbonate - base metal sulfide veins with chlorite - montmorillonite ± muscovite ± illite halos. These features are typical of IS epithermal deposits (Einaudi et al., 2003; Sillitoe and Hedenquist, 2003). Most of the veins have chlorite - montmorillonite halos; the muscovite-bearing halos to the Link Zone veins near the Compass fault (e.g., Fig. 4.38) may be indicative of higher temperature or more porphyry-proximal IS mineralisation (Einaudi et al., 2003). Pyrite fragments within the carbonate veins west of Golpu contain trace pyrrhotite inclusions, and Link Zone mineralisation contains trace amounts of both pyrrhotite and arsenopyrite in association with adularia (e.g., Fig. 4.40 A,B,F).

Unlike HS epithermal deposits, IS deposits do not commonly demonstrate close spatial relationships with porphyry (or HS) deposits (Sillitoe and Hedenquist, 2003). Wafi-Golpu is an exception, wherein the Wafi carbonate - base metal sulfide veins are related spatially to the Golpu porphyry deposit and the Wafi high sulfidation mineralisation (e.g., Fig. 4.24).

Timing of intermediate sulfidation veins

The Wafi carbonate veins are interpreted to have formed during and shortly after the adjacent alunite - kaolinite alteration and associated veins. The IS epithermal veins contain gold adjacent to the HS epithermal domain (Figs. 4.24, 4.25 C, 4.41). This relationship was also noted by Leach (1999), who suggested that higher gold grades occur at the transition from high to intermediate sulfidation styles. This implies that either (1) both the high and intermediate sulfidation fluids were gold-bearing, and happened by coincidence to deposit gold in approximately the same C-shaped region defined by the gold grade shells in Figure 4.24, or (2) the high sulfidation fluid was (at least in part) parent to the intermediate sulfidation fluid, and gold mineralisation occurred in the transition from high to intermediate sulfidation conditions.

In IS epithermal veins along the lithocap margin, the chronological and vein wall-to-centre transition from quartz ± sulfide into carbonate - sulfide ± gold (e.g., Figs. 4.36 C-F, 4.37 A,C,D) may indicate that gold precipitation occurred during a similar transition to carbonate-stable conditions. Possible causes of the high to intermediate sulfidation transition are further explored in Chapter Five.

4.4.2.3 Structural controls on epithermal mineralisation

The broadly concentric to C-shaped pattern of epithermal veins and altered rocks (e.g., Figs. 4.2, 4.24, 4.41) reflects structural controls from both the east-dipping stratigraphy and the north-dipping Compass fault. Sillitoe (1999 and 2013) and Morehari et al. (2008) suggested that the Wafi breccia complex contacts localised much of the Wafi epithermal mineralisation. However, the distribution of gold in Figure 4.24 suggests that the Compass fault, which occurs along and extends beyond the southern diatreme contact, has localised most of the

Wafi mineralisation. Link Zone mineralisation, for example, does not occur within or along the contact of the Wafi breccia complex, but instead occurs along the Compass fault about 100 metres west of the complex. The westernmost zones of 1 ppm Au mineralisation likewise occur along the Compass fault, up to 310 metres west of the Wafi breccia complex (e.g., Figs. 4.24, 4.41).

The zones of stage III muscovite and stage IV kaolinite altered rocks along the shoulders of the Golpu diorites (Figs. 4.23 A, 4.25 A) are similar to the "barren advanced argillic shoulders" described by Corbett and Leach (1998). Sillitoe (1999) interpreted such features as the roots of lithocaps that were controlled by the mechanical (and resulting permeability) contrasts between porphyry intrusions and their host rocks.

The stage III quartz-pyrite veins and early muscovite alteration appear to have been nearly symmetrically distributed to the east and west sides of the stage II diorite (Fig. 4.23 A), whereas the stage IV epithermal vein and alteration domains are notably asymmetrical (Fig. 4.25 A). For example, the deepest zones of stage IV pervasive kaolinite - dickite altered rocks and high sulfidation mineralisation are centred over the eastern shoulder of the stage II Golpu diorite, whereas stage IV carbonate veins with montmorillonite-, chlorite-, and muscovite-altered rocks are more prevalent to the west. This asymmetry can be explained by several factors that may have influenced the locations and/or durations of upflow of the lithocap-forming and adjacent vein-producing fluids:

- East-dipping host stratigraphy has likely influenced the location and density of veins (rock type or bedding contacts affecting fracture development) as well as alteration (e.g., lithocap-forming fluids diffusing or dissolving along stratigraphic units; Figs. 3.5, 4.25 A).
- The vertical intrusive contacts and stockwork veins associated with the stage I and II diorite intrusions may have influenced the locations of upflow and alteration. For example, the stage I Golpu diorite may have been the site of more focussed or more prolonged stage IV veining and alteration, due to its rheological contrast with metasedimentary rocks.
- Eruption of the Wafi breccia complex may have shifted the hydrothermal system during stage III, so that the buoyant magmatic vapour plume was more widespread west of Golpu (e.g., through the Wafi breccia complex and along its contacts; Fig. 4.25).

The westernmost portion of the IS epithermal domain has cross-cut the upper Nambonga diorite. This may reflect rheological controls on vein density in the epithermal environment; that is, the more coherent Nambonga diorite prefentially allowed the development of veins. Alternatively, it is possible that the Nambonga diorite served as a fluid channel and / or fluid source (?) to the intermediate sulfidation veins, in a manner perhaps analogous to lithocaps fed by multiple intrusive centres. This hypothesis could be tested with further geochronological constraints on the emplacement of the Nambonga diorite and the formation of the IS epithermal veins.

4.5 Summary

The veins and altered rocks of the Wafi-Golpu deposit record a four stage transition from porphyry to high and intermediate sulfidation epithermal styles of mineralisation. The first two stages (I and II) comprise calc-alkalic porphyry-style mineral assemblages that are concentrically zoned about the Golpu diorites (Figs.

4.3, 4.5, 4.10, 4.14). These stages include veins of quartz - anhydrite - molybdenite, orthoclase, and quartz - magnetite - specularite, along with alteration domains of biotite - actinolite to distal actinolite - chlorite - epidote. Stage I porphyry mineralisation was a minor ore forming event; the main stage of Cu-Au porphyry mineralisation occurred during stage II, following intusion of the stage II hornblende-phyric Golpu diorite. The main stage of Cu-Au mineralisation involved vein and disseminated chalcopyrite, pyrite, and bornite. Native gold inclusions occur in the sulfides, along with magnetite - hematite intergrowths and accessory phases including hypogene calcite, barite, rutile, native bismuth, and cubanite. The porphyry mineralisation has resulted in an unusually sulfide-rich and vertically elongate orebody (Fig. 4.14).

Stage II intrusion-concentric porphyry mineralisation was overprinted by upward-flaring epithermal domains of quartz, muscovite, and pyrite veins and alteration (stage III; Fig. 4.23). The Wafi breccia complex is interpreted to have erupted during stage III, after Golpu porphyry mineralisation, and before the epithermal mineralisation. Diatreme eruption was followed by the main stage of Wafi epithermal mineralisation and alteration (stage IV), which overprinted metasedimentary host rocks, the mineralised Golpu diorites, and the Wafi breccia complex (Figs. 4.24, 4.25). These late mineral domains include zones of pervasive alteration containing quartz, alunite, pyrophyllite, kaolinite, dickite, and diaspore at the current erosional surface, and sparse kaolinite - pyrite veins at depth.

Epithermal mineral assemblages are also broadly zoned with distance from the Golpu intrusions, with an outermost zone of carbonate - sulfide ± quartz ± adularia veins and montmorillonite - chlorite ± muscovite ± illite altered rocks. The IS domain contains most of the epithermal gold mineralisation, which was mainly localised by the north-dipping Compass fault (Fig. 4.41). Along the Compass fault, IS epithermal veins have cross-cut stage II biotite-altered rocks associated with the Golpu porphyry deposit (Figs. 4.25 C, 4.38). Some of the IS epithermal mineralisation contains pyrrhotite and high-As pyrite, which imply reducing conditions locally (e.g., Einaudi et al., 2003).

Considered separately, the Golpu porphyry deposit and Wafi high and intermediate sulfidation deposits can be easily classified into their respective deposit types. As a whole, however, the particular configuration of zoned and overprinting epithermal styles of mineralisation that have significantly overprinted a porphyry deposit is unique. In Chapter Five, additional constraints on the mineral zoning and paragenesis documented here will further establish that the configuration of porphyry and epithermal deposit styles in Wafi-Golpu offers compelling evidence for a genetic relationship between porphyry and epithermal environments.

Chapter 5
Geochronology and Geochemistry of Alteration and Mineralisation

5.1 Introduction

The absolute timing and origin of the Wafi-Golpu veins and alteration is constrained in this chapter using geochronological and geochemical analyses. Specifically, new Re-Os and Ar-Ar age determinations are provided for veins and alteration minerals, together with mineral and whole rock geochemical analyses and $\delta^{34}S$ compositions of sulfides and sulfates. Geochemical data are used to characterise the mass balance changes that occurred during alteration. The discussion addresses the timescales involved in the transition from porphyry to epithermal styles of mineralisation, and highlights new evidence for genetic links between the porphyry and epithermal environments at Wafi-Golpu.

5.2 Geochronology of Veins and Alteration

5.2.1 Introduction and Methods

The absolute timing of veins and alteration at Wafi-Golpu have been constrained by Re-Os (molybdenite), Ar-Ar (biotite), Ar-Ar (muscovite), and Ar-Ar (alunite) analyses. These results provide independent evidence for the relative timing of veins and alteration documented in Chapter Four, and provide constraints on the duration of hydrothermal activity.

Re-Os analysis

Two samples of quartz - molybdenite veins were analysed by R. Creaser at the University of Alberta for Re-Os dating of molybdenite. The samples were crushed, and molybdenite was recovered by magnetic and gravity separation methods. Concentrations of ^{187}Re and ^{187}Os in the molybdenite were measured by isotope dilution mass spectrometry, employing the method described by Markey et al. (2007). The age determination errors quoted in the Re-Os results include uncertainty in the ^{187}Re decay constant. Detailed results of the Re-Os analyses are provided in Appendix G.

Ar-Ar analysis

Five samples were submitted to M. Heizler at the New Mexico Geochronology Research Laboratory for Ar-Ar dating of biotite, muscovite, and alunite. Two samples of syn-mineralisation coarse-grained biotite were separated at the University of Tasmania from two diorite core samples. Coarse grained alunite was separated from an alunite vein using a hand-held drill. A further two samples of whole drill core (one biotite and one muscovite - pyrite altered metasandstone sample) were submitted with the biotite and alunite samples for heavy liquid mineral separation at New Mexico Tech.

The five mineral samples were irradiated at the USGS reactor in Denver, Colorado, for 19.5 hours.

Samples were step-heated with 75 W Photon-Machines, and Ar isotope contents were measured by M. Heizler using a Thermo-Fisher Scientific ARGUS VI mass spectrometer. Plateau Ar-Ar ages were calculated relative to the FC-2 Fish Canyon Tuff sanidine standard, with weighted 2σ errors calculated as in Taylor (1982). Detailed results of the Ar-Ar geochronological analyses are provided in Appendix G.

5.2.2 Results

Re-Os (molybdenite) results of 8.831 ± 0.036 Ma and 8.731 ± 0.036 Ma were obtained from two samples of stage IIa quartz - molybdenite veins (Table 5.1, Fig. 5.1). These dates constrain the first stage of veins and alteration to within error of the intrusion of the stage II diorite (8.86 ± 0.22 Ma to 8.59 ± 0.22 Ma; Fig. 5.1). A biotite separate from stage II biotite-altered metasandstone, adjacent to the stage II diorite, yielded an Ar-Ar (biotite) age of 8.74 ± 0.04 Ma, which is almost identical to the youngest of the Re-Os results (Table 5.1, Fig. 5.1). This is interpreted to indicate that the biotite closure temperature of wallrock alteration was reached during the development of the stage IIa quartz - molybdenite veins. Stage IIc chalcopyrite - bornite ± pyrite mineralisation within the stage II diorite is, in some intervals, intergrown with coarse-grained biotite. Two samples of this stage IIc biotite yielded Ar-Ar ages of 8.70 ± 0.02 and 8.67 ± 0.02 Ma (Table 5.1, Fig. 5.1).

One muscovite separate from stage III muscovite - pyrite altered rock yielded an Ar-Ar age of 9.17 ± 0.18 Ma (Table 5.1). This is interpreted to be inconsistent with all other age determinations in this study, as addressed in section 5.2.3. A final Ar-Ar age of 8.51 ± 0.04 Ma was obtained from a stage IVb alunite vein (Table 5.1, Fig. 5.1). This provides an age constraint on the most recent documented stage of Wafi-Golpu veins and alteration.

5.2.3 Discussion

Establishing the duration of magmatic-hydrothermal activity is a crucial step in developing a genetic model for porphyry-epithermal systems (e.g., Chiaradia et al., 2013). Geochronological results from this study provide a valuable contribution to the porphyry-epithermal model, indicating that Golpu and Wafi were formed over a few hundred thousand years.

In general, the geochronological results define a history of Golpu diorite emplacement around 9.01 - 8.59 Ma, followed by Golpu porphyry veins and alteration around 8.83 - 8.67 Ma, to the final stage of Wafi epithermal veins around 8.51 Ma (Fig. 5.1). The 2 - 3 % error in the U-Pb intrusive ages overlap the age determinations for veins and alteration (Fig. 5.1), so they cannot be used to discriminate the duration of later magmatic-hydrothermal events. However, the Re-Os and Ar-Ar results are distinct at the 2σ confidence level, and are sufficient to establish the duration from the earliest of the porphyry veins (interpreted to have occurred shortly following emplacement of the Stage II diorite) to the latest epithermal vein.

The development of stage II porphyry veins began with the earliest (stage IIa) quartz - molybdenite veins following diorite intrusion. It culminated with the main stage of Golpu porphyry mineralisation (stage IIc), and lasted between 105,000 and 217,000 years at the reported 2σ confidence. This period includes the time taken for the porphyry to cool from ~ 530 °C to ~ 325 ºC, based on the closure temperatures for Re-Os in molybdenite and Ar-Ar in biotite (Suzuki et al., 1996; Knapp and Heizler, 1990).

The difference between the youngest Ar-Ar (biotite) and the Ar-Ar (alunite) age determinations suggests that Wafi-Golpu evolved from the main stage of porphyry mineralisation to the latest epithermal veins (a period which includes the eruption of the Wafi breccia complex and formation of Wafi epithermal mineralisation) over a period lasting between 100,000 and 220,000 years. Comparing the oldest Re-Os (molybdenite) to the Ar-Ar (alunite) age determinations, the total interval from the first (stage IIa) porphyry vein to the last (stage IVb) epithermal vein lasted between 250,000 and 400,000 years. Magmatic-hydrothermal activity of the Lepanto-FSE porphyry-epithermal deposit, which began to form around 1.5 Ma, occurred over a similar ~ 300,000 year period (Arribas et al., 1995).

Given that the epithermal veins and alteration have overprinted the Golpu porphyry, a few kilometres of uplift must have occurred within the same ~ 0.25 - 0.40 m.yr. period. Such is consistent with the tectonic evolution and related development of regional thrust faults described in Chapter Two.

Table 5.1: Geochronology of Wafi district intrusions, veins, and alteration

Material dated	Sample ID	Age (± 2σ)	Dating method	Source	Inferred age
Nambonga diorite	N5	10.33 ± 0.50	K-Ar (hornblende)	Tau-Loi (1996)	Nambonga intrusion ~ 10.33 - 9.95 Ma
	H6	9.95 ± 0.50			
Stage I plagioclase- and hornblende-phyric Golpu diorite	397-1084.0	9.01 ± 0.14	U-Pb (zircon)	this study	Stage I Golpu diorite intrusions ~ 9.01 - 8.79 Ma
Stage I plagioclase- and quartz-phyric Golpu diorite	392-1830.9	8.93 ± 0.2	U-Pb (zircon)	this study	
	392-1790.0	8.79 ± 0.17	U-Pb (zircon)	this study	
Stage II Golpu diorite	392-1413.0	8.86 ± 0.22	U-Pb (zircon)	this study	Stage II Golpu diorite intrusion ~ 8.86 - 8.59 Ma
	321-H	8.86 ± 0.19	U-Pb (zircon)	A. Harris (2010)	
	220-H	8.70 ± 0.19	U-Pb (zircon)	A. Harris (2010)	
	392-1280.5	8.59 ± 0.22	U-Pb (zircon)	this study	
Stage IIa quartz - molybdenite vein (earliest Stage II)	347-806.0	8.831 ± 0.036	Re-Os (molybdenite)	this study	Stage II quartz - molybdenite veins ~ 8.83 - 8.73 Ma
Stage IIa quartz - molybdenite vein (Stage II)	347-854.0	8.731 ± 0.036	Re-Os (molybdenite)	this study	
Stage II biotite-altered metasandstone	377-1081.5	8.74 ± 0.04	Ar-Ar (biotite)	this study	Stage II biotite alteration ~ 8.74 Ma
Stage IIc biotite in quartz - chalcopyrite - biotite vein	397-1120.4	8.70 ± 0.02	Ar-Ar (biotite)	this study	Main stage porphyry mineralisation ~ 8.70 - 8.67 Ma
Stage IIc biotite in pegmatitic biotite - chalcopyrite clot	377-1171.5	8.67 ± 0.02	Ar-Ar (biotite)	this study	
Wafi breccia complex	199-154.9	9.05 ± 0.23	U-Pb (zircon)	this study	Age of breccia fragments entrained in breccia complex
Stage III muscovite alteration	398-817.5	9.17 ± 0.18	Ar-Ar (muscovite)	this study	Plateau age inconsistent with field observations; muscovite alteration post-dates stage II biotite alteration and Wafi breccia complex
Stage IVb alunite vein	398-150.5	8.51 ± 0.04	Ar-Ar (alunite)	this study	Youngest Wafi epithermal veins ~ 8.50 Ma

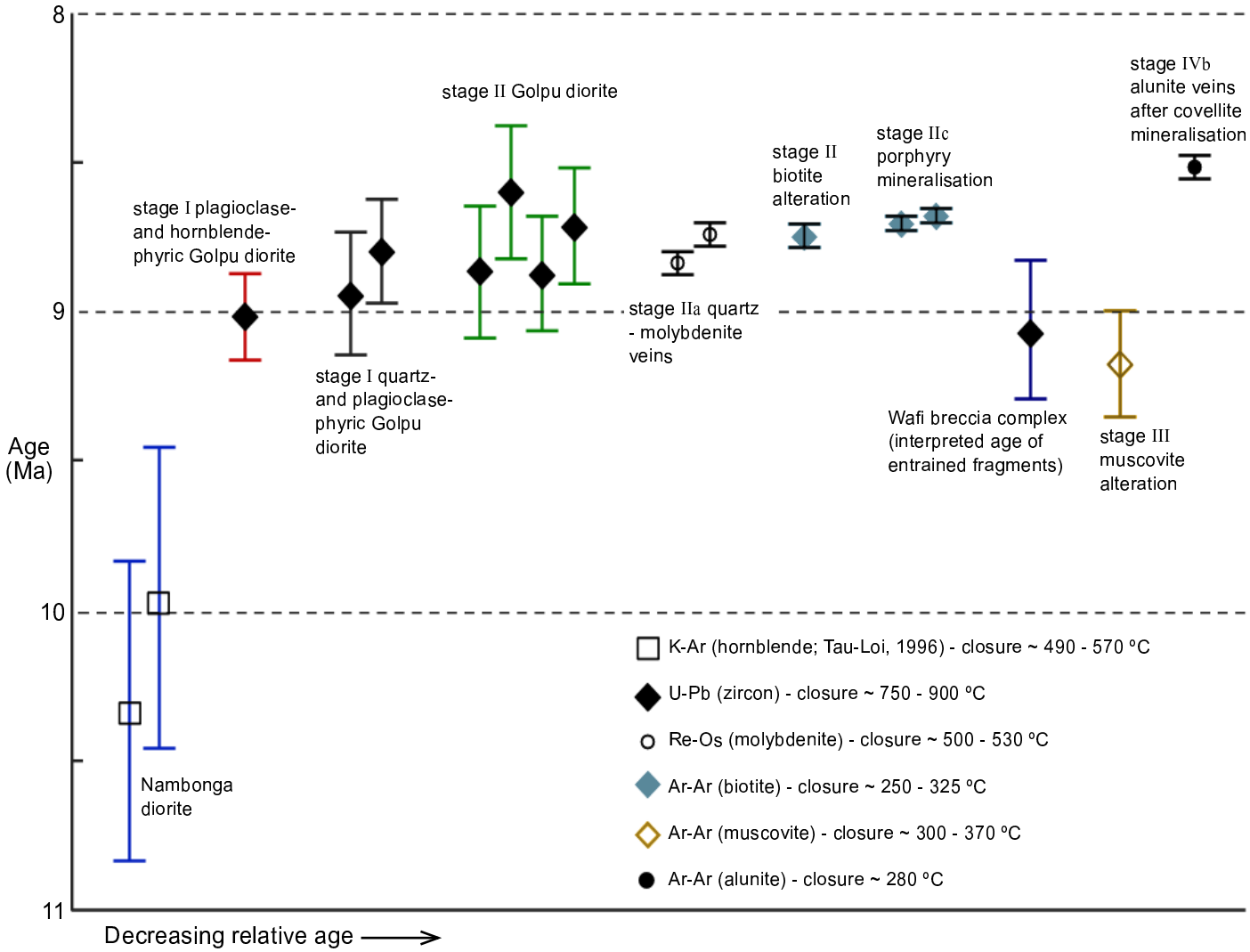

Figure 5.1: Summary of the geochronology of magmatic-hydrothermal events in the Wafi district, illustrating the transition from Golpu diorite intrusions around 9.01 - 8.59 Ma, to Golpu porphyry mineralisation around 8.83 - 8.67 Ma, to the final stage of Wafi epithermal mineralisation around 8.51 Ma. Error bars are drawn at 2σ. The Ar-Ar age indicated for stage III muscovite alteration is interpreted to be erroneous, because it has overprinted stage II biotite alteration. Estimated closure temperatures are from Knapp and Heizler (1990), Suzuki et al. (1996), Love et al. (1998), Cherniak and Watson (2001), and Chiaradia et al. (2013).

Anomalous Ar-Ar (muscovite) age

The sample WR398-817.5 is a fine-grained, pervasively muscovite-altered metasandstone, collected from a zone of muscovite - pyrite altered rocks with quartz - pyrite veins. The veins and alteration in this larger zone have cross-cut and overprinted stage II biotite-altered rocks adjacent to the Golpu porphyry (Appendix B), so the returned Ar-Ar age of 9.17 ± 0.18 Ma (Table 5.1) is interpreted to be erroneous. This may be the result of (1) excess argon or potassium loss in the sample, or (2) ^{39}Ar recoil during sample irradiation, which is more likely to produce anomalously old ages in fine-grained samples such as WR398-817.5 (e.g., Foland et al., 1992). Alternatively, the result may indicate a more complex paragenesis involving an earlier, undocumented stage of muscovite alteration. These problems could be resolved with additional geochronology of stage III events, perhaps sampling more coarse-grained muscovite (Ar-Ar) or sulfides (Re-Os).

5.3 Whole Rock Geochemistry

5.3.1 Methods

Classification of samples

A total of 87 core samples were selected to represent the range of styles and intensities of veins and altered rocks that occur at Wafi-Golpu. Analytical methods are described in Chapter Three (section 3.2). In this chapter, the sample data have been classified into eight spatial domains dominated by characteristic vein and alteration types, as shown in Figure 5.2.

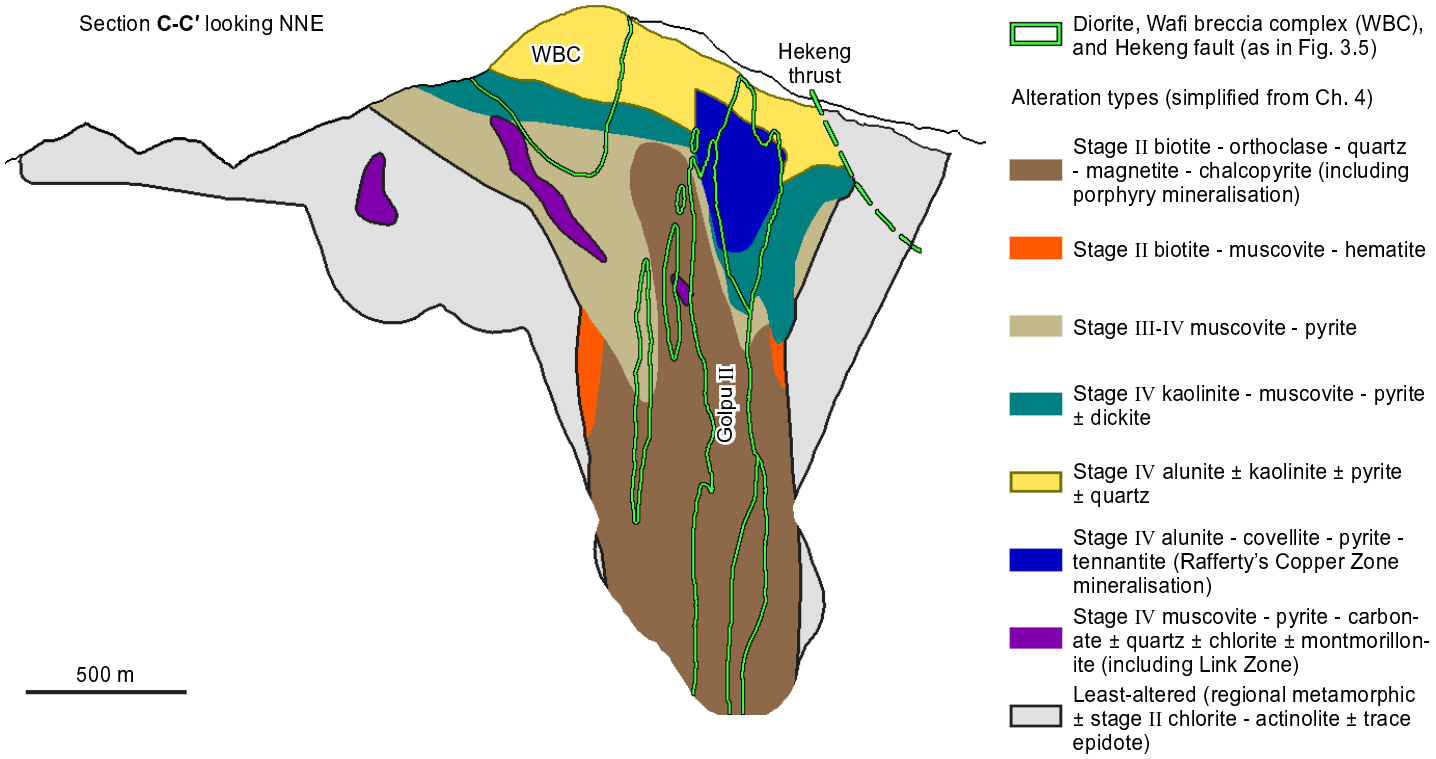

Figure 5.2: Vein and alteration domains described in Chapter Four have been simplified into eight alteration types, shown here in section C. Note that Golpu porphyry mineralisation occurs in the stage II biotite - orthoclase - quartz - magnetite - chalcopyrite domain, HS epithermal mineralisation (i.e., Rafferty's Copper Zone) occurs in the stage IV alunite - covellite - pyrite - tennantite domain, and IS epithermal mineralisation (including Link Zone, not visible in section C) occurs in the stage IV muscovite - pyrite - carbonate ± quartz ± chlorite ± montmorillonite domain.

MMJV assay data

Whole rock assays of Au, Ag, Cu, Mo, Fe, As, Sb, S, K, Mn, Pb, and Zn contents have been collected by MMJV geologists from every metre of drill core in the study area, with the exception of Fe and K (missing in some drill holes). Samples were pulverised in a steel mill to 200 mesh, and analysed at PT Intertek Laboratories in Indonesia. Ag, As, Cu, Fe, Mn, Mo, Pb, Sb, and Zn were determined by ICP-MS following aqua regia digest. Au contents were determined by 30 g fire assay and atomic absorption spectrometry. Reported detection limits for the assay methods are: 0.01 ppm for Au; 0.1 ppm for Ag; 1 ppm for Cu, Mn, Mo, Sb, and Zn, and S; 2 ppm for As and Pb; and 0.01 % for Fe (Morehari et al., 2009).

Grade shells of assay data

Isotropic grade shells of the MMJV assay data have been constructed from 10 m composite intervals using Leapfrog Mining software. The grade shells were constrained to a volume within 200 metres of assay data, and are shown in Figures 5.9 - 5.14. A description of the method used to produce the grade shells is provided in Appendix C.

5.3.2 Results

5.3.2.1 Whole rock geochemical data

Zr appears to have the been least-mobile element during hydrothermal alteration. It has a positive correlation with Hf in all samples, which passes through the origin (Fig. 5.3 A). The sample suite includes rocks that have undergone intense acid alteration and quartz veining. Accordingly, many other species commonly applied as immobile tracers in variation diagrams (e.g., TiO_2; Fig. 5.3 B) are not appropriate as least-mobile tracers for the Wafi-Golpu data.

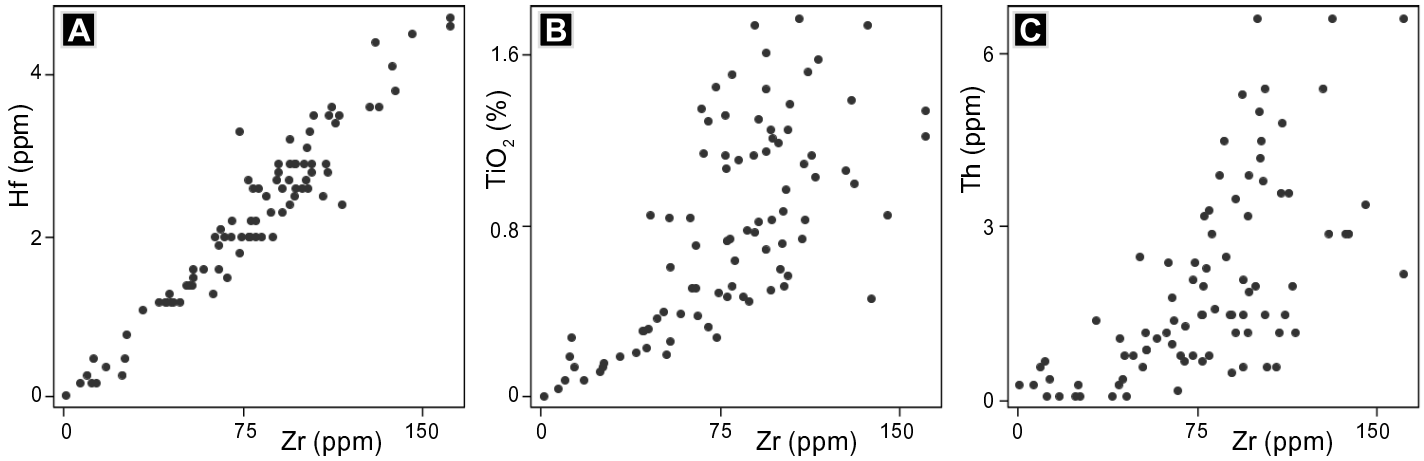

Figure 5.3: Variation of selected elements in 87 veined and altered Wafi-Golpu samples. A) Hf vs. Zr. B) TiO_2 vs. Zr. C) Th vs. Zr.

Of the 87 samples, 13 metasedimentary rock and three diorite samples are weakly altered, based on visual estimate in hand sample and thin section. These samples allow a limited assessment of the geochemical variability within protolith units (Fig. 5.4). Among the weakly altered samples of Owen Stanley metasedimentary rocks, there is little geochemical variation within rock types (apart from one sample of weakly altered quartz-rich metasandstone, which contains the highest SiO_2 and lowest Na_2O and CaO contents of the weakly altered metasedimentary rock samples; Fig. 5.4 E,L,O). Most metasandstone samples contain higher MgO contents than metaconglomerate and metasiltstone samples (Fig. 5.4 I). Metasiltstone samples, on average, contain slightly lower MgO and CaO contents compared to the other metasedimentary units (Fig. 5.4 E,I).

The three weakly altered samples of the stage II Golpu diorite display little variation in major and trace element compositions (Fig. 5.4). The mean composition of these three samples is provided in Table 5.2. Weakly altered intervals of the stage I intrusions or the Wafi breccia complex were not observed and therefore could not

Table 5.2: Geochemistry of altered and mineralised rocks from Golpu and Wafi

Alteration type (as in Fig. 5.2)	Least-altered		Stage II biotite - orthoclase - quartz - magnetite - chalcopyrite		Stage II biotite - muscovite - hematite	Stage III-IV muscovite - pyrite
Sample ID	Mean of 13 samples*	Mean of 3 samples**	392-1402.0	402-700.0	396-975.8	347-395.0
Sample description	Least-altered metasedimentary rock mean	Least-altered Golpu diorite mean	Intense, orthoclase- and biotite-altered diorite with 25 % quartz - sulfide veins	Intense, pervasive, biotite-altered metasandstone	Strong, pervasive, muscovite-, biotite-, and hematite-altered metasandstone	Moderate, pervasive and vein halo, muscovite- and pyrite-altered metasandstone
SiO_2	54.66	62.25	63.96	58.48	55.76	51.06
TiO_2	1.17	0.38	0.37	1.45	1.19	1.74
Al_2O_3	14.41	13.50	11.72	13.61	14.27	21.40
Fe_2O_3	8.39	9.22	8.81	7.07	8.37	10.44
MnO	0.24	0.07	0.02	0.03	0.06	0.03
MgO	7.11	1.31	1.60	8.25	8.71	0.09
CaO	4.53	2.61	0.36	0.46	1.18	0.15
Na_2O	2.33	2.66	2.31	3.26	0.25	0.04
K_2O	0.75	4.20	3.98	4.40	2.35	0.32
P_2O_5	0.13	0.18	<0.01	<0.01	0.17	0.04
S	3.15	1.85	4.50	1.48	4.42	8.41
LOI†	2.97	2.73	0.02	0.97	3.20	6.12
Sum	99.84	99.06	97.65	99.46	99.93	99.84
Ag	0.35	0.94	3.45	0.18	0.06	0.27
As	10.7	2.1	12.4	0.7	1.8	19.1
Au	0.08	0.37	1.53	0.07	0.03	0.14
B	4	3	3	<1	9	5
Ba	166	270	187	84	144	60
Be	2	<1	2	<1	2	<1
Bi	1.25	0.29	0.12	0.15	0.37	1.48
Cd	0.33	0.14	0.18	0.07	<0.01	0.16
Co	28.0	6.3	4.5	24.0	37.5	25.1
Cr	214.5	8.5	4.9	307.9	280.7	163.6
Cs	1.9	2.0	3.6	3.4	2.9	1.1
Cu	199.4	7518.5	28170.0	2560.6	114.3	173.5
Ga	15.0	18.1	18.8	14.2	14.4	20.0
Hf	2.4	1.7	1.2	3.3	2.6	4.1
Hg	0.07	0.02	<0.01	0.03	<0.01	<0.01
Mo	22.8	8.0	1.9	51.1	28.2	0.3
Nb	3.2	2.6	2.9	1.8	4.2	11.9
Ni	165.6	11.3	6.5	125.0	164.5	175.7
Pb	25.2	4.5	6.7	4.1	1.5	39.5
Rb	17.9	51.3	50.1	139.7	64.3	9.8
Sb	0.15	0.06	0.21	<0.02	0.04	<0.02
Sc	29	6	7	35	31	45
Se	4.0	7.9	28.1	2.7	3.7	17.5
Sn	3	3	3	4	4	5
Sr	108.0	236.7	82.3	72.7	37.8	45.6
Ta	0.2	0.2	0.3	<0.1	0.3	0.4
Te	0.49	0.14	0.26	0.44	0.24	3.90
Th	1.7	1.5	0.8	0.8	2.0	2.9
Tl	0.40	0.07	0.20	0.89	0.44	4.70
U	0.6	0.2	0.2	0.3	0.7	0.7
V	228	120	154	240	264	302
W	3.4	1.9	2.9	1.0	5.8	1.1
Y	23.1	9.3	2.0	19.0	19.0	41.6
Zn	190	62	47	57	25	451
Zr	88.4	62.0	48.2	73.1	99.5	137.4

Major element oxides and sulfur are reported in wt. %. Trace elements are reported in ppm. Lanthanide series elements are omitted from this table, but are provided in Appendix G. *Mean of samples 321-467.7, 323-457.7, 337-157.7, 347-98.8, 377-218.6, 377-910.0, 392-150.2, 392-276.3, 396-1226.3, 396-284.7, 396-44.0, 396-674.8, and 397-353.2. **Mean of samples 337-991.5, 349-260.6, 377-1650.0. †Loss on ignition values exclude sulfur.

Table 5.3: Geochemistry of altered and mineralised rocks from Golpu and Wafi

Alteration type (as in Fig. 5.2)	Stage IV kaolinite - muscovite - pyrite	Stage IV alunite ± kaolinite ± pyrite ± quartz		Stage IV alunite - covellite - pyrite - tennantite	Stage IV muscovite - pyrite - carbonate ± quartz ± chlorite ± montmorillonite	
Sample ID	349-188.4	301-115.7	398-25.0	398-272.6	397-74.2	177-389.8
Sample description	Strong, pervasive, kaolinite-, dickite-, and pyrite-altered metasandstone	Intense, pervasive, quartz- and alunite-altered Wafi breccia complex	Intense quartz-altered Golpu diorite with vuggy texture	Intense, quartz- and alunite-altered and pyrite-covellite mineralised metasandstone with relict quartz stockwork veins	Moderate, chlorite-, muscovite-, and montmorillonite-altered metasandstone with 20% quartz - carbonate - pyrite veins	Moderate, pervasive muscovite-altered metasiltstone with quartz - pyrite - adularia - rhodochrosite veins (Link Zone)
SiO_2	53.99	53.76	97.96	66.68	31.07	62.13
TiO_2	0.85	1.00	0.74	0.08	0.47	0.71
Al_2O_3	16.18	15.74	0.23	4.09	8.11	10.39
Fe_2O_3	9.49	3.77	0.2	16.36	31.48	7.93
MnO	0.06	<0.01	<0.01	0.01	0.36	2.83
MgO	5.03	0.02	0.02	<0.01	3.93	1.28
CaO	0.54	0.08	0.01	0.03	4.98	1.1
Na_2O	3.86	0.35	<0.01	0.03	0.07	0.12
K_2O	5.49	3.93	0.02	0.05	1.34	3.96
P_2O_5	0.27	0.19	0.04	0.12	0.11	0.12
S	2.65	5.22	<0.05	10.64	17.90	5.21
LOI†	0.86	15.71	0.77	0.00	0.00	4.12
Sum	99.27	99.77	99.99	98.09	99.82	99.90
Ag	0.75	3.74	0.04	5.25	0.3	7.53
As	6.2	80.3	15.5	41.6	22.5	1455.0
Au	0.15	1.6	0.08	0.6	0.09	15.35
B	<1	<1	<1	<1	3	7
Ba	586	512	16	905	152	289
Be	2	<1	1	2	<1	<1
Bi	0.65	9.22	0.17	1.86	2.31	0.54
Cd	0.27	0.03	0.01	1.6	0.28	0.22
Co	96.2	<0.2	0.5	46.8	53.6	26.1
Cr	179.4	16.2	1.7	4.4	85.2	52.7
Cs	4.6	0.2	0.1	0.2	3.5	10.5
Cu	3893.7	52.9	16.6	26860	20.6	100.1
Ga	13.3	39.8	<0.5	2.6	7.6	12.8
Hf	4.5	3.6	2.9	0.3	2.2	1.9
Hg	0.05	2.78	0.02	0.09	0.08	1.69
Mo	53.1	2.5	2.5	246.1	5.8	1.8
Nb	5	5.2	6.1	0.7	2.3	1.5
Ni	152.9	0.6	0.5	26.5	239.8	284.3
Pb	16.7	306.1	2.9	46.2	39.8	36.2
Rb	131.2	3	0.6	1	38.3	112.8
Sb	0.14	7.91	0.93	0.28	0.14	15.79
Sc	23	10	1	2	9	19
Se	4.6	6.9	<0.5	>100.0	7.7	8.3
Sn	7	6	5	58	2	3
Sr	59.2	502.6	3.4	731.4	35.6	26.7
Ta	0.4	0.5	0.5	0.1	0.1	0.2
Te	0.43	13.19	2.53	3.43	1.23	6.76
Th	3.4	6.6	1.2	0.6	3.2	1.8
Tl	0.61	0.09	<0.02	0.43	0.25	15.37
U	0.9	1.5	0.5	<0.1	1	0.5
V	118	139	<8	33	71	151
W	1.6	4.4	2.4	5.5	3	7.9
Y	21.3	6.5	3.1	0.4	28.5	18.7
Zn	544	18	2	385	62	107
Zr	145.8	131.8	109.6	9.1	77.9	64.5

Major element oxides and sulfur are reported in wt. %. Trace elements are reported in ppm. Lanthanide series elements are omitted from this table, but are provided in Appendix G. †Loss on ignition values exclude sulfur.

be sampled in this study.

The major and trace element contents of Wafi-Golpu samples vary significantly between alteration types (Tables 5.2, 5.3; Figs. 5.4 - 5.8). Among all alteration types, the most common mass changes involved losses of CaO and MgO, and gains of K_2O and / or SiO_2 (Figs. 5.5 - 5.8).

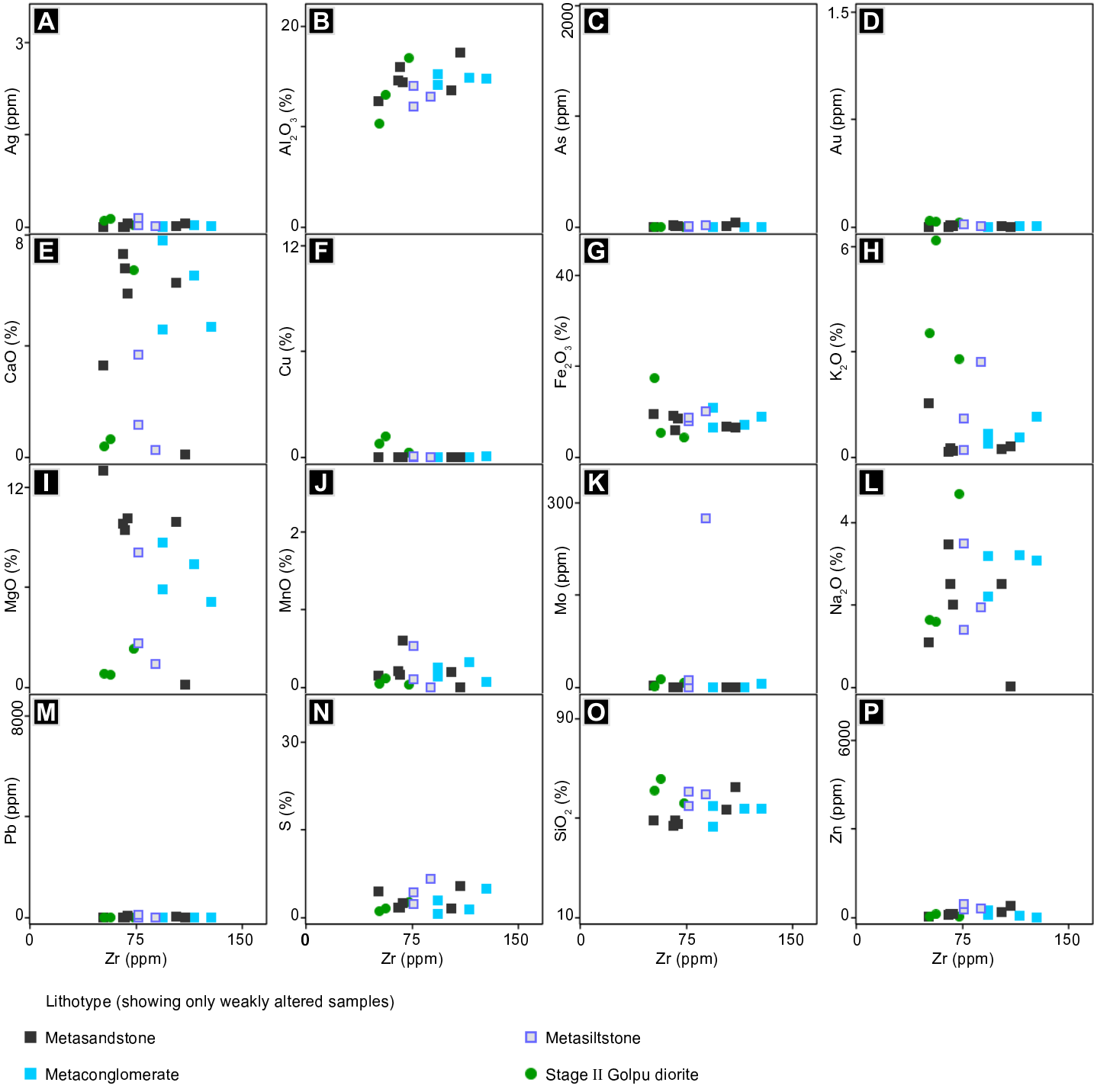

Figure 5.4: Selected major and trace element variation in weakly altered samples of Owen Stanley metasedimentary rocks and stage II Golpu diorite. Other lithotypes (e.g., stage I diorite intrusions, Wafi breccia complex) are not included on this diagram because they do not contain weakly altered samples. A) Ag vs. Zr. B) Al_2O_3 vs. Zr. C) As vs. Zr. D) Au vs. Zr. E) CaO vs. Zr. F) Cu vs. Zr. G) Fe_2O_3 vs. Zr. H) K_2O vs. Zr. I) MgO vs. Zr. J) MnO vs. Zr. K) Mo vs. Zr. L) Na_2O vs. Zr. M) Pb vs. Zr. N) S vs. Zr. O) SiO_2 vs. Zr. P) Zn vs. Zr.

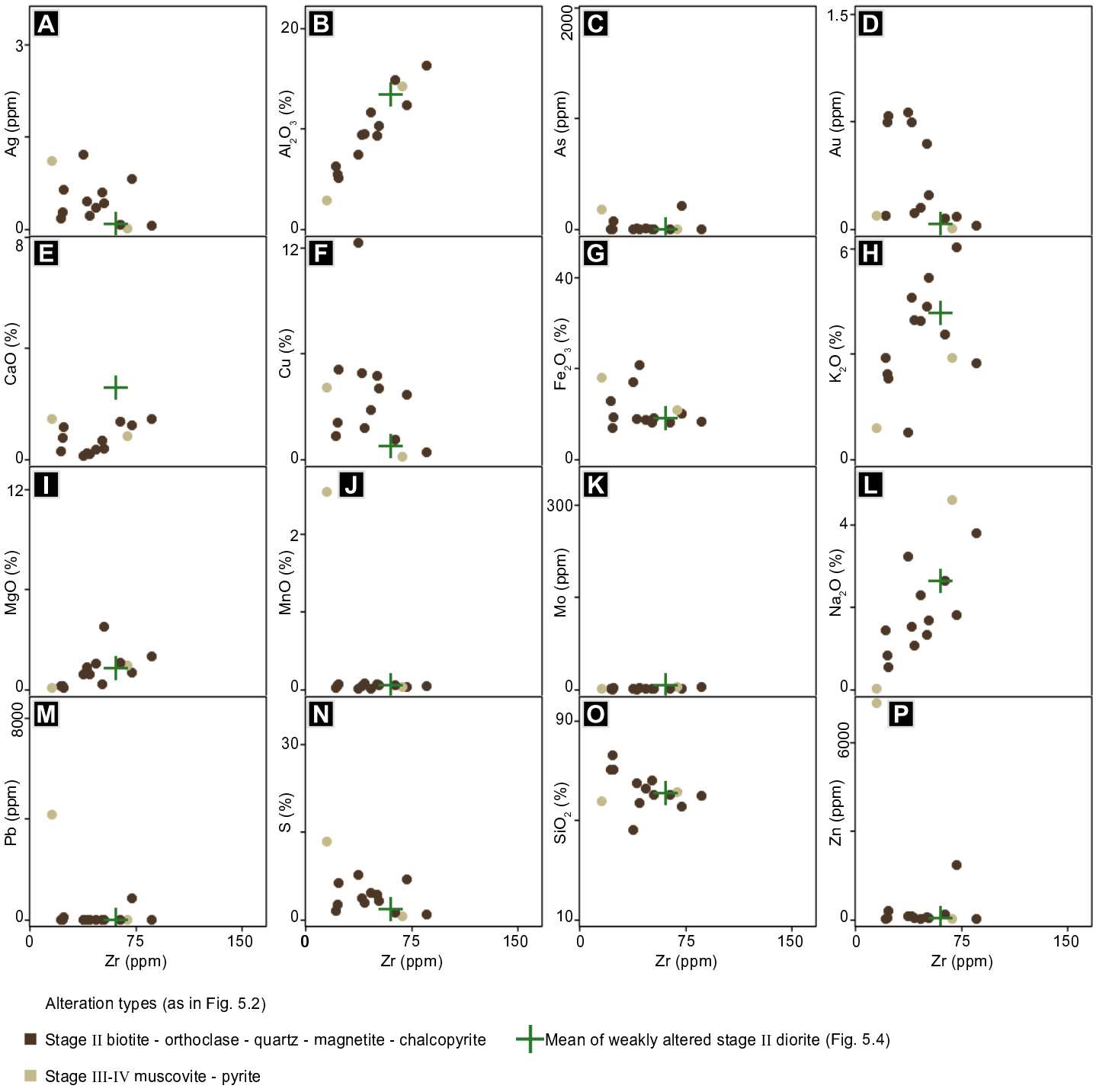

Figure 5.5: Selected major and trace element variation in altered samples of stage II Golpu diorite. A) Ag vs. Zr. B) Al_2O_3 vs. Zr. C) As vs. Zr. D) Au vs. Zr. E) CaO vs. Zr. F) Cu vs. Zr. G) Fe_2O_3 vs. Zr. H) K_2O vs. Zr. I) MgO vs. Zr. J) MnO vs. Zr. K) Mo vs. Zr. L) Na_2O vs. Zr. M) Pb vs. Zr. N) S vs. Zr. O) SiO_2 vs. Zr. P) Zn vs. Zr.

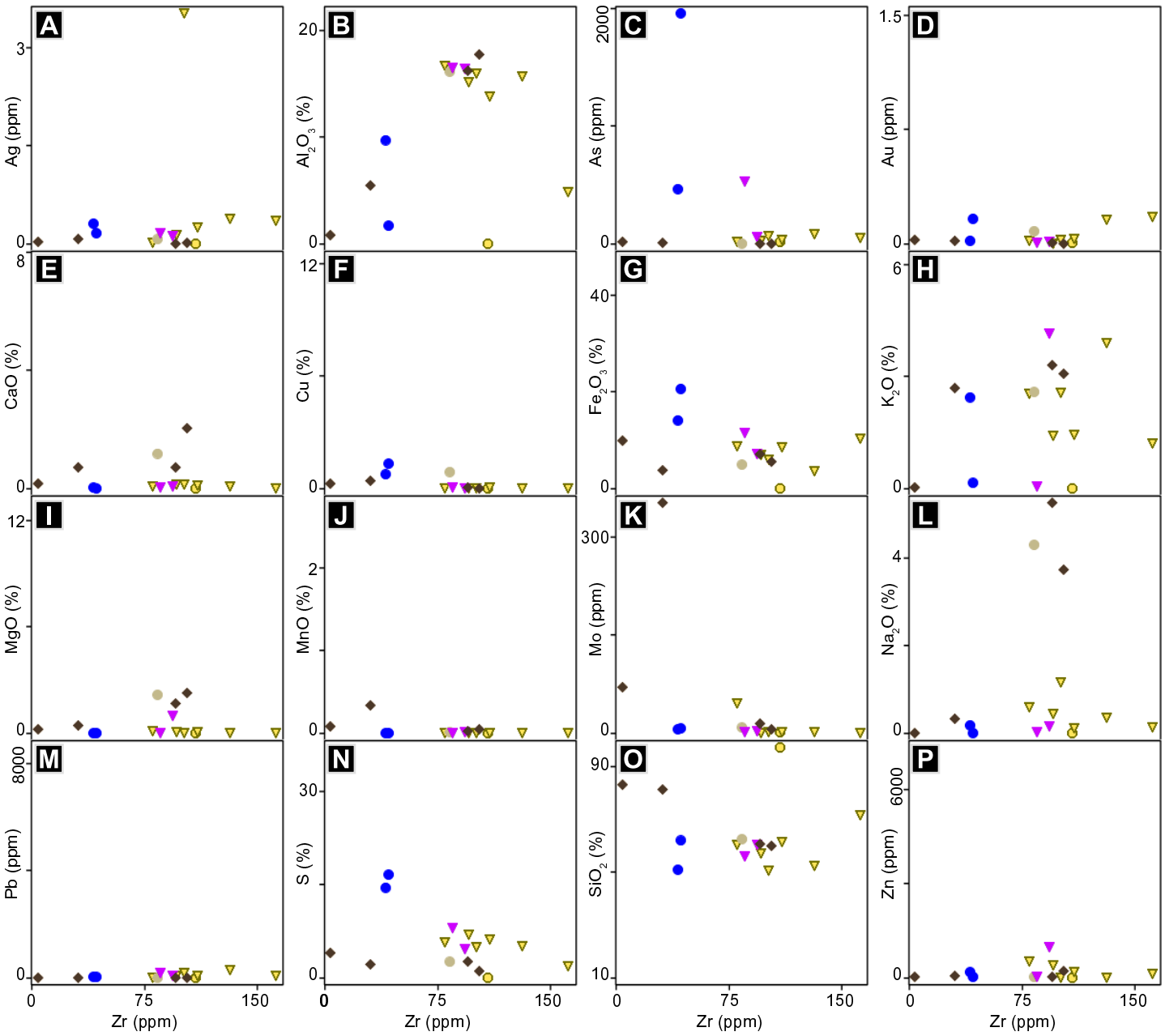

Figure 5.6: Selected major and trace element variation in altered samples of stage I Golpu diorite intrusions and the Wafi breccia complex. A) Ag vs. Zr. B) Al_2O_3 vs. Zr. C) As vs. Zr. D) Au vs. Zr. E) CaO vs. Zr. F) Cu vs. Zr. G) Fe_2O_3 vs. Zr. H) K_2O vs. Zr. I) MgO vs. Zr. J) MnO vs. Zr. K) Mo vs. Zr. L) Na_2O vs. Zr. M) Pb vs. Zr. N) S vs. Zr. O) SiO_2 vs. Zr. P) Zn vs. Zr.

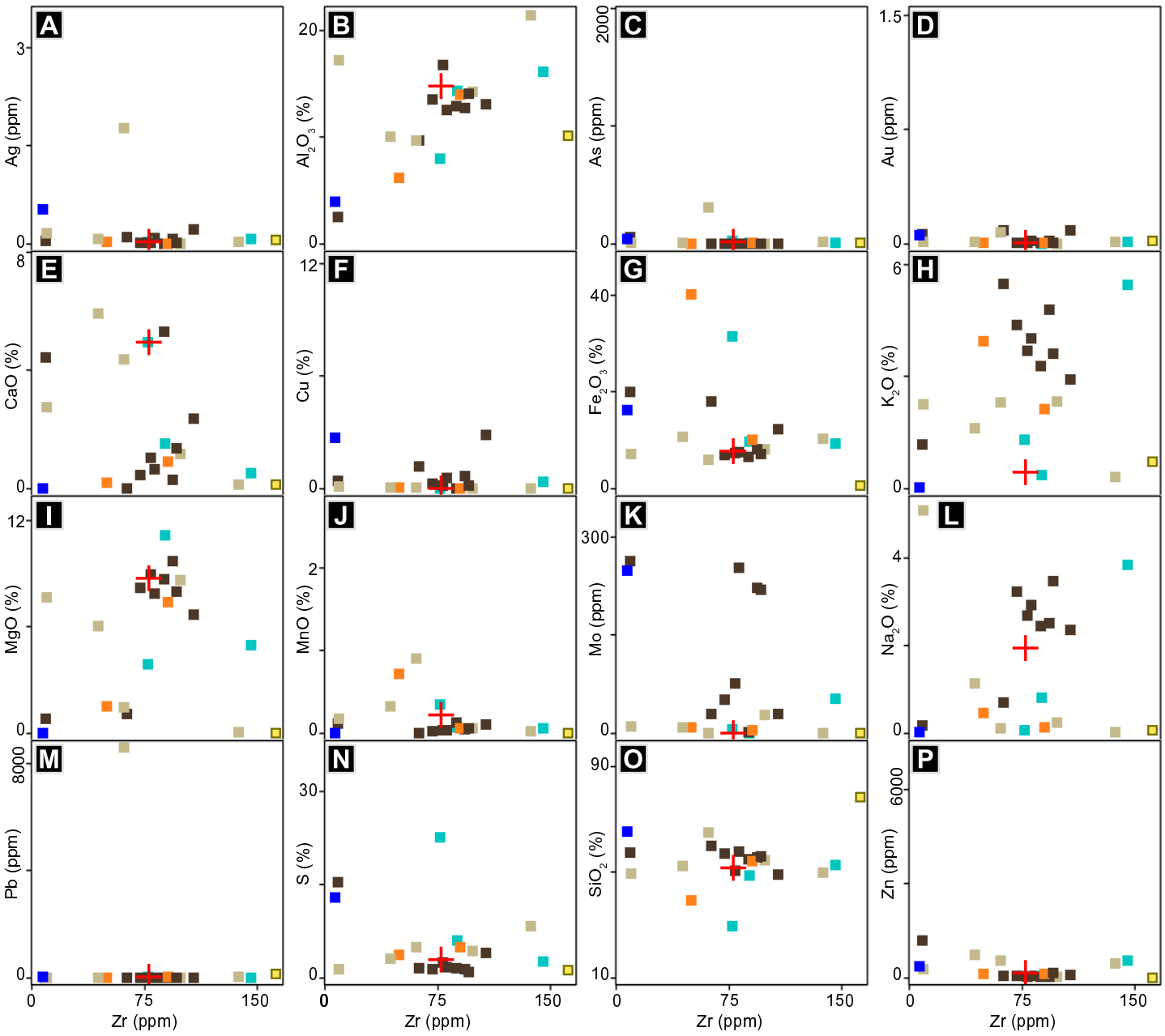

Figure 5.7: Selected major and trace element variation in altered samples of Owen Stanley metasandstone. A) Ag vs. Zr. B) Al_2O_3 vs. Zr. C) As vs. Zr. D) Au vs. Zr. E) CaO vs. Zr. F) Cu vs. Zr. G) Fe_2O_3 vs. Zr. H) K_2O vs. Zr. I) MgO vs. Zr. J) MnO vs. Zr. K) Mo vs. Zr. L) Na_2O vs. Zr. M) Pb vs. Zr. N) S vs. Zr. O) SiO_2 vs. Zr. P) Zn vs. Zr.

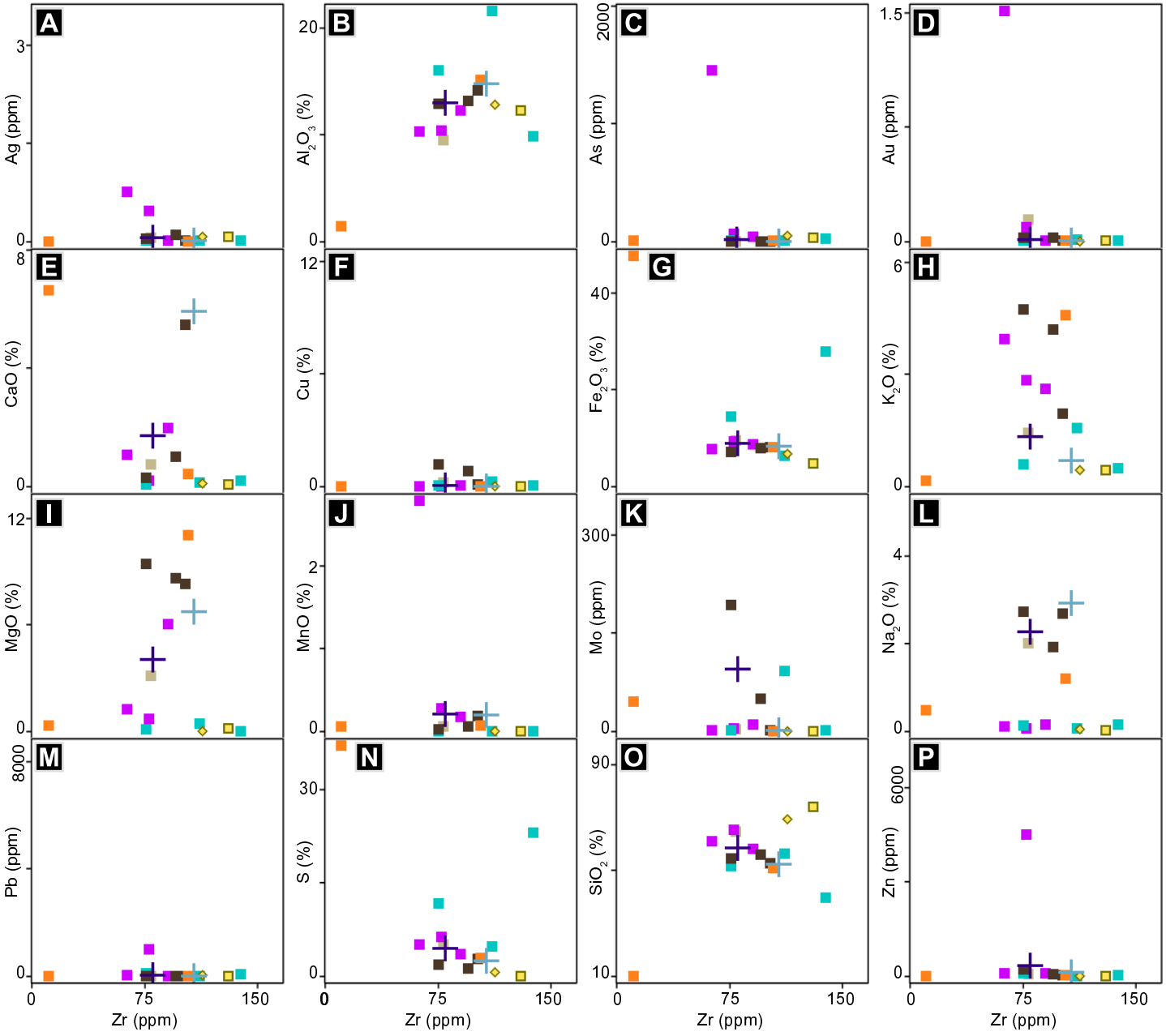

Alteration types (as in Fig. 5.2)

- Stage II biotite - orthoclase - quartz - magnetite - chalcopyrite
- Stage II biotite - muscovite - hematite
- Stage III-IV muscovite - pyrite
- Stage IV kaolinite - muscovite - pyrite ± dickite
- Stage IV alunite ± kaolinite ± pyrite ± quartz
- Stage IV muscovite - pyrite - carbonate ± quartz ± chlorite ± montmorillonite

Lithotype

- Metasiltstone
- Metaconglomerate (1 alunite-altered sample)
- Mean of weakly altered metasiltstone (Fig. 5.4)
- Mean of weakly altered metaconglomerate (Fig. 5.4)

Figure 5.8: Selected major and trace element variation in altered samples of Owen Stanley metasiltstone and metaconglomerate. A) Ag vs. Zr. B) Al_2O_3 vs. Zr. C) As vs. Zr. D) Au vs. Zr. E) CaO vs. Zr. F) Cu vs. Zr. G) Fe_2O_3 vs. Zr. H) K_2O vs. Zr. I) MgO vs. Zr. J) MnO vs. Zr. K) Mo vs. Zr. L) Na_2O vs. Zr. M) Pb vs. Zr. N) S vs. Zr. O) SiO_2 vs. Zr. P) Zn vs. Zr.

Stage II veins and alteration

Most of the stage II biotite - orthoclase - quartz - magnetite - chalcopyrite altered and mineralised samples have lower Ca and Al, and higher S, Ag, Au, Cu, and Fe contents than their weakly altered equivalents (Figs. 5.5 and 5.7). Biotite-altered metasandstone samples have markedly higher K and Na contents than weakly altered metasandstone (Fig. 5.7 H,L). Among stage II diorite samples, Si, K, and Na contents vary little from the weakly altered mean (Fig. 5.5 H,L,O). The 12 biotite-altered samples of stage II diorite contain means of 3.0 ppm Ag, 2.3 ppm Au, and 2.7 % Cu, whereas the three weakly altered diorite samples contain means of 0.9 ppm Ag, 0.4 ppm Au, and 0.8 % Cu (Table 5.2).

Rocks along the biotite - muscovite transition have compositions similar to the biotite-altered rocks nearer to the porphyry (Figs. 5.7, 5.8). Unlike the biotite-altered samples, a possible loss of Na, and a greater gain of Fe are evident in most of the biotite - muscovite - hematite altered samples (Figs. 5.7 G,L, 5.8 G,L).

Stage III-IV veins and alteration

The muscovite - pyrite altered rocks, comprising the basal portions of upward-flaring stage III-IV alteration, generally have higher K, Mn, S, and Zn contents than their weakly altered equivalents (Fig. 5.7 H,J,N,P). They also have overall lower Ca, Mg, and Na concentrations (Fig. 5.7 E,I,L). One sample of muscovite - pyrite altered stage II diorite has elevated Ag, Mn, Pb, S, and Zn (Fig. 5.5 A,J,M,N,P). Pervasive kaolinite-altered rocks have compositions similar to the muscovite - pyrite altered rocks, except for possible gains of Fe and S (Figs. 5.7 G,N, 5.8 G,N).

Alunite-altered samples generally have the highest concentrations of Zr (Figs. 5.6 - 5.8). Among metasedimentary rocks, the samples are characterised by low concentrations of most major elements (particularly Ca, Mg, and Na; Figs. 5.7 E,I,L, 5.8 E,I,L), and elevated Si contents (Figs. 5.7 O, 5.8 O). Alunite-altered samples of the Wafi breccia complex and the Stage I quartz-phyric Golpu diorite are dominated by oxides of Si and Al, with minor K, Fe, and S (Table 5.3; Fig. 5.6 B,G,H,N,O).

Covellite - pyrite - tennantite mineralised samples have some of the lowest Zr contents of all samples analysed, but contain elevated As, Cu, Fe, and S (Table 5.3; Figs. 5.6 C,F,G,N, 5.7 C,F,G,N). In the IS epithermal altered rocks, muscovite - pyrite - carbonate ± quartz ± chlorite ± montmorillonite alteration has resulted in mass changes similar to the adjacent kaolinite - muscovite - pyrite altered rocks (Table 5.3; Fig. 5.8), except for generally higher Ag, As, Au, K, Mn, Pb, and Zn contents in the former (Fig. 5.8 A,C,D, H, J, M, P).

5.3.2.2 MMJV assay data

The geochemical characteristics of veins and altered rocks at Wafi-Golpu are further evident in the assay data (Figs. 5.9 - 5.14), which constrain the locations of porphyry and epithermal styles of mineralisation. Specifically, in the lowermost drilled kilometre of the Golpu intrusive complex (between 250 m and -1250 m elevation), the grade shells indicate the locations of porphyry-related veins and alteration. In the uppermost 800 m of the intrusive complex (rocks above 250 m elevation), grade shells are mostly the result of stage III-IV epithermal overprints and surface oxidation.

Metal, sulfur, arsenic, and antimony zonation at depth (below 250 m ASL)

At depth, Au, Ag, Cu, and K contents are highest within the Golpu (and, to a lesser extent, Nambonga) diorites, and taper to background values with increasing distance from the intrusions (Figs. 5.9 - 5.11). Mo contents indicate the locations of porphyry-concentric stage I and II quartz - molybdenite veins, which are most abundant 70 - 120 metres from the diorite contacts (sections 4.3.1, 4.3.2; Figs. 5.9 - 5.11).

The highest Fe, As, Sb, and S contents are located in the upward-flaring pyrite-bearing domains of stage III-IV, the basal portions of which extend along the shoulders of the Golpu porphyry (Figs. 5.9 - 5.13). Although Fe-bearing phases such as magnetite, pyrite, and chalcopyrite occur in the Golpu diorites, overall Fe contents in the porphyry are about the same as in least-altered wallrock (e.g., Table 5.2 and Figs. 5.9 - 5.11).

Mn, Zn, and Pb contents are elevated in the rocks containing sparse carbonate-base metal sulfide veins. At depth, these veins occur near the porphyry, and are interpreted to be the root zones of epithermal mineralisation (e.g., Fig. 4.36; Figs. 5.9 - 5.11). Elevated Pb and Zn contents also occur at depth along the Compass fault, as part of a corridor of elevated K, Mo, Pb, and Zn contents that extends from the porphyry up to Link Zone mineralisation (Fig. 5.13).

Metal, sulfur, arsenic, and antimony zonation near surface (above 250 m ASL)

Nearer to the current erosional surface, geochemical profiles related to porphyry veins and alteration have been masked by epithermal overprints and surface oxidation. A porphyry-concentric ring of elevated Mo has been preserved in the quartz - alunite and vuggy quartz-altered rocks, whereas the porphyry-concentric Au, Ag, Cu, and K contents, originally associated with stages I and II, have been remobilised or overprinted (Fig. 5.14).

Gold in the near-surface environment occurs in zones containing carbonate veins, with the highest values near the Compass fault (Figs. 5.9 - 5.14). The distribution of Ag contents is similar to that of Au, except for some association with Zn along the margins of the alunite-altered rocks (e.g., Fig. 5.14).

Elevated As, Sb, and Pb contents coincide roughly with the locations of near-surface alunite alteration (Fig. 5.14). The highest As contents indicate sulfosalt mineralisation in Rafferty's Copper Zone, where elevated Cu, Sb, S, and Ag grades are associated with HS epithermal ore (Fig. 5.11). Although elevated Au values occur in pyrite within Rafferty's Copper Zone (section 5.4), the Au grade shells in section C illustrate that the high sulfidation contribution to the overall Au resource is minor (Fig. 5.11).

Among all whole rock assay data, the most distal manifestation of Wafi-Golpu veins and alteration is an arcuate zone of elevated Mn, Zn, and (to a lesser extent) Pb contents that coincide with the locations of carbonate veins (Fig. 5.14). At the present erosional surface, the zone of elevated Mn contents occurs up to 1.5 km west of the Golpu porphyry.

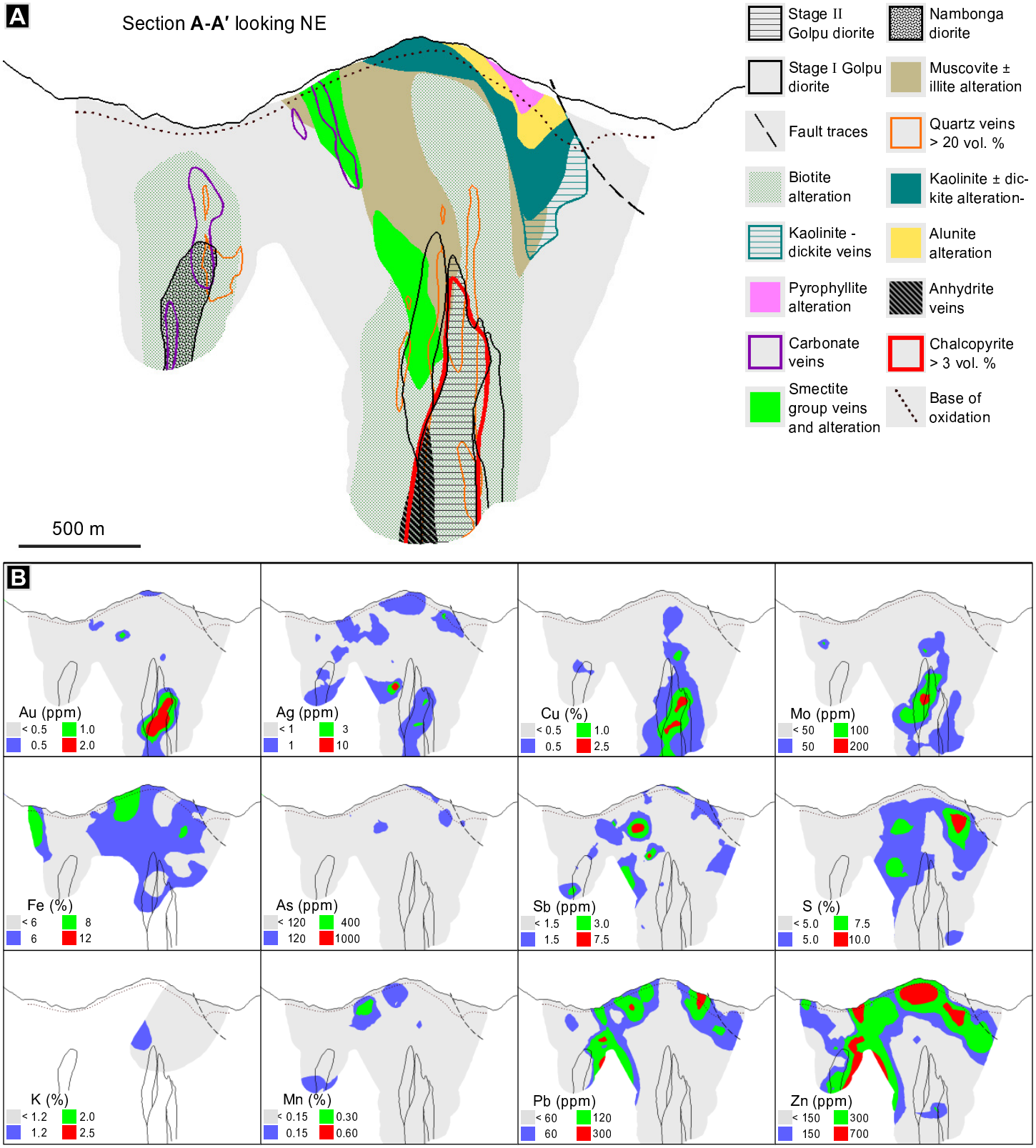

Figure 5.9: A) Simplified vein and alteration domains in section A. Light grey is propylitic to least-altered (regional metamorphic) rock. The location of this section is indicated in Figure 3.2 B. B) Isotropic grade shells for selected metals with As, Sb, and S in the same section, clipped to within 200 metres of assay data. White areas have no available assay data. Note Fe and K data are missing in some drill holes. Faults, diorite outlines, and the base of surface oxidation are also indicated in these sections.

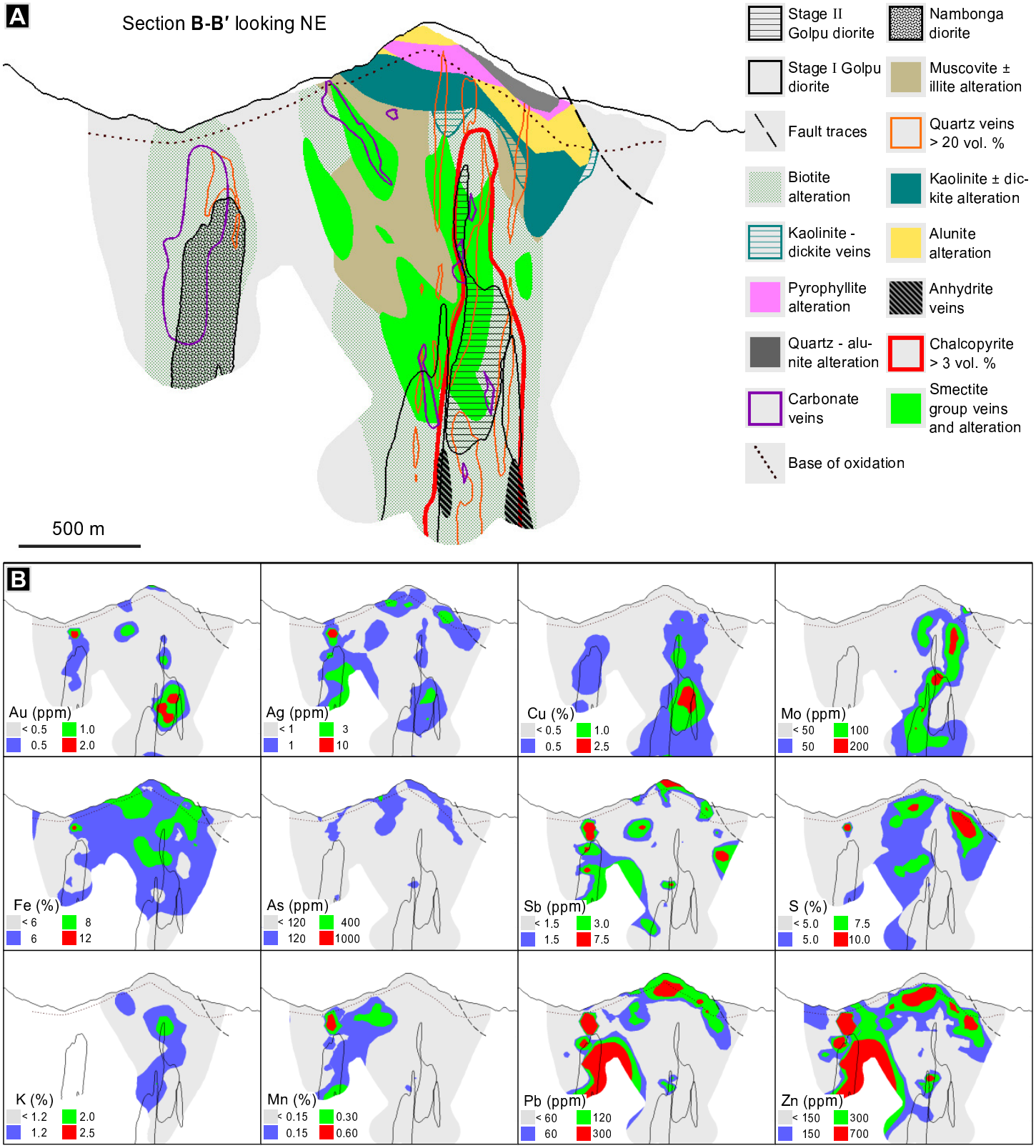

Figure 5.10: A) Simplified vein and alteration domains in section B. The location of this section is indicated in Figure 3.2 B. B) Isotropic grade shells for selected metals with As, Sb, and S in the same section, clipped to within 200 metres of assay data.

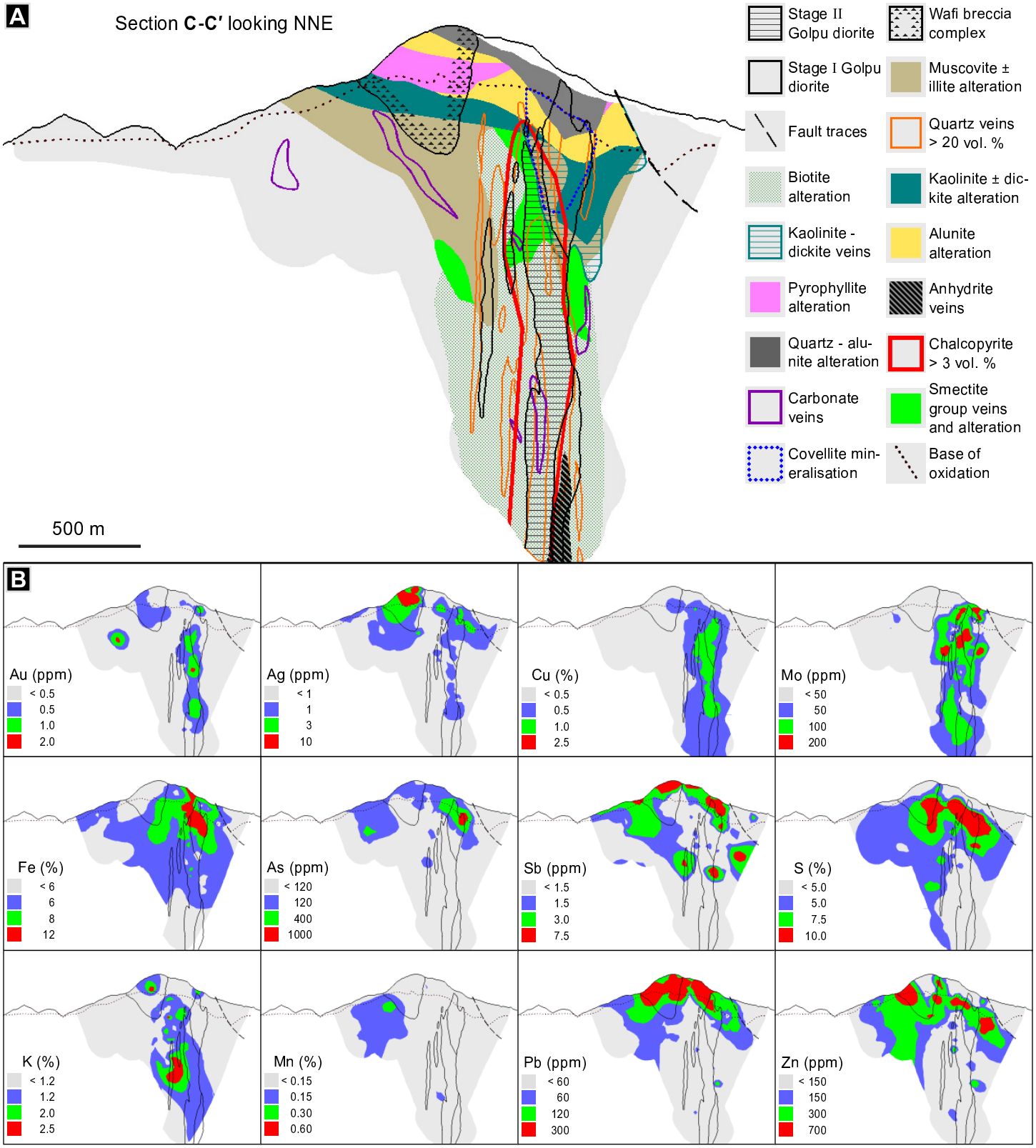

Figure 5.11: A) Simplified vein and alteration domains in section C. The location of this section is indicated in Figure 3.2 B. B) Isotropic grade shells for selected metals with As, Sb, and S in the same section, clipped to within 200 metres of assay data.

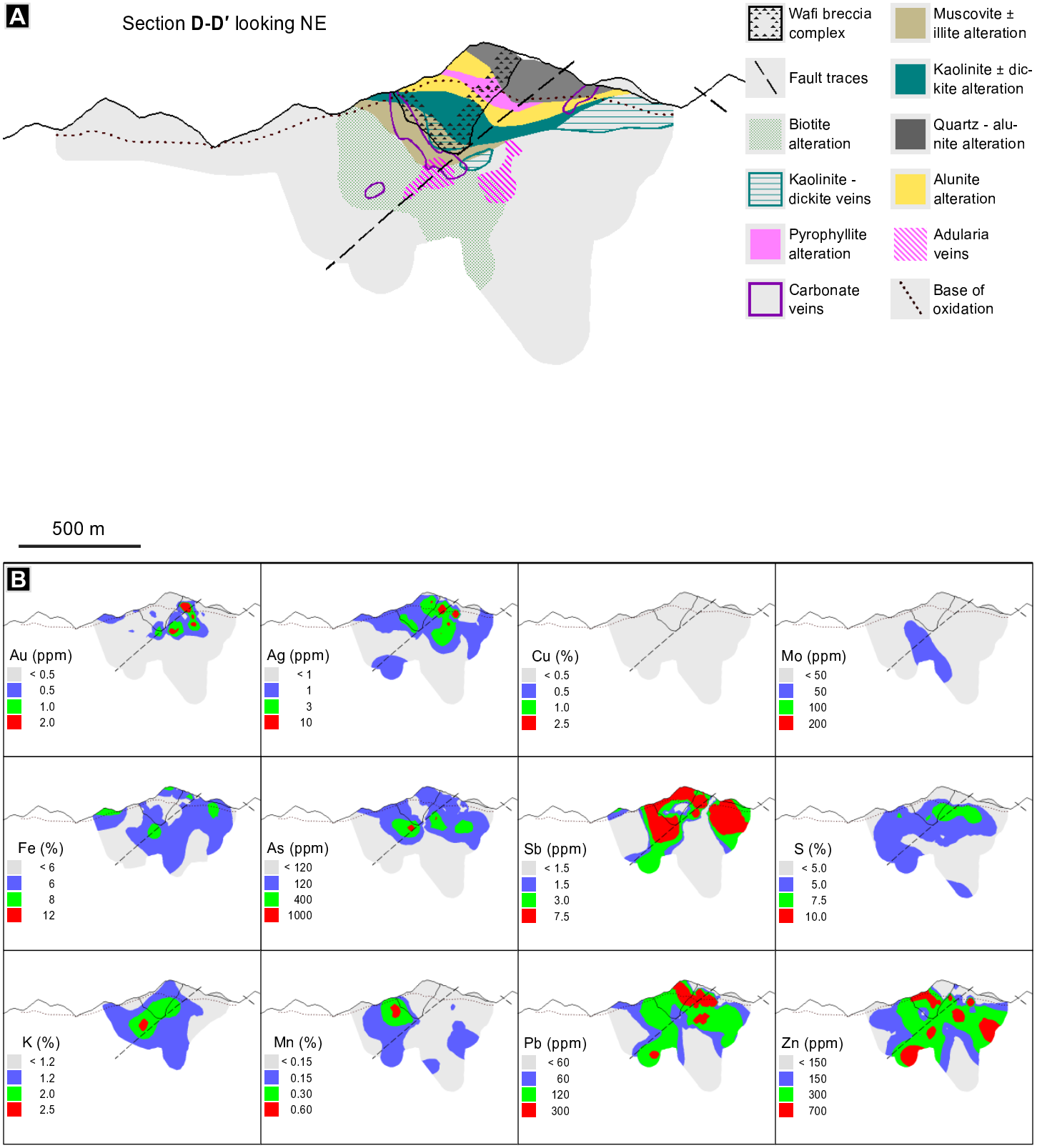

Figure 5.12: A) Simplified vein and alteration domains in section D. The location of this section is indicated in Figure 3.2 B. B) Isotropic grade shells for selected metals with As, Sb, and S in the same section, clipped to within 200 metres of assay data.

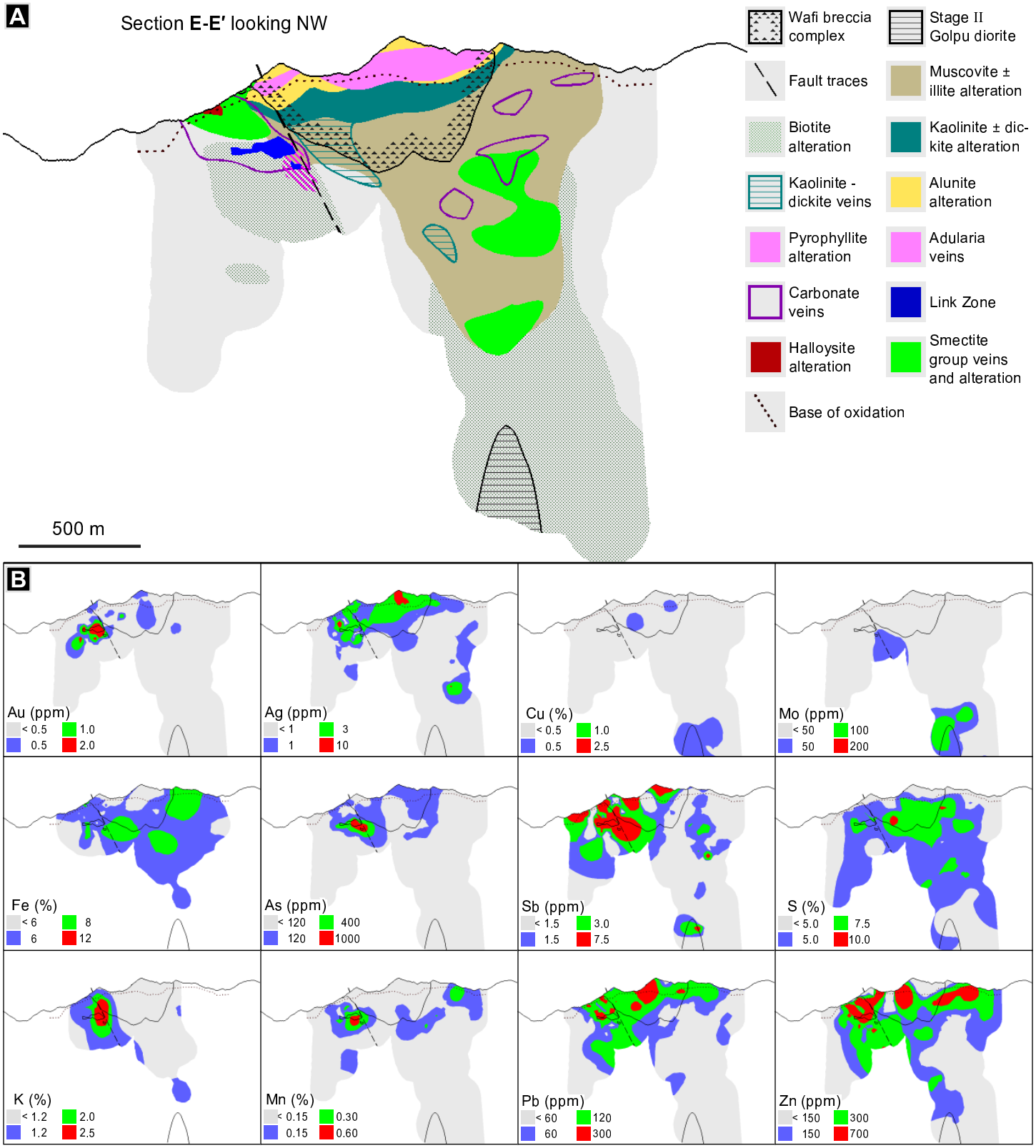

Figure 5.13: A) Simplified vein and alteration domains in section E. The location of this section is indicated in Figure 3.2 B. B) Isotropic grade shells for selected metals with As, Sb, and S in the same section, clipped to within 200 metres of assay data.

Figure 5.14: A) Simplified Wafi-Golpu vein and alteration domains in plan view, looking below overburden and Hekeng Andesite, as in Figure 4.3. Note that the diorite outlines are projected from depth. B) Grade shells for selected metals with As, Sb, and S, at surface. These isotropic grade shells are clipped to within 200 metres of available assay data, and are constructed from 10 metre composites. White indicates no data. Note that Fe and K assays are not available for all drill holes.

Metal contents of Wafi and Golpu ore

Selected metal and As contents of the porphyry and epithermal styles of mineralisation are shown in Figure 5.15 B-E. The assay data in Figure 5.15 are classified by location. Golpu porphyry mineralisation includes all assays within Golpu diorites and adjacent wallrocks, excluding zones that have been overprinted by epithermal veins and alteration. HS epithermal mineralisation includes assays from Rafferty's Copper Zone. IS epithermal mineralisation has been divided into two groups, as in Chapter Four: western mineralisation includes carbonate veins that have cross-cut the Nambonga diorite; and Compass fault mineralisation contains assays within 500 m of the Compass fault, including Link Zone mineralisation.

The Golpu porphyry deposit contains Cu, Mo, and Au assay values that are consistent with its classification as a high-K calc-alkalic Cu-Au porphyry deposit (e.g., Sillitoe, 2010; Fig. 5.15 A; section 3.4.3). The porphyry mineralised rocks have high Cu contents that generally increase with increasing Au (Fig. 5.15 B), and lower As contents than the epithermal ores (Fig. 5.15 D). HS epithermal mineralisation has high As and Cu contents, along with the lowest Mn contents of all mineralisation styles. IS epithermal mineralisation has the lowest Cu contents, except where carbonate - sulfide veins have cross-cut the weakly porphyry mineralised Nambonga diorite (Fig. 5.15 B).

Most rocks with greater than 10 ppm Ag occur in the IS epithermal domain; otherwise, there is little variation in Ag contents or Au:Ag ratios between any of the mineralisation styles (Fig. 5.15 C). Overall As and Mn contents are also highest in the IS epithermal mineralisation, particularly near the Compass fault (Fig. 5.15 B-E). A positive correlation between As and Au contents is evident in the IS epithermal ore (Fig. 5.15 D). Although there is little correlation between Mn and Au contents evident in the assay data, most of the assays containing very high gold grades (e.g., > 10 ppm Au) have about 0.5 - 5 wt. % Mn (Fig. 5.15 E), indicative of rhodochrosite veins within the assayed metre intervals (section 4.3.4.2).

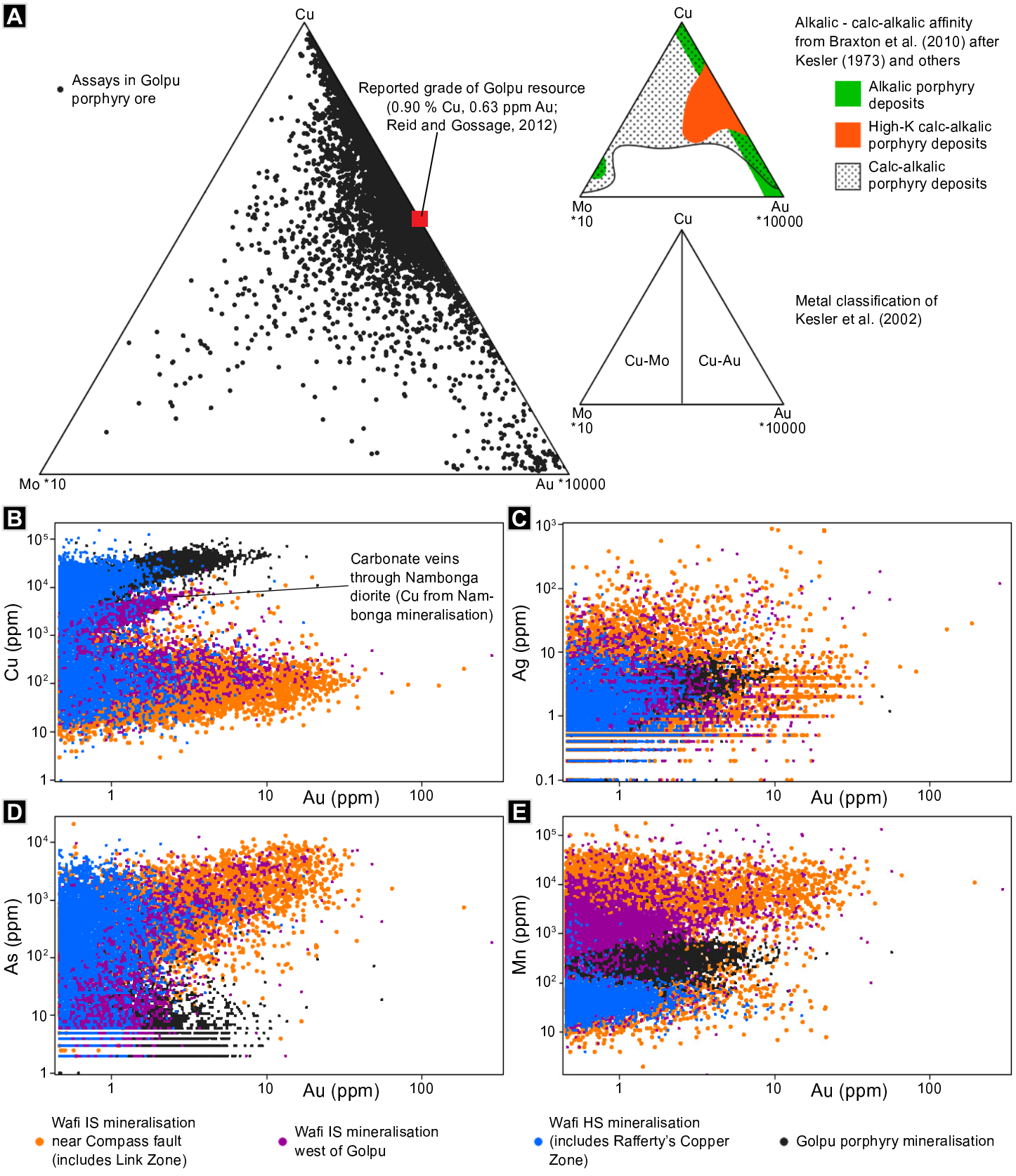

Figure 5.15: Selected metal and As compositions of Golpu and Wafi mineralised rocks. A) Ternary Cu-Mo-Au diagrams illustrate that the metal contents of Golpu ore are consistent with high-K calc-alkalic Cu-Au porphyry deposits. B) Cu vs. Au in Golpu porphyry and Wafi epithermal mineralised samples. Porphyry mineralised samples contain high Cu contents that increase with Au. C) Ag vs. Au showing little variation in Ag:Au ratios between mineralisation styles. D) As vs. Au showing low As contents in the porphyry samples, and high As in the epithermal samples. As is weakly correlated with Au contents in the IS epithermal samples. E) Mn vs. Au. HS epithermal mineralisation resulted in low Mn contents. Most intervals with Au > 10 ppm occur in carbonate veined rocks with ~ 0.5 - 10 wt. % Mn.

5.4 Mineral Chemistry and Gold Deportment

5.4.1 Introduction and Methods

Laser ablation inductively coupled plasma mass spectrometry (LA-ICPMS) was used to investigate the gold content of sulfides and sulfosalts in key mineralised samples. Analyses were collected in order to determine whether gold occurs in inclusions or in a lattice-hosted configuration. In the case of lattice-hosted gold, analyses were used to identify trace elements that are associated with gold. Elements analysed were (in alphabetical order): Ag, Al, As, Au, Bi, Cd, Co, Cu, Fe, Gd, Hf, La, Mn, Mo, Ni, Pb, Pt, Sb, Se, Sn, Ta, Te, Tl, W, Zn, and Zr.

A total of 212 LA-ICPMS spot analyses were carried out at CODES, University of Tasmania, following the method described by Large et al. (2009). Spots were ablated with a 50 μm beam for a total of 90 s, including a 30 s background measurement before sample ablation. The laser was fired at a frequency of 5 Hz, and typically resulted in a fluence / laser energy of ~ 4.2 J/cm^2 for sulfides. A lithium borate glass standard (STDGL2b2 of Danyushevsky et al., 2003) was analysed with a 100 μm beam before and after each run of between 5 and 20 spot analyses. Internal standards used were Fe (pyrite, chalcopyrite, and pyrrhotite), Cu (bornite, tennantite, and covellite), and Zn (sphalerite).

5.4.2 Results

The LA-ICPMS mineral chemistry results presented here reveal several contrasts in the compositions of sulfides and sulfosalts from the porphyry, HS epithermal, and IS epithermal samples (Table 5.4). Porphyry pyrite contains the lowest trace overall element contents, except for higher Cu, Pt, Se, Cd, and Sn. HS epithermal pyrite contains the highest Au, Ag, Pb, Bi, Se, and Te. IS epithermal pyrite contains the highest As contents (up to 9.5 wt. % As occurs in both disseminated pyrite grains and acicular pyrite rims), along with Sb, Tl, Zn, Mn, Co, Ni, and W contents (Table 5.4). HS epithermal bornite contains higher As, Tl, Cd, Sb, Te, and Au, but lower Ag and Se contents than porphyry bornite. Among sphalerite grains analysed: porphyry sphalerite contains the highest Au, Cu, Pb, W, and Se contents; HS epithermal sphalerite contains the highest Ag, Bi, Sb, and Tl contents; and IS epithermal sphalerite contains the highest As, Sn, Mn, Co, Ni, and Fe contents (Table 5.4).

Table 5.4: Summary of LA-ICPMS analyses of Golpu and Wafi sulfides and sulfosalts

Paragenetic stage and mineral	stage IIc (main stage porphyry mineralisation)					IVa (high sulfidation mineralisation)				IVa (intermediate sulfidation mineralisation)					
	vein and disseminated pyrite (n=38)	vein chalcopyrite (n=17)	vein bornite (n=12)	vein sphalerite (n=2)	vein tennantite (n=1)	disseminated pyrite (n=29)	disseminated covellite (n=19)	disseminated bornite (n=4)	disseminated sphalerite (n=7)	vein pyrite (n=35)	disseminated pyrite (n=18)	acicular pyrite rims (n=9)	vein sphalerite (n=5)	pyrrhotite inclusions in disseminated pyrite (n=2)	pyrrhotite inclusions in vein pyrite (n=5)
Au	0.43	0.52	0.52	6.82	2.56	50.81	2.23	2.88	2.93	4.74	6.33	21.19	0.47	0.04	0.00
Ag	2.35	37.57	102.41	134.52	877.29	46.12	11.67	15.56	543.86	14.92	2.28	15.80	24.81	0.10	0.12
As	54	11	6	48	255024	621	196	32	247	452	7827	52069	249	3	1
Al	225	66	64	426	11	4327	2478	9317	1	6085	7926	3418	505	92	23
Bi	1.15	1.38	3.25	2.32	6.43	26.34	13.16	3.91	86.07	8.34	5.72	31.45	31.84	3.43	0.64
Cd	0.50	0.65	2.92	1817.89	734.66	0.68	4.30	7.24	1655.57	0.53	0.47	0.49	2789.63	<0.07	<0.07
Co	283.57	34.12	0.32	0.18	0.11	70.77	18.47	6.01	0.03	757.42	331.73	38.17	20.34	44.50	1023.23
Cu	1932	345325	633100*	24833	475100*	9856	664600*	633100*	527	628	143	449	437	81	18
Fe	465000*	304300*	143826	8870	7697	465000*	46257	48982	152	465000*	465000*	465000*	116828	623300*	623300*
Gd	<0.01	<0.02	2.23	5.45	0.06	0.02	<0.02	<0.06	<0.01	0.15	0.72	0.91	0.58	0.02	<0.01
Hf	<0.005	<0.01	<0.01	<0.01	<0.004	0.01	<0.01	<0.01	<0.01	1.00	0.32	0.09	<0.01	0.21	0.02
La	0.00	0.05	3.13	31.53	0.24	0.42	0.18	1.59	<0.002	0.31	4.55	5.19	1.90	0.01	<0.002
Mn	6	22	101	3251	250	336	16	15	22	55	331	651	50302	42	41
Mo	0.04	<0.05	<0.04	0.42	0.17	0.19	14.93	3.71	<0.03	0.31	0.14	0.19	5.27	0.15	0.38
Ni	266.7	10.3	5.7	0.9	0.2	44.9	14.4	4.2	0.4	436.0	1308.6	348.4	37.5	4766.3	3873.9
Pb	21.5	1325.2	1991.0	29309.0	459.2	764.2	638.1	453.8	313.7	109.2	37.7	261.4	296.5	1.4	3.4
Pt	0.07	<0.02	<0.03	<0.01	<0.01	<0.01	<0.02	<0.03	<0.01	<0.01	<0.01	<0.01	<0.01	<0.01	<0.01
Sb	7.09	0.43	0.13	1.13	496.95	74.73	11.81	4.10	127.97	12.24	46.03	496.48	26.52	0.04	0.03
Se	266.07	323.50	241.51	73.78	202.21	341.98	110.98	104.84	4.74	47.44	36.88	24.15	22.68	37.98	69.60
Sn	5.12	15.68	13.04	22.29	3.99	7.77	32.14	10.24	13.28	4.56	0.94	1.73	39.31	0.40	0.14
Ta	<0.002	<0.005	<0.005	<0.002	<0.001	<0.002	<0.003	0.02	<0.002	0.06	0.03	0.01	<0.002	0.02	<0.002
Te	2.75	3.16	1.50	1.35	28839.12	190.05	28.13	44.26	0.43	10.27	6.90	14.35	2.71	1.52	0.42
Tl	0.65	0.16	0.20	0.49	1.54	19.24	99.71	168.57	2.88	2.59	43.27	346.86	0.31	0.01	0.02
W	0.06	0.26	0.09	0.88	0.26	0.11	1.09	1.34	<0.02	2.19	2.94	6.70	0.05	0.82	0.05
Zn	102	184	940	640600*	97225	224	46	66	640600*	41	47	159	640600*	5	6
Zr	<0.01	<0.01	<0.01	<0.01	<0.005	0.22	0.03	0.15	<0.01	34.71	11.17	3.47	<0.01	7.26	0.27

All elements are reported in ppm. *denotes the standard used in the calculation of LA-ICPMS results.

Gold in the Golpu porphyry environment

LA-ICPMS results from this study do not indicate the presence of lattice-hosted (solid solution) gold within stage IIc chalcopyrite, pyrite, or bornite (Figs. 5.4 and 5.16). Instead, gold occurs primarily as native inclusions up to 80 microns across within stage IIc veins and disseminated grains of chalcopyrite, bornite, and pyrite. Gold inclusions are evident in some of the LA-ICPMS spot profiles of Cu- and Fe-sulfides (e.g., Fig. 5.16 B).

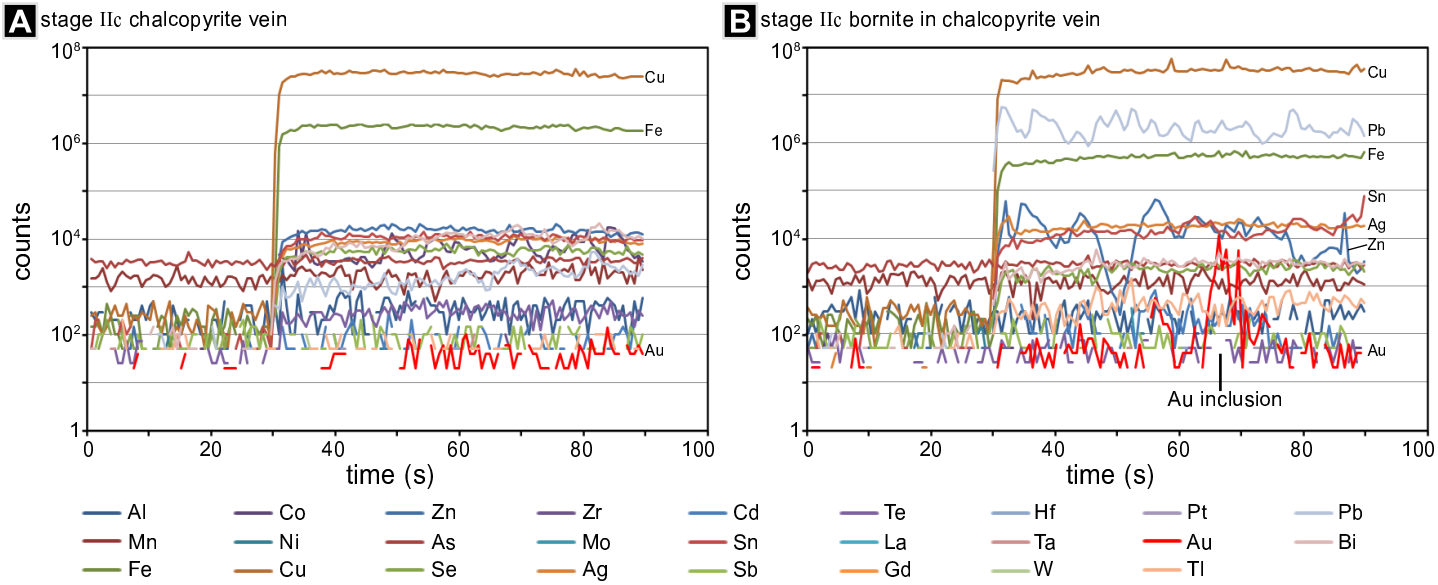

Figure 5.16: A) LA-ICPMS profile for a spot analysis of stage IIc vein chalcopyrite. This analysis yields no evidence for lattice-hosted gold, as is typical for sulfides in the Golpu porphyry. Note that there is little variation in any of the trace element contents (sample WR337, 1220.2 m). B) LA-ICPMS profile of stage IIc vein bornite, which contains a gold inclusion, and displays some variation in Pb and Zn contents (sample WR392, 1546.3 m).

Gold in the Wafi HS epithermal domain

Gold in the HS epithermal domain occurs primarily in stage IVa disseminated pyrite (Table 5.4). The relatively smooth laser ablation profiles for Au suggest that it occurs within the pyrite lattice (e.g., Fig. 5.17). However, five of 29 analyses yield a Au:As ratio greater than 0.02 (such as in Fig. 5.17 A), which Reich et al. (2005) showed to be indicative of gold in nanoparticles as opposed to solid solution. The pyrite-hosted gold occurs in association with Te, Se, Mn, Ag, Zn, Sb, Tl, Sn, and Bi contents (e.g., Fig. 5.17 B). Stage IVa HS epithermal bornite, covellite, and sphalerite also contain 2 - 3 ppm Au, whereas bornite and sphalerite are gold-poor in the porphyry environment (Table 5.4).

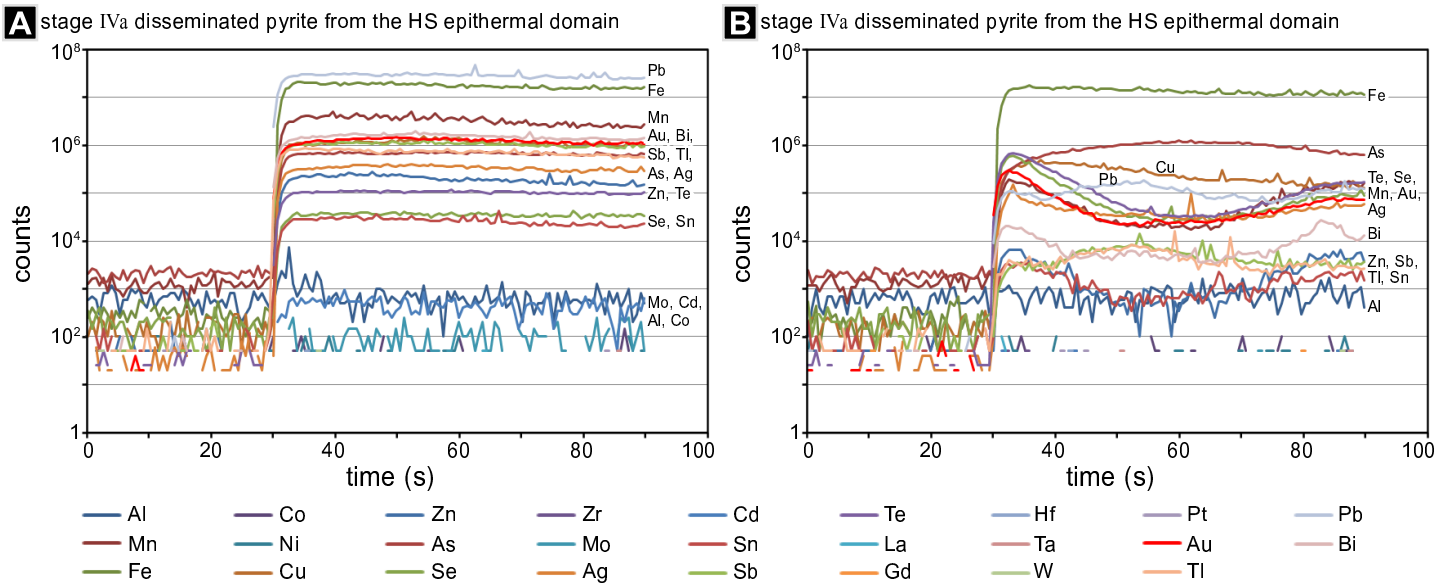

Figure 5.17: A) LA-ICPMS profile representative of stage IVa HS epithermal pyrite with refractory gold. This spot ablation yielded an average of 511 ppm Au and 2287 ppm As. Note that there is little variation in any of the other trace element contents (sample WR402, 220.0 m). B) LA-ICPMS profile of stage IVa HS epithermal pyrite with an average of 27 ppm Au. The refractory gold varies with tellurium, selenium, manganese, silver, and bismuth (sample WR402, 220.0 m).

Gold in the Wafi IS epithermal domain

Gold in the IS epithermal domain occurs primarily in stage IVa vein and disseminated pyrite (Table 5.4). In Link Zone, the stage IVa pyrite grains are rimmed by acicular pyrite which contains an average of 21 ppm Au and 5.2 wt. % As (Table 5.4). Although some native gold inclusions up to 8 µm across were documented in carbonate - sulfide veins (Chapter Four), most of the Wafi gold occurs in the pyrite crystal lattice, and varies in association with As, Sb, Tl, Bi, and Ag contents (Fig. 5.18).

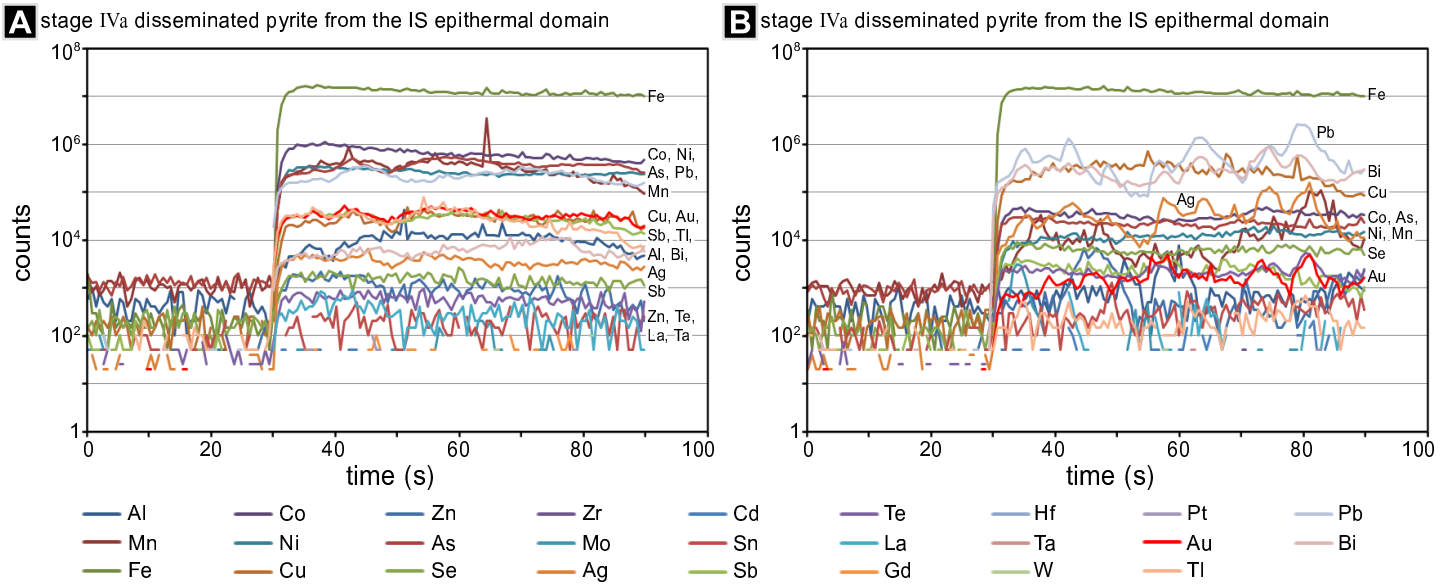

Figure 5.18: A) LA-ICPMS profile representative of stage IVa pyrite from the IS epithermal domain. This analysis yielded an average of 19.5 ppm refractory gold. Gold varies with arsenic, manganese, lead, thallium, antimony, and to a lesser extent, silver (sample WR177, 310.7 m). B) LA-ICPMS profile of stage IVa pyrite from the IS epithermal domain, with an average of 1.0 ppm Au. Gold varies with bismuth and lead, and to a lesser extent with silver and manganese (sample WR199, 319.8 m).

5.4.3 Discussion

LA-ICPMS analyses, together with petrography and SEM results (Chapter Four), indicate that gold in the Golpu porphyry occurs mainly as native inclusions in chalcopyrite, pyrite, and bornite. The native gold inclusions comprise up to 0.003 vol. % of the sulfide host in some samples (e.g., WR337, 1220.2 m and WR377, 1466.2 m; Appendix A). This is equivalent to approximately two 20 μm diameter gold inclusions per square centimetre of porphyry sulfide in thin section, and is more than sufficient to account for the 0.63 ppm Au grade of the porphyry resource. For example, in a typical interval of Golpu diorite containing 5 vol. % sulfide, 0.003 vol. % sulfide-hosted Au would account for 10.0 ppm Au.

Gold inclusions up to 8 μm across were documented in some carbonate - sulfide veins (Chapter Four) as well as in vein and disseminated pyrite and pyrrhotite from Link Zone samples (Tudor et al., 1997). However, LA-ICPMS results suggest that refractory gold in pyrite is the primary mode of epithermal gold mineralisation. In all samples of epithermal mineralisation, gold contents are associated with other trace elements in pyrite, particularly Tl, Bi, Ag, Sb, and to a lesser extent, Pb and Mn. Au contents in pyrite also vary with As in the IS epithermal samples, whereas Au and As vary independently in some HS epithermal pyrite grains.

5.5 Sulfur Isotopes

5.5.1 Introduction and Methods

The sulfur isotopic compositions of sulfides and sulfosalts can be used to trace variations in reduction potential, temperatures, and sulfur sources, provided there is some control of variables such as water:rock ratio and paragenetic stage (Ohmoto and Rye, 1979). Sulfur isotopic compositions have been analysed for sulfides and sulfates in Wafi-Golpu. The analysed samples were constrained paragenetically, and mixed sulfide-sulfate samples were generally avoided. Coarse-grained material (mostly vein infill) was sampled using a hand-held drill, with the drill bit cleaned on a quartz block after each sample was taken. Fine-grained material (most of the disseminated grains) was sampled along predefined paths and spots using a mechanically controlled micromill at CODES, University of Tasmania. Core samples selected for micromill sampling of alunite contained an average of 44 wt. % alunite (based primarily on XRD data; Appendix E). Micromill drilling of alunite was performed over short intervals, so that slightly darker powders (indicating contamination by very fine-grained sulfides) could be rejected in batches. Contamination by quartz could not be avoided in most of the alunite samples.

Sulfur isotopic compositions of the mineral powders were measured by C. Cook at the University of Tasmania Central Science Laboratory, following the methods of Robinson and Kusakabe (1975). ^{34}S and ^{32}S contents were measured using a VG SIRA Series II spectrometer. The $\delta^{34}S$ values are reported with respect to the Canyon Diablo Troilite standard. Detailed sulfur isotope results are provided in Appendix G.

5.5.2 Results

Sulfur isotopic compositions of Wafi-Golpu sulfides and sulfates differ by paragenetic stage and sample location (Table 5.5). In general, $\delta^{34}S$ values decrease from early porphyry to epithermal stages of alteration and mineralisation (Figs. 5.19 and 5.20), and increase from porphyry to distal samples (Figs. 5.21 and 5.22).

The stage IIa sulfides and sulfates have $\delta^{34}S$ values within range of typical porphyry $\delta^{34}S_{sulfide}$ values of near 0 ‰, and $\delta^{34}S_{sulfate}$ values of near +10 ‰ (Ohmoto and Rye, 1979; Taylor, 1987). Specifically, anhydrite from the stage IIa veins (n = 5) has $\delta^{34}S$ values from +9.2 to +11.3 ‰. Stage IIa vein chalcopyrite, pyrite, and molybdenite (n = 5) have $\delta^{34}S$ values from +0.6 to +0.8 ‰. Stage IIc pyrite (n = 3) has similar $\delta^{34}S$ values (+0.8 to +1.3 ‰), whereas stage IIc chalcopyrite and bornite (n = 10) have lower and more widely spread $\delta^{34}S$ values from -0.9 to +0.1 ‰ (Fig. 5.19). Four samples of pyrite in distal stage II chlorite - actinolite ± epidote ± muscovite altered rocks yielded $\delta^{34}S$ values from +0.6 to +2.0 ‰ (Figs. 5.19, 5.21).

Pyrite from stage III muscovite - pyrite veins (n = 9) has $\delta^{34}S$ values from -1.2 to +1.3 ‰ (Fig. 5.19). Disseminated and vein pyrite associated with stage IV alunite (n = 13) have $\delta^{34}S$ values from -3.6 to +2.4 ‰ (Figs. 5.19 and 5.20). The lowest values occur above the Golpu porphyry (Fig. 5.22). One sample of vein covellite from the top of the Golpu porphyry yielded a $\delta^{34}S$ value of -23.2 ‰, the lightest of all values obtained in this study (Table 5.5, Fig. 5.19).

Samples of stage IVa disseminated alunite (n = 8) returned a wide range of $\delta^{34}S$ values, from +6.3 to +19.4 ‰ (Figs. 5.19, 5.20). This is within the lower range of values typical for high sulfidation deposits (Fifarek and Rye, 2005). The $\delta^{34}S$ values are zoned from lower values at the covellite-mineralised zone above Golpu, to isotopically heavier values with increasing distance from Golpu (Fig. 5.22). Two samples of coarse-grained alunite from a stage IVb colloform alunite vein above the Golpu porphyry yielded $\delta^{34}S$ values of +7.9 and +9.9 ‰, which are among the lightest values for sulfates in this study (Table 5.5, Fig. 5.19).

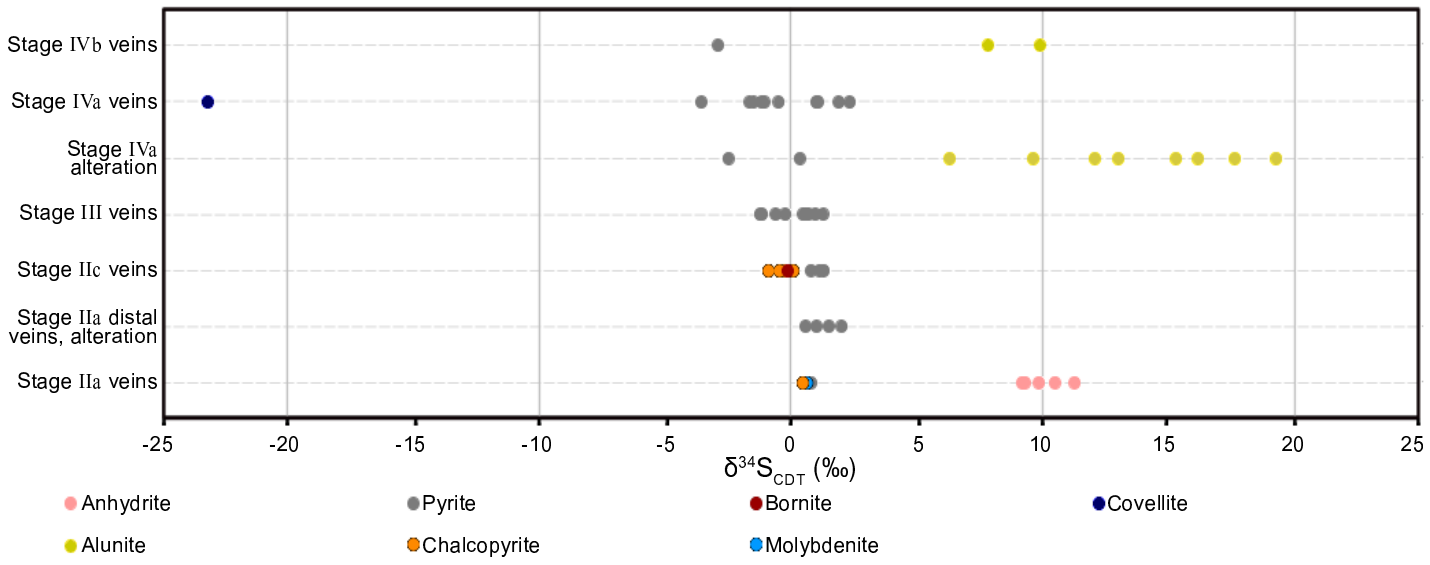

Figure 5.19: Distribution of $\delta^{34}S$ values in Golpu and Wafi sulfides and sulfates, arranged by paragenetic stage from oldest (bottom) to youngest (top). Note a weak trend towards progressively decreasing values from early to late stages of mineralisation.

Table 5.5: $\delta^{34}S$ values in Golpu and Wafi sulfides and sulfates

Sample ID	Paragenetic stage	Mineralisation style	Mineral	Mineral occurrence	$\delta^{34}S$ (‰)
377-1707.5	Stage IIa	Porphyry veins	Anhydrite	Anhydrite veins with weak actinolite halos in biotite-altered rock	9.2
377-1791.5	Stage IIa	Porphyry veins	Anhydrite	Laminated anhydrite - quartz - molybdenite - chalcopyrite vein	9.3
377-1825.2	Stage IIa	Porphyry veins	Pyrite	Anhydrite - pyrite - chalcopyrite vein in biotite-altered rock	0.8
377-1825.2	Stage IIa	Porphyry veins	Anhydrite	Anhydrite - pyrite - chalcopyrite vein with actinolite halo in biotite-altered rock	11.3
392-1126.0	Stage IIa	Porphyry veins	Pyrite	Pyrite (+ trace chalcopyrite) veins with actinolite halos after biotite-altered rock	0.6
392-1650.0	Stage IIa	Porphyry veins	Anhydrite	Anhydrite veins in stage II Golpu diorite	9.9
392-1879.0	Stage IIa	Porphyry veins	Chalcopyrite	Chalcopyrite (+ 5 % pyrite) vein in biotite- and actinolite-altered rock	0.6
392-1879.0	Stage IIa	Porphyry veins	Anhydrite	Anhydrite vein after chalcopyrite - pyrite veins	10.5
392-1891.0	Stage IIa	Porphyry veins	Pyrite	Pyrite (+ trace chalcopyrite, anhydrite) veins with actinolite halos after biotite-altered rock	0.7
396-1320.4	Stage IIa	Porphyry veins	Molybdenite	Molybdenite fragments in pyrite-cemented breccia vein after stage I diorite	0.7
315-437.2	Stage IIa	Porphyry (distal)	Pyrite	Pyrite vein in chlorite- and muscovite-altered rock	1.5
323-505.1	Stage IIa	Porphyry (distal)	Pyrite	Pyrite vein in chlorite - muscovite - epidote altered rock	2.0
377-761.0	Stage IIa	Porphyry (distal)	Pyrite	Fine-grained disseminated pyrite in weakly chlorite- and epidote-altered rock	0.6
396-92.0	Stage IIa	Porphyry (distal)	Pyrite	Pyrite vein in chlorite - epidote - hematite altered rock	1.0
337-1220.2	Stage IIc	Porphyry veins	Chalcopyrite	Chalcopyrite vein (+ trace native gold) in stage II Golpu diorite	0.0
377-1171.5	Stage IIc	Porphyry veins	Chalcopyrite	Chalcopyrite vein with diffuse margins into coarse-grained biotite	0.1
377-1210.0	Stage IIc	Porphyry veins	Pyrite	Pyrite - chalcopyrite vein	1.3
377-1210.0	Stage IIc	Porphyry veins	Chalcopyrite	Pyrite - chalcopyrite vein	0.1
377-1466.2	Stage IIc	Porphyry veins	Chalcopyrite	Chalcopyrite (+ trace pyrite) vein	-0.1
377-1472.7	Stage IIc	Porphyry veins	Chalcopyrite	Pyrite - chalcopyrite vein	-0.4
377-1472.7	Stage IIc	Porphyry veins	Pyrite	Pyrite - chalcopyrite vein	1.2
377-1581.2	Stage IIc	Porphyry veins	Pyrite	Pyrite fragments in chalcocite-cemented breccia vein in stage II Golpu diorite	0.8
392-1277.1	Stage IIc	Porphyry veins	Chalcopyrite	Chalcopyrite vein cross-cutting stage II Golpu diorite intrusive contact	0.0
392-1495.6	Stage IIc	Porphyry veins	Chalcopyrite	Chalcopyrite interstitial to coarse-grained biotite clots in stage II Golpu diorite	-0.2
392-1546.3	Stage IIc	Porphyry veins	Bornite	Chalcopyrite - bornite - magnetite (+ trace carbonate) vein in stage II Golpu diorite	-0.1
392-1546.3	Stage IIc	Porphyry veins	Chalcopyrite	Chalcopyrite - bornite - magnetite (+ trace carbonate) vein in stage II Golpu diorite	0.1
397-1359.3	Stage IIc	Porphyry veins	Chalcopyrite	Chalcopyrite vein with orthoclase halo	-0.9
301-315.6	Stage III	Porphyry veins	Pyrite	Pyrite veins with muscovite (+ trace kaolinite) halos	1.3
301-317.2	Stage III	Porphyry veins	Pyrite	Pyrite in hydrothermal sandstone infill to breccia veins near Wafi breccia complex margins	-1.1
347-200.0	Stage III	Porphyry veins	Pyrite	Pyrite veins in muscovite-altered rock overprinted by alunite -kaolinite alteration	-1.2
347-259.5	Stage III	Porphyry veins	Pyrite	Pyrite veins in muscovite-altered rock overprinted by alunite - kaolinite alteration	-0.6
349-468.5	Stage III	Porphyry veins	Pyrite	Pyrite (+ trace chalcopyrite) veins with muscovite halos after biotite-altered rock	0.5
377-1310.0	Stage III	Porphyry veins	Pyrite	Pyrite - chalcopyrite - carbonate vein after stage II diorite	0.6
396-912.3	Stage III	Porphyry veins	Pyrite	Quartz - pyrite veins with muscovite halos	1.0
397-1037.5	Stage III	Porphyry veins	Pyrite	Pyrite veins with muscovite halos after biotite - muscovite - hematite altered rock	0.7
397-987.0	Stage III	Porphyry veins	Pyrite	Pyrite vein with muscovite halo	-0.2
199-225.3	Stage IVa	HS epithermal alteration	Pyrite	Muscovite - pyrite - kaolinite (+ trace alunite) altered Wafi breccia complex	0.4
301-115.7	Stage IVa	HS epithermal alteration	Alunite	Pervasive quartz- and alunite-altered Wafi breccia complex	16.2
301-150.0	Stage IVa	HS epithermal alteration	Alunite	Pervasive alunite - quartz - pyrophyllite altered Wafi breccia complex	13.1
321-51.0	Stage IVa	HS epithermal alteration	Alunite	Pervasive alunite - quartz - kaolinite altered Wafi breccia complex	19.4
347-200.0	Stage IVa	HS epithermal alteration	Alunite	Pervasive alunite- and kaolinite-altered rock containing stage III pyrite veins	15.4
347-259.5	Stage IVa	HS epithermal alteration	Alunite	Muscovite-altered rock overprinted by alunite - kaolinite alteration	12.1
349-50.0	Stage IVa	HS epithermal alteration	Alunite	Pervasive quartz - alunite - kaolinite altered rock	17.7
393-23.8	Stage IVa	HS epithermal alteration	Alunite	Pervasive quartz - alunite - kaolinite (+ trace supergene hematite) altered rock	9.7
398-201.0	Stage IVa	HS epithermal alteration	Pyrite	Pyrite - covellite - alunite (+ trace chalcocite, tennantite) altered stage I diorite	-2.5
398-44.7	Stage IVa	HS epithermal alteration	Alunite	Pervasive quartz- and alunite-altered stage I Golpu diorite	6.3
377-335.6	Stage IVa	HS epithermal veins	Pyrite	Pyrite vein after stage III muscovite - pyrite - kaolinite altered rock	-1.1
377-586.2	Stage IVa	HS epithermal veins	Pyrite	Quartz - pyrite veins after muscovite-altered rock	-1.2
398-153.5	Stage IVa	HS epithermal veins	Covellite	Covellite vein with bornite fragments and alunite vein halo in stage I diorite	-23.2
398-168.0	Stage IVa	HS epithermal veins	Pyrite	Pyrite (+ trace chalcocite) vein with alunite halo in stage I Golpu diorite	-1.6
177-310.7	Stage IVa	IS epithermal veins	Pyrite	Link Zone: pyrite (+ quartz, trace carbonate) veins with muscovite halos	-0.5
392-193.7	Stage IVa	IS epithermal veins	Pyrite	Pyrite fragments in pyrite - calcite - rhodochrosite (+ trace sphalerite) vein	1.0
392-235.4	Stage IVa	IS epithermal veins	Pyrite	Pyrite - calcite - rhodochrosite vein with chlorite - montmorillonite halo	1.1
397-123.0	Stage IVa	IS epithermal veins	Pyrite	Pyrite fragments in rhodochrosite-cemented breccia vein	2.4
397-395.0	Stage IVa	IS epithermal veins	Pyrite	Pyrite fragments in pyrite-cemented breccia vein	-1.5
397-395.0	Stage IVa	IS epithermal veins	Pyrite	Pyrite (+ trace calcite) cement surrounding pyrite fragments in breccia vein	-3.6
397-74.2	Stage IVa	IS epithermal veins	Pyrite	Pyrite fragments in pyrite - calcite - rhodochrosite vein	1.9
398-150.5	Stage IVb	HS epithermal veins	Alunite	Coarse-grained alunite in colloform alunite - pyrite - orpiment - marcasite - galena vein	7.9
398-150.5	Stage IVb	HS epithermal veins	Alunite	Fine-grained alunite in colloform alunite - pyrite - orpiment - marcasite - galena vein	9.9
398-150.5	Stage IVb	HS epithermal veins	Pyrite	Small pyrite grains in colloform alunite - pyrite - orpiment - marcasite - galena vein	-2.9

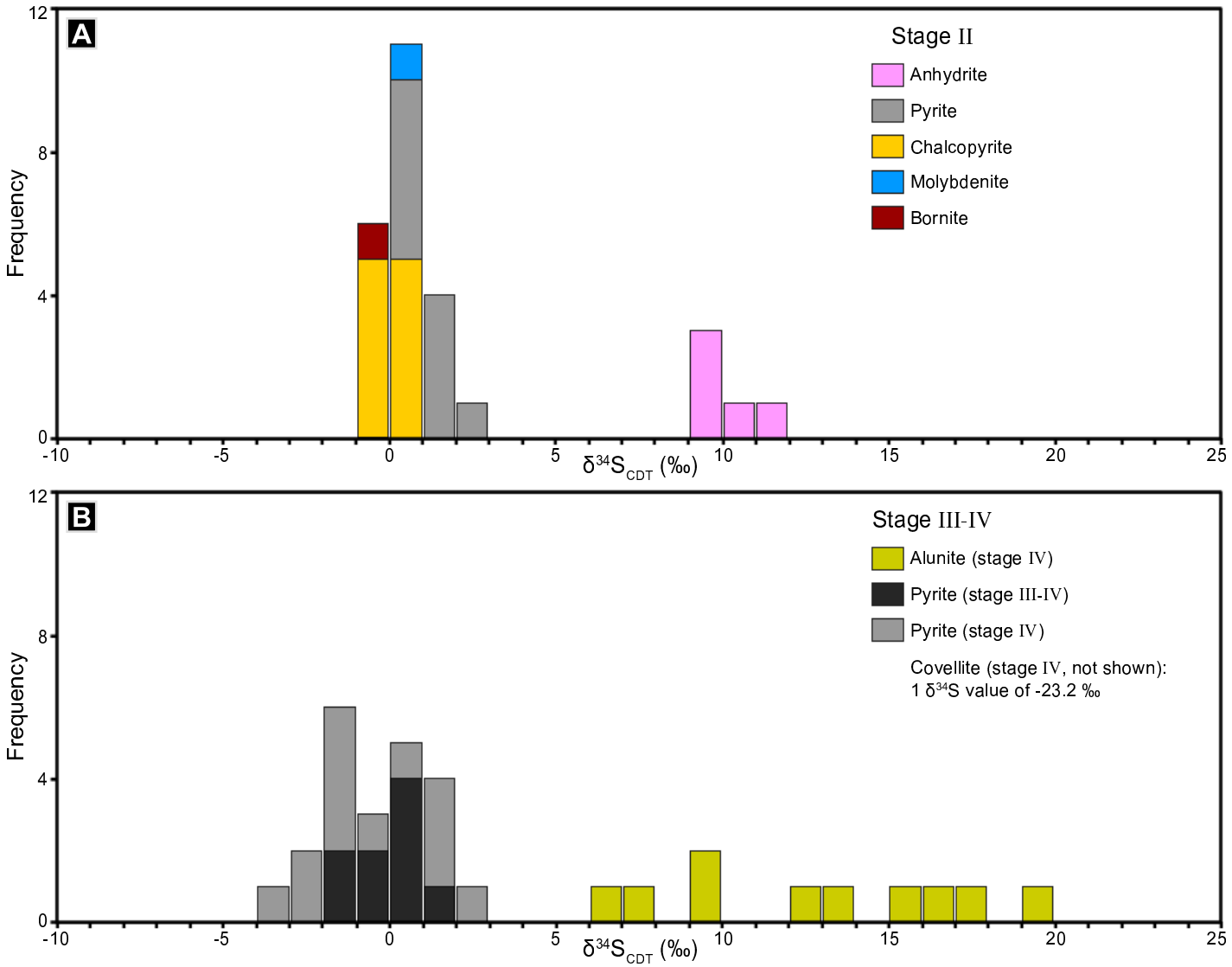

Figure 5.20: Cumulative frequency histograms of $\delta^{34}S$ values in Golpu and Wafi sulfides and sulfates. A) $\delta^{34}S$ values in stage II (porphyry) sulfides and anhydrite. B) $\delta^{34}S$ values in stage III-IV (epithermal) sulfides and alunite.

5.5.3 Discussion

If cooling of magmatic fluids were the only process responsible for changing $\delta^{34}S_{sulfide}$ values, then isotopically lighter values would be expected to occur in the distal porphyry samples (Rye, 1993). At Golpu, the isotopically heavier $\delta^{34}S$ values in distal samples of pyrite are instead interpreted to record a change in redox, from the Golpu porphyry to the relatively reduced, magnetite-bearing, greenschist facies wallrock. Wallrock reduction of magmatic sulfate was proposed to account for a similar pattern of $\delta^{34}S_{sulfide}$ enrichment with distance from the Cadia Cu-Au deposits (Wilson et al., 2007).

Assuming a constant H_2S / SO_4 ratio, $\delta^{34}S_{alunite}$ may increase due to decreasing temperature (cooling from 300 °C to 200 °C results in a ~ 5 ‰ increase in $\delta^{34}S_{alunite}$; Hikov et al., 2010) or mixing with meteoric water. At Wafi, heavier $\delta^{34}S_{alunite}$ values may therefore be explained as a result of cooling and / or mixing with meteoric water during outward dispersal of the lithocap-forming fluids. The lowest $\delta^{34}S_{alunite}$ (~ highest temperature and / or least mixed) values occur directly atop the stage II diorite, supporting the notion that the Golpu porphyry was

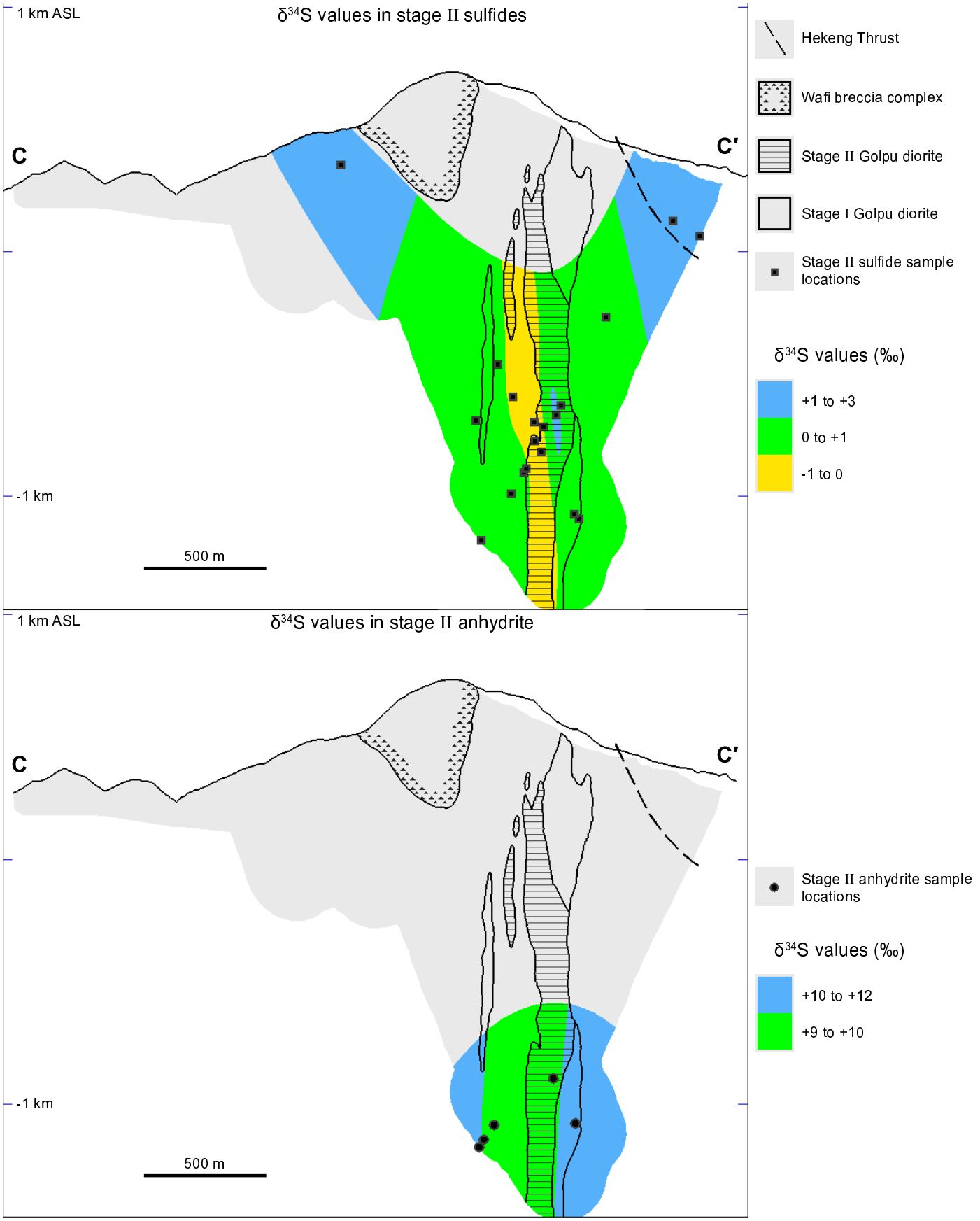

Figure 5.21: Distribution of $\delta^{34}S$ values in stage II sulfide (top) and sulfate (bottom) samples, shown in section C-C′. $\delta^{34}S$ values broadly increase with distance from the stage II Golpu intrusion.

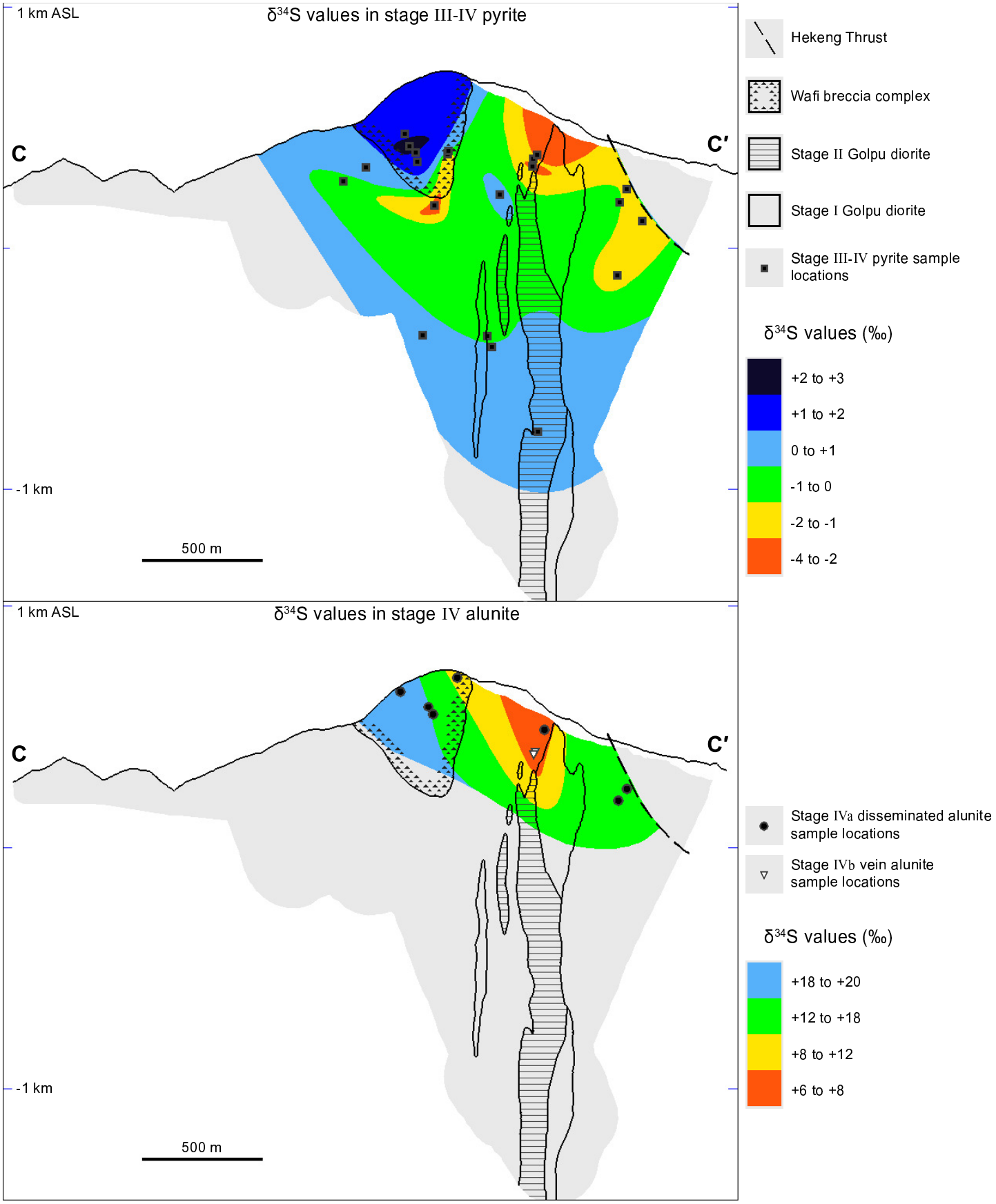

Figure 5.22: Distribution of $\delta^{34}S$ values in pyrite from stage III-IV (top), and alunite from stage IV (bottom), shown in section C-C′. $\delta^{34}S$ values broadly increase with distance from the top of the stage II Golpu intrusion.

a primary heat and magmatic fluid source in the Wafi lithocap. Rainbow et al. (2005) noted a similar zonation of isotopically lighter $\delta^{34}S_{alunite}$ values in the highest temperature portion of the Pierina high sulfidation epithermal deposit.

Although the disseminated alunite data presented here are interpreted to be from the same paragenetic stage, it is possible that the anatomy of the Wafi lithocap is more complex than recognised in this study. The Wafi lithocap may have been subjected to repeated incursions of meteoric water and / or fluctuations in the groundwater table, as well as repeated episodes of steam-heated overprinting. Sulfur isotopic compositions alone cannot be used to distinguish between magmatic-hydrothermal and steam-heated alunite (e.g., Fifarek and Rye, 2005). Thus, in the absence of oxygen and deuterium isotopic evidence for fluid source, alternative explanations for the spatial distribution of $\delta^{34}S_{alunite}$ values at Wafi, such as steam-heated overprints, should not be discounted.

5.6 Summary

Age determinations have constrained the paragenesis of Wafi-Golpu veins and alteration to timescales of a few hundred thousand years. Following the intrusion of the stage I and II Golpu diorites around 9.01 - 8.59 Ma, the stage II porphyry-concentric veins and related alteration assemblages formed around 8.83 - 8.67 Ma. The Re-Os (molybdenite) and Ar-Ar (biotite) ages constrain the development of stage II porphyry veins and alteration to a period lasting between 105 and 217 k.y.. Stages III and IV followed after porphyry mineralisation ended. This period encompassed the eruption of the Wafi breccia complex and the development of all epithermal mineralisation and alteration, and lasted between 100 and 220 k.y.. The final stage of Wafi epithermal veins, which cross-cut the main stage epithermal mineralisation, was dated by Ar-Ar (alunite) at 8.51 ± 0.04 Ma.

Comparisons of the most- and least-altered sample means suggest that the stage II porphyry veins and alteration have resulted mostly in mass gains to the host rocks, including additions of S, Ag, Au, Cu, Fe, K, and Na (Figs. 5.5 and 5.7). Such gains are consistent with the additions of perthitic orthoclase, biotite, magnetite, and locally gold-bearing sulfides during porphyry mineralisation. Similarly, gains of ~ 1-10 % K, Fe, and Cu have been noted in porphyry mineralised and biotite-altered zones of the Bajo de la Alumbrera and Sar Chesmeh porphyry Cu deposits (Ulrich and Heinrich, 2002; Hezarkhani, 2006). In cross section, elevated Au, Ag, Cu, and K assay values correspond to the location of porphyry mineralisation (Figs. 5.9 - 5.11). Elevated Mo contents, which indicate the locations of stage I and II quartz - molydenite veins near the Golpu intrusive contacts, are the only Golpu porphyry-related geochemical signature evident in the surface and near-surface assay data (Fig. 5.14).

Gold in the Golpu porphyry is weakly correlated with Cu assays, and occurs as native inclusions up to 80 µm across within the stage IIc vein and disseminated chalcopyrite, pyrite, and bornite. Elevated Cu-Mo-Au contents of the Golpu porphyry ore are consistent with the high-K calc-alkalic affinity of Golpu diorites (Chapter Three; Figs. 3.16, 5.15). Despite the presence of minor molybdenite, Golpu is classified geochemically as a Cu-Au porphyry deposit (Fig. 5.15; Kesler et al., 2002).

Sulfur isotopic compositions of the stage II sulfides and anhydrite are systematically zoned about the stage II Golpu diorite, with isotopically lighter values nearest the porphyry. The spatial distribution of stage II

$\delta^{34}S_{sulfide}$ values is interpreted to record a redox gradient, from the relatively oxidised porphyry to the relatively reduced, magnetite-bearing metasedimentary wallrock.

Stage III-IV muscovite - pyrite veins and alteration, which are transitional from the porphyry to the epithermal environment, appear to have resulted in gains of K and S (± Fe) contents, and losses of Ca, Mg, and Na contents. Such changes are consistent with additions of muscovite and pyrite at the expense of feldspars and other micas. The geometry of these upward-flaring zones is indicated by zones of elevated Fe, As, Sb, and S defined from the drill core assay data.

The upward-flaring domains of stage IV alunite - kaolinite alteration are characterised by low concentrations of most major elements (particularly Ca, Mg, and Na), and relatively high Zr (Figs. 5.6 - 5.8). This is interpreted to indicate mass loss by dissolution of non-Zr bearing phases, and is consistent with the textural evidence for dissolution, such as vuggy quartz, documented in Chapter Four. The Wafi HS epithermal domain contains minor Cu-Au mineralisation above the Golpu porphyry, and is marked by elevated Cu and As assays in cross section (Fig. 5.11). The high sulfidation gold is refractory in disseminated pyrite, and varies mostly with Te, Se, Mn, Ag, Tl, Sn, and Bi contents.

The sulfur isotopic compositions of stage IV disseminated alunite are zoned about the top of the Golpu porphyry and the deepest portions of the lithocap, with isotopically lighter values nearest the porphyry. The spatial distribution of stage IVa $\delta^{34}S_{alunite}$ values is interpreted to reflect temperature variations in a slowly rising, laterally migrating, and condensing column of magmatic steam atop the Golpu porphyry. Decreasing $\delta^{34}S$ values, corresponding to higher temperatures, point to the Golpu porphyry as the causative intrusion of the alunite - kaolinite alteration and Rafferty's Copper Zone mineralisation.

The stage IV IS epithermal domain is characterised by gains of Ag, As, Au, K, Mn, Pb, and Zn (Fig. 5.8). Such is consistent with the epithermal carbonate - base metal sulfide ± quartz ± adularia ± native gold veins and disseminated pyrite that occur throughout the carbonate veined rocks. The intermediate sulfidation mineralisation is expressed in the surface assays of Au, Ag, Mn, Zn, and Pb (Fig. 5.14).

Gold in the Wafi IS epithermal ore is mostly refractory in stage IVa vein and disseminated pyrite, in association with As, Sb, Tl, Zn, Mn, Co, Ni, and W contents. The IS epithermal pyrite contains the highest mean As contents of all pyrite grains examined in this study. Correspondingly, gold in the carbonate epithermal domain is correlated with whole rock As contents (Fig. 5.15). Higher gold grades typically occur in assay intervals containing Mn contents greater than 0.5 wt. %. Link Zone, the highest grade and most densely veined portion of the Wafi epithermal deposit, is transitional into the biotite-altered Golpu porphyry environment. In section, the Link Zone to Golpu transition can be discerned as a corridor of elevated K, Mo, Pb, and Zn contents along the Compass fault (Fig. 5.13).

This chapter has further constrained the timing, geochemical character, and spatial relationships between the Golpu porphyry and Wafi epithermal deposits. In the next chapter, results presented in this and previous chapters are compiled to produce a genetic model for Wafi-Golpu, summarising the evidence for a spatial, temporal, and ultimately genetic relationship between porphyry and epithermal environments.

Chapter 6
Genetic Model and Conclusions

6.1 Introduction

This chapter presents a genetic model for the Wafi-Golpu deposit, based on the deposit characteristics documented in previous chapters. The model identifies the regional tectonic controls on Golpu porphyry intrusion and uplift, highlighting an unusual style of low-angle subduction related to porphyry ore genesis. The model also summarises the deposit-scale transition from porphyry to epithermal styles of veins and alteration, highlighting the evidence for a genetic relationship between the porphyry and epithermal environments. A discussion of the implications of this study is followed by recommendations for future research.

6.2 Genetic Model

6.2.1 Regional Geodynamic and Metallogenic Model

In Chapter Two, a combination of seismic data, paleotectonic reconstructions, and porphyry deposit ages were compiled in a new tectonic-metallogenic model for the New Guinea Orogen (Fig. 2.8). In this model, most of the porphyry deposits in the New Guinea Orogen (including Golpu) are part of the Post-Maramuni metallogenic belt, which formed in a low-angle subduction related orogenic regime (Fig. 2.9). Key tectonic drivers to the formation of the Post-Maramuni metallogenic belt were:

- ~ 20 Ma: Initiation of southward subduction along the Trobriand-Wewak trench (Fig. 2.2) resulted in Maramuni belt porphyry-epithermal deposits forming between 17 and 12 Ma (Fig. 2.9).
- ~ 15 - 12 Ma: A combination of east to west closure of Trobriand subduction, initiation of north-directed subduction along the New Britain Trench, and accretion of the Melanesian Arc to the northern margin of New Guinea resulted in antiformal deformation of the Solomon Sea Plate (Figs. 2.3, 2.8).
- ~ 12 Ma to present day: Shallow west-directed subduction of the Solomon Sea Plate antiform resulted in a westward-migrating orogenic front. Compression, uplift, and exhumation driven primarily by the west-directed low-angle subduction were critical to the formation of Wafi-Golpu, along with most of the other porphyry deposits in the New Guinea Orogen (Fig. 2.9).

6.2.2 Genetic Model for Wafi-Golpu Mineralisation

The veins and altered rocks of the Wafi-Golpu deposit record a four stage evolution from porphyry to high and intermediate sulfidation epithermal styles of mineralisation, all of which are ultimately related to the Golpu intrusions (Figs. 4.1, 6.1). Stage I was a minor porphyry ore-forming event associated with the emplacement of two Golpu diorite intrusions at 9.01 ± 0.14 Ma and 8.93 ± 0.2 to 8.79 ± 0.17 Ma (Fig. 5.1). The stage II hornblende-phyric Golpu diorite was emplaced between 8.86 ± 0.22 Ma and 8.59 ± 0.22 Ma. The Golpu diorites have arc geochemical characteristics such as intermediate to felsic and calc-alkaline to high-K calc-alkaline compositions, fractionated REE patterns (e.g., least-altered La/Yb_{cn} ~ 3.2), and relative Ta, Nb, and

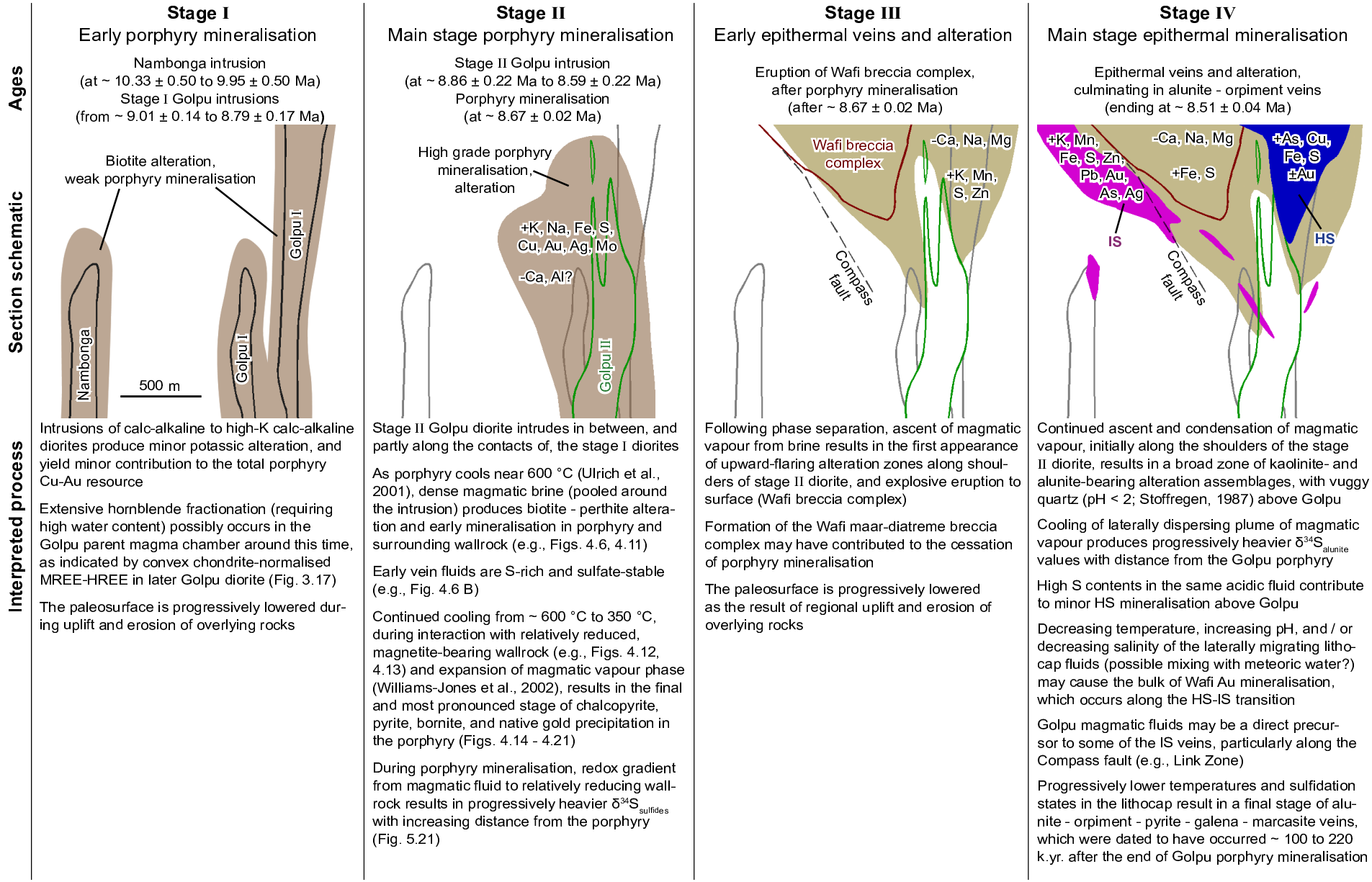

Figure 6.1: Summary of a genetic model for the Wafi-Golpu deposit, describing the ore deposit processes intepreted to have occurred during the evolution from early porphyry intrusions and mineralisation (stage I) to the final stage of epithermal mineralisation (stage IV). The schematics borrow elements from sections A, C, and E, looking generally NE or NW. The shaded regions correspond to zones of alteration and mineralisation. Mass changes indicated in each are estimated from comparisons of altered and weakly altered samples (section 5.3.2.1), and are partly indicated by the assay data in cross sections (Figs. 5.9 - 5.14). Continued uplift and exhumation of the deposit after stage IV (not shown) resulted in colluvium containing lithocap-altered clasts. Abbreviations in stage IV: HS = high sulfidation epithermal, IS = intermediate sulfidation epithermal.

Ti depletions (e.g., mean Nb/Nb* ~ 0.48; Fig. 3.16). The stage II Golpu diorite has lower total REE contents than the stage I intrusions, along with convex chondrite-normalised MREE to HREE profiles (Fig. 3.23) that are interpreted to indicate hornblende fractionation from a hydrous parent magma.

Stage IIa quartz - molybdenite ± anhydrite veins formed between 8.83 ± 0.04 and 8.73 ± 0.04 Ma, based on Re-Os dating of molybdenite (Table 5.1, Fig. 5.1). The associated alteration assemblages comprise biotite - perthite (orthoclase - albite) that transitions outwards to muscovite - chlorite and chlorite - actinolite - epidote alteration, with biotite dated at 8.74 ± 0.04 Ma (Table 5.1, Fig. 5.1). Stage IIb hematite veins with magnetite alteration halos, and disseminated hematite that occurs along the domain where biotite alteration transitions to muscovite alteration, indicate that Golpu magmatic fluids were relatively oxidised (sulfate-stable; e.g., Cooke and Simmons, 2000) with respect to the metasedimentary wallrock. The transition from dominantly oxidised magmatic conditions to relatively reduced conditions in the metasedimentary wallrock is interpreted to have resulted in the zonation of Golpu sulfur isotopic compositions ($\delta^{34}S_{anhydrite}$ from proximal values of +9.2 to distal +11.3‰, and $\delta^{34}S_{sulfides}$ from proximal -0.9 to distal +2.0 ‰; Fig. 5.21).

Stage II culminated in the main stage of Cu-Au mineralisation at 8.67 ± 0.02 Ma, based on Ar-Ar dating of stage IIc biotite (Table 5.1, Fig 5.1). Stage II vein and disseminated chalcopyrite, pyrite, and bornite are distributed about the stage II Golpu diorite (Fig. 4.14), and contributed to an unusually high-grade (1 Gt at 0.90 % Cu and 0.63 ppm Au) and vertically elongated (>1.8 km) porphyry orebody. Stage II sulfides define a broad zonation pattern from proximal chalcopyrite with trace bornite, to chalcopyrite > pyrite, to distal pyrite > chalcopyrite (Fig. 4.14). Gold occurs primarily as native inclusions up to 80 μm diameter in chalcopyrite, bornite, and pyrite (e.g., Fig. 4.20). Accessory phases include hypogene calcite, barite, rutile, native bismuth, and cubanite. Magnetite - hematite intergrowths occur in several of the main stage gold-bearing veins (e.g., Fig. 4.21 B), suggesting that oxidation of iron occurred during the formation of porphyry sulfide ore (as in Sun et al., 2013).

Stage II porphyry mineralisation was overprinted by upward-flaring domains of quartz, muscovite, and pyrite veins and alteration (stage III; Figs. 4.23, 6.1). Stage III quartz - pyrite veins transition upwards to muscovite alteration zones along the east and west shoulders of the stage II diorite (Fig. 4.23 A). The Wafi breccia complex, an upward-flaring multiphase polymictic breccia pipe that spans ~ 1 x 0.5 km at surface (Figs. 3.2 B, 3.5 - 3.7), is interpreted to have formed during stage III. It contains abundant metasedimentary country rock fragments (e.g., Fig. 3.18 F), biotite - orthoclase altered and chalcopyrite mineralised porphyry fragments, irregular dacite dykes, amoeboidal dacitic fragments interpreted to be juvenile magmatic clasts (Fig. 3.18 E), accretionary lapilli (Fig. 3.18 A), and base surge deposits (Tau-Loi, 1996). These features are together interpreted to constitute a maar-diatreme breccia complex that erupted at the end of main stage porphyry mineralisation, some time between 8.67 ± 0.02 Ma and 8.51 ± 0.04 Ma.

Diatreme eruption was followed by the main stage of Wafi epithermal mineralisation and alteration (stage IV), which comprises late mineral associations that overprinted metasedimentary host rocks, the Golpu diorites, and the Wafi breccia complex (Figs. 4.25, 6.1). The epithermal mineral associations are broadly zoned about the top of the Golpu intrusions, from (1) an inner high sulfidation epithermal domain of pervasive alteration containing alunite, kaolinite, pyrophyllite, quartz, dickite, and minor diaspore, to (2) an outer intermediate sulfidation epithermal domain, containing carbonate - sulfide ± quartz ± adularia veins and montmorillonite - chlorite ± muscovite ± illite alteration. Most of the Wafi epithermal gold resource

(136 Mt at 1.70 ppm Au) is hosted in the intermediate sulfidation epithermal ore, along the periphery of the high sulfidation epithermal domain (Fig. 4.41).

The high sulfidation epithermal domain exhibits a broad zonation in alteration mineralogy from vuggy quartz and alunite - kaolinite - quartz - pyrite that overprinted the top of the Golpu porphyry, through a domain of alunite - kaolinite - pyrophyllite - pyrite ± diaspore, to distal kaolinite - pyrite ± dickite (Fig. 4.25). The ore minerals are zoned outwards from the top of the Golpu porphyry, from vein and disseminated pyrite - covellite - chalcocite - tennantite ± enargite ± bornite, to distal disseminated pyrite - sphalerite ± tennantite. A zonation of $\delta^{34}S$ values in disseminated alunite (from +6.3 ‰, directly above Golpu, to +19.4 ‰, 600 metres west of Golpu) is interpreted to reflect temperature variations in the lithocap (Fig. 5.22). Molybdenite, originally precipitated in stage I diorite-concentric quartz - molybdenite veins, has been preserved in vuggy quartz altered zones atop the Golpu porphyry, resulting in a molybdenum halo that is visible in surface geochemical data (Fig. 5.14 B). Pyrite is the dominant gold host in the covellite-mineralised rocks, with ~ 50 ppm refractory Au in pyrite (Table 5.4).

Colloform alunite - orpiment - pyrite - galena - marcasite veins cross-cut the covellite-mineralised diorite at 8.51 ± 0.04 Ma (Ar-Ar alunite; Table 5.1). These veins are the last documented stage of Wafi epithermal activity, and are interpreted to indicate a return to cooler conditions and lower sulfidation states in the lithocap environment. Continued uplift and exhumation after the stage IV epithermal events produced colluvium containing clasts of advanced argillic altered rocks (Fig. 3.20 C,D).

The stage IV intermediate sulfidation epithermal domain comprises Mn-carbonate - base metal sulfide veins, with alteration halos of chlorite - montmorillonite ± muscovite ± illite and finely disseminated pyrite (e.g., Figs. 4.33, 4.34). The highest grade epithermal mineralisation (Link Zone) occurs along the north-dipping Compass fault (Figs. 4.25 C, 4.41), and contains adularia, pyrite containing up to 10 wt. % As, and trace amounts of pyrrhotite. The pyrrhotite and As-bearing pyrite are interpreted to indicate a lower sulfidation state than is typical for intermediate sulfidation deposits. Link Zone transitions down the Compass fault into the Golpu porphyry environment, where sparse veins of tennantite - sphalerite - galena - chalcopyrite are interpreted as the basal component of stage IV epithermal veins (Fig. 4.35).

Gold in the intermediate sulfidation epithermal domain is dominantly refractory in pyrite (6 to 20 ppm Au in pyrite; Table 5.4), and occurs as inclusions up to 8 microns across in carbonate - sulfide veins close to the epithermal kaolinite - alunite domain. Higher gold grades occur at Wafi coincide spatially with the transition from high to intermediate sulfidation assemblages (Fig. 4.41). Quartz and carbonate veins immediately outside the alunite alteration zone display a transition from outer quartz ± sulfide to central carbonate - sulfide ± native gold infill within individual veins. This may imply that the high sulfidation fluid was (at least in part) parent to the intermediate sulfidation fluid, and that gold precipitation occurred during a transition from quartz + alunite to quartz + carbonate stable conditions. Decreasing temperature, increasing pH, and / or decreasing salinity of the laterally migrating lithocap fluids were likely controls on gold mineralisation during this transition.

Genetic links between the porphyry and epithermal environments

The spatial and temporal relationships between the porphyry, high sulfidation, and intermediate sulfidation veins and altered rocks of the Wafi-Golpu deposit are consistent with a genetic relationship between the porphyry and both epithermal environments. A genetic relationship between the Golpu porphyry and Wafi

high sulfidation environments is supported by the following observations:

- The lowermost zones of kaolinite - alunite alteration and high sulfidation mineralisation at Wafi are centred above, and overprint part of the uppermost Golpu diorites (Fig. 4.25 A). The downward-tapering geometry of the kaolinite - alunite alteration zone points to Golpu as the source of buoyant, acid-generating magmatic fluids.
- A total of 0.25 - 0.40 m.y. elapsed from the formation of the early porphyry veins (stage IIa) to the youngest high sulfidation veins (stage IVb; Fig. 5.1). This time frame implies that the Golpu deposit formed as a precursor to high sulfidation veins and alteration. The time span is similar to that documented between the FSE porphyry and Lepanto high sulfidation mineralisation (Arribas et al., 1995).
- Decreasing $\delta^{34}S$ values in disseminated alunite, interpreted to correspond to higher temperatures, point to the Golpu porphyry as a heat (± fluid and metal) source at Wafi (Figs. 5.22, 6.1).

A genetic relationship between the Golpu porphyry and Wafi intermediate sulfidation mineralisation is supported by the following observations:

- There is a close spatial relationship between the carbonate - base metal sulfide veins and the Golpu porphyry. The carbonate - base metal sulfide veins occur in an arcuate zone that extends with depth into the Golpu porphyry. This spatial configuration possibly implies that the epithermal veins were (in part) precipitated from fluids derived from the porphyry. The epithermal veins were mostly located by the N-dipping Compass fault, particularly where it cuts E-dipping metaconglomerates (Fig. 4.41).
- The down-fault transition from Link Zone epithermal mineralisation to Golpu porphyry-related veins and alteration (Fig. 5.13) suggests that magmatic fluids may have been a precursor to some of the intermediate sulfidation veins in Link Zone.

Wafi-Golpu is particularly unusual in that very few lithocaps are known to have developed intermediate sulfidation deposits along their margins (Sillitoe, 2010). A genetic relationship between the Wafi lithocap and intermediate sulfidation environments is inferred by the following observations:

- There is a lateral transition from high to intermediate sulfidation mineral associations, from alunite ± covellite ± tennantite assemblages, outwards to kaolinite - muscovite - pyrite ± sphalerite, to gold-bearing carbonate - base metal sulfide assemblages (Figs. 4.24, 4.25). Disseminated and vein sphalerite occurs across the transition from high to intermediate sulfidation epithermal assemblages.
- High grade epithermal gold formed at the transition from high to intermediate sulfidation alteration assemblages (Figs. 4.41, 5.13 B, 5.14 B), possibly implying that gold precipitation occurred during a transition from alunite- to carbonate-stable conditions. Decreasing temperature, increasing pH, and / or decreasing salinity of the laterally migrating lithocap fluids may have triggered gold mineralisation during this transition.

6.3 Implications for Exploration

Some of the findings of this thesis are directly relevant to mineral exploration. At the regional tectonic scale, this study has shown that mantle seismic data and tomographic interpretations can be used to identify zones that are undergoing (or have recently undergone) low-angle subduction (e.g., Figs. 2.7, 2.8). In some environments – such as where hydrous magmas were generated by recent subduction – low-angle subduction may be involved in the formation of porphyry deposits (e.g., Cooke et al., 2005).

Geochemical profiles related to the Golpu and Wafi veins and alteration domains vary according to elevation (e.g., Figs. 5.9 B, 5.10 B, 5.11 B). In the deeper parts of the deposit, distal indicators of porphyry mineralisation include sparse pyrite - chalcopyrite veins with biotite halos (which may be clast-selective in Owen Stanley rocks; Fig. 4.7 D), reddening from disseminated hematite at the outer margins of biotite-altered rocks (Fig. 4.7 A,B), and decreasing $\delta^{34}S_{sulfide}$ values towards porphyry mineralisation (Fig. 5.21). Routine measurements of $\delta^{34}S_{sulfide}$ values in drill core may be a useful vector to porphyry in an exploration context, as proposed by Holliday and Cooke (2007).

Williamson and Hancock (2005) commented on a lack of geochemical manifestations of the Golpu porphyry at surface. The current study contradicts that finding, presenting two geochemical vectors to porphyry in the barren lithocap environment: $\delta^{34}S$ compositions in disseminated alunite decreasing from +20 ‰ at the edges of the lithocap to +6 ‰ above Golpu (Fig. 5.22); and whole rock Mo contents defining a halo ~ 600 m in diameter atop the porphyry (Fig. 5.14 B). The molybdenum halo occurs through the entire vertical extent of the Golpu porphyry, and is preserved in rocks altered to vuggy quartz. Elevated molybdenum assays at or near the surface may similarly point to underlying porphyry deposits in other lithocaps.

Surface indications of Wafi epithermal mineralisation include chlorite, montmorillonite, or muscovite alteration (Figs. 5.13, 5.14). Halloysite alteration also occurs at surface atop the Link Zone mineralisation, although it may have originated by supergene processes (section 4.3.4.3). Most of the intermediate sulfidation mineralisation and alteration occurs near faults or metaconglomerate units that dip towards the Golpu porphyry (Fig. 4.41). Targetting faults and relatively permeable units for identification of chlorite, montmorillonite, muscovite, and halloysite may therefore be an efficient surface exploration strategy in other regions.

Elevated Mn, Zn, and Pb contents are the most distal halos to Wafi-Golpu mineralisation documented in this study, occurring up to 1200 m west Golpu (Fig. 5.14 B). Similar geochemical halos have been documented in the distal portions of other porphyry deposits (e.g., Jones, 1992). This study further demonstrates that kilometre-scale patterns of base metal enrichment, when considered in the context of regional structure and gross dip of host stratigraphy, may point to epithermal and porphyry deposits elsewhere.

6.4 Contributions to the Porphyry-Epithermal Model

This study has significantly improved on current understanding of the tectonic-metallogenic evolution of New Guinea. It provides further evidence for the role of low-angle subduction in the generation of porphyry (± epithermal) deposits, such as proposed by Cooke et al. (2005). This study also demonstrates that the subduction of aseismic ridges or oceanic plateaus are not the only means of generating low-angle subduction. Subduction of an antiformal slab in a direction parallel to its hinge, as in the present day Solomon Sea Plate

(Fig. 2.8), appears to be an especially long-lived form of low-angle subduction. In New Guinea, this specific geodynamic configuration has been active for about 10 m.y. (Fig. 2.3), and has produced at least seven deposits in a belt several hundred kilometres long within the New Guinea Orogen (Fig. 2.9).

At the deposit scale, this study has shown that Golpu and Wafi have several characteristics that are consistent with the current understanding of calc-alkalic porphyry, IS epithermal, and HS epithermal deposits, as summarised in sections 4.4.1 and 4.4.2. Some of these characteristics have genetic implications, the following in particular:

- Inclusion trains of bornite in orthoclase (Fig. 4.11 B), and intergrowths of chalcopyrite and coarse-grained biotite (e.g., Fig. 4.18 D) illustrate that the fluids that produced sodic-potassic alteration assemblages in the porphyry were metal-bearing, probably wholly magmatic fluids (as opposed to fluids at least partially sourced from country rock; e.g., Dilles et al., 1995).
- The occurrence of anhydrite with quartz - chalcopyrite - molybdenite veins (Fig. 4.6 B) clearly shows that early porphyry fluids were sulfate-stable (i.e., oxidised; e.g., Cooke and Simmons, 2000).
- Magnetite - hematite intergrowths occur in the main stage of Golpu porphyry mineralisation, within late quartz - chalcopyrite - gold veins (e.g., Fig. 4.21 B,C). This is consistent with the findings of Sun et al. (2013), who suggested that the oxidation of ferrous to ferric iron may be a key driver in the reduction of magmatic sulfate to sulfide, in order to form porphyry deposits.
- New geochronological results demonstrate, with non-overlapping error, that stage II porphyry veins developed over 105 to 217 k.y., and that the transition from the first of stage II porphyry veins to the last epithermal veins occurred over 250 to 400 k.y.. The transition from the main and final stage of porphyry mineralisation to the last epithermal veins occurred over 100 to 220 k.y. (Fig. 5.1). These findings contribute to current understanding of the relatively brief durations of ore forming events in porphyry-epithermal systems (Chiaradia et al., 2013), and are consistent with timeframes documented in other deposits (e.g., Arribas et al., 1995).

As a whole, this study has documented three contrasting and uniquely overprinting styles of mineralisation in a large volume of rock, thoroughly constrained by drill core data and several new geochronological analyses. This work contributes to the porphyry-epithermal model by demonstrating that there is a spatial, temporal, and genetic relationship between the three deposit styles.

6.5 Recommendations for Future Work

In order to achieve a more thoroughly constrained genetic model for porphyry and epithermal mineralisation at Golpu and Wafi, some aspects of the deposit warrant further study:

- A distinction between regional metamorphic rock and weak chlorite - actinolite ± epidote altered rock has not been possible to make at the scale of this study. A wider study area could be used to document the extent of the chlorite - actinolite ± epidote alteration. Indicators of distal propylitic alteration in greenschist facies rock, such as elevated carbon contents or $\delta^{13}C_{\text{whole rock}}$ values (Djouka-Fonkwé et. al, 2012), could be applied as vectors to porphyry in Owen Stanley metasedimentary rocks regionally.

- The origin and timing of the Wafi breccia complex could be better constrained with clear examples of porphyry mineralised fragments and juvenile magmatic clasts, perhaps sampled from intervals containing elevated Cu and Au. Base surge beds, such as those documented by Tau-Loi (1996), need to be better documented at surface.
- A more thorough documentation of the anatomy of the high sulfidation epithermal alteration zone, including oxygen and deuterium isotopic compositions and alunite crystal habits, could resolve the possible role of steam-heated overprints and / or fluctuations in the groundwater table at Wafi. Better paragenetic constraints on alunite would then allow a more detailed investigation into the spatial distribution of $\delta^{34}S_{alunite}$ values above the Golpu porphyry, using a larger suite of disseminated alunite samples.
- More geochronological investigations are required. Specifically, new geochronology for the intermediate sulfidation veins would better constrain the deposit paragenesis. The intrusive age for the Nambonga diorite is based on prior K-Ar analyses of hornblende (Tau-Loi, 1996), which may have been disturbed by later magmatic-hydrothermal activity. Zircon U-Pb dates of the Nambonga diorite could resolve whether the Nambonga porphyry served as a fluid channel or fluid and / or metal source to some of the intermediate sulfidation mineralisation (as proposed in Chapter Four). The anomalous Ar-Ar (muscovite) age should be investigated with further sampling of stage III muscovite or pyrite.

References

Arribas, A., Jr., 1995, Characteristics of high-sulfidation epithermal deposits, and their relation to magmatic fluid, in Thompson, J. F., ed., Magmas, Fluids, and Ore Deposits: Mineralogical Association of Canada Short Course Series, v. 23, p. 419-454.

Arribas, A. Jr., Hedenquist, J. W., Itaya, T., Okada, T., Concepcion, R. A., and Garcia, J. S., 1995, Contemporaneous formation of adjacent porphyry and epithermal Cu-Au deposits over 3000 Ka in northern Luzon, Philippines: Geology, v. 23, p. 337-340.

Ayres, L. D., Averill, S. A., and Wolfe, W. J., 1982, An Archean molybdenite occurrence of possible porphyry type at Setting Net Lake, northwestern Ontario, Canada: Economic Geology, v. 77, p. 105-1119.

Ayuso, R. A., 2010, Trace-Element Geochemistry, in John, D. A., Ayuso, R. A., Barton, M. D., Blakely, R. J., Bodnar, R. J., Dilles, J. H., Gray, Floyd, Graybeal, F. T., Mars, J. C., McPhee, D. K., Seal, R. R., Taylor, R. D., and Vikre, P. G., 2010, Porphyry copper deposit model, Chapter B of Mineral deposit models for resource assessment: U.S. Geological Survey Scientific Investigations Report 2010–5070–B, p. 97-100.

Bainbridge, A. L., Hitchman, S. P., and DeRoss, G. J., 1998, Nena copper-gold deposit: in Berkman, D. A., and Mackenzie, D. H., eds., Geology of Australian and Papua New Guinean Mineral Deposits: The Australian Institute of Mining and Metallurgy Monograph Series v. 22, p. 855-862.

Barley, M. E., 1982, Porphyry-style mineralization associated with early Archean calc-alkaline igneous activity, Eastern Pilbara, Western Australia: Economic Geology, v. 77, p. 1230-1236.

Barton, P. B., Bethke, P. M., and Toulmin, P., 1963, Equilibrium in ore deposits: Symposium on the mineralogy of sulfides: International Mineralogical Association, 3rd General Meeting, Washington, DC, 1963, p. 171-185.

Barton, P. B., Jr., and Skinner, B. J., 1967, Sulfide mineral stabilities, in Barnes, H. L., ed., Geochemistry of Hydrothermal Ore Deposits: New York, Holt, Rinehart and Winston, p. 236-333.

Bates, R. L., and Jackson, J. A., 1987, Glossary of Geology: American Geological Institute: Alexandria, Virginia, 788 p.

Boyden, J. A., Müller, R. D., Gurnis, M., Torsvik, T. H., Clark, J. A., Turner, M., Ivey-Law,. H., Watson, R. J. and Cannon, J. S., 2011, Next-generation plate-tectonic reconstructions using GPlates: Geoinformatics: cyberinfrastructure for the solid earth sciences, p. 95-114.

Braxton, D., Cooke, D. R., Harris, A., Tosdal, R., Waters, P., and Wurst, A., 2010, Metallogeny of porphyry Cu-Au deposits: Workshop manual, Society of Economic Geologists Conference, Keystone, Colorado, 65 p.

Braxton, D. P., Cooke, D. R., Dunlap, J., Norman, M., Reiners, P., Stein, H., and Waters, P., 2012, From crucible to graben in 2.3 Ma: A high-resolution geochronological study of porphyry life cycles, Boyongan-Bayugo copper-gold deposits, Philippines: Geology, v. 40, p. 471-474.

Brimhall, G. H., Jr., 1977, Early fracture-controlled disseminated mineralization at Butte, Montana: Economic Geology, v. 72, p. 37-59.

Bruns, T. R., Vedder, J. G., and Culotta, R. C., 1989, Structure and tectonics along the Kilinailau Trench, Bougainville–Buka Island region, Papua New Guinea, in Vedder, J. G., and Bruns, T. R., eds., Geology and offshore resources of Pacific Islands arcs — Solomon Islands and Bougainville, Papua New Guinea region: Circum Pacific Council for Energy and Mineral Resources Earth Science Series, v. 12, p. 93-123.

Buddin, T., 1993, Petroleum evaluation of the Aure thrust belt, Gulf of Papua, Papua New Guinea: SOPAC Technical Report 183, 39 p.

Burnham, C. W., 1967, Hydrothermal fluids at the magmatic stage, in Barnes, H.L., ed., Geochemistry of hydrothermal ore deposits: New York, Holt, Rinehart and Winston, Inc., p. 34-76.

Burnham, C. W., 1979, Magmas and hydrothermal fluids, in Barnes, H.L., ed., Geochemistry of hydrothermal ore deposits, 2nd ed.: New York, John Wiley and Sons, p. 71-136.

Candela, P.A., 1997, A review of shallow, ore-related granites—Textures, volatiles, and ore metals: Journal of Petrology, v. 38, p. 1619-1633.

Chang, Z., Hedenquist, J. W., White, N. C., Cooke, D. R., Roach, M., Deyell, C. L., Garcia, J., Gemmell, J. B., McKnight, S., and Cuison, A. L., 2011, Exploration tools for linked porphyry and epithermal deposits: Example from the Mankayan intrusion-centered Cu-Au district, Luzon, Philippines: Economic Geology, v. 106, p. 1365-1398.

Cherniak, D. J., and Watson, E. B., 2003, Diffusion in zircon: Reviews in mineralogy and geochemistry, v. 53, p.113-143.

Chiaradia, M., Schaltegger, U., Spikings, R., Wotzlaw, J. F., and Ovtcharova, M., 2013, How accurately can we date the duration of magmatic-hydrothermal events in porphyry systems?—an invited paper: Economic Geology, v. 108, p. 565-584.

Cloos, M., Sapiie, B., Quarles van Ufford, A., Weiland, R. J., Warren, P. Q., and McMahon, T. P., 2005, Collisional delamination in New Guinea: The geotectonics of subducting slab breakoff: Geological Society of America Special Paper 400, 51 p.

Cooke, D. R., and Simmons, S. F., 2000, Characteristics and genesis of epithermal gold deposits, in Hagemann, S. G., and Brown, P. E., eds., Gold in 2000: Reviews in Economic Geology, v. 13, p. 221-244.

Cooke, D. R., Hollings, P., and Walshe, J. L., 2005, Giant porphyry deposits: characteristics, distribution, and tectonic controls: Economic Geology, v. 100, p. 801-818.

Corbett, G. J., 1990, Comments on the structure, alteration and mineralisation of the Wafi Project: Elders Mining PNG report (unpublished), 55 p.

Corbett, G. J., 1994, Regional structural control of selected Cu/Au occurrences in Papua New Guinea, in Rogerson, R., ed., Proceedings of the Geology, Exploration and Mining Conference, Lae, Papua New Guinea: The Australasian Institute of Mining and Metallurgy, p. 57-70.

Corbett, G. J., and Leach, T. M., 1998, Southwest Pacific Rim gold-copper systems: Structure, alteration and mineralization: Society of Economic Geologists Special Publication 6, 236 p.

Cox, K. G., Bell, J. D., and Pankhurst, R. J., 1979, The interpretation of igneous rocks: Allen & Unwin, London, 450 p.

Crawford, A. J., Meffre, S., Squire, R. J., Barron, L. M., and Falloon, T. J., 2007, Middle and Late Ordovician magmatic evolution of the Macquarie Arc, New South Wales: Australian Journal of Earth Sciences, v. 54, p. 181-214.

Crowhurst, P. V., Hill, K. C., Foster, D. A., and Bennett, A. P., 1996, Thermochronological and geochemical constraints on the tectonic evolution of northern Papua New Guinea, in Hall, R. and Blundell, D., eds., Tectonic evolution of Southeast Asia: Geological Society Special Publication, v. 106, p. 525-537.

Curtis, R. A., and Ryan, J., 1997, Mt Wanion EL 440 annual report: Rio Tinto Exploration (PNG) report (unpublished), 45 p.

Cussen, M. J., Wangu, A., McCulla, M. S., and Tau-Loi, D., 1986, Geology and mineralisation of the Wafi area, Papua New Guinea: Geological Survey of Papua New Guinea.

D'Addario, G.W., Dow, D. B., Swoboda, R., 1974, Geology of Papua New Guinea, 1 : 2,500,000 Map I — 875-C: Australian Bureau of Mineral Resources, Geology, and Geophysics.

Danyushevsky, L., Robinson, P., Gilbert, S., Norman, M., Large, R., McGoldrick, P., and Shelley, M., 2011, Routine quantitative multi-element analysis of sulphide minerals by laser ablation ICP-MS: Standard development and consideration of matrix effects: Geochemistry: Exploration, Environment, Analysis, v. 11, p. 51-60.

Davies, A. G., Cooke, D. R., Gemmell, J. B., and Simpson, K. A., 2008, Diatreme breccias at the Kelian gold mine, Kalimantan, Indonesia: Precursors to epithermal gold mineralization: Economic Geology, v. 103, p. 689-716.

Davies, H. L., 2012, The geology of New Guinea—the cordilleran margin of the Australian continent: Episodes—Newsmagazine of the International Union of Geological Sciences, v. 35, p. 87.

Davies, H. L. and Williamson, A. N., 2001, Explanatory notes to accompanyBuna 1:250,000 geological map: Geological Survey of Papua New Guinea.

Davies, H. L., and Smith, I. E., 1971, Geology of eastern Papua: Bulletin of the Geological Society of America, v. 82, p. 3299-3312.

Davies, J. F., and Luhta, L. E., 1978, An Archean "porphyry-type" disseminated copper deposit, Timmins, Ontario: Economic Geology, v. 73, p. 383-396.

Dewey, J. F., and Bird, J. M., 1970, Mountain belts and the new global tectonics: Journal of Geophysical Research, v. 75, p. 2625-2647.

Dilles, J. H., Farmer, G. L., and Field, C. W., 1995, Sodium-calcium alteration by non-magmatic saline fluids in porphyry copper deposits: Results fromYerington, Nevada: Mineralogical Association of Canada Short Course Series, v. 23, p. 309–338.

Djouka-Fonkwé, M. L., Kyser, K., Clark, A. H., Urqueta, E., Oates, C. J., and Ihlenfeld, C., 2012, Recognizing propylitic alteration associated with porphyry Cu-Mo deposits in lower greenschist facies metamorphic terrain of the collahuasi district, northern chile—implications of petrographic and carbon isotope relationships: Economic Geology, v. 107, p. 1457-1478.

Dow, D. B., 1977, A geological synthesis of Papua New Guinea: BMR Australia, Geology and Geophysics Bulletin 201, 41 p.

Dow, D. B., Smit, J. A. J, and Page, R. W., 1974, Wau, 1 :250,000 Geological Series - Explanatory Notes: Bureau of Mineral Resources, Geology and Geophysics and Department of Lands, Surveys and Mines: Canberra and Port Moresby, 33p.

Einaudi, M. T., Hedenquist, J. W., and Inan, E. E., 2003, Sulfidation state of fluids in active and extinct hydrothermal systems—Transitions from porphyry to epithermal environments: Society of Economic Geologists Special Publication 10, p. 285-313.

Engdahl, E. R., and Villaseñor, A., 2002, Global seismicity:1900-1999: International Geophysics, v. 81, p. 665-690, XV-XVI.

Erceg, M. M., 2008, Terry Leach: Contribution to the understanding of hydrothermal ore-forming processes of the Wafi high sulphidation epithermal gold deposit and his role in the discovery of the Wafi porphyry copper deposit: Terry Leach Symposium, Sydney, Australia: AUG Bulletin 48, p. 47-53.

Erceg, M. M., Craighead, G. A., Halfpenny, R., and Lewis, P. J., 1991, The exploration history, geology and metallurgy of a high sulphidation epithermal gold deposit at Wafi River, Papua New Guinea, in Rogerson, R., ed., Proceedings of the Geology, Exploration and Mining conference, Rabaul, Papua New Guinea: The Australasian Institute of Mining and Metallurgy, p. 58-65.

Fifarek, R. H., and Rye, R. O., 2005, Stable-isotope geochemistry of the Pierina high-sulfidation Au-Ag deposit, Peru: influence of hydrodynamics on SO4–H2S sulfur isotopic exchange in magmatic-steam and steam-heated environments: Chemical geology, v. 215, p. 253-279.

Findlay, R. H., Arumba, J., Abbott, L. D., Nekitel, D., Ninkama, J., Kopi, G., and Tekeve, B., 1997, The stratigraphy and tectonics of Markham: explanatory notes to accompany the revision of the MARKHAM 1:250,000 geological atlas: Papua New Guinea Geological Survey.

Fisher, N. H., 1975, Alluvial gold of the Morobe Goldfield, PNG, in Knight, C.L., ed., Economic geology of Australia and Papua New Guinea - 1. Metals: The Australian Institute of Mining and Metallurgy Monograph Series v. 5, p. 1045-1049.

Foland, K. A., Hubacher, F. A., and Arehart, G. B., 1992, 40Ar39Ar dating of very fine-grained samples: An encapsulated-vial procedure to overcome the problem of 39Ar recoil loss: Chemical Geology, v. 102, p. 269-276.

Garcia, J. S., Jr., 1991, Geology and mineralization characteristics of the Mankayan mineral district, Benguet, Philippines, in Matsuhisa, Y., Aoki, M., and Hedenquist, J. W., eds., Chishitsu Chosajo Hokoku = Geological Survey of Japan, Report 277: Kawasaki, Geological Survey of Japan, p. 21-30.

Garwin, S., Hall, R., and Watanabe, Y., 2005, Tectonic setting, geology, and gold and copper mineralization in Cenozoic magmatic arcs of Southeast Asia and the West Pacific: Economic Geology 100th Anniversary Volume, p. 891-930.

Gernon, T. M., Gilbertson, M. A., Sparks, R. S. J., and Field, M., 2009, The role of gas-fluidisation in the formation of massive volcaniclastic kimberlite: Lithos, v. 112, p. 439-451.

Gladczenko, T. P., Coffin, M. F., and Eldholm, O., 1997, Crustal structure of the Ontong Java Plateau: modeling of new gravity and existing seismic data: Journal of Geophysical Research: Solid Earth (1978-2012), v. 102, p. 22711-22729.

Gorton, M. P., and Schandl, E. S., 2000, From continents to island arcs: a geochemical index of tectonic setting for arc-related and within-plate felsic to intermediate volcanic rocks: The Canadian Mineralogist, v. 38, p. 1065-1073.

Grainger, D. J., and Pillinger, D. M., 1973, Markham, Papua New Guinea, 1:250 000 map SB/55-10, 1st edition: Bureau of Mineral Resources, Australia.

Grant, J. N. and Nielson, R. L., 1975, Geology and geochronology of the Yandera porphyry copper deposit, Papua New Guinea: Economic Geology, v. 70, p. 1157-1174.

Groves, D. I., Vielreicher, R. M., Goldfarb, R. J., and Condie, K. C., 2005, Controls on the heterogeneous distribution of mineral deposits through time: Geological Society of London Special Publications, v. 248, p. 71-101.

Gustafson, L. B., and Hunt, J. P., 1975, The porphyry copper deposit at El Salvador, Chile: Economic Geology, v. 70, p. 857-912.

Hall, R., 2002, Cainozoic geological and plate tectonic evolution of SE Asia and the SW Pacific: computer-based reconstructions, model and animations: Journal of Asian Earth Sciences, v. 20, p. 353-434.

Hall, R., and Spakman, W., 2002, Subducted slabs beneath the eastern Indonesia-Tonga region: insights from tomography: Earth and Planetary Science Letters, v. 201, p. 321-336.

Harmony Gold Mining Company Limited, 2003, Annual Investment Report, http://www.harmony.co.za/assets/investors/reporting/annual-reports/harmony_ar2003.pdf

Harris, A., 2010, Summary of petrological observations from drillholes WR315, WR316, WR318, WR320, WR321, WR323 (66 samples), Morobe Mining Joint Ventures report (unpublished), 40 p.

Hastie, A. R., Kerr, A. C., Pearce, J. A., and Mitchell, S. F., 2007, Classification of altered volcanic island arc rocks using immobile trace elements: development of the Th-Co discrimination diagram: Journal of Petrology, v. 48, p. 2341-2357.

Head, J. W. and Wilson, L., 2002, Diatremes and kimberlitic magmas and production of crater, diatreme and hypabyssal facies (extended abstract): Microsymposium 36, Moscow, Russia.

Hedenquist, J. W., 1987, Volcanic-related hydrothermal systems in the Circum-Pacific basin and their potential for mineralisation: Mining Geology, v. 37, p. 347-364.

Hedenquist, J. W., and Lowenstern, J. B., 1994, The role of magmas in the formation of hydrothermal ore deposits: Nature, v. 370, p. 519-527.

Hedenquist, J. W., Matsuhisa, Y., Izawa, E., White, N. C., Giggenbach, W. F., and Aoki, M., 1994, Geology, geochemistry, and origin of high sulfidation Cu-Au mineralization in the Nansatsu district, Japan: Economic Geology, v. 89, p. 1-30.

Hedenquist, J. W., Izawa, E., Arribas, A. Jr., and White, N. C., 1996, Epithermal gold deposits: Styles, characteristics, and exploration: Resource Geology Special Publication 1, 17 p.

Hedenquist, J. W., Arribas, A. Jr., and Reynolds, T. J., 1998, Evolution of an intrusion-centred hydrothermal system: Far Southeast-Lepanto porphyry and epithermal Cu-Au deposits, Philippines: Economic Geology, v. 93, p. 373-404.

Hedenquist, J. W., Arribas, A, Jr., and Gonzalez-Urien, E., 2000, Exploration for epithermal gold deposits, in Hagemann, S. G., and Brown, P. E., eds., Gold in 2000: Reviews in Economic Geology, v. 13, p. 245-277.

Hehnke, C., Ballantyne, G., Martin, H., Hart, W., Schwarz, A., and Stein, H., 2012, Geology and exploration progress at the Resolution porphyry Cu-Mo deposit, Arizona: Society of Economic Geologists Special Publication 16, p.147-166.

Heinrich, C. A., 2007, Fluid-fluid interactions in magmatic-hydrothermal ore formation: Reviews in Mineralogy and Geochemistry, v. 65, p. 363-387.

Heinrich C. A., Driesner T., Stefánsson A., and Seward, T. M., 2004, Magmatic vapor contraction and the transport of gold from porphyry to epithermal ore deposits: Geology, v. 32, p. 761-764.

Henley, R. W., and McNabb, A., 1978, Magmatic vapor plumes and ground-water interactions in porphyry copper emplacement: Economic Geology, v. 73, p. 1-20.

Hezarkhani, A., 2006, Mass changes during hydrothermal alteration/mineralization at the Sar-Cheshmeh porphyry copper deposit, southeastern Iran: International Geology Review, v. 48, p. 841-860.

Hikov, A., Lerouge, C., Velinova, N., Хиков, А., Катрин, Л., and Велинова, Н., 2010, Geochemistry of alunite group minerals in hydrothermally altered rocks from the Asarel porphyry copper deposit, Central Srednogorie: Review of the Bulagrian Geological Society, v. 71, p.133-148.

Hill, K. C., and Raza, A., 1999, Arc-continent collision in Papua Guinea: Constraints from fission track thermochronology: Tectonics, v. 18, p. 950-966.

Hill, K. C., Keetley, J. T., Kendrick, R. D., and Sutriyono, E., 2002, Structure and hydrocarbon potential of the New Guinea Fold Belt, in McClay, K., ed., Proceedings of the Thrust Tectonics 1999 Conference, Egham, England: American Association of Petroleum Geologists.

Holliday, J. R., and Cooke, D. R., 2007, Advances in geological models and exploration methods for copper ± gold porphyry deposits, in Milkereit, B. ed., Proceedings of the Fifth Decennial International Conference on Mineral Exploration, Toronto, Canada, p. 791-809.

International Seismological Centre, 2009, Global seismic data from 1964-2009: Bulletin of the International Seismological Centre, Thatcham, United Kingdom, www.isc.ac.uk/iscgem

Irvine, T. N., and Baragar, W. R. A., 1971, A guide to the chemical classification of the common volcanic rocks: Canadian Journal of Earth Sciences, v. 8, p. 523-548.

Jobin, Y., 2004, High sulfidation enargite-pyrite veins at Cerro de Pasco, Peru: A mineralogical study of ore and alteration minerals and an infra-red fluid inclusion study on enargite: Unpublished MSc Thesis, University of Geneva, 139 p.

John, D. A., Ayuso, R. A., Barton, M. D., Blakely, R. J., Bodnar, R. J., Dilles, J. H., Gray, Floyd, Graybeal, F. T., Mars, J. C., McPhee, D. K., Seal, R. R., Taylor, R. D., and Vikre, P. G., 2010, Porphyry copper deposit model, Chapter B of Mineral deposit models for resource assessment: U.S. Geological Survey Scientific Investigations Report 2010–5070–B, 169 p.

Jones, B. K., 1992, Application of metal zoning to gold exploration in porphyry copper systems: Journal of Geochemical Exploration, v. 43, p. 127-155

Kearey, P., Klepeis, K. A., and Vine, F. J., 2009: Global tectonics. John Wiley & Sons, Oxford, England.

Kesler, S. E., 1973, Copper, molybdenum, and gold abundances in porphyry copper deposits: Economic Geology, v. 68, p. 106-112.

Kesler, S. E., Chryssoulis, S. L., and Simon, G., 2002, Gold in porphyry copper deposits: its distribution and fate: Ore Geology Reviews, v. 21, p. 103-124.

Knapp, J. H., and Heizler, M. T., 1987, Thermal history of crystalline nappes of the Maria fold and thrust belt, west central Arizona: Journal of Geophysical Research, v. 95, no. B12, p. 20049-20073.

Knesel, K. M., Cohen, B. E., Vasconcelos, P. M., and Thiede, D. S., 2008, Rapid change in drift of the Australian plate records collision with Ontong Java plateau: Nature, v. 454, p. 754-757.

Kopi, G., Findlay, R. H., and Williams, I., 2000, Age and provenance of the Owen Stanley Metamorphic Complex, East Papuan Composite Terrane, Papua New Guinea: Geological Survey of Papua New Guinea, Report (unpublished).

Kuno, H., 1968, Differentiation of basalt magmas, in Hess, H. H., and Poldervaart, A. A., eds., Basalts: The Poldervaart Treatise on Rocks of Basaltic Composition: Interscience, New York, p. 623-688.

Large, R. R., Danyushevsky, L., Hollit, C., Maslennikov, V., Meffre, S., Gilbert, S., Bull, S., Scott, R., Emsbo, P., Thomas, H., Singh, B., and Foster J., 2009, Gold and Trace Element Zonation in Pyrite Using a Laser Imaging Technique: Implications for the Timing of Gold in Orogenic and Carlin-Style Sediment-Hosted Deposits: Economic Geology, v. 102, p. 1232-1267.

Leach T. M., 1977, Petrographic and XRD study of a suite of twenty four core samples from the drill holes WR153 and WR154, Wafi River, PNG. CRA Exploration report (unpublished).

Leach, T. M., 1989, Evaluation of rock chips, drillcore, bench and regional surface samples from the Wafi River prospect, PNG: Elders Resources report (unpublished), 261 p.

Leach, T. M., 1990a, Mineralogy of ninety-eight fresh, transitional, and oxide intervals from the Wafi Deposit, PNG: Elders Resources report (unpublished), 110 p.

Leach, T. M., 1990b, The occurrence and distribution of gold in samples from Wafi, PNG: Elders Resources report (unpublished), 52 p.

Leach, T. M., 1990c, Rock type and mineralogy of forty-nine metallurgical crushed core and percusion [sic] chip samples from the Wafi deposit, PNG: Elders Resources report (unpublished), 116 p.

Leach, T. M., 1990d, Surface petrology of silica cap, Zone C and Malaria, Denge [sic] and Hesson Creek Zones, Wafi Deposit, PNG: Elders Resources report (unpublished), 136 p.

Leach, T. M., 1991a, Interpretation of petrological data from drillholes WR 87, 89, 91, 92, 93, 94, and 95; and surface samples from the Wafi River prospect, PNG: Elders Resources / CRA Exploration JV report (unpublished), v. 1, 103 p.

Leach, T. M., 1991b, Interpretation of petrological data from drillholes WR 87, 89, 91, 92, 93, 94, and 95; and surface samples from the Wafi River prospect, PNG: : Elders Resources / CRA Exploration JV report (unpublished), v. 2, 243 p.

Leach, T. M., 1995, Field report on models of gold mineralisation and advanced argillic alteration at Wafi River, PNG: CRA Exploration report (unpublished), 6 p.

Leach, T. M and Erceg, M. M., 1990. The Wafi high sulphur epithermal gold deposit, Papua New Guinea, Proceedings of the Pacific Rim Congress, Melbourne, Australia: The Australian Institute of Mining and Metallurgy, p. 451-456.

Leach, T. M., and Corbett, G. J., 1993, Porphyry-related carbonate base metal gold systems: The transition between the epithermal and porphyry environments, in Second national meeting, Specialist Group in Economic Geology, Armidale, New South Wales: Geological Society of Australia Abstracts, v. 34, p. 39-40.

License P. S., 1994, Zone A mineralization (a bulk disseminated sediment hosted hybrid high sulphidation gold deposit situated along the edge of the Wafi diatreme): CRA Exploration report (unpublished).

Loffler, E., 1977, Geomorphology of Papua New Guinea. Australian National University Press, Canberra, Australia, 195 p.

Love, D. A., Clark, A. H., Hodgson, C. J., Mortensen, J. K., Archibald, D. A., and Farrar, E., 1998, The timing of adularia-sericite-type mineralization and alunite-kaolinite-type alteration, Mount Skukum epithermal gold deposit, Yukon Territory, Canada; 40Ar-39Ar and U-Pb geochronology: Economic Geology, v. 93, p. 437-462.

Lus, W. Y., McDougall, I., and Davies, H. L., 2004, Age of the metamorphic sole of the Papuan Ultramafic Belt ophiolite, Papua New Guinea: Tectonophysics, v. 394, p. 85-101.

Mahoney, J. J., Storey, M., Duncan, R. A., Spencer, K. J., and Pringle, M., 1993, Geochemistry and geochronology of Leg 130 basement lavas: Nature and origin of the Ontong Java Plateau: Proceedings of the Ocean Drilling Program, Scientific Results, v. 130, p. 3-22.

Markey, R., Stein, H. J., Hannah, J. L., Zimmerman, A., Selby, D., and Creaser, R. A., 2007, Standardizing Re-Os geochronology: a new molybdenite reference material (Henderson, USA) and the stoichiometry of Os salts: Chemical Geology, v. 244, p. 74-87.

Martin, U., Németh, K., Lorenz, V., and White, J. D. L., 2007, Maar-diatreme volcanism and associated processes: Journal of Volcanology and Geothermal Research, Special Issue 159, 312 p.

Masterman, G. J., 2003, Geology of the Rosario Cu-Mo-Ag mine, Collahuasi, Chile: Unpublished PhD thesis, CODES Centre for Ore Deposit Research, University of Tasmania, 253 p.

Montgomery, D. R., and Brandon, M. T., 2002, Topographic controls on erosion rates in tectonically active mountain ranges: Earth and Planetary Science Letters, v. 201, p. 481-489.

Morehari G. I., 2007, Annual report for EL440 - Mt Wanion, Morobe Province, Papua New Guinea: Harmony Mining Limited report (unpublished), 31 p.

Morehari G. I., Tekeve, B., and Spence, B.A., 2009, Annual report for EL440 - Mt Wanion, Morobe Province, Papua New Guinea: Morobe Mining Joint Ventures report (unpublished), 40 p.

Nelson, R. W., Bartram, J. A., and Christie, M. H., 1990, Hidden Valley gold-silver deposit, in Hughes, F.E., ed., Geology of the mineral deposits of Australia and Papua New Guinea: Australasian Institute of Mining and Metallurgy, Monograph Series, v. 14, p. 1763-1767.

Newcrest Mining Limited, 2012, Golpu Pre-Feasibility Study and Reserve Announcement, http://www.newcrest.com.au/media/resource_reserves/2012/August_2012_Golpu_Pre-Feasibility_Study_and_Reserve_Announcement.pdf

Ohmoto, H., and Rye, R. O., 1979, Isotopes of sulfur and carbon, in Barnes, H. L., ed., Geochemistry of Hydrothermal Ore Deposits: Wiley Interscience, New York, p. 509-567.

Pearce, J. A., 1982, Trace element characteristics of lavas from destructive plate boundaries: in Thorpe, R. S., ed., Andesites: Wiley, New York, p. 525-548.

Pearce, J. A., Harris, N. B., and Tindle, A. G., 1984, Trace element discrimination diagrams for the tectonic interpretation of granitic rocks: Journal of petrology, v. 25, p. 956-983.

Pearce, J. A., and Peate, D. W., 1995, Tectonic implications of the composition of volcanic arc magmas: Annual Review of Earth and Planetary Sciences, v. 23, p. 251-285.

Peccerillo, A., and Taylor, S. R., 1976, Geochemistry of Eocene calc-alkaline volcanic rocks from the Kastamonu area, northern Turkey: Contributions to Mineralogy and Petrology, v. 58, p. 63-81.

Pegler, G., Das, S., and Woodhouse, J. H., 1995, A seismological study of the eastern New Guinea and the western Solomon Sea regions and its tectonic implications: Geophysical Journal International, v. 122, p. 961-981.

Plane, M., 1972, A New Guinea fossil macropodid (Marsupiala) from the marine Pliocene of the National Museum, Victoria: National Museum Memoirs,v. 33, p 33-36.

Pohn, H. A., 2000, Lateral ramps in the folded Appalachians and in overthrust belts worldwide: a fundamental element of thrust-belt architecture, U.S. Dept. of the Interior, U.S. Geological Survey, v. 2163.

Pollard, P. J., Taylor, R. G., and Peters, L., 2005, Ages of intrusion, alteration, and mineralization at the Grasberg Cu-Au deposit, Papua, Indonesia: Economic Geology, v. 100, p. 1005-1020.

Rainbow, A., Clark, A. H., Kyser, T. K., Gaboury, F., and Hodgson, C. J., 2005, The Pierina epithermal Au-Ag deposit, Ancash, Peru: Paragenetic relationships, alunite textures, and stable-isotope geochemistry: Chemical geology, v. 215, p. 235-252.

Reich, M., Kesler, S. E., Utsunomiya, S., Palenik, C. S., Chryssoulis, S. L., and Ewing, R. C., 2005, Solubility of gold in arsenian pyrite: Geochimica et Cosmochimica Acta, v. 69, p. 2781-2796.

Reid, R., and Gossage, B., 2012, Wafi Resource Model Report. Morobe Mining Joint Ventures internal report (unpublished), 1 p.

Richards, J. P., 2009, Post-subduction porphyry Cu-Au and epithermal Au deposits—Products of remelting of subduction modified lithosphere: Geology, v. 37, p. 247-250.

Richards, J. P., 2011, Magmatic to hydrothermal metal fluxes in convergent and collided margins: Ore Geology Reviews, v. 40, p. 1-26.

Ripper, I. D., 1982, Seismicity of the Indo-Australian / Solomon Sea plates boundary in the southeast Papua region: Tectonophysics, v. 87, p. 355-369.

Robinson, B. W., and Kusakabe M., 1975, Quantitative preparation of sulfur dioxide, for 34S/32S analyses, from sulfides by combustion with cuprous oxide: Analytical Chemistry, v. 47, p. 1179-1181.

Roedder, E., 1971, Fluid inclusion studies on porphyry-type ore deposits at Bingham (Utah), Butte (Montana), and Climax (Colorado): Economic Geology, v. 66, p. 98-120.

Rohrlach, B. D., and Loucks, R. R., 2005, Multi-million-year cyclic ramp-up of volatiles in a lower crustal magma reservoir trapped below the Tampakan copper-gold deposit by Mio-Pliocene crustal compression in the southern Philippines, in Porter, T.M., ed., Super porphyry copper and gold deposits—A global perspective: Porter GeoConsultancy Publishing, Adelaide, Australia, v. 2, p. 369-407.

Ryan, S.J., and Vigar, A., 1999, Discovery of the high-grade gold Link Zone at Wafi, PNG: Pacrim '99 Congress, Bali, Indonesia, 1999, Proceedings: Melbourne, Australasian Institute of Mining and Metallurgy, p. 65–72.

Ryan, W. B. F., Carbotte, S. M., Coplan, J.O., O'Hara, S., Melkonian, A., Arko, R., Weissel, R.A., Ferrini, V., Goodwillie, A., Nitsche, F., Bonczkowski, J., and Zemsky., R., 2009, Global Multi-Resolution Topography synthesis, Geochemistry, Geophysics, Geosystems, v. 10, Q03014.

Rye, R.O., 1993, The evolution of magmatic fluids in the epithermal environment: The stable isotope perspective: Economic Geology, v. 88, p. 733-753.

Sapiie, B., Natawidjaya, D. H., and Cloos, M., 1999, Strike-slip tectonics of New Guinea: Transform motion between the Caroline and Australian plates, in Busono, I., and Alam, H., eds., Developments in Indonesian tectonics and structural geology: Proceedings of the 28th Annual Convention of the Indonesian Association of Geologists, Jakarta, Indonesia, p. 1-15.

Schmid, R., Fettes, D., Harte, B., Davis E., and Desmons, J., 2007, A systematic nomenclature for metamorphic rocks: 1. How to name a metamorphic rock: Recommendations by the IUGS Subcommission on the Systematics of Metamorphic Rocks, https://www.bgs.ac.uk/scmr/docs/papers/paper_1.pdf

Seedorff, E., Dilles, J. H., Proffett, J. M., Jr., Einaudi, M. T., Zurcher, L., Stavast, W. J. A., Johnson, D. A., and Barton, M. D., 2005, Porphyry deposits: Characteristics and origin of hypogene features: Economic Geology 100th Anniversary Volume, p. 251-298.

Self, S., Kienle, J., and Huot, J. P., 1980, Ukinrek maars, Alaska, II. Deposits and formation of the 1977 craters: Journal of Volcanology and Geothermal Research, v. 7, p. 39-65.

Shedden, S. H., 1979, First annual report for EL440 - Mt Wanion, Morobe Province, Papua New Guinea: Conzinc Riotinto of Australia report (unpublished).

Sillitoe, R. H., 1972, A plate tectonic model for the origin of porphyry copper deposits: Economic Geology, v. 67, p.184-197.

Sillitoe, R. H., 1985, Ore-related breccias in volcanoplutonic arcs: Economic Geology, v. 80, p. 1467-1514.

Sillitoe, R. H., 1994, Comments on recent exploration results from the Wafi porphyry copper-gold system, Papua New Guinea. CRA Exploration report (unpublished).

Sillitoe, R. H., 1995, Exploration of porphyry copper lithocaps, in Mauck, J. L., and St George, J. D., eds., Proceedings of the Pacific Rim Congress, Auckland, New Zealand: The Australian Institute of Mining and Metallurgy, p. 527-532.

Sillitoe, R. H., 1997, Characteristics and controls of the largest porphyry copper-gold and epithermal gold deposits in the circum-Pacific region: Australian Journal of Earth Sciences, v. 44, p. 373-388.

Sillitoe, R. H., 1999, Styles of high-sulphidation gold, silver and copper mineralisation in porphyry and epithermal environments: Proceedings of the Pacific Rim Congress, Bali, Indonesia: Australasian Institute of Mining and Metallurgy, p. 29-44.

Sillitoe, R. H., 2000, Gold-rich porphyry deposits: Descriptive and genetic models and their role in exploration and discovery: Reviews in Economic Geology, v. 13, p. 315-345.

Sillitoe, R. H., 2010, Porphyry copper systems: Economic Geology, v. 105, p. 3-41.

Sillitoe, R. H., and Hedenquist, J. W., 2003, Linkages between volcanotectonic settings, ore-fluid compositions, and epithermal precious metal deposits: Society of Economic Geologists Special Publication 10, p. 315-343.

Sillitoe, R. H., Tolman, J., and Van Kerkvoort, G., 2013, Geology of the Caspiche porphyry gold-copper deposit, Maricunga Belt, northern Chile: Economic Geology, v. 108, p. 585-604.

Singer, D. A., Berger, V. I., and Moring, B. C., 2002, Porphyry copper deposits of the world—Database, maps, and preliminary analysis: U.S. Geological Survey Open File Report 2002–268, 62 p.

Singer, D.A., Berger, V.I., and Moring, B.C., 2008, Porphyry copper deposits of the world—Database and grade and tonnage models, 2008: U.S. Geological Survey Open File Report 2008–1155, 45 p.

Smit, J. A. J., Dow, D. B., Pitt, R. P. B., and Pillinger, D. M., 1974, Wau Sheet SB55-14, Papua New Guinea 1:250,000 Geological Series: Bureau of Mineral Resources, Geology and Geophysics and Department of Lands, Surveys and Mines, Canberra and Port Moresby.

Stoffregen, R. E., 1987, Genesis of acid-sulfate alteration and Au-Cu-Ag mineralization at Summitville, Colorado: Economic Geology, v. 82, p. 1575-1591.

Streckeisen, A. L., 1976, Classification and nomenclature of igneous rocks: Earth Science Reviews, v. 12, p. 1-35.

Sun, S. S., and McDonough, W. F., 1989, Chemical and isotopic systematics of oceanic basalts: Implications for mantle composition and processes, in Saunders, A. D., and Norry, M. J., eds., Magmatism in the ocean basins: Geological Society of America Special Publication 42, p. 313-345.

Sun, W. D., Liang, H. Y., Ling, M. X., Zhan, M. Z., Ding, X., Zhang, H., Yang, X. Y., Li, Y., Ireland, T.R., Wei, Q. R., and Fan, W. M., 2013, The link between reduced porphyry copper deposits and oxidized magmas: Geochimica et Cosmochimica Acta, v. 103, p. 263-275.

Suzuki, K., Shimizu, H., and Masuda, A., 1996, ReOs dating of molybdenites from ore deposits in Japan: Implication for the closure temperature of the ReOs system for molybdenite and the cooling history of molybdenum ore deposits: Geochimica et Cosmochimica Acta, v. 60, p. 3151-3159.

Tau-Loi, D., 1996, Geology and genesis of the Wafi porphyry and high sulphidation epithermal Cu-Au system: Unpublished MSc thesis, University of Western Australia, 119 p.

Tau-Loi, D., and Andrew, R. L., 1998, Wafi copper-gold deposit: Geology of Australian and Papua New Guinean Mineral Deposits, p. 827-831.

Taylor, B. E., 1987, Stable isotope geochemistry of ore-forming fluids, in Kyser, T. K., ed., Short course in stable isotope geochemistry of low temperature fluids: Mineralogical Association of Canada Shortcourse Handbook, v. 13, p. 337-445.

Taylor, B. E., Goodliffe, A. M., and Martinez, F., 1999, How continents break up: Insights from Papua New Guinea: Journal of Geophysical Research, v. 104, p. 7497-7512.

Taylor, J. R., 1982, An Introduction to Error Analysis: The Study of Uncertainites in Physical Measurements: University Science Books, Mill Valley, California, 270 p.

Tingey, R.J., and Grainger, O.J., 1976, Markham 1:250,000 geological map and exploratory notes, sheet SB/55-10: Papua New Guinea Geological Survey.

Titley, S. R., 1982, The style and progress of mineralization and alteration in porphyry copper systems, in Titley, S. R., ed., Advances in geology of the porphyry copper deposits, southwestern North America: University of Arizona Press, Tucson, Arizona, p. 93-116.

Tregoning, P., McQueen, H., Lambeck, K., Jackson, R., Little, R., Saunders, S. and Rosa, R., 2000, Present-day crustal motion in Papua New Guinea: Earth Planets Space, v. 52, p. 727-730.

Tregoning, P., and Gorbatov, A., 2004, Evidence for active subduction at the New Guine Trench: Geophysical research letters, v. 31, L13608.

Tudor A., Morehari G., Sine J., Tau-Loi D., and Mesak F., 1997, Annual report for EL440 - Mt Wanion, Morobe Province, Papua New Guinea: CRA Exploration report (unpublished), 45 p.

Ulrich, T., Günther, D., and Heinrich, C. A., 2001, The evolution of a porphyry Cu-Au deposit, based on LA-ICP-MS analysis of fluid inclusions: Bajo de la Alumbrera, Argentina: Economic Geology, v. 96, p. 1743-1774.

Ulrich, T., and Heinrich, C. A., 2002, Geology and alteration of the porphyry Cu-Au deposit at Bajo de la Alumbrera, Argentina: Economic Geology, v. 97, p. 1865-1888.

Verave, R. T., and Kawagle, S. A., 2010, The Geological framework of Papua New Guinea - An overiew, in Miura, S., Noguchi, N., Coffin, M. F., Kawagle, S. A., and Verave, R. T.: R/V Kairei KR10-05 Cruise Report (unpublished), 88 p.

Vespermann, D., and Schmincke, H.-U., 2000, Scoria cones and tuff rings, in Sigurdsson, H., Houghton, B.F., McNutt, S.R., Rymer, H., and Stix, J. eds., Encyclopedia of Volcanoes: Academic Press, San Diego, p. 683-694.

Whalen, J. B., Britten, R. M., and McDougall, I., 1982, Geochronology and geochemistry of the Frieda River prospect area, Papua New Guinea: Economic Geology, v. 77, p. 592-616.

White, N. C., 1991, High-sulfidation epithermal gold deposits: Characteristics and a model for their origin: Geological Survey of Japan Report, v. 277, p. 9-20.

Wilkinson, J. J., 2013, Triggers for the formation of porphyry ore deposits in magmatic arcs: Nature Geoscience, v. 6, p. 917-925.

Williams-Jones, A. E., Migdisov, A. A., Archibald, S. M., and Xiao, Z. F., 2002, Vapor-transport of ore metals: Geochemical Society Special Publication 7, p. 279–305.

Williamson, A., and Hancock, G., 2005, The geology and mineral potential of Papua New Guinea: Papua New Guinea Department of Mining, Port Moresby, Papua New Guinea, 154 p.

Wilson, A. J., Cooke, D. R., Harper, B. J., and Deyell, C. L., 2007, Sulfur isotopic zonation in the Cadia district, south-eastern Australia—Exploration significance and implication for the genesis of alkalic porphyry gold-copper deposits: Mineralium Deposita, v. 42, p. 465-487.

Winter, J. D., 2010, Principles of igneous and metamorphic petrology, v. 2, Cambridge University Press, New York, 702 p.

Zhang, L., Leach, T., and Merchant, R., 1997, Petrographic investigations of drill core samples from holes WR158, WR159, and WR160, Wafi River Prospect, Papua New Guinea: CRA Exploration report (unpublished).

Appendix A
Detailed Petrographic Descriptions

Selected thin section descriptions are provided in the following tables. Identified phases are described by modal abundance, crystal size (if possible), and mineral habit and occurrence. The abundances of relict phases, where identified, are indicated in brackets. For example, 8 vol % relict hornblende phenocrysts up to 1.5 mm long may be described as follows: "(8) / 0.6 - 1.5 mm / subhedral rhombs replaced by biotite and trace disseminated chalcopyrite." Relict phases do not contribute to the total mineral abundance in the sample. The third row in each sample ("Representative of:") indicates whether the thin section area was sampled as approximately representative of a wide interval, or particular features such as a single vein. Gold assays from the corresponding metre interval are included for each sample. Abbreviations used are:

vfgr: very fine-grained, grains < 0.1 mm

fgr: fine-grained, 0.1 - 1 mm in diameter (longest dimension)

mgr: medium-grained, 1 - 3 mm in diameter

cgr: coarse-grained, > 3 mm in diameter

cpy, sph, py (used sparingly): chalcopyrite, sphalerite, pyrite

Hole ID	177	177	199
Depth (m)	310.7	369.5	269.8
Representative of:	Zone	Zone	Zone
Protolith lithotype	Metasiltstone	Metasiltstone	Metasiltstone
Mineral assemblage	Muscovite-pyrite, quartz-pyrite-adularia	Muscovite-pyrite, quartz-pyrite-adularia	Biotite, muscovite, quartz-pyrite-adularia
Alteration texture	Pervasive, vein, and vein halo	Pervasive, vein, and vein halo	Vein and vein halo
Alteration intensity	Intense	Intense	Intense
Description	Light tan to rusty (jarosite + hematite-stained), intensely muscovite-altered metasiltstone with disseminated and vein pyrite. Most of the protolith minerals are obscured by intense muscovite (+ clay?) alteration. Quartz - pyrite veins make up ~ 8 % of the thin section.	Tan muscovite - clay - pyrite altered metasiltstone cut by ~ 10 % quartz - pyrite veins < 2 mm wide. Thin section reveals that the quartz-pyrite veins taper to anastomosing arrays of veinlets < 0.1 mm wide.	Mottled dark grey and tan, intensely altered metasiltstone with ~ 10 % quartz-pyrite veins < 3 mm across, with muscovite alteration halos < 1 cm wide. The muscovite alteration halos have overprinted fine-grained biotite (+ chlorite?) alteration.
Notes, interpretation	Link Zone sample. Pyrrhotite inclusions < 0.1 mm across occur in some disseminated pyrite grains	Link Zone. 8.3 % S	Link Zone. Earlier biotite evident in replacement of plagioclase grains between vein halos, also visible in hand sample
Au (ppm)	16	7.35	0.95
	vol % / size (mm) / habit, occurrence	vol % / size (mm) / habit, occurrence	vol % / size (mm) / habit, occurrence
Quartz (disseminated)	50 / vfgr / rounded clasts throughout	44 / vfgr / rounded clasts throughout	40 / vfgr / rounded clasts throughout
Quartz (vein)	5 / < 4 mm wide / irregular veinlets with pyrite and trace orthoclase (adularia)	10 / < 2 mm wide	5 / < 3 mm wide / veins with pyrite and trace orthoclase (adularia)
Plagioclase	(30?) / vfgr / possible relict clasts, rounded as in quartz grains	(30?) / vfgr / possible relict clasts, rounded as in quartz grains, muscovite altered	(30?) / vfgr / possible relict clasts, rounded as in quartz grains
Orthoclase	< 1 / vfgr / irregular sericite-dusted lenses within quartz - pyrite veins		< 1 / vfgr / irregular aggregates in quartz - pyrite veins
Hornblende (relict)			
Biotite			6 / vfgr / pleochroic brown replacement of siltstone grains (plagioclase?)
Chlorite			< 1 ? / possible association with biotite
Actinolite			
Muscovite (visible)	5 / vfgr / vein halos to quartz - pyrite veins		8 / vfgr / vein halos to quartz - pyrite veins
Muscovite (sericite) and / or clays	30 / throughout sample, producing semi opaque appearance	40 / throughout sample, weakly selective after grains (of plagioclase?)	30 / throughout sample, more pronounced with proximity to veins
Hematite (dusty)	2 / throughout sample, mostly near pyrite	1 / throughout sample	
Calcite			
Other carbonate		< 1 ? / vfgr high-birefringence grains in quartz veins	
Epidote			
Alunite			
Anhydrite			
Pyrite	8 / < 0.2 / most as very finely disseminated grains, some irregular aggregates in veins	5 / < 0.4 / mostly irregular aggregates in veins, some as very small disseminations	8 / < 0.1 / most as very finely disseminated grains, larger grains occur in veins
Chalcopyrite			
Bornite			
Magnetite			
Specular hematite			
Molybdenite			
Galena			
Covellite			
Chalcocite			
Marcasite			
Arsenopyrite			3 ? / fine coatings on pyrite
Other mineral (specified)	Pyrrhotite < 1 / < 0.1 / rounded inclusions within disseminated pyrite grains		
Other mineral (specified)			

Hole ID	199	301	301
Depth (m)	285.0	150.0	353.8
Representative of:	Zone	Zone	Zone
Protolith lithotype	Metasiltstone	Wafi breccia complex	Metasiltstone
Mineral assemblage	Muscovite-pyrite, quartz-pyrite-adularia	Kaolinite-alunite-muscovite-pyrite	Muscovite-kaolinite-pyrite
Alteration texture	Pervasive and vein halo	Pervasive to selective	Pervasive, vein, and vein halo
Alteration intensity	Intense	Strong	Intense
Description	Tan to light grey, muscovite - clay - pyrite altered metasiltstone cross-cut by quartz - pyrite - adularia veins. Grey-tinged high-As pyrite or arsenopyrite occur as acicular rims to some pyrite grains. Many pyrite grains contain inclusions of chalcopyrite and pyrrhotite.	White or very pale tan, strongly sericite - clay - alunite (+pyrophyllite) altered, fragment-supported chaotic polymict breccia, with angular fragments 0.1-2 mm across.	Light tan-pink, intensely clay (kaolinite?) - muscovite - hematite altered metasiltstone, with several quartz - pyrite - muscovite veins containing quartz and muscovite alteration halos
Notes, interpretation	Link Zone.	Appears to contain few fragments in hand sample, but thin section shows abundant fragments < 2 mm long	
Au (ppm)	3.67	0.08	0.58
	vol % / size (mm) / habit, occurrence	vol % / size (mm) / habit, occurrence	vol % / size (mm) / habit, occurrence
Quartz (disseminated)	41 / vfgr / rounded clasts	20 / < 0.5 / anhedral	60 / vfgr / rounded clasts
Quartz (vein)	20 / < 8 mm wide		5 / < 1 mm wide
Plagioclase		(20) / < 0.5 / anhedral in infill, and relict (sericite-replaced) fragments < 2 mm long	(20?) likely relict siltstone grains, not identifiable due to clay alteration
Orthoclase	5 (adularia) / < 1 / aggregates in quartz veins, confirmed by SEM		
Hornblende (relict)		(10) / 0.2 - 0.6 / anhedral to subhedral relict fragments replaced by biotite or clays	
Biotite	5 / vfgr / throughout sample	3 / < 0.2 / disseminated anhedral grains	
Chlorite			
Actinolite			
Muscovite (visible)	5 / vfgr / as halos to quartz - pyrite veins		
Muscovite (sericite) and / or clays	15 / pervasive	45 // preferentially after breccia infill	25 / pervasive
Hematite (dusty)	5 / most near pyrite veins	2 // preferentially along fragment margins	5 / throughout sample
Calcite			
Other carbonate			
Epidote			
Alunite		15 / 0.1 / subhedral, randomly oriented blades throughout breccia infill	
Anhydrite			
Pyrite	8 / vfgr / disseminated grains and in quartz veins	5 / 0.1-1 / disseminated anhedral aggregates and diffuse veins or lenses < 0.2 mm wide	5 / < 0.1 / veins and rounded disseminated grains
Chalcopyrite	< 1 / < 0.1 / rounded inclusions in pyrite		
Bornite			
Magnetite			
Specular hematite			
Molybdenite			
Galena			
Covellite			
Chalcocite			
Marcasite	< 1 ? / < 0.1 / acicular inclusions in py		
Arsenopyrite	1 / acicular coatings < 0.2 mm on pyrite		
Other mineral (specified)	pyrrhotite < 1 / < 0.1 / incl in py	Enargite < 1 / < 0.1 / very finely disseminated after relict hornblende (?) fragments	One grain of pleochroic yellow mineral (?) < 0.2 mm across in quartz - pyrite veins
Other mineral (specified)		Pyrophyllite 10 ? / < 0.1 / blades (low birefringence, otherwise similar to alunite)	

Hole ID	321	321	321
Depth (m)	812.2	949.4	952.1
Representative of:	Zone	Zone	Zone
Protolith lithotype	Metasiltstone	Diorite II (hornblende-plag)	Diorite II (hornblende-plag)
Mineral assemblage	Biotite-muscovite-hematite	Orthoclase-biotite-quartz, muscovite	Biotite-orthoclase-quartz-magnetite-cpy
Alteration texture	Pervasive and vein	Selective and vein	Selective and vein
Alteration intensity	Strong	Strong	Strong
Description	Red-tinged, biotite - muscovite - hematite altered metasiltstone cross-cut by quartz - pyrite - chalcopyrite veins	Light grey-green, strongly orthoclase-altered, crowded plagioclase- and hornblende-phyric diorite	Grey-green, strongly orthoclase-altered, plagioclase- and hornblende-phyric diorite containing ~ 10 % quartz - sulfide veins
Notes, interpretation		Examples of well preserved relict hornblende phenocrysts in strongly altered diorite	
Au (ppm)	0.17	0.72	1.11
	vol % / size (mm) / habit, occurrence	vol % / size (mm) / habit, occurrence	vol % / size (mm) / habit, occurrence
Quartz (disseminated)	25 / vfgr / grains in protolith	30 / vfgr / alteration throughout groundmass	39 / vfgr / throughout groundmass
Quartz (vein)	20 / 1 - 7 mm wide	5 / 1 - 3 mm wide	10 / 1 -2 mm wide
Plagioclase	(20) ? / vfgr / clasts in protolith	(30) / 0.5 - 2 / subhedral phenocrysts	(40) / 1 - 2 / subhedral (mostly rectangular) phenocrysts
Orthoclase		15 / vfgr / throughout groundmass and rimming phenocrysts	13 / vfgr / throughout groundmass and rimming phenocrysts
Hornblende (relict)		(20) / 1 - 2.5 / subhedral-euhedral rhombs	(15) / 1.5 - 2 / subhedral rhombs
Biotite	35 / < 0.5 / laths throughout sample	20 / < 0.5 / after hornblende	20 / < 0.5 / after hornblende
Chlorite		5 / < 0.5 / after hornblende	3 / as in biotite
Actinolite			
Muscovite (visible)			
Muscovite (sericite) and / or clays	14 / distributed throughout sample (between quartz veins)	19 / after plagioclase and groundmass	10 / throughout sample
Hematite (dusty)	5 / as in sericite		
Calcite		2 / vfgr / disseminated throughout sample	
Other carbonate			
Epidote			
Alunite			
Anhydrite			
Pyrite	< 1 / vfgr / disseminated grains throughout sample, some in quartz veins	1 / vfgr / disseminated grains and diffuse veins < 2 mm wide	2 / vfgr / disseminated grains and diffuse veins < 1 mm wide
Chalcopyrite	1 / as in pyrite	3 / < 0.5 / as in pyrite	3 / < 0.5 / as in pyrite
Bornite			
Magnetite			
Specular hematite			
Molybdenite			
Galena			
Covellite			
Chalcocite			
Marcasite			
Arsenopyrite			
Other mineral (specified)			
Other mineral (specified)			

Hole ID	337	337	347
Depth (m)	1182.4	1220.2	669.3
Representative of:	Zone	Patch (chalcopyrite-molybdenite)	Zone
Protolith lithotype	Diorite II (hornblende-plag)	Diorite II (hornblende-plag)	Metasandstone
Mineral assemblage	Orthoclase-quartz-cpy, magnetite-hematite	Quartz-orthoclase-chalcopyrite-molybdenite	Kaolinite-muscovite-pyrite
Alteration texture	Vein and pervasive	n/a	Pervasive and vein halo
Alteration intensity	Strong	n/a	Strong
Description	Mottled green, red, and white diorite with quartz - chalcopyrite veins. hornblende phenocrysts are replaced by biotite and magnetite + hematite; plagioclase phenocrysts are replaced by orthoclase	~ 60% of the thin section is an irregular zone of chalcopyrite (+Mo, Au), remainder is quartz - orthoclase altered diorite	Grey, strongly kaolinite- and muscovite-altered metasandstone, with sparse quartz - pyrite veins < 1 mm wide lined with diffuse kaolinite alteration halos
Notes, interpretation	Late chalcopyrite veins contain specularite and magnetite	Example of native gold as rims to magnetite	
Au (ppm)	1.55	1.61	0.02
	vol % / size (mm) / habit, occurrence	vol % / size (mm) / habit, occurrence	vol % / size (mm) / habit, occurrence
Quartz (disseminated)	19 / vfgr /throughout groundmass	29 / 1 - 2 / aggregates with orthoclase	43 / < 1.5 / rounded grains
Quartz (vein)	20 / < 4 mm wide		5 / < 1 mm wide
Plagioclase	(30) / < 2 / subhedral phenocrysts		(30) ? / grains as in quartz
Orthoclase	20 / perthitic replacement of plagioclase and groundmass	8 / < 0.5 / dusty (sericite-biotite), locally perthitic aggregates with quartz	
Hornblende (relict)	5 / 1 - 2 / subhedral phenocrysts		
Biotite	3 / vfgr / after hornblende	2 / < 0.2 / interstitial to quartz + orthoclase, and as small inclusions in orthoclase	5 / vfgr / possible early alteration stage (prior to kaolinite - muscovite)
Chlorite			5 / as in biotite
Actinolite			
Muscovite (visible)			10 / < 1 / randomly oriented throughout
Muscovite (sericite) and / or clays	10 / after plagioclase and groundmass	6 / dusting orthoclase, particularly near chalcopyrite aggregates	30 / throughout sample, and as halos < 3 mm wide to quartz - pyrite veins
Hematite (dusty)			
Calcite	< 1 / vfgr / after plag	1 / < 0.2 / sparse within quartz-orthoclase	
Other carbonate			
Epidote			
Alunite			
Anhydrite			
Pyrite	1 / vfgr / disseminated grains and veins	2 / 0.05 - 0.2 / subhedral - euhedral crystals in chalcopyrite	2 / vfgr / disseminated grains
Chalcopyrite	4 / < 0.4 / disseminated grains and veins	50 / irregular vein fill > 2 cm wide / contains Au, Mo, pyrite inclusions	< 1 / as in pyrite
Bornite			
Magnetite	15 / vfgr / disseminated grains and aggregates < 1 mm across	< 1 / vfgr / anhderal, mostly as rims to pyrite inclusions in chalcopyrite	< 1 ? / vfgr / disseminated grains (ID is unclear)
Specular hematite	3 / specularite in magnetite aggregates		
Molybdenite		2 / 0.1 - 3.5 / laths within chalcopyrite, 1 large hexagonal plate 3.5 mm across	
Galena		< 1 / 1 possible inclusion in Mo lath	
Covellite			
Chalcocite			
Marcasite			
Arsenopyrite			
Other mineral (specified)		Native gold < 1 / irregular grains 0.06 - 0.1 mm across in chalcopyrite, 1 around mt	
Other mineral (specified)			

Hole ID	347	349	349
Depth (m)	1033.6	50.0	260.6
Representative of:	Zone	Zone	Zone (least-altered)
Protolith lithotype	Diorite II (hornblende-plag)	Metasandstone	Diorite II (hornblende-plag)
Mineral assemblage	Quartz-orthoclase-magnetite-chalcopyrite	Quartz-alunite-clays	Quartz-orthoclase-magnetite-chalcopyrite
Alteration texture	Veins and selective	Pervasive and vein	Selective
Alteration intensity	Intense	Intense, texturally destructive	Weak
Description	Green and white, hornblende-phyric diorite with abundant quartz - sulfide veins and chalcopyrite - magnetite mineralisation. Relict hornblende phenocrysts are pale green in hand sample, and have been replaced by chlorite and possibly clays.	Light pink-beige to white, intensely quartz- and alunite-altered sample with some clay and supergene hematite. A soft white vein of alunite 1 - 5 mm wide cross-cuts the sample.	Grey-green, weakly to moderately altered hornblende- and plagioclase-phyric diorite with well-preserved porphyritic texture. Part of hand sample (not in thin section) contains a zone of pervasive orthoclase alteration (possible vein halo?).
Notes, interpretation			
Au (ppm)	1.33	0.63	0.25
	vol % / size (mm) / habit, occurrence	vol % / size (mm) / habit, occurrence	vol % / size (mm) / habit, occurrence
Quartz (disseminated)	12 / vfgr / alteration throughout diorite	80 ? / vfgr / dusted with clay	10 / vfgr / throughout groundmass
Quartz (vein)	45 / 2 - 15 mm		
Plagioclase	(20) ? / relict phenocrysts < 2 mm replaced by orthoclase		(30),15 / relict phenocrysts < 1 .5 mm replaced by orthoclase, quartz, and muscovite
Orthoclase	20 / throughout diorite (between quartz veins), especially after plagioclase		35 / perthitic throughout groundmass and after plagioclase
Hornblende (relict)	(10) / < 1.5 / anhedral to subhedral rhombs mostly replaced by chlorite (?)		(15) / < 1 / dark anhedral phenocrysts mostly replaced by biotite
Biotite	5 / throughout diorite, mostly after hornblende		14 / vfgr / throughout diorite, mostly after hornblende phenocrysts
Chlorite	2 / as in biotite		
Actinolite			
Muscovite (visible)			
Muscovite (sericite) and / or clays	10 / dusting throughout sample, and after hornblende phenocrysts	9 / dusting throughout sample produces semi-opaque thin section, impedes ID	20 / after plagioclase, hornblende, and groundmass
Hematite (dusty)		1 / throughout sample	
Calcite			
Other carbonate			
Epidote			
Alunite		10 ? / vfgr / possible disseminated alunite as high-birefringence blades, clay-coated	
Anhydrite			
Pyrite	2 / < 0.5 / most in veins, some grains and irregular aggregates throughout sample		2 / vfgr/ disseminated grains, a few aggregates up to 0.4 mm across
Chalcopyrite	3 / as in pyrite, most occurring in quartz veins		3 / as in pyrite, some rimming magnetite
Bornite			
Magnetite	1 / disseminated grains throughout sample		1 / disseminated grains throughout sample, some after hornblende
Specular hematite			
Molybdenite			
Galena			
Covellite			
Chalcocite			
Marcasite			
Arsenopyrite			
Other mineral (specified)			
Other mineral (specified)			

Hole ID	349	377	377
Depth (m)	388.0	761.0	843.0
Representative of:	Zone	Zone (least-altered)	Veins (deep clays-pyrite + carbonate-pyrite)
Protolith lithotype	Metasandstone	Metasandstone	Metasandstone
Mineral assemblage	Biotite-magnetite-chalcopyrite	Chlorite-actinolite-pyrite-epidote	Biotite, kaolinite-pyrite, carbonate-sulfide
Alteration texture	Pervasive	Selective to pervasive	Pervasive and vein
Alteration intensity	Intense	Weak	Moderate
Description	Dark brown to black, intensely biotite-altered metasandstone	Grey-green, weakly propylitic altered, massive metasandstone with clasts 0.5 - 3 mm across	Grey-green to grey-brown, moderately biotite-altered metaconglomerate-metasandstone, cross-cut by (1) a soft, green kaolinite (?) - pyrite vein 2.5 cm wide (most of the sample), in turn cross-cut by (2) a carbonate - pyrite vein 7 mm wide
Notes, interpretation		Possible brownish epidote in this sample	0.03% Cu; 6.43% S; low As-Pb-Zn-Mn
Au (ppm)	0.28	0.14	0.1
	vol % / size (mm) / habit, occurrence	vol % / size (mm) / habit, occurrence	vol % / size (mm) / habit, occurrence
Quartz (disseminated)	40 ? / < 1 / grains masked by biotite	36 / vfgr / grains throughout sandstone	10 / vfgr / grains throughout sandstone
Quartz (vein)	2 / < 0.5 / sparse veinlets with thin quartz alteration halos	1 / 1 mm wide	
Plagioclase		(20) ? / < 0.5 / some relict clasts ? twinning barely visible	(15) ?
Orthoclase			
Hornblende (relict)			
Biotite	42 / vfgr / randomly oriented throughout sample	15 / vfgr / throughout sample	15 / vfgr / throughout sample (outside of veins)
Chlorite	3 / small zones associated with biotite	10 / as in biotite, some blue birefringence	5 / as in biotite
Actinolite		3 / < 0.1 / randomly oriented acicular crystals throughout sample	
Muscovite (visible)		15 / < 0.3 / after sandstone clasts	
Muscovite (sericite) and / or clays	10 / throughout sample, with biotite alteration	10 / throughout sample	55 / throughout sample, and as semi-opaque vein infill to clay-pyrite vein
Hematite (dusty)		5 / dusting selective after some clasts	
Calcite			
Other carbonate			10 / < 2 / within a carbonate-sulfide vein
Epidote		< 1 / < 0.3 / disseminated aggregates	
Alunite			
Anhydrite			
Pyrite	< 1 / < 0.1 / disseminated grains throughout sample	2 / < 0.4 / aggregates with magnetite, some pyrite rimming disseminated magnetite	2 / < 0.5 / disseminated aggregates throughout sample, and in both veins
Chalcopyrite	1 / < 0.1 / disseminated grains throughout sample, more common adjacent to veins	< 1 / < 0.3 / fine rims to magnetite-pyrite aggregates	2 / as in pyrite, and mostly within carbonate-sulfide vein
Bornite			
Magnetite	2 / < 0.1 / vfgr aggregates throughout sample	3 / vfgr - 0.2 / disseminated grains and aggregates, some clast-selective	1 / vfgr / small disseminated grains in biotite-altered wallrock only
Specular hematite			
Molybdenite			
Galena			
Covellite			
Chalcocite			
Marcasite			
Arsenopyrite			
Other mineral (specified)			
Other mineral (specified)			

Hole ID	377	377	377
Depth (m)	887.0	1171.5	1246.0
Representative of:	Zone	Zone	Vein (sulfide breccia vein)
Protolith lithotype	Metasandstone-metaconglomerate	Diorite II (hornblende-plag)	Diorite II (hornblende-plag)
Mineral assemblage	Biotite-chlorite-pyrite-magnetite	Biotite-orthoclase-quartz-magnetite-cpy	Chalcopyrite-bornite-pyrite-molybdenite
Alteration texture	Selective, vein, and vein halo	Pervasive and vein	n/a
Alteration intensity	Moderate	Intense	n/a
Description	Grey-brown to grey-green, moderately biotite - chlorite - epidote - magnetite altered and sparsely veined pebbly metasandstone. The hand sample contains dark vein halos of actinolite which are less obvious in the thin section.	Mottled white and brown, intensely orthoclase-biotite-magnetite-chalcopyrite-pyrite altered diorite with relict, orthoclase-replaced phenocrysts < 1.5 mm across, and abundant quartz-sulfide veins	70% of thin section is a chaotic, infill-supported breccia vein containing 40% sub-angular pyrite fragments 0.1 - 2 mm across in chalcopyrite + bornite cement; remainder is quartz - orthoclase along vein margins
Notes, interpretation	Example of disseminated magnetite associated with biotite alteration	Gold inclusions in late chalcopyrite veins	Cu_pct=3.0
Au (ppm)	0.1	3.57	2.76
	vol % / size (mm) / habit, occurrence	vol % / size (mm) / habit, occurrence	vol % / size (mm) / habit, occurrence
Quartz (disseminated)	27 / < 1 / dusty grains throughout sandstone	10 / vfgr / throughout groundmass	
Quartz (vein)	1 / 1 mm wide	47 / 1 - 8 mm wide / containing sulfides	10 / 0.1 - 1.5 / breccia vein margins, containing chalcopyrite inclusions
Plagioclase	(30) ? / < 1.5 / rounded relict clasts	(10) / 0.7 - 1.5 / subhedral, orthoclase-replaced phenocrysts	
Orthoclase		15 / < 2 / sericite-dusted perthitic grains after plagioclase and rimming hornblende	20 / < 2 / anhedral, weakly twinned, with chalcopyrite inclusions
Hornblende (relict)		(5) / < 2 / subhedral rhombs replaced by biotite-chlorite and some orthoclase	
Biotite	10 / vfgr / throughout sample, possible weak vein halos	5 / < 0.4 / some diffuse with orthoclase alteration, most as selvages to veins	
Chlorite	15 / as in biotite, some after clasts	1 / as in biotite	
Actinolite	5 / vfgr / as in biotite		
Muscovite (visible)			
Muscovite (sericite) and / or clays	30 / evenly distributed throughout sample	5 / dusting after orthoclase or plagioclase	
Hematite (dusty)			
Calcite			
Other carbonate			< 1 / < 1.6 / euhedral terminations into orthoclase
Epidote	5 / vfgr / replacement of some plag grains		
Alunite			
Anhydrite			
Pyrite	4 / < 0.5 / disseminated aggregates	1 / < 2 / aggregates in late chalcopyrite veins	30 / 0.1 - 2 / angular and broken (cpy-veined) fragments
Chalcopyrite	< 1 / vfgr / thin rims to disseminated pyrite	9 / < 8 / disseminated aggregates and late veins with quartz	40 / breccia vein cement
Bornite			< 1 / < 0.5 / irregular aggregates at vein margins, some inclusions in pyrite
Magnetite	3 / vfgr / disseminated grains and aggregates, usually with biotite	7 / vfgr / disseminated grains and diffuse veins < 3 mm wide	
Specular hematite		< 1 / cores in magnetite in late veins	
Molybdenite			< 1 / < 0.6 / anhedral grains at chalcopyrite vein margins
Galena			
Covellite			< 1 / / tarnish (?) after bornite
Chalcocite			
Marcasite			
Arsenopyrite			
Other mineral (specified)	Talc (?) < 5 / irregular, diffuse fibrous patches associated with chlorite	Native gold < 1 / <0.02 (20 microns) across / inclusions in late chalcopyrite veins	
Other mineral (specified)			

Hole ID	377	377	377
Depth (m)	1306.6	1310.0	1328.6 -1
Representative of:	Zone	Veins (porphyry and IS veins?)	Zone
Protolith lithotype	Diorite II (hornblende-plag)	Diorite II (hornblende-plag)	Diorite II (hornblende-plag)
Mineral assemblage	Chlorite-orthoclase-magnetite-chalcopyrite	Orthoclase, carbonate-sulfide, tennantite	Biotite-orthoclase-quartz-magnetite-cpy
Alteration texture	Selective, vein halo, and vein	Selective and vein halo	Vein and pervasive
Alteration intensity	Strong	Strong	Strong
Description	Green, hornblende-phyric diorite, cross-cut by (1) a perthitic orthoclase vein < 3 mm wide, in turn cross-cut by (2) a magnetite vein < 1 mm wide, in turn cross-cut by (3) quartz - chalcopyrite veins	Mottled grey and white, strongly orthoclase-altered and quartz - sulfide veined diorite, cross-cut by (1) a rhodochrosite - pyrite - chalcopyrite vein 1 cm wide (most of the thin section), cross-cut by (2) a rhodochrosite - tennantite - sphalerite - galena vein < 1 mm wide	20% of sample is white, strongly orthoclase-altered, hornblende-phyric diorite. Perthitic feldspar occurs as rims < 0.2 mm wide to some of the hornblende phenocrysts.
Notes, interpretation	Example of magnetite after orthoclase veins, and late (stage IIc) mineralisation	Late rhodochrosite - tennantite - sphalerite - galena vein may be deep portion of intermediate sulfidation veins?	
Au (ppm)	2.21	1.52	3.21
	vol % / size (mm) / habit, occurrence	vol % / size (mm) / habit, occurrence	vol % / size (mm) / habit, occurrence
Quartz (disseminated)	20 / vfgr / groundmass		30 / vfgr / groundmass alteration of plagioclase
Quartz (vein)	18 / < 3 mm wide	85 / < 0.6 / most of sample is vein	
Plagioclase	(20) ? / < 2 / replaced by orthoclase and muscovite		(20),27 / vfgr / groundmass with quartz, some phenocrysts < 1.5 mm (orthoclase altered)
Orthoclase	32 / < 3 / perthitic, occurring throughout diorite, and in a vein 2 - 3 mm wide		15 / rims < 0.2 mm wide / perthitic rims to hornblende, and after plagioclase
Hornblende (relict)	(15) / < 1.5 / subhedral rhombs mostly replaced by chlorite (?)		(20) / 0.5-1.2 / rounded to rhombic relict phenocrysts
Biotite	4 / throughout diorite, mostly after hornblende		5 / vfgr / after hornblende phenocrysts
Chlorite	4 / as in biotite, mostly after hornblende		5 / vfgr / after hornblende phenocrysts
Actinolite			
Muscovite (visible)			
Muscovite (sericite) and / or clays	15 / throughout sample, some after phenocrysts		15 // after phenocrysts
Hematite (dusty)			
Calcite			
Other carbonate		5 / < 0.2 / cement in both vein sets	
Epidote			
Alunite			
Anhydrite			
Pyrite	1 / < 0.5 / disseminated grains and irregular aggregates throughout sample	2 / < 0.5 / grains in both vein sets	1 / < 0.4 / disseminated grains
Chalcopyrite	3 / disseminated as in pyrite, most occurring in late quartz veins	6 / < 0.8 / most occurring in quartz - chalcopyrite - pyrite (+ carbonate) vein	1 / < 0.8 / disseminated grains and aggregates
Bornite			
Magnetite	3 / < 0.5 / disseminated grains and aggregates, and in a vein after orthoclase		1 / vfgr / disseminated throughout sample
Specular hematite			
Molybdenite			
Galena		< 1 / < 0.5 / in late tennantite veinlet	
Covellite			
Chalcocite			
Marcasite			
Arsenopyrite			
Other mineral (specified)		Tennantite 2 / < 0.5 / in late vein with galena, sphalerite, and rhodochrosite	
Other mineral (specified)		Sphalerite < 1 / as in galena, and containing small chalcopyrite inclusions	

Hole ID	377	377	377
Depth (m)	1328.6 -2	1365.0	1392.0
Representative of:	Veins / patches (biotite-quartz)	Zone	Veins (quartz-chalcopyrite-pyrite)
Protolith lithotype	Diorite II (hornblende-plag)	Diorite II (hornblende-plag)	Diorite II (hornblende-plag)
Mineral assemblage	Biotite-orthoclase-quartz-magnetite-cpy	Orthoclase-quartz-magnetite-chalcopyrite	Quartz-chalcopyrite-pyrite
Alteration texture	n/a	Pervasive and vein	n/a
Alteration intensity	n/a	Intense	n/a
Description	80% of sample consists of irregular veins of coarse perthitic feldspar transitioning into biotite laths < 5 mm long, with interstitial quartz and sulfides. The biotite laths contain inclusions of chalcopyrite, magnetite, and possible rutile.	Mottled grey-green and pale pink, intensely orthoclase-chlorite-biotite-magnetite altered, hornblende-phyric diorite, cut by magnetite and quartz - chalcopyrite veins	Mottled white, intensely orthoclase-altered diorite containing abundant quartz - chalcopyrite - pyrite veins, and disseminated chalcopyrite. This thin section description applies to the porphyry quartz - sulfide veins only.
Notes, interpretation			
Au (ppm)	3.21	1.92	3.7
	vol % / size (mm) / habit, occurrence	vol % / size (mm) / habit, occurrence	vol % / size (mm) / habit, occurrence
Quartz (disseminated)		28 / vfgr / alteration throughout groundmass	
Quartz (vein)	29 / < 5 / anhedral aggregates in vein centre	25 / 1 -12 mm wide / planar and undulating veins after a magnetite vein	90 / < 15 mm wide / planar and undulating quartz - sulfide veins
Plagioclase		(20) / < 1.5 / subhedral phenocrysts, altered to orthoclase and muscovite	
Orthoclase	50 / 0.5-2 / Perthitic aggregates at V margins	25 / perthitic alteration after plagioclase, some rimming hornblende phenocrysts	
Hornblende (relict)		(8) / < 0.8 / subhedral phenocrysts generally replaced by biotite - chlorite	
Biotite	15 / < 5 / euhedral laths radiating into vein centre	6 / vfgr / after hornblende	
Chlorite		1 / as in biotite	
Actinolite			
Muscovite (visible)			
Muscovite (sericite) and / or clays		10 / throughout diorite	
Hematite (dusty)			
Calcite			
Other carbonate			
Epidote			
Alunite			
Anhydrite			
Pyrite		1 / vfgr / disseminated grains and aggregates < 0.5 mm, some in quartz veins	2 / < 0.6 / anhedral - subhedral grains mostly within chalcopyrite
Chalcopyrite	5 // Interstitial to biotite, especially near vein walls	4 / < 0.2 / disseminated grains and aggregates, mostly in veins	8 // irregular aggregates throughout quartz veins, some along vein seams
Bornite			
Magnetite	1 / vfgr / most within biotite laths along cleavage	5/ vfgr / disseminated throughout sample, and as a vein < 1 mm wide	< 1 ?/ vfgr / possible inclusions in pyrite grains (ID is unclear)
Specular hematite			
Molybdenite			
Galena			
Covellite			
Chalcocite			
Marcasite			
Arsenopyrite			
Other mineral (specified)	Rutile < 1 / vfgr / elongate inclusions along cleavage planes of large biotite laths		
Other mineral (specified)			

Hole ID	377	377	377
Depth (m)	1399.0	1403.5	1453.4
Representative of:	Zone	Zone (note: quartz veins are over-represented)	Zone
Protolith lithotype	Diorite II (hornblende-plag)	Diorite II (hornblende-plag)	Diorite II (hornblende-plag)
Mineral assemblage	Orthoclase-quartz-magnetite-chalcopyrite	Orthoclase-quartz-magnetite-chalcopyrite	Orthoclase-quartz-magnetite-chalcopyrite
Alteration texture	Vein, vein halo, and selective	Selective and vein	Selective and vein
Alteration intensity	Intense	Strong	Strong
Description	White, intensely orthoclase-altered diorite with 20% quartz-sulfide veins, and ~ 40% sulfides in total, including bornite. The porphyry veins have been cross-cut by minor sphalerite-tennantite veinlets < 1 mm wide.	Patchy red+yellow, hornblende- and plagioclase-phyric diorite. 80% of the thin section consists of quartz - chalcopyrite - pyrite veins. Chalcopyrite veins contain cubanite exsolution lamellae, and native gold inclusions tens of microns across.	Light tan, orthoclase - quartz - biotite - magnetite altered and mineralised hornblende- and plagioclase-phyric diorite, cross-cut by abundant quartz - sulfide veins containing gold inclusions. Disseminated sulfides are abundant throughout the sample.
Notes, interpretation	8 ppm Au is from WR sample (assayed 4 ppm Au)	Evidence of Au (in chalcopyrite) associated with specularite-magnetite intergrowths. Disseminated hematite produced red colour.	Cu_pct=4.3
Au (ppm)	8	6.43	5.33
	vol % / size (mm) / habit, occurrence	vol % / size (mm) / habit, occurrence	vol % / size (mm) / habit, occurrence
Quartz (disseminated)	15 / vfgr / throughout diorite		20 / vfgr / groundmass
Quartz (vein)	15 / < 1 cm wide	77 / 3.5 mm wide	35 / 1 -20 mm wide / planar and undulating veins with orthoclase halos
Plagioclase	(15) / < 1 / subhedral phenocrysts altered to orthoclase and muscovite	(4) / < 2 / subhedral phenocrysts (relict)	(20) / 1 - 3 / subhedral phenocrysts, altered to orthoclase and muscovite
Orthoclase	21 / < 3 / perthitic grains, most as halos to quartz-sulfide veins	10 / perthitic alteration after plagioclase	14 / perthitic alteration after plagioclase, most as halos to quartz - sulfide veins
Hornblende (relict)	(6) / < 1 / subhedral phenocrysts, some partially replaced by magnetite and biotite	(8) / 0.6 - 1.5 / subhedral rhombs replaced by biotite and trace disseminated chalcopyrite	(5) / < 2 / subhedral phenocrysts
Biotite	6 / vfgr / after hornblende	2 / vfgr to 1 / in groundmass and after hornblende	5 / vfgr / after hornblende
Chlorite	1 / as in biotite	< 1 / as in biotite	1 / as in biotite
Actinolite			
Muscovite (visible)			5 / < 0.5 / after plagioclase phenocrysts
Muscovite (sericite) and / or clays	5 / throughout diorite	3 / after plagioclase and hornblende	10 / throughout diorite (between quartz veins)
Hematite (dusty)		< 1 / diffuse around specularite hematite	1? / possible fine hematite throughout sample
Calcite		< 1 / after plagioclase	5 / vfgr / disseminated throughout sample
Other carbonate	<1 / possible minor component in veins	< 1 / in quartz - chalcopyrite veins	
Epidote			
Alunite			
Anhydrite			
Pyrite	5 / < 0.2 / subhedral grains mostly within chalcopyrite veins, some fragmented	2 / in veins and vfgr disseminations	1 / vfgr / disseminated grains and aggregates < 1 mm, some in veins
Chalcopyrite	32 // occurring in irregular clots and as vein infill	4 / veins and disseminations, some replacing hornblende	3 / vfgr / disseminated grains and aggregates < 3 mm, mostly in veins
Bornite	< 1 / < 0.1 / anhedral inclusions in chalcopyrite		< 1 / vfgr / disseminated grains, fine rims to magnetite
Magnetite	< 1 / vfgr / disseminated throughout diorite, none in veins	2 / mostly disseminated grains in halos to quartz - chalcopyrite veins	1 / vfgr / disseminated throughout sample
Specular hematite		< 1 / small patches replaced by magnetite	
Molybdenite			< 0.5 / vfgr / disseminated throughout diorite, not within quartz veins
Galena			
Covellite			
Chalcocite			
Marcasite			
Arsenopyrite			
Other mineral (specified)	Sphalerite < 1 / < 0.3 / within late veinlet, grains show red internal reflections	Cubanite < 1 / exsolution lamellae in Au-bearing chalcopyrite Vs	Native gold < 1 / two inclusions 0.015 mm (15 microns) in vein and disseminated sulfide
Other mineral (specified)	Tennantite (?) < 1 / vfgr / within sphalerite vein < 1 mm wide	Native gold < 1 / < 0.03 mm / inclusions in chalcopyrite veins	

Hole ID	377	377	377
Depth (m)	1466.2	1530.0	1650.0
Representative of:	Zone	Zone	Zone (least-altered)
Protolith lithotype	Diorite II (hornblende-plag)	Diorite II (hornblende-plag)	Diorite II (marginal hornblende~plag)
Mineral assemblage	Orthoclase-quartz-magnetite-chalcopyrite	Biotite-orthoclase-quartz-magnetite-cpy	Biotite-orthoclase, anhydrite-sulfides
Alteration texture	Selective and vein	Pervasive and vein	Selective and vein
Alteration intensity	Intense	Intense	Weak
Description	Intensely orthoclase-altered diorite with 40% quartz-chalcopyrite veins, containing four round gold inclusions 0.02 mm across	Intensely orthoclase- and biotite-altered diorite, porphyritic texture barely evident in hand sample due to alteration. Native gold occurs in the quartz - chalcopyrite veins.	Grey-green, weakly orthoclase-, muscovite-, and chlorite-altered plagioclase- and hornblende-phyric diorite, cut by anhydrite - molybdenite - chalcopyrite veins < 7 mm wide
Notes, interpretation			Example of anhydrite after diorite; 0.29 ppm Au is from WR (assayed 1.24 ppm)
Au (ppm)	4.33	3.43	0.29
	vol % / size (mm) / habit, occurrence	vol % / size (mm) / habit, occurrence	vol % / size (mm) / habit, occurrence
Quartz (disseminated)	26 / vfgr / groundmass	8 / vfgr / throughout groundmass	10 / vfgr groundmass
Quartz (vein)	31 / veins 0.5-15 mm wide	36 / 1 - 22 mm wide	
Plagioclase	(15) / 0.2-2 / rounded phenocrysts replaced by sericite - orthoclase and rimmed by orthoclase	(?)	45 / 0.5 - 3 / subhedral zoned phenocrysts partly replaced by orthoclase, muscovite
Orthoclase	19 / vfgr / alteration through groundmass and as thin rims around phenocrysts	20 / < 0.8 / pervasive perthitic alteration of groundmass and phenocrysts	(10) / < 2 / zoned phenocrysts
Hornblende (relict)	(10) / 0.4-1.5 / subhedral phenocrysts	(?) / < 2	(10) / < 2 / subhedral phenocrysts replaced by flaky biotite
Biotite	8 / < 0.2 / most after hornblende phenocrysts	15 / < 0.3 / anhedral laths associated with orthoclase and chalcopyrite	15 / < 0.5 / throughout groundmass, some after hornblende
Chlorite	2 / < 0.2 / most after hornblende phenocrysts	3 / diffuse patches in biotite	4 / mostly after hornblende
Actinolite			
Muscovite (visible)			
Muscovite (sericite) and / or clays	5 // after groundmass and Plag phenocrysts		8 / after plagioclase phenocrysts
Hematite (dusty)			
Calcite			
Other carbonate		1 / diffuse zones 1 - 3 mm wide within quartz - chalcopyrite veins	
Epidote			
Alunite			
Anhydrite			12 / veins < 7 mm wide
Pyrite	4 / < 0.6 / tarnished anhedral grains in chalcopyrite Vs	5 / < 0.4 / tarnished anhedral grains in chalcopyrite	1 / vfgr in anhydrite veins
Chalcopyrite	15 / Vs 4 mm across and diss < 0.5 mm	12 / veins < 4 mm across, and disseminated aggregates 0.1 - 1 mm across	5 / vfgr in anhydrite veins, and disseminated throughout diorite
Bornite			
Magnetite		< 1 / aggregates < 0.2 / diffuse aggregates within late chalcopyrite - biotite	
Specular hematite			
Molybdenite		< 1 / < 0.1 / inclusions in early chalcopyrite veins	< 1 / vfgr in anhydrite veins
Galena			
Covellite			
Chalcocite			
Marcasite			
Arsenopyrite			
Other mineral (specified)	Native gold < 1 / 0.02 (20 microns) / 4 round inclusions in centre of cpy veins	Native gold < 1 / one inclusion 0.02 mm across observed in quartz vein	
Other mineral (specified)			

Hole ID	377	377	392
Depth (m)	1707.5	1837.3	369.0-1
Representative of:	Vein (anhydrite-cemented breccia)	Zone	Vein
Protolith lithotype	Metasandstone	Metasandstone	n/a
Mineral assemblage	Biotite-actinolite, anhydrite-sulfides	Biotite-actinolite, quartz-anhydrite	Rhodochrosite-pyrite-sphalerite-galena-gold
Alteration texture	Vein, vein halo, and selective	Pervasive and vein + vein halo	n/a
Alteration intensity	Strong	Intense	n/a
Description	60% of the sample is strongly biotite-altered metasandstone; 40% is anhydrite-cemented breccia vein with rotated, angular, biotite-altered wallrock fragments. The anhydrite veins are lined in places by weak actinolite alteration halos.	65% of thin section is biotite-altered metasandstone; remainder is a single quartz - anhydrite vein	40% of thin section consists of rhodochrosite - pyrite veins 0.5 - 30 mm wide, transitioning from quartz along vein walls, to zoned rhodochrosite + pyrite (+ native gold, indicated in SEM), to pyrite
Notes, interpretation		Chlorite more common near magnetite - chalcopyrite aggregates, biotite elsewhere	
Au (ppm)	0.15	0.41	8.75
	vol % / size (mm) / habit, occurrence	vol % / size (mm) / habit, occurrence	vol % / size (mm) / habit, occurrence
Quartz (disseminated)	28 / < 1 / rounded grains	20 / vfgr (some < 0.4) / rounded grains	
Quartz (vein)		13 / along margins to quartz-anhydrite vein, and disseminated in vein halo	15 / < 0.5 / inward-radiating crystals from vein walls
Plagioclase		(10) / vfgr / grains in sandstone	
Orthoclase			
Hornblende (relict)			
Biotite	30 / vfgr / randomly oriented throughout wallrock	35 / <0.4 / randomly oriented throughout sandstone	
Chlorite	5 / intergrown with biotite	8 / as in biotite, especially near magnetite	
Actinolite	5 / vfgr / disseminated acicular crystals as weak halos to anhydrite vein		
Muscovite (visible)		2 / < 0.3 / acicular along pyrite vein margins	
Muscovite (sericite) and / or clays			
Hematite (dusty)			
Calcite			
Other carbonate			20 / < 2 / zoned euhedral crystals radiating into vein
Epidote			
Alunite			
Anhydrite	29 / < 30 / breccia vein cement	15 / < 11 / anhedral in vein centre	
Pyrite	1 / vfgr disseminated grains throughout wallrock	4 / vfgr / disseminated grains, and some aggregates < 1 mm in late pyrite-chlorite vein	65 / aggregates intergrown with quartz - rhodochrosite
Chalcopyrite	2 / vfgr disseminated grains and veins < 1 mm wide	3 / vfgr / aggregates after disseminated pyrite, some in late veins	
Bornite			
Magnetite			
Specular hematite			
Molybdenite		< 1 / < 0.1 / a few inclusions in quartz-dominated part of quartz-anhydrite vein	
Galena			< 1 / < 0.5 / inclusions in pyrite
Covellite			
Chalcocite			
Marcasite			
Arsenopyrite			
Other mineral (specified)			Sphalerite < 1 / < 0.5 / inclusions in pyrite
Other mineral (specified)			Native gold < 1 / inclusions in pyrite fragments near vein walls, indicated by SEM only

Hole ID	392	392	392
Depth (m)	369.0-2	1495.8	1546.3
Representative of:	Zone	Patches (coarse-grained biotite)	Vein (IS vein after porphyry?)
Protolith lithotype	Metaconglomerate	Diorite II (hornblende-plag)	Diorite II (hornblende-plag)
Mineral assemblage	Muscovite-chlorite-montmorillonite	Quartz-biotite-chalcopyrite	Orthoclase-chalcopyrite, tennantite-galena
Alteration texture	Pervasive and vein halo	n/a	Vein and selective
Alteration intensity	Strong	n/a	Moderate
Description	60% of thin section is beige/pale tan and locally pale green, muscovite-chlorite and clay-altered metaconglomerate	Coarse-grained, irregular zones of quartz-biotite-chalcopyrite near diorite margins, containing chalcopyrite, magnetite, and possible rutile (?) interstitial to biotite laths, and as small inclusions along biotite cleavage planes	Biotite- and orthoclase-altered diorite, cross-cut by an 8 mm wide vein consisting of ~ 1/2 bornite - covellite - tennantite - galena, and 1/2 pyrite - chalcopyrite
Notes, interpretation	S_pct=7.32, As_ppm=1050, Mn_ppm=14700		Possible evidence of transition from porphyry mineralisation to intermediate sulfidation mineralisation containing tennantite and galena?
Au (ppm)	8.75	3.01	1.19
	vol % / size (mm) / habit, occurrence	vol % / size (mm) / habit, occurrence	vol % / size (mm) / habit, occurrence
Quartz (disseminated)	32 / vfgr throughout (large clasts not visible in this section)		37 / vfgr / throughout diorite groundmass
Quartz (vein)		57 / < 7 / anhedral and containing several smaller quartz inclusions	5 / 0.5 - 9 mm wide
Plagioclase	10 / vfgr throughout		(40) / 1 - 2 / subhedral phenocrysts
Orthoclase			13 / perthitic zones after plagioclase
Hornblende (relict)			(15) / 0.5 - 2 / subhedral phenocrysts
Biotite	5 / vfgr disseminated laths throughout sample	30 / < 5 / subhedral fans	15 / vfgr / after hornblende
Chlorite	5 / as in biotite	1 / < 0.3 / diffuse patches after biotite	
Actinolite			
Muscovite (visible)			
Muscovite (sericite) and / or clays	35 / evenly distributed throughout metaconglomerate		20 / mostly after plagioclase phenocrysts
Hematite (dusty)	7 / as in muscovite		
Calcite			
Other carbonate			4 / vfgr / as vein selvage
Epidote			< 1 / vfgr / disseminated throughout diorite
Alunite			
Anhydrite			
Pyrite	6 / < 0.2 / subhedral disseminated grains and aggregates, some rimmed by 2nd stage of pyrite	1 / < 0.5 / anhedral inclusions in chalcopyrite	2 / vfgr to 0.5 / disseminated grains and in vein
Chalcopyrite		11 / < 10 / aggregates interstitial to biotite, and vfgr inclusions along biotite cleavage planes	3 / as in pyrite
Bornite			1 / < 0.5 / in bornite - covellite - tennantite - galena - pyrite - chalcopyrite vein
Magnetite		< 1 / < 0.5 / inclusions in pyrite and along biotite cleavage planes	
Specular hematite			
Molybdenite			
Galena			< 1 / as in bornite
Covellite			< 1 / as in bornite
Chalcocite			< 1 / as in bornite
Marcasite			
Arsenopyrite	<1 / Possible rims to disseminated pyrite (?)		
Other mineral (specified)	Gypsum (?) < 1 / anisotropic laths exhbiting up to 3rd order birefringence throughout sample	Rutile (?) < 1 / <0.3 / inclusions in pyrite and along biotite cleavage planes	Tennantite < 1 / as in bornite
Other mineral (specified)			

Hole ID	392	392	392
Depth (m)	1662.6	1662.8	1699.2
Representative of:	Zone	Zone	Zone
Protolith lithotype	Metasandstone	Metasandstone	Diorite I (plag>hornblende, quartz)
Mineral assemblage	Biotite-orthoclase-quartz-chalcopyrite	Biotite-chalcopyrite-quartz-molybdenite	Othoclase-biotite-chalcopyrite-pyrite
Alteration texture	Pervasive and vein halo	Vein and pervasive	Vein and selective
Alteration intensity	Intense	Intense	Strong
Description	Dark brown, biotite-altered metasandstone cross-cut by quartz - chalcopyrite - pyrite veins	Dark brown to black, biotite-altered metasandstone cross-cut by quartz - chalcopyrite - pyrite - molybdenite veins	Mottled light grey and brown, strongly orthoclase- and biotite-altered plagioclase- and quartz-phyric diorite with late chalcopyrite - magnetite mineralisation
Notes, interpretation			
Au (ppm)	0.78	0.78	1.52
	vol % / size (mm) / habit, occurrence	vol % / size (mm) / habit, occurrence	vol % / size (mm) / habit, occurrence
Quartz (disseminated)	23 / < 2 / grains in metasandstone	30 / < 2 / grains in metasandstone	26 / < 1 / groundmass and phenocrysts
Quartz (vein)	18 / 1 - 22 mm wide	18 / 1 - 30 mm wide	8 / 0.5 - 12 mm wide
Plagioclase	(10) ? / protolith grains	(10) ? / protolith grains	(40) / 0.6 - 1.5 / subhedral phenocrysts
Orthoclase	1 / vfgr / as selvages to quartz - chalcopyrite veins	1 / vfgr / as selvages to quartz - chalcopyrite veins	35 / < 0.5 / throughout sample, mostly after plagioclase and groundmass
Hornblende (relict)			(5) / possible subhedral rhombs, replaced by biotite, orthoclase, and muscovite?
Biotite	50 / < 0.2 / throughout sample, particularly in vein halos ~ 1 cm wide	40 / < 0.2 / throughout sample, particularly in vein halos ~ 1 cm wide	11 / throughout groundmass and as phenocrysts < 0.5 mm long
Chlorite			
Actinolite			
Muscovite (visible)			
Muscovite (sericite) and / or clays			13 / after plagioclase
Hematite (dusty)			
Calcite	< 1 / vfgr / in aggregates to diffuse lenses up to 0.5 mm long in quartz veins		1 / vfgr / associated with biotite
Other carbonate			
Epidote			
Alunite			
Anhydrite		2 / < 0.5 / within quartz veins	
Pyrite	2 / < 0.5 / disseminated grains, diffuse aggregates, and in quartz veins	2 / < 0.5 / disseminated grains, diffuse aggregates, and in quartz veins	2 / < 0.5 / disseminated grains and diffuse veins < 1 mm wide
Chalcopyrite	6 / as in pyrite	6 / as in pyrite	4 / as in pyrite, and some rimming early pyrite
Bornite			
Magnetite	< 1 / vfgr / disseminated grains in metasandstone	< 1 / vfgr / disseminated grains in metasandstone	<1 / <0.5 / disseminated grains throughout diorite
Specular hematite			
Molybdenite	< 1 / 0.1 / disseminated grains mostly associated (in contact with) chalcopyrite	1 / <0.5 / as diffuse laminae in quartz veins	
Galena			
Covellite			
Chalcocite			
Marcasite			
Arsenopyrite			
Other mineral (specified)			
Other mineral (specified)			

Hole ID	392	392	392
Depth (m)	1728.3	1824.6	1851.5
Representative of:	Zone	Zone	Zone (least-altered)
Protolith lithotype	Diorite I (plag>hornblende, quartz)	Diorite I (plag>hornblende, quartz)	Diorite I (plag>hornblende, quartz)
Mineral assemblage	Orthoclase-biotite-muscovite-chalcopyrite	Orthoclase-biotite-muscovite-chalcopyrite	Orthoclase-biotite-muscovite-chalcopyrite
Alteration texture	Selective		
Alteration intensity	Moderate	Moderate	Weak
Description	Mottled grey and brown, moderately orthoclase- and biotite-altered diorite with ~ 5 % quartz - sulfide veins	Grey, moderately orthoclase-altered plagioclase-phyric diorite, cross-cut by a quartz - chalcopyrite - pyrite vein with a disseminated chalcopyrite vein halo.	Grey, weakly to moderately orthoclase-altered plagioclase-phyric diorite. The sample contains < 1 % secondary chalcopyrite as coatings to disseminated sulfides, and secondary biotite + muscovite.
Notes, interpretation		Example of Stage II chalcopyrite coating disseminated stage I sulfides	Extinction angles in plagioclase phenocrysts (R1-L1): 41,45,49,33,40; ~ labradorite
Au (ppm)	0.55	0.13	0.12
	vol % / size (mm) / habit, occurrence	vol % / size (mm) / habit, occurrence	vol % / size (mm) / habit, occurrence
Quartz (disseminated)	30 / < 1 / groundmass and phenocrysts	17 / < 0.5 / interstitial to plag (microphenocrysts and groundmass)	20 / < 0.5 / interstitial to plag (microphenocrysts and groundmass)
Quartz (vein)	5 / 1 - 3 mm wide	5 / 1-2 mm wide + 7 mm halo	
Plagioclase	(30),20 / 0.5 - 2 / phenocrysts and groundmass, <1/2 are preserved w zoning	53 / 1.5-3 / subhedral, strongly zoned phenocrysts	65 / 1.5-3 / subhedral, strongly zoned phenocrysts
Orthoclase	15 / < 0.5 / throughout groundmass, mostly as halos to quartz - sulfide veins	4 / < 0.5 / throughout sample, mostly after plagioclase and groundmass	
Hornblende (relict)			
Biotite	10 / < 0.5 / after plagioclase, and as sparse phenocrysts < 1 mm	8 / 0.2-1 / groundmass + anhedral-subhedral laths after plagioclase	8 / aggregates < 0.5 / microphenocrysts and groundmass, minor secondary biotite
Chlorite			
Actinolite			
Muscovite (visible)			
Muscovite (sericite) and / or clays	15 / throughout groundmass	8 / / dusting plag	5 / / dusting plag
Hematite (dusty)			
Calcite			
Other carbonate			
Epidote			
Alunite			
Anhydrite			
Pyrite	2 / < 0.5 / disseminated grains throughout diorite	3 / aggregates with magnetite 0.2-1 and coating Mt	2 / aggregates with magnetite 0.2-1
Chalcopyrite	3 / vfgr / disseminated grains, some in quartz veins	1 / < 0.5 / coating diss pyrite and as diss halo to vein	< 1 / vfgr / veinlets and coating diss pyrite
Bornite			
Magnetite	< 0.5 / vfgr / as in pyrite	1 / aggregates with early pyrite 0.2-1	< 1 / aggregates with pyrite 0.2-1
Specular hematite			
Molybdenite	< 0.5 / vfgr / as in pyrite		< 1 / vfgr / sparse disseminated grains
Galena			
Covellite			
Chalcocite			
Marcasite			
Arsenopyrite			
Other mineral (specified)			
Other mineral (specified)			

Hole ID	392	396	396
Depth (m)	1891.0	284.7	975.8
Representative of:	Zone	Zone (least-altered)	Zone
Protolith lithotype	Metasandstone-metasiltstone	Metaconglomerate	Metasandstone
Mineral assemblage	Biotite-actinolite-anhydrite-chalcopyrite	Actinolite-pyrite-biotite-chlorite	Biotite-muscovite-hematite-pyrite
Alteration texture	Pervasive to selective and vein	Selective and vein halo	Pervasive and vein halo
Alteration intensity	Intense	Weak	Strong
Description	~80% of sample is brown-grey, biotite- and actinolite-altered metasandstone, cross-cut by (20 %) anhydrite and chalcopyrite-pyrite-actinolite veins. Trace bornite occurs as rims to chalcopyrite in the anhydrite veins.	Grey-green and brown, weakly chlorite- and actinolite-altered, rounded clast- to matrix-supported metaconglomerate. Part of the sample contains a quartz - pyrite - chalcopyrite vein with a clast-selective biotite alteration halo.	Red-brown metasandstone, cross-cut by ~ 5 % quartz - pyrite veins < 2 mm wide. Fine-grained hematite produced the red colour.
Notes, interpretation			
Au (ppm)	0.24	0.17	0.08
	vol % / size (mm) / habit, occurrence	vol % / size (mm) / habit, occurrence	vol % / size (mm) / habit, occurrence
Quartz (disseminated)	25 / vfgr rounded grains	15 / vfgr / within conglomerate matrix	50 / < 2 / rounded sandstone grains
Quartz (vein)	3 / veins with anhydrite	2 / < 1 mm wide	5 / < 2 mm wide with pyrite
Plagioclase	14 / vfgr rounded grains	40 / vfgr / grains within conglomerate matrix, minor component is < 2mm in gabbroic clasts	(20) / < 2 / rounded grains
Orthoclase			
Hornblende (relict)			
Biotite	19 / vfgr / throughout sandstone	2 / vfgr / mostly as very thin rims to large clasts	20 / < 0.2 / randomly oriented laths throughout sample, weak replacement of plagioclase grains
Chlorite	5 / as in biotite	5 / vfgr / as in actinolite, and a few crystals < 1 mm	
Actinolite	12 / as in biotite, and as vein halos to selvages of acicular crystals 0.5 mm long	15 / vfgr / within conglomerate matrix and selective after gabbroic clasts	
Muscovite (visible)			8 / as in biotite
Muscovite (sericite) and / or clays		10 / occurring mostly along clast edges, as in biotite	10 / throughout matrix, and after plagioclase grains
Hematite (dusty)		3 / throughout matrix and along clast edges	3 / throughout, imparting red colour
Calcite		1 / vfgr / mostly after plagioclase	
Other carbonate			
Epidote		1 / vfgr / disseminated throughout matrix	
Alunite			
Anhydrite	12 / in veins < 6 mm wide with sulfides		
Pyrite	6 / fgr disseminated grains and in anhydrite veins	5 / vfgr / disseminated grains, some in vein < 1 mm wide	1 / vfgr / disseminated grains, some in quartz - pyrite veins
Chalcopyrite	1 / as in pyrite, most in anhydrite veins	< 1 / vfgr / disseminated grains mostly adjacent to or within biotite laths	3 / < 0.5 / round disseminated grains throughout sample
Bornite	< 1 / fine rims to chalcopyrite in veins		
Magnetite	1 / vfgr disseminated grains and inclusions in chalcopyrite	1 / vfgr / disseminated grains throughout sample	
Specular hematite			
Molybdenite			
Galena			
Covellite			
Chalcocite			
Marcasite			
Arsenopyrite			
Other mineral (specified)			
Other mineral (specified)			

Hole ID	396	396	396
Depth (m)	1189.2	1309.0	1320.4
Representative of:	Zone	Zone (least-altered)	Vein (intermediate sulfidation?)
Protolith lithotype	Metasandstone	Diorite I (hornblende-plag)	Diorite I (hornblende-plag)
Mineral assemblage	Actinolite-biotite-pyrite-chalcopyrite	Biotite-orthoclase-quartz-magnetite-cpy	Pyrite-molybdenite-galena-calcite-marcasite
Alteration texture	Pervasive, vein, and vein halo	Vein and selective	n/a
Alteration intensity	Moderate	Strong	n/a
Description	Light grey, massive, moderately biotite- and actinolite-altered metasandstone, cross-cut by quartz-pyrite-chalcopyrite-actinolite veins with prominent black actinolite halos < 4 mm wide	Hornblende- and plagioclase-phyric diorite with chlorite - biotite - muscovite altered and orthoclase-rimmed and altered phenocrysts 1 -2 mm across, cut by quartz - magnetite veins, and overprinted by a late stage of sulfide mineralisation.	Breccia vein 1 cm wide containing quartz and molybdenite fragments supported in a pyrite - marcasite - calcite - galena cement. The vein cross-cuts white or pale tan, strongly ortho-clase-altered diorite.
Notes, interpretation	Actinolite alteration halos are diffuse, but more sharply defined than in comparable samples	Stage I sulfides rimmed by stage II sulfides	Possible example of root zone to IS mineralisa-tion
Au (ppm)	0.02	0.27	0.46
	vol % / size (mm) / habit, occurrence	vol % / size (mm) / habit, occurrence	vol % / size (mm) / habit, occurrence
Quartz (disseminated)	45 / < 1 / rounded grains	35 / vfgr sugary throughout sample, likely secondary (alteration)	
Quartz (vein)	3 / < 1 mm wide	7 / 1 - 8 mm wide / late quartz - magnetite veins	
Plagioclase	? none visible	(15) / < 1 / relict subhedral laths replaced by muscovite - chlorite - orthoclase	
Orthoclase		20 / vfgr / throughout groundmass and as rims to phenocrysts	
Hornblende (relict)		(30) / 1 - 2 / subhedral - euhedral rhombs and hexagons	
Biotite	15 / vfgr / pervasive throughout wallrock, and intergrown with actinolite in vein halos	7 / vfgr / mostly replacing hornblende, some in groundmass	
Chlorite		10 / as in biotite	
Actinolite	32 / < 0.5 / within, and as halos to, quartz-py-rite-cpy-actinolite veins, smaller in wallrock		
Muscovite (visible)			
Muscovite (sericite) and / or clays		10 / throughout groundmass	
Hematite (dusty)			
Calcite			45 / irregular patches as infill to breccia frag-ments
Other carbonate			
Epidote			
Alunite			
Anhydrite			
Pyrite	< 1 / some disseminated grains, most as aggre-gates < 1 mm long within actinolite veins	4 / < 0.5 / subhedral disseminated grains throughout diorite	25 / fragments < 1 mm across / some in breccia infill
Chalcopyrite	4 / as in pyrite	2 / < 0.5 / vfgr disseminated grains and late rims to disseminated pyrite	
Bornite			
Magnetite	1 / vfgr / disseminated grains throughout wallrock	5 / vfgr / disseminated grains in diorite and in quartz - magnetite and magnetite veins	
Specular hematite			
Molybdenite			10 / 0.3 - 3 / rounded fragments in breccia vein, some interstital to marcasite laths
Galena			
Covellite			
Chalcocite			
Marcasite			20 / < 1 mm long / randomly oriented in infill
Arsenopyrite			
Other mineral (specified)			
Other mineral (specified)			

Hole ID	396	396	397
Depth (m)	1489.5	1501.0	123.0
Representative of:	Zone	Patch (orbicular diorite?)	Vein (carbonate-base metal sulfide)
Protolith lithotype	Diorite II (marginal hornblende~plag)	Diorite II (marginal hornblende~plag)	Metaconglomerate
Mineral assemblage	Quartz-orthoclase-biotite-chlorite-magnetite	Quartz-orthoclase-biotite-chlorite-magnetite	Rhodochrosite-pyrite-sphalerite-galena
Alteration texture	Selective	Pervasive, after relict orbicular (?)	Vein and pervasive
Alteration intensity	Moderate	Strong	Strong
Description	Marginal quartz-rich diorite (locally hornblende ~ plagiclase, grades over several metres into hornblende > plagioclase w/ less quartz). The sample contains < 1 % vein and disseminated calcite, generally replacing perthitic feldspar.	Orthoclase-altered diorite containing rounded diffuse patches of biotite - chlorite - muscovite < 1 cm across, possibly relict orbicules.	Hand sample is light beige MCO cut by late rhodochosite-pyrite veins; thin section is through one such breccia vein, with ~40% pyrite fragments < 5 mm across, supported by rhodochosite cement, and fragment-supported along one of the vein walls.
Notes, interpretation	High quartz content in this sample reflects quartz saturation/"flooding" near intrusive margin?	Orbicular texture?	Distribution of sulfides suggests settling against up-hole side, may be mis-oriented core? 292 ppm Pb; 781 ppm Zn; 13.2 pct S; 1.26 pct Mn
Au (ppm)	0.29	0.5	0.19
	vol % / size (mm) / habit, occurrence	vol % / size (mm) / habit, occurrence	vol % / size (mm) / habit, occurrence
Quartz (disseminated)	80 / < 0.2 and some aggregates (phenocrysts?) < 2 /	50 / vfgr / possible sparse phenocrysts < 1.5 mm across (?)	
Quartz (vein)			
Plagioclase		(10)	
Orthoclase	5 / < 0.5 / groundmass and perthitic grains < 1 mm	15 / < 1 / groundmass and perthitic grains	
Hornblende (relict)		(5) ?	
Biotite	9 / < 0.6 / anhedral in groundmass, sparse subhedral phenocrysts	14 / < 0.5 / throughout groundmass and in orbicular patches	
Chlorite		5 / as in biotite	
Actinolite			
Muscovite (visible)		3 / as in biotite	
Muscovite (sericite) and / or clays	4 / / throughout groundmass	10 / as in biotite	
Hematite (dusty)			
Calcite	2 / Vs < 0.3 mm wide, diss < 0.1 / Ct after perthitic Or		55 / < 1 / zoned from vein margin into dusty rhodochrosite
Other carbonate			6 / < 1.5 / at centre of vein
Epidote			
Alunite			
Anhydrite			
Pyrite		< 1 / vfgr disseminated grains and aggregates < 2 mm across	35 / < 5 / rounded to angular fragments within carbonate cement
Chalcopyrite		3 / as in pyrite	
Bornite			
Magnetite		< 1 / as in pyrite	
Specular hematite			
Molybdenite		<1 / vfgr disseminated grains throughout diorite	
Galena			1 / < 0.2 / sparse aggregates with pyrite, sph
Covellite			
Chalcocite			
Marcasite			
Arsenopyrite			
Other mineral (specified)			Sphalerite 3 / < 0.2 / irregular aggregates, mostly disseminated in calcite near vein margins
Other mineral (specified)			

Hole ID	397	397	397
Depth (m)	396.0	1037.5	1093.5
Representative of:	Vein (carbonate-base metal sulfide)	Zone	Zone
Protolith lithotype	Metasandstone-metasiltstone	Metasiltstone	Diorite I (hornblende-plag)
Mineral assemblage	Carbonate-pyrite-sphalerite-galena	Biotite-muscovite-hematite	Biotite-muscovite-hematite
Alteration texture	n/a	Pervasive and vein halo	Pervasive and vein
Alteration intensity	n/a	Intense	Intense
Description	Multiphase, chaotic to locally jigsaw-fit, mostly infill-supported breccia vein. Fragments (65 % of sample) are pyrite, containing up to 30 % quartz inclusions and rims of lighter coloured (As-rich?) inclusion-free pyrite. One fragment is a quartz-cemented pyrite breccia. Infill (35 % of sample) is ~ 40 % calcite and 60 % hydrothermal sandstone to mudstone with pyrite fragments and calcite cement.	Mottled red-brown, biotite - muscovite - hematite altered metasiltstone, with lighter coloured, round patches of diffuse quartz interpreted to be an alteration texture	Mottled red and white diorite with intense, texturally destructive biotite - muscovite - hematite alteration in between quartz veins. Iron oxides occur as rims to disseminated (stage I porphyry?) sulfides.
Notes, interpretation	Very high Au and Ag (86.7 ppm Ag), low Cu (0.18% Cu), 39% S		Mottled red, green, white, yellow
Au (ppm)	40.7	0.38	0.24
	vol % / size (mm) / habit, occurrence	vol % / size (mm) / habit, occurrence	vol % / size (mm) / habit, occurrence
Quartz (disseminated)	5 / < 0.1 / rounded inclusions in some pyrite fragments	37 / vfgr throughout sample / some in diffuse patches	?
Quartz (vein)		4 / < 15 mm wide	57 / 1 - 15 mm wide
Plagioclase		(20) ?	?
Orthoclase			?
Hornblende (relict)			
Biotite		40 / vfgr / throughout sample	10 / vfgr / throughout diorite (between quartz veins)
Chlorite			3 / as in biotite
Actinolite			
Muscovite (visible)			
Muscovite (sericite) and / or clays		10 / as in biotite	17 / as in biotite
Hematite (dusty)		5 / as in biotite, producing red colour	5 / as in biotite
Calcite	28 / < 5 / cement infill		
Other carbonate	5 / as in calcite, slightly more opaque in thin section		
Epidote			
Alunite			
Anhydrite			
Pyrite	59 / < 0.1 to 30 / fragments in breccia	< 1 / vfgr / disseminated with chalcopyrite	1 / < 0.5 / disseminated grains throughout diorite
Chalcopyrite		4 / vfgr / in veins and disseminated in halos to quartz veins	3 / as in pyrite, and in quartz veins
Bornite			
Magnetite			< 1 / vfgr / minor inclusions in specular hematite
Specular hematite			4 / as rims to disseminated pyrite and chalcopyrite
Molybdenite			
Galena	< 1 / < 0.1 / inclusions in some pyrite fragments		
Covellite			
Chalcocite			
Marcasite			
Arsenopyrite	3 / Possible rims to pyrite fragments ?		
Other mineral (specified)	Sphalerite < 1 / < 0.1 / inclusions in some pyrite fragments		
Other mineral (specified)			

Hole ID	397	397	397
Depth (m)	1124.0	1206.3	1359.3
Representative of:	Zone	Zone	Zone
Protolith lithotype	Diorite I (hornblende-plag)	Diorite I (hornblende-plag)	Diorite II (hornblende-plag)
Mineral assemblage	Quartz-biotite	Biotite-orthoclase-quartz-magnetite, py+clays	Biotite-orthoclase-quartz-magnetite-cpy-pyrite
Alteration texture	Pervasive, texturally destructive	Vein and pervasive	Selective and vein halo
Alteration intensity	Intense	Intense	Intense
Description	Grey, intensely quartz-altered diorite containing < 1 hematite and magnetite, and ~4 % chalcopyrite + pyrite.	Mottled white, light brown, and light green, biotite-orthoclase-chlorite and clay-altered, crowded hornblende- and plagioclase-phyric diorite with quartz-chalcopyrite veins and orthoclase vein halos	Biotite- and orthoclase-altered and mineralised diorite, with vein halos of perthitic feldspar after hornblende and plagioclase phenocrysts. Late mineralisation veins contain co-genetic chalcopyrite, pyrite, native gold, and magnetite.
Notes, interpretation	Unusual example of quartz as an alteration product (as opposed to veins)	Possible replacement of stage I magnetite by stage II pyrite	More magnetite than in nearby sample 297-1361.0
Au (ppm)	0.38	0.07	4.81
	vol % / size (mm) / habit, occurrence	vol % / size (mm) / habit, occurrence	vol % / size (mm) / habit, occurrence
Quartz (disseminated)	85 / vfgr / diffuse alteration throughout sample	10 / vfgr / throughout groundmass	25 / vfgr / groundmass
Quartz (vein)		40 / < 2 mm wide	6 / veins < 7 mm wide
Plagioclase		(30) / 1 - 3 / subhedral rectangles, some twinning preserved	16 / < 2 / groundmass and relict phenocrysts
Orthoclase		11 / vfgr / mostly replacing plagioclase, in vein halos	26 / vfgr / vein halos of perthitic feldspar
Hornblende (relict)		(5) / 2 / subhedral rhombs	(15) / 0.6-2 / subhedral
Biotite	5 / vfgr / in diffuse patches < 1 cm	10 / vfgr / after hornblende and throughout groundmass	13 / < 0.5 / secondary disseminated
Chlorite		5 / as in biotite	2 / vfgr / after or with biotite
Actinolite			
Muscovite (visible)			
Muscovite (sericite) and / or clays	3 / throughout sample	15 / after plagioclase and hornblende phenocrysts	3
Hematite (dusty)	2 / throughout sample	1 / throughout sample	
Calcite			
Other carbonate			
Epidote			
Alunite			
Anhydrite			
Pyrite	1 / vfgr / disseminated grains	3 / < 0.01 - 2 / disseminated aggregates and veins, some containing magnetite inclusions	2 / < 0.4 / anhedral grains in chalcopyrite Vs and rims to Mt
Chalcopyrite	3 / vfgr / disseminated grains	4 / < 0.5 / rimming pyrite-magnetite	6 / veins < 7 mm wide and anhedral dissem
Bornite			
Magnetite	0.5 / vfgr / disseminated grains	1 / < 0.05 / inclusions in some disseminated pyrite grains	4 / < 0.6 / anhedral disseminated grains in diorite, and in diffuse veins < 5 mm wide
Specular hematite	0.5 / vfgr / disseminated grains		
Molybdenite			
Galena			
Covellite			
Chalcocite			
Marcasite			
Arsenopyrite			
Other mineral (specified)			Native gold < 0.1 / 0.02 mm / inclusions in pyrite of quartz - cpy - pyrite - magnetite veins
Other mineral (specified)			

Hole ID	397	398	398
Depth (m)	1361.0	44.7	101.0
Representative of:	Zone	Zone	Zone
Protolith lithotype	Diorite II (hornblende-plag)	Diorite I (plag>hornblende, quartz) ?	Diorite I (plag>hornblende, quartz) ?
Mineral assemblage	Biotite-orthoclase-quartz-magnetite	Quartz-alunite-clays, hematite	Quartz-alunite-clays, hematite
Alteration texture	Selective, vein, and vein halo	Pervasive, texturally destructive	Pervasive, texturally destructive
Alteration intensity	Intense	Intense	Intense
Description	Mottled black and pale pink, biotite- and orthoclase-altered and mineralised diorite, with chalcopyrite-pyrite-magnetite(+quartz) veins with wide alteration halos of perthitic feldspar after hornblende and plagioclase phenocrysts	White (quartz+alunite) and red (hematite) altered rock with wormy quartz veins and fragments of quartz veins	Pitted / vuggy red, black, and white, intensely quartz- and alunite-altered quartz vein stockwork through plagioclase- and quartz-phyric diorite, with two preserved quartz phenocrysts < 3 mm across. Vuggy pits occur mostly in between the quartz veins.
Notes, interpretation	Examples of orthoclase halos after relict hornblende phenocrysts.	Acid-altered quartz stockwork veins; 106 ppm As; 11 ppm Mo	Quartz phenocrysts preserved in quartz-veined and acid-altered stage I diorite; 116 ppm Mo; 871 ppm As; 0.08 % S;
Au (ppm)	4.35	1.6	0.69
	vol % / size (mm) / habit, occurrence	vol % / size (mm) / habit, occurrence	vol % / size (mm) / habit, occurrence
Quartz (disseminated)	15 / vfgr / groundmass	95 / < 0.5 mm (including vein quartz in protolith)	84 / < 0.8 mm / throughout, including vein quartz in protolith
Quartz (vein)	9 / veins 1-6 mm wide		
Plagioclase	10 / vfgr to 2 / groundmass and relict phenocrysts		
Orthoclase	25 / vfgr / vein halos of perthitic alteration and thin rims to phenocrysts		
Hornblende (relict)	(10) / 0.5-1.5 / subhedral		
Biotite	13 / < 0.5 / secondary disseminated		
Chlorite	2 / vfgr / after or with biotite		
Actinolite			
Muscovite (visible)			
Muscovite (sericite) and / or clays	5 / throughout sample	4 / distributed throughout sample (between quartz veins)	6 / pervasive alteration throughout sample
Hematite (dusty)		1 / throughout sample, some after breccia infill	8 / pervasive dusting throughout, between veins
Calcite			
Other carbonate			
Epidote			
Alunite			
Anhydrite			
Pyrite	4 / < 0.6 / anhedral grains in chalcopyrite Vs and rims to Mt		
Chalcopyrite	15 / veins < 20 mm wide and anhedral dissem in vein halos	< 1 / < 0.1 / within some relict quartz vein fragments	
Bornite			
Magnetite	2 / < 0.5 / anhedral disseminated in diorite and some inclusions in chalcopyrite veins		
Specular hematite			2 / secondary, as small reflective patches in hematite zones
Molybdenite			
Galena			
Covellite			
Chalcocite			
Marcasite			
Arsenopyrite			
Other mineral (specified)			
Other mineral (specified)			

Hole ID	398	398	398
Depth (m)	150.5	153.5	201.0
Representative of:	Vein (colloform alunite)	Zone	Zone
Protolith lithotype	Diorite I (plag>hornblende, quartz)	Diorite I (plag>hornblende, quartz)	Diorite I (plag>hornblende, quartz)
Mineral assemblage	Alunite-orpiment-pyrite-marcasite-galena	Quartz-alunite-pyrite-covellite-quartz	Quartz-alunite-clays-pyrite-covellite-tennantite
Alteration texture	n/a	Pervasive and vein	Pervasive and vein
Alteration intensity	n/a	Intense	Intense
Description	Colloform banded alunite-sulfide-sulfosalt vein, through alunite- and covellite- altered relict quartz diorite. ~1/3 of the vein alunite is inward-radiating botryoidal fans of subhedral laths < 2.5mm long. Minor chalcocite occurs in colloform bands as lamellae and wormy symplectite bands within pyrite. Trace galena grains occur within the alunite vein.	Mottled grey, intensely quartz- and alunite-altered plagioclase- and quartz-phyric diorite with abundant pyrite and minor covellite. Covellite-bornite veins occur in the hand sample, but are not evident in the thin section area. Covellite occurs mostly as a fine coating to disseminated pyrite grains.	Mottled dark grey (quartz veins) and white (alunite), intensely altered diorite containing relict quartz-molybdenite stockwork veins, and abundant secondary disseminated pyrite.
Notes, interpretation	Trace galena with alunite. Orpiment indicates relatively low T.		Stage I quartz-molybdenite veins preserved in lithocap; 330 ppm Mo; malachite developed on surface of drill core; 0.8 % Cu; 1120 ppm Zn
Au (ppm)	0.69	0.35	0.63
	vol % / size (mm) / habit, occurrence	vol % / size (mm) / habit, occurrence	vol % / size (mm) / habit, occurrence
Quartz (disseminated)		15 / vfgr / groundmass	66 / < 0.9 / vfgr throughout sample, and < 0.9 mm in veins
Quartz (vein)		31 / veins 1-9 mm wide / relict barren Vs	(40) (included in protolith abundance above)
Plagioclase		(10) / vfgr / groundmass with quartz	
Orthoclase			
Hornblende (relict)			
Biotite			
Chlorite			
Actinolite			
Muscovite (visible)			
Muscovite (sericite) and / or clays		5 // after groundmass	15 / diffuse patches in between quartz veins, producing semi opaque appearance
Hematite (dusty)	3 // on Alun laths		
Calcite			
Other carbonate			
Epidote			
Alunite	95 / vfgr sugary and some < 2.5 / most of vein contains small equant grains, some bands are	28 / < 0.5 / randomly oriented anhedral laths (tabular)	10 / < 0.2 / fine randomly oriented laths in diorite, commonly radiating from pyrite grains
Anhydrite			
Pyrite	2 / < 0.5 / f dissem and in colloform bands < 0.5mm wide with orpiment and chalcocite	20 / 0.2-1 / anhedral diss outside of quartz Vs	7 / < 0.6 / anhedral grains and aggregates throughout sample +late veinlets < 0.4mm wide
Chalcopyrite			
Bornite			
Magnetite			
Specular hematite			
Molybdenite			
Galena	< 1 / < 0.5 / sparse anhedral crystals in alunite		
Covellite		1 / vfgr / partly rims some pyrite	2 / < 0.3 / mostly as fine rims to pyrite
Chalcocite	< 1 / < 1 / in colloform bands, py symplectite		
Marcasite			
Arsenopyrite			
Other mineral (specified)	Orpiment < 1 / < 0.5 / in round concentric radial growths in alunite, some in bands with py	Tennantite < 1 / < 0.5 / disseminated and as rims to pyrite	Tennanite < 1 / < 0.1 / small inclusions in disseminated pyrite and covellite
Other mineral (specified)	Digenite < 1 // thin rims to some pyrite		

Hole ID	398	402	402
Depth (m)	358.9	566.3	569.3
Representative of:	Zone	Zone	Zone
Protolith lithotype	Metasandstone	Metasiltstone	Metasiltstone
Mineral assemblage	Covellite-chalcocite, after muscovite-hematite	Biotite-magnetite-hematite	Biotite-magnetite-hematite-chalcopyrite
Alteration texture	Vein and pervasive texturally destructive	Vein, vein halo, and pervasive	Vein, vein halo, and pervasive
Alteration intensity	Intense	Strong	Strong
Description	Unusual peach, white, and red coloured quartz-veined rock; peach colour in altered wallrock is due to combination of very finely disseminated covellite - chalcocite and hematite. Paragenesis indicated is: biotite - muscovite - hematite alteration and quartz - chalcopyrite veins // clay veins and alteration with covellite - chalcocite mineralisation.	Dark grey-brown, strongly biotite-altered metasiltstone, cross-cut by a quartz-specularite-chalcopyrite-pyrite vein 1 cm wide, with disseminated magnetite vein halos that are diffuse over several mm.	Black, biotite-altered metasiltstone with a quartz-specularite-chalcopyrite-pyrite vein > 7 cm wide (a part of which is seen in the thin section), rimmed by disseminated magnetite vein halos.
Notes, interpretation	147 ppm Mo; 587 % Zn; 1.16 % Cu; 4.6 % Cu;	Evidence of redox front, from (relatively) oxidised vein fluid into wallrock	
Au (ppm)	0.87	0.12	0.22
	vol % / size (mm) / habit, occurrence	vol % / size (mm) / habit, occurrence	vol % / size (mm) / habit, occurrence
Quartz (disseminated)	20 / vfgr throughout sample	35 / vfgr / rounded grains in wallrock	11 / vfgr / grains in wallrock
Quartz (vein)	40 / 1 - 12 mm wide	25 / 0.5 - 60 / locally laminated veins	64 / wide vein containing specularite, chalcopyrite, and pyrite
Plagioclase	(20) ?	(10)? / vfgr / grains in wallrock	(10)? / vfgr / grains in wallrock
Orthoclase			
Hornblende (relict)			
Biotite	12 / vfgr throughout sample	25 / vfgr / pervasive in wallrock only	9 / vfgr / pervasive in wallrock only
Chlorite		3 / as in biotite	1 / as in biotite
Actinolite			
Muscovite (visible)		7 / vfgr / as in biotite	1 / vfgr / as in biotite
Muscovite (sericite) and / or clays	11 / throughout sample, and in covellite-bearing veins		
Hematite (dusty)	10 / throughout sample, fragments in later veins		
Calcite			
Other carbonate			
Epidote			
Alunite			
Anhydrite			
Pyrite	1 / vfgr / disseminated grains	1 / vfgr / in small aggregates interstitial to specularite in quartz veins, some in veinlets	3 / vfgr / in small aggregates interstitial to specularite in quartz-specularite vein
Chalcopyrite	2 / < 1 / in quartz - chalcopyrite veins	3 / as in pyrite	3 / as in pyrite
Bornite	< 1 / vfgr / intergrown with chalcocite-covellite		
Magnetite		2 / < 0.1 / disseminated grains in wallrock, most abundant nearest the quartz vein margins	1 / < 0.3 / disseminated grains in wallrock, most abundant nearest the quartz vein margins
Specular hematite	3 / vfgr disseminated grains throughout sample	1 / 0.3 - 1.2 / subhedral laths in quartz vein	12 / < 10 / aggregates with chalcopyrite in quartz veins
Molybdenite	< 1 / as in chalcopyrite		
Galena			
Covellite	1 / vfgr / disseminated, some halos to clay veins		
Chalcocite	< 1 / as in covellite, some as halos to clay veins		
Marcasite			
Arsenopyrite			
Other mineral (specified)			
Other mineral (specified)			

Hole ID	402	402
Depth (m)	657.0	921.2
Representative of:	Zone	Vein (quartz-pyrite-molybdenite)
Protolith lithotype	Metasandstone	Metasandstone-metasiltstone
Mineral assemblage	Biotite-magnetite-quartz-chalcopyrite	Biotite-quartz-cpy, quartz-pyrite-molybdenite
Alteration texture	Vein halo	Vein and pervasive
Alteration intensity	Strong	Strong
Description	Dark grey-brown, biotite-altered metasandstone with disseminated magnetite and quartz - chalcopyrite (+ trace anhydrite) veins < 5 mm wide. Biotite alteration occurs as diffuse alteration halos < 1.5 cm wide, near quartz-chalcopyrite vein margins.	65% of the sample is a laminated and pitted quartz - pyrite - molybdenite vein ~2.5 cm wide. Remainder (35%) is dark brown-grey, biotite- and minor muscovite-altered metasandstone.
Notes, interpretation	Possible shallowest occurrence of anhydrite documented at Golpu	Example of a stage I quartz-molybdenite-pyrite vein which has not been overprinted by acid alteration. Insufficient molybdenite for Re-Os
Au (ppm)	0.14	not available
	vol % / size (mm) / habit, occurrence	vol % / size (mm) / habit, occurrence
Quartz (disseminated)	49 / < 1 / rounded grains	14 / < 1 / rounded grains
Quartz (vein)	6 / < 5 mm wide	65 / 25 mm wide / quartz crystals up to 1.5 mm long occur at vein margins, terminating inward
Plagioclase	(20) / < 1 / rounded grains in protolith	(5) / < 1 / rounded grains in protolith
Orthoclase		
Hornblende (relict)		
Biotite	24 / < 0.2 / disseminated throughout, more common near vein margins (i.e., vein halos)	12 / < 0.1 / disseminated in wallrock
Chlorite		
Actinolite	5 ? / < 0.3 / as in biotite (pleochroic green, possibly chlorite)	
Muscovite (visible)		
Muscovite (sericite) and / or clays	12 / throughout sample	5 / throughout wallrock
Hematite (dusty)		
Calcite		
Other carbonate		
Epidote		
Alunite		
Anhydrite	< 1 ? / < 0.5 / possible anhydrite in quartz veins	
Pyrite	2 / vfgr / disseminated grains and in quartz veins	1 / < 0.4 / disseminated anhedral grains, mostly in quartz vein
Chalcopyrite	2 / within quartz veins	3 / < 0.2 / disseminated grains in wallrock+ quartz vein, some irregular aggregates <0.9 mm
Bornite		
Magnetite	< 1 / vfgr / disseminated throughout wallrock with biotite	< 1 / vfgr / disseminated throughout wallrock with biotite
Specular hematite		
Molybdenite		< 1 / vfgr / disseminated grains within quartz vein
Galena		
Covellite		
Chalcocite		
Marcasite		
Arsenopyrite		
Other mineral (specified)		
Other mineral (specified)		

Appendix B
Graphic Logs

Digitised versions of graphic drill core logs are provided on the following pages, in order of drill hole ID. The logs were recorded by the author at Wafi camp and the Nine Mile core site in Papua New Guinea. Based on detailed petrographic and XRD data collected after the core logging was completed, displayed biotite contents in the following logs were adjusted to 1/2 of the original estimates. Blank spaces in the core logs indicate intervals of missing or very poorly preserved drill core. In addition to the terms defined in Table 4.1, terms and abbreviations used are:

TCA: "to core axis," describing the minimum acute angle of planar features with respect to the drill core axis; e.g., "beds at 90 TCA" describes bedding planes perpendicular to the drill core

fine-grained: grains < 1 mm in diameter (longest dimension)

medium-grained: grains 1 - 3 mm in diameter

coarse-grained: grains > 3 mm in diameter

Rock types (left column)

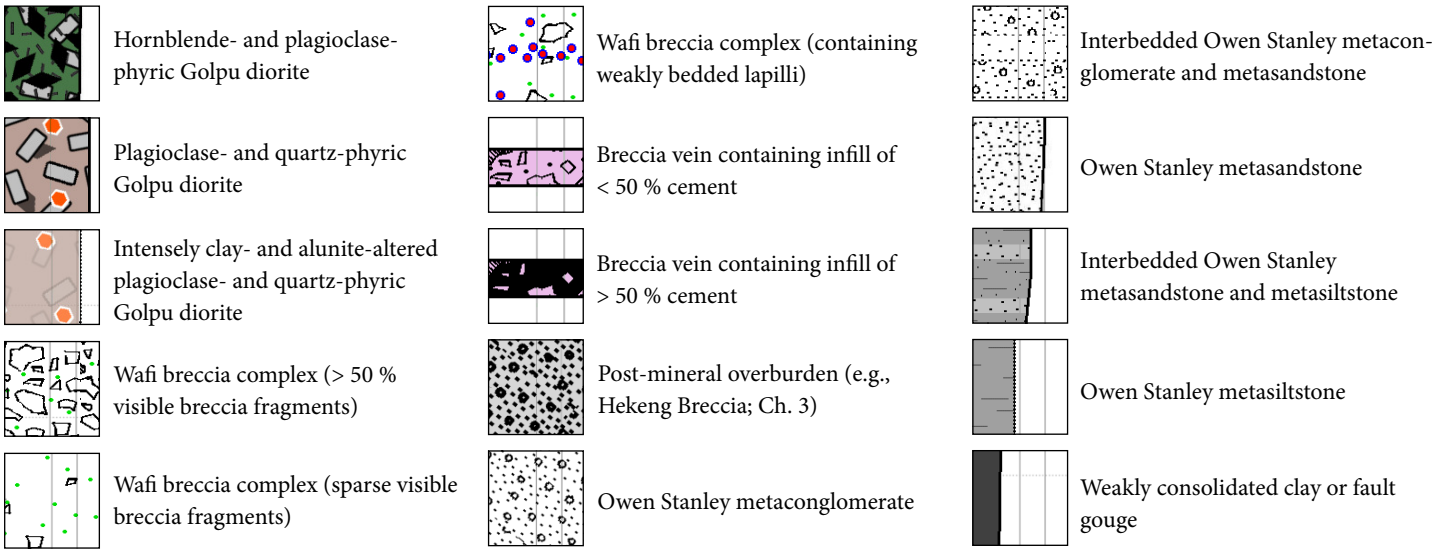

Alteration and vein minerals (abundance columns)

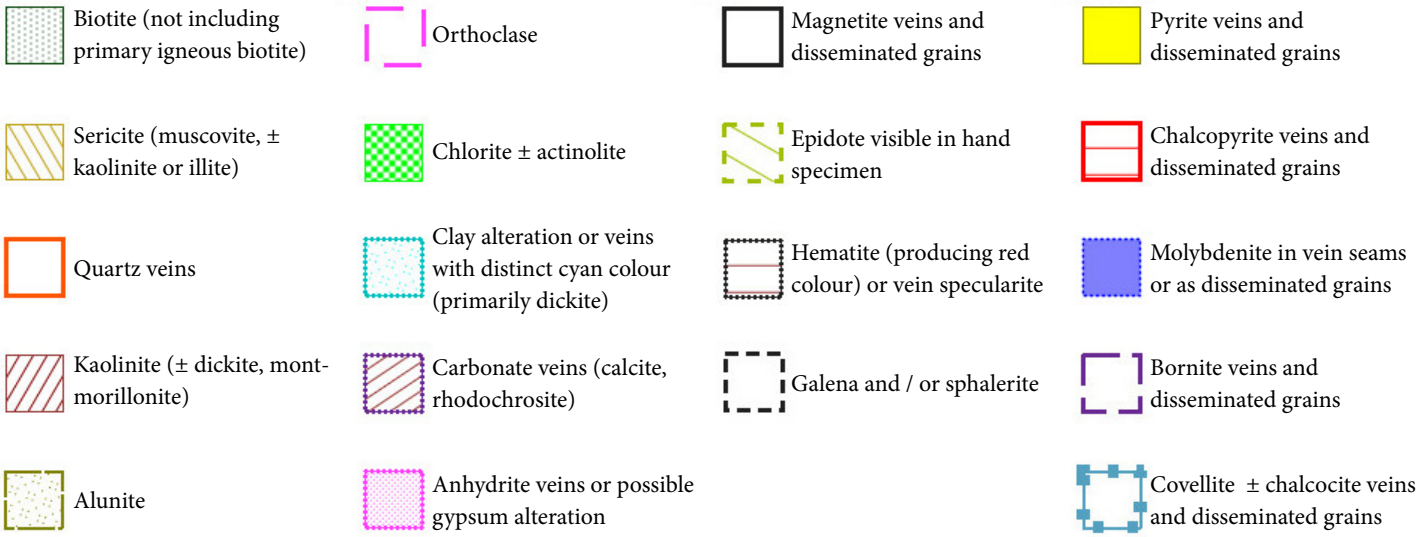

WR199

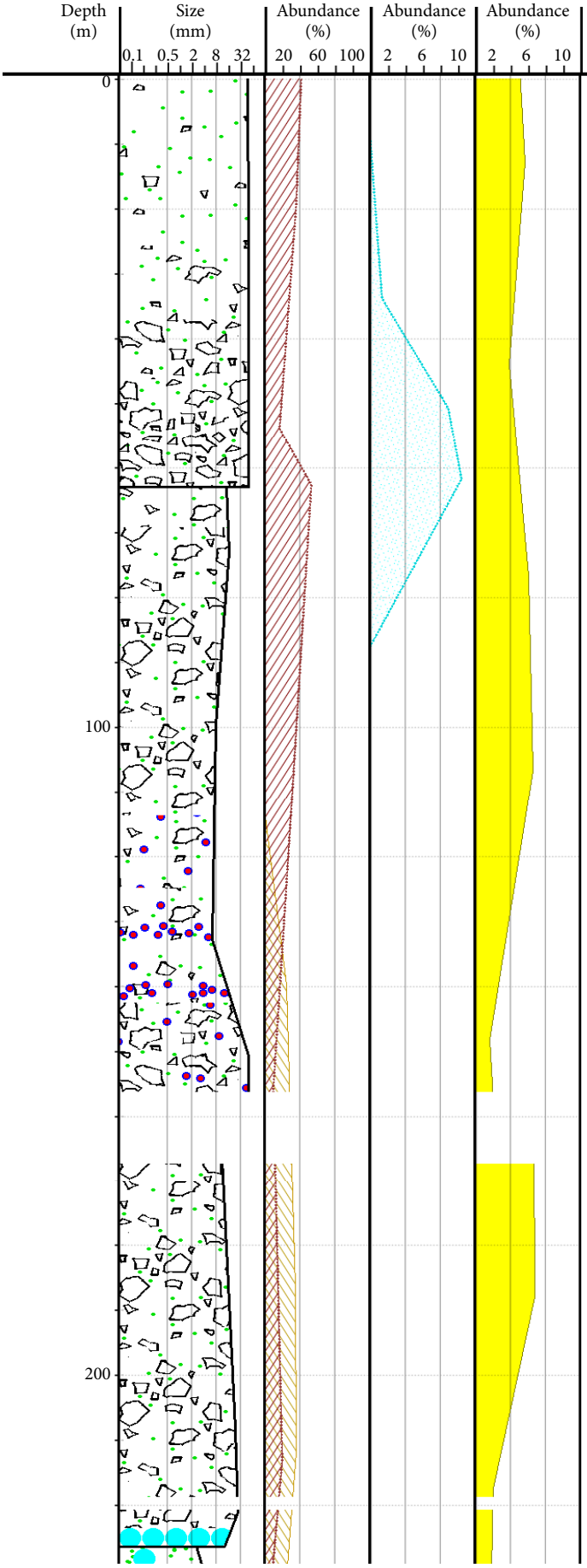

Description, interpretation

2.0 m: Polymictic, 60 %-infill-supported chaotic breccia with angular to subangular fragments < 4 cm (most < 1 cm), of which: 70 % are light tan metasiltstone (?), and 30 % are light grey mottled and strongly kaolinite-replaced (possible diorite?). Infill is kaolinite-altered, possibly tuffaceous with sparse bedding planes.

18.5 m: 5 cm fine tuff (?) at 80 TCA.

48.8 m: Quartz-veined metasiltstone fragment > 10 cm

55.0 m: Breccia as above, but 10 % of fragments are plagioclase-phyric crystal tuff(?)

70.0 m: Monomictic 75 %-infill-supported chaotic breccia with light tan angular metasiltstone(?) fragments.

155.3 m: Larger kaolinite-replaced amoeboid fragments have irregular margins -- juvenile magmatic fragments?

227.9 m: Lower contact marked by 10 cm of 0.6-1 cm round grey lapilli(?) with pyrite-replaced centres.

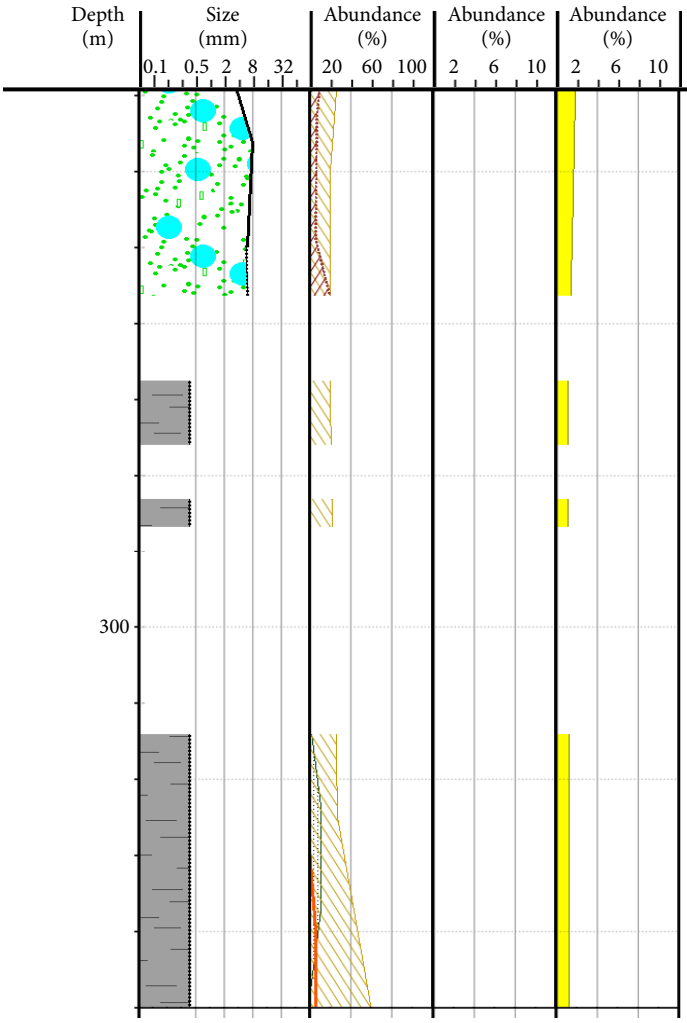

Description, interpretation

235.0 m: Massive plagioclase crystal tuff(?) with 30-50 % small white plagioclase laths 0.5-1.5 mm, 10-20 % rounded grey lapilli(?) 4-8 mm.

265.0 m: Core chips are jarosite-stained sericite-altered metasiltstone as in rock below.

305.0 m: Jarosite+hematite-stained rock chips (poor core recovery).

End of hole

WR301

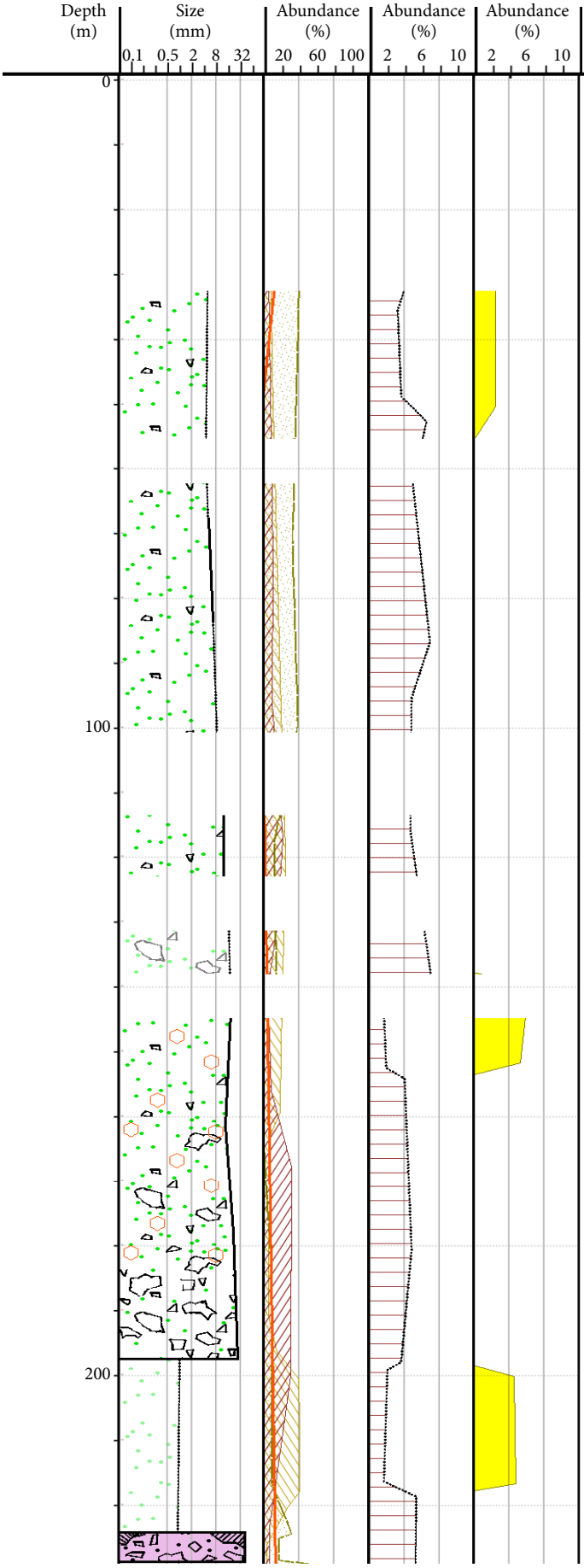

Description, interpretation

150.0 m: Pyrite preserves relict texture of flattened tuff or fiamme(?)

155.0 m: Fragment-poor (< 5 %) plagioclase-phyric rock w < 1 % rounded quartz phenocrysts ~ 1 mm. fragment content increases down hole.

180.0 m: Polymictic 70 %-infill(tuff matrix?)-supported breccia with rounded-subangular fragments, of which: 50 % are light tan (metasiltstone?), 50 % are strongly kaolinite+/-dickite+pyrite-replaced fragments (barely visible; relict).

210.0 m: Fine-grained plagioclase-phyric crystal tuff(?)

229.0 m: Fragment-poor (< 5 %) plagioclase-phyric rock w < 1 % rounded quartz phenocrysts ~ 1 mm. fragment content increases down hole.

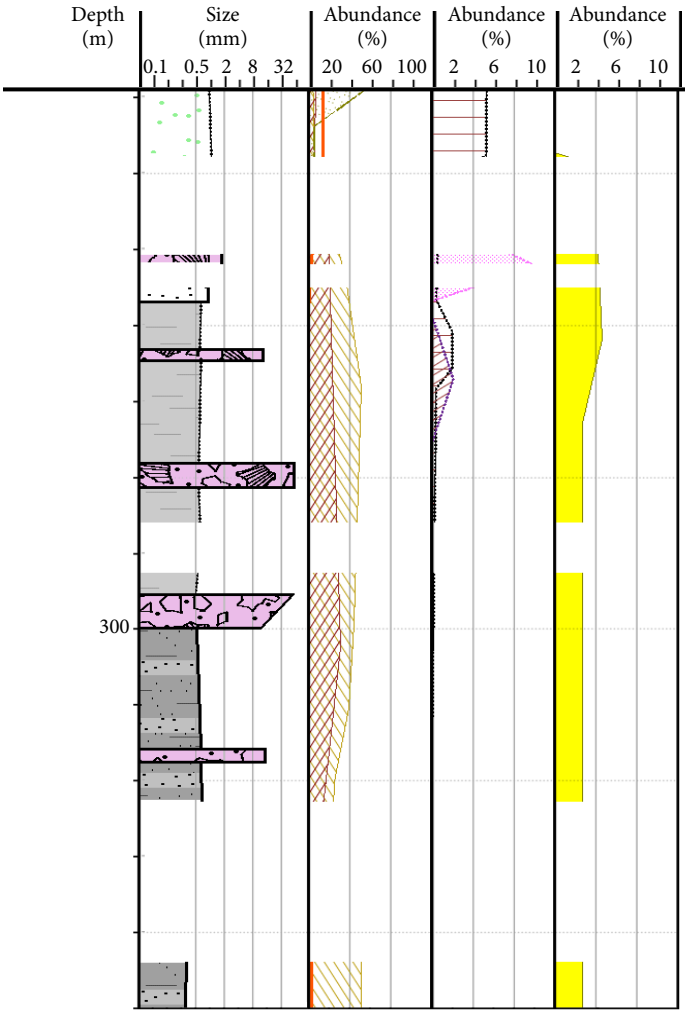

Description, interpretation

245.0 m: Box 60 (missing) contains 10.2 m of core, whereas even strongly faulted intervals typically contain < 5m -- suggests wide fault zone?

254.0 m: Soapy gypsum(?)+kaolinite-altered core chips.

263.0 m: Monomictic fragment-supported chaotic breccia with rounded fragments of metasiltstone, and clay+sericite-altered hydrothermal sandstone infill. cross-cut by (1) pyrite veins and (2) rhodochrosite?chrosite-pyrite+/-sphalerite vein.

270.8 m: Molymictic chaotic 50 % infill- to fragment-supported breccia with angular fragments, of which: 90 % are sericite-altered metasiltstone, some pyrite-veined, and one rounded 6 cm fragment of quartz-cemented sericite-altered-fragment breccia. Infill is opaque mix of sericite+30 % pyrite+/-kaolinite, likely hydrothermal sandstone.

280.0 m: Monomictic fragment-supported chaotic breccia with angular fragments of metasiltstone and sericite+ very fine-grained pyrite hydrothermal sandstone infill.

297.0 m: Polymictic chaotic fragment- (top) to infill- (bottom) supported breccia with overall 50 % subangular fragments, of which: 50 % (the largest) are weakly sericite+kaolinite-altered metasiltstone, 40 % are grey-yellow moderately sericite-altered and minor quartz-pyrite-veined fragments, and 10 % are pyrite-veined breccia fragments of composition similar to breccia at 317.3m. 10 cm of tan sericite-kaolinite infill (no fragments) at 296.5m. Both contacts apparently missing or obscured by broken core.

317.3 m: Polymictic chaotic 70 %-infill-supported breccia with angular fragments, of which: 90 % are sericite-altered metasiltstone, some pyrite-veined, and 10 % calcite+pyrite fragments < 2 cm. Infill is opaque mix of kaolinite+sericite+30 % pyrite, likely hydrothermal mudstone.

335.0 m: Light grey to tan chips, likely sericite-altered metasiltstone.

350.0 m: End of hole.

WR321

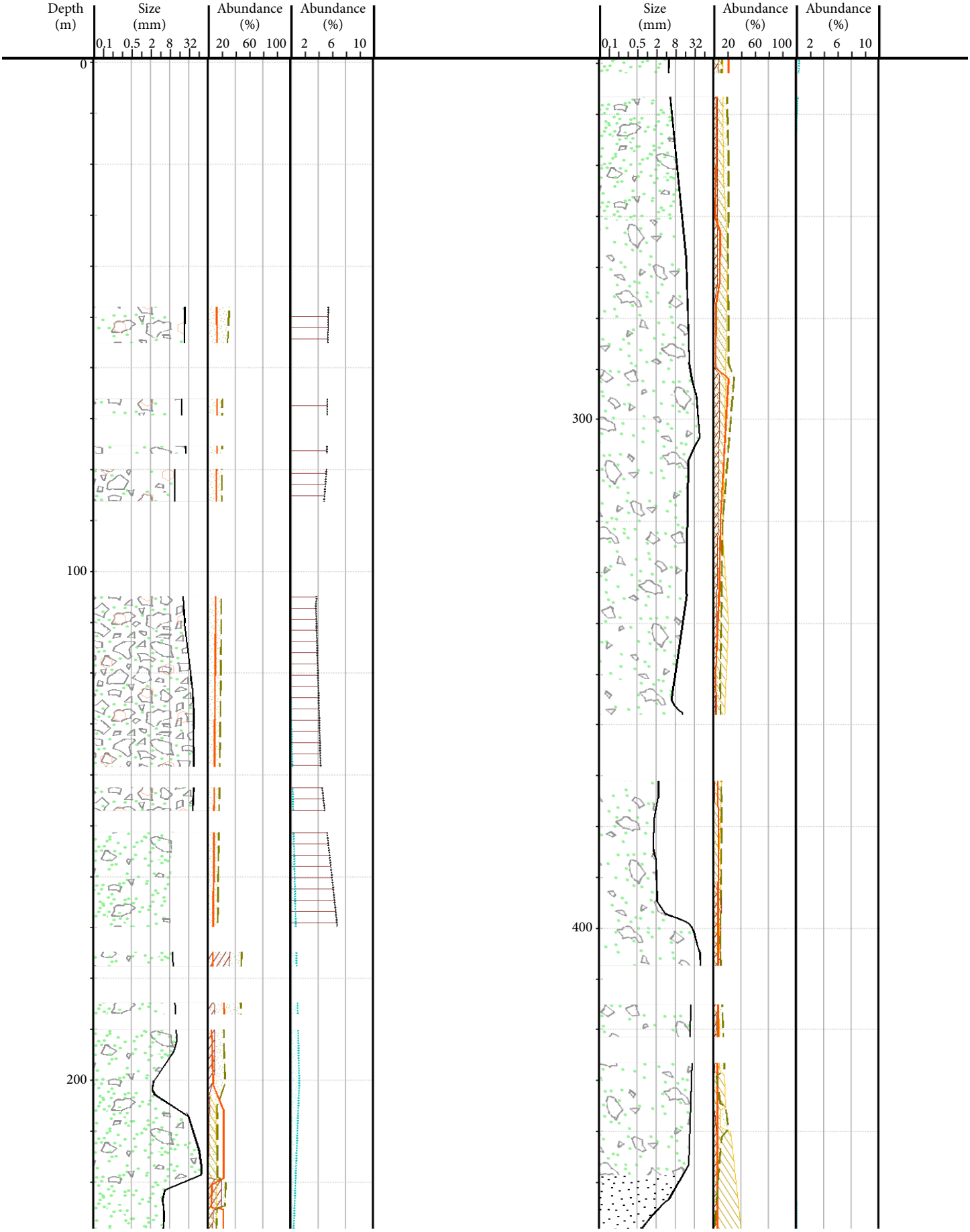
Depth (m)
Size (mm)
0.1 0.5 2 8 32
Abundance (%)
20 60 100
Abundance (%)
2 6 10
0
100
200
300
400

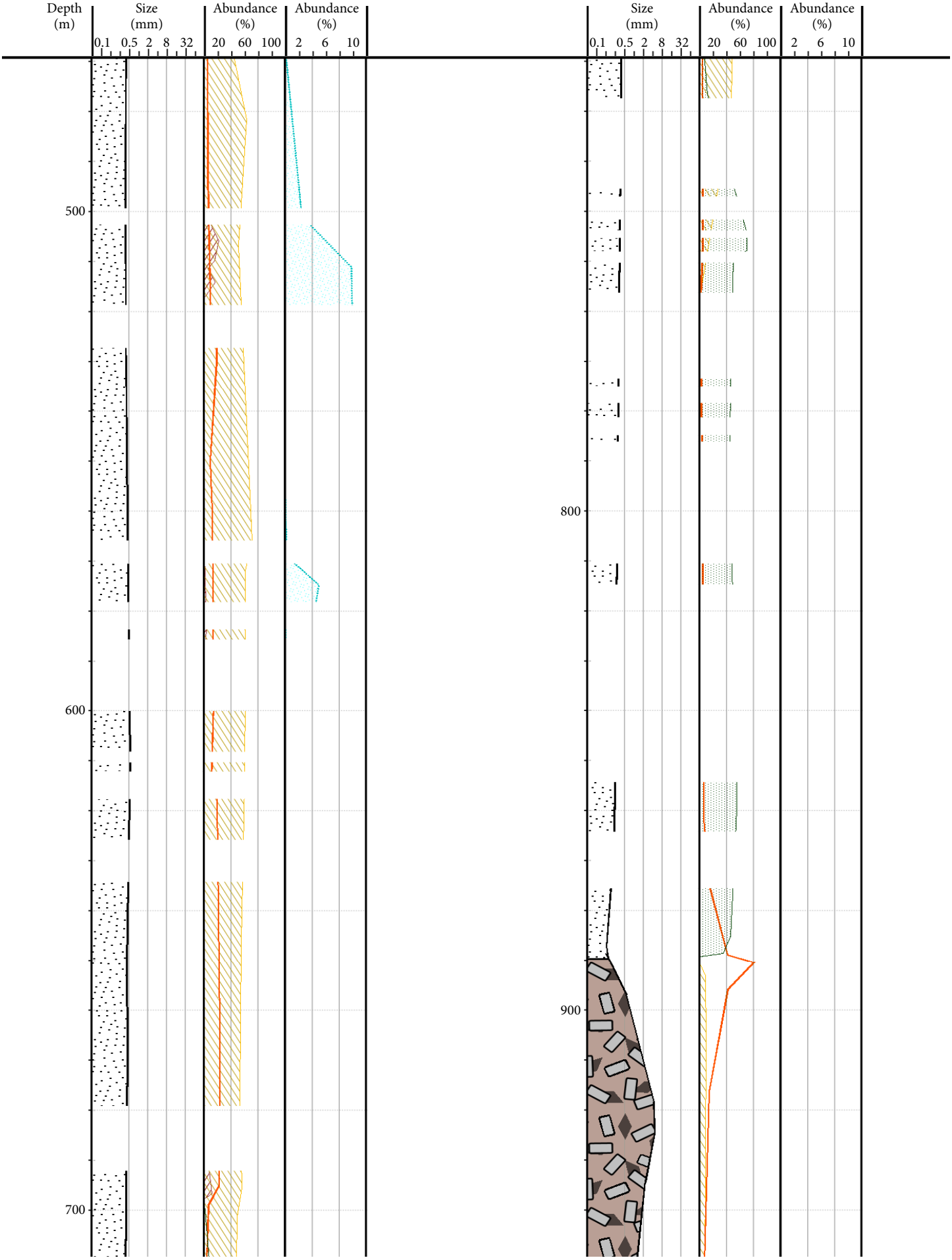
Depth (m)
Size (mm)
0.1 0.5 2 8 32
Abundance (%)
20 60 100
Abundance (%)
2 6 10
500
600
700
800
900

WR347

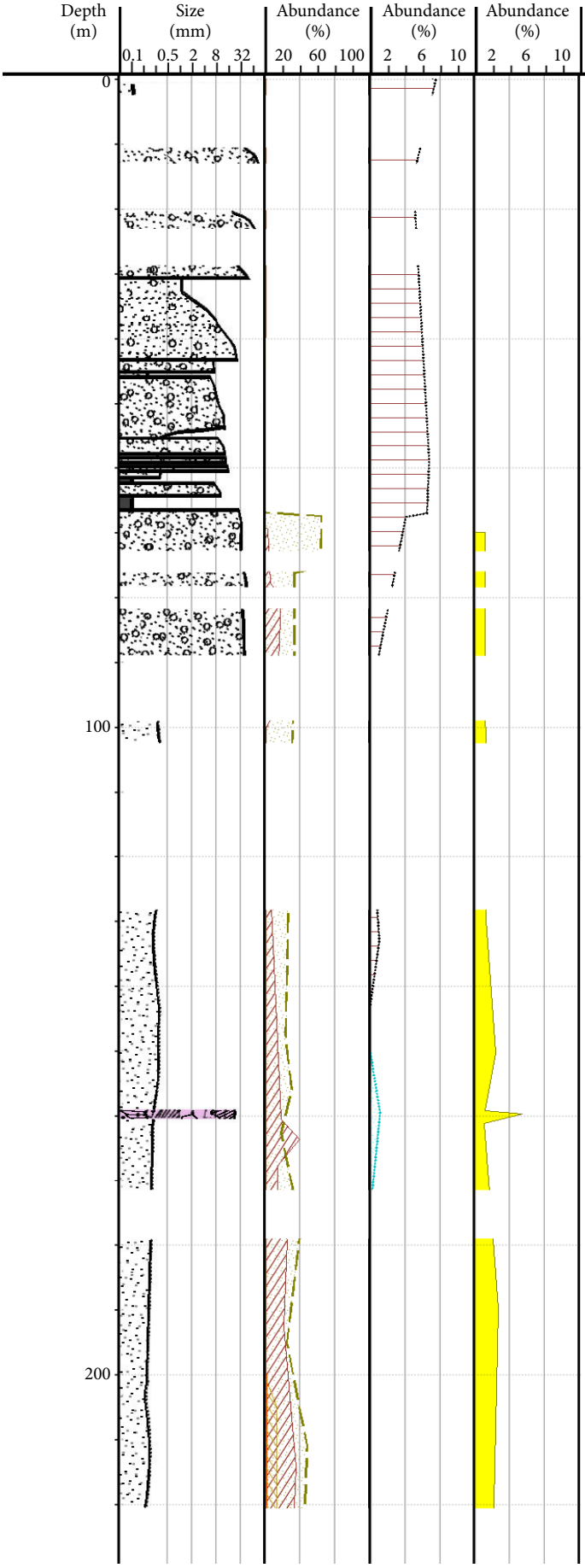

Description, interpretation

46.7 m: Dark tan/red, mostly poorly consolidated polymictic conglomerate to breccia, most above 28 metres obscured by broken core. ~3/4 is clast-supported, with rounded to sub-angular clasts, most slightly elongate parallel to bedding. ~95% of clasts are red fine-grained mudstone , ~5% pale grey quartz+/-clay and quartz-chlorite fragments increasing to ~60% to the base of the unit. lower contact is obscured by broken/missing core.

61.0 m: Light grey-green, locally pale grey sandstone to polymictic conglomerate, matrix and clasts very weakly foliated and consisting of very fine-grained. chlorite. ~60% of clasts are green chloritic phyllite, 30% dark grey mudstone, 10% light grey quartz+/-alunite(?), and <1% graphitic fragments. Locally very strongly hematite-altered [61.0-68.5] and locally quartz-alunite-bearing [70-72].

68.5 m: Light grey-green clast-supported polymictic conglomerate similar to [46.7-61.0], of larger (<15cm long) rounded clasts of 60% grey-green mudstone or phyllite to alunite-altered conglomerate, and 40% weakly sericite-altered andesite (?) with sub-ophitic plagioclase laths enclosing dark green pyroxene. lower contact is missing (broken/missing core)

127.3 m: Light grey strongly alunite-altered fine-grained metasiltstone to metasandstone cut by several irregular fractures at ~15TCA. Most of this interval is missing.

127.6 m: Finely cross-jointed and fractured clay+hematite-altered metasandstone. At the upper contact, hematite has bled into fractures at 16-20TCA a few cm into the overlying rock.

159.0 m: Pale grey, locally green- to light tan yellow-tinged fine-grained metasedimentary rock (chlorite-bearing phyllite) with a moderate planar fabric at 18TCA. Foliation-parallel fractures are spaced a few cm apart. Very weakly pyrite- and magnetite-mineralised minor faults (displacement <1cm) have cross-cut these fractures.

159.2 m: Light pink-grey/beige polymictic chaotic fragment-supported breccia. Fragments, making ~80% of the interval, are mostly sub-angular. 95% of fragments are light beige schistose and possibly laminated/finely bedded sericite-altered metasedimentary rock as in adjacent intervals, 3% are similar but have a darker yellow colour, 2% are dark grey siliceous fragments, and <<1% are rounded pyrite clasts up to 5mm across. Infill (~20% of interval) is about half pink-grey to darker grey very fine-grained milled rock, and half hydrothermal cement consisting of pyrite and green dickite/kaolinite. Dickite-pyrite veins are lined by thin (<0.5mm) dark selvages (oxidised pyrite?) and at least one has cross-cut both fragments and infill. upper contact and lower contact are both missing.

202.5 m: Pale grey to yellow-tinged alunite- and clay-altered metasedimentary rock as in interval [127.6-159.0], barring locally higher diffuse clay contents (judged mostly from softness and from yellow colour on wet core surface; see alt'n). At 179.4m, quartz-pyrite veins are parallel to what may be bedding planes at 12 TCA, and jog across planes every few cm.

202.9 m: Mottled grey and beige chaotic clast-supported breccia. Very similar to interval [159.0-159.2], apart from a lack of dickite (about half of infill is quartz-pyrite cement, the other half hydrothermal mudstone to sandstone), and 3-5% pink angular (orthoclase-altered?) fragments 0.2-1cm across. upper contact is sharp and irregular at 26 TCA, and is marked by a vein 3-8mm wide of soft white material (sericitic?) and very fine-grained dark green (chl?) with pyrite and <5% epidote. lower contact is sharp and irregular at ~30TCA.

228.9 m: Pale grey to yellow-tinged alunite- and clay-altered metasedimentary rock as in [159.2-202.5], containing a few metre-scale intervals of brown-grey as opposed to yellow colour (possibly smectite group clays, or different protolith composition.)

229.2 m: Mottled grey (slightly darker than breccia at [202-5-202.9]) chaotic fragment-supported breccia. Clasts are angular to sub-angular, making up about 85% of the interval. Of the fragments: 1) 95% are yellow-grey to darker brown-grey clay-altered metasedimentary rock as in adjacent wallrock, 0.3-5cm across, some cross-cut by arrays of subparallel quartz veins a few mm wide; 2) 3% are white/translucent grey quartz or strongly silicified fragments (possibly of quartz vein origin), most rounded and <6 mm across; 3) 2% are pale yellow, strongly clay (?) + pyrite-replaced clasts up to 2cm across, one of which contains possible relict zoning preserved by the distribution of pyrite. Of the infill (~15% of total interval): 1) 65% resembles a cement of soft yellow-grey clay (?) and pyrite, although this may represent later replacement of very fine-grained rock flour infill; 2) 30% is grey to beige hydrothermal mudstone to sandstone; 3) 5% is green-blue dickite, most in veins <1mm wide through infill only.

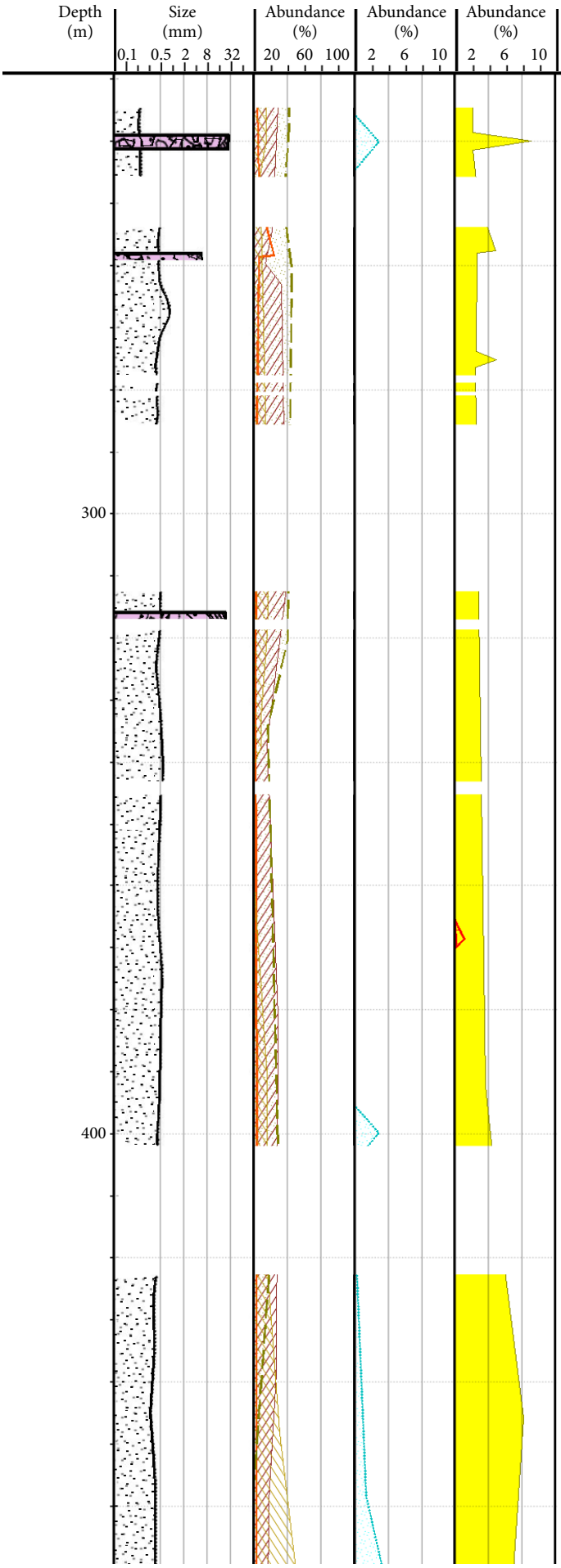

237.2 m: Pale grey to yellow-tinged, locally darker grey (see colour scale), clay-altered metasedimentary rock as in [202.9-228.9].

239.0 m: Mottled grey chaotic fragment-supported polymictic breccia similar to [228.9-229.2], apart from less cement infill; infill makes up ~20% of the interval and consists of 70% hydrothermal sandstone and 30% pyrite-clay+/-dickite veining/cement. Decreasing fracture density towards upper contact from chaotic to about 10cm of jigsaw-fit breccia.

246.0 m: alunite, clay-altered metasandstone to siltstone

246.1 m: Chaotic to rotated fragment-supported breccia similar to previous intervals apart from entirely hydrothermal sandstone infill. Both contacts are missing (broken core).

263.1 m: clay-altered metasandstone to siltstone as in interval [202.9-228.9]. Quartz-pyrite veins make up about 5-10% of the interval, except for the lowermost four metres, with about 20% veins

266.3 m: Angular fragment-supported chaotic breccia similar to breccia intervals above [246-246.1] in terms of fragment types and abundances, but containing two large (5-6cm across) angular fragments of clay-altered yellow-grey rock rimmed by yellow alteration halos 1mm wide (as in clay vein selvages and diffuse alteration in adjacent rocks; suggestive of breccia fluid relationship to diffuse clay alteration elsewhere uphole?). upper contact is sharp at 50TCA, lower contact missing.

275.6 m: clay-altered metasandstone to siltstone as in interval [202.9-228.9].

275.7 m: Chaotic, rounded, infill- to fragment-supported polymictic breccia containing quartz-rich grey-brown and yellow clasts 0.1-6cm across (fewer fragment varieties than in most breccia intervals). Infill makes up ~30% of rock, of which: 1) 50% is soft (H~4) pink very fine-grained cement (hematite+clays?); 2) 40% is very fine-grained anhedral pyrite, in irregular aggregates or blebs, some of which may have a secondary vein origin (i.e., cross-cutting the breccia infill, though not the fragments); 3) 10% is grey-beige hydrothermal mudstone. upper contact is sharp and nearly planar at 56TCA.

318.6 m: clay-altered metasandstone to metasiltstone as in interval [202.9-228.9].

~319 m: Breccia similar to [159.0-159.2]. upper contact is sharp and planar at 60TCA, lower contact is missing.

331.2 m: clay-altered metasandstone to metasiltstone as in interval [202.9-228.9].

339.0 m: clay-altered metasandstone to metasiltstone as in interval [202.9-228.9], but with slight epidote-green colour (possible minor sericite-epidote component?).

431.6 m: Light grey-green, locally yellow-tinged (see colour specs) sericite-altered metasandstone, containing a few intervals of clay veins (or clay selvages to quartz veins). [367.4-370.0] contains several pyrite veins, at ~15% of total interval, and minor chalcopyrite.

440.4 m: As above, but quartz-pyrite, pyrite, and minor dickite-pyrite have wider (0.1-3cm) dark/black selvages.

443.3 m: quartz-pyrite and later dickite veined sericite+/-clay altered metasandstone.

451.0 m: Light grey-green sericite-altered metasandstone as in [339.0-431.6], with diffuse contacts on the basis of colour only.

456.5 m: Slightly yellow-tinged, weakly clay-altered and quartz-pyrite veined rock similar to interval [440.4-443.3].

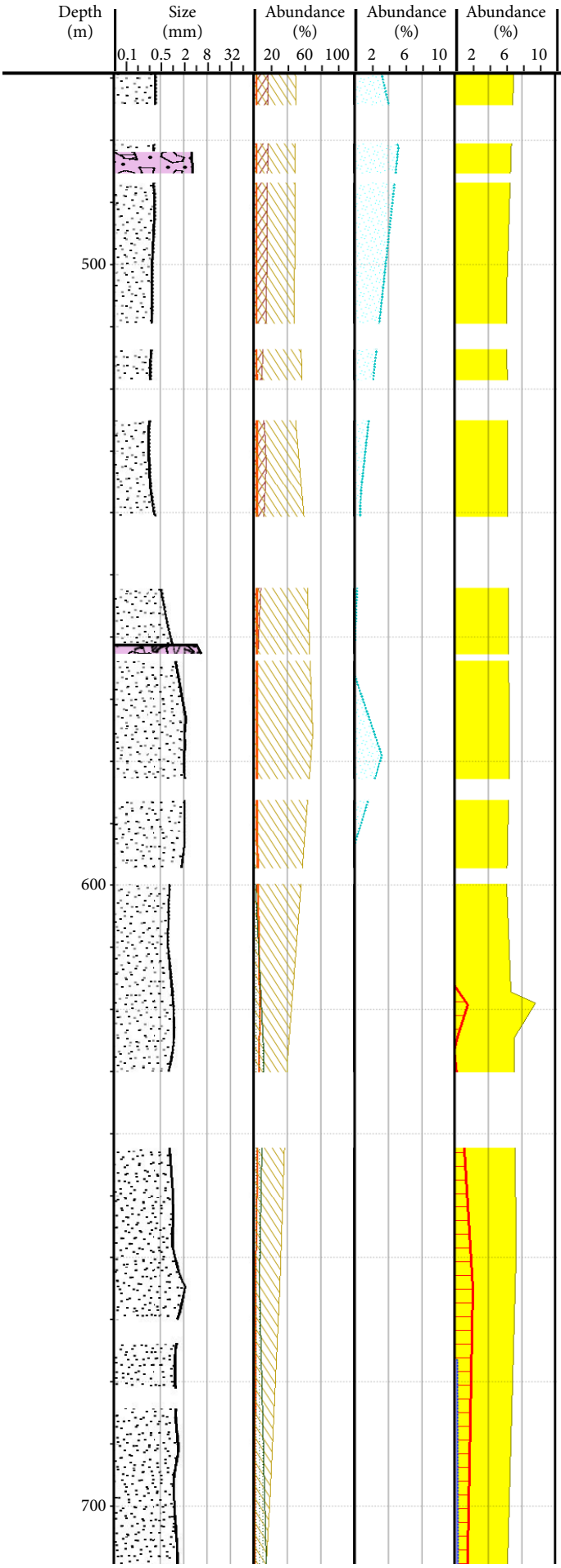

Description, interpretation

483.0 m: Variably yellowish (clay) to greenish (sericite-epidote) tinged metasandstone with two dominant vein series: V1: quartz <2cm at 11TCA, without selvages, V2: Dark brown (oxidised or possibly marcasite?) pyrite veins <3mm wide at 55-70 TCA.

484.6 m: Very poorly consolidated light grey rock, likely a strongly weathered/ porous uphole equivalent of vuggy Mo-bearing veins (e.g., at [716.4]). Resembles a poorly consolidated breccia, but unlike breccia intervals above, contains ~equant white and grey sub-angular quartz fragments 0.3-1cm across. Infill, where preserved, is quartz or amorphous silica (possible soft white clay material as well), very porous/vuggy, and contains finely disseminated euhedral pyrite coated in sooty black material (overall pyrite content is ~5-10%). Infill also contains <3% light blue dickite, as later diffuse veins through infill or open spaces. Both contacts are missing (broken core).

506.0 m: As in interval [456.5-506.0].

528.0 m: As in previous sericite+/-epidote-altered intervals barring fewer subintervals of yellow/clay selvages.

551.0 m: As above, light beige, locally yellow and green-tinged

618.0 m: Largely sericite-altered metasandstone as in [528.0-551.0], but with greater local variation in strong orange to red colour from core weathering, likely reflecting sulfide abundance; intervals [585-592], [614-616], [620.5-625] have a strong orange to red colour.

620.5 m: Dark brown-grey, soft phyllite with 2-3% finely disseminated pyrite and 5-8% vein pyrite+/-chalcopyrite. Contacts of this unit are missing/obscured by broken core.

625.4 m: As in interval [551.0-618.0], with lower contact diffuse over several metres on the basis of biotite content and/or grey-brown colour.

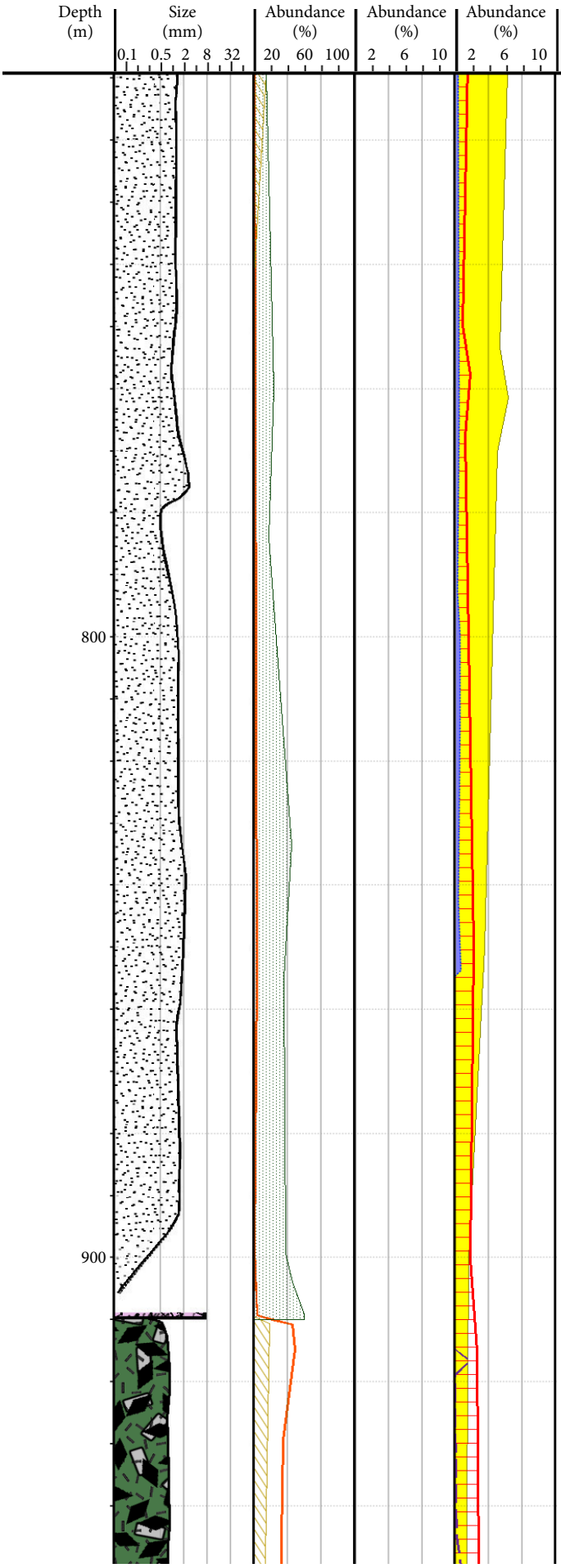

733.4 m: Metasandstone similar to above sericite+/-clay-altered intervals apart from a slightly darker brown colour from weak (~10%) diffuse biotite alteration, not distinctly associated with vein selvages (photo). Density of veining and overall biotite content (associated with darker colour) gradually increases downhole, and lower contact is arbitrarily based on a transition to very dark grey-brown. At [628], sericitic selvages have overprinted biotite/potassic alteration (photos).

756.4 m: Black or very dark grey-brown, strongly biotite-altered metasandstone (rounded quartz grains of protolith are more obvious in a biotite-altered matrix). Several softer sub-intervals contain fractures or veinlets weathered to jarosite (yellow) and hematite (red), producing an overall dark tan tinge.

805.7 m: As above, with slightly higher overall vein %. This interval also contains several molybdenite-bearing quartz-pyrite veins as described in the interval below. Sub-interval [759-765] has a dark red tinge reflecting higher sulfide content (V pyrite ~5-20%, V chalcopyrite 1-2%).

806.0 m: Grey or weakly pink-grey vein 15cm wide of translucent to opaque quartz (98%), pyrite (2%, most finely disseminated in diffuse bands parallel to veining), and molybdenite (<1%, along seven distinct hair-thin bands parallel to veining, not symmetrical, but most concentrated towards the middle of the vein). Distinct texture is produced from vugs/pores up to 6mm wide, between quartz fragments, lined with prismatic-terminating quartz crystals and euhedral pyrite. This is similar to other veins hosting Mo above and below this interval, though most are a few mm wide. Veins at [716.4] and [483.0-484.6] are more vuggy/pitted and poorly consolidated.

809.0 m: Black or very dark grey-brown strongly biotite-altered metasandstone as in interval [733.4-756.4].

809.5 m: Dark grey-brown strongly biotite-altered metasandstone as in interval [733.4-756.4], but with strong red tinge (weathering of pyrite in core).

847.0 m: Black or very dark grey-brown strongly biotite-altered metasandstone as in interval [733.4-756.4].

850.0 m: Biotite-altered metasandstone, with slightly lighter colour (lower biotite content?) than adjacent intervals.

892.0 m: Dark grey-brown biotite-altered rock as in interval [733.4-756.4], with a few slightly lighter coloured or dark tan-red sub-intervals.

907.0 m: As in interval [733.4-756.4], with dark red tinge likely reflecting higher sulfide content. Lowermost ten metres contain texturally desctructive biotite alteration; little/no indication of protolith composition or grain size.

910.2 m: Black, strongly biotite-altered very fine-grained rock. Lower contact to porphyry is sharp and marked by 5cm of strongly magnetic medium-grained chaotic infill-supported breccia of light grey porphyry or quartz vein fragments in a black biotite infill.

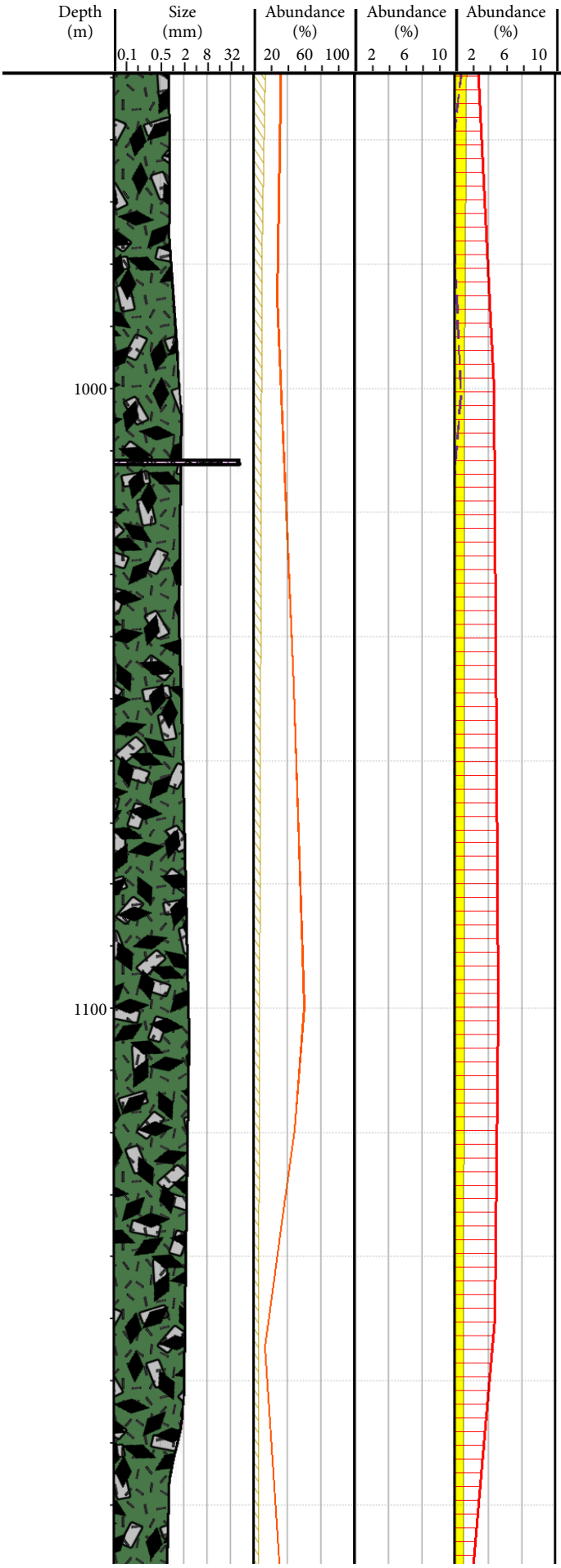

Description, interpretation

1012.0 m: Light grey, fine-grained hornblende- and plagioclase-phyric diorite porphyry. It consists of ~50% plagioclase laths <0.5mm long, ~5% orthoclase (?) interstitial to plag and hornblende (no quartz phenocrysts), 20% soft pale green subhedral hornblende rhombs (some laths?) 0.5-2mm long, and 10-25% finely disseminated to clotty magnetite (though the interval is non-magnetic within a few metres of the upper contact). Most of the unit is cut by ~10-30% sharp-walled and laminated quartz and quartz-magnetite veins (magnetite usually at vein margins, minor chalcopyrite+/-bornite in centres). Some bornite observed may be distinctly blue-violet weathered/oxidised chalcopyrite (?) based on yellow colour on fresh surfaces, though bornite at [913.1] was reported in earlier logs. The composition of this unit varies mostly in amounts of quartz+/-bornite+/-chalcopyrite+/-magnetite veins, in amounts of biotite, and in the ratio of black (least-altered) to pale green and soft (sericite+chl-altered) hornblende phenocrysts.

1012.1 m: Chaotic fragment- to infill-supported breccia containing ~60% fragments, of which: 99% are angular clear or milky quartz (vein) fragments 0.1 to at least 3cm across, the largest also brecciated (i.e. some breccia fragments are brecciated quartz vein material in a quartz infill); and 1% are bornite which may either be fragments 1mm across, or they may have been originally hosted withing the quartz fragments. Of the infill, 70% is hydrothermal sandstone and 30% is very fine-grained brown to black material (likely biotite).

1145.0 m: Light grey porphyry as above, with little variation apart from paucity of quartz-bornite veins. Minor variation in maximum plagioclase phenocryst size.

B - 200

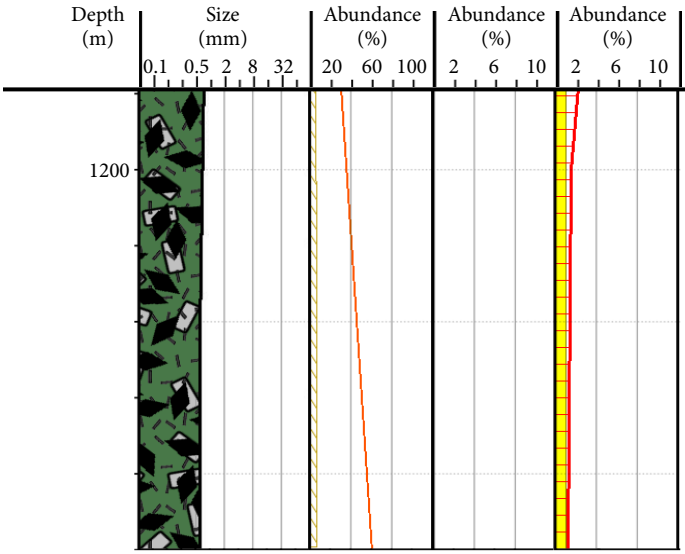

Description, interpretation

End of log.

WR349

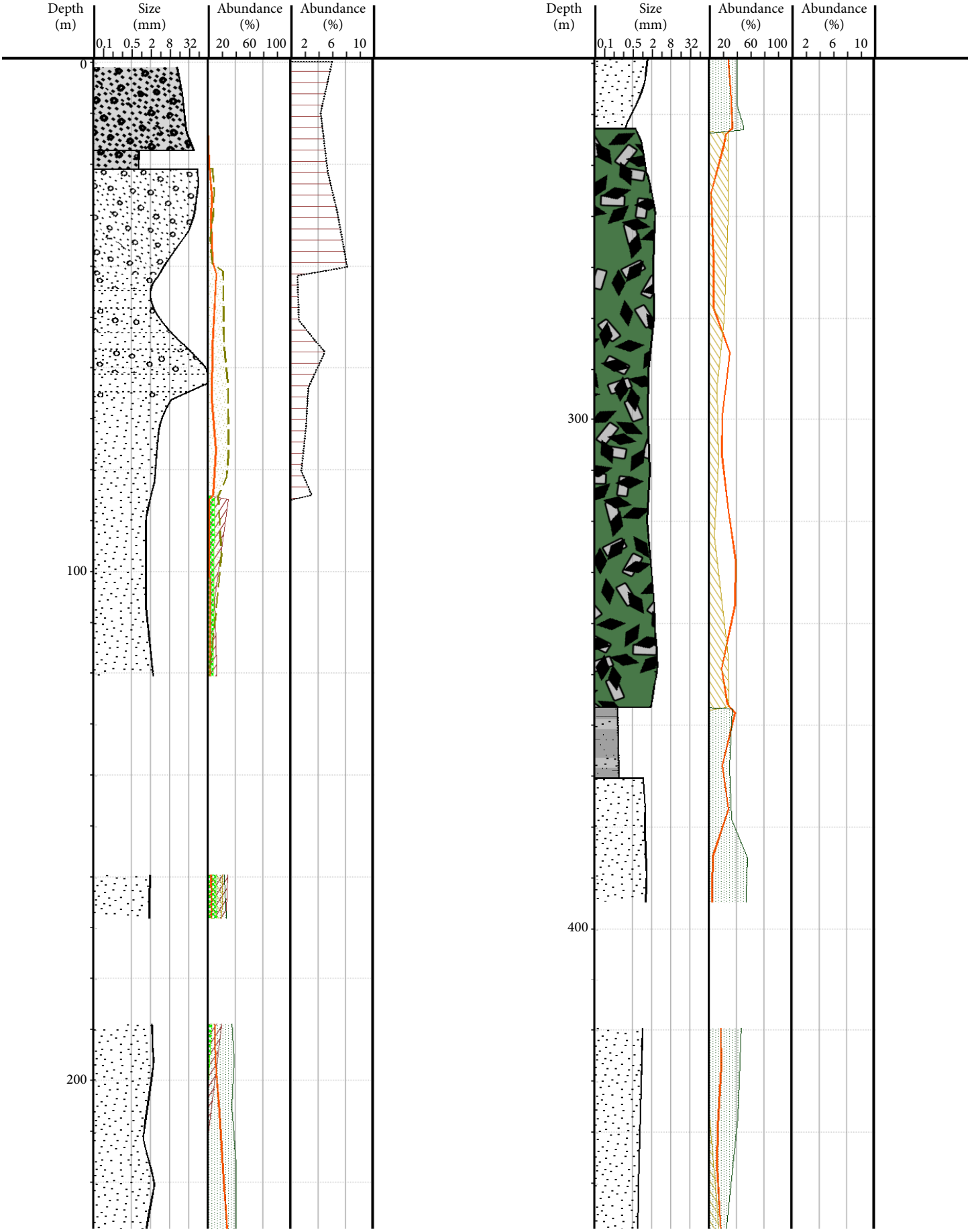
Depth (m)
Size (mm)
0.1 0.5 2 8 32
Abundance (%)
20 60 100
Abundance (%)
2 6 10
0
100
200
300
400

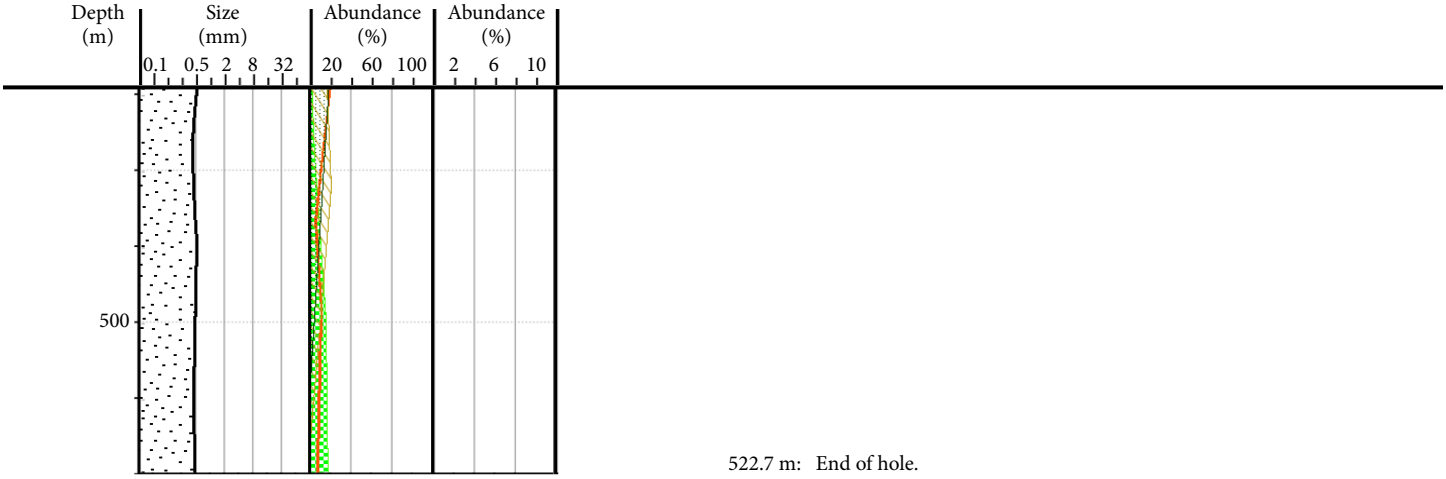

522.7 m: End of hole.

WR377

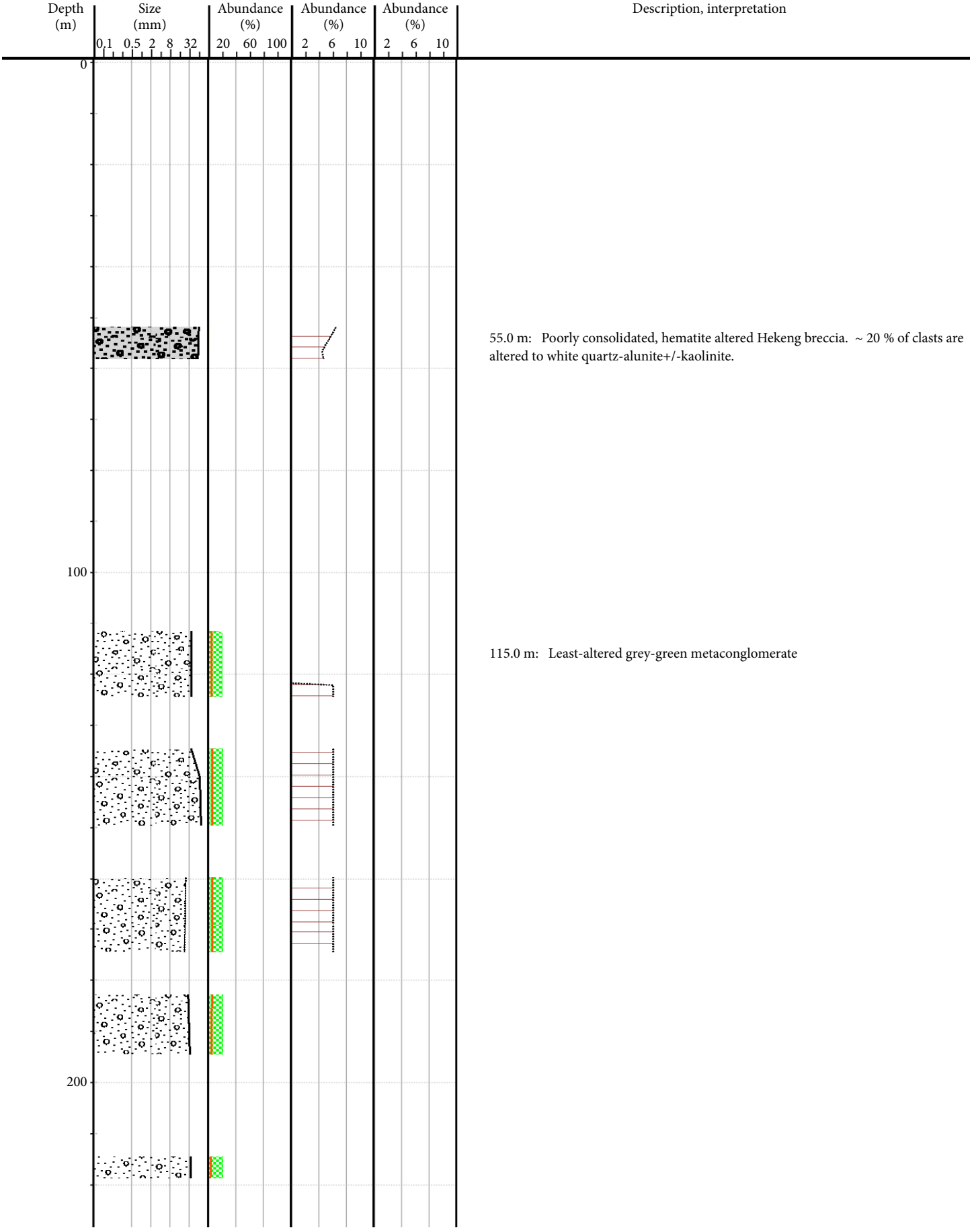
Depth (m)
Size (mm)
0.1 0.5 2 8 32
Abundance (%)
20 60 100
Abundance (%)
2 6 10
Abundance (%)
2 6 10
Description, interpretation
0
100
200
55.0 m: Poorly consolidated, hematite altered Hekeng breccia. ~ 20 % of clasts are altered to white quartz-alunite+/-kaolinite.
115.0 m: Least-altered grey-green metaconglomerate

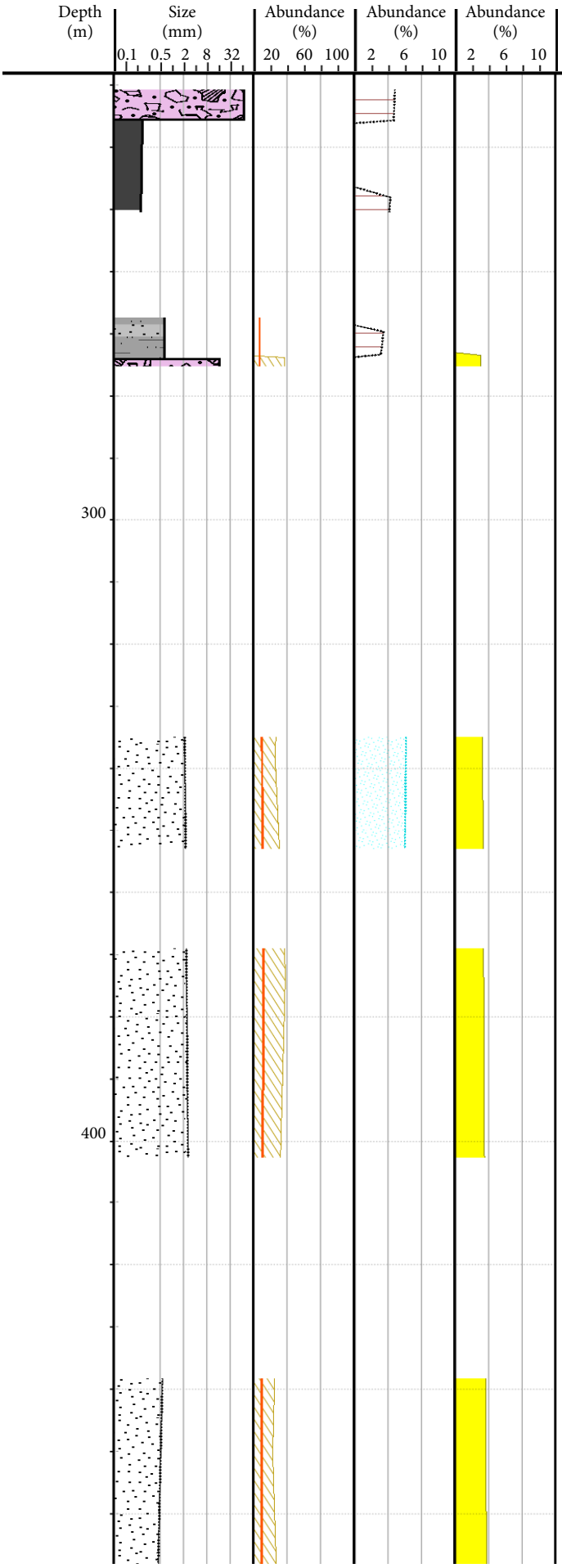

231.0 m: Polymictic 40 %-infill- to fragment-supported chaotic breccia with angular fragments, of which: 55 % (the largest) are quartz-veined metasiltstone, 30 % (< 2 cm) are metasandstone, and 15 % are quartz (possible fragments of quartz veins). Infill is hematite-altered hydrothermal sandstone of similar composition to larger fragments, locally quartz-cemented hydrothermal sandstone. Infill and fragments are hematite-altered, fragments were hematite-replaced mostly at their margins.

245.0 m: Poorly consolidated, black clay. fault(?)

274.0 m: Polymictic fragment-supported chaotic to (along walls) jigsaw-fit breccia with angular fragments, of which: 90 % are sericite-altered metasiltstone as in wallrock, and 10 % are translucent kaolinite+dickite kaolinite fragments. Infill is ~ 95 % kaolinite with < 5 % finely disseminated pyrite. One contact visible, sharp and irregular at approx 0 TCA.

340.0 m: Locally dark colour to sericite+/clay alteration (smectite?).

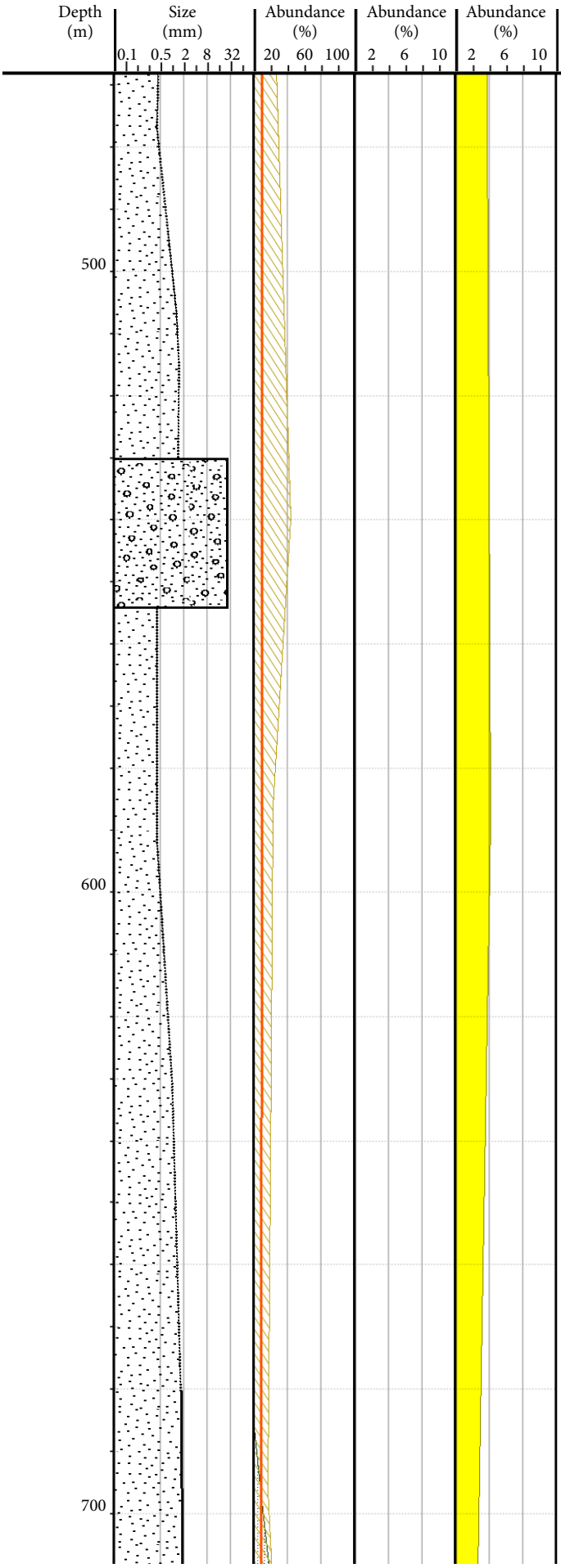

Description, interpretation

580.0 m: Early quartz-pyrite veins are irregular/patchy, second set are thin, linear.

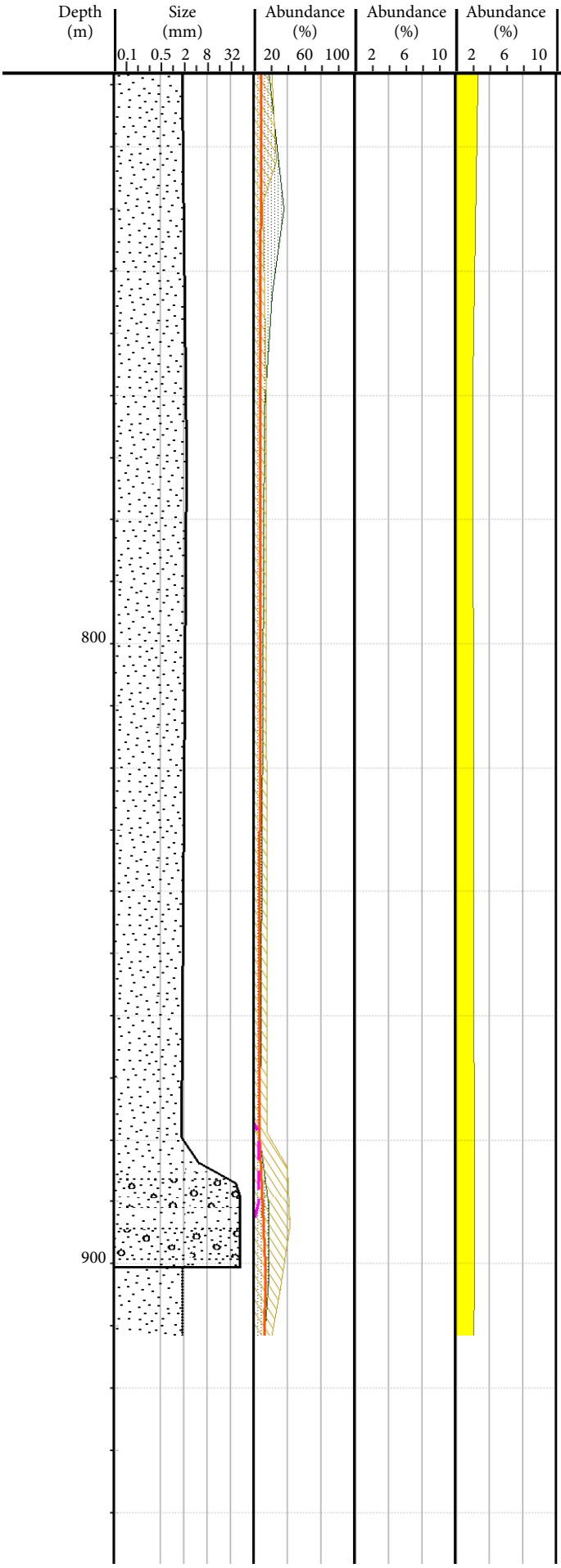

Description, interpretation

760.0 m: Almost least-altered metasandstone, barring decimetre-scale intervals of quartz-pyrite veins with sericite halos and weak biotite alteration (biotite halos to quartz veins at depth).

905.0 m: Undulating, patchy early quartz veins.

914.0 m: Core chip colour changes from grey-yellow (sericite) to darker (biotite) downhole.

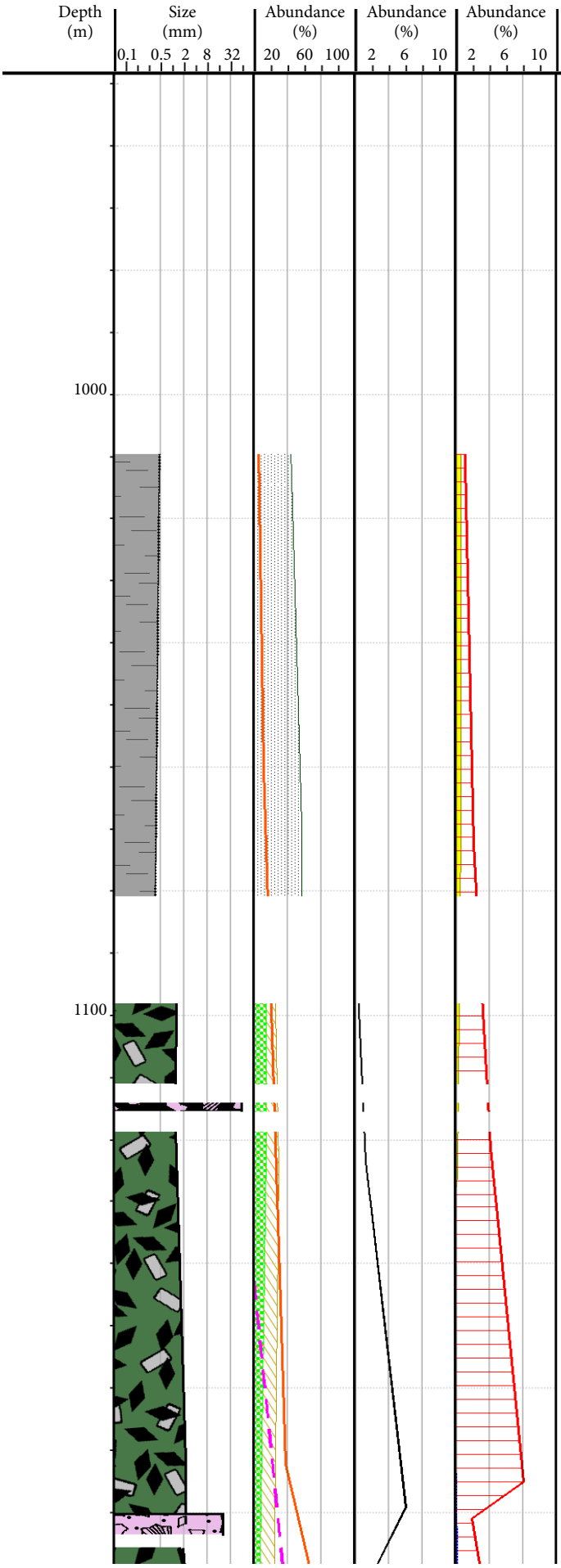

Description, interpretation

1116.4 m: Possible monomictic rotated fragment-supported breccia (?--poor core recovery). fragments (80 %) are quartz-veined diorite, infill (20 %) is quartz-chalcopyrite-orthoclase-biotite cement. No contacts preserved. May be dense vein network after quartz-veined diorite, as opposed to breccia?

1120.0 m: Sericite + chlorite after plagioclase phenocrysts and throughout groundmass.

1171.5 m: Coarse-grained biotite patch 10 cm wide with very fine-grained chalcopyrite interstitial to biotite laths.

1182.0 m: Monomictic 80 %-infill-supported chaotic breccia with angular fragments 1-40 mm of pale orthoclase+/-sericite-altered diorite (?) floating in a weakly sericite-altered hydrothermal sandstone infill replaced by ~ 70 % magnetite and chlorite after sericite (N.B. magnetite replacement, not cement). Upper contact obscured by quartz veins, lower is missing core. breccia contains no visible sulfides, and (along with magnetite-replaced infill) was cross-cut by 2 generations of quartz-chalcopyrite+/-pyrite veins (+/-trace bornite?) with orthoclase halos.

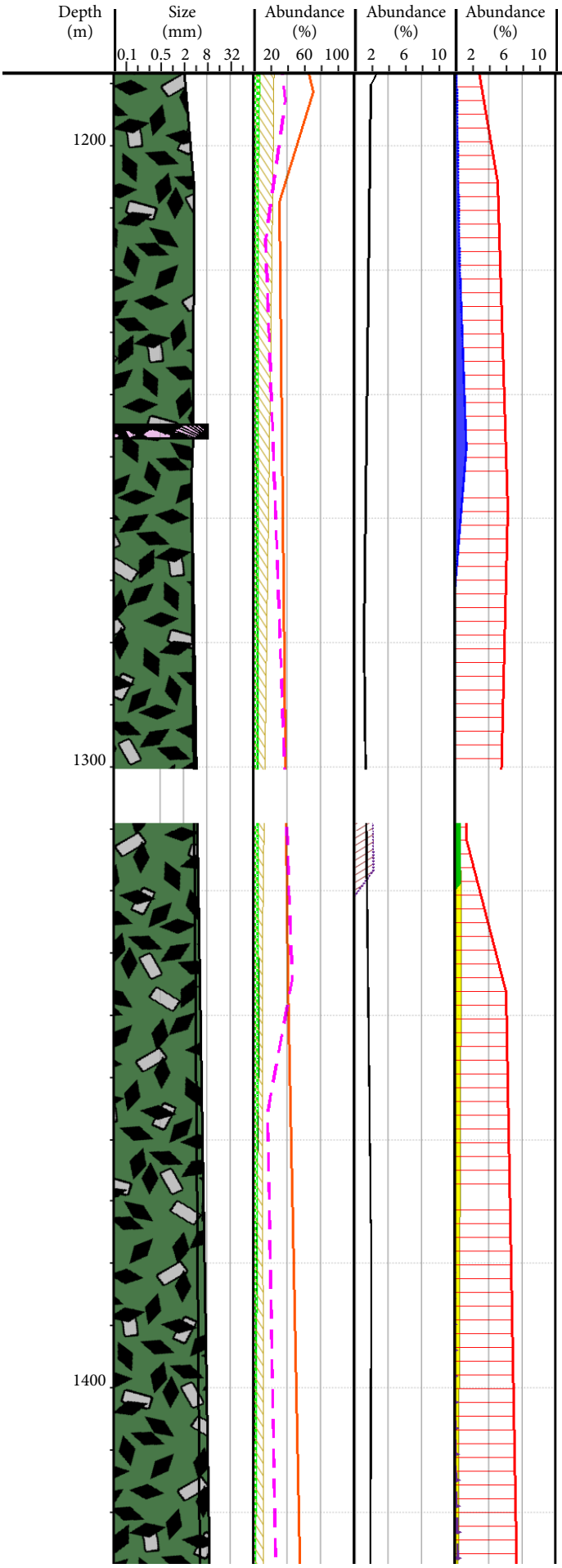

Description, interpretation

1200.0 m: Orthoclase alteration is patchy, diffuse.

1210.0 m: Large (4 mm) round sericite+chlorite-altered plagioclase phenocrysts.

1220.2 m: Late chalcopyrite veins (after quartz veins with orthoclase halos) are locally molybdenite-bearing as round inclusions 1-2 mm across.

1246.0 m: Monomictic 95 %-infill-supported breccia vein with angular quartz fragments floating in a chalcopyrite(+trace patchy molybdenite) cement infill. Both contacts are irregular at ~ 35 TCA, and marked by euhedral inward-terminating quartz crystals ~ 1-2 mm long.

1306.6 m: Vein and alteration sequence observed as follows: 1 (first) - disseminated magnetite, chlorite alteration of phenocrysts, and orthoclase vein at 11 TCA, 2- quartz-biotite vein, 3- magnetite veinlet, 4- quartz veins at 40 TCA, 5(last)-chalcopyrite veinlets cross-cutting and locally exploiting (running parallel to) previous vein contacts.

1310.0 m: Pyrite-rhodochrosite-quartz+/-chalcopyrite cross-cuts porphyry, quartz veins with orthoclase+/-sericite halos, and chalcopyrite veins. This was cross-cut by a few subparallel hair-thin to locally mm-wide metallic grey (tennantite? enargite? non-magnetic, grey streak) veinlets at ~ 10 TCA.

1328.6 m: Irregular patch ~ 6 cm long of coarse-grained biotite laths with interstitial quartz and terminating into quartz+chalcopyrite. Margins of this coarse-grained biotite-quartz vein/zone are at ~ 5-20 TCA and rimmed by a white orthoclase selvage 1-4 mm wide into host diorite.

1345.0 m: A few cm-scale patches of texturally destructive orthoclase flooding.

1370.0 m: Chlorite after biotite phenocrysts is spatially associated with diffuse magnetite. Red-tinged mineral in magnetite-rich patches may be secondary hematite (?).

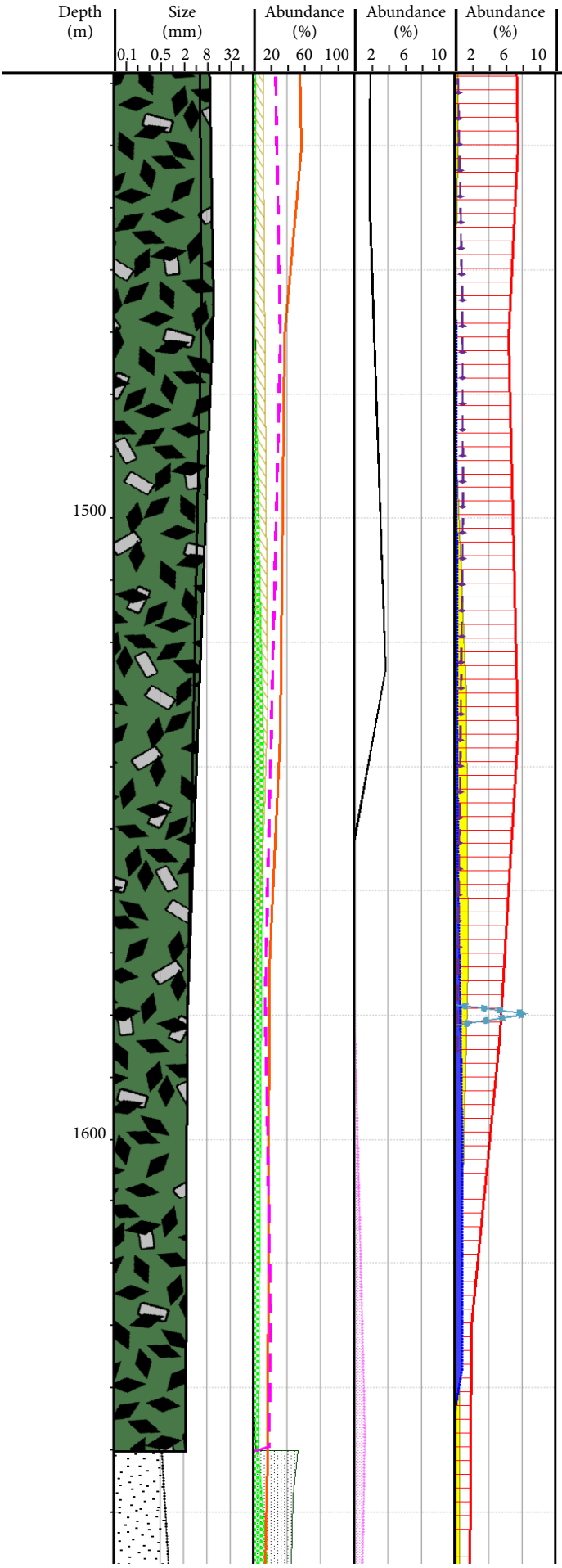

Description, interpretation

1433.5 m: Interpreted sequence: 1- orthoclase halos, magnetite throughout groundmass, 2-quartz veins with orthoclase halos, thin quartz-chalcopyrite+/- bornite veins.

1470.0 m: Bornite is very finely disseminated through porphyry. bornite associated with region of largest phenocrysts?

1476.6 m: Bornite is very finely disseminated in quartz veins. molybdenite is very finely disseminated through porphyry.

1530.0 m: High magnetite content is mostly diffuse vein halos, but some may be primary magmatic. This magnetite-rich interval contains fewer preserved plagioclase phenocrysts than adjacent porphyry.

1549.0 m: Chlorite clots ~ 7 mm across with finely disseminated chalcopyrite along margins.

1581.2 m: ~ 1m of diffuse quartz + 5-10 % finely disseminated chalcocite, pyrite, and chalcopyrite, cross-cut by two breccia veins 0.5-2 cm wide of quartz-pyrite fragments < 5 mm in a pyrite-chalcocite cement infill. Both breccia veins have sharp contacts at 12-20 TCA, marked by 3-5 mm of inward-terminating quartz crystals.

1620.0 m: Very finely disseminated molybdenite through porphyry.

1628.0 m: 3 cm long rounded grey xenolith of plagioclase-phyric very fine-grained (sub-mm phenocrysts) diorite, within plagioclase-phyric diorite.

1640.0 m: Light grey hornblende+plagioclase-phyric crowded diorite porphyry with ~ 65 % hornblende and 15 % plagioclase phenocrysts 2-3 mm in a hard, quartz-rich groundmass. In strongly chlorite-altered zones, plagioclase and hornblende phenocrysts can be distinguished by rhombic (hornblende) or rounded and blurry (plagioclase) crystals.

1650.0 m: Irregular anhydrite vein at ~ 10 TCA occurs with quartz veins in porphyry.

1670.0 m: Darker biotite, possible minor very fine-grained actinolite(?)

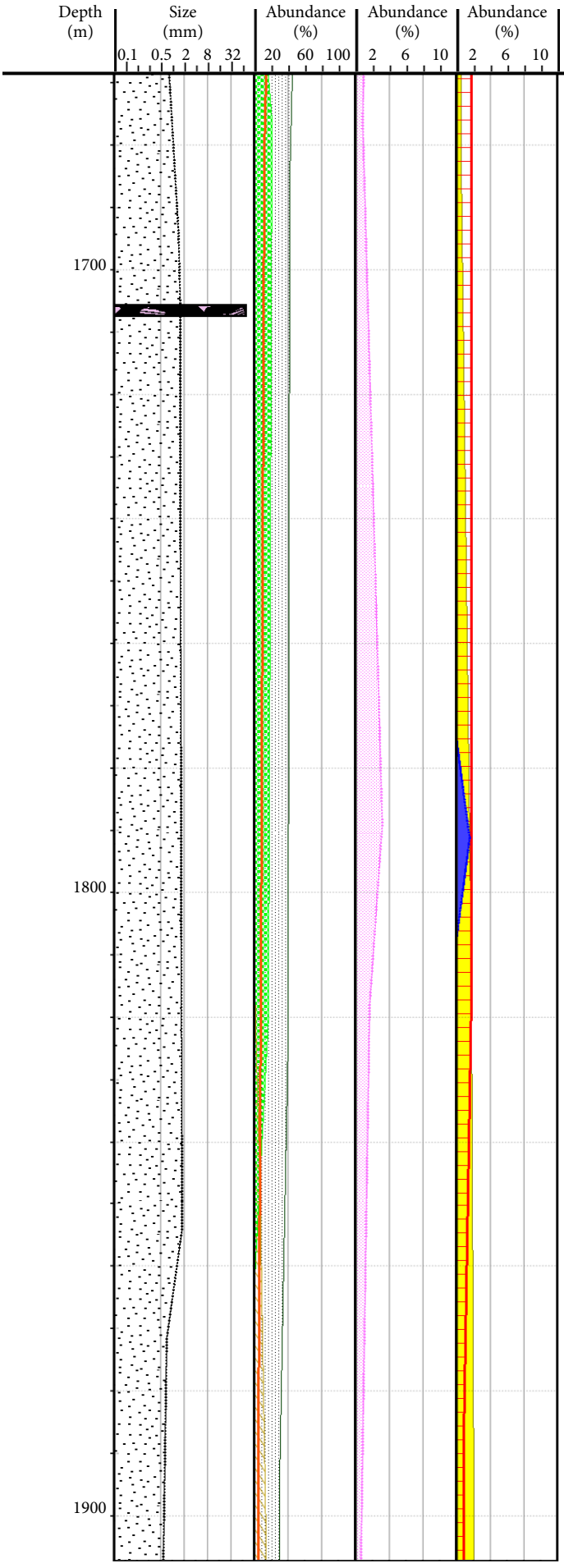

Description, interpretation

1707.5 m: Monomictic 60 %-infill-supported rotated to in-situ breccia vein with angular biotite-altered metasandstone fragments (wallrock) in mm-scale crystalline anhydrite cement infill. breccia vein has dark biotite+/-actinolite halos < 1 cm wide with trace very finely disseminated chalcopyrite at its margins.

1791.5 m: Coarse-grained to laminated quartz veins with seam molybdenite and disseminated to seam chalcopyrite cross-cut by sub-parallel anhydrite veins at ~ 30 TCA.

1810.0 m: Where diffuse/patchy, chalcopyrite is generally associated with higher magnetite content.

1820.0 m: Very finely disseminated pyrite is associated with biotite halos.

1825.2 m: Chalcopyrite is only hosted in anhydrite veins, whereas pyrite occurs with anhydrite vein and disseminated in host.

1837.3 m: Chlorite halos around pyrite veins, after diffuse biotite.

1890.0 m: 2 stages of anhydrite-pyrite veins with biotite halos. Pyrite and chalcopyrite more abundant in biotite-actinolite halos.

End of hole.

WR392

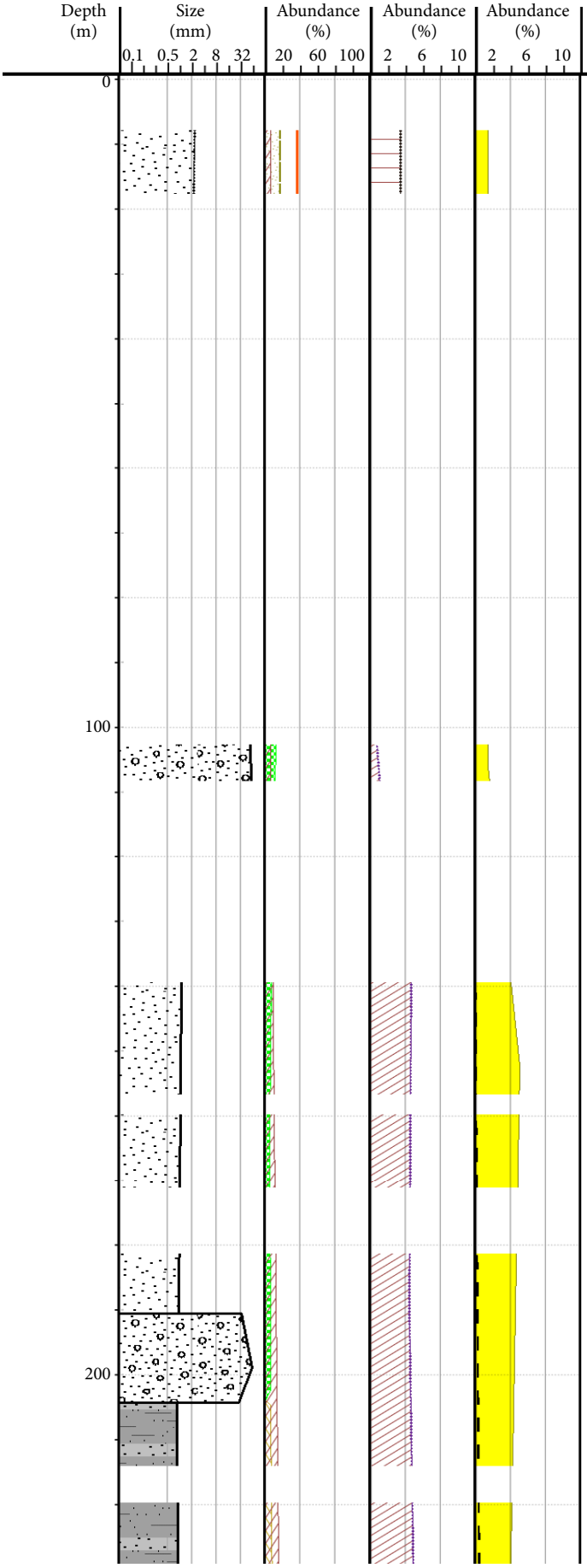

Description, interpretation

15.0 m: Vuggy quartz-hematite-alunite altered rock (metasandstone?)

106.0 m: Least-altered metaconglomerate, excepting sparse calcite-pyrite veins.

186.9 m: Observed vein sequence: 1- quartz-pyrite veins, 2- carbonate-chalcopyrite veins, 3- calcite veins

204.0 m: Downhole transition from white calcite veins to pink/orange carbonate (mostly rhodochrosite?) veins.

220.0 - 275.0 m: ~ 10 vol % linear carbonate+base metal sulfide veins throughout interval.

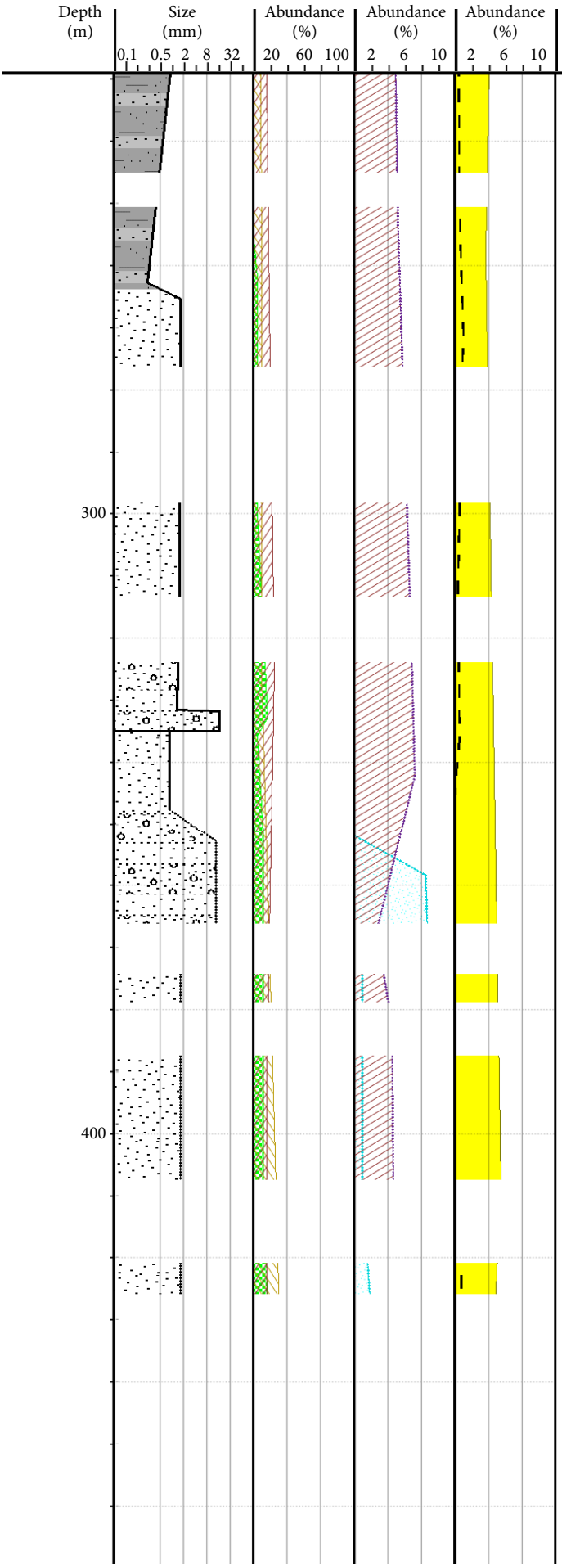

Description, interpretation

326.6 m: Monomictic 60 %-infill-supported chaotic to rotated breccia vein, with angular sericite-altered wallrock fragments 3-9 mm long in a carbonate cement+kaolinite+trace pyrite infill. Cement is ~ 60 % pink (rhodochrosite?) at margins of vein and ~ 40 % calcite, towards centre with higher kaolinite content. Both vein contacts are sharp and irregular at ~ 10 TCA. One sphalerite+carbonate+trace galena vein extends at ~ 5 TCA from the margin of the breccia vein.

371.0 m: Rusty, degraded core. Few small chips remaining contain carbonate-pyrite veins.

390.6 m: Black Mn oxide on unpolished core surface.

395.8 m: Calcite-pyrite+trace galena vein, locally breccia (sulfide fragments in calcite cement) after a quartz vein.

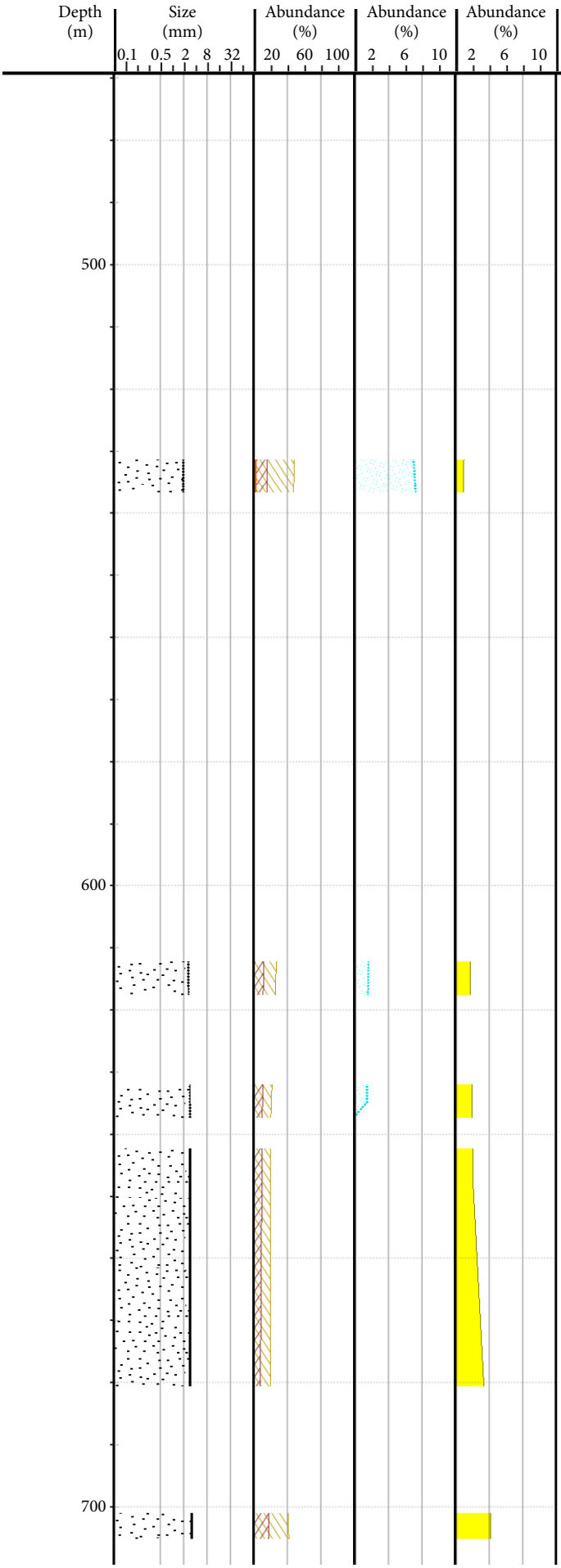

Description, interpretation

515.0 m: End of WR392 log. Start of WR392W_1 log.

625.0 m: Light blue clay (dickite?) visible on core chip surfaces.

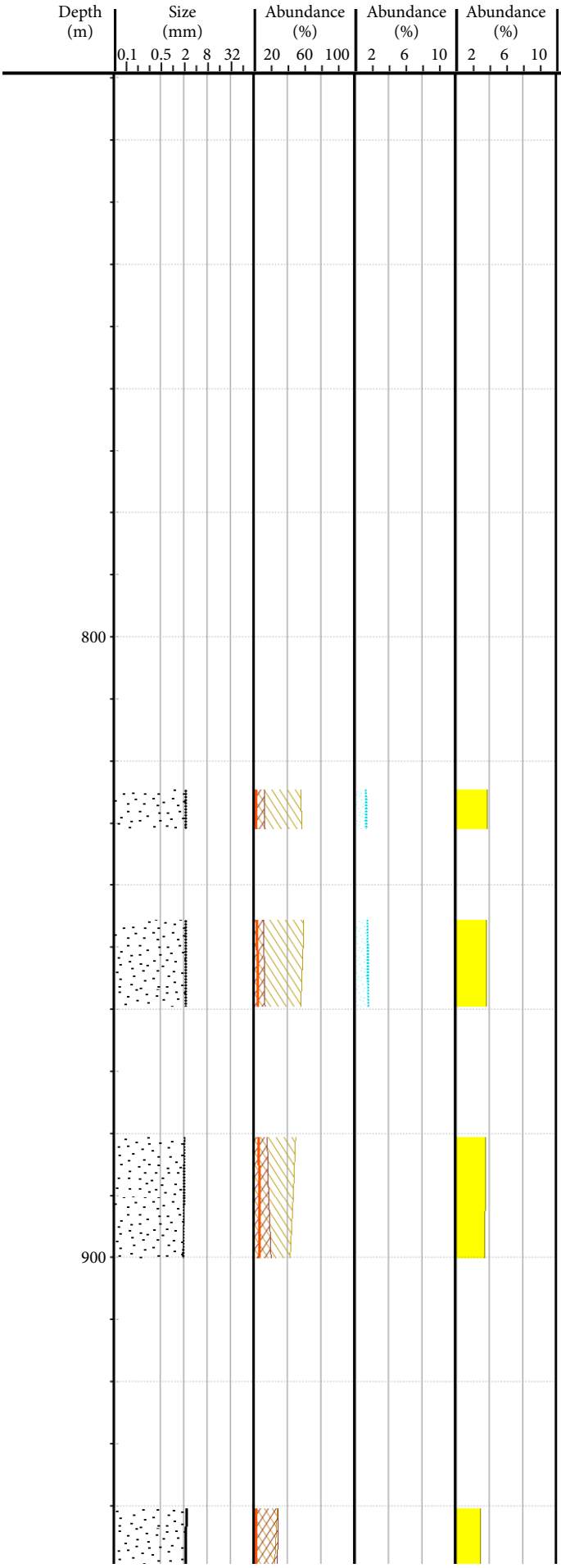

950.0 m: Grey colour from diffuse kaolinite alteration.

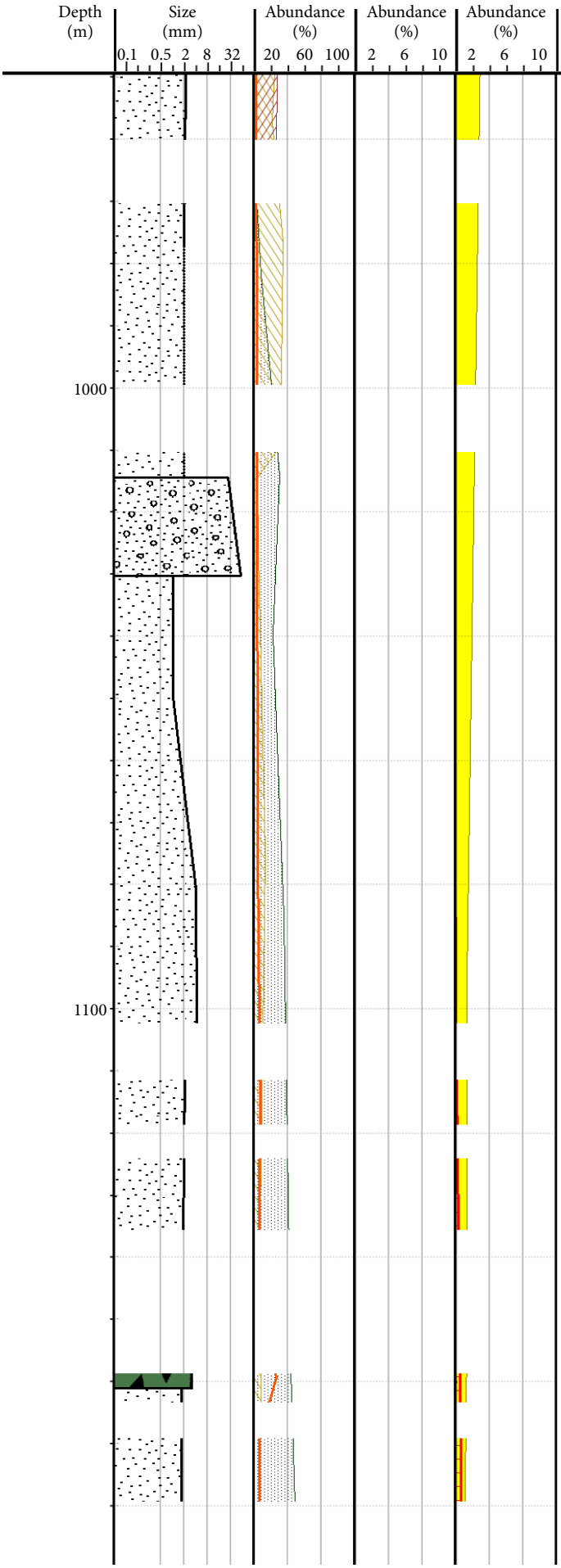

Description, interpretation

1090.0 m: Biotite halos to quartz veins grades over several cm to sericite halos.

1100.0 m: Pyrite vein with chlorite halos after diffuse biotite.

1151.0 m: Linear pyrite+marcasite(?) vein 6 mm wide has cross-cut porphyry at 5 TCA.

1160.0 m: Light grey plagioclase-phyric(?) diorite porphyry, possible weakly preserved hornblende phenocrysts (replaced by orthoclase-quartz-sericite alteration).

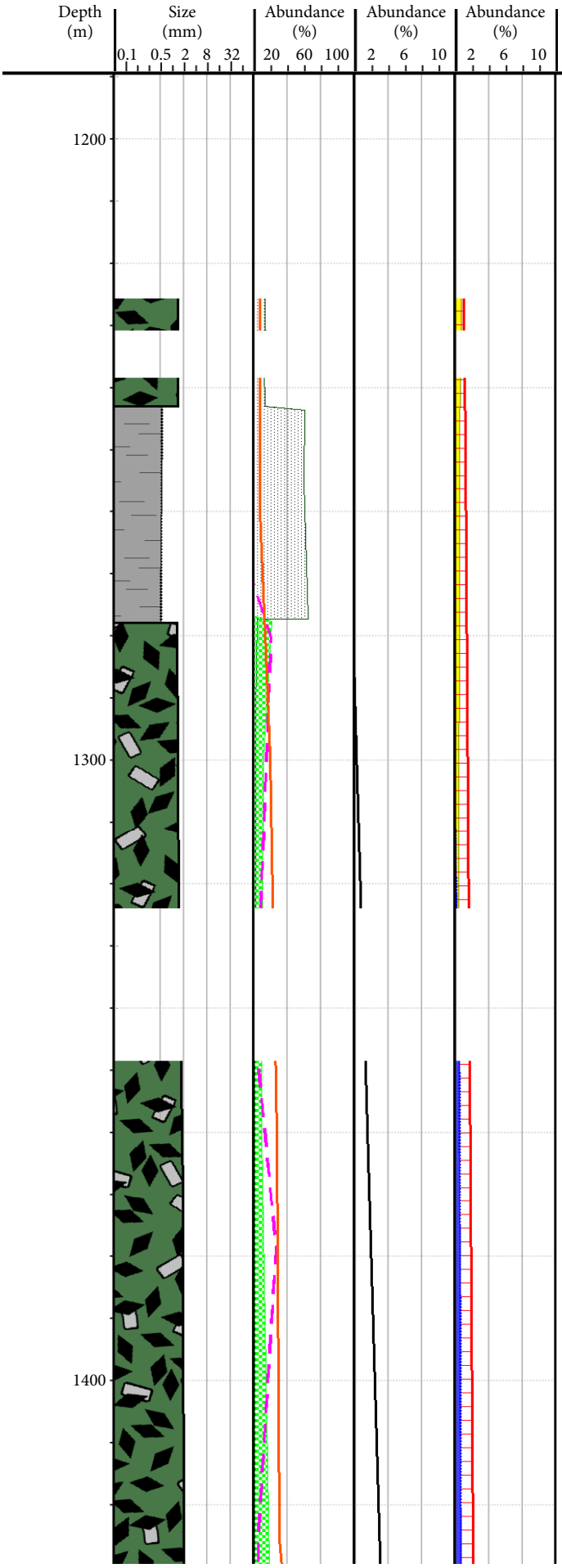

Description, interpretation

1240.0 m: Weakly biotite-altered fine-grained (1 mm) plagioclase+minor hornblende-phyric porphyry dyke. Poor core recovery. upper contact missing. lower contact is sharp with no clear chill margin, angular, and offset by several thin quartz veins, in turn cross-cut by chalcopyrite veins. chlorite content increases within 1 cm of dyke contact with biotite-altered host.

1277.1 m: Porphyry upper contact is sharp and planar at 70 TCA, contact was cross-cut by quartz veins and later chalcopyrite veins.

1280.0 m: Linear biotite veinlets through porphyry were cross-cut by chalcopyrite veins at 80 TCA.

1300.0 m: Grey to darker grey-green, locally pink, plagioclase+hornblende-phyric diorite with 40-70 % subhedral chlorite-replaced hornblende phenocrysts mostly < 1 mm, some < 3 mm. Contains trace very finely disseminated molybdenite, chalcopyrite, and bornite, and 3-15 % disseminated to clotty magnetite throughout. bornite, magnetite, and chlorite content increase downhole towards the lower contact.

1380.0 m: Chlorite throughout porphyry, after hornblende and biotite phenocrysts and biotite in groundmass, and as halos to magnetite, pyrite, and chalcopyrite veins.

1398.0 m: White quartz+orthoclase-replaced hornblende phenocrysts superficially resemble plagioclase, apart from rhombic habit.

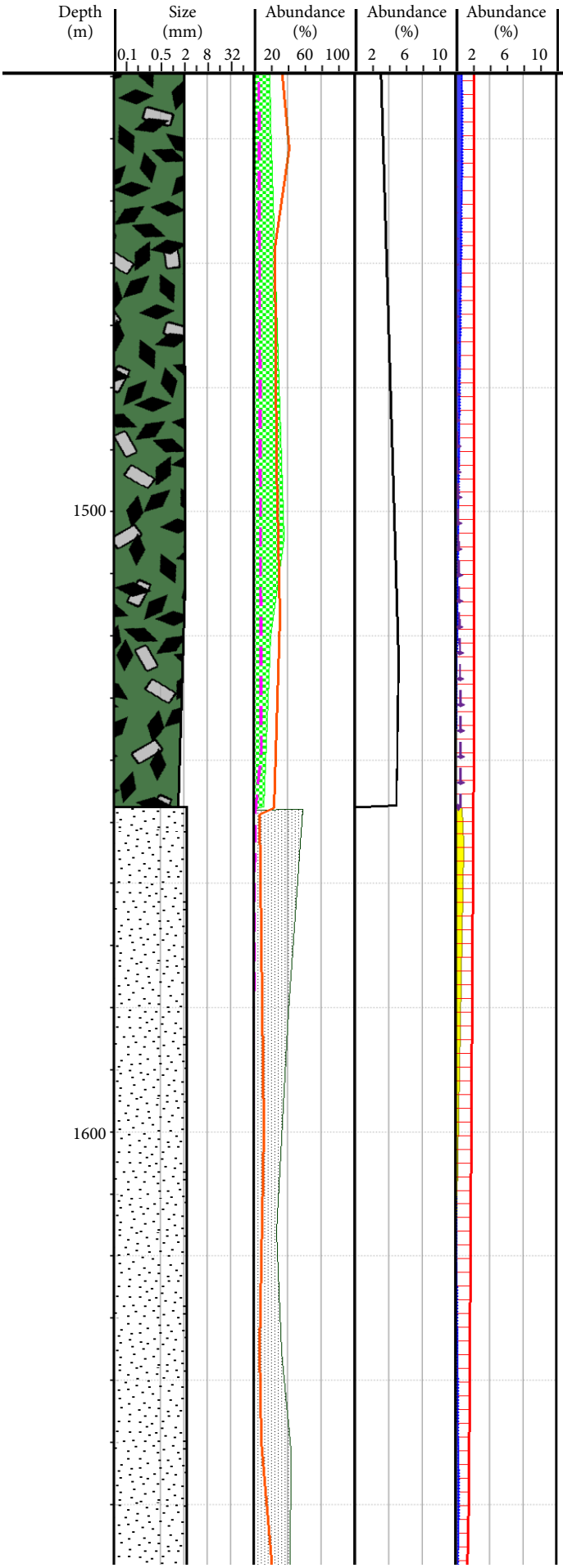

Description, interpretation

1431.7 m: Carbonate-pyrite-chalcopyrite vein with trace very fine-grained molybdenite(?) cross-cuts porphyry at 60 TCA.

1450.0 m: Quartz veins increasingly undulating and diffuse (margins ~ 1 mm) with depth.

1495.8 m: ~ 5 cm irregular patch of coarse-grained quartz (6 mm) terminating centrally to coarse-grained biotite (plates/laths up to 1 cm) with chalcopyrite interstitial to biotite laths.

1530.0 m: cm-scale diffuse magnetite patches/clots with chlorite halos several cm.

1545.0 m: < 0.5 % bornite, very finely disseminated in groundmass and in chalcopyrite veins. Sublinear chalcopyrite-bornite veins cross-cut all other veins (quartz, magnetite, chalcopyrite) at ~ 5 TCA.

1662.8 m: Molybdenite in laminar quartz veins with minor chalcopyrite, cross-cutting both early undulating and later sublinear veins.

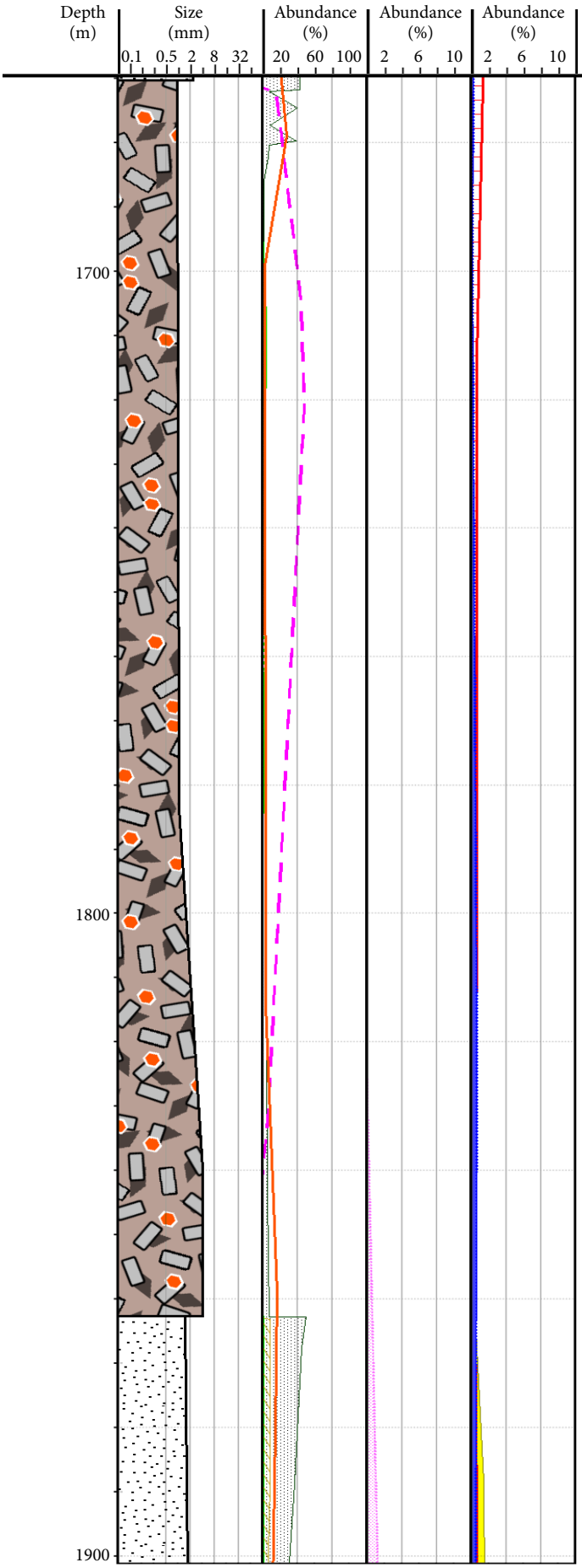

Description, interpretation

1673.0 - 1680.0 m: Several cm-wide porphyry dykes within strongly biotite-altered and quartz veined metasandstone. Dyke contacts are irregular, but overall trend 40-70 TCA.

1685.0 m: Coarse-grained biotite clots < 1 cm across are most abundant within several metres of porphyry upper contact.

1699.2 m: Trace molybdenite+chalcopyrite-bearing quartz veins cross-cut barren quartz and orthoclase veins+halos.

1710.0 m: Decimetre-scale patches of diffuse chlorite alteration after biotite in groundmass, some after plagioclase phenocrysts.

1711.0 - 1740.0 m: Diffuse, round biotite clots < 1 cm sparsely distributed throughout porphyry.

1743.0 m: Possible fine-grained quartz+plagioclase-phyric diorite xenolith 5 cm long, margins diffuse.

1790.0 m: Grey non-magnetic hornblende+quartz+plagioclase-phyric diorite, phenocrysts mostly < 2 mm with fine-grained biotite in quartz-rich groundmass. ~ 10-30 % hornblende as subhedral rhombs < 1.5 mm, ~ 5 % quartz phenocrysts up to 3 mm. Locally magnetic (diffuse finely disseminated magnetite) with associated chlorite, and contains sparsely distributed biotite phenocrysts < 5 mm, as well as several intervals containing round clots of coarse-grained biotite. ~ 0.5 % very finely disseminated chalcopyrite and << 0.5 % molybdenite throughout.

1851.5 m: Subangular xenoliths < 2 cm of very fine-grained biotite-altered diorite (?), chlorite replacing biotite a few mm into xenolith margins.

1890.0 m: End of hole.

WR393

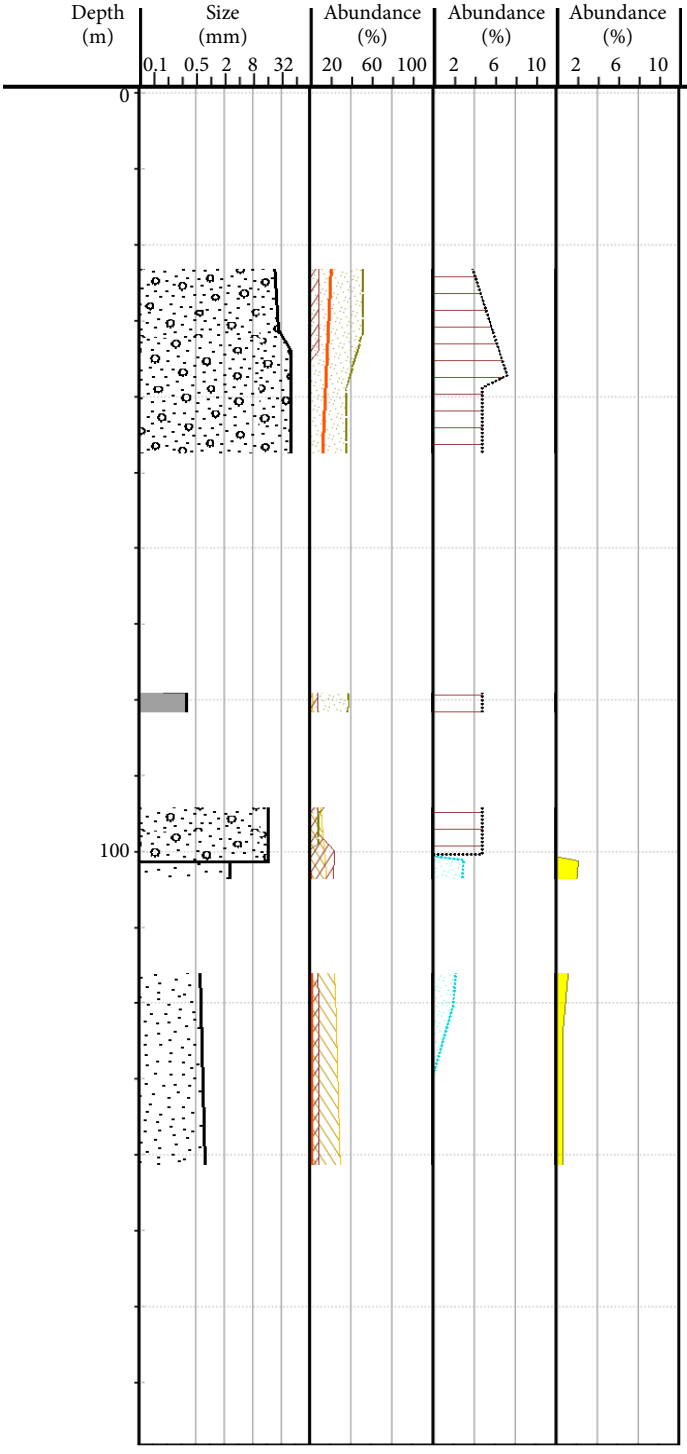

Description, interpretation

25.0 m: Metaconglomerate as in other Owen-Stanley metaconglomerate intervals: poorly sorted rounded clasts 0.5-5 cm, some slightly elongate with weakly preferred orientation at ~ 40 TCA, supported in a chloritic sandy matrix. A few cm-scale intervals of low quartz-alunite-hematite content have colour typical of greenschist facies metaconglomerate (mostly chlorite). This interval was previously logged as Wafi breccia complex.

46.0 m: Vuggy; < 5 % irregular, generally round cavities < 6 mm across throughout quartz-alunite-altered rock

81.0 m: Locally least-altered grey-green metasiltstone between quartz-alunite-hematite veins. hematite veins into metasiltstone have alunite halos with sharp margins, and no hematite veins occur within 5 mm of alunite-metasiltstone boundary.

160.0 m: Core chips (few available) are moderately sericite-altered metasandstone with pyrite veins.

End of hole.

WR396

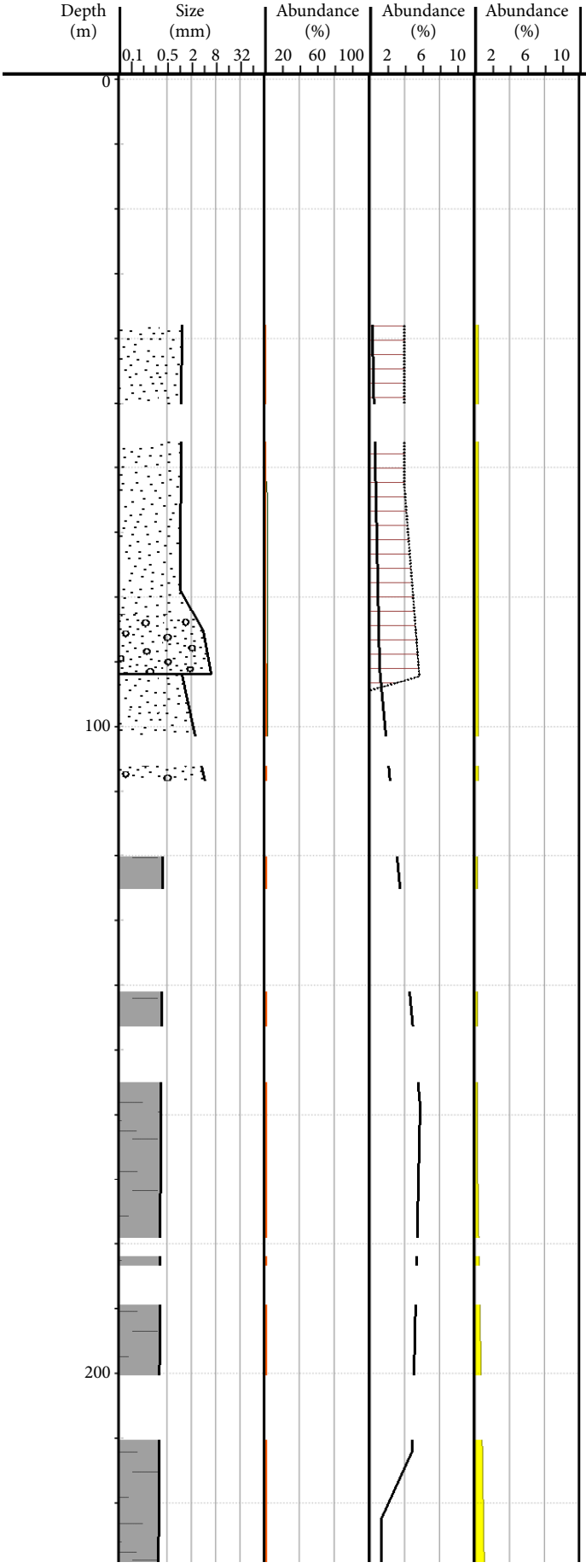

Description, interpretation

10.0 m: Rusty and unconsolidated drill core.

41.0 m: Sparse pyrite-quartz+/-magnetite veins have dark green halos < 1 mm (chlorite?)

80.0 m: Diffuse hematite altered metaconglomerate cross-cut by magnetite-pyrite veins.

155.0 - 192.0 m: Grey-green weakly altered metasedimentary rock apart from slightly darker to brown colour from weak biotite+/-chlorite halos to magnetite veins. A few sparse intervals < 1 m wide contain rounded clasts several cm across; otherwise, the interval is dominantly composed of silt-sized grains.

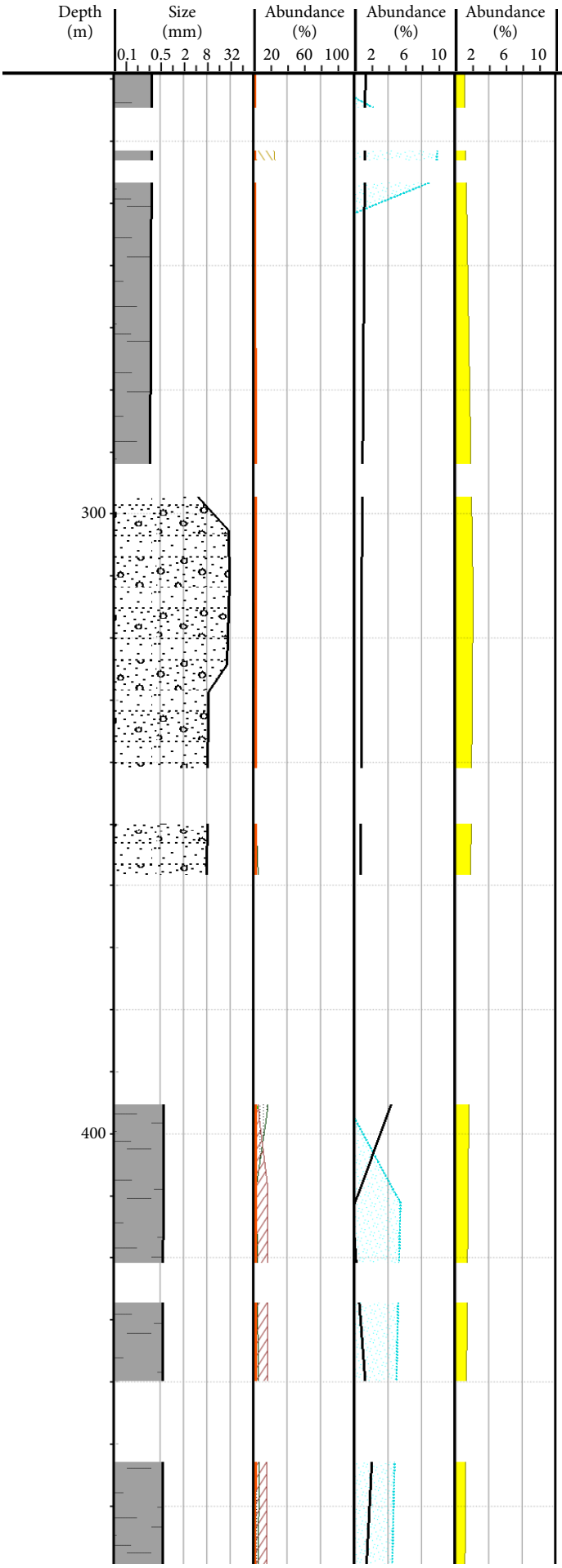

Description, interpretation

238.0 m: Strongly hematite + jarosite stained chips to mud.

284.0 m: In small metaconglomerate interval, selective replacement of metaconglomerate clasts at intersection of two magnetite veinlets shows cm-scale alteration zoning from dark brown (biotite only)-->light tan, soft (sericite?)-->darker grey-green (least-altered/metamorphic) with increasing distance from magnetite veins.

400.0 m: Weak red tinge to biotite alteration. chlorite halos to quartz-magnetite veins.

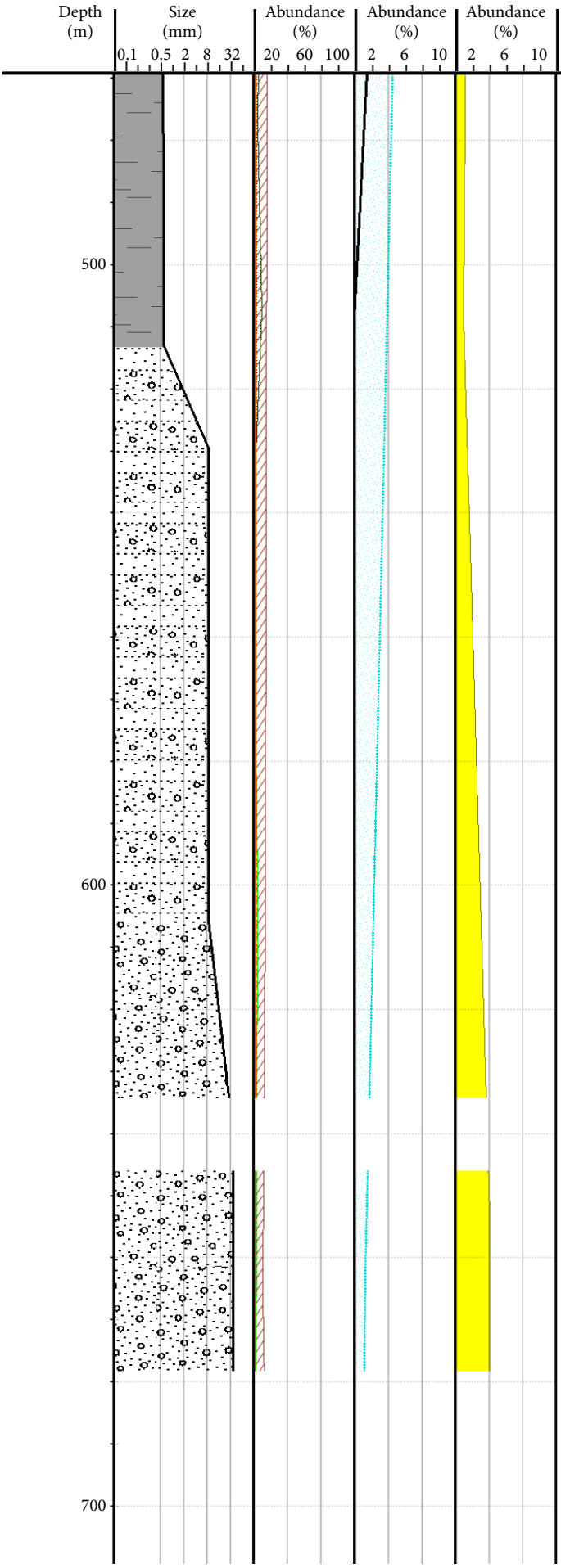

Description, interpretation

678.0 - 743.0 m: Rusty core chips through ~ 90 % of interval.

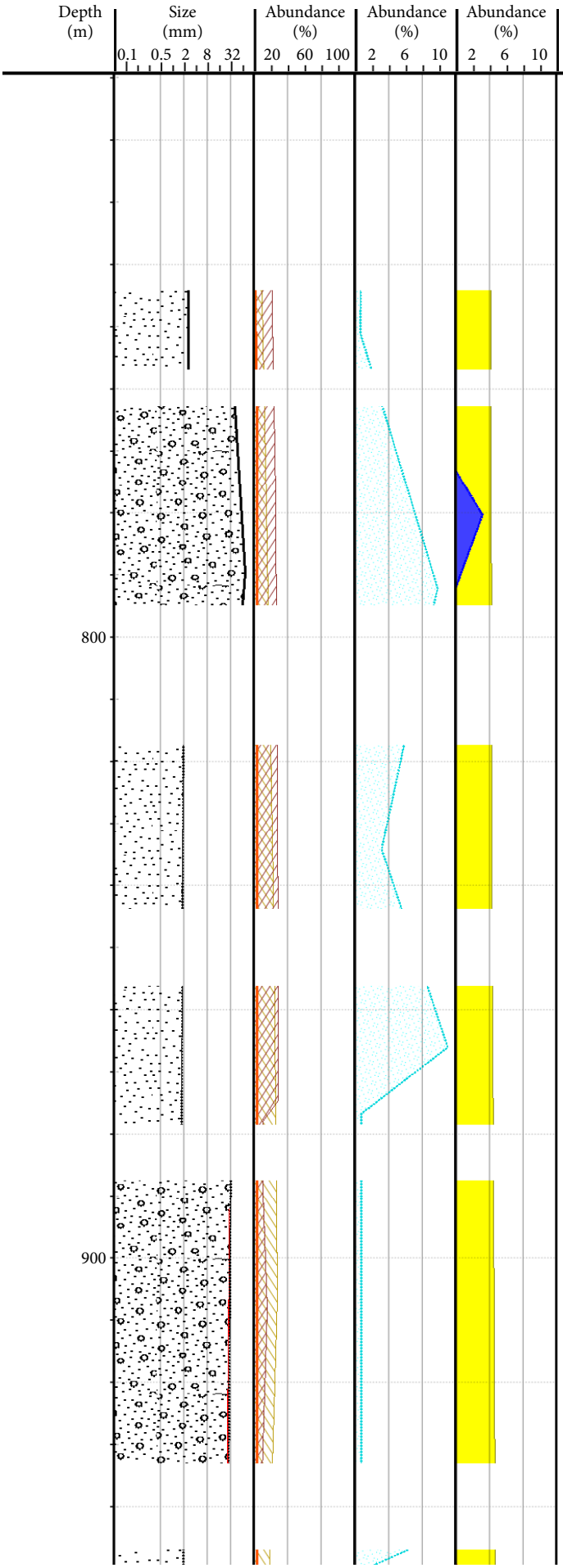

Description, interpretation

785.6 m: Molybdenite-bearing quartz vein was cross-cut by irregular pyrite v.

934.0 m: End of WR396 log. Start of WR396W_2 log.

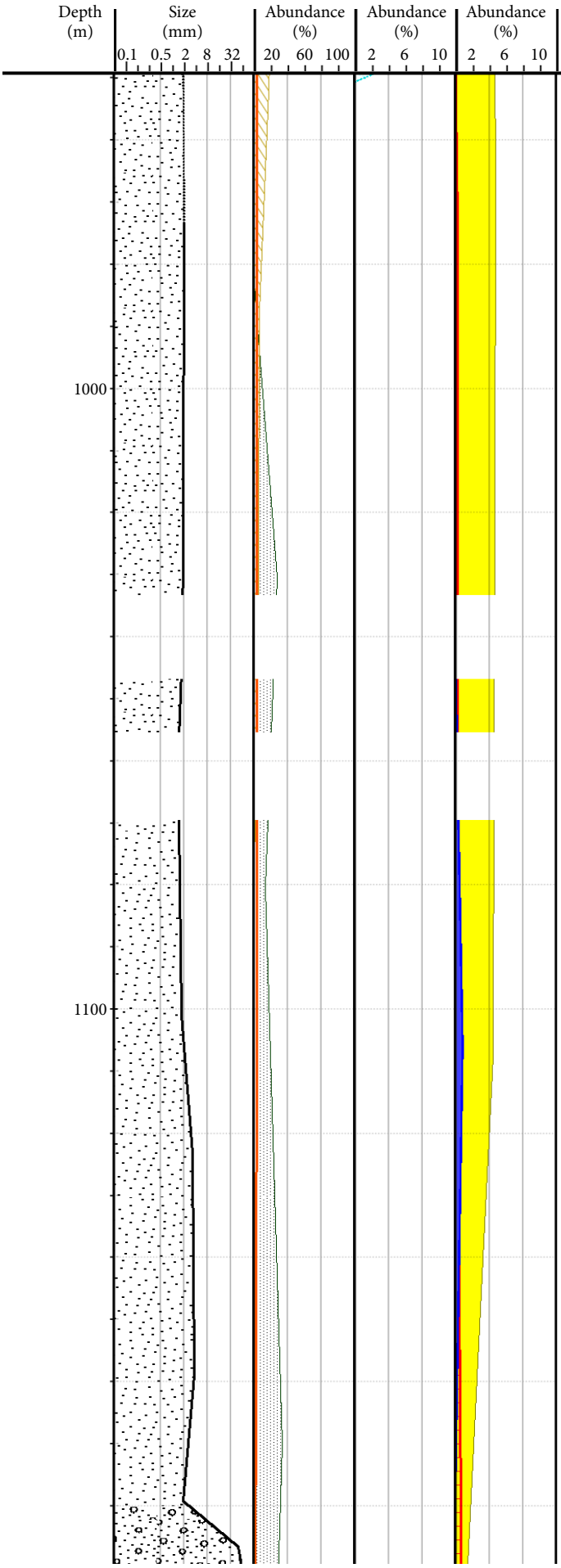

Description, interpretation

975.8 m: ~ 1 m interval of sericite-altered rock has unusual red tinge (hematite?)

1035.0 m: Quartz-pyrite veins with sericite halos after diffuse biotite alteration.

1060.0 m: Jarosite-stained core chips.

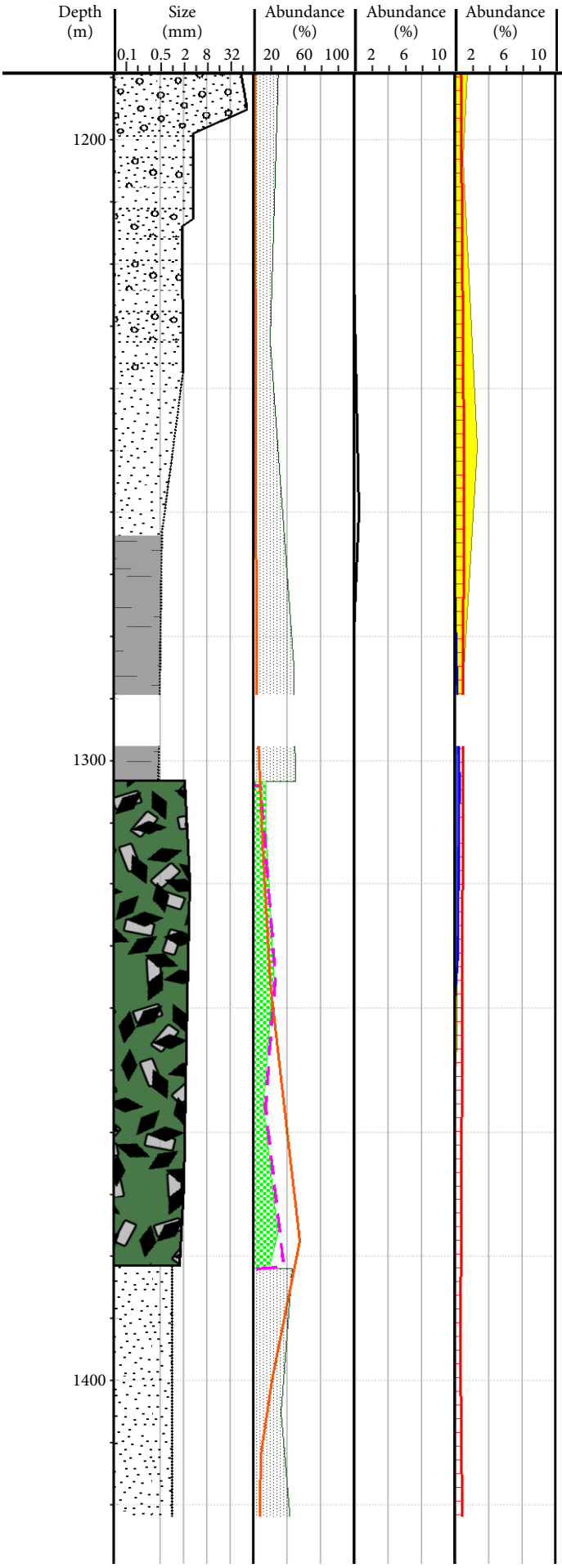

Description, interpretation

1305.0 m: Upper diorite contact is sharp and ~ planar at 90 TCA. Uppermost 5 m of porphyry contains moderately planar fabric from elongation of chlorite-replaced hornblende phenocrysts along with quartz veins (cross-cutting other quartz veins), both parallel to upper contact at 90 TCA.

1315.5 m: Mottled grey-green crowded hornblende-phyric weakly magnetic porphyry, with ~ 60 % chlorite-replaced subhedral hornblende phenocrysts < 2 mm, locally < 2.5 mm, in ~ 40 % grey to (where sericite-altered) light grey groundmass with very fine-grained biotite + orthoclase(?).

1318.6 m: Very finely disseminated molybdenite and disseminated chalcopyrite to diffuse chalcopyrite veins throughout porphyry.

1320.4 m: Quartz-pyrite-molybdenite vein, with molybdenite as rounded blebs ~ 1 mm.

1366.0 - 1380.0 m: Most quartz veins are laminated and subparallel at 50-60 TCA (i.e., sheeted quartz veins) 0.2-5 cm wide, with sparse rounded biotite blebs < 5 mm parallel to veins in small spaces between veins.

1382.9 m: No planar fabric evident. Sparse biotite patches < 8 mm across partially replaced by chlorite.

1383.2 m: Lower contact of porphyry is planar at 40 TCA, appears to be diffuse over ~ 1 cm(!?).

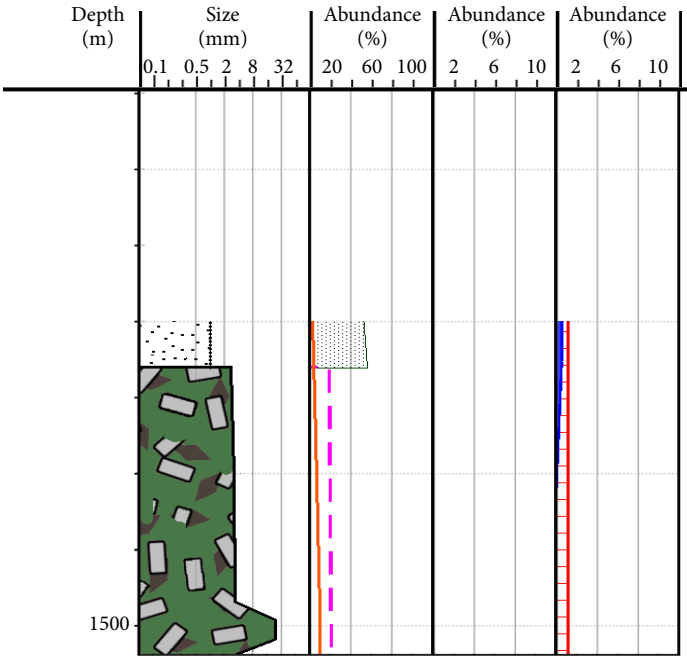

Description, interpretation

1470.0 m: Mottled light grey quartz+plagioclase-phyric non-magnetic diorite porphyry, with ~ 70 % rounded white (not clear) quartz and plagioclase phenocrysts 1.5-2.5 mm and < 5 % hornblende phenocrysts < 4 mm in a grey very fine-grained quartz-rich groundmass.

1499.7 m: Porphyry contains black biotite-altered and quartz-veined angular xenoliths (wallrock?) < 4 cm.

1500.9 m: Orbicular diorite? Up to 60 % round patches of randomly to radially oriented biotite 3-12 mm across, partially interconnected, over ~ 4m. Only a few patches are near-spherical; most are slightly polygonal/blocky. very finely disseminated chalcopyrite occurs mostly along margins of the biotite patches. chlorite has replaced ~ 30 % of the biotite. Possible minor hematite content in groundmass (to judge from red colour).

WR397

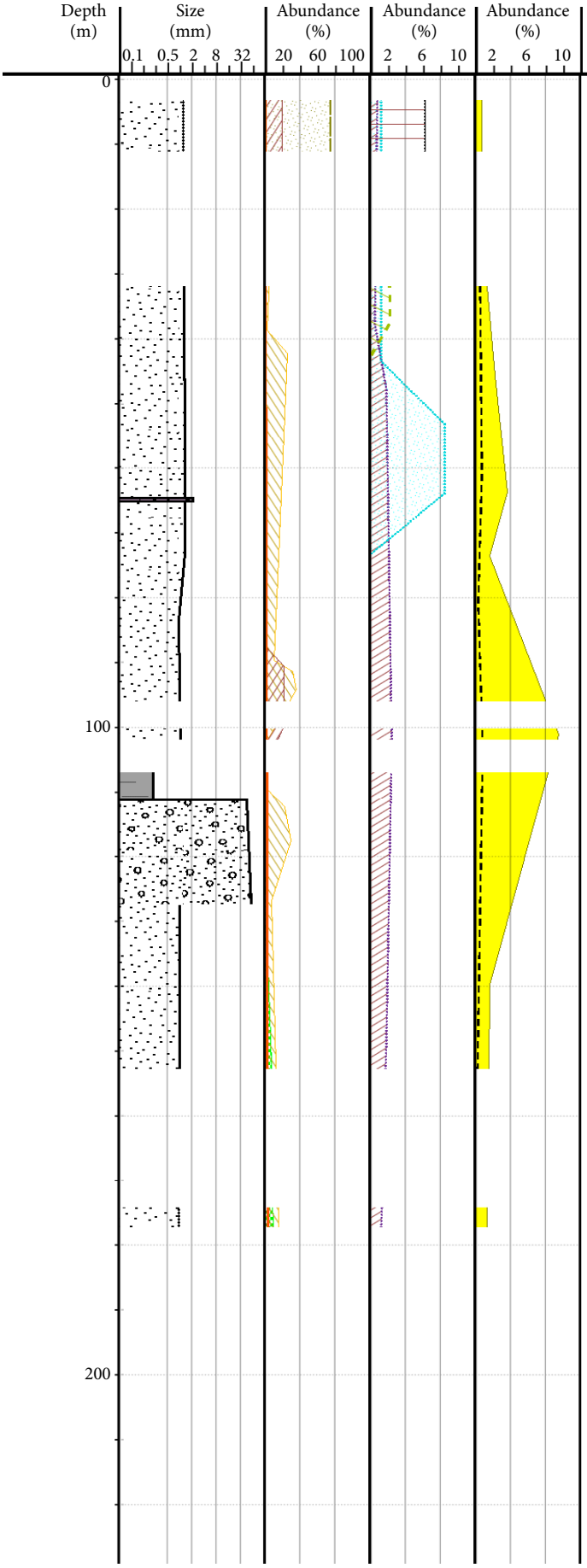

Description, interpretation

9.0 m: Mn oxide on fracture surfaces.

34.7 m: Disseminated epidote after rounded grains (plagioclase?) < 1 mm.

60.0 - 150.0 m: Several calcite to pink carbonate (rhodochrosite?)-cemented rounded pyrite(+/-sphalerite, galena) fragment-supported breccia veins make up about 1-2 % of this interval. Most are 2-15 mm wide, with no consistent orientation noted (e.g., from 20-80 TCA).

64.4 m: Pyrite-fragment-supported carbonate-cement infill breccia vein 6 cm wide at 75 TCA. Diffuse dickite-kaolinite veining runs through infill and is diffuse from margins of breccia vein over several cm.

112.0 m: Upper contact of metaconglomerate is sharp, planar, possibly weakly sheared, at 10 TCA.

123.0 m: Rhodochrosite-cemented pyrite-fragment breccia vein, containing two red sphalerite clasts and very finely disseminated galena (both < 1 % of vein). breccia vein is 2-3 cm wide with ~ 5 mm pyrite along both sharp irregular/undulating margins at ~ 30 TCA.

123.5 m: Thin carbonate cement vein with sparse pyrite fragments contains pink

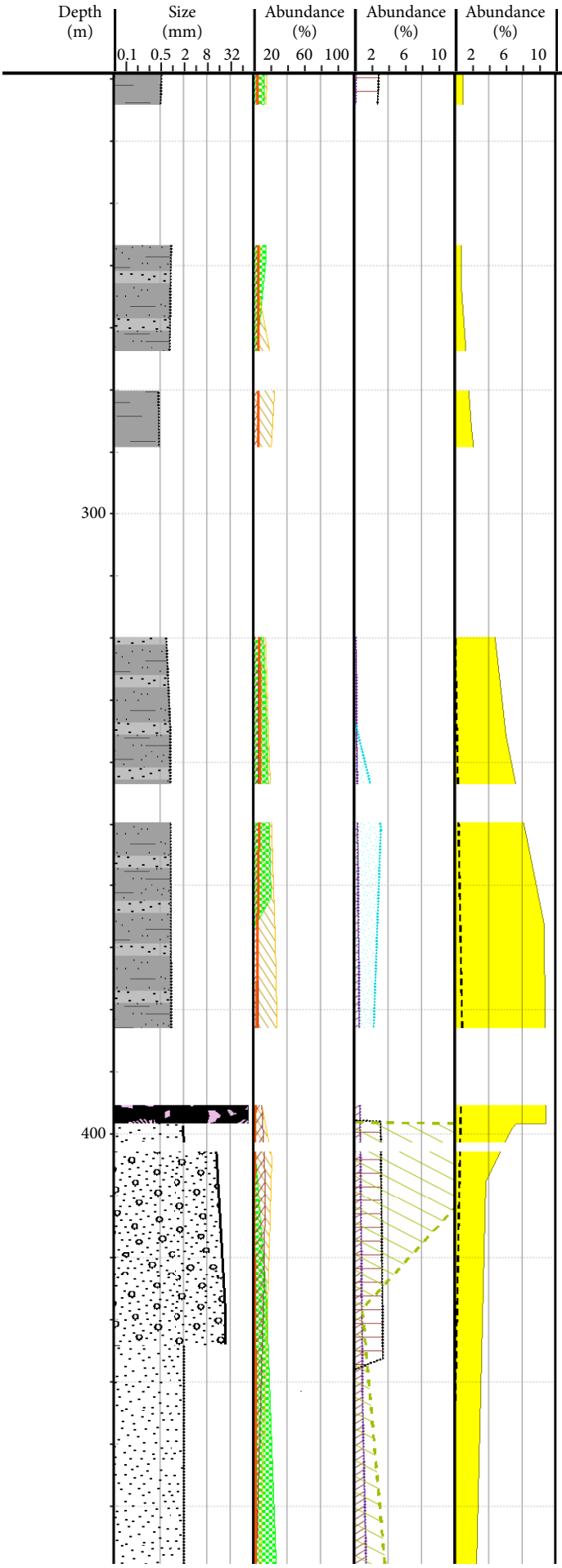

Description, interpretation

331.4 m: Metasandstone bedding/laminae 1-15 mm wide at 52 TCA.

340.0 m: mm-scale quartz-sericite intergrowths produced mottled texture in sericite-altered metasandstone.

395.5 m: Polymictic chaotic fragment-supported breccia, with 80-90 % angular pyrite fragments 0.1-10 cm, of which 20 % are distinctly pitted on fresh surface ("vuggy pyrite"?). Infill is ~ 90 % pyrite+/-marcasite cement and ~ 10 % medium-grained crystalline calcite cement. breccia vein is > 70 cm wide, with both upper contact and lower contact obscured by broken core and jarosite-altered clay.

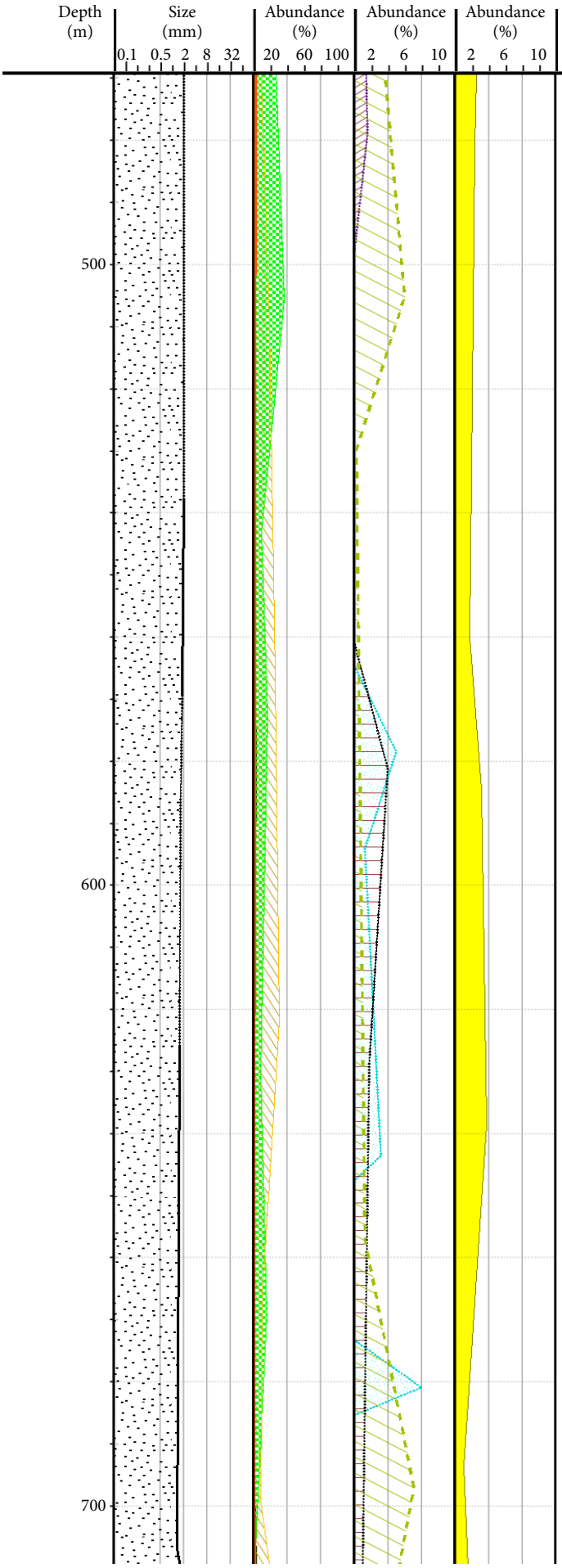

Description, interpretation

479.8 m: Pyrite fragments in calcite-cemented breccia vein 2 cm wide at 22 TCA.

510.0 m: Weak diffuse chlorite-epidote alteration.

545.0 m: ~ Equally sparse veins of early deformed quartz+/-pyrite veins and late ~ planar quartz-pyrite veins < 1 mm.

690.0 m: ~ 5 % epidote is diffuse/very finely disseminated.

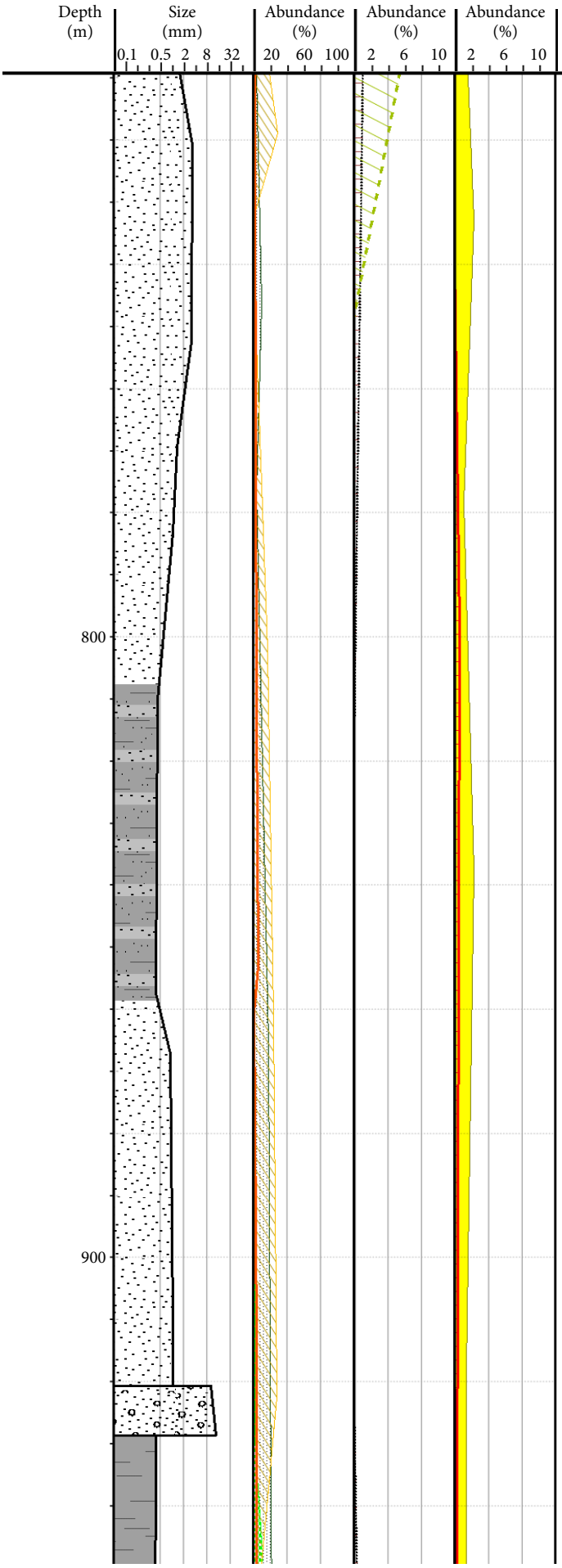

Description, interpretation

759.0 m: Quartz-pyrite-kaolinite vein at 45 TCA with diffuse dickite+kaolinite halos over several cm.

840.0 m: Relict sand to silt beds 0.2-2 cm wide at 81 TCA, fining up hole.

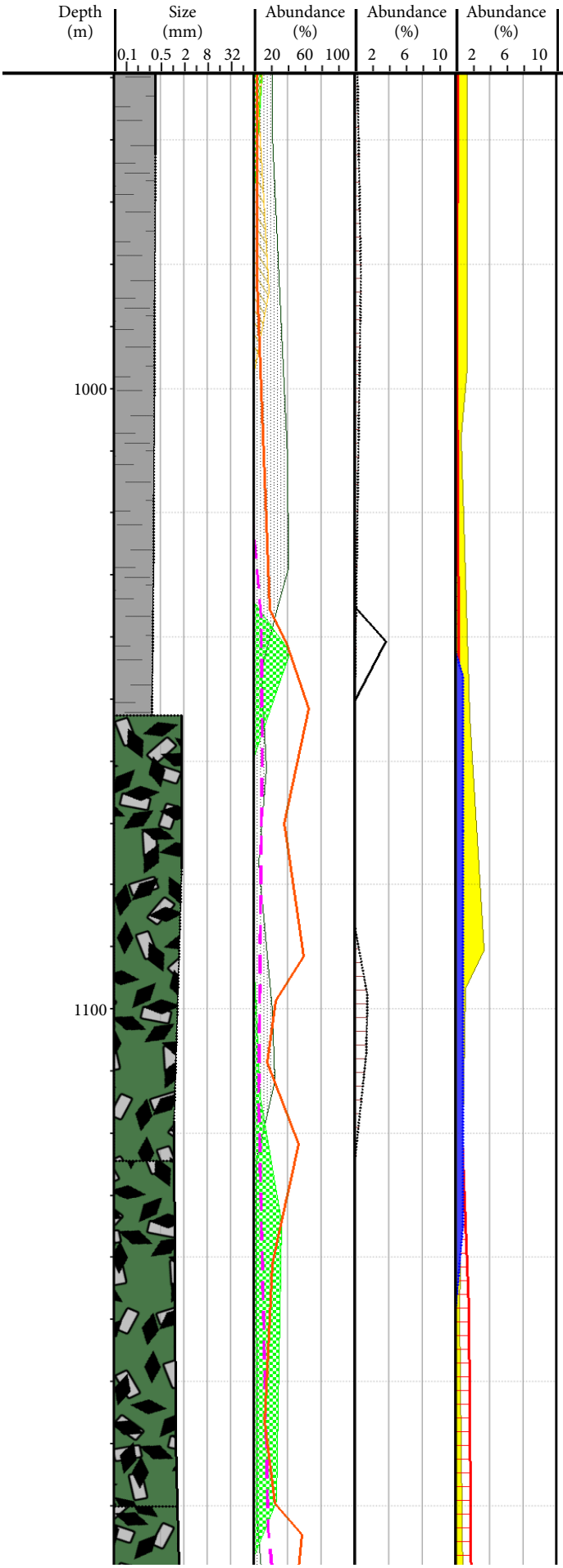

Description, interpretation

983.4 m: Most biotite is diffuse, some in selvages or sharp halos 1-2 mm wide. Most quartz-pyrite veins with biotite halos are lined by < 0.5 mm dark green chlorite (or actinolite?).

987.0 m: Quartz-pyrite vein 3.5 cm wide with broad (4 cm) orthoclase halos into biotite-altered wallrock, at 50 TCA.

~ 1000.0 m: Red hue to biotite alteration (disseminated hematite?).

1037.5 m: Quartz+orthoclase with biotite in round and ~ evenly distributed diffuse blotches/spots 0.5-2 mm

1055.0 m: ~ 1 % chalcopyrite is very finely disseminated through quartz veins and as 1 mm blebs in chlorite-magnetite interstices to quartz veins. magnetite is diffuse to clotty and red (hematite-altered) on polished surface.

1055.0 - 1124.0 m: Light grey to dark grey-green hornblende-phyric (?) diorite with blurry relict hornblende phenocrysts < 2 mm and 20-70 % quartz veins. Contains ~ 0.5 % very finely disseminated chalcopyrite and < 0.5 % molybdenite. upper contact obscured/cross-cut by quartz veins. Locally mottled red-orange.

1093.5 m: Stockwork quartz-veined porphyry with unusual red-orange colour from < 5 % hematite staining in sericite halos to quartz veins.

1119.0 m: Mottled red, green, and white to yellow quartz-flooded (diffuse alteration without distinct veins) to 20-30 % quartz-veined chlorite-magnetite-hematite-altered porphyry with very finely disseminated chalcopyrite, molybdenite, and pyrite between quartz veins. Red and green colours of porphyry are from hematite-altered magnetite clots and diffuse chlorite, respectively; yellow is hematite staining to sericite alteration.

1124.0 m: Possible quartz-veined upper contact of later porphyry phase [1130-1180m]?

1130.0 - 1180.0 m: Hornblende-phyric porphyry with trace chalcopyrite as in adjacent intervals, apart from ~ 30 % bright green to teal chlorite after hornblende and diffuse through groundmass. hornblende occurs anhedral-subhedral phenocrysts 1-2 mm, and possibly in groundmass with biotite?

1138.0 m: Fragment- to infill-supported quartz-cemented breccia vein with ~ 60 % fragments ~ 1 mm, of which 70 % are magnetite, 30 % pyrite. pyrite fragments occur in irregular patches segregated from magnetite-fragment vein. breccia vein upper contact and lower contact are planar at 50 TCA, and have 1 cm chlorite halos into adjacent porphyry.

1180.0 - 1220.5 m: Light grey to mottled brown+grey hornblende-phyric(?) porphyry with white quartz+sericite-altered phenocrysts 1-2 mm (hornblende?) in a locally orthoclase-bearing groundmass. orthoclase alteration, disseminated + vein biotite, and disseminated + vein chalcopyrite are more abundant than in porphyry intervals up hole.

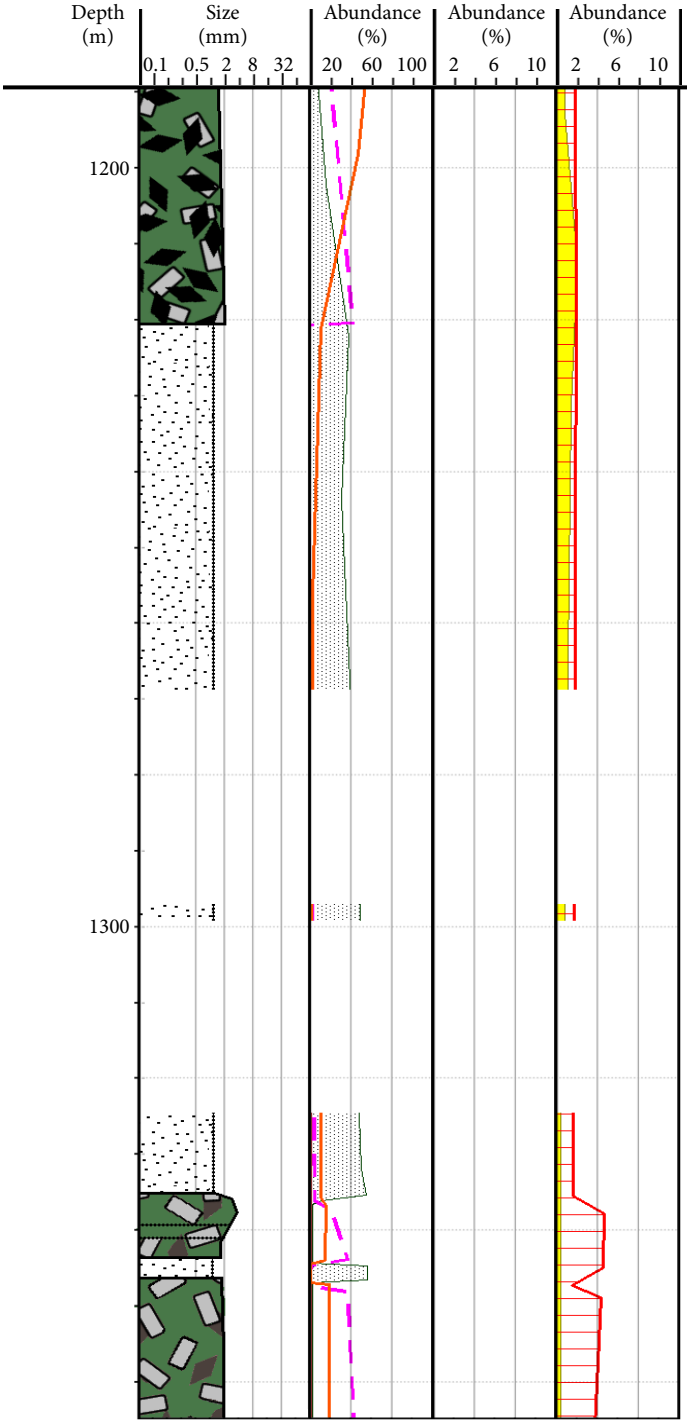

Description, interpretation

1211.5 m: Vein sequence as follows: 1- diffuse ~ planar biotite (+/- chlorite) veins through porphyry, 2- planar quartz veins > 5 mm, 3-undulating quartz+/-chalcopyrite veins ~ 2 mm

1300.3 m: Weak red hue to biotite alteration.

1361.0 m: Orthoclase altered hornblende- and plagioclase-phyric porphyry.

1364.4 m: End of hole.

WR398

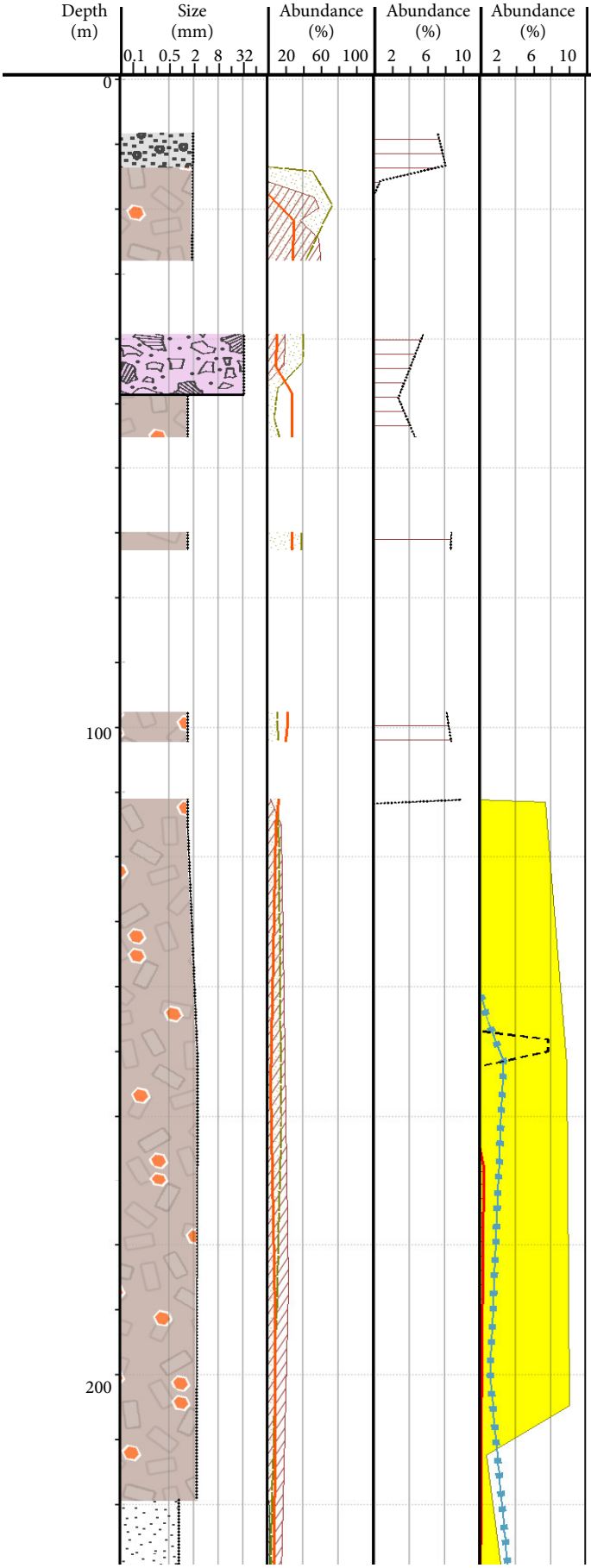

13.0 - 49.5 m: Alternating intervals of monomictic breccia veins with quartz or quartz vein fragments in alunite-kaolinite-quartz infill, and strongly alunite-quartz-kaolinite+/-hematite-altered quartz-phyric diorite (?) without clasts.

15.5 m: 20 cm interval of dark green clay-rich degraded core corresponding to ~ 300 ppm Mo. No molybdenite visible in core sample.

25.0 m: Monomictic chaotic infill-supported breccia vein 0.5-2 cm wide with rounded to angular quartz or quartz veins fragments 0.5-3 mm in alunite-kaolinite+/-quartz infill (infill is powdery; cannot determine whether cement or clastic). upper contact and lower contact very irregular at ~ 30-80 TCA.

44.7 m: Polymictic chaotic infill- to fragment-supported breccia with subangular diorite fragments < 4 cm, each containing multiple cross-cutting ~ planar quartz veins, and < 30 % quartz fragments < 5 mm. breccia was cross-cut by thin alunite-hematite-quartz hydrothermal sandstone breccia vein (small fragments < 2 mm likely quartz only). lower contact obscured by quartz-alunite alteration and quartz veins, drawn based on downhole transition to no visible fragments.

54.0 m: Relict wormy, deformed laminated quartz veins (laminated quartz stock-work protolith?).

79.0 m: Degraded core: dark red to purple (strongly hematite altered) mud

90.3 m: Core chips are relict quartz stockwork with >30 % quartz veins.

120.0 m: Quartz stockwork-veined and kaolinite-altered diorite as in above intervals apart from preserved pyrite (below surface oxidation zone) and less alunite.

146.0 m: Lowest porous/vuggy quartz-kaolinite-pyrite.

149.0 m: Chalcocite veins and halos after vein and disseminated pyrite.

150.5 m: ~ 20 cm interval of vein soft pale yellow-grey colloform alunite veins with fine-grained pyrite and possible orpiment or native sulfur visible along laminae. Both vein contacts are missing / obscured by broken core

153.5 m: Chalcocite vein 1 cm with halos of vein-parallel veinlets up to 5 cm from vein, some of which have cross-cut pyrite veins (i.e., not only pyrite replacement),and diffuse chalcocite after pyrite. vein is slightly undulating at 30-40 TCA.

201.0 m: Trace disseminated chalcocite after pyrite.

207.6 m: White kaolinite and/or alunite(?) veins < 2 mm follow and locally cross-cut pyrite veins.

213.3 m: Chalcopyrite-molybdenite vein (molybdenite as inclusions < 5 mm) was cross-cut and partially replaced along margins by a diffuse pyrite vein, both at ~ 80-85 TCA.

220.0 m: 5 cm window of biotite+chlorite-altered metasandstone between kaolinite alteration (kaolinite as halos to quartz-pyrite veins).

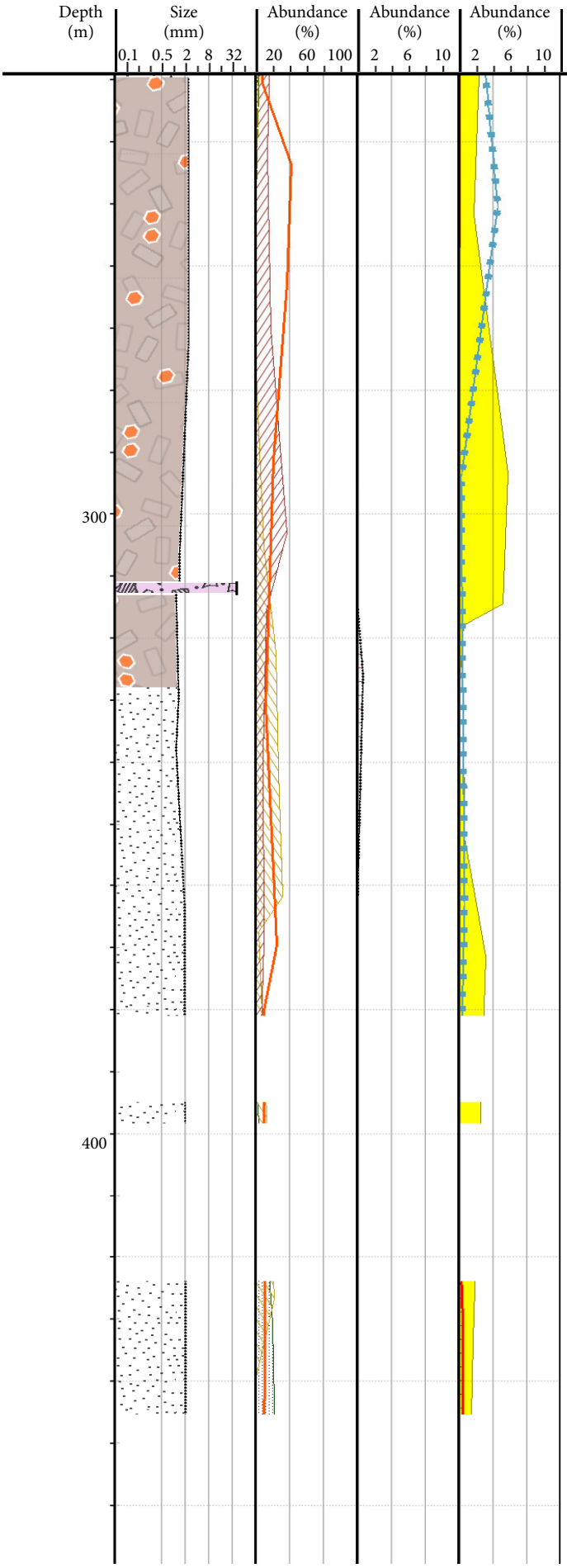

Description, interpretation

232.4 m: Diorite (?) cross-cut by irregular quartz veins 4 cm wide. Diorite contains ~ 2 % very finely disseminated pyrite. upper contact and lower contact unclear, estimated on basis of hardness (harder quartz-phyric diorite).

255.8 m: Strongly deformed/wormy and moderately kaolinite-altered quartz stockwork veins < 6 mm wide, mostly sub-parallel, with very fine-grained chalcocite and pyrite in quartz-phyric diorite(?) between veins.

272.6 m: Grey crowded quartz- and plagioclase-phyric diorite porphyry(?) with pyrite rimmed by chalcocite (later chrysocolla-altered on core faces) mostly in groundmass. kaolinite alteration occurred almost throughout groundmass.

313.3 m: Monomictic chaotic fragment-supported breccia with subangular diorite fragments 0.2-2.5 cm in a biotite-altered hydrothermal sandstone infill, cross-cut by a chalcopyrite-molybdenite vein.

335.2 m: Dark grey quartz-rich metasandstone(?) was cross-cut by quartz veins and later specular hematite+chalcopyrite veins. Specular hematite veins have magnetite halos over a few cm into wallrock.

425.0 m: Diffuse biotite is preserved with distance from clay veins.

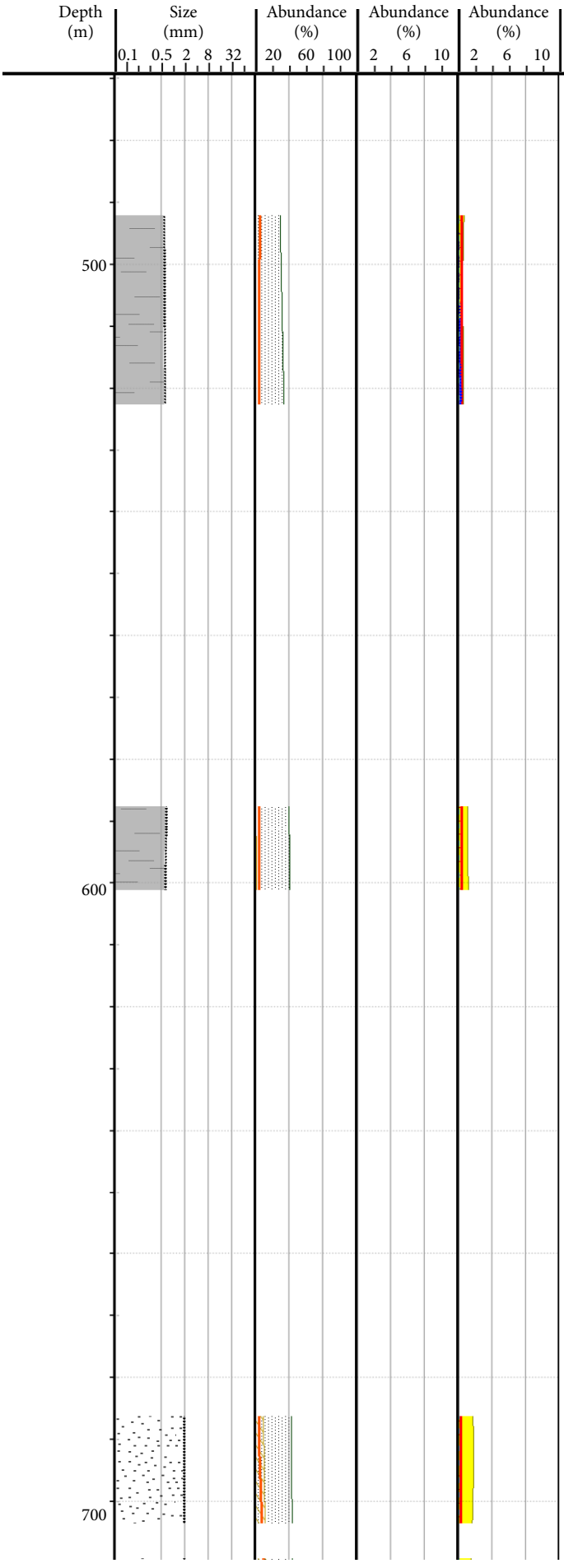

Description, interpretation

470.0 m: Hematite, jarosite, and minor dickite (not chrysocolla) on core chips and clay.

520.8 m: 1.5 cm quartz-molybdenite vein through metasandstone at 25 TCA.

620.0 m: Biotite-altered (dark brown/black) to hematite+jarosite-stained core chips and clay.

690.0 - 712.0 m: ~ 1 % quartz-pyrite-molybdenite veins < 2 cm.

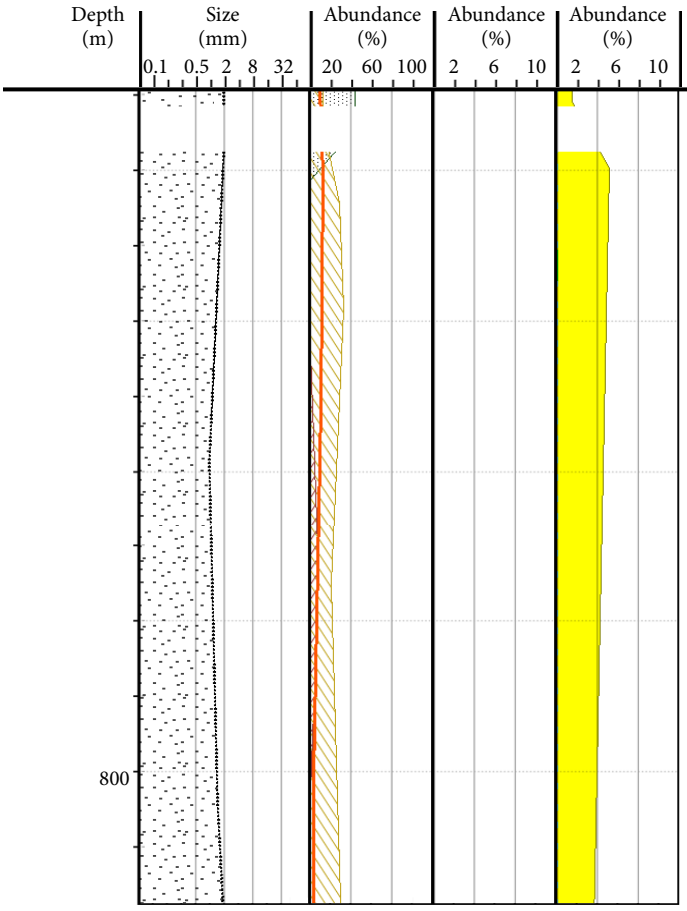

Description, interpretation

730.0 m: Quartz-rich metasandstone(?)

790.0 m: White sericite+kaolinite+pyrite altered quartz-rich metasandstone(?). Sparse quartz grains < 1 mm occur throughout the interval.

810.0 m: Most quartz veins < 1 mm.

817.6 m: End of hole.

WR402

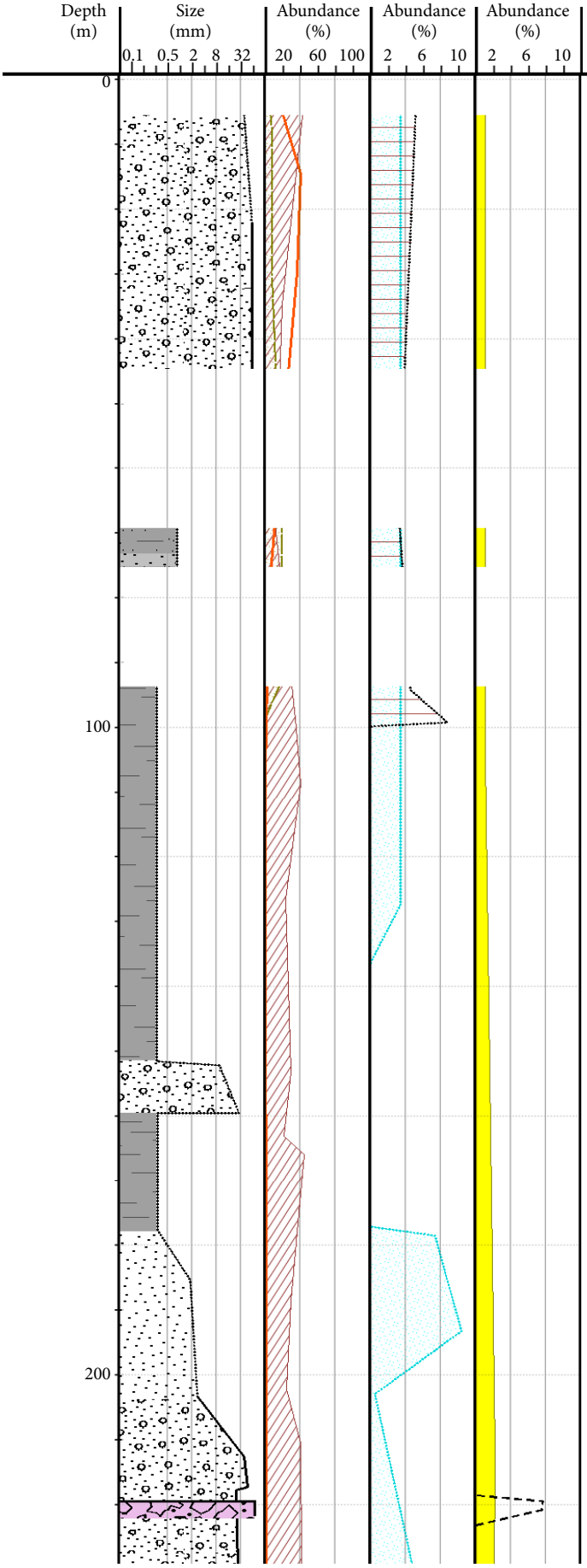

Description, interpretation

30.0 m: Rounded and elongated metaconglomerate clasts barely visible due to vuggy quartz-alunite (+hematite vein infilling fractures).

175.8 m: Relict beds/laminae 2-6 mm, a few containing quartz clasts < 3 mm, at 20 TCA.

220.0 m: Monomictic chaotic infill-supported breccia vein with ~ 20 % rounded and quartz-pyrite veined metaconglomerate fragments < 7 cm in a pyrite (+trace sphalerite) hydrothermal sandstone infill (same proportion of sulfides as both sub-mm fragments and cement of the hydrothermal sandstone infill). The infill also includes or was later replaced by kaolinite, mostly along its irregular margins, at 10 TCA.

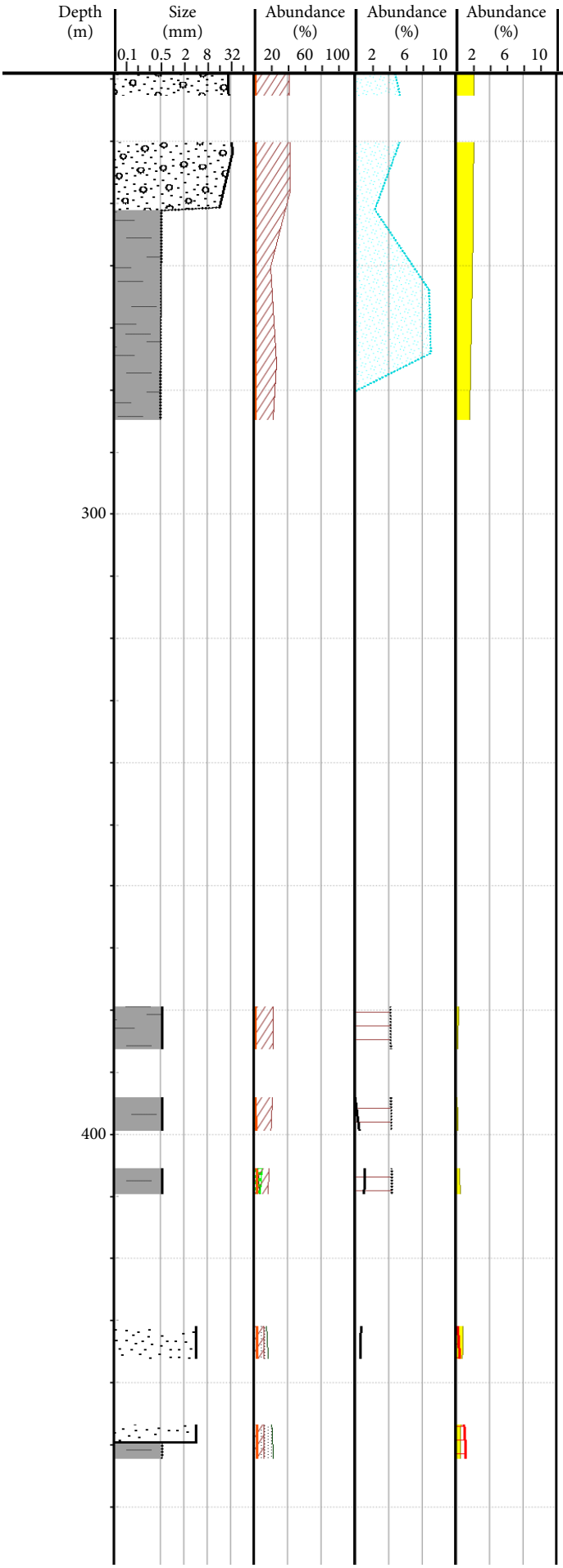

242.0 m: Dickite(+kaolinite, pyrite) preferentially replaced some metaconglomerate clasts; other clasts, in particular quartz-rich clasts, are effectively unaltered except within a few mm of clast margins.

295.0 m: Quartz veins in core chips have kaolinite selvages (not halos, as normally observed) < 1 mm, and sericite and/or clay halos over several cm.

406.2 m: Specular hematite-quartz-pyrite+/-chalcopyrite veins with magnetite halos several cm into biotite(+chlorite)-altered wallrock, at ~ 15 TCA and 80-90 TCA. These were cross-cut by sparse chalcopyrite veins < 0.5 mm.

433.0 m: 5 mm wide magnetite-seamed quartz veins at 5 TCA through non-magnetic biotite-altered metasandstone.

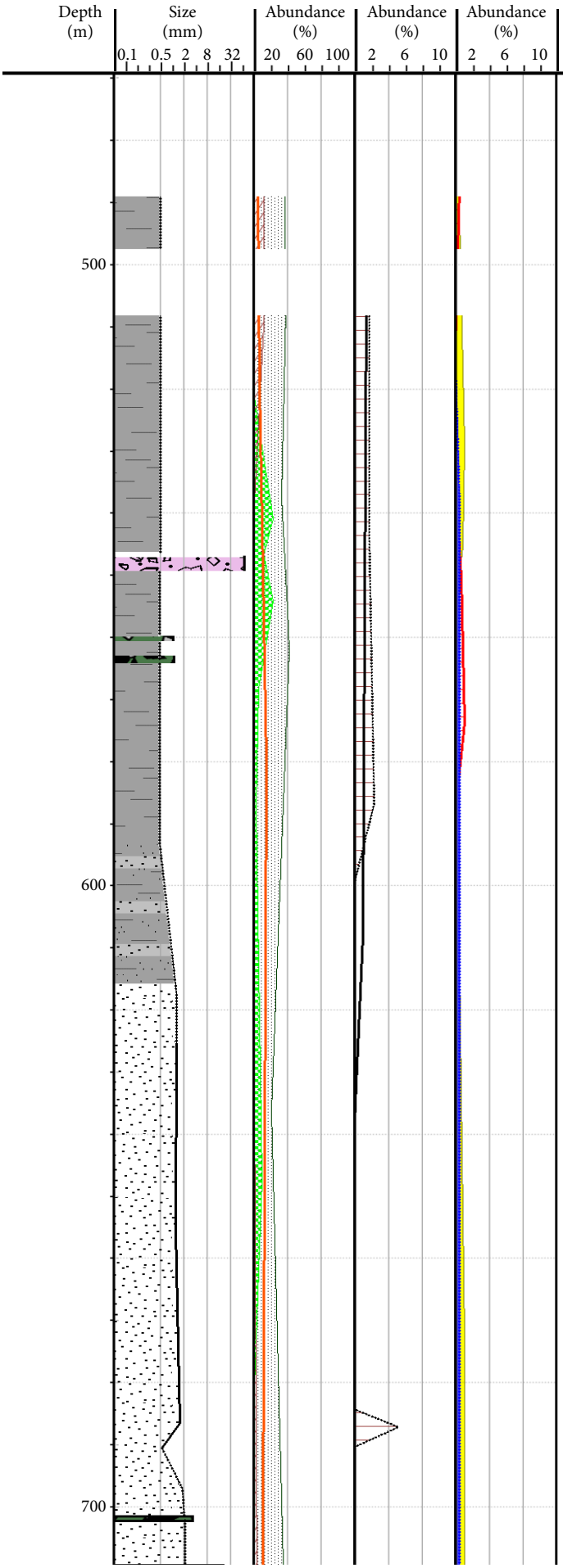

490.0 - 585.0 m: Interval containing ~ 10 % quartz-specularite veins (+/-pyrite,chalcopyrite) with magnetite halos. (Also note quartz-specular hematite veins at 406.2 and 686.0m.)

510.2 m: Planar laminated quartz-pyrite vein 6 cm wide at 90 TCA.

528.1 m: Chlorite after diffuse biotite is associated with magnetite halos of quartz-specularite veins.

529.3 m: Quartz-chalcopyrite-pyrite-hematite veins without halos were cross-cut by specular hematite veins with magnetite halos.

544.0 - 545.0 m: ~ 1m interval (with gradational contacts) superficially resembles a shear zone, from multiple parallel laminated quartz veins to sub-mm veinlets at ~ 40-46 TCA.

547.0 m: Monomictic rotated to in-situ fragment-supported breccia vein 7 cm wide with 80 % angular biotite-altered metasiltstone-metasandstone (wallrock) fragments 2-4 cm and 20 % weakly quartz-sericite-altered hydrothermal sandstone-mudstone infill. upper contact and lower contact are planar and parallel at 40 TCA. The breccia vein was cross-cut by two generations of quartz-pyrite veins < 1 cm.

561.6 - 564.8 m: Intervals [561.6-562.0] and [564.4-564.8] are crowded weakly sericite+chlorite-altered hornblende+plagioclase-phyric porphyry dykes with subhedral chlorite-replaced hornblende phenocrysts < 1.5 mm and subhedral lath to rounded plagioclase phenocrysts < 1 mm with weak foliation parallel to sharp planar contacts at 38-50 TCA. hornblende phenocrysts are more abundant than plagioclase phenocrysts. The dykes are weakly magnetic with < 1 % finely disseminated chalcopyrite associated with biotite patches to stringers, especially within a few cm of contacts with wallrock.

564.4 m: Sharp and planar upper contact of porphyry dyke at 48 TCA has cross-cut both quartz-biotite veins (with sericite halos) and quartz-pyrite veins in wallrock.

566.3 m: Quartz veins with specularite-chalcopyrite at centre, magnetite-chlorite halos a few cm.

559.0 m: Orange carbonate (wrongly identified by the author as a possible mix of sericite+hematite) veins < 4 mm wide cross-cut quartz-specularite veins.

563.3 - 585.0 m: Several planar laminated quartz-specularite+/-chalcopyrite-pyrite veins with < 15 cm wide with magnetite halos a few cm wide. Some veins contain a weakly magnetic combination of specular hematite and magnetite. Most veins are at 5-15 TCA.

569.3 m: In pyrite-chalcopyrite veins that have cross-cut quartz-specular hematite veins (with magnetite halos), at mm to cm scale, chalcopyrite is most common where the wallrock host is a hematite vein; pyrite is more common where the wallrock host is magnetite-altered metasedimentary rock.

602.0 m: Very finely disseminated molybdenite in dark clay-filled gouge (possibly degraded core, originally sulfide veins?).

634.7 m: sericite-chlorite-altered fine-grained (< 1 mm) plagioclase+hornblende-phyric porphyry dyke 2-4 cm wide with sharp undulating contacts at 50-80 TCA. plagioclase phenocrysts are more abundant than hornblende phenocrysts in this interval.

640.0 m: Biotite alteration occurs as wide halos in intervals containing < ~ 30 % biotite.

662.7 m: Pitted quartz-pyrite veins with trace very finely disseminated molybdenite 6-9 mm at 70-80 TCA were cross-cut by thin pyrite+/-quartz veins with sericite halos several cm wide at 20 TCA.

686.0 m: Laminated quartz-pyrite-specularite vein 5.5 cm at 85 TCA, cross-cut by pyrite veinlet < 0.5 mm.

700.0 m: Dark biotite-altered hornblende+plagioclase-phyric porphyry dyke 6 cm wide with 5 % finely disseminated chalcopyrite in groundmass (none in wallrock). Most phenocrysts are < 1 mm, plagioclase phenocrysts sericite+chlorite-altered, hornblende biotite+chlorite-replaced. Foliation is parallel to near-planar contacts at 30 TCA. upper contact is a 2-3 cm quartz veins breccia with orthoclase-altered(?) rotated wallrock breccia fragments 0.5-2 cm.

Description, interpretation

708.4 m: Monomictic chaotic fragment-supported breccia vein 4.5 cm with 70 % fragments of biotite-altered wallrock (variably quartz-veined) 0.5-1.4 cm in a biotite (+ trace very finely disseminated chalcopyrite) cement replaced (?) by soft white sericite (?) mostly at margins of infill. upper contact is sharp and irregular at ~ 50 TCA, lower contact has been cross-cut by a laminated and pitted quartz-pyrite vein at 74 TCA.

740.0 m: A few pitted and laminated quartz-pyrite veins at ~ 80 TCA.

795.0 m: Centimetre-scale patchy chlorite alteration (after diffuse biotite) is associated with early irregular/undulating quartz veins.

921.0 m: Finely disseminated molybdenite in early pitted, undulating quartz veins.

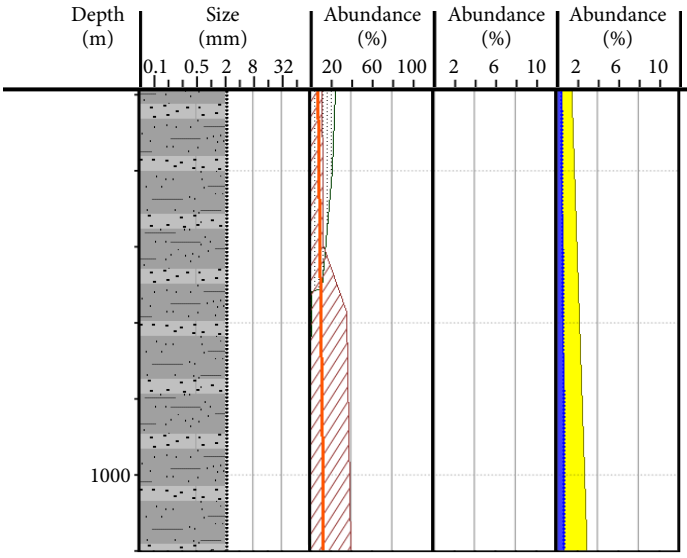

975.8 m: Downhole change from biotite-dominant to sericite-dominant alteration occurs over < 1 m. There is no visible change in host protolith or fault density at or near this transition.

975.9 m: Quartz-pyrite stockwork with wide sericite halos, some veins containing trace molybdenite. These were cross-cut by irregular pyrite veinlets < 2 mm wide.

End of hole.

Appendix C
Lithotype and Assay Modelling Methods

Lithotype volumes, fault traces, and assay grade shells (as shown in Figs. 3.2 - 3.7, 4.3, 4.5, 4.10, 4.14, 4.23, 4.24, 4.25, 4.41, 5.2, 5.9 - 5.14, 5.21, and 5.22) were constructed from all available drill core data using Leapfrog software, following the steps listed below. Note that the software terms used (e.g., “distance buffer”) are explained in the Leapfrog help files and tutorials.

1) Group interval names or lithotypes into fewer categories (e.g., “fault,” “fault breccia,” and “cataclasite” intervals are grouped in “fault zone”).
2) Define a volume bound by topography and a surface 200 metres around all drill traces, using a distance buffer.
3) Define an approximate structural trend along the gross dip of the Owen Stanley units. In the study area this is about 55° to the ESE.
4) Simplify the lithotype intervals (using the Leapfrog compositing functions “ignore small gaps” and “window processing”), so that an interval containing e.g., 25 metres of metaconglomerate with 5 metres of interbedded metasandstone is reclassified as “metaconglomerate dominant”. This is effectively the same as producing a table of average lithotype (per composite interval) that maintains the location/depth of contacts between changes in dominant lithotype.
5) Build volumes bounding the metasandstone dominant and metaconglomerate dominant intervals (using the interpolate function in Leapfrog), with a 5:5:1 aspect ratio parallel to the structural trend defined in step 3. The remainder is metasiltstone dominant, which can be verified by viewing the raw lithology data in 3D.
6) Interpolate volumes for the Wafi breccia complex using an isotropic (1:1:1) structural trend, and a vertical (3:1:1) structural trend for diorite intrusions.
7) Construct 10 metre composite intervals from all assay data, and interpolate the composite data using an isotropic structural trend. The cutoff values used for each of the grade shells are indicated in Figures 5.9 - 5.14.
8) Limit the extent of all rock volumes and grade shells to within the boundary defined in step 2, using “domains” in Leapfrog. This ensures that all models are constrained to a region no more than 200 metres from drill core (or, in the case of grade shells, available drill core assay data).
9) Display the modeled lithotype volumes, grade shell volumes, and fault surfaces in map and section view. Defining a section clip is irrelevant, as the modelled volumes are cut exactly along the surface of the section. A section clip is, however, required to display point and interval data (e.g., drill traces, sample locations), as indicated in Figures 3.2 - 3.7.

Appendix D
Modal Abundance and Core Photography Methods

Estimation of modal mineral abundance in thin section images, and colour correction of drill core images displayed in this thesis were carried out using the java-based freeware imageJ, available at < http://imagej.nih.gov >.

The modal abundance of key mineral phases, such as chalcopyrite or relict hornblende phenocrysts, were measured as follows:

1) Acquire thin section images in reflected and transmitted light, using various instruments and software at CODES, University of Tasmania. Save images in uncompressed formats whenever possible.
2) For each mineral measured, create a mask or binary image using RGB or HSL pixel values that highlights only the mineral phase.
3) Measure the pixel count for the portion of the binary image that corresponds to the phase of interest, and divide by the total number of image pixels to determine the mineral area %.

In a few samples of altered diorite, the abundance of relict hornblende phenocrysts was estimated by phenocryst shape. Shape identification algorithms attempted for this task did not produce reliable results, likely because of the irregular margins of biotite- and orthoclase-replaced hornblende and plagioclase phenocrysts. Instead, rhomb-shaped phenocrysts (subhedral-euhedral hornblende) were identified and coloured manually in the thin section images, and their abundance was then estimated by the method described above.

Colour adjustment of core photos was undertaken in order to correct for poor control on lighting intensity and direction. In particular, core photos taken in overcast conditions resulted in a measurably bluer colour to the rock photos compared to the same rock in full sun. A standard colour card (below right) was placed in each image. "Auto white balance" was disabled, and core photos were stored in RAW image format when possible. The following imageJ macro was then used for each photograph:

```
// This macro corrects to standard card values from the red, green,
// and blue channels of an image (need standard card in photo)
// It also measures the mean colour values of the rock
// Marc Rinne

dir = <core photo directory>;

Rstandard = 236;
Gstandard = 246;
Bstandard = 253;

WhiteVal = 0.7  // This is the upper cutoff for card values normalised to white (standards above)
                // in each channel (i.e., 0.9 is 90th percentile and brighter)
BlackMinR = 48   // These are the RGB value minima for grey square "1" of the standard card.
BlackMinG = 54
BlackMinB = 63

//setBatchMode(true);

requires("1.35b");
  if (bitDepth!=24)
     exit("This macro needs an RGB image");

setTool("line");

  title = "";
  msg = "Draw line from middle of 1 to middle of 8 and Enter or \"OK\".";
  waitForUser(title, msg);
```

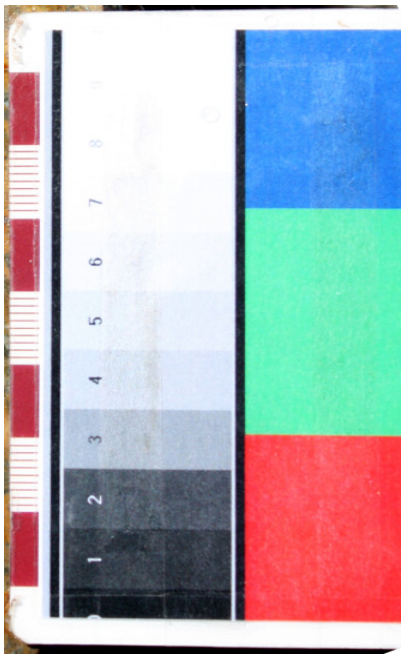

```
setRGBWeights(1, 0, 0);  //=====    RED
//=================================
  // Get profile and display values in "Results" window
  run("Clear Results");
  Rprofile = getProfile();
  for (i=0; i<Rprofile.length; i++)
      setResult("Value", i, Rprofile[i]);
  updateResults;
//-------------------------------------------------
Array.sort(Rprofile);
Rbrighter_index = parseInt(WhiteVal*Rprofile.length);
Rcutoff = (Rprofile[Rbrighter_index]);   //  value of the ~90th percentile cut-off
print(Rcutoff);
//=============================

setRGBWeights(0, 1, 0);  //=====    GREEN
//=================================
  // Get profile and display values in "Results" window
  run("Clear Results");
  Gprofile = getProfile();
  for (i=0; i<Gprofile.length; i++)
      setResult("Value", i, Gprofile[i]);
  updateResults;
//-------------------------------------------------
Array.sort(Gprofile);
Gbrighter_index = parseInt(WhiteVal*Gprofile.length);
Gcutoff = (Gprofile[Gbrighter_index]);   //  value of the ~90th percentile cut-off
print(Gcutoff);
//=============================

setRGBWeights(0, 0, 1);  //=====    BLUE
//=================================
  // Get profile and display values in "Results" window
  run("Clear Results");
  Bprofile = getProfile();
  for (i=0; i<Bprofile.length; i++)
      setResult("Value", i, Bprofile[i]);
  updateResults;
//-------------------------------------------------
Array.sort(Bprofile);
Bbrighter_index = parseInt(WhiteVal*Bprofile.length);
Bcutoff = (Bprofile[Bbrighter_index]);   //  value of the ~90th percentile cut-off
print("B 90% is"+(Bcutoff));
//=============================

Darker_index = parseInt(0.01*Rprofile.length);  // index of the lowest 5th percentile RGB value
                                                // (note array length will be same for R,G,and B)

Rshift = (BlackMinR-Rprofile[Darker_index]);
Gshift = (BlackMinG-Gprofile[Darker_index]);
Bshift = (BlackMinB-Bprofile[Darker_index]);

if(Rshift<0)
        {Rcorrect = Rstandard/(Rcutoff+Rshift);
        }
else
        {Rcorrect = Rstandard/Rcutoff;
        }

if(Gshift<0)
        {Gcorrect = Gstandard/(Gcutoff+Gshift);
        }
else
        {Gcorrect = Gstandard/Gcutoff;
        }
if(Bshift<0)
        {Bcorrect = Bstandard/(Bcutoff+Bshift);
        }
else
        {Bcorrect = Bstandard/Bcutoff;
        }


//=============================

run("RGB Stack");

setSlice(1);
if(Rshift<0)
        {
        run("Add...", "value=Rshift");
        }
run("Multiply...", "value=Rcorrect");

setSlice(2);
if(Gshift<0)
        {
        run("Add...", "value=Gshift");
        }
run("Multiply...", "value=Gcorrect");
```

```
setSlice(3);
if(Bshift<0)
		{
		run("Add...", "value=Bshift");
		}
run("Multiply...", "value=Bcorrect");

run("RGB Color");

print("R -- correct = "+Rcorrect+", shift = "+Rshift);
print("G -- correct = "+Gcorrect+", shift = "+Gshift);
print("B -- correct = "+Bcorrect+", shift = "+Bshift);
print("------");

if((Rshift+Bshift+Gshift)<-100)
		{rename(getTitle+"_overexposed");
		print("Photo was overexposed");
		}

else if((Rshift+Bshift+Gshift)>100)
		{rename(getTitle+"_underexposed");
		print("Photo was underexposed");
		}
else
		{rename(getTitle+"_corrected");
		}

run("Clear Results");

setTool("rectangle");
  title = "";
  msg = "Select photo area (rock only) and Enter or \"OK\".";
  waitForUser(title, msg);

run("Measure RGB");

MeanR = d2s(getResult("Mean",0),1);
MeanG = d2s(getResult("Mean",1),1);
MeanB = d2s(getResult("Mean",2),1);
```

Appendix E
X-Ray Diffraction Results

X-ray diffraction traces were collected from 70 Wafi-Golpu drill core samples, and analysed according to the methods described in Chapter Three (section 3.2). S. McKnight used Rietveld analysis to identify and estimate the relative proportions of minerals in each sample, which are given here in alphabetical order of identified phases, in weight %. Results below ~ 2 wt. % should be considered as not detected. The raw data (XRD traces) from each sample are provided as space-separated value files in Appendix G.

Hole ID	177	177	199	199	199	301	301	301	301	315	315	318	321	321	323	323	337	337	337	342	347	347	347	349	349
Depth (m)	341.6	389.8	48.8	155.3	337.9	115.7	184.0	229.2	317.2	315.8	444.8	26.0	175.3	467.7	404.0	457.7	157.7	804.0	958.5	1005.0	98.8	259.5	1075.0	50.0	188.4
Actinolite										0.0	0.0	0.5									12.7	2.0	0.0	0.1	0.0
Albite	0.5	0.9	0.0	17.4	0.0	0.0	1.0	0.0	1.0	20.5	16.2	0.8	0.0	10.6	3.9	30.3	0.4	15.6	18.7	19.3	29.8	0.0	16.6	0.9	1.1
Alunite						36.8	15.8	13.0	0.0	0.0	0.0	40.0	9.2	4.2	0.2	0.4					0.0	26.3	0.0	9.3	0.3
Anhydrite						0.2	0.2	0.2	0.4	0.0	0.0	0.0					0.0	0.1	0.3		0.3	0.0	0.1	0.1	0.0
Ankerite	0.6	0.5								0.3	0.2		0.1	0.0			0.0	0.0	0.0		0.3	0.1	0.0	0.2	0.1
Arsenopyrite																	0.0	0.0	0.3						
Augite										0.3	0.0						0.0	0.0	0.8	0.7	15.3	0.0	2.0	0.2	0.7
Biotite	2.0	1.0	6.4	26.1	7.9					0.8	4.8		0.0	0.3	5.3	1.9	0.0	37.4	41.0	12.3	0.7	0.5	6.3	0.8	0.0
Bornite										0.0	0.0										0.0	0.0	0.0	0.0	0.0
Calcite	0.0	0.0	0.0	0.0	2.4	0.0	0.0	0.0	0.0	0.0	0.0		0.0	0.1	8.3	0.7				0.3	0.0	0.0	0.7	0.3	0.5
Chalcocite	0.0	0.4															0.0	0.4	0.3	0.2	0.3	0.0	0.4	0.0	0.0
Chalcopyrite	0.4	0.4	0.2	0.0	4.9	0.0	0.1	0.0	0.0	0.2	0.6	0.0	0.0	0.0	0.3	0.4	0.0	0.4	0.2	0.2	0.1	0.0	2.2	0.0	0.0
Chlorite			0.0	0.7	0.0					1.6	2.0	0.4			1.3	3.5	0.0	1.0	0.2	1.0	17.9	0.0	0.4	0.0	0.0
Epidote																									
Galena																									
Goethite						0.7	0.0	1.2	0.0			0.0													
Gypsum			0.0	0.0	0.6																				
Hematite												3.5	0.3	0.0							0.0	0.4	0.0	0.0	0.0
Kaolinite			0.9	0.5	5.4	0.0	0.8	0.0	21.3						1.1	0.9	21.7	4.1	0.2	1.1	1.9	0.8	7.0	14.1	38.4
Labradorite	0.0	0.0	0.0	18.3	1.8	0.0	0.0	1.4	0.0	3.4	1.9		0.8	5.2	6.1	9.9	0.0	11.0	15.4	22.3	12.8	0.7	12.1	0.2	0.0
Magnetite	0.1	0.2	0.0	0.4	0.0					0.3	0.0						0.3	0.0	0.0	0.1	0.0	0.1	3.0	0.0	0.0
Marcasite																									
Molybdenite																					0.0	0.2	0.0	0.0	0.0
Montmorillonite																				5.6					
Muscovite	21.9	19.6	40.3	6.8	25.7	0.6	0.0	0.0	0.0	29.9	29.0		3.0	19.8	28.5	2.0	7.5	10.7	1.6	6.5	0.0	0.0	1.5	0.0	0.5
Orthoclase	0.0	7.8	0.0	15.1	0.0	0.0	0.0	0.0	0.0	0.0	0.0		0.0	0.0	0.0	0.0	0.0	0.0	0.0	7.5	1.9	0.0	15.2	0.0	0.0
Pyrite	11.7	8.8	11.4	7.9	6.4	0.3	9.6	0.2	24.6	9.7	7.6	0.5	10.7	16.6	7.5	10.5	12.6	3.8	0.6	1.1	4.0	8.0	0.7	0.0	11.9
Pyrophyllite						0.0	26.0	0.6	0.6				32.2	2.4			0.8	1.5	0.3	0.6	0.0	0.0	1.4	1.2	0.5
Quartz	61.4	55.0	40.8	6.7	43.9	60.4	45.6	81.8	50.8	32.1	36.6	54.3	43.6	40.8	35.4	31.1	56.4	14.0	20.1	21.3	0.7	59.3	29.1	69.2	44.0
Rhodochrosite	0.0	4.0																							
Rutile	1.4	1.4				1.0	0.9	1.6	1.3															1.2	0.8
Siderite			0.0	0.1	0.0	0.0	0.0	0.0	0.0												0.0	0.0	0.0	0.0	0.0
Smectite					1.0					1.1	1.0				1.1	7.3	0.3	0.0	0.0		1.2	1.5	1.2	2.1	1.2
Talc															1.0	1.1									
Total	100.0	100.0	100.0	100.0	100.0	100.0	100.0	100.0	100.0	100.2	99.9	100.0	99.9	100.0	100.0	100.0	100.0	100.0	100.0	100.1	99.9	99.9	99.9	99.9	100.0

Hole ID	349.0	377	377	377	377	377	377	377	377	377	377	377	377	377	392	392	392	392	392	392	392	396	396	396	396
Depth (m)	260.6	218.6	586.2	910.0	1116.4	1182.4	1310.0	1399.0	1433.5	1466.2	1549.0	1650.0	1791.5	1890.0	150.2	276.3	396.0	1402.0	1635.5	1728.3	1891.0	44.0	284.7	674.8	975.8
Actinolite	0.0	22.6	0.3	0.9	0.1	0.4	1.5	0.0	0.0	0.0	0.0	0.0	0.2	11.0	2.0	8.7	0.0	0.0	0.0	0.0	6.5	23.3	21.1	1.5	0.0
Albite	11.2	24.2	0.3	0.0	21.2	6.8	0.0	2.0	3.5	6.3	7.0	17.8	0.0	0.0	4.6	2.9	0.0	8.4	2.5	28.6	1.1	2.0	3.7	2.7	0.2
Alunite	0.0	0.0	0.0	0.0	0.7	0.0	0.7	0.0	0.0	0.0	0.0	0.3	0.0	0.0	0.1	0.1	3.1	0.8	0.3	0.0	0.1	0.0	0.2	0.0	0.1
Anhydrite	0.0	0.0	0.2	0.0	0.0	0.0	0.3	0.0	0.1	0.2	0.2	7.6	23.3	0.9	0.0	0.2	0.0	0.0	1.4	0.0	6.8	0.0	0.0	0.0	0.0
Ankerite	0.1	1.4	0.0	0.0	0.9	0.3	0.5	0.4	0.4	1.1	0.6	0.0	0.4	0.0	0.2	0.7	6.3	0.6	0.9	0.7	0.0	0.0	0.0	0.0	0.0
Arsenopyrite															0.0	0.0	0.0	0.5	0.7	0.0	1.0	0.0	0.0	0.3	0.0
Augite	2.8	11.5	0.5	2.3	0.0	1.3	1.7	0.3	2.2	0.0	0.0	0.1	1.9	1.6	1.9	2.4	0.3	0.5	0.0	0.0	0.0	0.2	0.4	0.3	0.0
Biotite	0.9	1.2	0.9	7.4	3.0	1.1	0.8	0.6	0.0	1.6	3.6	9.7	0.2	16.5	0.4	0.7	3.1	10.1	28.9	6.8	31.1	0.4	1.6	0.2	9.4
Bornite	0.0	0.0	0.0	0.3	0.0	0.0	0.0	0.0	0.1	0.0	0.0	0.0	0.0	0.1	0.1	0.0	0.1	0.1	0.2	0.0	0.0	0.0	0.0	0.0	0.0
Calcite	0.0	0.0	0.0	0.0	1.0	0.9	1.5	3.5	1.0	10.1	8.6	0.4	0.7	0.0	2.5	0.1	0.0	0.0	0.8	0.1	0.0	0.1	0.0	1.6	1.0
Chalcocite	0.5	0.3	0.0	0.0	0.4	0.2	0.0	0.0	0.0	0.0	0.0	0.7	0.0	0.0	0.0	0.2	0.0	0.0	0.0	0.7	0.0	0.4	0.1	0.0	0.0
Chalcopyrite	2.0	0.2	0.3	0.9	31.5	4.4	11.6	13.8	5.9	14.5	16.2	0.9	1.0	1.5	1.0	0.5	1.6	8.8	9.1	2.9	0.5	0.1	1.3	0.5	0.2
Chlorite	0.0	18.4	0.0	17.3	1.2	0.1	0.0	0.0	0.4	0.9	2.8	1.9	0.0	1.8	22.6	28.5	0.0	0.0	6.6	0.4	0.6	1.7	1.7	5.3	9.5
Epidote		5.1	0.0	0.0	0.0	0.0	1.3	0.0	0.0	0.8	0.0	0.0	0.0	0.0	0.0	0.8	0.0	0.0	0.0	0.0	0.0	0.1	0.0	0.0	0.5
Galena		0.0	0.1	0.1	0.0	0.0	0.6	0.0	0.1	0.0	0.0	0.0	0.2	0.1											
Goethite																									
Gypsum		0.0	1.1	0.2	0.4	0.6	0.1	0.2	0.6	0.0	0.0	0.5	0.0	0.0											
Hematite	0.8	0.0	0.0	0.0	0.0	2.5	0.0	0.3	0.1	0.6	0.2	0.0	0.1	0.0	0.0	0.0	0.0	0.0	0.0	0.0	0.0	0.0	0.0	0.0	0.0
Kaolinite	0.5	0.1	10.1	1.6	0.1	0.8	0.4	0.4	1.0	1.3	0.5	0.5	0.3	0.0	0.0	2.3	0.6	2.3	0.6	0.0	0.0	0.3	0.4	1.1	0.3
Labradorite	2.5	7.4	0.0	26.6	11.4	7.8	1.2	2.4	3.7	4.6	4.4	37.8	2.4	43.9	42.4	26.9	0.0	11.8	24.3	12.1	31.1	46.0	50.0	34.7	0.9
Magnetite	0.4	0.0	0.3	0.1	0.0	4.6	0.0	0.0	1.0	0.0	0.0	0.1	0.0	0.0	0.0	0.0	0.6	0.0	0.2	0.0	0.0	0.0	0.0	0.1	0.0
Marcasite																									
Molybdenite	0.0	0.0	0.0	0.0	0.0	0.0	0.0	0.0	0.0	0.0	0.0	0.0	0.2	0.0	0.0	0.0	0.0	0.0	0.0	0.0	0.1	0.0	0.0	0.0	0.0
Montmorillonite																									
Muscovite	3.0	0.0	7.8	0.0	1.5	2.5	7.7	3.6	1.1	2.2	0.3	3.3	0.0	0.0	0.0	0.0	18.9	1.6	3.3	19.8	0.0	0.1	0.0	0.3	24.8
Orthoclase	34.0	1.5	0.0	4.4	2.3	18.4	0.0	7.0	9.5	21.2	20.7	8.4	0.0	0.4	0.0	0.0	0.0	20.7	1.3	0.6	0.6	2.2	2.0	1.4	0.0
Pyrite	1.1	1.5	39.7	7.6	0.1	0.9	17.0	4.6	1.1	1.2	0.7	0.3	0.0	3.9	3.3	4.8	9.9	2.5	2.0	3.3	0.0	4.2	4.9	7.3	14.8
Pyrophyllite	0.9																								
Quartz	37.9	2.4	38.1	11.3	23.9	46.5	51.1	60.8	67.9	32.9	33.9	9.8	69.0	17.8	15.0	17.9	55.0	30.7	13.9	23.7	20.4	17.4	10.4	33.7	36.3
Rhodochrosite																									
Rutile	0.4																					0.5	0.5	1.6	1.8
Siderite	0.0														0.0	0.0	0.0	0.0	0.3	0.0	0.0	0.0	0.0	0.0	0.0
Smectite	1.0	1.2	0.1	0.1	0.1	0.0	0.0	0.1	0.0	0.0	0.2	0.1	0.1	0.0	1.0	0.8	0.1	0.2	2.2	0.0	0.0	1.2	2.2	7.4	0.2
Talc		0.9	0.1	18.8	0.3	0.0	2.0	0.0	0.1	0.4	0.1	0.0	0.0	0.3	2.9	1.4	0.4	0.4	0.5	0.3	0.1	0.3	0.0	0.0	0.0
Total	100.0	99.9	99.9	99.9	100.1	100.1	100.0	100.0	99.8	99.9	100.0	100.2	100.0	99.8	100.0	99.9	100.0	100.0	100.0	100.0	100.0	100.5	100.5	100.0	100.0

Hole ID	396	396	397	397	397	397	397	398	398	398	398	398	398	398	398	402	402	402	402	402
Depth (m)	1226.3	1339.7	74.2	353.2	759.0	1124.0	1361.0	25.0	118.4	168.0	272.6	335.2	441.6	711.6	817.5	23.3	220.0	406.2	700.0	979.3
Actinolite	2.8	0.0						0.0	0.2	0.0	0.0	0.0	0.3	0.0	0.0	0.0	0.0	0.0	0.0	0.0
Albite	0.4	4.1	1.1	10.3	4.3	0.9	19.1	0.0	0.0	0.7	0.7	2.6	1.7	20.5	0.0	0.2	0.6	1.1	28.4	0.1
Alunite	0.5	0.0	0.0	0.0	0.0	0.8	0.0	0.0	1.0	20.0	1.8	0.0	0.9	0.0	1.0	0.2	7.8	0.0	0.0	0.2
Anhydrite	0.0	0.1	0.0	0.0	0.0	0.8	0.0	0.0	0.0	0.4	1.3	0.0	0.4	0.5	0.0	0.3	1.4	0.0	0.0	0.2
Ankerite	0.0	0.6	3.3	0.0	0.2	0.5	0.3	0.0	0.1	1.3	0.8	0.0	0.6	0.0	0.0	0.0	0.0	0.0	0.0	0.3
Arsenopyrite	0.0	0.0						0.1	0.0	0.0	0.0	0.0	0.0	0.6	0.0	0.1	0.0	0.0	0.3	0.0
Augite	0.0	1.4																		
Biotite	2.5	1.1	1.2	0.4	0.0	0.7	15.7	0.2	0.2	0.0	0.0	2.8	3.6	39.2	4.2	0.2	0.0	3.7	43.3	0.7
Bornite	0.0	0.1	0.0	0.0	0.0	0.0	0.1	0.0	0.1	0.0	0.0	0.0	0.0	0.0	0.0	0.0	0.0	0.1	0.0	0.0
Calcite	0.5	0.0	6.0	1.0	0.0	0.7	0.4	0.0	0.2	0.7	0.0	0.5	2.3	0.4	0.0	0.1	0.0	0.0	0.0	0.0
Chalcocite	0.0	0.0	0.0	0.0	0.0	0.0	0.0	0.0	0.3	0.0	0.0	0.0	0.0	0.0	0.0	0.0	0.4	0.2	0.0	0.0
Chalcopyrite	0.2	1.7	1.1	0.5	0.1	0.9	11.6	0.0	2.7	0.4	0.4	1.7	2.1	2.2	0.3	0.0	0.0	0.0	0.8	0.8
Chlorite	0.4	0.0	5.4	14.0	30.6	0.0	2.5	0.0	0.0	0.0	0.0	0.0	0.0	0.4	0.0	0.0	0.0	0.0	0.0	0.0
Epidote	1.3	0.0																		
Galena																				
Goethite																				
Gypsum																				
Hematite	0.0	0.0						0.0	0.0	0.0	0.0	14.2	0.1	0.0	0.0	0.7	0.0	15.3	0.0	0.0
Kaolinite	0.6	1.2	3.2	9.4	5.5	2.8	0.0	0.2	0.7	0.0	2.3	1.0	0.2	0.1	2.7	30.6	12.2	0.0	0.0	40.7
Labradorite	51.2	0.0	0.0	11.8	7.6	1.5	0.0	0.1	1.1	0.8	1.0	0.0	0.0	0.6	0.6	0.6	0.0	0.0	0.3	0.0
Magnetite	0.0	0.0	0.9	1.3	2.7	0.7	0.0	0.0	0.0	0.1	0.3	0.2	0.1	0.0	0.0	0.0	0.7	22.3	0.0	0.0
Marcasite								0.0	0.0	0.0	0.0		15.1	0.7	0.0	0.2			0.1	0.5
Molybdenite	0.0	0.0	0.0	0.1	0.0	0.4	0.0	0.0	0.1	0.2	0.0	0.0	0.0	0.1	0.0	0.0	0.0	0.0	0.0	0.0
Montmorillonite																				
Muscovite	5.2	3.8	6.5	1.5	5.0	0.0	1.3	0.4	0.4	0.1	0.0	0.0	0.0	3.7	38.1	1.0	0.0	2.9	5.8	11.5
Orthoclase	0.0	11.4	0.0	0.0	0.0	0.0	21.7	0.0	0.0	0.0	0.0	30.1	0.0	1.6	0.0	0.0	0.0	13.6	0.0	0.0
Pyrite	10.7	3.3	46.9	9.4	12.2	4.8	0.4	0.0	31.6	23.4	24.8	1.6	15.1	1.7	7.9	0.3	42.4	8.5	1.3	9.4
Pyrophyllite																				
Quartz	21.3	69.5	23.4	38.1	28.0	81.8	25.9	97.9	60.4	50.6	64.6	43.7	56.1	26.7	43.4	64.3	33.7	22.8	19.0	34.9
Rhodochrosite																				
Rutile	1.1	1.0	0.8	1.5	2.0	0.9	1.0	0.8	0.7	0.9	1.2	1.0	1.1	0.7	1.0	0.9	0.8	0.8	0.7	0.6
Siderite	0.0	0.1	0.1	0.1	0.0	1.9	0.0	0.0	0.0	0.3	0.4	0.0	0.2	0.0	0.0	0.0	0.0	8.5	0.0	0.0
Smectite	1.2	0.2	0.1	0.3	2.0	0.0	0.0	0.2	0.2	0.2	0.0	0.2	0.1	0.0	0.1	0.1	0.0	0.2	0.0	0.0
Talc	0.2	0.3	0.0	0.2	0.0	0.0	0.0	0.1	0.0	0.0	0.3	0.2	0.2	0.4	0.6	0.2	0.0	0.0	0.0	0.2
Total	100.1	99.9	100.0	99.9	100.2	100.1	100.0	100.0	100.0	100.1	99.9	99.8	100.2	100.1	99.9	100.0	100.0	100.0	100.0	100.1

Appendix F
SWIR Mineral Identification Results

Short wavelength infrared (SWIR) spectra were measured as described in Chapter Four (Section 4.2.2). Minerals, or mineral groups, were identified by comparing each spectrum to a reference database using The Spectral Geologist (TSG) software. The SWIR mineral identification results are provided in the following table. Minerals are listed from left to right in decreasing order of confidence in identification (i.e., curve fitting), which may not reflect mineral abundance. Note that a few analyses yielded no identification. The peak positions or inflection points near 1485 nm (alunite), 1410 nm (micas), and 2250 nm (micas) are also listed, where measured. The raw data (SWIR spectra) are provided in Appendix G. Note that the 3-digit spectrum ID numbers listed in the last column are 1 digit higher than the TSG spectrum file names; for example, spectrum 001 in the table below corresponds to spectrum "WG.000" in Appendix G.

Hole ID	Depth (m)	Bulk rock mineral 1	Bulk rock mineral 2	Bulk rock mineral 3	Vein or alteration halo mineral 1	Vein or alteration halo mineral 2	1485 nm peak (nm)	1410 nm peak (nm)	2250 nm peak (nm)	Spectrum ID numbers (Appendix G)
177	310.7	Muscovite							2249.1	333, 334
199	48.8	Muscovite	Kaolinite					1410.4		326, 327
199	123.9	Illite	Paragonite	Montmorillonite				1411.4		348, 349
199	154.9	Dickite	Kaolinite				1482.8	1414.4		030, 031
199	155.3	Kaolinite	Dickite					1414.3		131, 132
199	225.3	Kaolinite					1479.0	1414.6		339, 340
199	253.7	Illite	Kaolinite	Muscovite				1413.3		014, 015
199	269.8	Muscovite	Kaolinite		Kaolinite			1414.0		341, 342
301	115.7	K Alunite					1478.3	1427.5		226, 227
301	150.0	Pyrophyllite	K Alunite	Kaolinite			1478.8	1393.7		123,124, 152, 153, 154
301	239.0	K Alunite					1479.0	1428.4		324, 325
301	253.5	Kaolinite	K Alunite				1478.3	1394.1	2230.1	331 , 350
301	256.4	K Alunite					1478.7	1428.7		332
301	258.3	K Alunite	Kaolinite				1480.2			337, 338
301	263.2	K Alunite					1481.0			328, 329
301	270.8	K Alunite					1481.1			258, 259
301	295.0	Pyrophyllite	K Alunite				1480.5	1393.7		343, 344
301	296.0	K Alunite					1484.3		2233.5	345, 346, 347
301	299.3	K Alunite					1482.3			223, 224
301	299.9	K Alunite	Kaolinite				1479.5	1429.8		330
301	315.6	K Alunite					1482.3			208 , 209
301	317.2	Kaolinite	Muscovite	Dickite	Kaolinite	Dickite		1414.4		039, 040
301	353.8	Dickite	Kaolinite				1475.7	1414.2		335, 336
321	51.0	Dickite	K Alunite				1478.8	1414.4		369, 370
321	395.0	Paragonite	Kaolinite				1478.6	1412.7		146
321	395.0	Paragonite	Kaolinite				1480.7	1412.4	2233.0	351, 352
321	467.7	Muscovite	K Alunite				1478.6	1410.4		147, 148
321	467.7	Muscovite	K Alunite	Paragonite			1478.9	1410.0		356, 357

Hole ID	Depth (m)	Bulk rock mineral 1	Bulk rock mineral 2	Bulk rock mineral 3	Vein or alteration halo mineral 1	Vein or alteration halo mineral 2	1485 nm peak (nm)	1410 nm peak (nm)	2250 nm peak (nm)	Spectrum ID numbers (Appendix G)
321	612.0	Kaolinite					1478.0	1414.3		359, 360, 361
321	711.0	Kaolinite					1476.5	1414.1	2232.6	358
321	812.2	Biotite						1392.9	2246.0	367
321	877.9	Biotite					1483.9	1395.0	2245.2	353
321	949.4	Montmorillonite	FeMgChlorite				1475.6	1413.1	2248.2	368
323	404.0							1414.4	2248.1	188
337	157.7	Dickite					1482.4	1414.5	2234.5	364, 365
337	158.0	Kaolinite					1481.4	1414.7	2231.8	354, 355
337	310.0						1481.7	1428.7	2233.4	366
337	593.7	Kaolinite						1414.5		041
337	768.7	FeMgChlorite	Montmorillonite				1480.0	1413.3	2247.6	362, 363
337	804.0	Montmorillonite	Phlogopite					1413.0	2246.5	144
337	991.5	FeChlorite	Kaolinite					1411.9	2251.5	091, 233
337	1220.2						1493.1	1398.6	2249.2	313
337	1242.4						1491.6	1405.9	2251.6	135
342	1203.0	FeChlorite	Montmorillonite		Siderite		1478.6	1411.0	2252.5	150, 151, 384
342	1276.0	FeMgChlorite	Illite				1478.9	1408.2	2249.4	028
347	190.0	Kaolinite					1489.4	1414.4		382, 383
347	200.0	K Alunite	Kaolinite				1478.7	1427.9		379, 380
347	231.5	K Alunite	Kaolinite				1479.5	1414.6		371, 372
347	259.5	K Alunite					1480.3			145
347	395.0	Kaolinite					1477.1	1414.6	2232.7	373, 374
347	483.1	Muscovite					1491.2	1409.9		377, 378
347	669.3	Kaolinite						1414.5	2245.3	149
347	732.4	Montmorillonite	Phlogopite					1414.7	2247.4	376
347	805.9							1427.9		099
347	836.0	MgChlorite	Phlogopite					1395.2	2249.5	375
347	854.2	Biotite					1488.0	1416.9	2249.6	381, 398
347	1075.0							1414.1	2245.9	066
347	1120.4	Biotite					1485.5	1394.6	2248.1	067, 068
349	50.0	Kaolinite	K Alunite				1478.6	1395.0		046, 391, 392
349	106.4	Paragonite	Kaolinite	Dickite			1488.5	1413.0		386, 387
349	196.4	Montmorillonite	Kaolinite				1477.4	1414.5		385
349	260.6	Montmorillonite	Muscovite				1475.5	1414.0	2230.8	020, 021
349	260.6	Kaolinite	FeMgChlorite					1414.1	2232.7	033, 034, 117
349	365.7						1490.3	1395.1	2241.4	395
349	387.7	Biotite					1486.5	1395.4	2245.5	389, 390
349	423.4	Muscovite	Phlogopite				1488.5	1415.2	2243.9	394
349	425.6	Biotite	Montmorillonite				1488.4	1414.9	2244.0	393
349	468.5	Paragonite	Montmorillonite				1489.7		2239.1	397
349	519.0	Biotite	Montmorillonite				1475.3	1413.9	2246.5	388, 396
377	218.6	MgChlorite	Actinolite				1478.7	1399.2	2254.9	253, 254

Hole ID	Depth (m)	Bulk rock mineral 1	Bulk rock mineral 2	Bulk rock mineral 3	Vein or alteration halo mineral 1	Vein or alteration halo mineral 2	1485 nm peak (nm)	1410 nm peak (nm)	2250 nm peak (nm)	Spectrum ID numbers (Appendix G)
377	335.6	Kaolinite	Dickite				1491.7	1414.7	2232.3	308
377	507.8	Kaolinite	FeMgChlorite				1483.5	1414.2	2248.6	320 , 321
377	761.0	Actinolite	MgChlorite	Biotite			1479.1	1393.5		073, 166
377	843.0	Biotite	Actinolite		Muscovite	Montmorillonite		1412.3		317, 318, 319
377	887.0	Actinolite					1481.6	1393.5	2247.5	323
377	910.0	MgChlorite	Talc				1475.8	1393.3	2244.7	315
377	1171.5									085
377	1205.0							1413.4		095
377	1210.0						1493.0	1409.0	2236.4	109
377	1306.6							1413.8		310
377	1310.0	Muscovite			FeMgCarbonate		1483.3	1411.5		056, 057, 120
377	1342.3							1412.1	2250.7	098
377	1358.2						1477.5	1412.6	2248.2	314
377	1365.0	Kaolinite					1477.1	1413.5	2251.1	027, 049, 050, 128
377	1365.5						1493.4	1422.4	2255.1	309
377	1380.0	Muscovite						1410.7	2248.0	110
377	1399.0	Muscovite	Kaolinite				1490.4	1414.6		306
377	1403.5	FeMgChlorite	Kaolinite	Muscovite			1477.6	1413.8	2249.3	304, 305
377	1433.5	Kaolinite	Muscovite				1478.4	1413.7		097
377	1452.5	Muscovite	Kaolinite				1477.6	1413.5	2252.9	311, 312
377	1453.4	Muscovite	Kaolinite					1413.5		107 , 108, 307
377	1466.2	Muscovite	Montmorillonite	Kaolinite				1413.7		053, 054, 055
377	1472.7	Muscovite					1475.3	1411.0	2232.2	121
377	1479.9	Kaolinite	FeMgChlorite		Muscovite			1413.6		113, 114
377	1530.0						1492.0	1409.1	2256.2	129, 130
377	1549.0						1478.3	1405.8	2251.0	316
377	1581.2						1482.3	1412.5	2235.4	069, 070
377	1586.2	Muscovite						1412.2		096
377	1626.0	Montmorillonite	Biotite					1412.7	2244.4	025, 026
377	1650.0						1482.6	1411.0	2249.6	322
377	1707.5	Biotite					1478.8	1395.7	2247.3	064, 065
377	1791.5						1491.5	1428.2	2261.2	138, 139
377	1825.2	Biotite	Actinolite				1475.8	1393.4	2249.1	118, 119
377	1890.0	Actinolite					1490.2	1394.7	2268.5	220
392	150.2	FeMgChlorite	Zoisite				1478.2	1395.9	2244.0	189, 190
392	193.7	MgChlorite	Montmorillonite		FeMgCarbonate			1414.1	2239.5	408, 409
392	235.4	FeMgChlorite	Montmorillonite	Muscovite	FeMgCarbonate			1401.6	2245.8	405, 406
392	326.5	Muscovite			FeMgCarbonate		1478.0	1409.7		411, 412
392	341.0	Paragonite					1478.2	1409.1	2235.4	407
392	369.0	Muscovite	Montmorillonite		FeMgCarbonate		1475.5	1411.2		401, 402
392	854.5	Kaolinite	Muscovite	Montmorillonite	Kaolinite			1414.3	2245.1	420, 421, 422, 423, 424
392	1029.0	Biotite	Montmorillonite				1476.5	1413.5	2247.2	261

Hole ID	Depth (m)	Bulk rock mineral 1	Bulk rock mineral 2	Bulk rock mineral 3	Vein or alteration halo mineral 1	Vein or alteration halo mineral 2	1485 nm peak (nm)	1410 nm peak (nm)	2250 nm peak (nm)	Spectrum ID numbers (Appendix G)
392	1038.0	Biotite	Montmorillonite		Kaolinite	Montmorillonite	1477.7	1414.5	2245.3	404
392	1126.0	Biotite			FeMgChlorite	Muscovite	1477.0	1397.0	2247.2	262, 263
392	1164.8						1492.4	1395.1	2248.1	255
392	1268.5	Biotite					1491.3		2248.4	264
392	1277.1	Biotite					1492.7	1391.6	2247.8	203 , 204
392	1281.5	Kaolinite					1485.1	1414.8	2241.0	022
392	1431.7	Kaolinite					1490.6	1413.3	2251.0	403
392	1495.8						1475.4		2232.5	176
392	1528.5						1475.8	1413.5		102
392	1546.3	Muscovite			FeMgCarbonate		1475.8	1412.5		083, 169
392	1635.5	Magnesium Clays					1478.8	1413.2	2245.1	192
392	1662.6	Biotite							2246.8	060, 061, 141
392	1662.8	Biotite	Muscovite				1488.5	1396.1	2245.1	080, 081
392	1673.3	Biotite			Muscovite		1478.6	1391.7	2245.5	413, 414, 415
392	1699.2	Montmorillonite	Biotite	Muscovite				1412.8		104, 416, 417
392	1728.3	Muscovite					1476.2	1411.1		180
392	1790.0						1475.5	1413.8	2244.6	024
392	1824.6	Biotite	Muscovite	Montmorillonite	Montmorillonite	Muscovite	1483.9	1414.8	2246.8	076, 077, 078, 079, 175
392	1851.5						1475.3	1417.5	2245.8	032, 052, 410
392	1879.0	Actinolite			Biotite		1484.0	1394.3	2251.4	197, 198, 199
392	1891.0	Biotite			Actinolite	FeMgChlorite	1481.4		2244.7	200, 201, 202
393	138.8	Kaolinite	Muscovite					1414.5	2230.8	300, 301, 302, 303
396	44.0	MgChlorite	Actinolite				1475.7	1394.8	2248.9	193, 194
396	92.0							1395.3	2246.9	103
396	214.9	Actinolite	MgChlorite					1395.1	2264.9	285
396	284.7				MgChlorite	Montmorillonite	1484.2	1395.4	2263.7	074, 075, 183
396	479.0	FeMgChlorite	Biotite				1485.1	1397.2	2248.4	282
396	674.8	Muscovite	Montmorillonite		Kaolinite	Montmorillonite		1413.9	2232.9	284
396	869.9	Illite	FeMgChlorite	Muscovite				1409.4	2247.7	295, 296
396	912.3	FeMgChlorite	Kaolinite	Muscovite	Muscovite	Kaolinite		1413.6	2247.2	286, 287, 288
396	975.8	Kaolinite	Phlogopite	Muscovite				1414.1	2245.4	172
396	1167.3	Magnesium Clays					1477.3	1394.9	2243.8	292, 293
396	1189.2	Actinolite	Biotite					1395.1	2267.1	090, 170
396	1226.3	Magnesium Clays	Montmorillonite					1414.0	2242.1	187
396	1259.7						1491.8	1395.1	2246.5	294
396	1300.0	Biotite			Muscovite		1477.7	1404.6	2248.9	298, 299
396	1303.0	FeMgChlorite	Montmorillonite				1476.0	1412.5	2251.9	289
396	1309.0	Kaolinite	Montmorillonite	Muscovite	Muscovite		1477.2	1403.2	2250.5	029, 142, 143
396	1315.8								2254.2	011
396	1320.4	Montmorillonite	Paragonite	Muscovite	Siderite			1412.6	2230.6	093, 178, 179
396	1339.7	MgChlorite	Montmorillonite					1414.5	2233.7	019
396	1388.3	Biotite					1491.1	1412.1	2249.7	297

Hole ID	Depth (m)	Bulk rock mineral 1	Bulk rock mineral 2	Bulk rock mineral 3	Vein or alteration halo mineral 1	Vein or alteration halo mineral 2	1485 nm peak (nm)	1410 nm peak (nm)	2250 nm peak (nm)	Spectrum ID numbers (Appendix G)
396	1466.8	Biotite	Montmorillonite				1485.1	1397.7	2246.7	283
396	1489.5	Montmorillonite	Kaolinite					1414.3	2233.4	082, 173
396	1501.0	Biotite	Montmorillonite				1485.4	1412.6	2232.7	058, 059, 163, 164
397	74.2	Paragonite	Montmorillonite	Muscovite	FeMgCarbonate			1407.6	2245.0	035, 036, 037, 038, 215, 216, 217, 218, 219
397	117.8	MgChlorite	Muscovite	Actinolite				1406.8	2247.9	251, 252
397	119.6	FeMgChlorite	Illite		FeMgCarbonate			1409.0	2248.2	221, 222, 225
397	123.0	MgChlorite	Illite		FeMgCarbonate		1475.4	1410.1		042, 044, 045
397	123.5	MgChlorite	Muscovite	Illite	FeMgCarbonate		1478.4	1407.9	2246.9	246, 247, 248
397	271.0	MgChlorite	Montmorillonite					1399.5	2248.9	088, 089, 167
397	353.2						1486.8	1394.4	2251.2	237
397	395.0						1492.3	1429.1	2235.3	260
397	396.0				Calcite		1487.4		2232.9	230, 231, 232
397	759.0	MgChlorite	Illite		Montmorillonite	Illite		1412.8		016, 017
397	983.4							1395.5	2245.7	195,196
397	987.0	Biotite	Montmorillonite		Montmorillonite		1475.7	1396.3	2246.6	212, 213
397	1025.0	Biotite			Muscovite		1483.4	1394.2	2246.8	235, 236
397	1026.5	Biotite			Kaolinite		1492.8	1392.4	2247.7	205, 206, 207
397	1037.5	Biotite	Montmorillonite	Illite			1475.7	1411.5	2246.6	094, 161, 162
397	1051.8						1488.7	1410.8	2249.0	214
397	1055.0							1410.7	2253.4	023
397	1068.0	FeMgChlorite	Muscovite				1488.1	1410.5	2254.5	228, 229
397	1093.5	Muscovite					0.0	0.0	0.0	086, 087, 171, 210
397	1111.4							1411.9	2252.1	111
397	1119.4								2266.9	010
397	1124.0	FeChlorite	Muscovite				1476.3	1410.1	2255.5	181, 184
397	1138.0								2249.1	001, 002, 003, 004
397	1195.7	Muscovite	Phlogopite					1410.9	2246.1	112
397	1206.3								2245.9	005, 006, 007, 009, 140
397	1209.5	Biotite	Muscovite	Kaolinite				1414.1	2246.3	256, 257
397	1221.4	Biotite					1475.1	1396.5	2247.0	101
397	1359.3						1476.2		2248.2	115, 116, 127
397	1361.0							1411.7	2246.4	051, 100
398	44.7							1428.1	2231.3	239, 240
398	51.4						1487.2	1416.4		244, 245
398	90.3						1488.1	1415.9	2232.4	243
398	101.0	Kaolinite					1492.1	1428.1	2231.9	271
398	118.4						1476.9	1414.9	2231.2	211
398	150.5				K Alunite		1477.7	1427.5		047, 048, 125, 155, 156, 157
398	153.3	K Alunite	Kaolinite		Kaolinite		1478.8	1428.3	2232.0	018
398	153.5				K Alunite		1478.9	1428.7	2230.1	062, 063, 126
398	168.0	K Alunite					1479.6	1428.1	2231.7	234
398	207.6	K Alunite					0.0	0.0	0.0	084, 177

Hole ID	Depth (m)	Bulk rock mineral 1	Bulk rock mineral 2	Bulk rock mineral 3	Vein or alteration halo mineral 1	Vein or alteration halo mineral 2	1485 nm peak (nm)	1410 nm peak (nm)	2250 nm peak (nm)	Spectrum ID numbers (Appendix G)
398	220.0	Kaolinite			Dickite	K Alunite	1478.1	1414.8		290, 291
398	232.4	K Alunite			K Alunite		1478.8	1414.0	2232.0	265 , 266
398	255.8	Kaolinite	Muscovite	Paragonite				1414.2	2232.6	071, 072, 174
398	272.6						1475.8	1415.1	2269.9	012
398	297.0	Kaolinite					1493.2	1414.6		270
398	313.3	Kaolinite					1475.6	1414.3	2250.3	272, 273
398	335.2						1491.1	1402.0	2252.5	133, 134
398	358.9	Kaolinite						1413.8	2232.8	267, 268, 269
398	441.6						1477.2	1425.8	2245.4	191
398	517.0	Biotite						1391.6	2247.1	274
398	711.6	Biotite					1487.3	1393.4	2245.8	238
398	730.0	Paragonite	Muscovite	Kaolinite				1410.1		249, 250
398	817.5	Kaolinite	Muscovite	Pyrophyllite				1394.5		241, 242
402	44.4	K Alunite					1481.1			280, 281
402	220.0								2231.9	275, 276
402	547.0	Biotite					1478.7	1405.2	2246.0	418
402	559.0	Kaolinite	Phlogopite		FeMgCarbonate		1477.5	1414.5	2247.1	277, 278, 279
402	564.4	Biotite	Kaolinite				1478.3	1394.5	2245.8	185, 186
402	566.3	Biotite					1491.6	1394.7	2245.4	136, 137, 160
402	569.3	Biotite					1493.0	1394.2	2249.8	105, 106, 158, 159
402	657.0	Biotite			Biotite			1395.9	2244.7	182
402	700.0	Biotite	Montmorillonite				1476.8	1412.4	2243.4	168
402	807.5				Kaolinite		1477.5	1415.7	2231.4	092, 165
402	921.2	Biotite					1493.1	1426.1		419, 420